CHARACTERIZATION OF THE UPPER MAIN ZONE, BUSHVELD COMPLEX, SOUTH AFRICA

Julie E. Bourdeau

A thesis submitted to the Faculty of Science, University of the Witwatersrand,
in partial fulfillment of the requirements for the degree of Doctor of Philosophy.

UNIVERSITY OF THE
WITWATERSRAND,
JOHANNESBURG

September 17, 2020
Johannesburg, South Africa.

Candidate's Declaration

I declare that this thesis is my own, unaided work with the exception of the numerical magmatic transport modeling code which was written by Dr. S. E. Zhang. This work is hereby submitted for the degree of Doctor of Philosophy at the University of the Witwatersrand, Johannesburg, South Africa. This work has not been submitted before for any degree or examination at this or any other university.

Julie E. Bourdeau

Julie Ellen Bourdeau
M.Sc., B.Sc. Earth Sciences

September 17, 2020
Ottawa, Ontario, Canada.

Abstract

The Main Zone of the Bushveld Complex is often described as an unspectacular ∼3 km thick succession of gabbronorite. As such, few studies have focused on the Main Zone. However, it is punctuated with localized layered anorthosite sequences and pyroxenite layers.

One such anorthosite sequence is found in the Upper Main Zone, ∼165 m below the base of the Upper Zone in the eastern lobe. The sequence consists of eight poikilitic anorthosite layers which are exposed along a road-cut, 5.3 km north-east of the town of Apel. Anorthosite layers are meter-scale in thickness (0.4 - 10 m), have sharp contacts with distinct mineral compositional breaks and are defined on the size and shape of pyroxene oikocrysts they contain. The sequence hosts numerous centimeter to meter-scale blocks of distinct cumulate lithologies (olivine-bearing norite, norite and poikilitic norite). The distinct textures of the blocks, their modal, mineral, chemical and isotopic compositions (average initial $^{87}Sr/^{86}Sr$: 0.707344 and initial εNd: -5.23) suggests that they represent recycled cumulate material from Bushveld's magmatic plumbing system. Based on the consistent plagioclase crystal morphologies throughout the sequence, relatively constant mineral and whole-rock chemistries within each layer, presence of magmatic flow textures, and a numerical model, I propose that each layer was formed by the injection of a plagioclase slurry (5 - 30 vol% crystals).

Two distinct pyroxenite layers associated with the Pyroxenite Marker (Upper Main Zone) are exposed in the Mooimeisjesfontein area, ∼36.5 km SW of Burgersfort in the eastern lobe. Progressing up-section, the first layer is a ∼2 m thick orthopyroxenite, followed by a second ∼40 cm thick melagabbronorite. Based on field observations, mineral and whole-rock chemical trends, each pyroxenite layer was formed by a less differentiated replenishing magma which mixed with a resident one. The pyroxenite layers host numerous centimeter to decameter-scale blocks of distinct cumulate textures or lithologies (anorthosite, gabbronorite, norite and websterite). Field and petrographic observations combined with numerical modeling support layer formation by injection of slurries (5 - 15 vol% crystals).

The evidence presented in this study attests to a far more dynamic origin for the Upper Main Zone of the Bushveld Complex.

Acknowledgments

First to Steven E. Zhang and Andrew Logue who provided invaluable field support and endured many difficult treks up and down mountains. Special thanks to Andrew Logue who used his patented rock-throwing caveman method to obtain difficult-to-reach samples. Thanks to Sophia Chistyakova who introduced me to the study locations. To Caiphas Majola, Sam Tshabalala and Mphefu (Joe) Aphane (University of the Witwatersrand) for the preparation samples for geochemistry or thin sections. To Glen Poirier (University of Ottawa - Canadian Museum of Nature) for helping me conduct microprobe analyses. To Marlin Patchappa and Allan Wilson (Earth Lab - University of the Witwatersrand) for helping me prepare samples for and conducting geochemical analyses. To Peter Edmondston from Intertek Laboratories who provided me with detailed insight into geochemical analyses and all standard certificates. Thanks to Linda Iaccheri (University of the Witwatersrand) and Henriette Ueckermann (University of Johannesburg) for laboratory and instrument training for isotopic analyses. Thanks to Ben Hayes, Andrew Logue and Kimberley Beaton who performed some of my isotopic analyses. Thanks to Richard Montjoie (Lesego Platinum) and Paul Nex (University of the Witwatersrand) for providing crucial information regarding the geology of the Phosiri Dome area. To Steven E. Zhang, Ben Hayes, Lewis Ashwal and Grant Cawthorn (University of the Witwatersrand) for insightful discussions regarding the Bushveld Complex and providing constructive feedback for several chapters of this thesis. To Roger Scoon, Geoff Howarth and James Roberts for their review of the anorthosite sequence chapter, now accepted for publication in South African Journal of Geology. Thanks to Marlina Elburg (University of Johannesburg) for editorial handling and critical discussions about isotopic results. To Danielle Simmons Duarte, who from the first day guided me though the lengthy and convoluted process of the administration that is the University of the Witwatersrand.

This study was supported by research grants to R. Latypov from DSI-NRF CIMERA. The support of CIMERA towards this research is hereby acknowledged.

Special thanks are given to Steven E. Zhang, Grant M. Bybee, Ben Hayes, Glen Nwaila, Musa S. D. Manzi, Cleo Solomon, Andrew Logue, Tony D. Fowler and André E. Lalonde (deceased) for their continuous support and mentorship through difficult times.

This thesis is dedicated to my better half, Steven E. Zhang, who never fails to brighten my day.

Contents

Declaration ii

Abstract iii

Acknowledgments iv

List of Figures ix

List of Tables x

1 Introduction 1
- 1.1 Scope of this study . . . 1
- 1.2 Formation hypotheses . . . 3
  - 1.2.1 Frequency of magma emplacement . . . 3
  - 1.2.2 Origin of cumulus crystals . . . 3
  - 1.2.3 Origin of transported cumulate blocks . . . 5

2 Geological setting 6
- 2.1 The Bushveld Complex . . . 6
  - 2.1.1 Rooiberg Group . . . 6
  - 2.1.2 Rustenburg Layered Suite . . . 6
  - 2.1.3 Rashoop Granophyre Suite . . . 10
  - 2.1.4 Lebowa Granite Suite . . . 12
- 2.2 The Phosiri Dome area . . . 12
  - 2.2.1 Stratigraphic sequence . . . 12
  - 2.2.2 Formation of the Phosiri Dome . . . 14
  - 2.2.3 Geology of the study area . . . 14
- 2.3 The Mooimeisjesfontein area . . . 15
  - 2.3.1 Stratigraphic sequence . . . 15
  - 2.3.2 Deformation and hydrothermal alteration . . . 17
  - 2.3.3 Geology of the study area . . . 17

3 Sampling and analytical techniques 18
- 3.1 Field and sampling methods . . . 18
- 3.2 Sample preparation . . . 18
- 3.3 Whole-rock density measurement . . . 18
- 3.4 Electron microprobe analyses . . . 19
- 3.5 Whole-rock chemical analyses . . . 19
  - 3.5.1 Intertek Laboratories . . . 19
  - 3.5.2 Earth Lab, University of the Witwatersrand . . . 20
- 3.6 Whole-rock Rb-Sr and Sm-Nd isotopic analyses . . . 21

4 Layered anorthosite sequence in the Upper Main Zone 23
- 4.1 Introduction . . . 23
- 4.2 Field descriptions . . . 24
  - 4.2.1 The anorthosite sequence and host rocks . . . 24

4.2.2 Deformation and hydrothermal alteration . . . 27
4.3 Petrography and mineral chemistry . . . 29
4.3.1 Anorthosite layers . . . 29
4.3.2 Norite layer . . . 31
4.3.3 Gabbronorite . . . 31
4.4 Density . . . 34
4.5 Bulk rock chemistry . . . 35
4.5.1 Major elements . . . 35
4.5.2 Incompatible and trace elements . . . 35
4.6 Discussion . . . 35
4.6.1 Stratigraphic position of the anorthosite sequence . . . 35
4.6.2 Origin of layering in the Upper Main Zone anorthosite sequence . . . 39
4.6.3 Alternative hypotheses . . . 41
4.6.4 Implications for the origin of anorthosites in large layered ultramafic-mafic intrusions . . . 41
4.7 Conclusions . . . 43

5 Staging chambers, plagioclase slurries and cumulate recycling 44
5.1 Introduction . . . 44
5.2 Summary of previous work: Poikilitic anorthosite layers and bounding gabbronorite . 45
5.2.1 Field descriptions . . . 45
5.2.2 Petrography and mineral chemistry . . . 46
5.3 Field descriptions . . . 46
5.4 Petrography and mineral chemistry . . . 48
5.4.1 Poikilitic norites . . . 48
5.4.2 Olivine-bearing norites . . . 48
5.4.3 Norites . . . 52
5.5 Abundance of Al_2O_3 in orthopyroxene . . . 54
5.6 Density . . . 54
5.7 Whole-rock chemistry . . . 55
5.7.1 Major and minor elements . . . 55
5.7.2 Incompatible and trace elements . . . 55
5.7.3 Sr-Nd isotopes . . . 57
5.8 Discussion . . . 59
5.8.1 Relationship between the blocks and their host rocks . . . 59
5.8.2 Block relationship to the Bushveld magmatic plumbing system . . . 60
5.8.3 The origin of the blocks and the role of staging chambers during the emplacement of the Main Zone . . . 67
5.9 Conclusions . . . 69

6 Pyroxenite layers and blocks in the Upper Main Zone: a case of magmatic replenishment via slurries 71
6.1 Introduction . . . 71
6.2 Field descriptions . . . 72
6.2.1 The orthopyroxenite sequence . . . 73
6.2.2 The melagabbronorite sequence . . . 73
6.2.3 Blocks . . . 73

6.2.4 Deformation and hydrothermal alteration . . . 74
6.3 Petrography and mineral chemistry . . . 75
6.3.1 The orthopyroxenite sequence . . . 75
6.3.2 The melagabbronorite sequence . . . 76
6.3.3 Blocks . . . 80
6.4 Abundance of Al_2O_3 in orthopyroxene . . . 82
6.5 Rock density . . . 83
6.6 Whole-rock chemistry . . . 84
6.6.1 Major elements . . . 84
6.6.2 Incompatible and trace elements . . . 85
6.7 Discussion . . . 87
6.7.1 Magmatic model: Magma replenishment with mixing . . . 88
6.7.2 Relationship between the pyroxenite sequences . . . 90
6.7.3 Relationship of the blocks with the host rocks and putative RLS parent magmas 91
6.7.4 Implications for the style of magmatic replenishment . . . 95
6.8 Conclusions . . . 97

7 Conclusions **99**

A List of samples **102**

B Mooimeisjesfontein block outcrop maps **106**

C Calculation of mineral formula and error propagation **109**
C.1 Calculation of a mineral formula . . . 109
C.2 Calculation of error propagation for a mineral formula . . . 110
C.3 Step by step process used in this study . . . 111

D Mineral chemistry data and analytical uncertainties **113**

E Whole-rock chemical data and analytical uncertainties **158**

F Whole-rock density data and analytical uncertainties **168**

References **182**

List of Figures

2.1 Geological map of the Bushveld Complex . . . 7
2.2 Stratigraphy of the Rustenburg Layered Suite . . . 9
2.3 Stratigraphy of the Main Zone . . . 11
2.4 Simplified geological map of the Phosiri Dome area . . . 13
2.5 Geological map of the Mooimeisjesfontein area . . . 16

4.1 Stratigraphic succession at the road-cut . . . 25
4.2 Overview of the west side of the road-cut . . . 26
4.3 Textural variations found in the anorthosite sequence . . . 28
4.4 Cross-polarized thin section scans of anorthosites . . . 30
4.5 Euhedral primocrystic plagioclase laths in anorthosites . . . 31
4.6 Stratigraphic compositional variations of plagioclase, orthopyroxene and clinopyroxene for select anorthosite layers . . . 32
4.7 Petrography and mineral chemistry of a composite oikocryst . . . 33
4.8 Cross-polarized thin section scans of the norite layer and the basal gabbronorite . . . 34
4.9 Densities of anorthosite, gabbronorite and norite at the road-cut . . . 36
4.10 Whole-rock major element oxide and molar Mg# variations . . . 38
4.11 Chondrite-normalized incompatible and rare earth element diagrams . . . 38

5.1 Stratigraphic succession at the road-cut . . . 47
5.2 Overview of poikilitic anorthosite layers . . . 48
5.3 Cross-polarized light photomicrographs of the anorthosite and gabbronorite . . . 49
5.4 Representative photographs of blocks found at the road-cut . . . 49
5.5 Close-up of a contact between a block and its host anorthosite . . . 50
5.6 Cross-polarized light photomicrographs of blocks . . . 51
5.7 Photomicrographs of distinct features found in some of the blocks . . . 52
5.8 Abundance of Al_2O_3 (wt%) versus CaO (wt%) in orthopyroxene crystals . . . 54
5.9 Scatter matrix of major oxides (wt%) between different blocks . . . 55
5.10 Chondrite-normalized incompatible and rare earth element diagrams . . . 59
5.11 Whole-rock Sr-Nd isotopes of road-cut lithologies compared to the RLS . . . 60
5.12 Abundance of Al_2O_3 (wt%) versus Mg# (mol%) in orthopyroxene crystals . . . 63
5.13 Numerical model for the transport of the blocks . . . 66
5.14 Illustration of a proposed model of the origin and evolution of the blocks and host poikilitic anorthosite . . . 70

6.1 Geology and stratigraphic succession of the Mooimeisjesfontein area . . . 72
6.2 Overview of the pyroxenite sequences . . . 74
6.3 Representative photographs of blocks found in the incised valley . . . 75
6.4 Cross-polarized photomicrographs from the pyroxenite sequences . . . 77
6.5 Stratigraphic modal mineralogy and compositional variations for pyroxenite sequences 78
6.6 Cross-polarized light photomicrographs of the blocks . . . 84
6.7 Abundance of Al_2O_3 (wt%) versus CaO (wt%) in orthopyroxene crystals . . . 85
6.8 Densities of the pyroxenite sequences . . . 87
6.9 Whole-rock major element oxide variations . . . 88
6.10 Chondrite-normalized incompatible and rare earth element diagrams . . . 89
6.11 Chondrite-normalized incompatible and rare earth element diagrams of the blocks . . . 90

6.12 Abundance of Al_2O_3 (wt%) versus Mg# (mol%) in orthopyroxene crystals 93
6.13 Numerical model for the transport of the blocks 94

B.1 Outcrop map of large blocks in the Mooimeisjesfontein area 106
B.2 Outcrop map of small blocks in the Mooimeisjesfontein area 107
B.3 Outcrop map of large blocks in the Mooimeisjesfontein area 108

List of Tables

3.1 Whole-rock chemistry of an in-house standard sample analyzed at Intertek and at the Earth Lab . . . 20

4.1 Representative mineral analyses from an anorthosite layer . . . 34
4.2 Average core, mantle, rim and overgrowth compositions for plagioclase laths . . . 34
4.3 Average whole-rock chemical results of all layers at the road-cut . . . 37

5.1 Representative mineral analyses from the blocks . . . 53
5.2 Average whole-rock chemical results for all lithologies . . . 56
5.3 Sr and Nd isotope data from blocks and host rocks . . . 58

6.1 Representative mineral analyses from the pyroxenite layers . . . 80
6.2 Representative mineral analyses from select blocks . . . 83
6.3 Average whole-rock densities of pyroxenite sequences and blocks . . . 85
6.4 Average whole-rock geochemical results of all lithologies . . . 86

A.1 List of samples from the anorthosite sequence . . . 102
A.2 List of samples from blocks in the anorthosite sequence . . . 103
A.3 List of samples from pyroxenite sequences . . . 104
A.4 List of samples from blocks in pyroxenite sequences or in modally-graded gabbronorite 105

C.1 Steps taken in the calculation of a mineral formula . . . 111
C.2 Steps taken in the calculation of error propagation . . . 112

D.1 Mineral chemistry for epidote . . . 114
D.2 Mineral chemistry for epidote. Analytical uncertainties . . . 114
D.3 Mineral chemistry for hornblende . . . 114
D.4 Mineral chemistry for hornblende. Analytical uncertainties . . . 116
D.5 Mineral chemistry for micas . . . 118
D.6 Mineral chemistry for micas. Analytical uncertainties . . . 119
D.7 Mineral chemistry for olivine, including analytical uncertainties . . . 120
D.8 Mineral chemistry data for plagioclase, including analytical uncertainties . . . 120
D.9 Mineral chemistry for pyroxenes . . . 134
D.10 Mineral chemistry for pyroxenes. Analytical uncertainties . . . 145
D.11 Mineral chemistry for spinels, including analytical uncertainties. . . . 155

E.1 Whole-rock chemical data . . . 159
E.2 Relative errors form Earth Lab and coefficients for expanded uncertainties from Intertek . . . 167

1 Introduction to the Upper Main Zone of the Bushveld Complex

The Paleoproterozoic-aged Bushveld Complex is located in South Africa and contains some of the richest ore deposits in the world, notably in Platinum Group Elements along with iron, tin, chromium, titanium and vanadium. One component of the complex includes the world's largest layered ultramafic-mafic intrusion, called the Rustenburg Layered Suite (RLS), with an areal coverage of 40 000 km^2 and a thickness of $\leq$8 km (Eales and Cawthorn, 1996; Cawthorn et al., 2016). The RLS is divided into the Marginal, Lower, Critical, Main and Upper Zones (from bottom to top), based on major mineralogical and isotopic changes (SACS, 1980). Altogether, the suite broadly grades upwards from ultramafic, through mafic, to intermediate and silicic rock varieties (Wager and Brown, 1968; Cawthorn, 2015). Given its size and complexity, the origin and formation mechanisms of the RLS has attracted a plethora of hypotheses, more than any other intrusion. To date, the continuity between the different lobes, the origin, composition and number of parental magma(s) and their emplacement mechanism(s) remain highly debated. Overall, the bulk of the existing research has been focused on areas of economic interest, such as the Merensky and UG chromitite reefs in the Critical Zone, leaving less endowed areas, such as the Main Zone, comparatively understudied.

The Main Zone is by far the thickest zone of the RLS with a maximal thickness between 3000 and 3400 m (Molyneux, 1974). Generally, the Main Zone is described as unspectacular and unlayered, but only in comparison to the other zones (Wager and Brown, 1968; Molyneux, 1974; Nex et al., 1998; Cawthorn, 2015). Most of the Main Zone is characterized by unlayered norites and gabbronorites that are composed of plagioclase, clinopyroxene and orthopyroxene and/or inverted pigeonite (von Gruenewaldt, 1970; Molyneux, 1974; Mitchell, 1986). Locally, thin or poorly developed pyroxenite, anorthosite and modally graded gabbronorite layers have been documented (e.g. von Gruenewaldt, 1973; Molyneux, 1974; von Gruenewaldt and Weber-Diefenbach, 1977; Quadling and Cawthorn, 1994; Nex et al., 1998 and others). Even though most of the Main Zone is unlayered, its most striking feature is a pervasive igneous lamination, defined by plagioclase laths aligned parallel to the plane of layering (Eales and Cawthorn, 1996; Cawthorn, 2015).

The Main Zone is further divided into two sub-zones: a lower (2200 - 3100 m thick) and an upper (300 - 800 m thick) sub-zone (von Gruenewaldt, 1973; Mitchell, 1990; Cawthorn, 2020). The Pyroxenite Marker, defined by a single or multiple (up to 4) $\leq$2 m thick orthopyroxenite layers found in three of the major lobes of the RLS, marks the boundary between the sub-zones (von Gruenewaldt and Weber-Diefenbach, 1977; Mitchell, 1990). The Upper Main Zone continues up-section with unlayered gabbronorite, porphyritic gabbro and several layers of pure or poikilitic anorthosites (Molyneux, 1974 and this study). Molyneux (1970, 1974) also recorded a number of transgressive magnetitite plugs in the Upper Main Zone.

1.1 Scope of this study

This study began as an integrated view of various outcrops in the Bushveld Complex. From numerous field excursions, it became apparent that sequences of the Upper Main Zone differ from the overall 'unspectacular' gabbronorite of wording used to describe the Main Zone (Wager and Brown, 1968; Molyneux, 1974; Nex et al., 1998; Cawthorn, 2015). I observed dykes and layered sequences of texturally varied anorthosites, which occasionally contained transported cumulate blocks, modally-graded sequences of gabbronorite (or banded gabbronorite units Molyneux, 1974; Kruger,

1990; Quadling and Cawthorn, 1994; Nex et al., 1998) with and without transported cumulate blocks, pyroxenite layers underlain by pure or poikilitic anorthosites, magnetitite plugs, pegmatite bodies and evolved pegmatoidal dykes. Locally, even the 'unspectacular' gabbronorite displayed optically continuous units of inverted pigeonite that form copper-colored patches in the reflected sunlight measuring up to 30 cm in diameter (von Gruenewaldt, 1970). All of these observations suggest a nuanced, potentially complex and dynamic origin for the Upper Main Zone. Furthermore, there have been relatively few studies on the Main Zone and certainly even less on the origin of some specific features such as layers in the Upper Main Zone (e.g. von Gruenewaldt, 1973; von Gruenewaldt and Weber-Diefenbach, 1977; Hayes et al., 1985; Mitchell, 1990; Cawthorn et al., 1991; Quadling and Cawthorn, 1994; Nex et al., 1998; Ashwal et al., 2005; Cawthorn and Ashwal, 2009; Roelofse and Ashwal, 2012; VanTongeren and Mathez, 2013; Cawthorn et al., 2016; Cawthorn, 2020).

This study first seeks to document various outcrops and their included blocks using combined geological, petrographical, geochemical, isotopic and geophysical techniques. The multi-sourced data is then used to examine the known magmatic emplacement hypotheses for the Upper Main Zone. Specifically, this study will first examine if the Upper Main Zone is the result of a single or multiple injections of magma. Second, this study seeks to contribute to the broader magmatic emplacement debate in the Upper Main Zone, where magmas were either emplaced as superheated and aphyric magmas that crystallized *in situ* or as crystal-bearing slurries. Third, this study seeks to constrain possible origins for the hundreds of transported cumulate blocks found in the Upper Main Zone. To do so, I explore some of the unique textures and features encountered in the Upper Main Zone in the eastern lobe of the RLS through the multi-sourced data and observations. The studied outcrops and their corresponding chapters in this thesis are: 1) a sequence of eight texturally distinct poikilitic anorthosite layers in Chapter 4, 2) the nature and origin of transported cumulate blocks hosted by the poikilitic anorthosite layers in Chapter 5, and 3) two pyroxenite layers associated with the Pyroxenite Marker, as well as the hundreds of transported cumulate blocks within, in Chapter 6. The unique contribution of this study lies in its integrated multi-disciplinary approach. This study makes use of field geology, petrography, mineral and whole-rock chemistry, isotope geochemistry, whole-rock density and numerical modeling in order to gain a much broader perspective regarding the origin of the magma/blocks, the rheological conditions of the magma upon emplacement and the frequency of magmatic emplacements. These methods were used to examine both large-scale features (i.e. outcrops) and several small-scale features (i.e. cm - m scale blocks).

As with any study dealing with large-scale intrusions, it is impossible to document all features at all desirable scales and with all techniques. Large layered ultramafic-mafic intrusions are true examples of prolonged and continuously varied magmatic conditions (Marsh, 2006). This is true for the Upper Main Zone of the RLS, given its substantial stratigraphic thickness and areal coverage. The following study only addresses some main unique features found in the Upper Main Zone, which altogether indicate a complex and dynamic origin. Therefore, the following work should not be deemed as wholly representative of the entire Upper Main Zone and even less so for the RLS of the Bushveld Complex.

Chapters 4, 5 and 6 are intended for publication as research articles in international journals. Chapter 4, detailing the texturally distinct poikilitic anorthosite layers has been accepted for publication in the South African Journal of Geology (volume: 123, number: 3, year: 2020). All materials associated with the chapter are reproduced with permission from the journal. Chapters 5 and 6 are in preparation for submission.

1.2 Formation hypotheses

Among the plethora of hypotheses proposed to date for the origin of the Bushveld Complex, and hypotheses pertaining to other aspects of the complex, three major themes are explored in this study. These are the frequency of magma emplacement, the origin of cumulus crystals and the origin of transported cumulate blocks.

1.2.1 Frequency of magma emplacement

Many large layered ultramafic-mafic intrusions, including the RLS, are considered to be the products of multiple injections of magma. Magmatic replenishments can be documented: 1) structurally (e.g. cross-cutting dykes and layers), 2) mineralogically (e.g. addition or loss of a crystallizing phase), 3) texturally (e.g. crystal zoning or resorption), 4) chemically, and/or 5) isotopically. For the RLS, a total of 4 major additions of magma have been identified (Eales, 2002 and references therein). The Upper Main Zone of the RLS is interpreted to be the result of one of these injections, based on drastic changes in mineral assemblage/composition (decrease of $\sim$10 mol% in both An-content in plagioclase and Mg# in orthopyroxene; Molyneux, 1974; Hayes et al., 1985; Mitchell, 1990; VanTongeren and Mathez, 2013) and isotopic values (decrease of initial $^{87}Sr/^{86}Sr$ of 0.70827 to 0.70694, calculated at 2.056 Ga; Sharpe, 1985; Mitchell, 1986; Kruger, 1994; Cawthorn et al., 1991). To date, essentially two models have been proposed for the origin of the Upper Main Zone.

The first model proposes that the entire stratigraphic succession spanning the Pyroxenite Marker in the Upper Main Zone to the topmost layer in the Upper Zone is the product of a single pulse of magma that subsequently embarked on an uninterrupted (closed system) course of differentiation. This model was first proposed and supported by the large-scale field and petrographic studies of Wager and Brown (1968); von Gruenewaldt (1970) and Molyneux (1974). Subsequently, studies by Sharpe (1985); Kruger et al. (1987); Cawthorn et al. (1991); Kruger (1994) and others demonstrated that the stratigraphic succession in question shares a common initial $^{87}Sr/^{86}Sr$ ratio of $\sim$0.7073, which differs from the remainder of the Main Zone ($\sim$0.7085). Based on these data, the aforementioned studies proposed that a major influx of less-differentiated magma occurred at the level of the Pyroxenite Marker. The recharge magma thoroughly mixed with a resident one without further addition or contamination during subsequent crystallization.

Another model proposes that the same stratigraphic succession was emplaced from multiple (open system) and at times discrete pulses of magma. This model was first proposed by Mitchell (1986, 1990) based on the the identification of several petrographic, mineral and whole-rock chemically distinct units in the Lower Main Zone. Subsequently, Scoon and Mitchell (2012) and Yuan et al. (2017) noted the same for the Upper Zone. Further work by Ashwal et al. (2005) and Hayes et al. (2017) identified numerous (up to 22) units with reversals in modal mineralogies, whole-rock densities and mineral compositions in the Main and Upper Zones. Also recently, work by Roelofse and Ashwal (2012) and VanTongeren and Mathez (2013) regarded the lack of differentiation in the Lower Main Zone to be the result of repetitive injections of discrete pulses of magma. Mitchell (1986) demonstrated that initial $^{87}Sr/^{86}Sr$ ratios of the Lower Main Zone also vary significantly (0.70737 - 0.70902). However, Mitchell (1986) did not have the necessary resolution to either support or refute the model.

1.2.2 Origin of cumulus crystals

Regardless of the frequency of magma emplacement, the nature of the emplacement of specific recharges is also a highly debatable topic. Currently, much of the debate in the RLS is focused on

the style and dynamics of magma emplacement, specifically regarding the origin of cumulus crystals (e.g. Cawthorn, 2015). Essentially, only two opposing models dominate the debate today: crystal-free versus crystal-bearing magma recharges (Chapters 4, 6). As large layered ultramafic-mafic intrusions are solidified from multiple magmatic replenishments over prolonged periods of time, it is reasonable to assume that replenishment magma exists along a continuum of crystallinities, whereby some magmas were extremely crystal-laden while others were possibly devoid of crystals.

One end-member model proposes that melts were superheated, aphyric and solidified *in situ* upon emplacement in the magma chamber (e.g. Campbell, 1977; McBirney and Noyes, 1979; Latypov et al., 2017). This model is thought to explain a number of features that are deemed inconsistent with predictions of the traditional cumulus theory. Among the most pertinent are: 1) inverted graded rhythmic layering, whereby less dense cumulates are overlain by denser cumulates (Campbell, 1977), 2) poorly hydraulically sorted layers, suggesting a significant chemical control rather than a mechanical one (Campbell, 1977), 3) cumulate layers formed on steeply dipping and at times overhanging surfaces (e.g. chromitite layers at Rum and the Merensky Reef; Campbell, 1977; Latypov et al., 2013, 2017), 4) textures including cross-bedding and graded-bedding in layered sequences with near-vertical primary dips (Campbell, 1977), 5) plagioclase buoyancy in a tholeiitic magma, whereby the crystals would float rather than settle as a cumulate (Morse, 1973; Campbell et al., 1978; Scoates, 2000), 6) the formation of monomineralic chains forming optically continuous units for up to 30 cm (von Gruenewaldt, 1970) which is interpreted to indicate self-nucleation (Campbell, 1977), and 7) cryptic rhythmic layering (e.g. chromitite bands in the Critical Zone of the RLS and in the Banded series of the Stillwater Complex), which is more akin to chemical precipitates from a saturated solution rather than cumulus accumulation (Jackson, 1961; Latypov et al., 2017). Specifically for the RLS, potholes in the Merensky Reef are interpreted by Latypov et al. (2017) as a thermal erosion feature that can be explained to some extent by magma mixing between a superheated, aphyric recharge magma and a cooler, crystal-laden resident one. However, most of the factors presented above are based on field and petrographic evidence. It is unclear from a rigorous theoretical or experimental thermodynamic perspective the exact requirements of the thermal and rheological conditions of the magma, in order to yield the observed evidence. Particularly a lower bound for the thermal and rheological state of the hypothetical recharge magma is not constrained. As such, and without exact bounds, it is impossible to understand the feasibility of an extremely end-member model in a given geological context that essentially encapsulates an otherwise wide and continuous range of possible crystalinities and injection temperatures. Furthermore, the effect(s) of the incorporation of minute crystal fractions, either from country rocks, in-chamber cumulates or from thermally eroded surfaces remains unknown. Lastly, it seems impossible for this model to be feasible for magmatic plumbing systems that feature multiple staging chambers.

The other model spans a comparatively much broader range of possible magmatic conditions and proposes that melts were injected as crystal-bearing slurries of varying crystalinity (e.g. Ashwal et al., 2005; Barnes et al., 2010; Roelofse and Ashwal, 2012; Eales and Costin, 2012; Yang et al., 2013; Maier et al., 2016; Yuan et al., 2017), although there is some academic dissonance in the definition of a slurry (at times referred to as a mush) and its exact crystalinity constraints. This model was initially based on the observation that lavas carry a portion of crystals (Wright and Okamura, 1977). In the context of the RLS, the notion of slurries is supported by: 1) significant Sr isotopic disequilibrium within and between individual plagioclase crystals that are both wide-spread and spatially consistent (Roelofse et al., 2015; Yang et al., 2013), 2) significant Sr isotopic disequilibrium between coexisting plagioclase and orthopyroxene crystals (Roelofse and Ashwal, 2012), 3) numerical thermodynamic modeling of parental melt crystallization that indicate a requirement of staging chambers in order to obtain the observed mineral/magmatic enrichment and assemblages (Barnes

et al., 2010; Eales and Costin, 2012), 4) nearly constant An-content in some anorthosite layers (Ashwal et al., 2005), 5) compositional reversals associated with magma replenishment events (Yuan et al., 2017), and 6) local irregular masses and seams of anorthosite that transgresses into the host rocks (Maier et al., 2016). One of the significant pitfalls of this model is that some lines of evidence (i.e. field, petrographic, geophysical) are sorely lacking. Furthermore, the majority of authors have not constrained nor placed educated guesses on the proportion of crystals carried in their proposed magma, and that crystal-bearing slurries at high viscosities, are difficult to form planar layers that are traceable for several kilometers. Lastly, the crystalinity of magmas and their effect on the hydrodynamic state of the magma is clearly dependent on the magma composition and thermodynamic state, and the ideal minimal slurry state may not be a well-defined concept.

1.2.3 Origin of transported cumulate blocks

A large portion of this study delves into the origin and nature of hundreds of transported cumulate blocks found in the Upper Main Zone. As chapters 5, 6 demonstrate, blocks are distinct from their host rocks (i.e. lithologically and/or texturally, chemically and isotopically). Autoliths and xenoliths are common features in many intrusions and lava flows worldwide. Altogether, they provide insights into pre-emplacement magma dynamics, magma rheology, flow dynamics as well as magmatic sources (e.g. Sparks et al., 1977; Clague, 1987; Irvine et al., 1998; Royse and Park, 2000; Yoshinobu et al., 2009). To date, only a single landmark study exists on the origin of blocks within large layered ultramafic-mafic igneous intrusions. Irvine et al. (1998) provided the first glimpse into the role that blocks can provide in the context of magmatic systems. Specifically, blocks in the Skaergaard Intrusion (Greenland) were derived from in-fallen roof and sidewall materials, which were scattered over the floor of the intrusion by magmatic crystal-liquid suspension currents. The paucity of research concerning blocks is an academic opportunity, as it leaves many possible hypotheses to explore in the context of the nature and provenance of the blocks in the RLS.

Could the blocks also represent in-fallen roof and sidewall materials, such as with those documented in the Skaergaard intrusion (Irvine et al., 1998)? If so, the blocks could provide the first evidence of a roof for the Bushveld Complex, since to date, no roof material has been found (Eales and Cawthorn, 1996; Cawthorn, 2015). Could the blocks represent disaggregated proto-cumulate layers? If so, this would provide insight into magma rheology and emplacement dynamics. Could the blocks have crystallized and been entrained from the base of the lithosphere/mantle, as demonstrated by mantle xenoliths from Hawaii's lava flows (Clague, 1987)? If so, this could provide insight into the roots of the Bushveld Complex. Finally, could the blocks have been entrained from staging chambers? If so, the blocks could provide insight into the processes and magma dynamics beneath the final RLS magma chamber. The concept of one or multiple staging chambers underneath the RLS has been proposed based on: 1) numerical modeling and magma mixing calculations (Barnes et al., 2010; Eales and Costin, 2012), 2) mass balance calculations of platinum-group elements in magmatic sulphides (McDonald and Holwell, 2007), 3) Sr-Nd isotopic disequillibrium between coexisting plagioclase and orthopyroxene, and neighboring plagioclase crystals (Roelofse and Ashwal, 2012; Roelofse et al., 2015). Altogether, these hypotheses highlight the crucial constraints, evolution and developmental condition(s) that can be provided by studying blocks in large layered ultramafic-mafic igneous intrusions.

2 Geological setting

2.1 Geological setting of the Bushveld Complex

The Bushveld Complex is located in the northeastern portion of the Kaapvaal Craton in South Africa (Fig. 2.1). The complex itself is Paleoproterozoic-aged, dated at 2.060 - 2.055 Ga and has been divided into the: 1) Rooiberg Group, 2) Rustenburg Layered Suite (RLS), 3) Rashoop Granophyre Suite, and 4) Lebowa Granite Suite (SACS, 1980).

The Complex is spatially divided into 5 lobes: the 1) eastern, 2) western, 3) northern, 4) south-eastern, and the 5) far-western lobes (Fig. 2.1a). The eastern lobe extends for $\sim$200 km and is well exposed due to a rugged terrain. The western lobe extends along a $\sim$200 km arc and is poorly exposed. The northern lobe is partially buried and the south-eastern lobe is completely buried. Both have been inferred using gravity data and drill cores. Finally, the far-western lobe is an eroded remnant of the Complex (Eales and Cawthorn, 1996; Cawthorn et al., 2006). It is thought that the layered units of the eastern and western lobes are connected at depth (Cawthorn et al., 1998; Nguuri et al., 2001; Webb et al., 2011). The Bushveld Complex also has a number of satellite intrusions. These are the Uitkomst, Losberg, Moloto and Rhenosterhoekspruit Intrusions and Molopo Farms Complex (Cawthorn et al., 2006).

2.1.1 Rooiberg Group

The Rooiberg Group unconformably overlies the Pretoria Group sediments of the Transvaal Supergroup (Buchanan, 2006). The group is $\sim$3 km thick and dated at 2061$\pm$2 Ma to 2052$\pm$48 Ma (Walraven, 1997; Walraven et al., 1987, 1990; Fig. 2.1a). The Rooiberg rocks are composed of $\sim$400 m thick silicic volcanic units which are separated by $\sim$meter thick and laterally extensive sedimentary units (Harmer and von Gruenewaldt, 1991; Eriksson et al., 1994; Cawthorn et al., 2006). Volcanic units are fine-grained with a variable amount of phenocrysts, porphyroblasts and amygdales. The sedimentary units consists of poorly sorted sandstones with lesser amounts of mudrocks and cherts from reworked Pretoria Group sediments and eroded materials from the lower units of the group (Eriksson et al., 1994; Buchanan, 2006).

The Rooiberg Group comprises the roof and forms the floor of the Bushveld Complex in the Stoffberg area (Fig. 2.1b). Whole-rock chemical and isotopic data suggests that the Rooiberg Group magmas were likely derived from same source and resided in the same mid-crustal magma chamber(s) as the RLS prior to emplacement (Buchanan et al., 2004; Buchanan, 2006). The subsequent intrusion of the RLS caused minor thermal metamorphism (low to medium metamorphic grades) of some of the Rooiberg Group rocks (Schweitzer and Hatton, 2005).

2.1.2 Rustenburg Layered Suite

The layered ultramafic-mafic rocks of the Bushveld Complex are known as the RLS. Rocks of the suite have been been dated at 2.055 - 2.060 Ga (Walraven et al., 1990; Scoates and Wall, 2015; Zeh et al., 2015; Mungall et al., 2016). The RLS intruded at shallow crustal levels ($<$12 km; Zeh et al., 2015) between the Neoarchean-Paleoproterozoic Transvaal sediments (floor) and the Rooiberg Group rocks (roof; Fig. 2.1b). Based on major mineralogical and isotopic changes, the suite is subdivided into 5 stratigraphic zones. These are (from bottom to top) the: 1) Marginal, 2) Lower, 3) Critical, 4) Main, and 5) Upper Zones (SACS, 1980; Fig. 2.2). Overall, rocks of the RLS grade from typically poorly layered norites, to layered dunite, pyroxenite and norite, to gabbro and anorthosite,

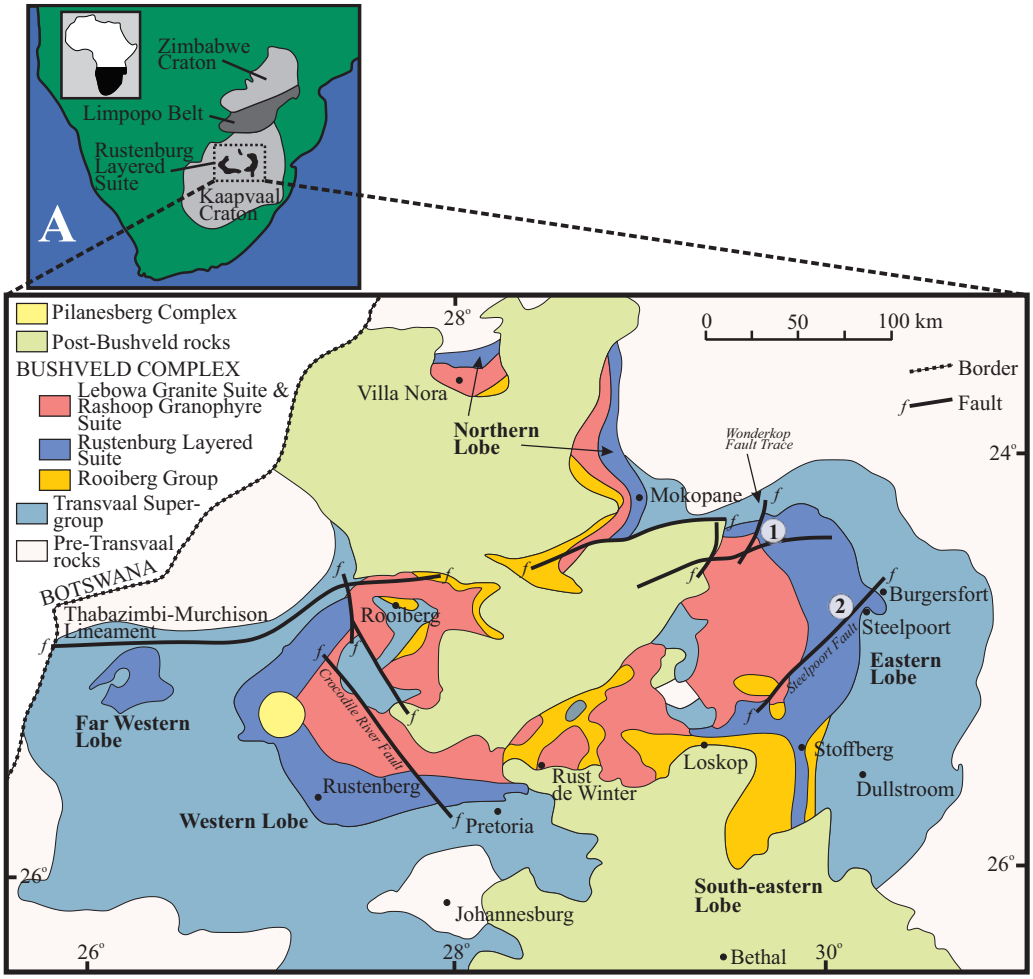

(a) Location of the Bushveld Complex in southern Africa (top) and simplified geological map of the Bushveld Complex (bottom). The white circles correspond to the Phosiri Dome (1) and the Mooimeisjesfontein (2) study areas.

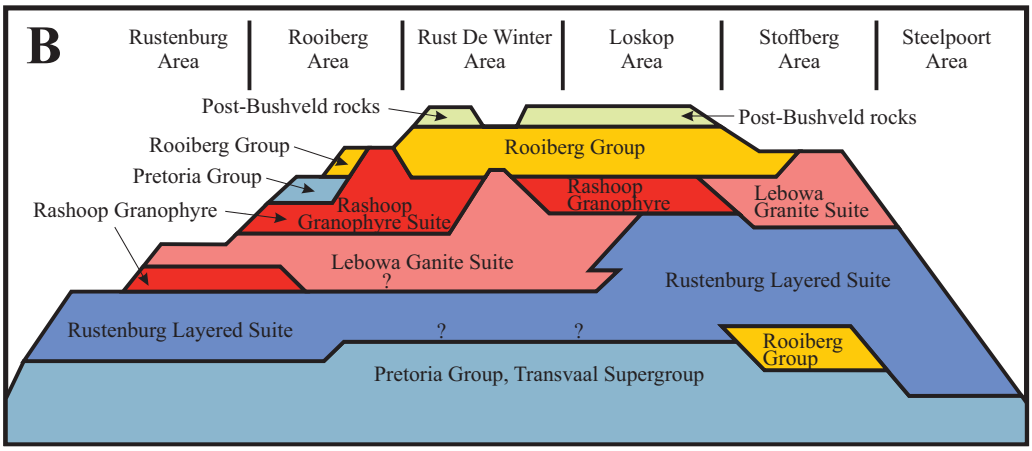

(b) Simplified cross-section of the Bushveld Complex. Axes not to scale.

Figure 2.1 – Simplified geological map of the Bushveld Complex and country rocks. Images sourced and modified from Cawthorn et al. (2006).

to magnetite- and apatite-rich diorite (Fig. 2.2). Initial magmas (i.e. Marginal, Lower and Critical Zones) were mantle-derived (possibly from a plume) Mg-andesites that were contaminated by the upper crust (Clarke et al., 2009; Zeh et al., 2015). The remainder of the magmas (i.e. Upper Critical, Main and Upper Zones) were tholeiitic in nature (Zeh et al., 2015). It is currently thought that the RLS magmas were quickly emplaced, in $\leq$0.1 Ma, yielding an accumulation rate of between 5 - 13 km^3/year (Cawthorn et al., 1998; Zeh et al., 2015).

Marginal Zone

The Marginal Zone is restricted to the floor, conformably overlying the Magaliesburg quartzite of the Pretoria Group sediments, Transvaal Supergroup, and encircling most of the RLS (Fig. 2.2). Rocks are fine- to coarse-grained, unlayered pyroxenites and layered norites with minor anorthosites (Wilson, 2012). Rocks of the Marginal Zone may contain variable amounts of quartz and biotite, indicating some assimilation of the Pretoria Group sediments (Fig. 2.2; Wager and Brown, 1968; Harmer and Sharpe, 1985).

The zone attains a maximum thickness of 800 m (Vermaak, 1976; Cawthorn et al., 2006) and is absent in some areas (Wilson, 2012). The Marginal Zone is not a true chill margin, but represents quickly crystallized magmas that were variably contaminated and differentiated compared to the remainder of the upcoming RLS magmas (Cawthorn et al., 2006; Cawthorn, 2015).

Lower Zone

The Lower Zone occurs as a series of troughs which may reach a thickness of $\sim$2 km (Cameron, 1978; Sharpe and Chadwick, 1982; Uken and Watkeys, 1997). This zone is composed of several cyclic units (up to 37 in the northern lobe) of dunite, harzburgites to pyroxenites (Fig. 2.2; Wager and Brown, 1968; Engelbrecht, 1985; Cawthorn et al., 2006). There are also a few, laterally impersistent, thin olivine layers which measure $\leq$6 m thick.

Critical Zone

The Critical Zone displays spectacular layering on the scale of a few millimeters to decametres (Fig. 2.2). In addition, the Critical Zone hosts the world's largest Platinum Group Elements (PGE) ore-bodies. The zone is subdivided into a Lower and Upper sub-zone based on the appearance of cumulus plagioclase (Fig. 2.2; Cawthorn, 2015).

The Lower Critical sub-zone is up to $\sim$800 m thick. It is defined by pyroxenite with rare olivine-bearing units and chromitite layer (SACS, 1980; Cawthorn, 2015). Layering in the Lower Critical sub-zone is not as pronounced compared to the Upper sub-zone.

The boundary between the Lower and Upper Critical sub-zones is defined on the appearance of cumulus plagioclase. The Upper Critical sub-zone is up to $\sim$1000 m thick and contains cyclic units ranging from chromitite (rarely harzburgite) to pyroxenite, norite and anorthosite at the top (Cawthorn et al., 2006). This sub-zone hosts the famous Merensky and Bastard cyclic units which contain PGE-enriched (1 - 4.5 m thick) chromitite layers (Wager and Brown, 1968).

Main Zone

The Main Zone is the thickest, attaining a thickness of 3400 m in the eastern lobe (Fig. 2.2; Molyneux, 1970, 1974). The zone is predominantly defined by poorly-layered norites and gabbronorites with minor layers of anorthosites and pyroxenites (Fig. 2.3). Rocks of the Main Zone

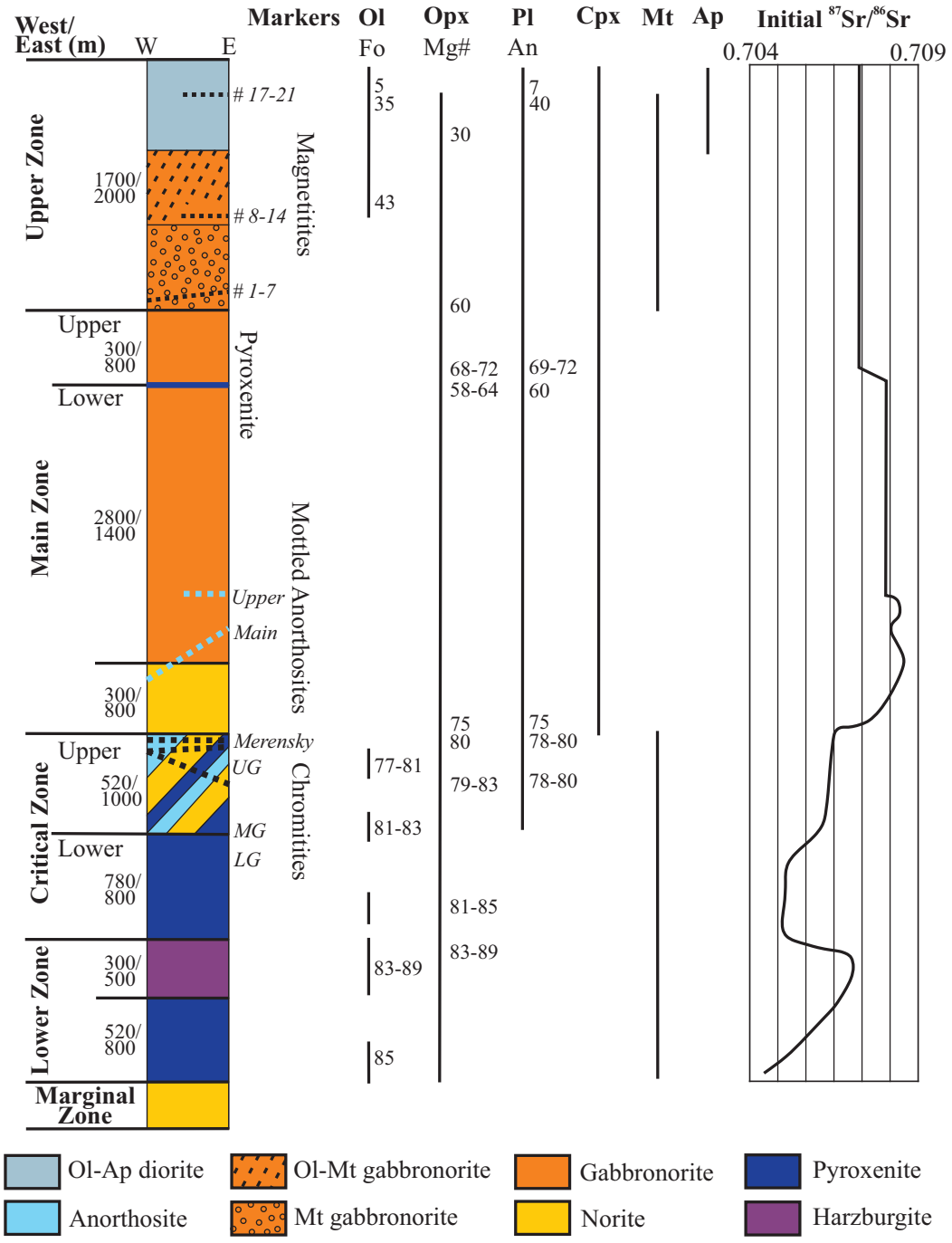

Figure 2.2 – Simplified stratigraphic column of the Rustenburg Layered Suite through the western and eastern lobes with the appearance/disappearance of major cumulus phases. Mineral compositional ranges and initial $^{87}Sr/^{86}Sr$ values are provided. Mineral abbreviations are those of Whitney and Evans (2010). Figure modified from Eales and Cawthorn (1996) and Cawthorn et al. (2006).

are ubiquitously laminated, caused by the alignment of plagioclase laths and to a lesser extent orthopyroxene crystals, roughly oriented parallel to the plane of layering. The Main Zone is also known for the disappearance of cumulus orthopyroxene and the appearance of inverted pigeonite at a stratigraphic height between 2200 - 3100 m (von Gruenewaldt, 1973; Molyneux, 1974; Mitchell, 1990).

The stratigraphy of the Main Zone has been developed and revised in large-scale studies by von Gruenewaldt (1973); Molyneux (1970, 1974); Mitchell (1986, 1990, 1996) and Nex et al. (1998). For simplicity, the division of the Main Zone into a lower (2200 - 3100 m thick) and an upper (300 - 800 m thick) sub-zone by Mitchell (1990); Cawthorn (2020) is kept for this thesis. Several unique textures and features found in the Upper Main Zone are the focus of this thesis. The lower and upper sub-zones are separated by the Pyroxenite Marker, a $\approx$2 m thick layer of orthopyroxenite that is found both in the Eastern and Western lobes (von Gruenewaldt and Weber-Diefenbach, 1977; Mitchell, 1990). This marker may be locally absent, but is typically recognized as 1 - 4 pyroxenite layers measuring $\leq$2 m in thickness (Molyneux, 1974; Cawthorn et al., 2006; Cawthorn, 2015; Chapter 6). The Pyroxenite Marker marks the top of a $\sim$350 m thick succession in which there are changes in: 1) major and trace element chemistries (VanTongeren and Mathez, 2013), 2) whole-rock initial $^{87}Sr/^{86}Sr$ ratios (Sharpe, 1985; Kruger, 1994; Cawthorn et al., 1991), and 3) mineral chemistries to more magnesian and calcic compositions, which altogether are interpreted by many (e.g. von Gruenewaldt, 1973; Molyneux, 1974; Hayes et al., 1985; Cawthorn et al., 1991; VanTongeren and Mathez, 2013) to represent a major magmatic replenishment event.

Upper Zone

The Upper Zone is defined by the appearance of cumulus magnetite, a few meters below the lowest magnetitite layer (Fig. 2.3; (Wager and Brown, 1968; Molyneux, 1974; Scoon and Mitchell, 2012; Cawthorn, 2015). This zone is intermittently well-layered and reaches up to 2000 m in thickness (Fig. 2.2; Molyneux, 1974; Cawthorn et al., 2006). The zone is dominated by gabbro, gabbronorite, diorite and anorthosite with variable amounts of cumulus Fe-pyroxenes, Fe-olivine, magnetite and apatite (Wager and Brown, 1968; Cawthorn et al., 2006; Scoon and Mitchell, 2012). The uppermost 200 m are defined by the presence of interstitial hornblende, biotite, quartz and K-feldspar (Wager and Brown, 1968; Cawthorn et al., 2006). The most striking feature of the zone are 25 melanocratic magnetitite layers ($\sim$cm - 6 m thick) alternating with leucocratic anorthosite layers which can be delineated along a strike of $>$150 km with the best examples found at Magnet Heights (Molyneux, 1964; Scoon and Mitchell, 2012).

2.1.3 Rashoop Granophyre Suite

Granophyric rocks belonging to the Rashoop Granopyre Suite are stratigraphically found between the Rustenburg Layered and Lebowa Granite Suites (Fig. 2.1). Rocks of the granophyre suite have been dated at 2053$\pm$12 Ma (Coertze et al., 1978). Altogether, rocks of the suite represent a significant component of the felsic phase of the Bushveld Complex. The suite is divided into a metamorphic type which formed by the melting of sedimentary rocks (Pretoria and Rooiberg Groups) by the RLS (Walraven, 1985) and a magmatic type which displays well-developed micro-graphitic intergrowths of quartz and K-feldspar (Cawthorn et al., 2006). These rocks have a similar chemical composition to some of the Rooiberg Group volcanic sequences and are therefore considered to be the intrusive, time-equivalent magmas, of the overlying volcanic sequences (Hatton and Schweitzer, 1995; Fig. 2.1b).

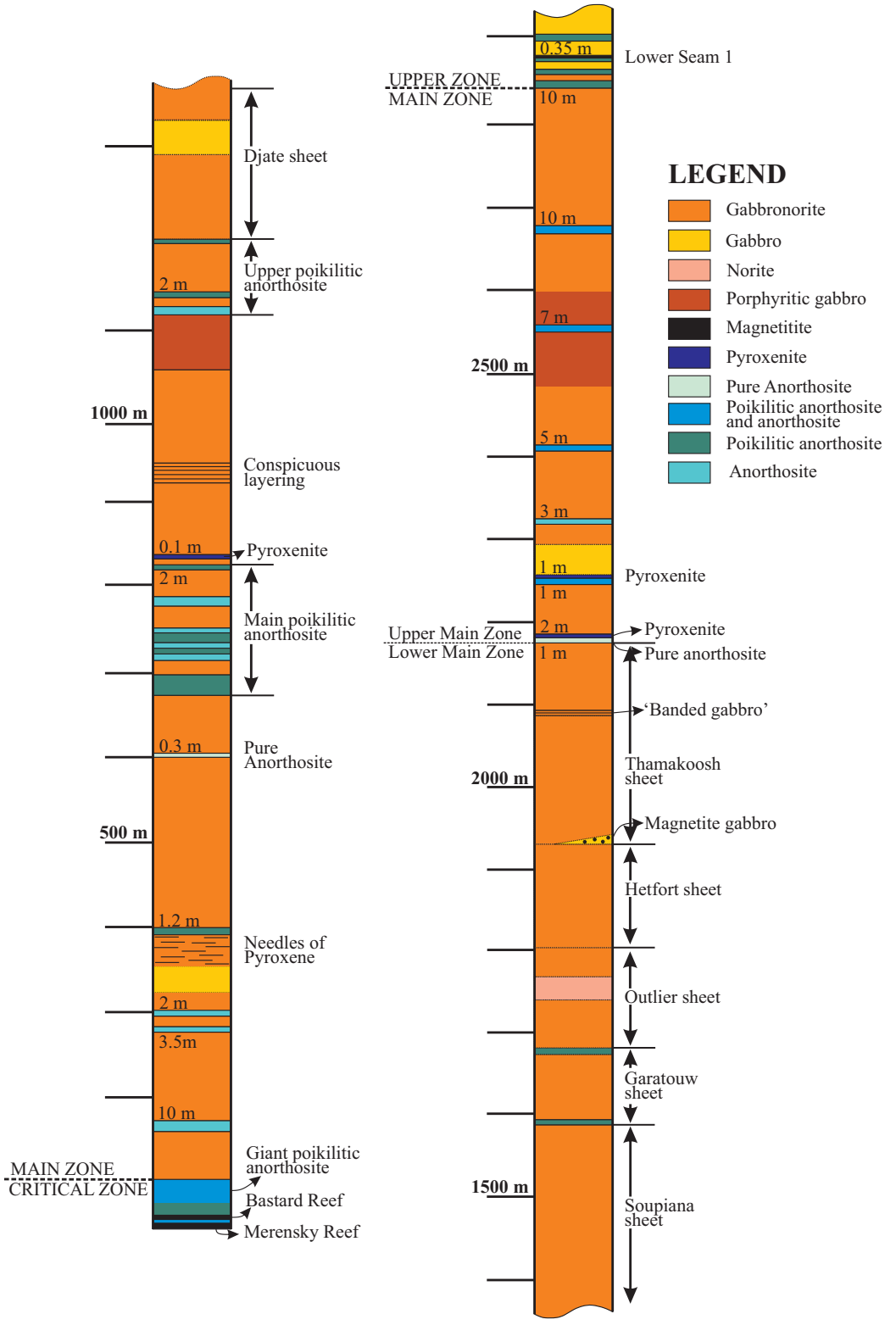

Figure 2.3 – Simplified stratigraphic succession of the Main Zone. The boundary between the Critical and Main Zones has been updated to the top of the Giant poikilitic anorthosite (also known as the Giant mottled anorthosite). The division of the Main Zone into 2 sub-zones follows Mitchell (1990). Figure modified from Molyneux (1974).

2.1.4 Lebowa Granite Suite

The last phase of the Bushveld Complex is defined by granitic magmatism, located above the RLS as two large semicircular lobes in the western and eastern lobes (Fig. 2.1a). The suite has been dated at 2054±2 Ma (Walraven and Hattingh, 1993) and attains a thickness of 2 - 3 km (Cawthorn, 2015). Most of the suite is dominated by the Nebo Granite. The Nebo Granite is coarse-grained, pink to gray in color and consists of perthite, quartz with minor hornblende, biotite and accessory minerals (Cawthorn et al., 2006). Other types of granites may be medium-grained and red-colored (Bobbejaankop Granite), finer-grained with extremely low contents of mafic minerals (Klipkloof Granite) or biotite-rich with schlieren textures defined by the trails of the mafic minerals (Makhutso Granite) (Cawthorn et al., 2006). Altogether, the granites present a continuous fractionation trend, with the exception of the Makhutso Granite (Cawthorn et al., 2006).

2.2 Geological setting of the Phosiri Dome area, Limpopo Province

The area of the Phosiri Dome applies to work discussed in Chapters 4 and 5.

The north-eastern region of the eastern lobe (Bushveld Complex) is structurally complex and crops out in a region of rugged topography (Hall, 1932). Part of this structural complexity is related to domal structures which expose the underlying, older sedimentary formations of the Pretoria Group (Fig. 2.4; Scoon, 2002). One of these domes is the Phosiri Dome, also known as the Fortdraai Anticline, the Phoshiri, Fosiri or Zaaikloof Dome. The Phosiri Dome is located north of the town of Apel, Limpopo Province. The dome is characterized by a ∼7 km wide anticline which curls in a SE direction and is bounded to the west by the NE-SW striking Stoffpoort Fault, which runs nearly parallel to the Wonderkop Fault system (Martin, 1999; Lesego Platinum Mining Ltd. and MSA, 2011). The area is economically important as there is an estimated 42 million ounces of PGE (Platinum, Palladium and Rhodium) and gold yet to be exploited (Lesego Platinum Mining Ltd. and MSA, 2011; Price, 2016).

2.2.1 Stratigraphic sequence

Most information regarding the geological setting of the Bushveld Complex has already been provided above (Section 2.1). The following only focuses on divergences documented in the study area detailed in Chapters 4 and 5.

Pretoria Group sediments, Transvaal Supergroup

The sedimentary and minor volcanic rocks from the Transvaal Supergroup overlie the Archean basement rocks which define the Kaapvaal Craton. Rocks of the Pretoria Group, Rb-Sr dated at 2224±21 Ma (Burger and Coertze, 1975), are exposed at the core of the Phosiri and Katkloof Domes. Five formations belonging to the Pretoria Group are found in the study area. These are, from bottom to top, the: 1) Daspoort Formation (∼10 - 120 m thick), composed of mature quartz arenites, subordinates mudrocks and ironstones, 2) Silverton Formation (1040 - 2230 m thick), characterized by shales (now andalusite metapelites), interbedded by subordinate carbonate rocks and tholeiitic basalts of the Machadodorp Member, 3) Magaliesberg Formation (∼225 - 550 m thick), composed of immature sandstones (now quartzites), 4) Vermont Formation (∼500 - 700 m thick), composed of immature feldspathic mudrocks (now cordierite hornfelses) and, 5) Lakenvalei Formation (200 - 350 m thick), characterized by immature feldspathic sandstones (now quartzites; Button, 1973; Eriksson and Reczko, 1995; Eriksson et al., 2006; Sharpe and Chadwick, 1982).

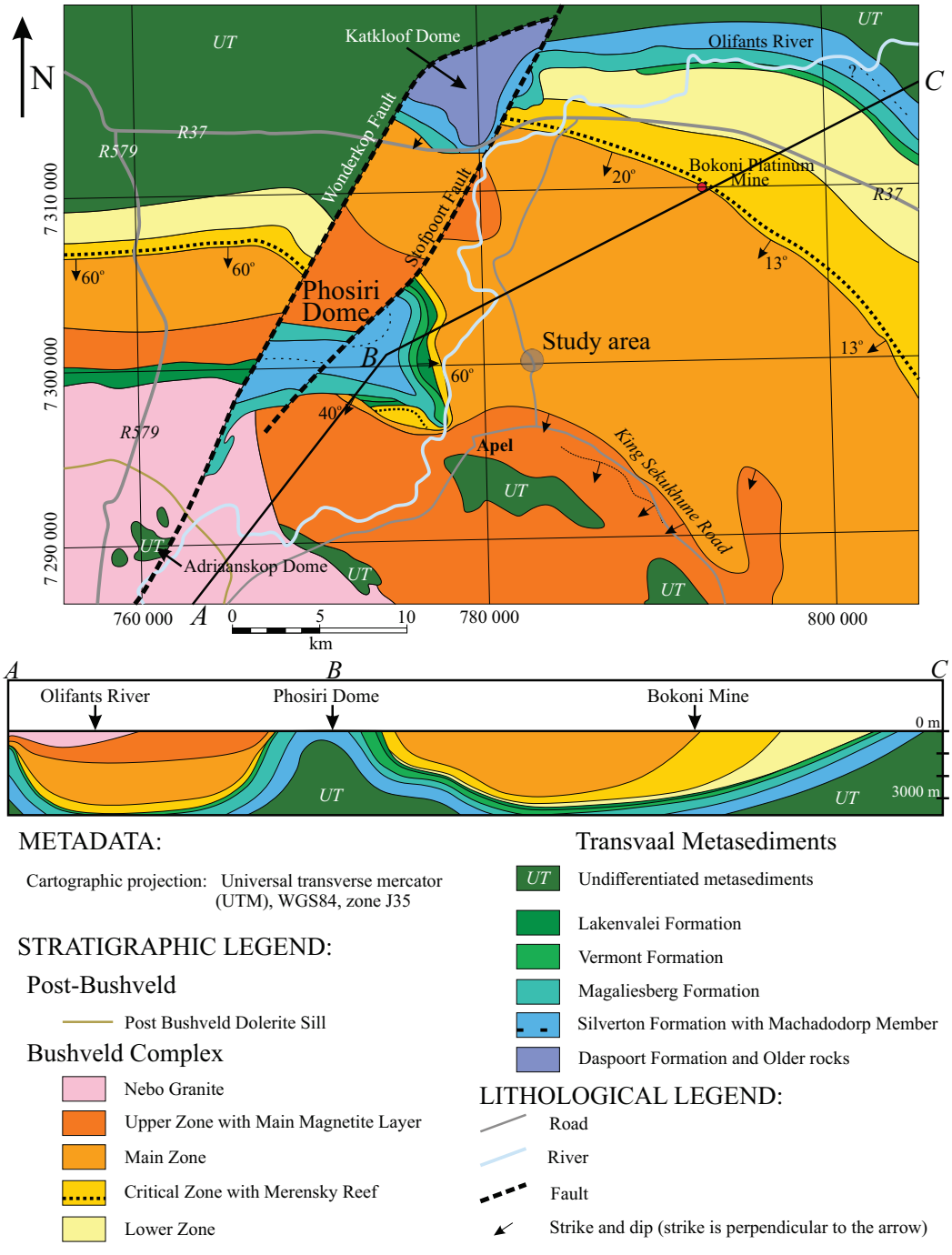

Figure 2.4 – Simplified geological map and cross-section of the Phosiri Dome area (UTM WGS84 ellipsoid, Zone J35). The original base map (2428 Nylstroom geological map, 1: 250 000 Series) was modified and updated using data from Scoon (2002); Molyneux (2008); Lesego Platinum Mining Ltd. and MSA (2011). The location of the studied road-cut, as detailed in Chapters 4 and 5 is highlighted by a gray circle.

Bushveld Complex

Rocks of the RLS are drastically thinner compared to the remainder of the Bushveld Complex, especially nearing the Phosiri Dome (Fig. 2.4). Consequently, some sequences or markers may be absent, highly sheared and/or discontinuous (Uken and Watkeys, 1997; Scoon, 2002). Rocks of the Main Zone on the eastern flank of the dome can be unusually thick, possibly caused by fold repetition (Scoon, 2002). Furthermore, lenses of pyroxenite, interpreted by Martin (1999) to correspond to an immature Pyroxenite Marker have been observed on the south-western flank of the dome. The contact between the Main and Upper Zones can be unconformable, where Upper Zone rocks truncate sequences from the Main and Critical Zones (Scoon, 2002). The unconformable contact was caused by subsequent faulting by the Wonderkop Fault system which laterally displaced the floor (Martin, 1999).

2.2.2 Formation of the Phosiri Dome

The RLS intruded into the Pretoria Group sediments with the Magaliesberg Formation forming the floor of the intrusion. The intrusion of the hotter, heavier and denser RLS magma not only produced a considerable contact metamorphism aureole ($\leq$5 km deep) but also increased the ductility of the Pretoria Group sediments such that they buckled (Sharpe and Chadwick, 1982; Gerya et al., 2003). Numerical models by Gerya et al. (2003) demonstrate that a dome, like the Phosiri Dome, would have grown rapidly ($\leq$6 Ma) from an initial anticline that existed in the Pretoria Group sediments. The Phosiri Dome developed throughout the solidification of the RLS, steepening and thinning the sequences (Uken and Watkeys, 1997; Martin, 1999; Scoon, 2002). The Wonderkop Fault system, which laterally displaced the floor rocks and produced widespread deformation, was also active during the formation of the Phosiri Dome (Sharpe and Chadwick, 1982; Martin, 1999). The widespread deformation facilitated the circulation of late-hydrothermal fluids which resulted in the sericitization and chloratization of the RLS (Scoon, 2002).

2.2.3 Geology of the study area

I studied a road-cut, located 5.3 km NE from the town of Apel (Fig. 2.4). The road-cut is encompassed under 'Government Grounds', reference 503 KS, on the Nylstroom geological map. The road-cut exposes a cross-sectional area of approximately 10 000 m^2. A total of 8, m-scale, texturally distinct layers of poikilitic anorthosite and a layer of norite, within gabbronorite, dominate the exposure. The poikilitic anorthosite layers also host 16 melanocratic, lithologically distinct cumulate blocks (0.2 - 5.75 m). A detailed study of the poikilitic anorthosite layers and the lithologically distinct cumulate blocks are presented in Chapters 4 and 5 respectively. The road-cut has not been directly affected by the formation of the Phosiri Dome. The layer thicknesses, strikes and dips are consistent with one another for the entirety of the exposure and correlate with the regional strike (ESE) and dip measurements (10 - 16° SSW; Molyneux, 2008; Lesego Platinum Mining Ltd. and MSA, 2011). The anorthosite sequence has been stratigraphically correlated to the Upper Main Zone by Molyneux (2008) and Lesego Platinum Mining Ltd. and MSA (2011), located $\sim$2685 m above the Critical-Main Zone contact (Chapter 4).

2.3 Geological setting of the Mooimesjesfontein area, Limpopo Province

The Mooimeisjesfontein area applies to work discussed in Chapter 6.

The eastern lobe of the Bushveld Complex is well known for its good exposure. Sequences of the Main Zone are well exposed midway though the eastern lobe, forming the spectacular Leolo Mountains. South of the Leolo Mountains is the Mooimeisjesfontein area (Afrikaans for: *Pretty girls fountain*), located 36.5 km SW of Burgersfort. Geographically, the area is encompassed under the 2430 Pilgrim's Rest geological map (1:250 000 Series) with an area of 18.6 km^2 (Fig. 2.5). The geology of the area was first mapped and documented by Molyneux (1970, 1974). The Mooimeisjesfontein area exposes a $\sim$1145 m stratigraphic section of the Main Zone, spanning from $\sim$1220 to $\sim$75 m below the Main and Upper Zone contact (Fig. 2.3). Notably, the area contains a N-S oriented incised valley where a small stream exposes numerous outcrops with pyroxenite layers and both unlayered and modally-graded gabbronorites.

2.3.1 Stratigraphic sequence

Most information regarding the main geological features of the Main Zone (Bushveld Complex) have already been described above (Section 2.1). The following only focuses on divergences documented in the study area.

Lower Main Zone

Regional geological mapping by Molyneux (1970, 1974) divided the area into 4 unlayered and homogeneous gabbronorite sheets below the Pyroxenite Marker. These are, from bottom to top: 1) Garatouw (90 m thick), 2) Outlier (120 m thick), 3) Hetfort (125 m thick), and 4) Thamakoosh (380 m thick) sheets. Altogether, the 4 sheets are petrographically very similar and are distinguished on the basis of differential erosion. A sequence of modally-graded gabbronorite (or banded gabbronorite, Molyneux, 1974) appears 250 m above the base of the Thamakoosh sheet. The unlayered, homogeneous gabbronorite is characterized by plagioclase laths (2 - 5 mm, 70 modal%) accompanied by orthopyroxene (0.4 - 4 mm; 15%) and clinopyroxene (0.2 - 3 mm; 15%). Plagioclase laths typically define a moderate to strong foliation aligned parallel to the plane of layering.

Upper Main Zone

The Pyroxenite Marker, defined as two $\leq$2 m thick pyroxenite layers, mark the base of the Upper Main Zone. The pyroxenite layers are separated by $\sim$60 m of unlayered gabbronorite (Molyneux, 1970, 1974). Progressing up-section from the Pyroxenite Marker to the Upper Zone contact, the Upper Main Zone is dominated by unlayered and homogeneous gabbronorite, with similar modal proportions as in the Lower Main Zone. Three thick poikilitic anorthosite layers (2 - 5 m thick), a few modally-graded gabbronorite horizons (1 - 10 m thick), as well as numerous modally-graded horizons (decimeter-scale) progressing from gabbronorite up to anorthosite (cm-scale) are found through the sub-zone.

Pegmatite bodies and evolved pegmatoidal dykes Several pegmatite bodies and evolved pegmatoidal dykes transect Main Zone rocks at the stratigraphic level of the Pyroxenite Marker. Pegmatite bodies are irregular-shaped, measuring 1 - 15 m across. Finer-grained (5 - 30 mm) zones are cut by coarser-grained (20 - 60 mm) ones. Contacts with the host gabbronorite tend to be finer-grained

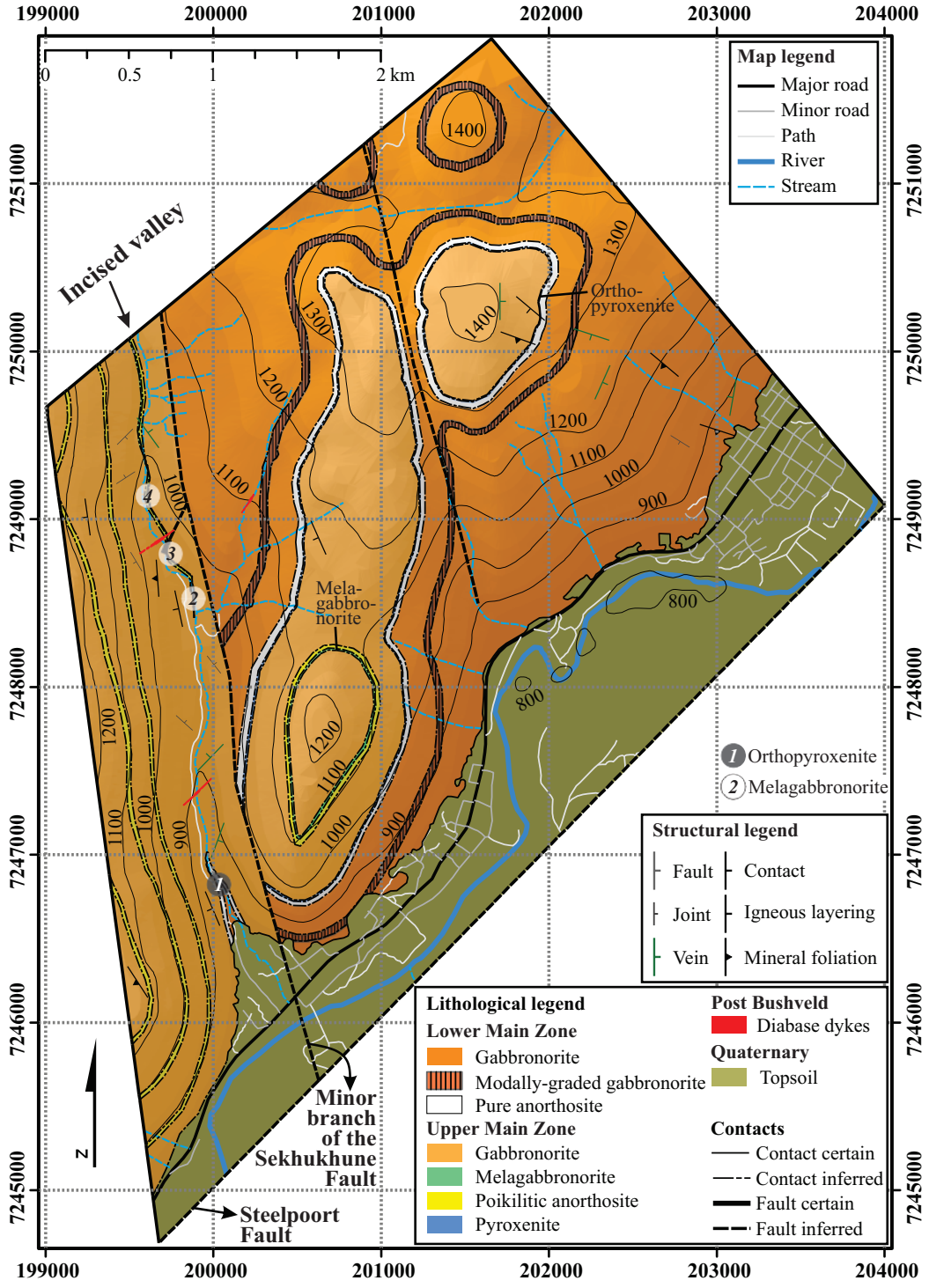

Figure 2.5 – Geological map of the Mooimeisjesfontein area (WGS84 ellipsoid, UTM, Zone J36). The original base map (2430 Pilgrim's Rest geological map, 1: 250 000 Series) was modified from Molyneux (1974) and updated by the author. The location of the studied pyroxenite outcrops, as detailed in Chapter 6, are highlighted by shaded circles.

for 0 - 35 cm inwards. The bodies are characterized by coarsened plagioclase, pyroxenes which are partially to completely replaced by hornblende with minor phlogopite and magnetite crystals.

Pegmatoidal dykes measure 2 - 30 cm across, strike NNE - SSW and dip between 85 to 90°. These dykes can be traced for several meters along strike. Pegmatoidal dykes have been described in detail by Hayes et al. (2018).

Post-Bushveld rocks

Diabase dykes A few very-fine grained diabase dykes (0.2 - 5 m wide) transect the Main Zone rocks. Diabase dykes strike NNE-SSW to NE-SW and dip between 85 to 90°. These dykes can be traced along strike for tens of meters. Rarely, the dykes may contain elongated enclaves of the host gabbronorite or rounded (0.01 - 0.1 m) xenolithic fragments of metamorphosed felsites and diorite. Most dykes are characterized by abundant jointing which strike perpendicular and parallel to the dyke's strike direction.

2.3.2 Deformation and hydrothermal alteration

Lithologies in the Mooimeisjesfontein area have been remarkably well preserved. The NE-SW trending Steelpoort Fault marks the southern edge of the Mooimeisjesfontein area. A minor N-S striking branch of the Sekhukhune Fault is found on the eastern slopes of the incised valley where it transects the Mooimeisjesfontein area until it intercepts the Steelpoort Fault (Fig. 2.5). Deformation associated with faulting is minimal in the Mooimeisjesfontein area, with the minor branch of the Sekhukhune Fault attaining a maximum throw of 30 m (Molyneux, 1970). Small ($\leq$3 cm wide) veins filled with dark green chlorite often transect the rocks, striking N-S to NE-SW and dipping between 85 to 90°.

2.3.3 Geology of the study area

We studied a $\sim$100 m section of the Upper Main Zone stratigraphy, starting at the stratigraphic level of the Pyroxenite Marker (Fig. 2.3). Several key outcrops exposing pyroxenite layers, blocks and their bounding lithologies are found in a N-S trending, incised valley which transects the Mooimeisjesfontein area (Fig. 2.5). Within the area, RLS lithologies strike SE and dip gently at $\sim$8° SW. The exposed pyroxenite sequences are detailed in chapter 6. The series of outcrops in the incised valley have been stratigraphically correlated to the level of the Pyroxenite Marker by Molyneux (1970, 1974).

3 Sampling and analytical techniques

3.1 Field and sampling methods

A Garmin eTrex 20 GPS was used to obtain geographic coordinates. Most coordinates are accurate to ± 3 m with the exception of specific locations (noted where appropriate) where a multi-point average ($n \geq 30$) was used to obtain an accuracy of ± 1 m. All coordinates reported here follow the UTM coordinate system, specifically the World Geodetic System (WGS84) ellipsoid. The complete list of all samples and coordinates are found in Appendix A.

I collected a total of 60 samples for the characterization of a layered anorthosite sequence in the Upper Main Zone exposed near Apel, Limpopo Province (Chapter 4). Anorthosite layers were sampled in detail ($\sim$10 samples per layer) with the exception of the bottom 3 and topmost layer for which only a representative sample was taken due to weathering/structural damage. Horizontal spacing between sampled layers ranges from 10 - 20 meters due to accessibility and degree of weathering. I also sampled a layer in multiple places along strike to test for any m-scale chemical heterogeneity. Additionally, I sampled a contact (between anorthosite layers 3 and 4) to test for chemical differences at the interface between two layers. A total of 13 lithologically distinct block samples were collected from the layered anorthosite sequence in the Upper Main Zone (Chapter 5).

I collected 65 samples for the characterization of pyroxenite sequences in an incised valley within the Mooimeisjesfontein (363-KT) area which exposes sections of the Upper Main Zone (Chapter 6). Two pyroxenite layers and their bounding lithologies were sampled in detail, every $\sim$10 cm on average. I also sampled one of the pyroxenite layers in multiple places along strike (up to 570 m) to test for any m-scale chemical and large-scale petrographic heterogeneity. A total of 29 lithologically and/or texturally distinct block samples were collected in the incised valley.

3.2 Sample preparation

Weathered edges, alteration and/or veins were separated from the samples by using a geological hammer and a diamond blade rock saw. Select samples were crushed in a Dickie & Stockler steel jaw crusher. Between samples, both the crusher and collection basket were wiped and cleaned. The crusher was also vacuumed to remove any dust or particles that could not be otherwise wiped off. A portion (40 - 60 g) of crushed specimen was pulverized in a Dickie & Stockler TS-250 Mill in a carbide and steel vessel. Both the vessel and preparation bench were wiped and cleaned between each sample to minimize contamination.

Thin sections were made at the Thin Section Preparation Laboratory, University of the Witwatersrand. Petrographic observations were made using an Olympus BX40 and Olympus BH2 microscopes. Thin sections were also scanned at high resolution (in both plane and cross-polarized light) using an Epson V550 to document larger-scale thin section textures.

3.3 Whole-rock density measurement

Whole-rock density of all lithologies were measured using the water immersion method. Data and analytical uncertainties are presented in Appendix F. Whole-rock densities were measured to further justify trends observed using conventional geological methods (e.g. whole-rock chemistry, petrography, mineralogy), as well as to construct a numerical model detailed in chapters 5 and 6.

3.4 Electron microprobe analyses

Electron microprobe analyses were conducted at the University of Ottawa (Canada), using a JEOL JXA-8230 SuperProbe. The beam operating conditions on the instrument were 40 degrees takeoff angle, 20 kV of bias voltage, 20 nA beam current. Beam diameters varied from 5 μm for pyroxene and spinel group minerals, and 10μm for feldspar, mica and amphibole group minerals. The microprobe was calibrated using the following standards for the following elements: albite for Na, celestine for Sr, diopside for Ca, sanidine for K and Si, hematite for Fe, rutile for Ti, sanbornite for Ba, chromite for Cr and smithsonian plagioclase for Al. Counting times were 10 seconds followed by an off-peak counting time of 10 seconds for all elements. Off-peak corrections were done using the linear method for all elements. Interference corrections of Donovan et al. (1993) were also applied to Ti for interference by Ba.

The data presented is the result of an average of three points with detection limits ranging from 0.012 wt% for Ti, 0.014 wt% for Al, 0.021 wt% for Si, 0.030 wt% for Fe, 0.100 wt% for Sr. Analytical sensitivities (at the 99% confidence level) ranged from 0.0360% relative for Al, 0.587% relative for Ca, 7.519% relative for K, 33.509% relative for Ba, 109.286% relative for Cr. All oxygen was calculated by cation stoichiometry and included in the matrix correction. The matrix correction method was ZAF or Phi-Rho-Z (Armstrong, 1988) by using the mass absorption coefficients dataset of FFAST. The complete set of data and analytical uncertainties are presented in Appendix D.

3.5 Whole-rock chemical analyses

A total of 83 whole-rock samples were analyzed for chemistry. Analyses were conducted at Intertek Genalysis (Perth, Australia) and the Earth Lab (University of the Witwatersrand, South Africa). In order to ensure that the results between laboratories are comparable, an in-house standard sample (gabbronorite: AR-9) was analyzed in both laboratories. Analyses from both laboratories are presented in Table 3.1. Results have an average variance of 0.015 wt%^{2} for major and minor elements, and 153 ppm^2 for trace elements. Results are therefore in good agreement between the laboratories. The complete set of data and analytical uncertainties are presented in Appendix E.

3.5.1 Intertek Laboratories

Major and minor elements

Major elements were analyzed via X-Ray Fluorescence (XRF) using a PanAnalytical MagixFast X-Ray Fluorescence instrument. Approximately 0.7 g of pulped sample was mixed with $LiBO_4$ flux and fused to produce a glass bead. The instrument was calibrated before each run by analyzing a monitor disk. Two standards (SARM-1 and SY-4) were included in the analyses to ensure quality and reproducibility. The Loss on Ignition (LOI) was determined by taking approximately 1 g of pulped sample and heating it to 1000°C. The difference in weight between the unheated and heated sample was measured using a Leco TGA701 Thermogravimetric Analyzer. Relative errors vary between 0.30 - 2.45%.

Trace elements

Trace elements Cr, Cu, Ni, V and Zn were analyzed via Inductively Coupled Plasma-Optical Emission Spectroscopy (ICP-OES), using the Thermo iCAP ICP-OES instrument. Trace elements Ag, As, Ba, Be, Bi, Cd, Ce, Co, Cs, Dy, Er, Eu, Ga, Gd, Ge, Hf, Ho, In, La, Li, Lu, Mo, Nb, Nd, Pb, Pr,

Table 3.1 – Whole-rock chemistry of an in-house standard sample analyzed at Intertek (Australia) and at the Earth Lab (South Africa).

Laboratory	Intertek	Earth Lab	Variance		Intertek	Earth Lab	Variance
SiO_2 (wt%)	50.87	50.87	6.018E-06	**In (ppm)**	0.03	0.00	0.000
TiO_2	0.18	0.18	3.655E-08	**La**	4.19	1.66	3.195
Al_2O_3	18.00	18.37	0.069	**Li**	4.00	2.01	1.983
Fe_2O_{3T}	6.52	6.15	0.068	**Lu**	0.10	0.05	0.001
MnO	0.14	0.13	5.197E-05	**Nb**	0.40	0.40	4.254E-06
MgO	8.46	8.30	0.013	**Nd**	3.70	1.90	1.626
CaO	13.44	13.58	0.010	**Ni**	152.70	139.06	93.013
Na_2O	1.69	1.72	0.000	**Pb**	1.80	1.69	0.006
K_2O	0.19	0.20	4.704E-05	**Pr**	0.86	0.42	0.097
P_2O_5	0.01	0.02	1.782E-05	**Rb**	3.45	2.99	0.105
LOI	0.35	0.48	0.008	**Sc**	31.30	14.89	134.570
Ba (ppm)	68.60	44.99	278.692	**Sm**	0.88	0.47	0.082
Ce	8.19	5.25	4.319	**Sn**	0.30	0.29	2.229E-05
Co	41.40	38.52	4.156	**Sr**	236.73	138.36	4838.611
Cr	176.00	200.88	309.565	**Ta**	0.04	0.06	0.000
Cs	0.23	0.19	0.001	**Tb**	0.17	0.09	0.004
Cu	24.30	28.35	8.216	**Th**	0.38	0.25	0.009
Dy	1.02	0.57	0.101	**Tm**	0.09	0.05	0.001
Er	0.68	0.33	0.061	**U**	0.10	0.10	2.653E-08
Eu	0.38	0.18	0.020	**V**	115.00	112.60	2.870
Ga	14.88	10.71	8.681	**Y**	5.72	2.94	3.869
Gd	0.93	0.53	0.079	**Yb**	0.62	0.34	0.039
Hf	0.36	0.33	0.000	**Zn**	42.00	40.37	1.324
Ho	0.22	0.12	0.005	**Zr**	12.40	10.57	1.672

Rb, Re, Sb, Sc, Se, Sm, Sn, Sr, Ta, Tb, Te, Th, Tl, Tm, U, W, Y, Yb and Zr were analyzed via Inductively Coupled Plasma-Mass Spectrometry (ICP-MS), using an Agilent 7700 ICP-MS instrument. Approximately 0.25 g of pulped sample was weighed and placed in a Teflon tube to which 1 mL of HNO_3 was added. The mixture was then warmed. Subsequently, a mix of HCl, HF and $HClO_4$ were added. The solution was kept at room temperature and subsequently increased and left to reflux and fume. AR-grade hydrochloric acid (37%) was then added to the sample and left to cool. Four standards (OREAS 24b, OREAS 45e, OREAS 45d and AMIS0170) and two blanks were included in the analyses to ensure quality and reproducibility. Relative errors vary between 2.8 - 17.93%.

3.5.2 Earth Lab, University of the Witwatersrand

Major and minor elements

Major elements were analyzed via XRF using a Axios Max Panalytical instrument. Approximately 1.75 g of $LiBO_4$ flux was added to Pt-crucibles and ignited to 1020°C for 40 minutes. Once cooled, approximately 0.34 g of sample was added to each crucible. The mixture was ignited to 1020°C for 50 minutes. The mixture was then poured out onto a hot plate and pressed into a disk. The fused disks were allowed to set and anneal for 2 hours on a hot plate. The LOI was determined via thermogravimetry. The instrument was calibrated before each run by analyzing 13 certified reference materials. Relative errors vary between 0.28 - 2.93%.

Trace elements

Trace elements were analyzed via ICP-MS using a Thermo Scientific iCAP RQ ICP-MS instrument. Samples were prepared for trace element analysis using a standard microwave digestion method. First, 50 mg of sample was weighed and added to a Teflon tube to which 6 mL of 2:1 HF:HNO_3 was added. The Teflon tubes were then sealed and heated to 190°C for 55 minutes in a CEM Mars

6 microwave and left to cool for 30 minutes to room temperature. The samples were transferred to small 15 mL Savillex beakers and the teflon tubes were rinsed with 10% HNO_3. Samples were then put on a hot plate (70°C) and left to dry. Once dry, 2 mL of pure HNO_3 was added to the sample. The mixture was capped and left to digest at 60°C for 24 hours. Afterwards, the sample was left to dry down at 70°C. Once dry, another 2 mL of pure HNO_3 was added. The sample was left to dry down again at 70°C. Finally, 3 mL of HNO_3 was added and the mixture was capped until analysis. Two standards (BCR-2 and BHVO-2) and three blanks were included in the analyses to ensure quality and reproducibility.

3.6 Whole-rock Rb-Sr and Sm-Nd isotopic analyses

A total of 15 whole-rock samples were analyzed via isotope dilution, ion exchange chemistry mass spectrometry to obtain Rb, Sr, Sm, Nd concentrations and isotopic ratios. Unfortunately, two of the samples (additional host anorthosite samples) were contaminated and yielded erroneous results. Consequently, these samples were not included in this study. The two samples are currently being re-prepared for analysis. Sample preparation was conducted at the Witwatersrand Isotope Geoscience Laboratory (WIGL), University of the Witwatersrand. Two standards (AVG-2 and BCR-2) and two blank were included in the analyses to ensure quality and reproducibility. JNdi standards measurements produced a running average of $^{143}Nd/^{144}Nd = 0.512105 \pm 0.000013$ (n = 50) compared to the accepted published values of $^{143}Nd/^{144}Nd = 0.512115 \pm 0.000007$; (Tanaka et al., 2000). The NIST-SRM987 standard was used for reporting Sr isotopic analyses and produced a running average of $^{87}Sr/^{86}Sr = 0.710236 \pm 0.000030$ (n = 71) compared to the accepted certified values of $^{87}Sr/^{86}Sr = 0.710340 \pm 0.000260$. Data and analytical uncertainties are presented in Table 5.3.

Approximately 300 mg of sample was spiked with mixed ^{85}Rb-^{84}Sr and ^{149}Sm-^{150}Nd tracers and dissolved in HF-HNO_3 acid in PFA beakers. The mixture was heated to 100°C on a hotplate for a minimum of two weeks. Samples were then dried down and 3 ml of HNO_3 and 3 ml of 6M HCl was added to the samples for the conversion of elements to chlorites. Solutions were visually checked for complete digestion and were centrifuged prior to being loaded into the PFA columns.

Rb, Sr and Light Rare Earth Elements (LREE) were separated from the matrix using PFA columns with a 2 ml resin bed of BioRad AG 50W-X8, 200 - 400 mesh. Columns were first washed and equilibrated. The samples were loaded into the columns and rinsed with 1 ml of 1.5M HCl three times. The sample matrix was eluted by adding 4 ml of 1.5M HCl before collecting Rb in new beakers by adding another 4 ml of 1.5M HCl. Ca was eluted from the column by adding 10 ml of 1.5M HCl. Following, Sr was collected in new beakers by adding 15 ml of 1.5M HCl. Heavy Rare Earth Elements (HREE) were then eluted from the columns by adding 2 ml of 6M HCl. The remaining LREE (for subsequent Sm-Nd extraction) were eluted from the columns and collected in new beakers by adding 7 ml of 6M HCl. Finally, the columns were then washed thrice with 10 ml HCl.

Nd and Sm were separated from the matrix using PFA columns with a 1 ml LNSpec resin bed as cation exchange medium. Columns were first washed and equilibrated. The samples were loaded in 0.3 ml of 0.17M HCl and rinsed twice with 0.4 ml of 0.17M HCl. La and Ce were then eluted and discarded by adding 11 ml of 0.17M HCl before collecting Nd in new beakers by adding 10 ml of 0.17M HCl. Subsequently, 3 ml of 0.4M HCl was added to the columns and discarded. Sm was then collected in new beakers by adding 4 ml of 0.4M HCl. Finally, the columns were then washed thrice with 6M HCl.

Isotopic measurements were performed in a low-resolution mode on a Nu Instruments Plasma II

Mass Collector-ICP-MS instrument at the Analytical Facility of the University of Johannesburg. The instrument is equipped with 16 Faraday detectors and 5 ion counters. Backgrounds were measured by offsetting the magnet away from the measuring position for 30 seconds prior to analyses and the signal was subtracted from the measurements. Automatic peak-centering was performed prior to each measurement. Samples and standards were introduced into the instrument in a 2% HNO_3 solution with a self-aspirating 200 μl/minute tube linked to a Glass Expansion MicroMist U-series nebuliser followed by sample ionization into plasma. Nd measurements were collected for 60 cycles ($\sim$10 minutes) and Sm for 20 cycles ($\sim$5 minutes), achieving an internal precision of $\leq\pm$0.001% (1 standard error: $\sigma_{\bar{x}}$) on fractionation-corrected ^{143}Nd/^{144}Nd ratios. Sr analyses were collected for 60 cycles and Rb for 20 cycles, achieving an internal precision of $\leq\pm$0.001% (1 $\sigma_{\bar{x}}$) on fractionation-corrected ^{87}Sr/^{86}Sr ratios. Washout between samples was carried out using a 2% HNO_3 solution to decrease the signal to background values ($\sim$5 minutes). Data reduction was performed using a customized Microsoft Excel spreadsheet created by the Analytical Facility. The initial Sr and Nd isotopic ratios were calculated to 2.060 Ga using the decay constants of 1.4×10^{-11}/year (^{87}Rb) and 6.54×10^{-12}/year (^{147}Sm).

4 Field, petrographical and geochemical characterization of a layered anorthosite sequence in the Upper Main Zone of the Bushveld Complex

4.1 Introduction

Stratiform or layered anorthosites are present in nearly all layered ultramafic-mafic intrusions (Wager and Brown, 1968; Charlier et al., 2015). Anorthosite layers can range from a few centimeters to meters (e.g. Bushveld Complex: Ashwal, 1993; Cawthorn, 2015), to hundreds of meters (e.g. Stillwater Complex: McCallum et al., 1980; Boudreau, 2016; Wall et al., 2018) in thickness. Anorthosite layers in layered ultramafic-mafic intrusions are commonly found at the uppermost portion of modally graded units (Ashwal, 1993). However, the varied thicknesses, textures and stratigraphic positions of layered anorthosites in layered ultramafic-mafic intrusions have promoted debate as to their origin.

Anorthosites comprise ∼6.5% of the Rustenburg Layered Suite (RLS) of the Bushveld Complex (Ashwal, 1993). Anorthosite layers are rare in the Main (∼6.5%) and overlying Upper (∼4.7%) Zones, but are more prominent in the underlying Upper Critical Zone (∼17%) of the RLS (Ashwal, 1993). Anorthosite layers in the Upper Critical Zone are typically found at the uppermost portion of cyclic-rhythmic units (e.g. from olivine-pyroxene-rich cumulates, through norites, to anorthosites: Cawthorn and Spies (2003)). However, recent contributions by Scoon and Costin (2018) and Mitchell et al. (2019) have questioned the validity of cyclic-rhythmic units in the Critical Zone. In the Main Zone, most anorthositic rocks appear at the top of modally-graded layers and rarely as layers within thick successions of norite or gabbronorite (e.g. Ashwal, 1993; Molyneux, 1974; Mitchell and Manthree, 2002; Cawthorn and Ashwal, 2009).

Anorthosites in the RLS are often poikilitic in texture and are colloquially termed 'mottled' or 'spotted', based on whether pyroxenes are an intercumulus or cumulus phase, respectively. Poikilitic anorthosites containing both cumulus and intercumulus pyroxenes have been referred as 'spottled' anorthosites. Rarely, intercumulus pyroxenes may define dendritic-shaped oikocrysts, referred to as 'dendritic mottles' and have been documented in the anorthosites associated with the UG1 chromitites (Scoon and Costin, 2018). Overall, there have been relatively few studies on the origin of poikilitic anorthosites in the RLS (e.g. de Klerk, 1995; Cawthorn et al., 2002; Cawthorn and Spies, 2003; Mitchell and Manthree, 2002; Cawthorn and Ashwal, 2009; Scoon and Costin, 2018).

Here, I describe a sequence of layered poikilitic anorthosites in the Upper Main Zone, from a road-cut located 5 km NE of the town of Apel, in the eastern lobe of the Bushveld Complex. The sequence is defined by eight m-scale poikilitic anorthosite layers and a thin (∼5 cm) norite layer, which are bounded by typical Main Zone gabbronorites. This sequence of anorthosite layers is the topmost sequence of 2 other layers or sequences mapped by Lesego Platinum Mining Ltd. and MSA (2011). The studied anorthosite layers correspond to leuco-norite, leuco-gabbronorite and anorthosite according to the IUGS rock classification scheme (Streckeisen, 1976), however for simplicity and in adherence with the Bushveld Complex nomenclature, I hereon refer to the layers as anorthosites. I document detailed field relationships together with petrographical, chemical (mineral and whole-rock) and density data and I propose an origin for this sequence of anorthosite layers in the Upper Main Zone of the RLS.

4.2 Field descriptions

The road-cut is composed of gabbronorite, which bounds 8 texturally-distinct (caused by variable pyroxene crystal habits) layers of anorthosite (labeled 1 - 8) and one thin (5 cm) layer of norite (Fig. 4.1). Thicknesses of the anorthosite layers (40 - >900 cm) and the norite layer remain relatively constant along strike for the entirety (∼450 m) of the outcrop (Fig. 4.2). Blocks of lithologically distinct cumulate material are also present in the anorthosite sequence. Contacts between anorthosites and blocks are always sharp (Figs. 4.2).

4.2.1 The anorthosite sequence and host rocks

Basal gabbronorite The basal gabbronorite is a medium-grained, homogeneous, mesocratic rock. Orthopyroxene crystals (15%) in the basal gabbronorite are euhedral, whereas plagioclase (56%) and clinopyroxene (17%) are subhedral. No up-section modal variation was noted. The gabbronorite is highly weathered in a 2 m zone immediately below the contact with anorthosite layer 1.

Anorthosite layer 1 The layer is 80 - 270 cm (each side of the road) in thickness (Fig. 4.2). At the base of the layer is a thin band (10 cm thick) of pure anorthosite (97% plagioclase and 3% chlorite) that grades upwards into poikilitic anorthosite. The remainder of the layer is defined by evenly distributed pyroxene oikocrysts (both clinopyroxene and orthopyroxene) in a matrix of plagioclase laths (1 - 5 mm) (e.g. Figs. 4.3A and B). Plagioclase laths typically have their long axis aligned parallel to the layering plane. Oikocrysts compose ∼20% of the layer, are roughly spherical and are 3 - 8 cm across. Oikocrysts contain abundant (20%) small (1 - 2 mm) plagioclase chadacrysts.

Anorthosite layer 2 Anorthosite layer 2 is 300 - 390 cm in thickness and is characterized by elongated clinopyroxene oikocrysts and subophitic crystals of orthopyroxene (1 - 3 mm, 5%) (e.g. Fig. 4.3B) both evenly distributed in a matrix of plagioclase laths. Plagioclase laths typically have their long axis aligned parallel to the layering plane. Orthopyroxene crystals may contain anhedral inclusions of plagioclase and clinopyroxene (≤5; ≤0.4 mm). Clinopyroxene oikocrysts are oblate, small (0.8 - 3 cm), compose 10% of the rock and contain 2 - 3% of plagioclase and orthopyroxene chadacrysts.

Anorthosite layer 3 This layer is 40 cm in thickness and is texturally similar to layer 1 (Fig. 4.3B). However, the band of pure anorthosite at the base is slightly thinner (5 cm) than that of layer 1.

Anorthosite layer 4 This layer is 110 - 120 cm in thickness and is texturally identical to layer 2 (Fig. 4.3B).

Anorthosite layer 5 The layer is 120 - 180 cm in thickness and is poikilitic, akin to layer 1, but contains numerous (5 - 8), mesocratic and laterally discontinuous norite bands (Fig. 4.3A). Orthopyroxene crystals (0.3 - 1 cm; 30 - 65% abundance) in the bands are subophitic. Clinopyroxene oikocrysts (2%) are also found in the norite bands.

Anorthosite layer 6 This layer is 320 - 450 cm in thickness. The basal part consists of small (3 - 6 cm) spherical pyroxene oikocrysts (∼20%; Fig. 4.3C). The modal proportion of oikocrysts remains constant through the layer. However, their size and shape gradually change. Midway through the

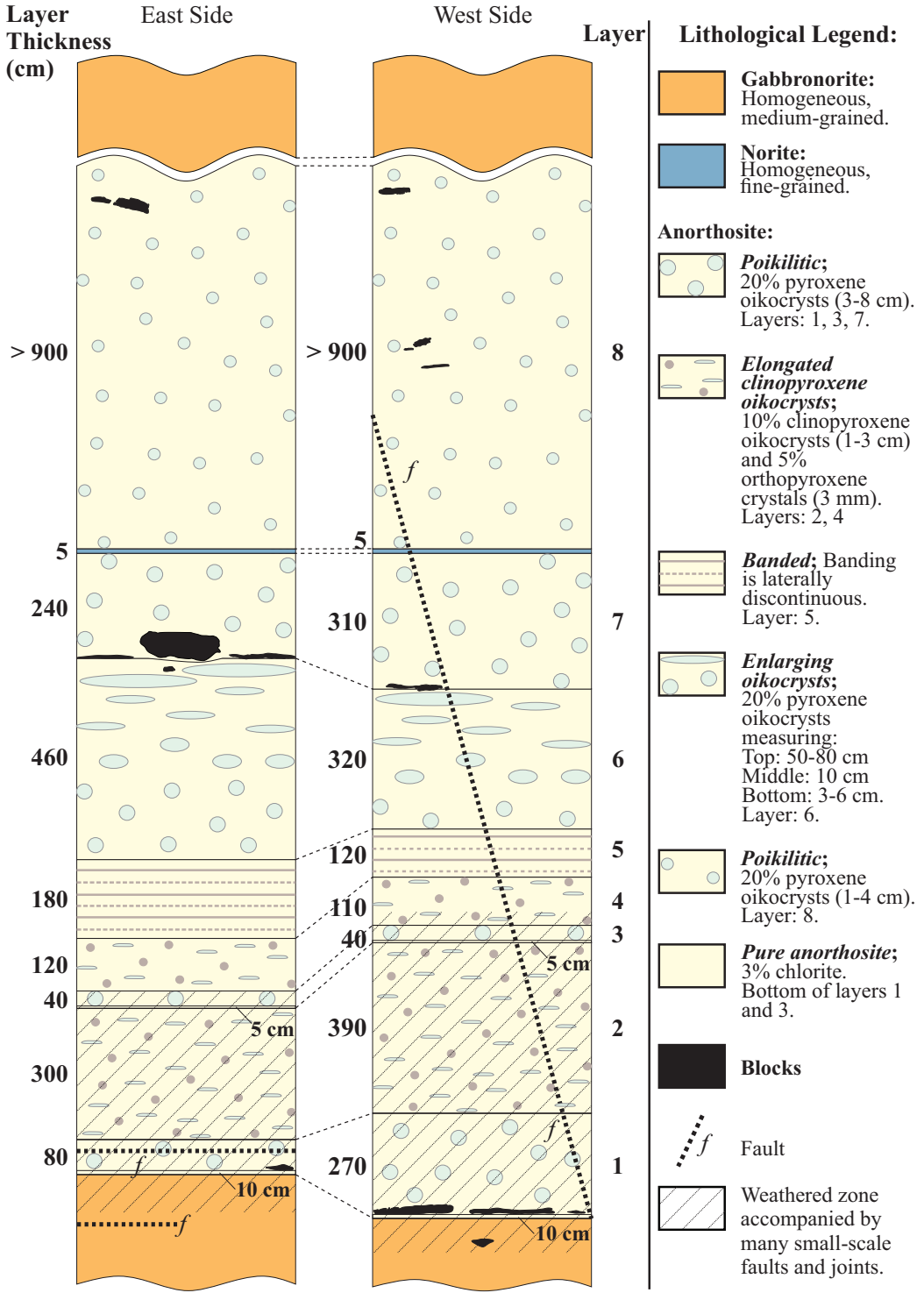

Figure 4.1 – Stratigraphic succession at the road-cut (on each side of the road), showing anorthosite layers 1 to 8, the norite layer and the bounding gabbronorite. Also shown are the locations of the blocks (i.e. cumulate fragments of distinct lithology).

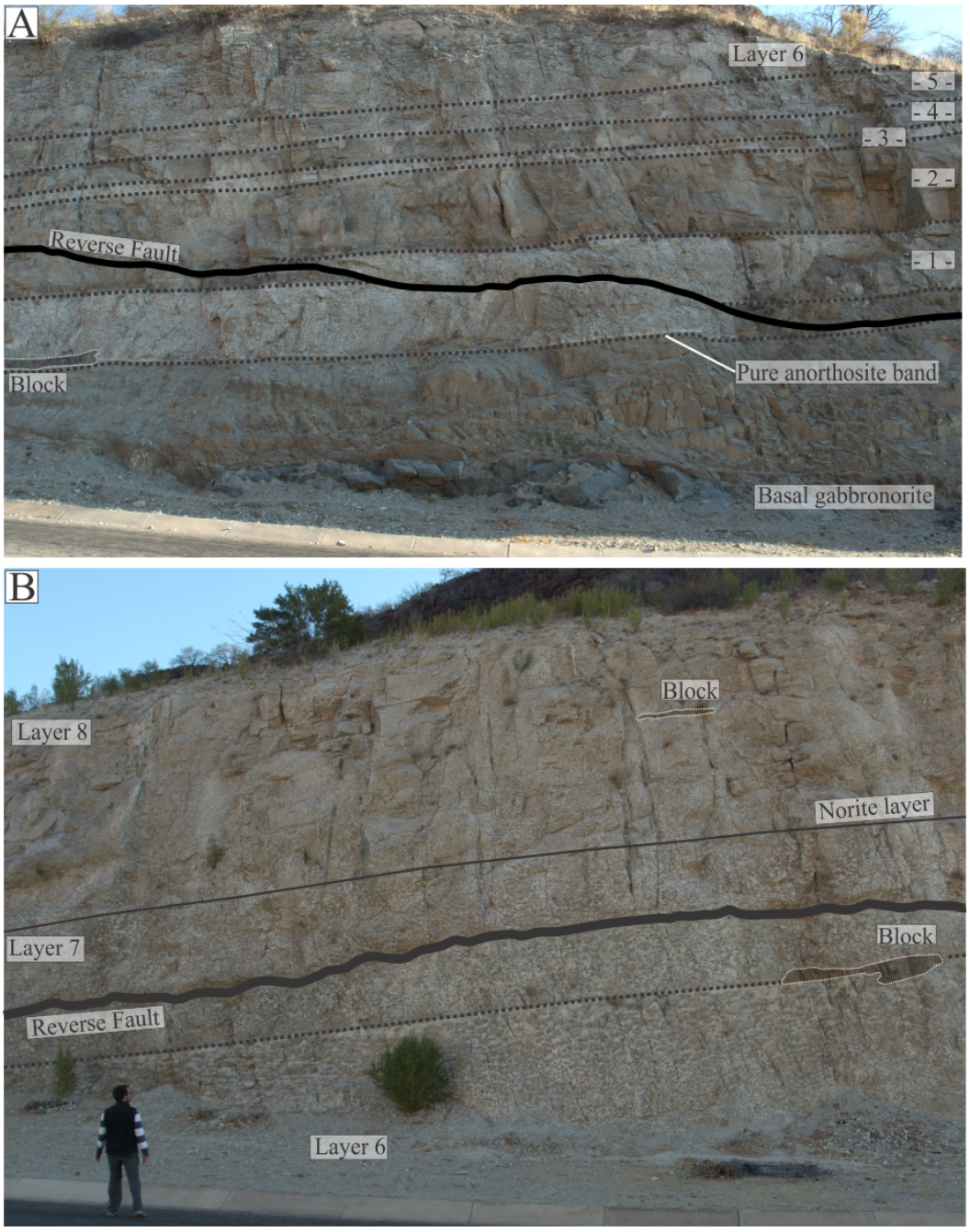

Figure 4.2 – Overview of the west side of the road-cut. Contacts between all layers and lithologies are sharp. **(A)** Anorthosite layers 1 to 6 are present with the layer contacts accentuated by dotted lines. A reverse fault with a lateral displacement of ∼8 m has offset contacts between the layers. Layer 1 is 2.7 m in thickness near the blocks (white dotted line) and has a 10 cm thick band of pure anorthosite at the bottom. **(B)** Top of the anorthosite sequence. Layer 6 (enlarging oikocrysts) lies at the bottom. A reverse fault (continued from subfigure **(A)**) cuts across layer 7 (poikilitic).The thin layer of norite (5 cm), between layers 7 and 8 is accentuated by a black line. Layer 8 (poikilitic) has been truncated by slope regrading and trimming.

layer the oikocryst size range increases to 3 - 15 cm. Smaller-sized (3 - 6 cm) oikocrysts are spherical, but larger ones are oblate (6 - 15 cm wide; 3 - 4 cm thick). Upwards, oikocrysts continue to increase in size, reaching 50 - 80 cm horizontally and 8 - 20 cm vertically. The uppermost 10 - 15 cm of the layer is generally pure anorthosite. The contact with layer 7 is typically highly weathered.

Anorthosite layer 7 This layer is 240 - 310 cm in thickness and is texturally similar to layer 1. The only difference is the lack of a pure anorthosite band at its base.

Norite layer A thin, 1 - 5 cm thick layer of homogeneous, mesocratic, fine-grained ($\leq$1 mm) norite occurs between anorthosite layers 7 and 8 (Figs. 4.1, 4.2B). No up-section modal variation was noted. The norite layer can be traced along strike for the entirety of the road-cut.

Anorthosite layer 8 This layer is between 900 and 1100 cm in thickness. Its thickness was estimated, as the upper section is missing due to slope trimming and regrading (Fig. 4.2B). It is similar to layers 1, 3 and 7, but lacks a pure anorthosite band at its base and contains small sized pyroxene oikocrysts (1 - 4 cm across).

Capping gabbronorite Outcrops on the hill slopes adjacent to the road-cut indicate that gabbronorite is the dominant lithology in the area. The contact between the gabbronorite and the anorthosite layer 8 is not exposed. The capping gabbronorite is mineralogically similar to the basal gabbronorite. The only difference is that orthopyroxene crystals are subhedral and contain numerous, small ($\leq$1 mm) inclusions of plagioclase crystals.

Blocks

The road-cut contains several meter-sized (0.5 - 6 m long), fine-grained ($\leq$1 mm), melanocratic blocks (Figs. 4.1, 4.2). In cross-section most blocks are rectangular, but with rounded margins with their long axis lying in the plane of layering. Blocks are typically found at the base of thicker poikilitic-textured layers (layers: 1, 7 and 8). Blocks are olivine-bearing norites, norites and poikilitic-textured norites, and do not appear to be related to any of the layered lithologies at the road-cut. The contact between a block and its host anorthosite is always sharp. Blocks are in direct contact with plagioclase laths (mm-sized) with their long-axis aligned parallel to the long-axis of the blocks.

4.2.2 Deformation and hydrothermal alteration

The road-cut does not exhibit intense deformation and hydrothermal alteration associated with the formation of the Phosiri and other domes. Nonetheless, the anorthosite sequence may have been thinned (viscous drag) or thickened (fold repetition), by an unknown amount, when compared to elsewhere in the Main Zone (Uken and Watkeys, 1997; Scoon, 2002). The sequence has also been steepened, with layers striking ESE and dipping at 16° SSW (Fig. 2.4). A reverse fault at the road-cut, related to the Wonderkop Fault system, has offset contacts between anorthosite layers by up to 8 m laterally (Fig. 4.2). All lithologies are transected by numerous, small-scale faults and joints aligned perpendicular to the plane of layering, striking NE-SW and dipping between 80 - 90°. Hydrothermal alteration at the road-cut is limited to small-scale faults and joints. Hydrothermal minerals include chlorite, sericite, minor quartz and clinozoisite.

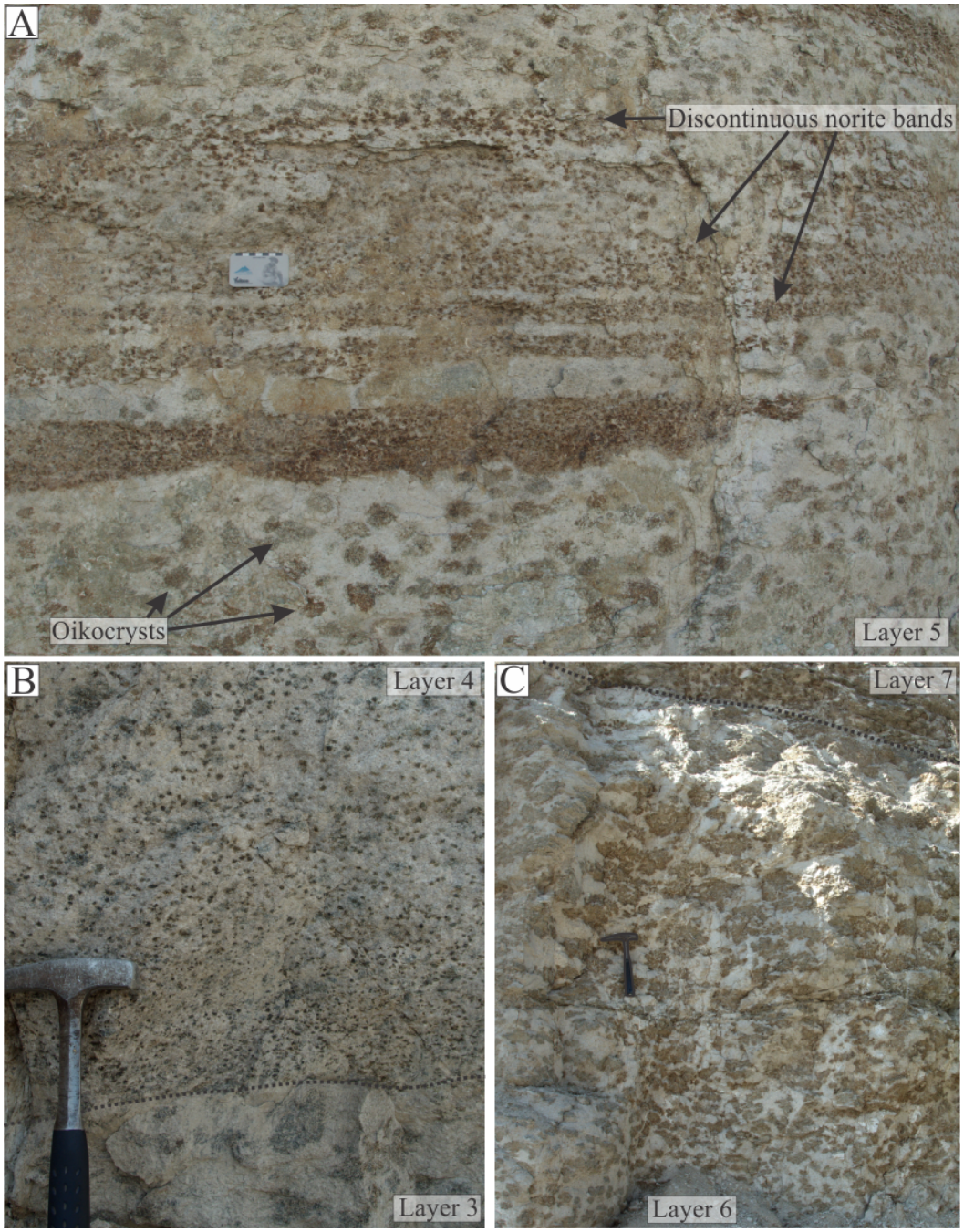

Figure 4.3 – Textural variations found in the anorthosite sequence. Photographs taken on the east side of the road-cut. **(A)** Layer 5 is poikilitic with numerous, laterally discontinuous norite bands that contain subophitic orthopyroxene crystals (30 - 65 modal%). **(B)** In layer 4, dark-green oikocrysts of clinopyroxene are elongated (0.8 - 3 cm) and evenly distributed amongst subophitic, dark-brown crystals of orthopyroxene. The contact between layers 3 and 4 is sharp (dotted line). Layer 3 is poikilitic. **(C)** The enlarging oikocrystic texture found in layer 6. The base of the layer has small (3 - 6 cm) spherical-shaped pyroxene oikocrysts. Oikocrysts gradually become larger (50 - 80 cm) and oblate-shaped towards the top. The contact between layers 6 and 7 is sharp but weathered (dotted line).

4.3 Petrography and mineral chemistry

4.3.1 Anorthosite layers

Plagioclase Euhedral-subhedral (0.2 - 5 mm) primocrystic laths of plagioclase (86 modal%) are identical in all anorthosite layers including at the contacts with the blocks and in the pure anorthosite bands. The laths define a moderate to strong foliation, creating a parting plane aligned parallel to the plane of layering (Fig. 4.4A). Rarely, the foliation may be inclined to an angle $\leq 60^{\circ}$. This inclination is prevalent around the tail edges of the blocks. Euhedral plagioclase chadacrysts in oikocrysts are smaller (by 0.2 - 0.4 mm on average) compared to plagioclase laths in the matrix and may occasionally define a weak foliation that is parallel to the foliation defined by the plagioclase laths (Fig. 4.4B). A few crystals are bent, to an angle $\leq 8^{\circ}$, resulting in a slight undulose extinction (Fig. 4.5A). Plagioclase has an average composition of $An_{72.5}$ (anorthite; atomic 100×Ca/(Ca+Na+K)) with a 1σ of 2.6 mol% for the entire anorthosite sequence. All crystals are slightly compositionally zoned. From core to mantle, crystals are normally zoned (average reduction of $\sim$1 mol% An). Rims are very thin (20 - 70 μm) (absent in chadacrysts) and are reversely zoned (Fig. 4.5), with an average increase of 2 mol% An (Tables 4.1, 4.2). Rarely, anhedral inclusions (37 - 300 μm) of albite ($Ab_{97.1\pm0.5}$) and orthoclase ($Or_{96.0\pm0.5}$) are found at the core of the euhedral plagioclase laths.

Overgrowths on primocrystic plagioclase laths are rare, but a good example is preserved at the base of layer 7 (Fig. 4.5B). These overgrowths are irregular in shape, are intergrown with interstitial quartz, have thicknesses between 12 and 130 μm and have an average composition of $An_{68.4}$ (1σ of 3.4 mol%). They are also enriched in SrO and depleted in TiO_2, FeO, MgO and K_2O compared to the rest of the laths (Table 4.2).

Over a thickness of 1100 cm (layers 3 - 7), the An-content of plagioclase crystal cores decreases by 2.5 mol% upwards (Fig. 4.6). At a sampled layer boundary (layers 3 and 4), the An-content of plagioclase increases abruptly by an average of 3.3 mol% An over 2 cm. Layer contact An-content variation is also greater and more abrupt than stratigraphic An-content changes within an individual layer (averaged core An-content changes of 0.5 - 3.8 mol% An at layer contacts over a less than a decimeter and 0.1 - 2.3 mol% An within layers, on the order of meters). In both cases, the changes across layers are consistently unaccounted for by the expanded (2σ) uncertainties of the stratigraphic An-content variation. Thus, the sharp changes across layers are unlikely to be associated with intra-layer An-content changes. No significant lateral change in composition was found within a sampled layer. The linearly-projected and measured values overlap. Intra-layer An-content of crystal cores (layers 4 - 7) typically increases by 0.2 - 2.0 mol% An upwards. Thinner layers also record the highest rate of change in An-content stratigraphically. Compared to other samples acquired at a single height, analyses within the pure anorthosite band at the bottom of layer 1 show the largest variance in An-content (15.9 mol% An).

Pyroxenes Interstitial orthopyroxene and clinopyroxene account for, on average, 7 and 4 modal% of each layer, respectively. Both occur as large oikocrysts (Figs. 4.4 B, 4.7). However, orthopyroxene crystals in layers 2, 4 and 5 (including within the discontinuous norite bands) are subophitic (primocrysts), enclosing few ($\leq$5) and significantly smaller (0.08 - 0.4 mm), typically equant plagioclase inclusions (Fig. 4.4C, D). Locally, clinopyroxene has exsolution lamellae and/or blebs of orthopyroxene, and orthopyroxene has blebs of clinopyroxene. Only a single crystal of inverted pigeonite (in layer 8), with numerous, regularly spaced, exsolution lamellae of clinopyroxene was observed.

Pyroxene oikocrysts are typically an amalgamation of several smaller-sized oikocrysts, which

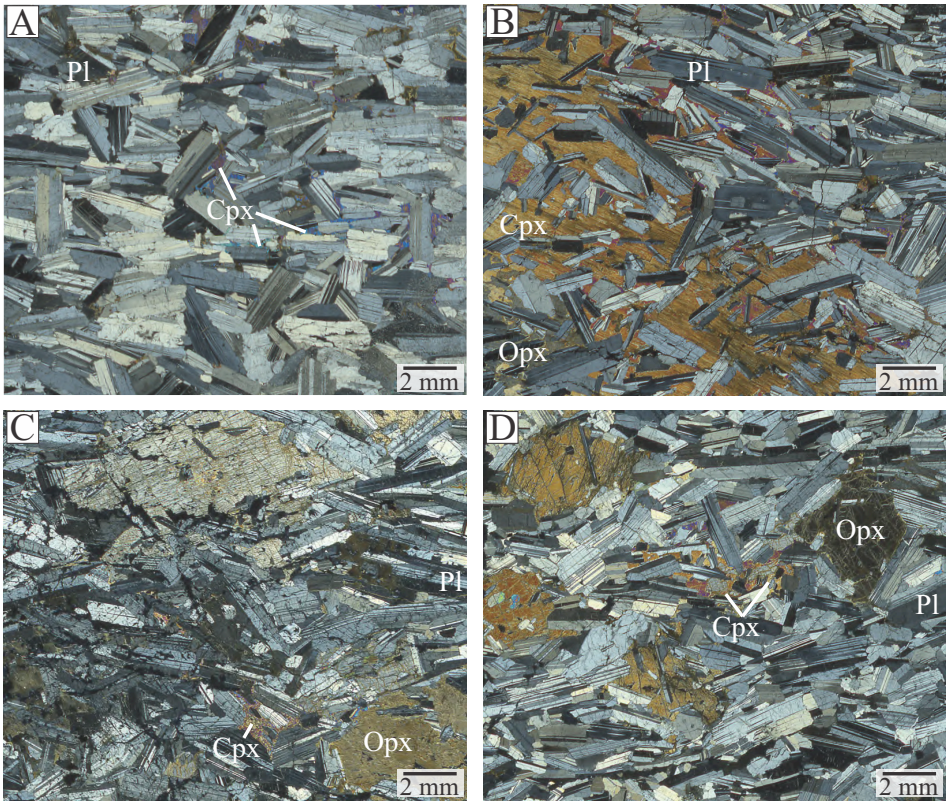

Figure 4.4 – Cross-polarized thin section scans of anorthosites from the sequence. All thin section scans are arranged with the top direction pointing upwards. **(A)** Plagioclase laths (Pl) define a moderate to strong foliation aligned parallel to the plane of layering. Clinopyroxene (Cpx) is interstitial. Specimen from layer 7. **(B)** Outcrop-scale oikocryst is composed of both clinopyroxene and orthopyroxene (Opx). Plagioclase chadacrysts define a weak foliation aligned in the same sense as plagioclase laths (horizontal; top right corner) in the anorthosite matrix. Specimen from layer 6. **(C)** Plagioclase and orthopyroxene crystals in the norite band from layer 5. Orthopyroxene crystals are subophitic and clinopyroxene is interstitial. **(D)** Subophitic orthopyroxene and interstitial clinopyroxene crystals from layer 4. Plagioclase laths define a moderate foliation.

have a slightly differing chemistry and crystallographic orientation (Fig. 4.7). Oikicrysts are rarely composed of large single crystals of clinopyroxene and orthopyroxene (Fig. 4.4B). Altogether, the composite oikocryst decreases in Mg# ($100\times$(Mg/(Mg+Fe$_T$); $\sim$4 mol%) from core to rim (Fig. 4.7C).

The average composition of orthopyroxene is enstatite $(En)_{60.7}$, ferrosilite $(Fs)_{36.8}$, wollastonite $(Wo)_{2.5}$ mol% (1σ En: 4.1, Fs: 4.6, Wo: 1.8 mol%) and clinopyroxene averages $En_{39.3}$, $Fs_{15.0}$, $Wo_{45.7}$ mol% (1σ En: 1.5, Fs: 1.5, Wo: 1.1 mol%). Over the analyzed stratigraphy of 1110 cm (layers 3 - 7), the Mg# decreases upwards by 13.0 mol% for orthopyroxene and 8.6 mol% for clinopyroxene (Fig. 4.6). At a sampled layer boundary (layers 3 and 4), the Mg# of clinopyroxene changes abruptly (by 1.3 mol% on average). The change is outside of the expanded (2σ) uncertainties of the stratigraphic Mg# variation. The layer contact Mg# variation is also greater and more abrupt than intra-layer changes (average Mg# change of 0.7 mol% for layer 4). No significant lateral change in orthopyroxene and clinopyroxene composition was found within a sampled layer. The linearly-projected and measured values overlap (Fig. 4.6). The intra-layer Mg# for layer 4 increases by 0.7 mol% upwards.

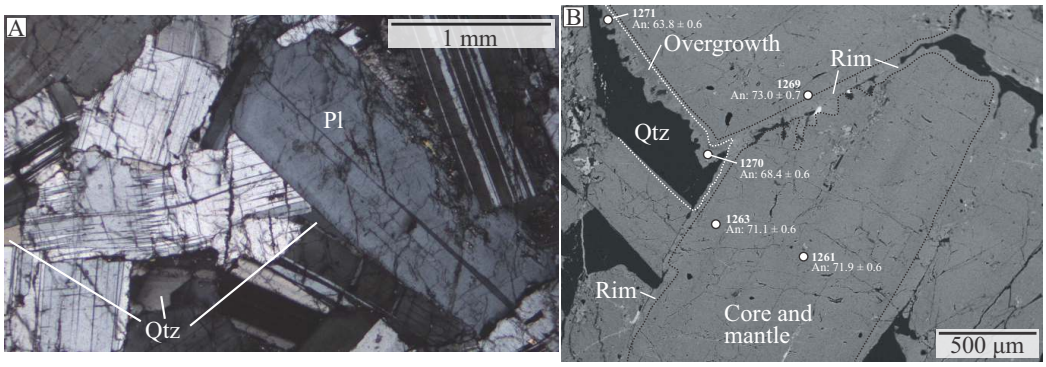

Figure 4.5 – Euhedral primocrystic plagioclase laths in anorthositic rocks. **(A)** Bent (center left) and zoned (center right) plagioclase laths with interstitial quartz (Qtz). Plagioclase laths are normally zoned from core to mantle, with a thin (darker) reversely zoned rim. Specimen from layer 1. **(B)** Electron back-scatter image of sodic plagioclase overgrowth on zoned plagioclase laths. Boundaries between the different compositional zones (An-contents in mol%) have been traced with dotted lines. The irregular boundaries of the sodic plagioclase overgrowths are intergrown with quartz, suggesting that they co-crystallized from an evolved, trapped interstitial residual liquid. Specimen from bottom of layer 7.

Accessory minerals Accessory minerals include: quartz (∼2%), magnesiohornblende (∼0.5%), magnetite (∼0.5%), phlogopite (∼0.5%), clinochlore and ilmenite (>0.5%). Quartz crystals (0.07 - 1.2 mm across) are interstitial, forming small (1 - 3.5 mm) interconnected networks (Fig 4.4E). Strongly pleochroic and zoned magnesiohornblende mantles (0.02 - 0.34 mm) pyroxenes and is intergrown with quartz (when present), indicating that magnesiohornblende and quartz co-crystallized. Amphibole zoning is characterized by a gradual decrease in Si and Mg, and an increase in Al, Fe, Na and K progressing away from the contact with the pyroxene. Magnetite crystals (0.03 - 0.48 mm) are commonly found as inclusions in pyroxenes, magnesiohornblende and/or phlogopite, and rarely as an interstitial phase. Magnetite commonly contains small (20 - 100 μm) oxy-exsolution lamellaes of ilmenite. Phlogopite and minor amounts of clinochlore partially mantle magnesiohornblende.

4.3.2 Norite layer

The norite layer is composed of very small (0.02 - 1 mm), anhedral crystals of cumulus plagioclase (66 modal%) and orthopyroxene (30%), with minor amounts of anhedral intercumulus clinopyroxene (3%) and magnetite (1%) (Fig. 4.8A). Plagioclase crystals have an average of $An_{77.2}$ (Carlsbad-albite method and CIPW norm) and orthopyroxene crystals have an average of $En_{70.0}$ (2V angle and birefringence). Clinopyroxene partially mantles (0.02 - 0.2 mm thick) orthopyroxene.

4.3.3 Gabbronorite

Euhedral cumulus plagioclase, orthopyroxene and subhedral clinopyroxene crystals with minor interstitial quartz (1%) and trace amounts of magnesiohornblende, phlogopite, magnetite crystals define the gabbronorite. Plagioclase crystals (0.2 - 4 mm) are tabular-shaped and define a good foliation (Fig. 4.8B). Locally, plagioclase crystals are bent, to an angle $\leq 8°$. Plagioclase crystals have an average composition of $An_{72.9}$ with a 1σ of 2.5 mol%. All crystals have a thin (20 - 75 μm), reversely zoned rim (average core: $An_{72.2}$ and rim: $An_{74.9}$; Fig. 4.6). Clinopyroxene ($En_{42.0}$, $Fs_{12.5}$, $Wo_{45.5}$ mol%; 1σ En: 0.5, Fs: 0.3, Wo: 0.6 mol%) crystals are elongated (0.5 - 3.4 mm) and commonly contain exsolution lamellae of orthopyroxene. Orthopyroxene ($En_{68.0}$, $Fs_{30.1}$, $Wo_{1.9}$ mol%; 1σ En: 1.1,

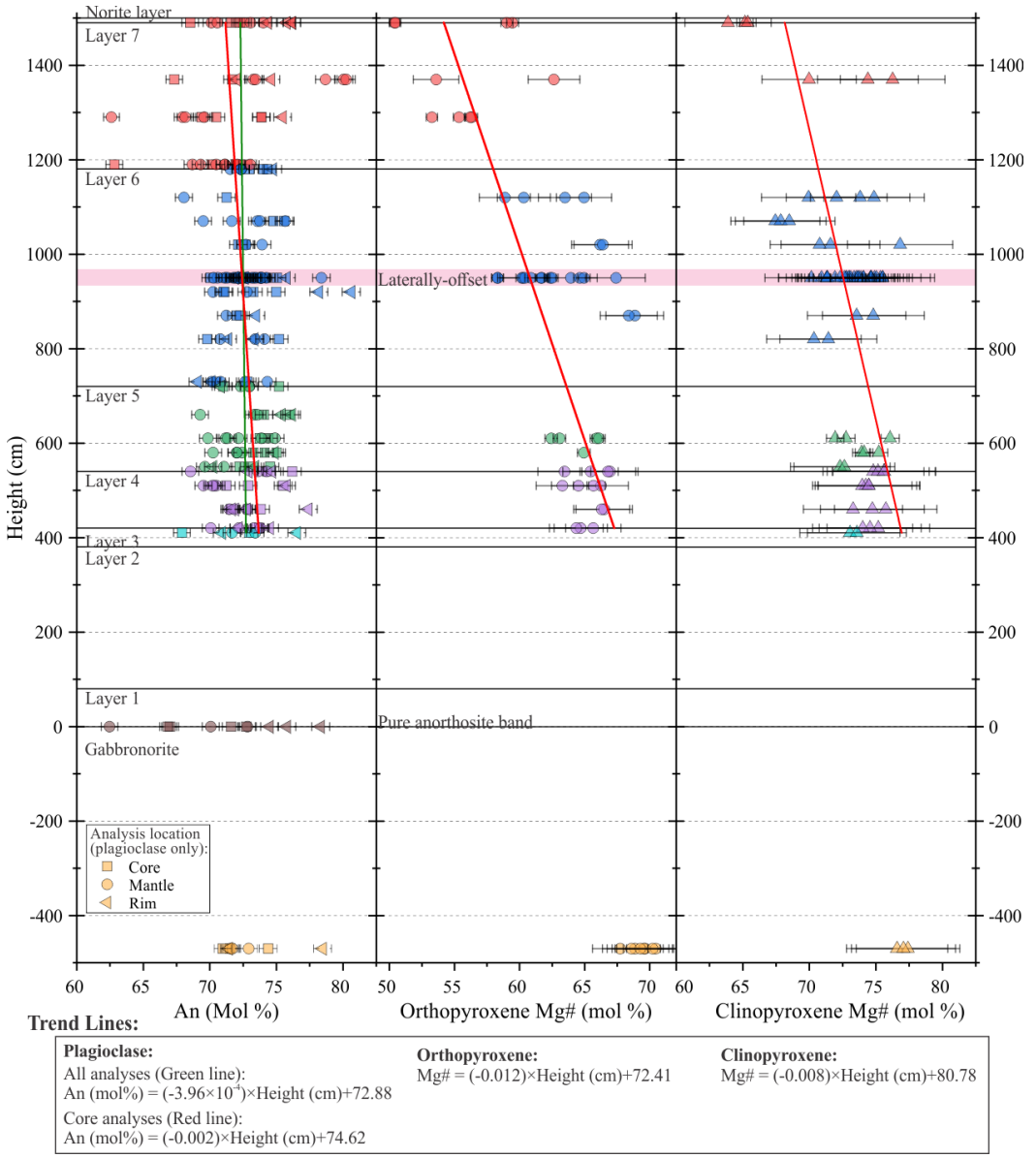

Figure 4.6 – Stratigraphic compositional variations of plagioclase, orthopyroxene and clinopyroxene for select anorthosite layers. Pyroxenes and plagioclase record an overall decrease in Mg# and An-content upwards. Equations for line of best fit (red or green lines) are given at the bottom. The pure anorthosite band (base of layer 1) was not considered for the line of best fit as it is texturally distinct and shows a large compositional range compared to the rest of the sequence. Results from the laterally-offset sample are highlighted in pink.

Fs: 0.9, Wo: 1.1 mol%) appears as large (1 - 4 mm), unzoned crystals with small (0.06 - 0.2 mm), partly rounded inclusions of plagioclase. Interstitial quartz crystals (0.2 - 0.4 mm) define small interconnected networks. Magnesiohornblende crystals partially mantle pyroxenes and are not strongly zoned. Phlogopite partially mantles magnesiohornblende. Subhedral magnetite crystals (0.002 - 0.2 mm) are commonly found as inclusions in pyroxenes and magnesiohornblende.

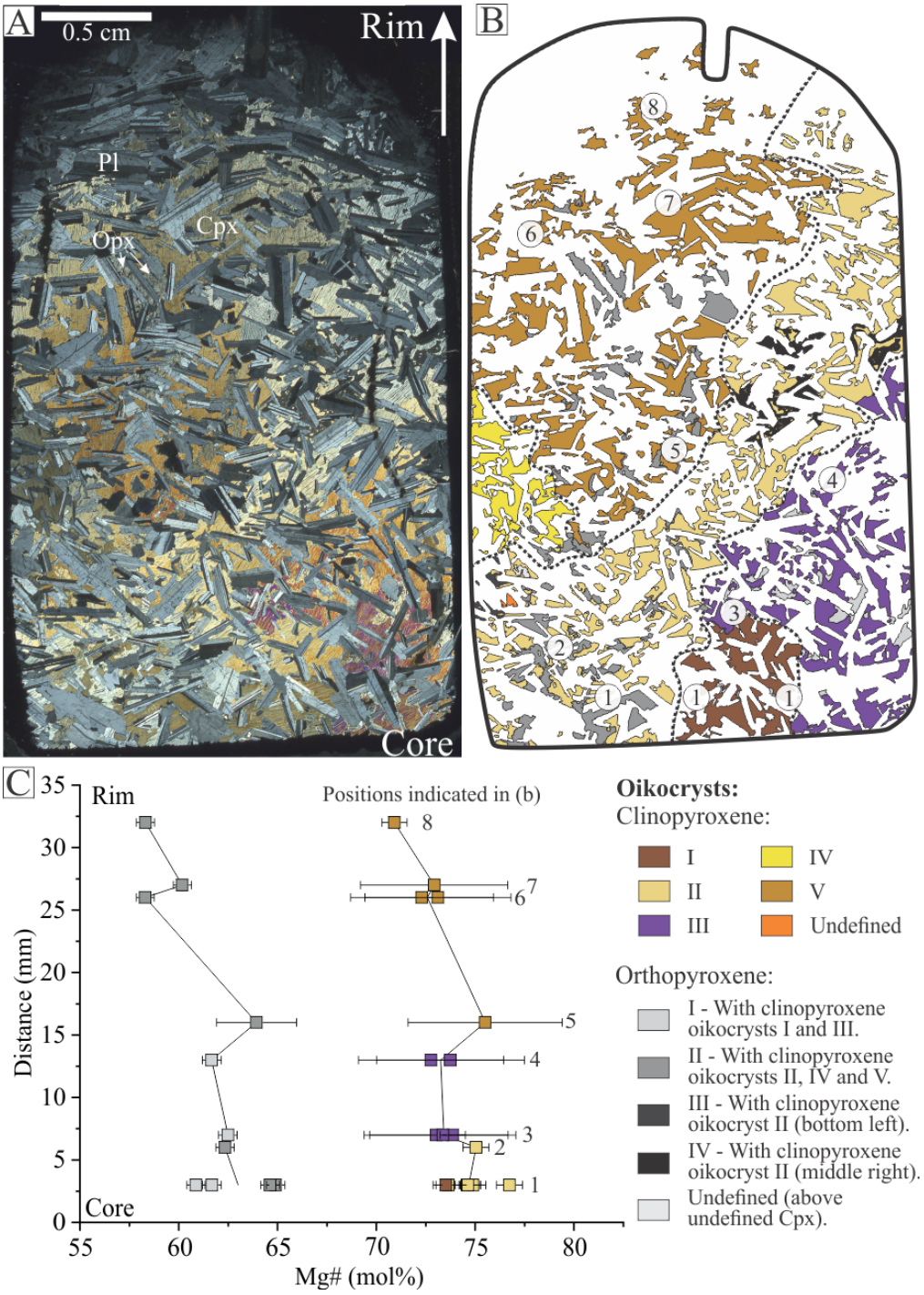

Figure 4.7 – Petrography and mineral chemistry of a composite oikocryst from layer 6. **(A)** Cross-polarized thin section scan of a large oikocryst from core (bottom) to rim (top). The outcrop-scale oikocryst is composed of an amalgamation of smaller-sized clinopyroxene and orthopyroxene (Cpx and Opx) oikocrysts. **(B)** Digitized version of **A** showing the arrangement of the smaller-sized oikocrysts. Individual oikocrysts were categorized based on their distinct extinction angle and birefringence. Plagioclase laths and chadacrysts are in white. **(C)** Molar Mg# of pyroxenes (both clinopyroxene and orthopyroxene) within the oikocryst. The Mg# of both clinopyroxene and orthopyroxene decreases by 4 mol% from core to rim. Pyroxene Mg#s vary between individual oikocrysts.

Table 4.1 – Representative mineral analyses (in wt%) from anorthosite layer 7 (for direct comparison). The complete set of data and their respective errors are presented in Appendix D.

Mineral	Plagioclase			Pyroxenes			Hornblende		Clinochlore	
Number	1290	1292	1291		1299	1306		1311		1308
	Core	Mantle	Rim		Cpx	Opx				
SiO_2	50.35	51.26	49.80	**SiO_2**	52.36	52.76	**SiO_2**	50.14	**SiO_2**	31.97
TiO_2	0.02	0.01	0.00	**TiO_2**	0.22	0.22	**TiO_2**	0.25	**TiO_2**	1.50
Al_2O_3	31.60	31.54	32.01	**Al_2O_3**	1.28	0.66	**Al_2O_3**	6.10	**Al_2O_3**	16.15
FeO	0.32	0.27	0.30	**V_2O_3**	0.07	0.03	**V_2O_3**	0.03	**V_2O_3**	0.06
MnO	0.01	0.01	0.00	**Cr_2O_3**	0.00	0.03	**Cr_2O_3**	0.02	**Cr_2O_3**	0.01
MgO	0.01	0.01	0.01	**FeO**	11.72	24.53	**FeO**	12.59	**FeO**	17.89
CaO	14.68	14.36	15.05	**NiO**	0.01	0.03	**NiO**	0.05	**NiO**	0.10
SrO	0.09	0.07	0.07	**MnO**	0.32	0.46	**MnO**	0.19	**MnO**	0.15
BaO	0.00	0.01	0.02	**MgO**	12.30	20.18	**MgO**	15.25	**MgO**	15.75
Na_2O	3.02	3.20	2.79	**CaO**	21.65	1.17	**CaO**	11.39	**CaO**	1.80
K_2O	0.14	0.17	0.13	**Na_2O**	0.23	0.00	**Na_2O**	0.54	**Na_2O**	0.03
Sum	100.25	100.91	100.17	**Sum**	100.16	100.06	**K_2O**	0.43	**K_2O**	0.25
							Cl	0.08	**Cl**	0.06
	End-members (mol%)						**F**	0.14	**F**	0.05
An	72.28	70.56	74.35	**En**	35.72	58.03	**H_2O**	1.97	**H_2O**	11.58
Ab	26.88	28.44	24.90	**Fs**	19.09	39.56	**OH=Cl**	0.02	**OH=F**	0.02
Or	0.84	1.01	0.75	**Wo**	45.19	2.41	**OH=F**	0.06	**OH=Cl**	0.01
				Mg#	65.16	59.46	**Sum**	97.22	**Sum**	85.78
									End-members (mol%)	
									Ccl	60.87
									Chm	38.80
									Pnn	0.33

Mineral abbreviations of Whitney and Evans (2010) with exception of Pnn = Pennanite.

Table 4.2 – Average core, mantle, rim and overgrowth compositions for the plagioclase laths for the entire anorthosite sequence. The complete set of data and their respective errors are presented in Appendix D.

Zones	n	SiO_2	TiO_2	FeO	MgO	CaO	Na_2O	K_2O	SrO	An-content	
		wt%	wt%	wt%	wt%	wt%	wt%	wt%	ppm	mol%	1σ
Core	68	49.45	0.019	0.368	0.017	14.840	2.969	0.158	425	72.8	1.9
Mantle	102	49.59	0.014	0.359	0.019	14.717	3.036	0.162	383	72.1	2.3
Rim	35	48.97	0.005	0.356	0.011	15.113	2.853	0.141	431	73.9	2.5
Overgrowth	4	51.04	0.000	0.304	0.004	14.024	3.518	0.111	656	68.4	3.4

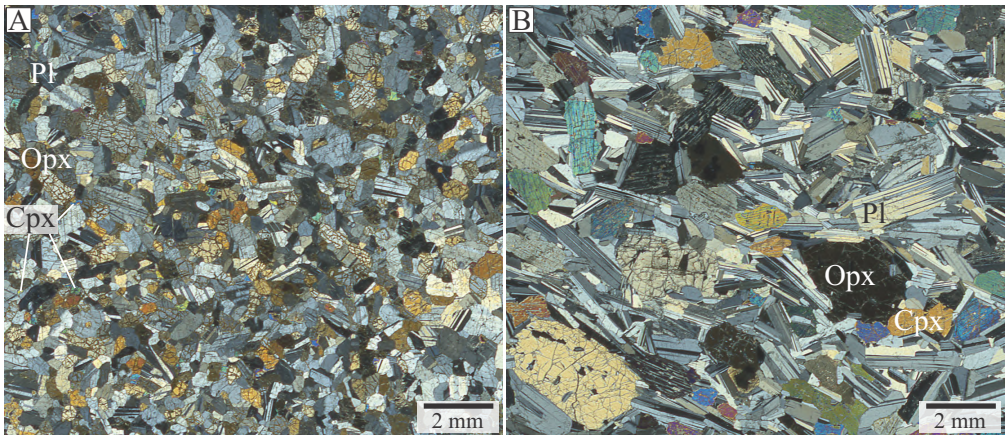

Figure 4.8 – Cross-polarized thin section scans of the norite layer between layers 7 and 8, and the basal gabbronorite. **(A)** Norite layer; composed of equidimensional plagioclase (Pl) and orthopyroxene (Opx), with minor amounts of clinopyroxene (Cpx). **(B)** Basal gabbronorite; composed of euhedral laths of plagioclase, orthopyroxene and clinopyroxene crystals.

4.4 Density

Rock densities average 2.73 g/cm^3 (1σ 0.03 g/cm^3) for anorthosite, 2.95 g/cm^3 (1σ 0.00 g/cm^3) for gabbronorite and 2.97 g/cm^3 (1σ 0.12 g/cm^3) for the norite layer (Fig. 4.9). My measurements

are in agreement with anorthosite (2.7 g/cm^3) and gabbronorite (3.0 g/cm^3) densities measured by Ashwal et al. (2005) and Cawthorn and Ashwal (2009). Over the measured stratigraphy of 2220 cm, anorthosites in the sequence increase by 0.11 g/cm^3 upwards (Fig. 4.9). Layer contact density variations are greater and more abrupt than intra-layer changes (layer contacts: 0.007 - 0.07 g/cm^3 and intra-layer: 0.005 - 0.05 g/cm^3). Changes at layer contacts are outside of the expanded (2σ) uncertainties, which supports the field, textural and chemical classification of multiple distinct anorthosite layers. No significant lateral change in density was observed within a sampled layer.

4.5 Bulk rock chemistry

4.5.1 Major elements

Whole-rock major element oxide data shows that the layers of the anorthosite sequence are chemically similar to each other. Over an analyzed thickness of 2260 cm, the layers decrease in TiO_2 from 0.12 $\pm$ 0.00 wt% to 0.09 $\pm$ 0.00 wt%, and Mg# from 64.0 $\pm$ 0.47 mol% to 59.32 $\pm$ 0.43 wt% upwards (Fig. 4.10). Both Al_2O_3 and K_2O increase, by 1.94 $\pm$ 0.89 wt% and 0.06 $\pm$ 0.01 wt% respectively, upwards within the analyzed stratigraphy. All trends are gradual with no abrupt changes/inflections between individual layers. No significant lateral change in composition is found within a sampled layer. The linearly-projected (for the layer) and measured values overlap.

Both the host gabbronorite and norite layer are chemically distinct from the anorthosite layers in that they are more enriched in TiO_2 (by 0.06 wt% gabbronorite only) and Mg# (by 12.52 mol% gabbronorite; 5.70 mol% norite), but are lower in Al_2O_3 (by 9.09 wt% gabbronorite; 7.02 wt% norite) and K_2O (by 0.04 wt% gabbronorite; 0.13 wt% norite) (Table 4.3; Fig. 4.10).

4.5.2 Incompatible and trace elements

In both chondrite-normalized incompatible and rare earth element diagrams (REE) (Fig. 4.11), the anorthosite, gabbronorite and norite patterns are similar. Incompatible and REE patterns for anorthosites lack any systematic variation with regards to stratigraphic height. Furthermore, the large, positive Eu-anomalies in the layers are consistent with accumulation of plagioclase crystals (Fig. 4.11B).

In comparison with the anorthosites, the gabbronorite and norite are enriched in heavy rare earth elements (HREE). Both the gabbronorite and the norite have positive Eu-anomalies which are consistent with accumulation of plagioclase crystals, although the positive Eu-anomaly is less pronounced for the gabbronorite.

4.6 Discussion

4.6.1 Stratigraphic position of the anorthosite sequence

There is doubt with regards to the stratigraphic position of the anorthosite sequence in this study. This is because the RLS near the Phosiri Dome has been steepened, thinned or thickened (Uken and Watkeys, 1997; Scoon, 2002). Regional-scale mapping by Molyneux (2008) and Lesego Platinum Mining Ltd. and MSA (2011) determined that the anorthosite belongs to the Upper Main Zone, stratigraphically above two other anorthosite layers or sequences. My stratigraphic depth calculations (using trigonometry from several field measurements) places the anorthosite sequence at the road-cut $\sim$166 m below the base of the Upper Zone. The anorthosite sequence at the road-cut could

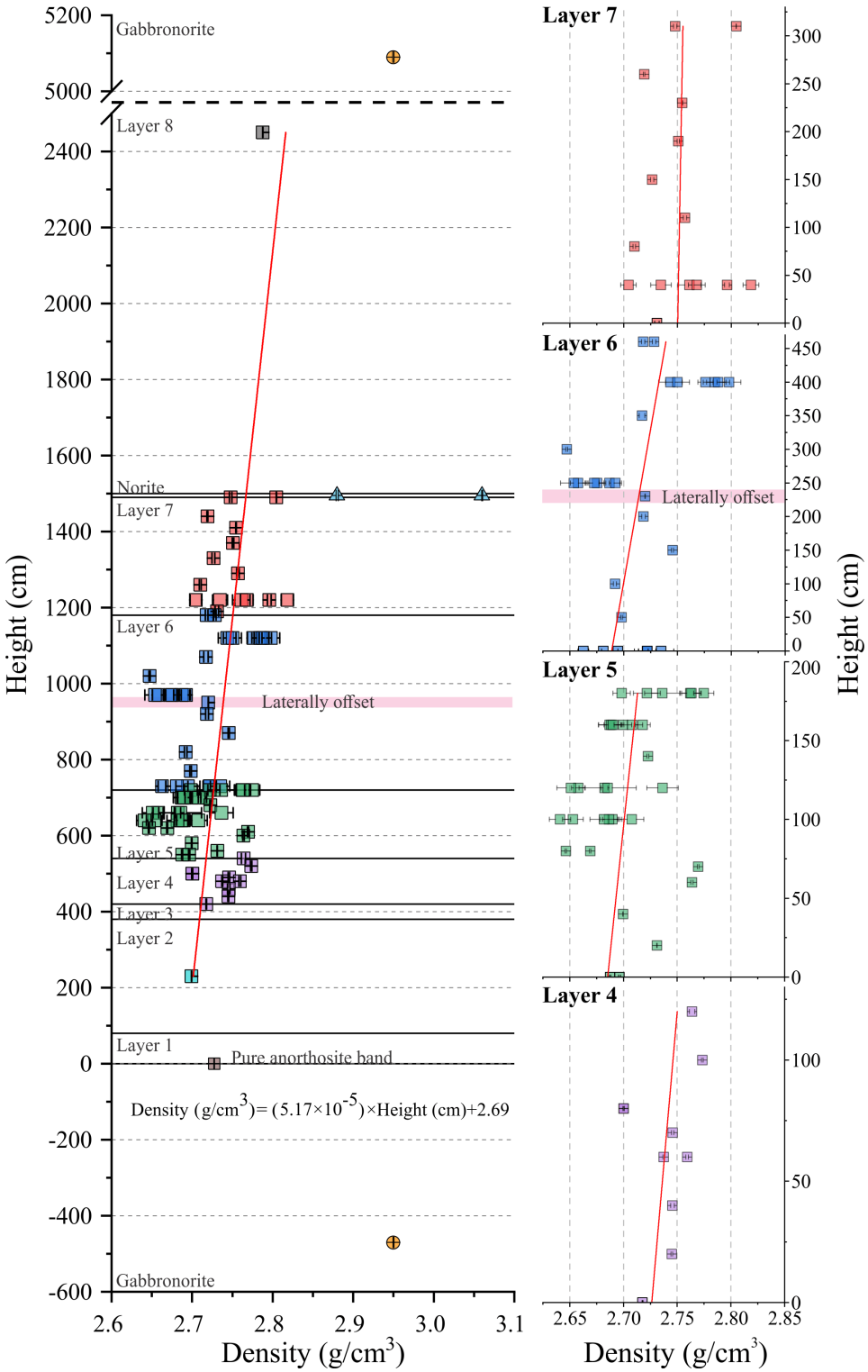

Figure 4.9 – Measured densities of anorthosite, gabbronorite and norite at the road-cut. Overall, the anorthosite layers increase in density upwards. The equation for the line of best fit (anorthosite layers only; red) is given. Results from the laterally-offset sample are highlighted in pink. Anorthosite layers 4 - 7 also record an increase in density upwards. Lines of best fit are presented (red). The contact between layer 8 and the capping gabbronorite is estimated (dashed line).

Table 4.3 – Average whole-rock chemistry. The complete set of data and their respective errors is presented in Appendix E.

Rock	**Anorthosite**						**Gabbronorite**		**Norite**
	Layer 8	**Layer 7**	**Layer 6**	**Layer 5**	**Layer 4**	**Layer 2**	**Top**	**Bottom**	
n	**1**	**5**	**7**	**5**	**6**	**1**	**1**	**2**	**1**
SiO_2 (wt%)	50.76	49.25	49.97	50.19	50.23	49.84	51.63	50.91	50.39
TiO_2	0.09	0.17	0.11	0.14	0.12	0.12	0.21	0.18	0.12
Al_2O_3	28.07	25.92	28.20	26.96	25.84	26.18	17.40	18.20	19.99
$Fe_2O_{3(T)}$	2.52	3.12	2.05	2.78	3.74	3.28	7.38	6.34	8.76
MnO	0.04	0.05	0.04	0.05	0.07	0.06	0.15	0.14	0.15
MgO	1.67	1.99	1.32	2.11	3.36	2.65	7.87	8.39	7.79
CaO	14.03	13.36	13.59	13.29	13.03	13.93	12.94	13.52	10.58
Na_2O	2.77	2.60	2.63	2.49	2.41	2.49	2.04	1.71	1.85
K_2O	0.20	0.28	0.24	0.26	0.18	0.15	0.20	0.20	0.10
P_2O_5	0.01	0.03	0.02	0.03	0.02	0.01	0.04	0.02	0.01
LOI	0.12	1.35	1.39	1.52	0.74	1.23	0.21	0.42	0.21
Total	100.39	98.15	99.61	99.83	99.78	100.05	100.10	100.11	100.09
n	**1**	**1**	**2**		**2**	**1**		**1**	**1**
V (ppm)	28.00	69.00	28.00		44.50	42.00		115.00	70.00
Cr	20.00	7.00	12.50		33.50	27.00		176.00	51.00
Zn	19.00	18.00	17.00		30.00	23.00		42.00	58.00
Rb	2.44	10.33	4.89		3.46	1.65		3.45	0.60
Sr	404.18	449.75	390.20		355.56	350.68		236.73	267.39
Y	1.97	3.58	2.52		2.91	2.65		5.72	2.93
Zr	7.40	26.80	11.65		13.70	10.10		12.40	4.80
Nb	0.37	2.24	0.69		0.65	0.43		0.40	0.28
Ba	79.80	141.50	95.00		79.70	70.20		68.60	53.00
La	2.47	4.45	4.15		3.42	3.30		4.19	1.95
Ce	4.29	8.52	7.60		6.35	5.97		8.19	3.53
Pr	0.50	0.98	0.85		0.72	0.69		0.86	0.41
Nd	2.02	3.89	3.18		2.80	2.71		3.70	1.69
Sm	0.35	0.79	0.57		0.55	0.52		0.88	0.35
Eu	0.43	0.46	0.45		0.46	0.45		0.38	0.33
Gd	0.35	0.75	0.51		0.52	0.48		0.93	0.41
Tb	0.06	0.12	0.08		0.10	0.08		0.17	0.08
Dy	0.33	0.66	0.47		0.52	0.49		1.02	0.46
Ho	0.08	0.14	0.10		0.11	0.10		0.22	0.11
Er	0.26	0.40	0.29		0.35	0.30		0.68	0.38
Tm	0.03	0.05	0.04		0.05	0.04		0.09	0.06
Yb	0.20	0.35	0.23		0.32	0.30		0.62	0.41
Lu	0.03	0.05	0.04		0.06	0.04		0.10	0.06
Hf	0.21	0.94	0.32		0.37	0.28		0.36	0.17
Ta	0.03	0.13	0.05		0.05	0.04		0.04	0.03
Pb	1.60	2.10	2.55		3.35	2.90		1.80	1.90
Th	0.29	0.84	0.64		0.64	0.48		0.38	0.15
U	0.06	0.17	0.07		0.11	0.07		0.10	0.03
$\sum$REE	11.36	21.74	18.52		16.33	15.47		22.03	10.23
$(La/Lu)_{cn}$	8.68	9.39	12.60		6.55	8.70		4.42	3.43
$(Eu/Eu^*)_{cn}$	3.77	1.83	2.68		2.67	2.76		1.29	2.67
La/Sm	7.06	5.63	7.57		6.21	6.35		4.76	5.57
Gd/Yb	1.75	2.14	2.27		1.64	1.60		1.50	1.00

$_{cn}$: Chondrite-normalized.
Eu/Eu*: Europium anomaly, Eu* obtained by straight line interpolation between plotted points for Sm and Gd.

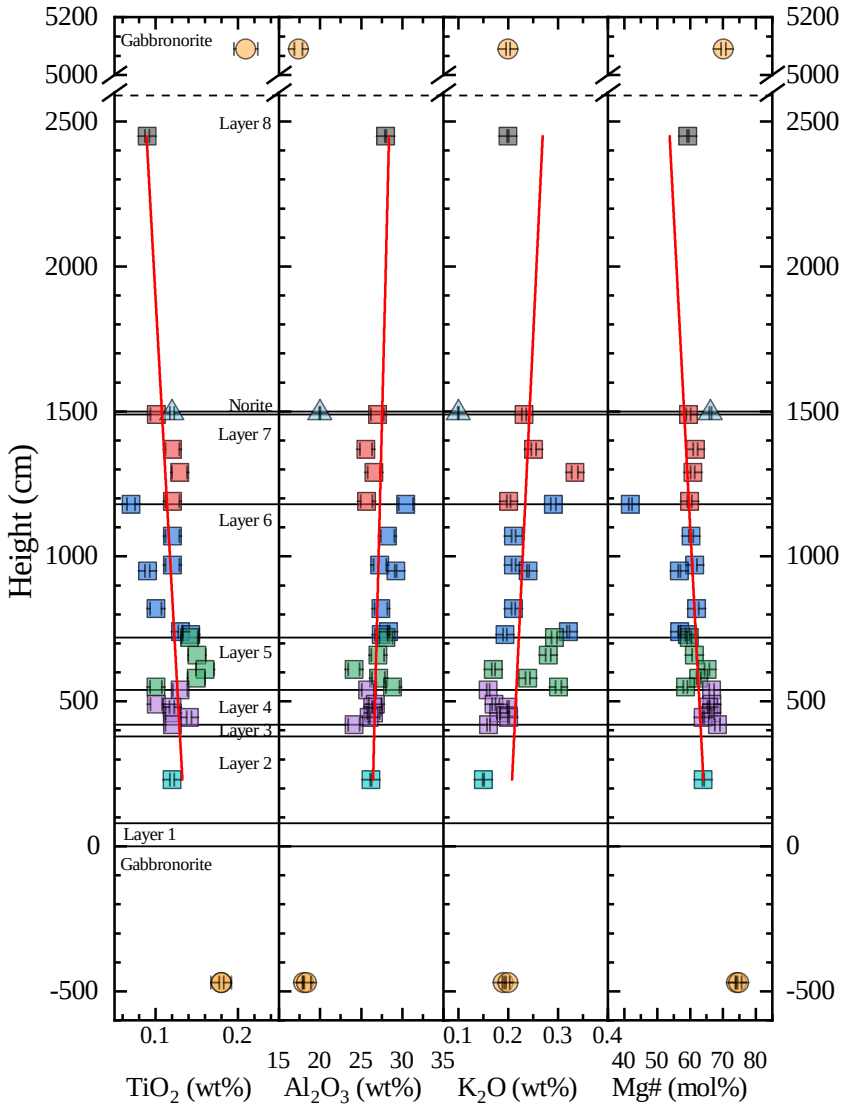

Figure 4.10 – Whole-rock major element oxide variations and molar Mg# in the anorthosite sequence. Lines of best fit (anorthosite layers only) are presented in red.

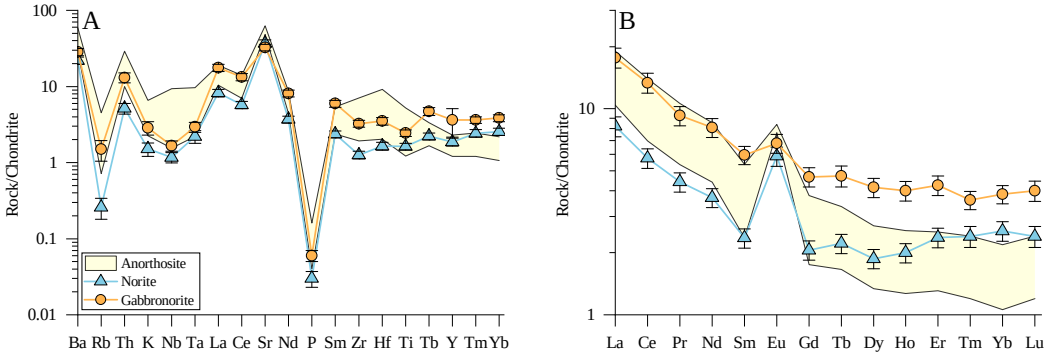

Figure 4.11 – Chondrite-normalized incompatible **(A)** and rare earth element **(B)** diagrams. Samples were normalized using the C1 carbonaceous chondrite values of McDonough and Sun (1995).

correlate with a 10 m thick layer of 'spotted' and 'mottled' anorthosites, located at a depth of ∼173 m below the base of the Upper Zone in Molyneux's (1974) stratigraphic column of the Main Zone. The exact stratigraphic position of the anorthosite sequence at the road-cut could not be determined using my mineral chemical data because of a paucity of data in the surrounding area, which is exacerbated when considering that mineral chemistries vary laterally in the RLS (Lundgaard et al., 2006; Clarke et al., 2009; Cawthorn et al., 2016; Setera and VanTongeren, 2018). From the Pyroxenite Marker upwards (eastern lobe), the dominant Ca-poor pyroxene is orthopyroxene (von Gruenewaldt, 1973; von Gruenewaldt and Weber-Diefenbach, 1977; Cawthorn et al., 1991) which gradually transitions to inverted pigeonite starting ∼200 m below the Main and Upper Zone contact (von Gruenewaldt and Weber-Diefenbach, 1977; Molyneux, 1974). The orthopyroxene-inverted pigeonite transition is followed by the appearance of myrmekite (Molyneux, 1974). Because only a single crystal of inverted pigeonite was observed and myrmekite was not observed, the most probable stratigraphic position of the anorthosite sequence corresponds to the beginning of the orthopyroxene-inverted pigeonite transition zone (von Gruenewaldt, 1973; von Gruenewaldt and Weber-Diefenbach, 1977; Molyneux, 1974), which is in agreement with my stratigraphic depth calculations. Therefore, the anorthosite sequence belongs to the Upper Main Zone, near the Main and Upper Zone contact, as suggested by Molyneux (2008); Lesego Platinum Mining Ltd. and MSA (2011) and by my stratigraphic depth calculations and petrography.

4.6.2 Origin of layering in the Upper Main Zone anorthosite sequence

The origin of anorthosite layers in layered ultramafic-mafic intrusions remains poorly understood and is highly debated. This problem is significant in the RLS, as relatively few studies have addressed the subject (e.g. de Klerk, 1995; Cawthorn et al., 2002; Cawthorn and Spies, 2003; Mitchell and Manthree, 2002; Cawthorn and Ashwal, 2009).

The anorthosite sequence can be divided into 8 individual layers. At the outcrop-scale, visually-distinct layers are either separated by a sharp contact or a thin layer of norite (between layers 7 and 8; Figs. 4.2, 4.3B). Each contact forms a relatively well-defined planar surface. Furthermore, each visually-distinct layer is defined by texturally-distinct oikocrysts of pyroxenes (e.g. poikilitic, banded), as defined by changes in both habit and size of pyroxenes. Variations in mineral chemistry (An-content and Mg#) and density are greater and more abrupt across layer contacts than within individual layers (Figs. 4.6, 4.9). Only layers 5 - 7 were analyzed in detail for their density, mineral and whole-rock chemistries. However my limited density measurements, mineral and whole-rock chemistries for the other layers are consistent with the observations for layers 5 - 7 and I therefore consider the trends observed here to be applicable to all layers. Whole-rock major element oxides were not sensitive enough to highlight changes across contacts (Fig. 4.10). The notion that each layer formed independently from a separate magmatic pulse is supported by the distinct textural changes, coupled with mineral compositional breaks across layer contacts.

Whole-rock normalized incompatible and REE patterns are identical between anorthosite layers, suggesting that each layer crystallized from magmas with a similar composition, and in this sense are co-magmatic. Furthermore, whole-rock normalized incompatible and REE patterns between the gabbronorite, norite and the anorthosite layers closely match, with the exception of higher HREE concentrations in both the norite and gabbronorite. These differences can be attributed to a higher modal% of pyroxenes in the norite and gabbronorite (Henderson, 1984). As such, the matching trace element chemistries between the anorthosite layers, gabbronorite and norite suggest that all of these rocks are from the same parental magma. Whole-rock normalized REE patterns of all lithologies at the road-cut are also comparable to Main Zone cumulate REE patterns published by Roelofse and

Ashwal (2012), and Maier and Barnes (1998).

For the anorthosite sequence, whole-rock major element oxides Al_2O_3 and K_2O increase, and TiO_2 and Mg# decrease upwards (Fig. 4.10). Similarly, plagioclase cores become more albitic (by 2.5 mol%), and both clinopyroxene and orthopyroxene crystals decrease in Mg# (8.6 and 13.0 mol% respectively) (Fig. 4.6) upwards. As the bulk of the outcrop consists of plagioclase adcumulates, parental magma fractionation effects are much more probable to account for the mineral and whole-rock chemistry trends through the layers as compared to the trapped liquid shift effect (e.g. Barnes, 1986; Cawthorn, 2015). Orthopyroxene oikocrysts and primocrysts are chemically identical in layers 4 and 5. Hence, I find it improbable for these two populations of crystals to be uniformly modified throughout the layers via the trapped liquid shift effect, to such an extent that both became chemically identical, regardless of crystal size, occurrence and distribution throughout the layers. However, minimal normal zonation in pyroxene oikocrysts (Fig. 4.7C) suggests that there was partial resetting of pyroxenes with trapped melt, but only on a local crystal-size scale, where oikocrysts were in contact with pockets of late-stage pore melt. Therefore, both large-scale whole-rock and mineral chemistry trends are much more consistent with magmatic fractionation. The lack of differentiation within the anorthosite sequence is consistent with the general lack of differentiation across the entire Main Zone (Cawthorn, 1996, 2015).

Intra-layer mineral (plagioclase and pyroxenes) and whole-rock chemistries remain relatively constant, both vertically and horizontally. Plagioclase crystal morphology (e.g. size, habit, zonation) remains constant throughout the layers, between contacts (including with the blocks) and within the pure anorthosite bands. Pure anorthosite bands occur at the base of some layers and help to delineate the sharp contacts. A hypothesis consistent with constant An-compositions, identical lath morphologies, and the overall non-cotectic proportions of plagioclase, is that each of these layers formed from the injection of a plagioclase slurry (Miller and Weiblen, 1990; Czamanske and Bohlen, 1990; Ashwal, 1993; Roelofse and Ashwal, 2012; Yuan et al., 2017; Hayes et al., 2017).

Several features and textures in the anorthosite sequence can be explained using the plagioclase slurry model. Mineral banding in igneous bodies may be produced by shearing in congested crystal-melt mixtures (i.e. a slurry) (Stickel and Powell, 2005; Petford and Mirhadizadeh, 2017). A congested plagioclase slurry, could explain the laterally discontinuous norite bands in layer 5 (Figs. 4.3A, 4.4C). Pure anorthosite bands (5 - 10 cm thick), noted at the base of some layers, grade into poikilitic anorthosite (Fig. 4.2A) and demonstrate the largest variance in An-content (Fig. 4.6). The large variance in An-content could have been produced because pure anorthosite bands formed where the thermal gradient was the greatest, although substantially less than chill margins found in many smaller intrusions or thin sills. Plagioclase laths within the pure anorthosite bands are morphologically identical (e.g. size, habit, zonation) to laths in the layers, indicating that the magma carried plagioclase crystals prior to emplacement. Plagioclase chadacrysts in pyroxene oikocrysts are also lath-shaped but are, on average, smaller-sized and lack reversely-zoned rims, further indicating that crystals within the incoming plagioclase slurry already possessed cores and mantles. The thin reversely zoned rims could either be products of an increase in temperature, caused by the emplacement of a new plagioclase slurry above the underlying resident layer (Sunagawa, 2005), a decrease in pressure caused by the ascent of the plagioclase slurry from greater depths (Longhi et al., 1993), or of the crystallization of a Ca-saturated intercumulus liquid caused by a trapped clinopyroxene component in the liquid (Morse and Nolan, 1984). Crystallization of the rims was followed by the crystallization of sodic overgrowths on some of the plagioclase laths (Fig. 4.5B). The sodic overgrowths are intergrown with quartz, with quartz being intergrown with magnesiohornblende, indicating that these phases likely co-crystallized from an evolved Si- and Na-rich trapped interstitial liquid (Humphreys, 2009; Vukmanovic et al., 2018; Hayes et al., 2018) (Table 4.2). Subophitic

crystals of orthopyroxene co-crystallized with plagioclase and were likely carried in with the plagioclase slurry. The interstitial nature of the pyroxene oikocrysts suggests that they crystallized after the emplacement of the slurry, likely through the coalescence and ripening (i.e. migration of pore fluid and diffusion of residual chemicals) of an interstitial pyroxene-saturated melt. In layer 6, where oikocrysts reach 80 cm across, this process was likely aided by either slow cooling or a higher mush porosity ($\geq$8 - 11%; Cheadle et al. (2004)) as to allow the substantial growth of the normally-zoned oikocrysts.

4.6.3 Alternative hypotheses

Several alternative hypotheses have been proposed to explain the origin of anorthosite layers in layered ultramafic-mafic intrusions and it is important to address some of these here. These include: 1) *in situ* crystallization (e.g. Campbell et al., 1978; Latypov et al., 2017) from a plagioclase-saturated magma, 2) supersaturation and nucleation effects (e.g. Maaloe, 1978; Morse, 1979a,b), 3) rhythmic pulses of crystallization followed by crystal settling and sorting under the influence of gravity (e.g. Wager and Brown, 1968, Cawthorn and Ashwal, 2009) and, 4) plagioclase flotation cumulates (e.g. Vermaak, 1976).

The hypothesis of *in situ* crystallization is rejected here since there is a magmatic flow fabric preserved in the anorthosite sequence, defined by the alignment of plagioclase laths which form a pervasive and consistent, moderate to strong foliation (Fig. 4.4). I consider the alignment of the plagioclase laths to be the result of magmatic flow as opposed to compaction since plagioclase laths show minimal evidence of deformation microstructures. Furthermore, the blocks would present the ideal nucleation surface on which crystals would grow during *in situ* crystallization. However, the blocks are in contact with morphologically-identical (e.g. size, habit, zonation) plagioclase laths to those within the bulk of the anorthosite layers, with the long axis of the crystals resting parallel to the long axis of the rectangular-shaped block, both aligned parallel to the plane of layering. Therefore, there is no evidence for *in situ* nucleation and crystallization at the margins of the blocks. The hypothesis of supersaturation and subsequent nucleation of a magma would require supercooling conditions in order to reach supersaturation. Supercooling would lead to the production of significant volumes of very fine-grained crystals of plagioclase, contrary to the preserved textures at the road-cut. Crystal settling and sorting under the influence of gravity and plagioclase flotation cumulates hypotheses are also rejected since the anorthosite layers at the road-cut lack any evidence of modal grading, are all in sharp contact with one another with no evidence of a pyroxenite cumulate counterpart to any single anorthosite layer as well as for the entire sequence. However, the hypothesis of plagioclase flotation cumulates could yield plagioclase slurries should they have accumulated in a staging chamber and been subsequently transported. The idea of a staging chamber below the RLS has been discussed in numerous studies (e.g. Eales, 2002; Ashwal et al., 2005; McDonald and Holwell, 2007; Roelofse and Ashwal, 2012).

4.6.4 Implications for the origin of anorthosites in large layered ultramafic-mafic intrusions

Anorthosite layers are common features of layered ultramafic-mafic intrusions and have been documented in the Stillwater (USA), Skaergaard (Greenland), Sept Îles (Canada), Kiglapait (Canada) and Jimberlana (Australia) intrusions, among others (a complete list is given in Ashwal, 1993). Typically, anorthosites are found at the tops of modally-graded layers, but may also appear as micro-rhythmic or thick (deca- to hectometer-scale) layers (Ashwal, 1993). Here I compare the anorthosite sequence

at the road-cut to other thick anorthosite layers in layered ultramafic-mafic intrusions, and discuss possible similarities in their origin.

Thick anorthosite layers have been well studied in the Stillwater Complex. Two anorthosite layers (Lower and Upper Anorthosites) attain thicknesses between 370 and 630 m (McCallum et al., 1980). These layers are characterized by:

- no variation in plagioclase grain-size or modal layering,
- transgressive, sharp basal contacts,
- unchanging major and minor-element chemistry,
- unvarying average plagioclase compositions (whole-rock normative An calculations),
- complexly zoned (normal, reverse and oscillatory) plagioclase crystals,
- large plagioclase crystal size compared to bounding rocks, and
- blocks of overlying troctolite (Hess, 1960; McCallum et al., 1980; Czamanske and Bohlen, 1990).

Many of these characteristics occur in our studied anorthosite sequence. In particular, individual layers at the road-cut exhibit:

- no variation in plagioclase-grain size or modal layering (with exception of norite bands in layer 5),
- sharp contacts,
- a relatively unchanging major and minor-element chemistry within layers,
- relatively unvarying plagioclase compositions within layers,
- zoned plagioclase crystals (although less complex compared to Stillwater), and
- exotic cumulate blocks within the layers.

However, there are differences. Plagioclase crystal sizes in the anorthosite layers are comparable to the bounding gabbronorites. The anorthosite layers at the road-cut are also thinner compared to those of the Stillwater Complex. However, comparable anorthosite layers in the Bushveld Complex are typically thinner ($\leq$50 m) and less well developed (Ashwal, 1993) as compared to those of the Stillwater Complex. Also, the blocks in the anorthosite sequence do not appear to be locally derived (i.e. from immediately above or below the layers) as opposed to those found in the Stillwater Complex. Nonetheless, given the similarities, the anorthosite sequence at the road-cut is therefore largely comparable to other thick layered anorthosites documented in layered ultramafic-mafic intrusions.

The features demonstrated by Stillwater's thick anorthosite layers have been used to support formation by the emplacement of plagioclase slurries (Czamanske and Bohlen, 1990; Miller and Weiblen, 1990; Ashwal, 1993). Here, I suggest a similar origin for the anorthosite sequence at the road-cut. A plagioclase slurry model for Main Zone anorthosites in the Bushveld Complex is also supported in various studies by Roelofse and Ashwal (2012), Roelofse et al. (2015) and Hayes et al. (2017).

Within the Main Zone of the Bushveld Complex, most anorthositic rocks appear at the top of modally-graded layers (Ashwal, 1993). Layers similar to those documented at the road-cut I studied are a rare occurrence in the Main Zone (G. Cawthorn (2018), personal communication). As such, they provide an invaluable insight into varied emplacement mechanisms of the Bushveld Complex and post-emplacement dynamics in a layered intrusion.

4.7 Conclusions

The anorthosite sequence located near the Phosiri Dome is defined by 8 texturally-distinct anorthosite layers and a layer of norite, all of which are hosted by gabbronorite. The stratigraphic position of the anorthosite sequence has been constrained to the Upper Main Zone, $\sim$166 m below the base of the Upper Zone. Anorthosite layers are defined by sharp mutual contacts, mineral composition breaks and local pure anorthosite bands, suggesting that each layer formed from a separate magma pulse. Based on identical chondrite-normalized incompatible and REE diagrams, each magma pulse was related to the same parent magma, however subtle changes in major element chemistry between each layer suggests that the parental source was partly fractionated prior to magma emplacement. Within layer plagioclase crystal morphology, mineral and whole-rock chemistries remain relatively constant, suggesting that the incoming magmas were plagioclase slurries. My study highlights the important role that plagioclase slurries play in the development of anorthosite layering in layered ultramafic-mafic intrusions.

5 Staging chambers, plagioclase slurries and cumulate recycling recorded in the Upper Main Zone

5.1 Introduction

Recycling of crystals and cumulate material is a common process in magma chambers during their emplacement and solidification (e.g. Hess, 1960; Irvine, 1974; Miller and Weiblen, 1990; Lightfoot et al., 1997; Irvine et al., 1998; Cashman et al., 2017). Blocks of transported cumulate material can therefore provide insights into pre-emplacement magma dynamics, sources, as well as rheology and flow dynamics of magmas during their emplacement (e.g. Sparks et al., 1977; Clague, 1987; Irvine et al., 1998; Yoshinobu et al., 2009). Cumulate blocks may therefore provide crucial constraints of the evolution and development for layered ultramafic-mafic igneous intrusions.

Irvine et al. (1998) studied igneous blocks in the Skaergaard intrusion that include a diverse assortment of both exotic xenoliths sourced from country rocks and cognate autoliths of troctolites, gabbros and anorthosites. He showed that these cognate autoliths were ripped from the Upper Border Series of the magma chamber roof during solidification. The Stillwater Complex also hosts numerous large blocks of cognate autoliths of troctolites, anorthosites and orthopyroxenites that were ripped up from underlying layers, as well as country rock xenoliths (McCallum, 1996; Wall et al., 2018).

The Rustenburg Layered Suite (RLS) of the Bushveld Complex in South Africa contains numerous cumulate blocks, sometimes referred to as 'autoliths' or 'inclusions'. The RLS also contains numerous xenoliths of quartzite, hornfels and dolomite that were derived from the underlying Pretoria Group sediments and, more rarely, xenoliths of metamorphosed felsites that were derived from the Rooiberg Group which overlies the RLS (Molyneux, 1970, 1974; Cameron, 1978). Cumulate blocks and xenoliths are found in particular horizons in the RLS of the Bushveld Complex, notably at the base of the Lower, Critical and Upper Zones and at the level of the Pyroxenite Marker in the Main Zone (e.g. Molyneux, 1970, 1974; Cameron, 1978). However, the origin of the cumulate blocks has not been previously studied, but as illustrated in this chapter, they may provide important insights into the evolution of its magma chamber.

Debate about magma emplacement in the RLS has become contentious across a continuum of models. One end-member view is that melts were aphyric, superheated, and solidified *in situ* (growth against a substrate) upon emplacement into the chamber (Campbell, 1977; McBirney and Noyes, 1979; Latypov et al., 2017), whereas another view is that magmas were injected as crystal-bearing slurries (Barnes et al., 2010; Roelofse and Ashwal, 2012; Eales and Costin, 2012; Hayes et al., 2017; Yuan et al., 2017). Both injection of crystal-bearing magmas and *in situ* crystallization of magma, following flow stagnation in the chamber, most likely contributed to the development of cumulates and igneous layering in the RLS. However, deciphering the origin and provenance of cumulate blocks will constrain minimum estimates of magma viscosity, flow rate and crystallinity, thereby providing insights into magma composition (aphyric versus crystal-bearing) upon its emplacement into the magma chamber.

This study presents field, petrological and geochemical data and its associated analyses of a suite of cumulate blocks hosted in a layered sequence of poikilitic anorthosites belonging to the Upper Main Zone of the RLS. Both blocks and host anorthosites are exposed along a road-cut located 5

km NE of the town of Apel, in the eastern lobe of the Bushveld Complex. These cumulate blocks are norites and olivine-bearing norites and are distinct from their leucocratic anorthosite host. High-precision Sr-Nd isotope results show that the blocks are indeed distinct from their host anorthosites and record crystallization events from a less-contaminated magma. This study also employs numerical modeling to constrain the magmatic conditions that are necessary to transport the observed blocks into the magma chamber. Together with all lines of evidence, I suggest that the cumulate blocks were derived from a deeper staging chamber system and were transported into the main magma chamber with the remobilization of plagioclase slurries. Therefore, transport of distinct cumulate blocks and their characteristics highlight the blocks' value in the study of important magmatic processes that may become obscured subsequent to emplacement (e.g. trapped liquid shift effect, compaction, subsequent hydrothermal alteration and deformation, etc.).

5.2 Summary of previous work: Poikilitic anorthosite layers and bounding gabbronorite

The field, petrography and mineral chemistry of the poikilitic anorthosite layers and the bounding gabbronorite were described for the entire sequence in detail in Chapter 4. The findings are summarized here.

5.2.1 Field descriptions

The layered sequence of poikilitic anorthosites ($\sim$25 m total thickness) has been divided into eight individual layers (ranging in thickness between 0.4 - 10 m) on the basis of textural and subtle mineral compositional breaks (Fig. 5.1). This layered sequence includes a thin (0.05 m) layer of norite (between anorthosite layers 7 and 8) and the entire sequence is hosted by gabbronorite (Fig. 5.2). The thicknesses of the layers remain relatively constant along strike for the entirety ($\sim$450 meters) of the road-cut. Contacts between layers are always sharp (Fig. 5.2).

The layers of poikilitic anorthosites (sensu lato) are composed of 80 - 97 modal% medium-grained (1 - 5 mm) euhedral-subhedral plagioclase laths that define a moderate to strong foliation that is aligned parallel to layering. Individual layers can be distinguished on the habit and sizes of pyroxenes (orthopyroxene and clinopyroxene). Layers may be: (1) poikilitic (layers 1, 3, 7 and 8); (2) spotted, with elongated oikocrysts of clinopyroxene (layers 2 and 4); (3) banded (layer 5); (4) poikilitic, with oikocrysts increasing in size upwards (layer 6); and (5) pure anorthosite ($\leq$97% plagioclase and 5 - 10 cm thick), found at the base of layers 1 and 3 (Fig. 5.1).

Poikilitic layers contain evenly distributed, spherical-shaped pyroxene oikocrysts (1 - 8 cm; $\sim$20 modal%; Fig. 5.2). Numerous (20%) plagioclase chadacrysts are found in the oikocrysts. Spotted layers are defined by evenly-distributed sub-ophitic orthopyroxene (1 - 3 mm; 5%) with oblate-shaped clinopyroxene oikocrysts (0.8 - 3 cm; 10%). The banded layer is poikilitic and is characterized by 5 - 8 laterally-discontinuous norite bands (4 - 12 cm thick). Orthopyroxene crystals (1 - 3 cm; 30 - 65%) in the bands are sub-ophitic and are intergrown with plagioclase laths. In layer 6, pyroxene oikocrysts (20%) increase in size upwards (from 3 - 6 cm spheres to 50 - 80 cm oblongs; Fig. 5.2). A thin layer (5 cm) of fine-grained ($\leq$1 mm) norite is present between layers 7 and 8 (Fig. 5.2).

The basal and capping gabbronorite, that hosts the layered sequence of poikilitic anorthosites, is medium-grained (2 - 5 mm) and does not show any modal layering. Euhedral orthopyroxene crystals in the gabbronorite contain fine-grained ($\leq$1 mm) inclusions of plagioclase and are reminiscent of

orthopyroxene crystals in the norite bands of anorthosite layer 5.

5.2.2 Petrography and mineral chemistry

The poikilitic anorthosite layers are composed of plagioclase laths (86 modal%; 0.2 - 4 mm), accompanied by interstitial orthopyroxene (7%) and clinopyroxene (4%) oikocrysts (Fig. 5.3A). Accessory minerals include quartz (2%), magnesiohornblende (0.5%), magnetite (0.5%), phlogopite (0.5%), clinochlore, clinozoisite and ilmenite (<0.5%). Plagioclase laths define a moderate to strong foliation and they are rarely bent (to an angle of $\leq 8^{\circ}$), resulting in a slight undulose extinction. Plagioclase laths have an average anorthite (An; atomic Ca/(Ca+Na+K)$\times$100) content of 72.6 mol%. They are slightly compositionally zoned, with normal zoning from the core to mantle (average $\sim$1 mol% An decrease) with a thin (20 - 70 μm) reversely zoned rim (average 2 mol% An increase). Both orthopyroxene and clinopyroxene form large oikocrysts with orthopyroxene present as sub-ophitic crystals (3 - 10 mm) in layers 2, 4 and 5. Orthopyroxene and clinopyroxene have an average Mg# (atomic Mg/(Mg+Fe)$\times$100) composition of 62.1 mol% and 72.5 mol%, respectively. Mineral compositional breaks occur between each layer, with an average An-content change of 0.5 - 3.8 mol% and an average Mg# change of 1.3 mol% (in clinopyroxene). Over the entire layered anorthosite sequence, the An-content decreases by 2.5 mol%, and the Mg# of orthopyroxene and clinopyroxene increases by 13.0 mol% and 8.6 mol% respectively.

The host gabbronorite is composed of euhedral-subhedral laths (0.2 - 4 mm) of plagioclase (56%) clinopyroxene (17%) and orthopyroxene (15%), accompanied by minor interstitial quartz (1%) and trace (>0.5%) amounts of magnesiohornblende, phlogopite and magnetite (Fig 5.3B). Plagioclase laths define a good foliation that is parallel to layering and they have an average composition of $An_{72.9}$ which is comparable to the anorthosite layers. Orthopyroxene and clinopyroxene have an average Mg# composition of 69.3 mol% and 77.0 mol%, respectively.

5.3 Field descriptions

The blocks are darker compared to their host anorthosites, are cm- to m-sized (0.2 - 5.75 m) and are fine- to medium-grained (0.1 - 2 mm; Fig. 5.4). Altogether, blocks represent $\sim$0.2% of the exposed surface area at the road-cut. Blocks are closely associated with the poikilitic anorthosite layers, being present at the base of layer 1, at the contact between layers 6 and 7, and in layer 8 (Figs. 5.1, 5.4). A single block is hosted by gabbronorite, below layer 1 (Fig. 5.4A). Typically, blocks are rectangular-shaped, but have rounded margins in cross-section (Fig. 5.4). A few blocks are asymmetrically-tapered towards the north (Figs. 5.2, 5.5). Rarely, they appear as fragmented and irregularly-shaped blocks, with tongues of the host anorthosite invading the block (Fig. 5.4C). All blocks are aligned with their longest axis parallel to layering. The largest block (labeled block 11) that sits 15 cm above the base of layer 7 has locally deformed of the upper part of layer 6 (Fig. 5.4D).

The contact between the blocks and their host is always sharp (Figs. 5.2, 5.4, 5.5). Plagioclase laths in the host anorthosite are aligned parallel to the margins of the block (Fig. 5.5B, C). Locally, there is a modal increase of pyroxenes (as clinopyroxene and orthopyroxene oikocrysts) at the block-anorthosite contact (Fig. 5.5). The block shown in Figure 5.5 shows grain size variations with fine- and medium-grained zones. Such zones are in irregular contact with one another.

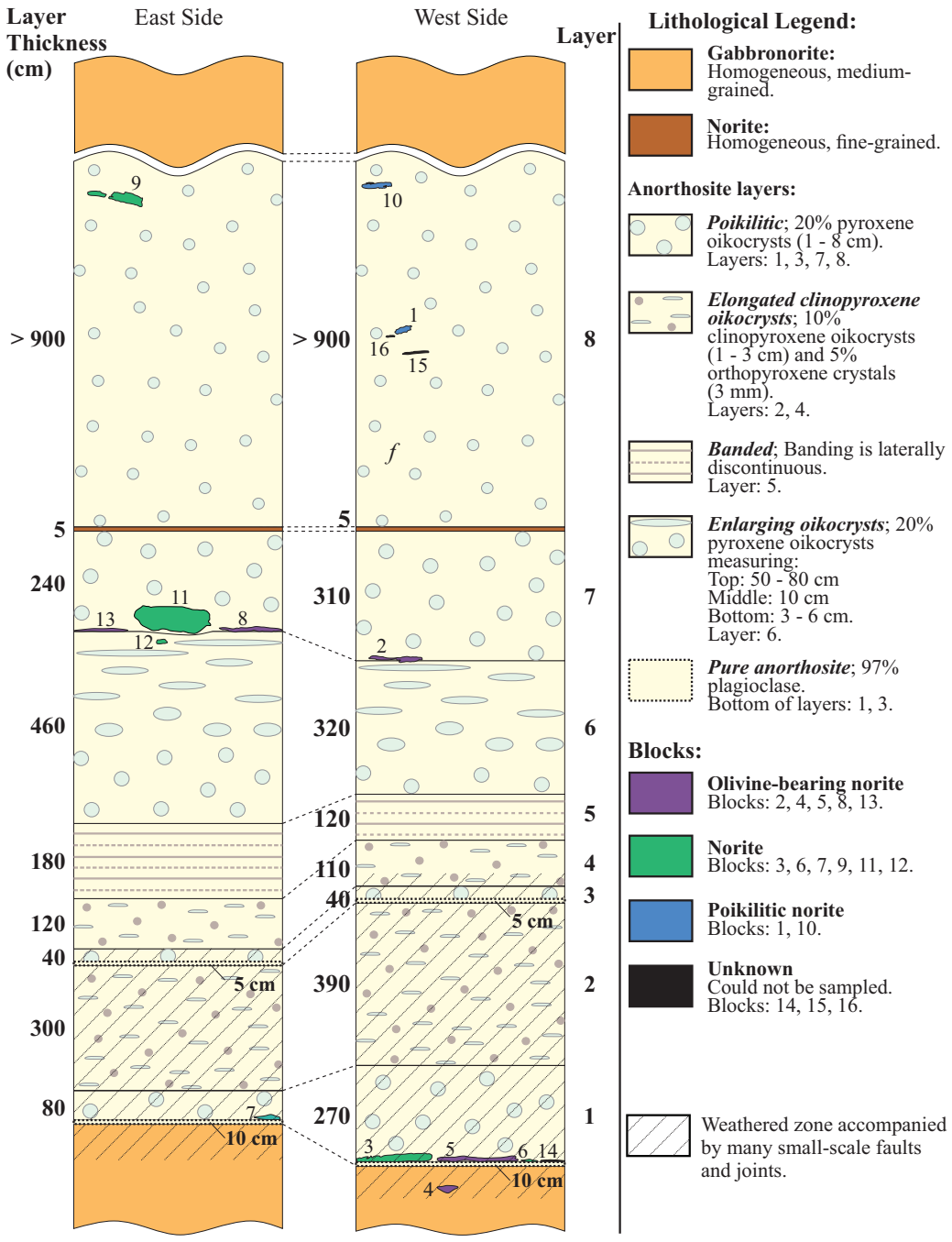

Figure 5.1 – Stratigraphic succession at the road-cut (on each side of the road), showing anorthosite layers 1 to 8, the norite band and bounding gabbronorite. At the bottom of the sequence is a pure anorthosite band (10 cm thick). Also shown in the stratigraphic log is the location and composition of the cumulate blocks (i.e. cumulate fragments of distinct lithology to their host).

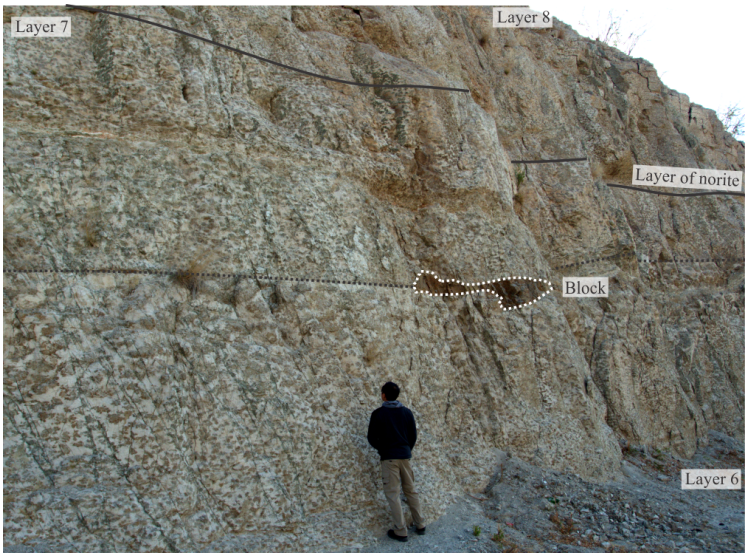

Figure 5.2 – Overview of poikilitic anorthosite layers 6 to 8 and the norite layer (accentuated by a black line) from west-side of the road-cut. Contacts between layers and blocks are always sharp (dotted lines). A melanocratic olivine-bearing norite block (block 2; white dotted line) is found at the contact between anorthosite layers 6 and 7.

5.4 Petrography and mineral chemistry

The suite of blocks can be classified into 3 petrological groups, namely: (1) poikilitic norites; (2) olivine-bearing norites; and (3) norites. Detailed descriptions of each group of blocks follows and their stratigraphic position is shown in Figure 5.1.

5.4.1 Poikilitic norites

Blocks 1 and 10 are poikilitic norites and are petrographically indistinguishable. They are medium-grained and consist of euhedral orthopyroxene (65%) chadacrysts that are hosted in large ($\leq$4 cm) oikocrysts of plagioclase (30%) and clinopyroxene (5%; Fig. 5.6A). Trace amounts of phlogopite, amphibole and magnetite are also found in the block. Plagioclase in hand specimens exhibit labradorescence. Orthopyroxene crystals may contain small inclusions of clinopyroxene (0.1 - 0.2 mm; Fig. 5.6B). Clinopyroxene oikocrysts commonly contain numerous, relatively evenly-spaced, orthopyroxene exsolution lamellae ($\leq$20 μm). Clinopyroxene may also partially mantle orthopyroxene chadacrysts in plagioclase oikocrysts (Fig. 5.6B).

Orthopyroxene crystals in block 1 have an average Mg# of 68.8 mol% (Table 5.1). Plagioclase in block 1 has an average An-content of 66.3 mol% An. Clinopyroxene in block 1 has an average Mg# of 78.8 mol%. Orthopyroxene crystals and clinopyroxene oikocrysts are unzoned. Plagioclase oikocrysts do exhibit zonation with narrow ($\leq$15 μm thick) reversely zoned rims at the contacts with orthopyroxene chadacrysts, with the average plagioclase An increasing by 10.5 mol%.

5.4.2 Olivine-bearing norites

Blocks 2, 4, 5, 7, 8 and 13 are olivine-bearing norites. They are defined by small to large (0.2 - 10 mm) poikilitic crystals of olivine (3%) that are hosted in a fine-grained matrix (0.1 - 0.6 mm) of anhedral orthopyroxene (50%) and plagioclase (43%), accompanied by minor amounts of clinopyroxene (3%) and magnetite (1%), and trace ($\leq$0.5%) amounts of phlogopite (Fig. 5.6C, D). A few

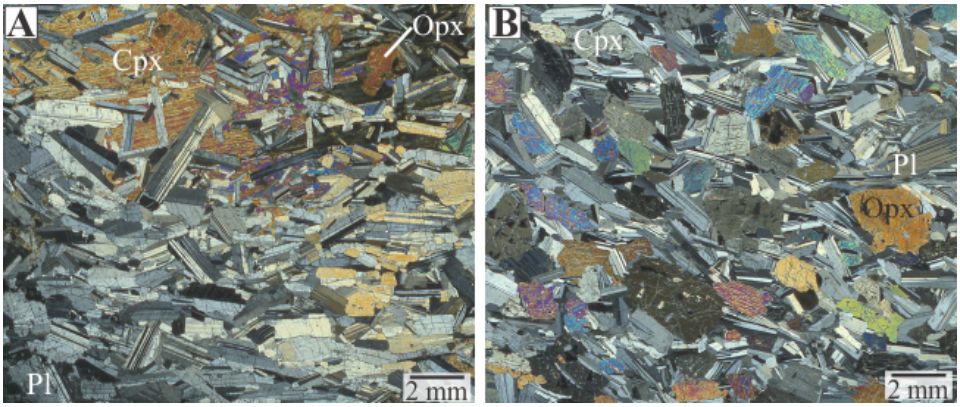

Figure 5.3 – Cross-polarized light photomicrographs of the anorthosite and gabbronorite. Photomicrographs are arranged with the top direction pointing upwards and were taken under crossed polars. **(A)** Plagioclase (Pl) laths in the anorthosite define a moderate to strong foliation (bottom). Interstitial clinopyroxene (Cpx) forms an interconnected network. Sub-ophitic orthopyroxene (Opx) is found as inclusions in interstitial clinopyroxene. Specimen is from layer 4. **(B)** The gabbronorite is composed of foliated plagioclase laths and euhedral-subhedral orthopyroxene and clinopyroxene.

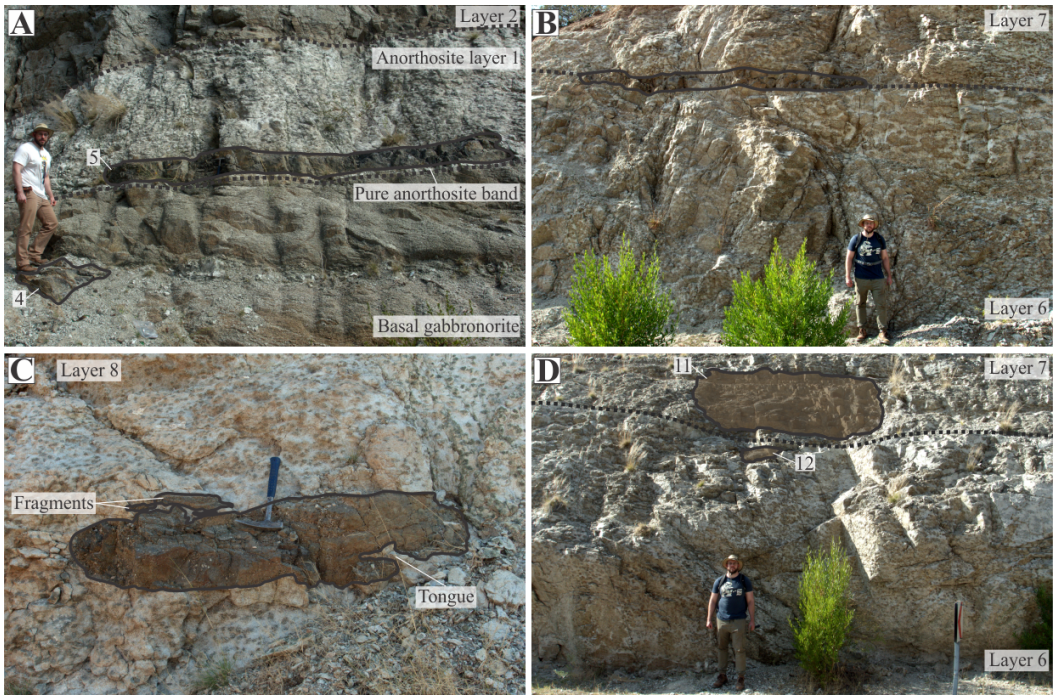

Figure 5.4 – Representative photographs of blocks found at the road-cut. **(A)** Olivine-bearing norite blocks 4 and 5 (traced by solid lines). Contacts between layers and lithologies are highlighted by dashed lines. Block number 4 is hosted in gabbronorite and is partially covered by talus. Block 5 is in anorthosite and it rests on a 10 cm thick band of pure anorthosite. **(B)** Olivine-bearing norite block 8 is at the boundary between anorthosite layers 6 and 7. The block indents into layer 6. **(C)** Poikilitic norite block 10, found in anorthosite layer 8 (735 cm above the base of the layer). This block is fragmented and there is a tongue of anorthosite penetrating it. **(D)** Norite blocks 11 and 12. The blocks have been shaded to aid their identification. Block number 11 is the largest of the blocks, measuring 2.7 by 1.5 m and it partially deforms the layer below (dotted line).

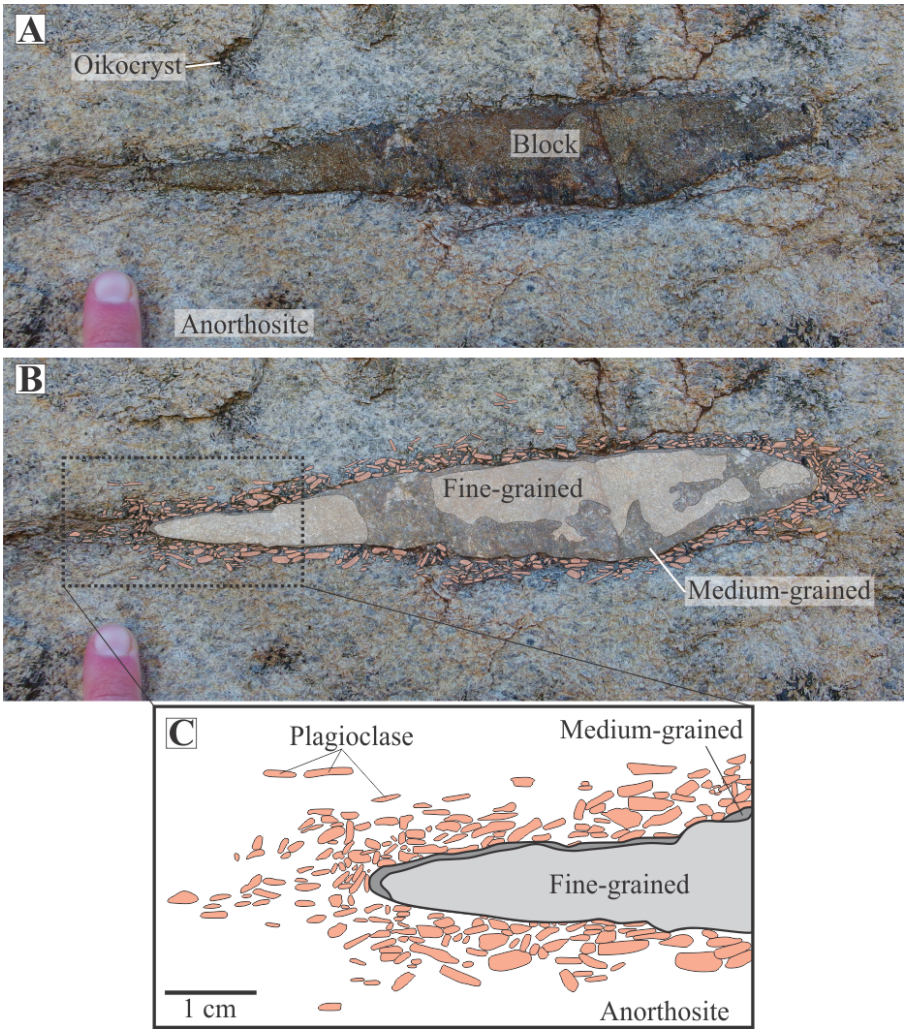

Figure 5.5 – A close-up of a contact between norite block 16 and its host anorthosite. This block is the smallest observed block at the road-cut and is hosted in anorthosite layer 8, 3.4 m above the base of the layer. **(B)** Digitized version of (A) showing the arrangement of the anorthosite plagioclase laths (pale orange) adjacent to the block's margins and the fine-grained (pale gray) and medium-grained (darker gray) zones within the block. Plagioclase laths near the block are clearly distinguishable because of the presence of oikocrystic pyroxenes immediately at the block-anorthosite contact. **(C)** A close up of the block-anorthosite contact showing major plagioclase laths aligned parallel to the margins of the block.

large ($\leq$3 mm) crystals of orthopyroxene are found randomly distributed through the fine-grained matrix (Fig. 5.7A). These large crystals, in comparison to the remainder of the fine-grained matrix, may contain small (25 - 100 μm) anhedral inclusions of plagioclase and clinopyroxene. In blocks 4 and 5 large orthopyroxene are more numerous (5%) and tend to form loosely-defined clusters. Olivine crystals are heavily embayed and are mantled by pyroxene (0.02 mm thick) or symplectitic-magnetite (0.01 - 0.4 mm; Fig. 5.7B). The smaller-sized olivine crystals tend to form crystallographically-aligned clusters, up to 3.3 mm across (Fig. 5.6D). Olivine crystals in blocks 4, 7 and 13 are completely altered to iddingsite. Clinopyroxene is interstitial and can occasionally form small (0.1 - 0.7 mm) interconnected networks.

Poikilitic olivine crystals are chemically homogeneous, with an average forsterite (Fo; atomic Mg/(Mg+Fe)$\times$100) content of 70.1 and 74.4 mol% in blocks 2 and 5, respectively (Table 5.1).

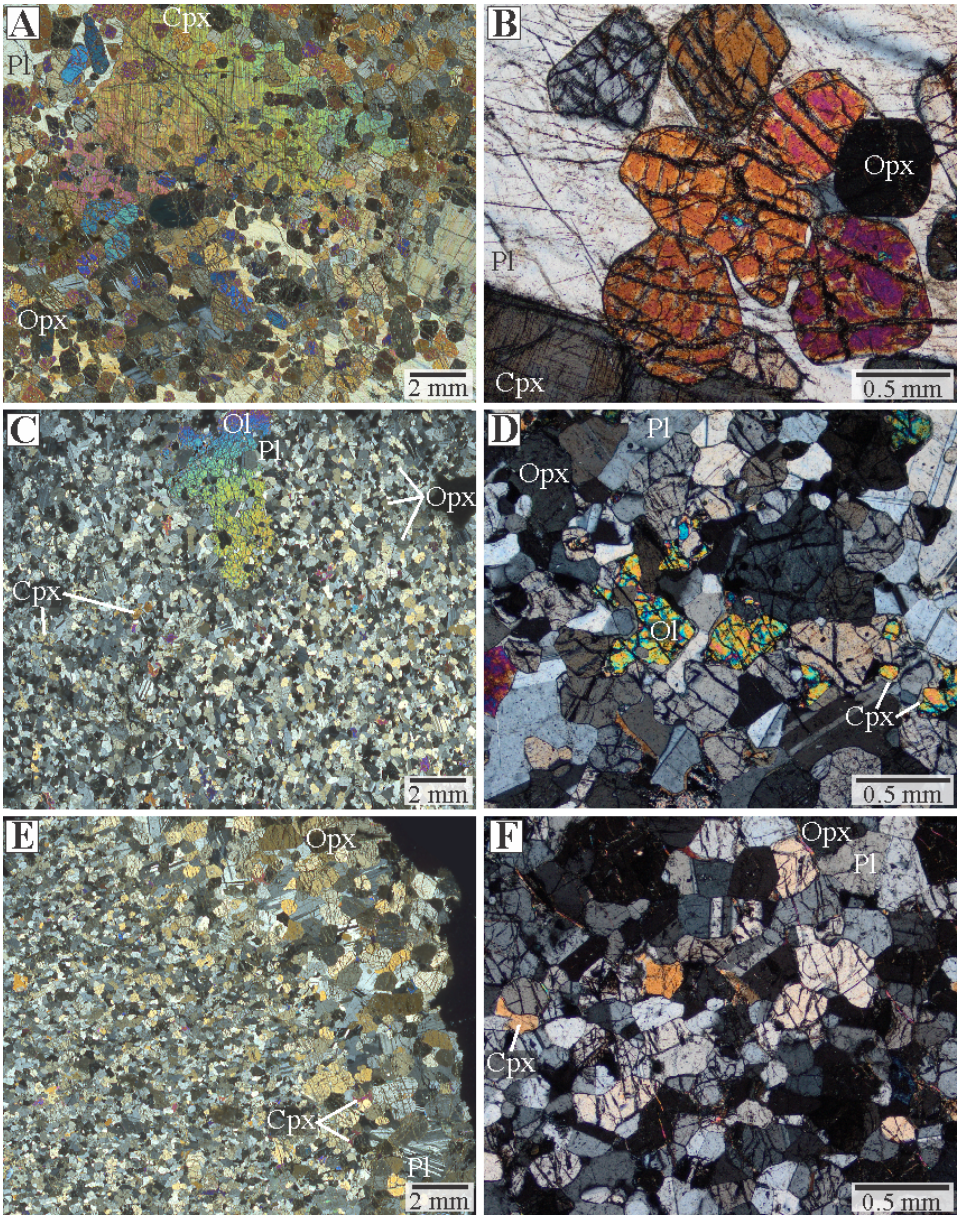

Figure 5.6 – Cross-polarized light photomicrographs of blocks. **A-B** are of poikilitic norite block 1, **C-D** are of olivine-bearing norite block 2 and **E-F** are of norite block 3. **(A)** Textural overview showing euhedral chadacrysts of orthopyroxene (Opx) in oikocrysts of plagioclase (Pl) and clinopyroxene (Cpx). **(B)** A cluster of euhedral orthopyroxene crystals hosted in plagioclase and clinopyroxene oikocrysts (bottom). **(C)** Textural overview of a large poikilitic olivine (Ol) crystal, hosted in a fine-grained matrix of plagioclase (Pl), orthopyroxene (Opx) and clinopyroxene (Cpx). **(D)** Small-sized olivine crystals that are crystallographically aligned are also mantled by pyroxene. **(E)** Textural overview showing both fine-grained and medium-grained zones. Orthopyroxene (Opx) crystals in the medium-grained zone are euhedral and hosted in interstitial plagioclase (Pl) as well as partially mantled by clinopyroxene (Cpx) **(F)** A fine-grained zone composed of anhedral crystals of orthopyroxene and plagioclase with interstitial clinopyroxene.

Plagioclase is typically unzoned and has an average core composition of $An_{83.0}$ and $An_{84.5}$ in blocks 2 and 5, respectively. Rarely, reverse zoning, with a maximum An-content of 95.1 mol%, is found at the rim (8 - 20 μm) of plagioclase crystals in block 2. Orthopyroxene crystals are also chemically homogeneous. Both large and small orthopyroxene crystals have an average Mg# of 74.5 and 77.0 mol% in blocks 2 and 5, respectively. Clinopyroxene has an average Mg# of 79.5 mol% and 81.3 mol% in blocks 2 and 5, respectively.

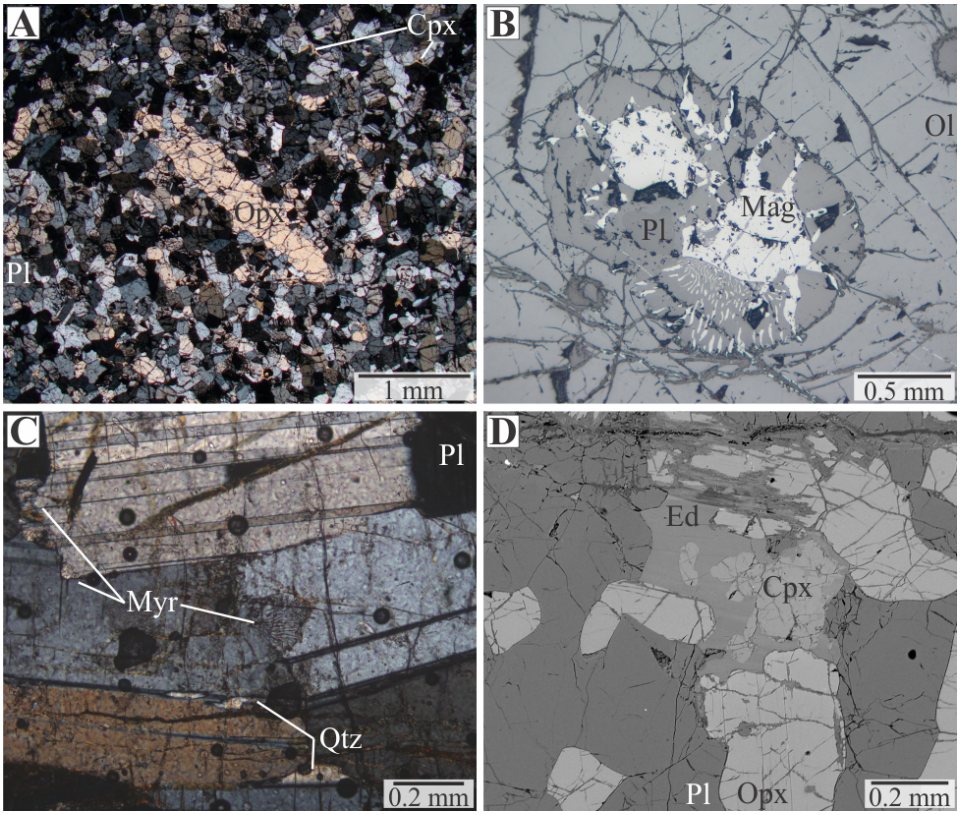

Figure 5.7 – Photomicrographs of distinct features found in some of the blocks. **(A)** A large orthopyroxene (Opx) crystal hosted in a fine-grained matrix of orthopyroxene, plagioclase (Pl) and clinopyroxene (Cpx) in norite block 14. Image taken under crossed polars. **(B)** Symplectite magnetite (Mag) with plagioclase in a circular embayment within a large poikilitic olivine (Ol) crystal in olivine-bearing norite block 7. The olivine in this specimen has been completely alteromorphed by iddingsite. Image taken under reflected light. **(C)** Myrmekite texture (Myr) and interstitial quartz (Qtz) in a medium-grained zone in norite block 6. Image taken under crossed polars. **(D)** Electron-back scatter image of a heavily embayed clinopyroxene crystal hosted in edenite (Ed) in norite block 11.

5.4.3 Norites

Blocks 3, 6, 9, 11 and 12 are norites. Most norite blocks are fine-grained (0.1 - 0.6 mm) with local medium-grained (0.5 - 2 mm) zones (Figs. 5.5B, 5.6E). Modal mineralogy is identical, regardless of grain size, and consists of anhedral orthopyroxene (55%) and plagioclase (42%), accompanied by minor amounts of interstitial clinopyroxene (3%), and trace amounts of phlogopite and magnetite. The fine-grained zones contain a few large (1 - 3; 1 - 3.4 mm), anhedral crystals of orthopyroxene (Fig. 5.7A). Large orthopyroxene crystals, in comparison to the remainder of the fine-grained matrix, contain small (25 - 100 μm) anhedral inclusions of plagioclase and clinopyroxene. In the

medium-grained zones, orthopyroxene crystals are euhedral and are hosted in interstitial plagioclase (Fig. 5.6E). However, compared to poikilitic norite blocks, the medium-grained zones in the norite blocks contain substantially less clinopyroxene, and plagioclase and clinopyroxene do not define oikocrysts. Minor amounts of clinopyroxene in the medium-grained zones partially mantle (15 - 30 μm thick) or form menisci between the orthopyroxene crystals. In block 6, interstitial quartz and the myrmekite texture was observed in a medium-grained zone, at the boundaries (0.04 - 0.16 mm thick) of plagioclase crystals (Fig. 5.7C). Block 11 also hosts small (0.1 - 0.3 mm), heavily-embayed crystals of clinopyroxene that are partially enclosed in orthopyroxene and rimmed by primary edenite (25 - 100 μm thick; Fig. 5.7D).

Blocks 3, 9 and 12 were investigated for mineral chemistry. Plagioclase crystals in the fine-grained zones have an average core An-content of 79.7 - 83.4 mol%. Orthopyroxene in the fine-grained zones has an average Mg# of 71.2 - 75.4 mol% and clinopyroxene has an average Mg# of 79.3 - 82.6 mol% (Table 5.1). All crystals are typically chemically homogeneous, with the exception of plagioclase in block 11, which has thin (8 - 20 μm), reversely zoned rims that reach an An-content of 93.3 mol%. The heavily-embayed crystals of clinopyroxene in block 11 are slightly more mafic, with an average Mg# of 81.4 mol%. Mineral compositions differ between fine- and medium-grained zones with the medium-grained zones being chemically more evolved, as reflected by a lower average An-content of 67.0 - 71.1 mol% for plagioclase and a lower average Mg# of 71.0 - 71.6 mol% for orthopyroxene (Table 5.1).

Table 5.1 – Representative mineral analyses from the blocks. Single point analyses were chosen being closest to the average. The complete set of data and their respective errors are presented in Appendix D.

Block	1: Poikilitic norite			2: Olivine-bearing norite				3: Norite (zones)				
								fine			medium	
Mineral	Pl	Opx	Cpx	Pl	Opx	Cpx	Ol	Pl	Opx	Cpx	Pl	Opx
ID number	2293	2299	2307	2271	2264	2260	2282	2219	2225	2227	2224	2236
SiO_2 (wt%)	50.66	52.98	52.99	46.69	53.43	51.85	37.80	47.14	53.71	52.45	48.87	53.74
TiO_2	–	0.19	0.34	–	0.12	0.33	–	–	0.19	0.43	–	0.33
Al_2O_3	30.20	0.96	1.57	33.66	1.40	2.25	–	33.52	1.07	2.21	32.02	0.86
V_2O_3		–	0.06		0.02	0.03	–		0.04	0.07		0.04
Cr_2O_3	–	0.18	0.43	–	0.16	0.49	–	–	0.28	0.49	–	0.06
FeO	1.54	20.08	6.83	0.23	15.90	7.35	26.86	0.26	15.41	5.98	0.30	18.60
NiO		0.04	0.03		0.04	0.02	0.23		0.06	0.03		0.06
ZnO		–	–		0.03	–	0.05		0.01	–		–
MnO	0.10	0.47	0.19	0.01	0.39	0.26	0.40	0.01	0.35	0.17	0.01	0.39
MgO	0.08	23.50	15.03	0.02	26.11	15.56	35.03	0.02	26.62	14.99	0.01	24.97
CaO	12.96	0.76	22.60	17.05	0.94	20.92	0.01	16.81	0.81	22.87	15.33	0.97
SrO	0.08	0.02	0.01	0.07	0.01	0.02	0.03	0.11	0.05	0.01	0.05	0.03
BaO	0.03	–	–	0.01	–	–	–	0.01	0.02	0.01	0.01	0.01
Na_2O	3.97	–	0.26	1.91	–	0.23	–	2.04	0.01	0.31	2.88	0.01
K_2O	0.21	–	–	0.03	–	–	–	0.05	–	–	0.15	–
Total	99.84	99.18	100.36	99.68	98.56	99.31	100.41	99.97	98.61	100.03	99.63	100.08
End-member (mol%)												
An	63.56			82.98				81.72			74.01	
Ab	35.21			16.85				17.97			25.13	
Or	1.23			0.17				0.32			0.87	
En		66.55	42.82		73.11	44.82			74.27	43.10		69.17
Fs		31.90	10.91		24.99	11.87			24.11	9.65		28.90
Wo		1.55	46.27		1.90	43.30			1.62	47.25		1.93
Fo							69.92					
Fa							30.08					
Mg#		67.59	79.70		74.53	79.06	0.70		75.49	81.71		70.53

All mineral and mineral group abbreviations follow Whitney and Evans (2010)
–: oxide analyzed but not detected

5.5 Abundance of Al_2O_3 in orthopyroxene

Orthopyroxene crystals in the host anorthosite and gabbronorite contain an average of 0.76 wt% (1σ: 0.14 wt%; n = 38) and 0.82 wt% (1σ: 0.12 wt%; n = 8) Al_2O_3, respectively (Fig. 5.8). Sub-ophitic orthopyroxene crystals in the anorthosite are consistently enriched in Al_2O_3 (average of 0.88, 1σ: 0.11 wt%) as compared to oikocrystic crystals (average of 0.71, 1σ: 0.12 wt%).

Orthopyroxene crystals in the poikilitic norite, olivine-bearing norite and norite blocks contain an average of 1.03 wt% (1σ: 0.30 wt%; n = 6), 1.41 wt% (1σ: 0.06 wt%; n = 12) and 1.02 wt% (1σ: 0.21 wt%; n = 26) Al_2O_3, respectively (Fig. 5.8). Interestingly, the fine-grained and medium-grained textures in the norite blocks correlate with high (e.g. average of 1.06 wt% in block 3) and low (e.g. average of 0.77 wt% in block 3) orthopyroxene Al_2O_3 concentrations, respectively (Fig. 5.8B). Furthermore, a large orthopyroxene crystal hosted in the fine-grained matrix of a norite block has a higher Al_2O_3-content (1.12±0.02 wt%) at its core compared to the rim (0.85±0.02 wt%; Fig. 5.8C).

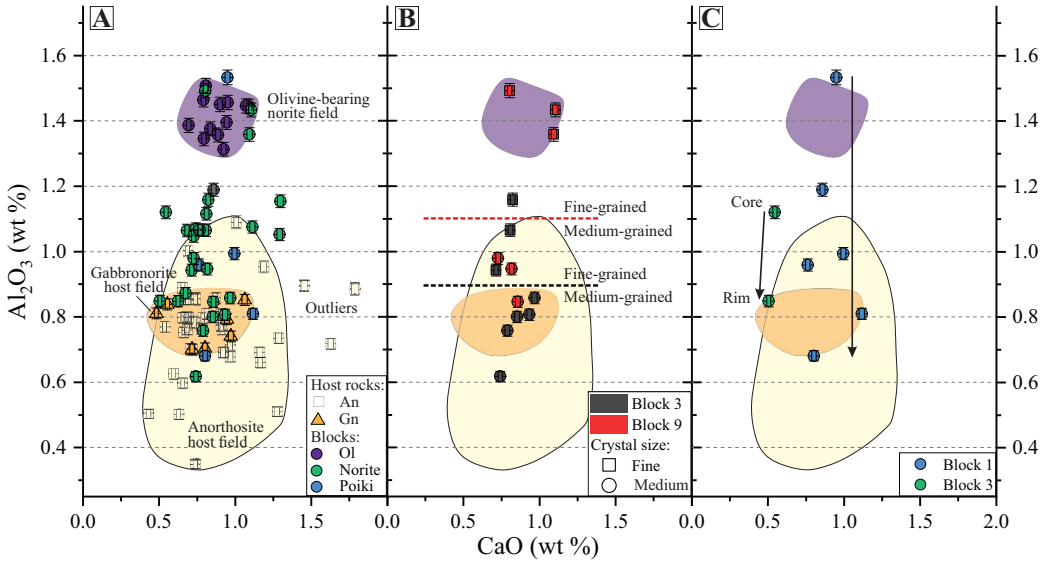

Figure 5.8 – Abundance of Al_2O_3 (wt%) versus CaO (wt%) in orthopyroxene crystals. **(A)** Comparison between the anorthosite (An) and gabbronorite (Gn) host rocks as well as the olivine-bearing norite (Ol), norite and poikilitic norite (Poiki) blocks. On average, host rocks contain less Al_2O_3 in orthopyroxene compared to the blocks. The remaining outliers (clinopyroxene contamination) in anorthosite are not included in the anorthosite field. **(B)** Difference in Al_2O_3-content in norite blocks with bi-modal grain sizes. Fine-grained zones always contain more Al_2O_3 (wt%) in orthopyroxene compared to the medium-grained zones. The boundaries between the zones is approximated by a dashed-line. **(C)** Changes in Al_2O_3-content in the poikilitic norite block (block 1) and in the core to rim of a large orthopyroxene crystal found in the fine-grained matrix of a norite block (block 3). Changes in Al_2O_3 are denoted by arrows.

5.6 Density

Rock densities for the host anorthosite and gabbronorite average 2.73±0.03 g/cm^3 (1σ, n = 42) and 2.95±0.00 g/cm^3 (n = 2), respectively (Chapter 4). These densities are in agreement with measured values for similar cumulates in Ashwal et al. (2005) and Cawthorn and Ashwal (2009).

Rock densities for all blocks average 3.09±0.00 g/cm^3 (n = 13). The poikilitic norites are the densest, averaging 3.24±0.00 g/cm^3 (n = 2), followed by the olivine-bearing norites, averaging

3.11±0.00 g/cm^3 (n = 6) and finally the norites average 3.00±0.00 g/cm^3 (n = 5).

5.7 Whole-rock chemistry

5.7.1 Major and minor elements

All blocks have high whole-rock Mg# of 71.8 - 76.1 mol%, compared to the host poikilitic anorthosites (Mg# of 60.5 mol%; Table 5.2). Major oxides show subtle variations and are controlled by the modal mineralogy of the blocks. Olivine-bearing norite and poikilitic norite blocks are chemically similar (Fig. 5.9). Norite blocks are commonly enriched in Al, Ca, and Na, and depleted in Ti, Fe, Mn and Mg. No correlation between blocks' chemistry and stratigraphic position was observed.

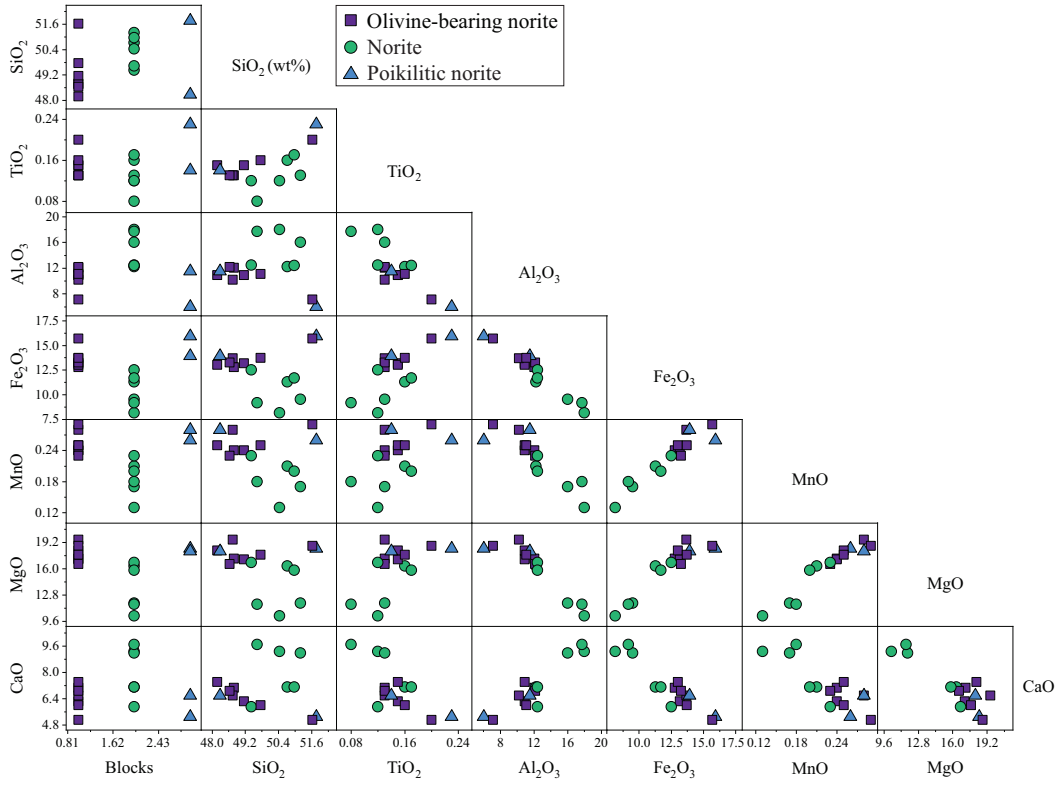

Figure 5.9 – Scatter matrix of major oxides (wt%) showing the chemical distributions between the different blocks based on their modal mineralogy.

5.7.2 Incompatible and trace elements

Chondrite-normalized incompatible and rare earth element (REE) diagrams are presented in Figure 5.10. All blocks possess positive Eu-anomalies (Eu/Eu*: 1.1 - 3.3; where Eu/Eu* = Eu$_{cn}$/ $\sqrt{Sm_{cn} \times Gd_{cn}}$) which are consistent with plagioclase accumulation (Fig. 5.10B). Blocks also have a similar range in $\sum$REE (6.0 - 8.2 ppm) and La/Lu$_{cn}$ ratios (1.6 - 3.6; Table 5.2). However, there are slight differences between the different block groups (Fig. 5.10B). Norite blocks are slightly more depleted in REE compared to the olivine-bearing norite blocks, even though both groups have similar La/Lu$_{cn}$ ratios (3.1 compared to 3.6) and Eu-anomalies (2.5 compared to 1.9). Poikilitic norite blocks are the most enriched in REE and have the lowest La/Lu$_{cn}$ ratio (1.6) and Eu-anomaly (1.3).

Table 5.2 – Average whole-rock chemical results from the blocks, anorthosite layers, bounding gabbronorite and norite layer. The complete set of data and respective errors are presented in Appendix E.

Rock	**Blocks**			**Road-cut lithologies**		
	Olivine-bearing norite	**Norite**	**Poikilitic norite**	**Anortho-site**	**Gabbro-norite**	**Norite layer**
n	**6**	**5**	**2**	**25**	**2**	**1**
SiO_2 (wt%)	49.61	50.33	50.03	49.96	51.25	50.39
TiO_2	0.15	0.13	0.19	0.13	0.20	0.12
Al_2O_3	10.75	14.58	8.76	26.84	17.70	19.99
Fe_2O_3	13.68	10.59	14.94	2.88	6.95	8.76
MnO	0.25	0.19	0.27	0.05	0.15	0.15
MgO	17.70	14.20	18.29	2.17	8.17	7.79
CaO	6.49	7.84	5.95	13.38	13.19	10.58
Na_2O	0.51	0.86	0.53	2.54	1.87	1.85
K_2O	0.05	0.04	0.05	0.23	0.20	0.10
P_2O_5	0.02	0.02	0.02	0.02	0.03	0.01
LOI	1.07	1.25	0.80	1.19	0.28	0.21
Total	100.58	100.21	100.16	99.45	100.05	100.09
V (ppm)	81.80	76.26	147.96	40.57	132.04	70.00
Cr	1482.74	735.70	877.43	20.86	148.35	51.00
Zn	119.97	72.53	82.65	22.00	41.98	58.00
Rb	0.89	0.55	0.55	4.45	3.47	0.60
Sr	131.80	175.19	70.02	385.16	220.81	267.39
Y	2.11	1.75	3.80	2.72	5.92	2.93
Zr	5.61	4.82	5.48	13.57	17.02	4.80
Nb	0.11	0.32	0.18	0.81	1.70	0.28
Ba	34.28	31.15	28.44	91.56	57.29	53.00
La	1.69	1.27	1.30	3.62	3.29	1.95
Ce	2.60	1.99	2.20	6.67	6.32	3.53
Pr	0.31	0.23	0.31	0.76	0.76	0.41
Nd	1.25	0.90	1.37	2.94	3.42	1.69
Sm	0.28	0.20	0.38	0.56	0.87	0.35
Eu	0.18	0.17	0.18	0.45	0.37	0.33
Gd	0.30	0.24	0.46	0.52	0.96	0.41
Tb	0.05	0.04	0.09	0.09	0.17	0.08
Dy	0.34	0.29	0.62	0.49	1.06	0.46
Ho	0.08	0.07	0.14	0.10	0.23	0.11
Er	0.24	0.22	0.46	0.32	0.67	0.38
Tm	0.04	0.04	0.08	0.04	0.09	0.06
Yb	0.29	0.27	0.55	0.28	0.64	0.41
Lu	0.05	0.04	0.09	0.04	0.10	0.06
Hf	0.15	0.15	0.19	0.40	0.52	0.17
Ta	0.01	0.09	0.01	0.06	0.13	0.03
Pb	1.87	1.60	10.40	2.63	1.32	1.90
Th	0.07	0.05	0.09	0.60	0.37	0.15
U	0.02	0.02	0.04	0.09	0.10	0.03
Mg#	74.04	74.56	72.97	61.17	72.10	66.19
$\sum$REE	7.70	5.97	8.21	16.87	18.95	10.23
$(La/Lu)_{cn}$	3.64	3.12	1.56	9.30	3.47	3.43
$(Eu/Eu^*)_{cn}$	1.95	2.47	1.31	2.72	1.23	2.67
$(La/Sm)_{cn}$	3.82	3.85	2.13	4.16	2.97	3.48
$(Gd/Lu)_{cn}$	6.26	5.58	5.24	1.54	1.17	0.86

$_{cn}$: Chondrite-normalized.
Eu/Eu*: Europium anomaly, Eu* obtained by straight line interpolation between plotted points for Sm and Gd.

Block trace element compositions are distinctly different to the host poikilitic anorthosite layers and gabbronorite. Anorthosites have greater $\sum$REE (11.4 - 21.7 ppm), are more enriched in LREE (La/Lu$_{cn}$ = 6.4 - 13.2) and have slightly greater positive Eu-anomalies (1.8 - 3.8; Table 5.2). The gabbronorite shows even greater enrichment in $\sum$REE (19.0 ppm), but the enrichment in LREE (La/Lu$_{cn}$ = 3.5) and Eu-anomalies (1.2) are comparable to the blocks.

I compared the trace element compositions of the blocks to putative parental melts (known as B1, B2 and B3) of the RLS. The discrepancy is quantified by the absolute relative deviation (ARD), although other metrics such as the mean-square-error could also suffice. The ARD is given by:

$$ARD = 100\% \times \frac{|B_{cn} - P_{cn}|}{P_{cn}} \tag{5.1}$$

where B_{cn} corresponds to a chondrite-normalized concentration of an element in a block, P_{cn} corresponds to the chondrite-normalized average concentration of an element in the parental magma. To calculate the total ARD for all elements on a per-block basis, the ARD per element is calculated and the total is averaged. This can also be performed at the petrographic group-level and for all the groups together.

All incompatible and REE patterns of the blocks (per block, per-petrographic group and all groups) best match the B3 melt composition (Fig. 5.10C, D), which has been considered as the parental melt to the Main Zone (Barnes et al., 2010). However, the blocks are much more depleted in incompatible elements and $\sum$REE compared to the B3 melt (7.3 ppm compared to 33.4 ppm), and is consistent with their cumulate composition.

5.7.3 Sr-Nd isotopes

Initial (calculated at 2.06 Ga) εNd and initial ^{87}Sr/^{86}Sr isotope ratios for the blocks and their host rocks are presented in Table 5.3. In general, the blocks, host anorthosite and gabbronorite all fall within the range of previously published RLS isotope compositions (Kruger, 1994; Maier et al., 2000; Roelofse and Ashwal, 2012; Fig. 5.11). The whole-rock initial εNd values measured by Roelofse and Ashwal (2012) tend to be more negative (-6.6 to -8.5) than those measured by Maier et al. (2000) for the Main Zone (-6.3 to -7.4). These differences might be caused by the location of the rocks, as Roelofse and Ashwal (2012) sampled in the northern lobe and Maier et al. (2000) sampled in the eastern lobe (Fig. 2.1a).

Host anorthosite and gabbronorite have an initial εNd between -8.31 and -6.27 and an initial ^{87}Sr/^{86}Sr ratio between 0.707279 and 0.707291. The poikilitic anorthosite has lower initial εNd values compared to gabbronorite and most other values measured for the Main Zone by Maier et al. (2000) and Roelofse and Ashwal (2012). Some anorthosites in the Upper Critical Zone also have lower initial εNd values (-7.1) compared to other lithologies Maier et al. (2000).

The blocks plot separately from the host poikilitic anorthosite and are loosely clustered together according to their group (Fig. 5.11; Table 5.3). Olivine-bearing norite blocks have an initial εNd between -5.76 and -4.43, and an initial ^{87}Sr/^{86}Sr ratio between 0.70614 and 0.70698. Norite blocks have an initial εNd between -6.15 and -3.92, and a ^{87}Sr/^{86}Sr ratio between 0.70712 and 0.70784. Poikilitic norite blocks have an initial εNd between -6.81 and -5.32, and an initial ^{87}Sr/^{86}Sr ratio between 0.70771 and 0.70840.

Table 5.3 – Sr and Nd isotope data from blocks and host rocks. Initial $^{87}Sr/^{86}Sr$ and εNd values are calculated at an age of 2.06 Ga.

Sample	**Block**	**Rb (ppm)**	**Sr (ppm)**	^{87}**Rb/** ^{86}**Sr**	^{87}**Sr/** ^{86}**Sr**	**2**σ	$(^{87}Sr/^{86}Sr)_i$ **2.06 Ga**	**2**σ	**Nd (ppm)**	**Sm (ppm)**	^{147}**Sm/** ^{144}**Nd**	^{143}**Nd/** ^{144}**Nd**	**2**σ	ε**Nd 2.06 Ga**
X1	Poiki.	0.72	67.96	0.0306	0.709292	23	0.708400	151	1.76	0.49	0.1667	0.511883	13	-6.81
X2	Ol.-b.	0.87	161.44	0.0155	0.706595	11	0.706142	52	1.10	0.23	0.1278	0.511461	11	-4.77
X3	No.	0.60	146.37	0.0118	0.707465	5	0.707122	14	1.05	0.24	0.1382	0.511531	23	-6.15
X4	Ol.-b.	1.51	130.72	0.0334	0.707957	4	0.706985	20	1.42	0.32	0.1370	0.511603	7	-4.43
X5	Ol.-b.	1.19	139.47	0.0247	0.707475	12	0.706755	38	1.13	0.27	0.1468	0.511667	11	-5.76
X9	No.	0.18	185.53	0.0028	0.707916	4	0.707836	6	1.44	0.29	0.1228	0.511374	9	-5.13
X10	Poiki.	0.44	88.69	0.0143	0.708127	5	0.707709	12	1.37	0.36	0.1588	0.511853	12	-5.32
X11	No.	0.26	322.37	0.0023	0.707568	10	0.707501	14	0.64	0.14	0.1303	0.511537	19	-3.92
X12	No.	0.45	144.24	0.0091	0.707915	4	0.707650	10	1.21	0.29	0.1437	0.511677	23	-4.75
	Hosts													
ARS-2-4	An.	5.53	331.88	0.0483	0.708698	10	0.707291	127	4.43	0.99	0.1353	0.511381	10	-8.31
AR-9	Gn.	3.72	249.89	0.0431	0.708535	11	0.707279	331	3.68	0.88	0.1446	0.511611	8	-6.27

Block abbreviations: Poiki. = poikilitic norite, Ol.-b. = olivine-bearing norite, No. = norite.
Host rocks abbreviations: An. = anorthosite, Gn. = gabbronorite.

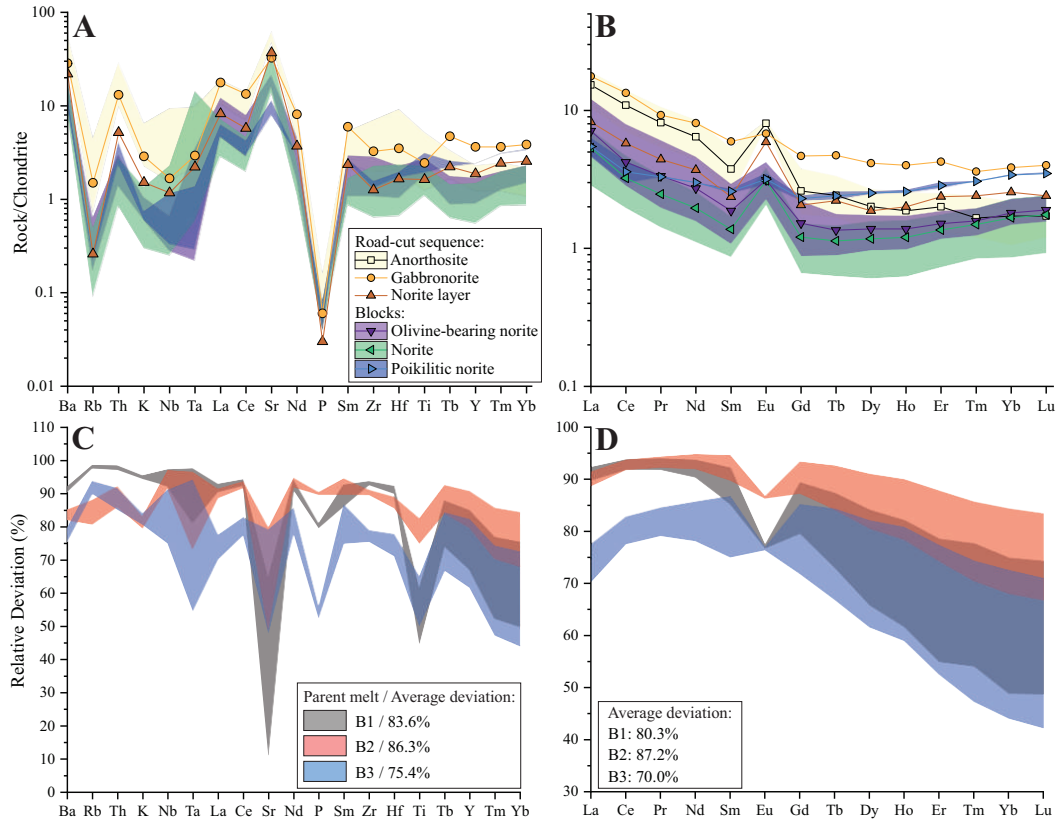

Figure 5.10 – Chondrite-normalized incompatible and rare earth element diagrams of the blocks, anorthosite, gabbronorite and norite layer (**A**, **B**). Ranges are provided for blocks and anorthosites. Samples were normalized using the C1 carbonaceous chondrite of McDonough and Sun (1995). **(B)** Data points and lines correspond to the average of the host (anorthosite only) and block groups. **(C)** and **(D)** Relative deviation of incompatible elements (**C**) and REE (**D**) of all block groups with respect to putative RLS parental melts (B1, B2, B3) proposed by Barnes et al. (2010). A lower relative deviation means a closer match.

5.8 Discussion

I presented a series of detailed field, textural and chemical (including high precision Sr-Nd isotopes) observations for suite of cumulate blocks in a layered sequence of poikilitic anorthosites in the Upper Main Zone of the RLS. The blocks have been categorized into 3 groups on the basis of textures and the presence or absence of olivine. Trace elements and Sr-Nd isotopes of the blocks show slight differences between each group and are very different from their host anorthosite and gabbronorite. In the following sections I discuss the relationship of the blocks to their host rocks, their origin, how they can be used to constrain the rheological conditions of the magmas, and how they provide insights into magma chamber dynamics in the Bushveld Complex.

5.8.1 Relationship between the blocks and their host rocks

The blocks are petrologically distinct from their host anorthosite and gabbronorite (Figs. 5.3, 5.6) and there is no cumulate layer present at the road-cut that is compositionally comparable to the blocks. Mineral compositions in the blocks are more magnesian and calcic compared to the host rocks. The blocks likely therefore crystallized from more primitive melts compared to those of the host anorthosites and gabbronorites. Isotopically the blocks are distinct when compared to the

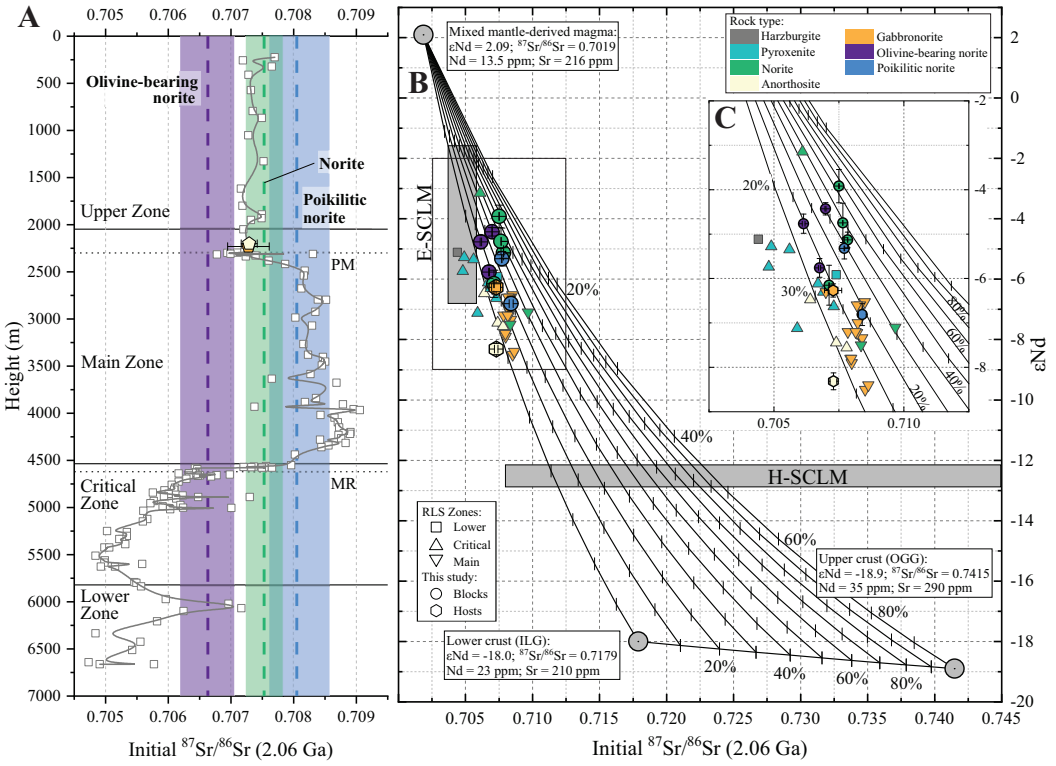

Figure 5.11 – Whole-rock Sr-Nd isotopes of the blocks, anorthosite and gabbronorite compared to the RLS. **(A)** Initial $^{87}Sr/^{86}Sr$ ratio profile of the RLS. Average ratios for the blocks (dashed lines) including the standard deviations (shaded area) as well as poikilitic anorthosite and gabbronorite hosts have been added to the profile for comparison. MR = Merensky Reef and PM = Pyroxenite Marker horizons. RLS data are from Kruger (1994). **(B)** Initial εNd versus initial $^{87}Sr/^{86}Sr$ ratios of blocks and their host anorthosite and gabbronorite, as well as measured RLS rocks (data from Maier et al., 2000; Roelofse and Ashwal, 2012). The diagram includes the crustal (gray circles) and SCLM (gray boxes) contamination models. The estimated reservoir compositions for the crustal model consist of: 1) mantle-derived magma, determined from a MORB-source (Zindler and Hart, 1986); 2) lower Kaapvaal Craton crust contaminant, represented by the Inlandsee Leucogranofels (ILG) exposed within the Vredefort Dome; and 3) upper Kaapvaal Craton crust contaminant; represented by the Outer Granite Gneiss (OGG) exposed within the Vredefort Dome (Hart et al., 1981, 1990). The isotopic mixing model between the reservoirs was developed following Roelofse and Ashwal (2012). The reservoir ranges for the SCLM model are: 1) initial $^{87}Sr/^{86}Sr$ ratio of 0.708 to 0.780 and εNd -12.16 to -12.88 for Harzburgite-SCLM (H-SCLM), and 2) initial $^{87}Sr/^{86}Sr$ ratio of 0.704 to 0.706 and εNd -6.79 to -1.57 for Eclogite-SCLM (E-SCLM). Data from Richardson et al. (1984, 1993); Richardson and Shirey (2008). **(C)** Enlarged portion of **B**.

anorthosites (Fig. 5.11). I suggest that the blocks must be derived from elsewhere in the Bushveld Complex plumbing system and investigate various possible sources in the following sections.

5.8.2 Block relationship to the Bushveld magmatic plumbing system

Despite the differences between the blocks and their host rocks, they are chemically affiliated with the RLS, and in this sense are cognate or comagmatic. This is reflected isotopically, as the blocks fall within the range of isotopic values previously measured for the RLS (Fig. 5.11; Kruger, 1994; Maier et al., 2000; Roelofse and Ashwal, 2012). Furthermore, blocks that are enriched in LREE (La/Lu_{cn} = 3.4) have comparable La/Lu_{cn} ratios to the rest of the Main Zone (3.3; Maier and Barnes, 1998).

The blocks' trace element patterns also best match the putative B3 melt composition that is inferred as the parental melt of the Main Zone (Barnes et al., 2010; Fig. 5.10C, D). However, the blocks are chemically more magnesian and calcic, more depleted in incompatible and REE concentrations and less radiogenic compared to the host Main Zone. Only a single block of poikilitic norite isotopically overlaps with the values measured for the Main Zone (Maier et al., 2000; Roelofse and Ashwal, 2012). Poikilitic olivine in the olivine-bearing norite blocks are unusual for the Main Zone, which is typically devoid of olivine (Eales and Cawthorn, 1996; Cawthorn, 2015). Comparatively, the norite blocks are systematically more silicic (i.e. orthopyroxene-bearing) are also and more radiogenic in initial $^{87}Sr/^{86}Sr$, which suggests that the olivine-bearing norites were formed from less crustally-contaminated melts (Maier et al., 2000). No trend could be interpreted using initial εNd as the values for both norite and olivine-bearing norite blocks overlap. I infer that the blocks represent chemically more primitive parts of the B3 melt system, and are possibly sourced from deeper parts of the magmatic plumbing system.

Isotopic mixing model

Isotopic studies by Maier et al. (2000); Roelofse and Ashwal (2012) and Zeh et al. (2020) have shown that the putative B3 parental melt composition, the closest matching parental melt for the blocks, was generated via a mixture of: 1) mixed asthenospheric and/or mixed mantle, 2) lower Kaapvaal Craton crust, and 3) minor amounts of upper Kaapvaal Craton crust. An isotopic mixing model was constructed using these three isotopic reservoirs, following methodologies/parameters discussed in Roelofse and Ashwal (2012) and is included in Figure 5.11B.

Under the prevailing crustal contamination model, the magma from which the blocks originated was variably contaminated by both the lower (16 - 29%) and upper Kaapvaal Craton crust (7 - 55%). On average, olivine-bearing norite blocks reflect less upper crustal contamination (15%) as compared to the norite (34%) and poikilitic norite blocks (28%). Blocks contain, on average, less crustal contamination as compared to the host Main Zone. The anorthosite host reflects a much stronger lower crustal contamination (39%) with no contribution from the upper crust (0%).

However, the scale of the RLS and the lateral homogeneity of PGE-enriched layers have long been problematic for the crustal contamination model (Schoenberg et al., 1999; Maier et al., 2000; Prevec et al., 2005; Richardson and Shirey, 2008). For this reason, it is important to consider the subcontinental lithospheric mantle (SCLM) contamination model, see 5.11B. The model indicates that both blocks and host rocks are closest to the eclogitic SCLM reservoir. These results are consistent with the putative B3 parental melt (Main Zone), which exhibits a greater contribution from the eclogitic SCLM reservoir (Richardson and Shirey, 2008). However, the contribution of the harzburgitic SCLM reservoir is difficult to quantify, as its range overlaps significantly with potential lower and upper crust signatures (Fig. 5.11B). This is further complicated by the observation that the RLS isotopic data's variance along the initial $^{87}Sr/^{86}Sr$-axis is much smaller than the variance of either the harzburgitic SCLM and the lower-upper crustal sources, and therefore, the εNd-$^{87}Sr/^{86}Sr$ system is unable to distinguish contributions from these reservoirs. However, the crustal contamination model is more similar with the variability of the RLS data compared to the SCLM model. Therefore, to within the available data, the crustal contamination model is a better fit.

Constraints using Al-in-orthopyroxene barometry

Here, I use the amount of Al_2O_3 in orthopyroxene to detect if the blocks were sourced from deeper parts of the RLS. Previous studies by Fram and Longhi (1992); Longhi et al. (1993, 1999) and Charlier et al. (2010) have demonstrated that the amount of Al_2O_3 (wt%) in orthopyroxene megacrysts

hosted in Proterozoic massif-type anorthosite plutons can be used to estimate their depth of crystallization (in kbar).

Longhi et al. (1993) and Charlier et al. (2010) calibrated the Al_2O_3 barometer for orthopyroxene crystals containing $\geq$3 wt% Al_2O_3. Our studied orthopyroxene crystals in the cumulate blocks contain an average of only 1.13 wt% Al_2O_3 (Fig. 5.8). However, the central idea that the amount of Al_2O_3 in orthopyroxene relates to its crystallization pressure is still exploitable, so long as it is demonstrable that major chemicals that could indicate other thermodynamic controls are essentially uncorrelated with Al_2O_3 and that the orthopyroxene is in equilibrium with plagioclase.

Al_2O_3 may be dependent on plagioclase melt saturation, as progressive crystallization of plagioclase results in depletion of aluminum and other plagioclase-forming elements, such as calcium. Therefore, if the aluminum in orthopyroxene is at least partially controlled by the depletion of aluminum in the parental melt, there should be an observable correlation within the data between Al_2O_3 and CaO. However, such a correlation is not observed, see Figure 5.8. Furthermore, all studied block samples are composed of orthopyroxene and plagioclase grains that are closely inter-grown, sometimes in a checkerboard pattern. Therefore, no evidence of disequilibrium is present between these phases. Several outliers in the host anorthosite (e.g. $>$1.3 wt% CaO) are caused by very-fine exsolution lamellae of clinopyroxene in orthopyroxene oikocrysts. Values with high CaO-contents and visible clinopyroxene exsolution lamellae nearby were eliminated from Figure 5.8. The remaining outliers that could not be eliminated by the criteria above (Fig. 5.8A) are likely contaminated by cryptic (non-visible) fine-exsolution lamellae, as in some cases additional analyses nearby did not exhibit the same CaO content (as a quality control). Correlations between Al_2O_3 and the Mg# in orthopyroxene for RLS lithologies have been used to suggest primary thermal and/or differentiation controls of Al_2O_3 in orthopyroxene Cawthorn (2018). However, this is not the case here. Al_2O_3 is essentially uncorrelated with the Mg#, which indicates an independence of the former on temperature and melt differentiation, see Figure 5.12. Indeed, no observable correlation (R^2 = 0.0241) is observed between Al_2O_3 and Mg# in the host anorthosite, which indicates that essentially all of the variability of Al_2O_3 is unexplained by the Mg#, and therefore aluminum is unlikely to be systematically controlled by primary crystallization temperature and differentiation processes.

The conjecture that the amount of Al_2O_3 in orthopyroxene crystals is related to pressure is best supported by observations comparing sub-ophitic crystals of orthopyroxene in poikilitic anorthosite (layers 4 and 5) and oikocrystic orthopyroxene. The sub-ophitic crystals are interpreted in this study to have co-crystallized with plagioclase and subsequently transported from depth in a plagioclase slurry. Sub-ophitic crystals consistently contain more Al_2O_3 (average of 0.88 wt%) compared to oikocrystic orthopyroxene (average of 0.71 wt%). In comparison, oikocrysts are interpreted to have crystallized from trapped pore melt, close to or at the final level of emplacement of the plagioclase slurry (Chapter 4). Given that Al_2O_3 in both groups of orthopyroxene crystals are unlikely to be related to crystallization temperature and differentiation processes, the pressure-control of Al_2O_3 in orthopyroxene is highly probable and is consistent with the data and observations. Furthermore, experimental data by Longhi et al. (1993, 1999) and modeling results by Charlier et al. (2010) suggest that the effects of temperature and other controls on the concentration of Al_2O_3 in orthopyroxene are relatively minor.

However, without a calibrated barometer for the range of Al_2O_3, I am unable to constrain an exact depth. Cawthorn (2018) attempted to calibrate the barometer for lesser amounts of Al_2O_3 using an assortment of natural and experimental samples. Cawthorn (2018) used sparse data with a relatively large variance, and chose a linear regression from Charlier et al. (2010), which poorly fits the data presented (and no R^2 was given). As presented, the data analysis, treatment and interpretation in Cawthorn (2018) is unreliable because of several issues. Firstly, Charlier et al. (2010) did not

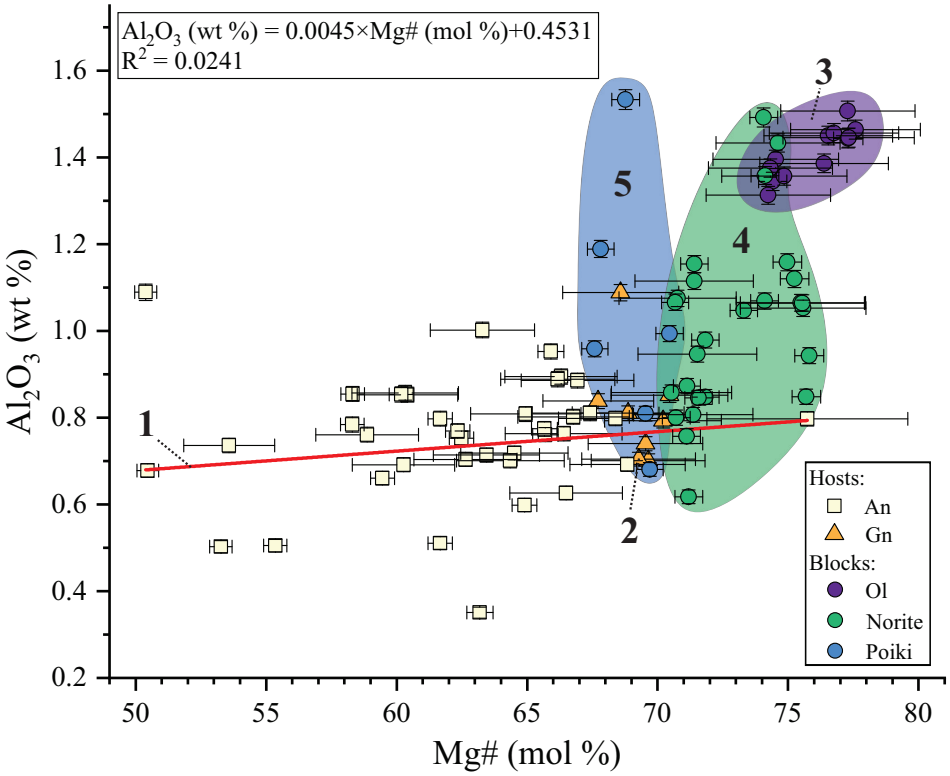

Figure 5.12 – Abundance of Al_2O_3 (wt%) versus Mg# (mol%) in orthopyroxene crystals. Patterns for each lithology are enumerated. The lack of a significant correlation indicates that the Mg# is not responsible for the observed variability in Al_2O_3. Thus, the concentration of Al_2O_3 is independent from temperature and/or melt differentiation. **1**: The host anorthosite (An) indicates a very weak correlation, indicated by the red line. The equation and R^2 of the fitted model are given above. The very weak correlation in anorthosite indicates that the majority of the variability in the data is not explained by the fitted model. Hence, other processes, such as pressure change, are needed to explain the variability. **2**: No correlation exists for gabbronorite (Gn). **3**: Each olivine norite (Ol) data cluster corresponds to a block. Therefore, no correlation could be validated. **4** and **5**: No correlation exists for the norite and poikilitic norite blocks, respectively.

use a linear regression to fit the data, the presented function is a non-linear one; and the fitted model is based on atoms per formula unit (*apfu*), whereas Cawthorn's (2018) model is based on Al_2O_3 in wt%. It is unclear how Cawthorn (2018) obtained a linear model from a non-linear one and the assumptions taken to re-parameterize the *apfu* model into wt%, as the model parameters and *apfu* calculation procedures are not stated except that it is derived from Charlier et al. (2010). Secondly, the data point closest to the Bushveld anorthosite composition was shown as a box with the chosen linear model intercepting this box at the center without any rationale. As Cawthorn (2018) seems to have chosen the intercept of the linear model, it implies that ultimately a circular logic was employed to demonstrate that, since the intercept is not at-depth, therefore an at-depth origin for the RLS (i.e. staging chamber) is unlikely. This is also a logical fallacy ("argument from ignorance"), in that Cawthorn (2018) assumes that a lack of data at low pressures implies that the data suggests a lack of low-pressure Al_2O_3 dependence. The region of low pressure <5 kbar has no experimental data conducted at pressure, the sole data in this region is conducted at atmospheric pressure, which implies that if there was a pressure dependence in this region of Al_2O_3 on pressure, there is simply no data to support this assertion, instead of functional independence. Therefore, Cawthorn's (2018)

utilization of his model (even if statistically sound) to suggest that a staging chamber is impossible within the RLS is an example of a false negative. Clearly, at low pressures, there is either a transition towards, or a continuity of the pressure-dependence in Al_2O_3 in orthopyroxene. The discrimination of the two types of behaviors, which is unexplored in Cawthorn (2018) is critical to the interpretation of the fitted model within the low pressure region. Thirdly, the goodness-of-fit of the model is more sensitive towards data points at the ends of the model's fitted range, and if a model were to be fitted quantitatively to the data (instead of the "semi-quantitative" approach), the slope would be substantially less. This counter-clockwise rotation of the linear model from as presented in Cawthorn (2018) would enable a completely disparate interpretation, that a staging chamber is possible. A refit of Cawthorn's (2018) model is impossible without raw data (not provided), as the data points presented are not of the same statistical relevance, i.e. some points, boxes and lines are multiple data points.

Previous study by Charlier et al. (2010) is statistically sound and proposed a non-linear relationship between Al_2O_3 and pressure. As this is contradictory to Cawthorn (2018), and given the concerns with the latter's non-rigorous methodology, this study deems the findings in Cawthorn (2018) to be unreliable. Since Charlier et al.'s (2010) barometer is non-linear, results from applications of it outside of its intended range exhibits a non-linear dependence of the error on the deviation of Al_2O_3 from the calibration range. With this caveat, and the fact that the RLS changed geometry during its cooling, the absolute depths of the samples is not useful. However, a semi-quantitative range spanned by the samples is roughly 12 km as per the Charlier et al.'s (2010) barometer. As Charlier et al.'s (2010) barometer is heavily non-linear in the region spanned by our study's data, and the slope is very steep, the range result of 12 km is most probably over-estimated.

On average, orthopyroxene crystals in the blocks contain more Al_2O_3 compared to the host anorthosite and gabbronorite (Fig. 5.8A). Given that the Al_2O_3 in orthopyroxene is unrelated to crystallization temperature and/or differentiation processes, its variability is likely to be due to crystallization pressure. Hence, blocks' orthopyroxene crystals likely crystallized at higher pressures and therefore at greater depths (most probably less than 12 km deep from the paleo-surface at the time of its formation) than orthopyroxene in the host poikilitic anorthosite. The highest Al_2O_3 values (average of 1.41 wt%) in orthopyroxene are present in the olivine-bearing norite blocks, indicating that these blocks crystallized deeper than any other blocks (Fig. 5.8A). Al_2O_3 values in the olivine-bearing norite blocks remain relatively constant, indicating that the blocks likely crystallized in isobaric conditions. Orthopyroxene in norite and poikilitic norite blocks contain a range of Al_2O_3 values, indicating that these blocks likely crystallized polybarically and therefore at variable depths. The fine-grained and medium-grained textures in the norite blocks correlate with high (e.g. 1.06 wt%) and low (e.g. 0.77 wt%) orthopyroxene Al_2O_3 concentrations respectively (Fig. 5.8B). The fine-grained zones are also more mafic in composition. Thus, the fine-grained zones of these heterogeneous norite blocks likely crystallized at greater depths in a more primitive magma. Furthermore, a large orthopyroxene crystal hosted in the fine-grained matrix (e.g. Fig. 5.7A) has a higher Al_2O_3-content at its core compared to its rim (Fig. 5.8C). A similar Al_2O_3-content pattern from core to rim has been recorded in large orthopyroxene megacrysts and interpreted to be a record of pressure-induced chemical zoning due to polybaric crystallization during magma/slurry ascent (Charlier et al., 2010). In short, the blocks were likely sourced from deeper parts of the RLS and record a variety of crystallization dynamics, ranging from isobaric (olivine-bearing blocks) to polybaric (norite and poikilitic blocks) conditions.

Block transport and plagioclase slurries

The density of the blocks was compared to their respective host rocks in order to assess the feasibility of RLS magmas transporting blocks from elsewhere in the magmatic system. A roughly linear and positive correlation is observed where the densest blocks are found in the densest anorthosite layers (Fig. 5.13A). This linear relationship could either result from: (1) the magmatic transport of the blocks, such that dense magmas were required to transport denser blocks; or (2) post-cumulus diffusive/infiltrative mass exchange during chemical re-equilibration between host layer and block. However, because there are: (1) sharp contacts; (2) distinct lithologies; (3) distinct mineral chemistries; (4) distinct whole-rock major and trace element chemistries; and (5) distinct Sr-Nd isotopic signature differences between the blocks and their host anorthosite, there is little evidence for any appreciable chemical homogenization between the blocks and the hosts. In addition, if the density correlation is solely due to mass exchange, the density correlation would also depend on the volume, shape and the mineralogy of blocks, as well as their time spent with their host rocks. To within available data, this does not appear to be the case. Therefore, this linear correlation in density between the blocks and host anorthosites is most probably explained by magmatic transport of blocks with denser magmas able to transport denser blocks.

A numerical model can be used to examine the magmatic conditions necessary for block transport. Specifically, the model is used to test the hypothesis that the blocks could have been transported by a host magma that resulted in the emplacement of the anorthosite sequence. As multiple lines of evidence (Chapter 4) suggests that the anorthosite layers were emplaced as slurries, the host magma is most probably an anorthosite slurry. A minimum transport velocity for the blocks can be calculated by balancing frictional forces acting on a spherical block settling at its terminal velocity within a magma column. Assuming the magma behaves as a non-Newtonian fluid, the terminal velocity (V_b) of the blocks can be calculated using the following equation developed by Spera (1980):

$$V_b = 0.344 \left(\frac{\Delta\rho g}{\rho_1}\right)^{\frac{5}{7}} \left(\frac{\rho_b}{\mu_e}\right)^{\frac{3}{7}} \left[r_b - \left(\frac{3K\sigma_0}{4\Delta\rho g}\right)\right]^{\frac{8}{7}}, \tag{5.2}$$

where ρ_b is the block density (average of 3.09 g/cm^3 by measurement), K is a dimensionless constant of $\sim$5, r_b is the radius of the block assuming a circular cross-section, ρ_1 is the density of the host magma that surrounds the block, g is the gravitational acceleration, $\Delta\rho$ is the difference in density between block and host, μ_e is the viscosity of the magma, and σ_0 is the yield strength of the magma, which can be approximated by (Spera, 1980):

$$\sigma_0 = k_1 F^3, \tag{5.3}$$

where, k_1 is an empirically derived constant having the dimension of stress equaling 3.0×10^4 Pa·s and F is the volume fraction of crystals in the magma.

If the host magma is more similar to the anorthosite hosts (average of 2.73 g/cm^3), then its density is likely better approximated by the hosts. As a specific parental host magma is unknown, and the depths of the blocks are also unknown, it is difficult to deduce an exact composition of the host magma that would have transported the blocks in this hypothesis. However, it is fair to argue that the host magma was rheologically and chemically more similar to the anorthosite hosts, e.g. a plagioclase slurry, than its primitive melt, e.g. a basalt (Ashwal and Bybee, 2017). The exact viscosity of a plagioclase slurry is difficult to constrain. Assuming that the plagioclase slurry was emplaced at a temperature of 1200°C (Cawthorn et al., 1998), experimental magma viscosity measurements by Getson and Whittington (2007) of chemically comparable experimental samples yield a viscosity between 1.0×10^6 - 2.0×10^7 Pa·s. Here, I take the lowest viscosity value since the magma likely

traveled at higher temperatures from greater depths. This leads to potential underestimation of the sizes of transportable blocks. The viscosity of the magma is also strongly dependent on its crystal load (Marsh, 1981; Spera, 1980; Getson and Whittington, 2007), which can be incorporated in the model with the Einstein-Roscoe equation (Marsh, 1981):

$$\mu_e = \mu\,(1 - 1.67F)^{-2.5}\,, \tag{5.4}$$

where μ_e is the effective viscosity of the magma with a crystal load as assessed by its volumetric crystal fraction, μ is the magma's viscosity (i.e. 1.0×10^6 Pa·s), and F is the crystal fraction.

The terminal velocities of the blocks as a function of a range of crystal fractions are presented in Figure 5.13B. Crystal fractions greater than 40 vol% are not considered since beyond that point, the magma quickly transitions from a slurry to a solid (Marsh, 1981; Spera, 2000; Takeuchi, 2011).

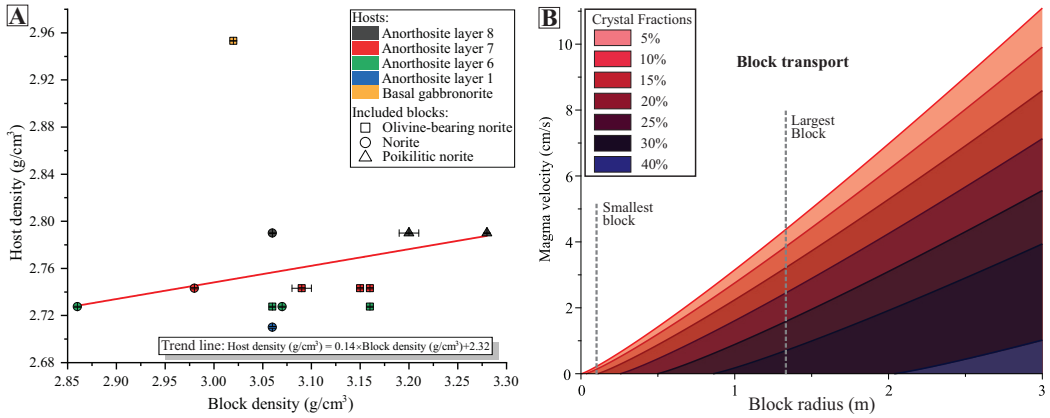

Figure 5.13 – Transport of the blocks. **(A)** Block densities versus host densities. A linear relationship (red line) shows that denser anorthosite layers host denser blocks. A block (number 4) hosted in gabbronorite (topmost data point) was not considered in the linear model as it is unique. The R^2 for the linear model equals 29.4%. **(B)** Numerical models showing minimum magma velocities required to transport given sizes of blocks for a plagioclase slurry with crystal fractions ranging from 5 to 40 vol%. Each color corresponds to maximum sizes of blocks that can be transported in the slurry given a certain crystal fraction. Vertical dashed lines correspond to the smallest and largest radii of blocks encountered in the layered sequence. Model parameters: host magma viscosity = 1.0×10^6Pa·s, average block density = 3.09 g/cm^3, average anorthosite density = 2.73 g/cm^3.

Figure 5.13B demonstrates a few key qualitative observations: (1) that the capacity for entrainment and transport of blocks is highly sensitive to the crystal fraction of the host magma in a non-linear manner; and, (2) all known sizes of blocks can be transported within a range of crystal fractions and flow velocities. With an aphric magma, transport is possible only at very high magma velocities, and therefore this case is much less probable in the sense that a spectrum of flow velocities exist within a magma chamber, similar to any other hydrodynamic system, and the highest velocities are the least abundant in both time and space. The largest block (block 11) has a radius of 133 cm. Since the blocks are semi-tabular, the model's assumption of a spherical shape for the blocks leads to a much smaller drag than that of semi-tabular-shaped blocks. This results in a large over-estimation of the magma velocity that is necessary to transport the blocks. Non-mutually exclusive implications of the spherical approximation of block shapes are: (1) the required crystalinity is lower than predicted by the model; (2) the required viscosity is lower than predicted by the model; and, (3) the required flow rate is much lower than that predicted by the model. Furthermore, transport along an incline requires less hydrodynamic force than that of vertical transport. Therefore, the numerical

model estimates are the absolute maximum upper bound of magma hydrodynamic conditions. With great over-estimation, a plagioclase slurry with a crystal fraction between 5 - 30 vol% would be able to entrain the observed blocks, if the blocks are spherical and if the magma ascent velocity is from 4.38 and 0.70 cm/s, respectively. The blocks would be entrained at crystal fractions greater than 30 vol% at any magma ascent velocity. These velocities correspond to the minimal magma ascent rates (greatly over-estimated) where the blocks would remain neutrally buoyant with the slurry. For transport to occur, the slurry needs to travel faster than the calculated terminal velocities and/or increase its crystal fractions and/or break up the blocks into smaller pieces. The model's estimated rates of magma/slurry ascent velocities are comparable to the ascent rates calculated for the Mount St. Helens May 18^{th} 1980 eruption, which are estimated to be between 0.7 - 70 cm/s from a 8 - 11 km deep storage zone (Scandone and Malone, 1985; Rutherford, 2008). Furthermore, recent U-Pb zircon dates reveal that the RLS was emplaced in less than 100 ka, implying a rapid accumulation of magma at a rate 5 - 13 km^3/year (Cawthorn et al., 1998; Zeh et al., 2015), which indirectly suggests that episodic conditions when and where ascending magma with sufficient velocity to transport blocks vertically could exist. Therefore, the numerical model of magma transport dynamics supports the hypothesis that the blocks could have been transported in a plagioclase slurry.

5.8.3 The origin of the blocks and the role of staging chambers during the emplacement of the Main Zone

The blocks are comagmatic with the RLS and can therefore be regarded as cognate xenoliths or autoliths. The blocks may therefore represent: (1) disaggregated proto-cumulate layers that originated at or near their present level during the evolution of the chamber; (2) recycled sidewall/roof cumulates; (3) deeper parts of the magmatic plumbing system.

Disaggregated proto-cumulate layers within the magma chamber?

The injection of plagioclase slurries during the formation of the layered anorthosite sequence within the magma chamber may have led to the disaggregation of resident layers of olivine-bearing norite, norite and poikilitic norite (e.g. Bergantz et al., 2015). Disaggregated layers may have then been transported, and in this sense recycled into the developing anorthositic layers as cumulate blocks. However, the blocks only constitute $\sim$0.2% of the exposed surface area and therefore do not appear to represent a sufficient volume of material for disaggregated cumulate layers – assuming that the disaggregation was local and that material was not transported further along-strike. Also, half of the blocks are randomly distributed throughout the layers (Fig. 5.1) that is more characteristic of transport and deposition. The blocks are generally large ($\sim$m-scale) and small examples ($<$1 m) are rare. I would expect a continuous distribution in block size if they were the result of local layer disaggregation. Furthermore, a variety of blocks from different groups are hosted in close proximity and sometimes co-aligned within the same anorthosite layer (Fig. 5.1; anorthosite layers 1, 7 and 8). I would expect similar cumulate lithologies to be clustered together if there was a layer disaggregation and the alignment of the blocks within the layers is more characteristic of magma flow. These lines of evidence suggest that the blocks do not represent material derived from disaggregated proto-cumulate layers in the chamber.

Entrainment from the roof or side walls of the magma chamber?

Blocks (up to several hundred meters across) in the layered sequence of the Skaergaard Intrusion have been interpreted as recycled roof and sidewall material that fell/became transported in magmatic

density currents (Irvine et al., 1998). The evidence for this includes: (1) crudely internally layered blocks; (2) leaching of mafic minerals in smaller blocks caused by thermal disequilibrium as the blocks settled in their cumulate hosts; (3) a large block that was cut by early basaltic (roof material, now eroded) dykes; and (4) cumulus minerals which drape the blocks caused by magmatic crystal-liquid suspension currents. However, the size and box-shaped nature of the Skaergaard Intrusion favored the development of sidewall and roof facies. Instabilities in these facies led to the collapse of crystal mushes and block transport. In comparison, the RLS does not exhibit such magma chamber geometry and has a large aspect ratio ($\sim$35:1; Eales and Cawthorn, 1996; Cawthorn, 2015). It is therefore unlikely that the blocks are derived from gravitational collapses of the sidewalls. Also, the RLS is lacking a roof sequence that is comparable to the basal parts of the magma chamber. Instead the RLS shows a continuous differentiation sequence with magnesian compositions at the base and more felsic compositions at the roof (Wager and Brown, 1968; Cawthorn, 2015). The development of a roof sequence depends on the size of the intrusion. Small ($<$100 m thick) intrusions typically develop thick roofs, whereas large intrusions, such as the RLS, develop thicker floor sequences since convection will maintain a large heat flux at the roof, inhibiting cooling and crystallization there (Jaupart and Mareschal, 2011). In summary, the blocks do not represent fallen roof or collapsed sidewall material during the solidification of the RLS.

Crystallization and entrainment from staging chamber(s)?

Staging chambers are conduit (sill or dyke) magma reservoirs located upstream and/or deeper in the magmatic plumbing system that process magmas prior to their final emplacement level. Various lines of evidence have been proposed for staging chambers, including mass balance calculations using the high platinum-group element tenors of magmatic sulfides (McDonald and Holwell, 2007), chromium concentrations (Eales and Costin, 2012), and Sr-Nd isotopic disequilibrium between co-existing plagioclase-orthopyroxene crystals (Roelofse and Ashwal, 2012).

The blocks' mineral and whole-rock chemistries, including normalized incompatible and REE patterns, as well as Sr-Nd isotopes reflect a signature closer to a mantle-derived magma (initial $^{87}Sr/^{86}Sr$: 0.707344 and εNd: -5.22; Fig. 5.11) as compared to the host rocks, other measured isotopic values for the Main Zone (initial $^{87}Sr/^{86}Sr$: 0.708244 and εNd: -7.30; Kruger, 1994; Maier et al., 2000; Roelofse and Ashwal, 2012) and the proposed putative parental melts for the RLS (e.g. B1, B2 and B3; Barnes et al., 2010). Such a signature should logically be produced closer to its source, at depth, deeper than within the main chamber. Additionally, orthopyroxene crystals in the blocks contain more Al_2O_3 (average of 1.13 wt%) that is uncorrelated with CaO or Mg#, than the oikocrystic orthopyroxene in the host anorthosites (average of 0.71 wt%; Fig. 5.8). This may mean that orthopyroxene crystals in the blocks crystallized at greater pressures and therefore greater depths than their current levels of exposure (Longhi et al., 1993; Charlier et al., 2010). The low Al_2O_3-contents of orthopyroxene crystals does not necessarily eliminate a staging chamber model as proposed by Cawthorn (2018), which is afflicted by serious data analysis and interpretation issues. Rather, even the minimum of 3 wt% Al_2O_3, which is the lowest calibrated range for the Al_2O_3-in-orthopyroxene barometer from Charlier et al. (2010), already corresponds to a crystallization pressure of $\sim$6 kbar, which is a depth of $\sim$22 km. Assuming that the RLS magma chamber was at a depth of $\sim$3 km below surface (Cawthorn et al., 1998), this leaves plenty of space to accommodate a staging chamber that is less than 12 km from the paleosurface. Thus, the evidence presented above is consistent with a deeper origin of the blocks.

Within the main chamber, it is improbable that there would have been such contrasting crystallization and contamination histories. For example, the olivine-bearing norite and fine-grained zones

in norite blocks share similar petrographies (Fig. 5.6D, F; with the exception of olivine crystals), mineral chemistries, Al_2O_3-concentrations in orthopyroxene crystals (Fig. 5.8), and whole-rock chondrite-normalized incompatible and REE patterns (Fig. 5.10A, B) suggesting that they began crystallizing from the same parent magma, likely at the same depth. However, the presence of olivine crystals and Sr-Nd isotopic systematics in the olivine-bearing norite blocks reflect crystallization from a less upper crustal contaminated melt (average of 15% upper crustal material) as opposed to the norite blocks (average of 34% upper crustal material; Fig. 5.11). The fine-grained zones in the norite blocks likely mingled and continued crystallizing elsewhere for a protracted period of time, likely at lesser depths, in a chemically evolving melt as evidenced by: their range of Al_2O_3-contents, which likely indicate polybaric crystallization; the ductile and mingled zones of larger and chemically more evolved crystals (Fig. 5.5, Table 5.1) and; more-radiogenic upper crustal isotopic signatures (Fig. 5.11). As for the poikilitic norite blocks, they reflect distinct petrographies, mineral and whole-rock chemistries, whole-rock chondrite-normalized incompatible and REE patterns (Fig. 6.11A, B) as well as a broad range in isotopic signatures as compared to the other blocks and host rocks. Given these differences, the poikilitic norite blocks likely originated from a chemically distinct environment, perhaps from another or different section of the magmatic plumbing system. Such differing crystallization and isotopic contamination histories are more consistent with a or perhaps a few staging chambers.

Sr-Nd isotopic data of the poikilitic anorthosite host at the road-cut reflect crystallization in a melt that assimilated larger amounts of lower crustal material (39%) as compared to the initial parental magmas of the blocks (average of 23%), the gabbonorite (28%) and the majority of known Main Zone (Fig. 5.11). A similar pattern is noted for some anorthosites in the Critical Zone as compared to other lithologies (Maier et al., 2000; Fig. 5.11B). The Sr-Nd isotopic similarity between the distinct anorthosite layers at the road-cut and the stronger lower-crustal signature compared to other analyzed rocks is well-explained by the crystallization of melts and slurries in deeper staging chambers. This interpretation is consistent with the widely-accepted Proterozoic massif-type anorthosite model (Ashwal, 1993; Ashwal and Bybee, 2017 and references therein).

Considering all these factors above, the blocks and host anorthosite layers likely originated from staging chambers below the RLS magmatic chamber. Staging chambers may experience large volumes of mantle-derived melt that undergo fractional crystallization and various mechanisms of mineral separation (e.g. olivine, pyroxene and plagioclase). Masses of crystals, such as plagioclase, can then be remobilized by further replenishments of the staging chamber and emplaced into the main chamber as slurries. Magmatic remobilization and emplacement into the main RLS chamber was likely of short duration, as evidenced by a general lack of more-radiogenic upper crustal isotopic signatures (Fig. 5.11). En route, these slurries entrained cumulate blocks from their original or other staging chambers as they ascended.

5.9 Conclusions

A total of 16 (olivine-bearing norite, norite and poikilitic norite) cm- to m-sized cumulate blocks are hosted in a sequence of layered poikilitic anorthosites in the Upper Main Zone of the RLS, Bushveld Complex. The sequence of poikilitic anorthosites is divided into 8 texturally and compositionally distinct layers and is hosted in unlayered gabbronorites that are typical of the Main Zone. Each layer of poikilitic anorthosite are formed by the injection of a plagioclase-charged slurry into the chamber with post-emplacement solidification, leading to the crystallization of orthopyroxene-clinopyroxene oikocrysts in the crystal mush. The field relations, whole-rock (major and trace elements), mineral

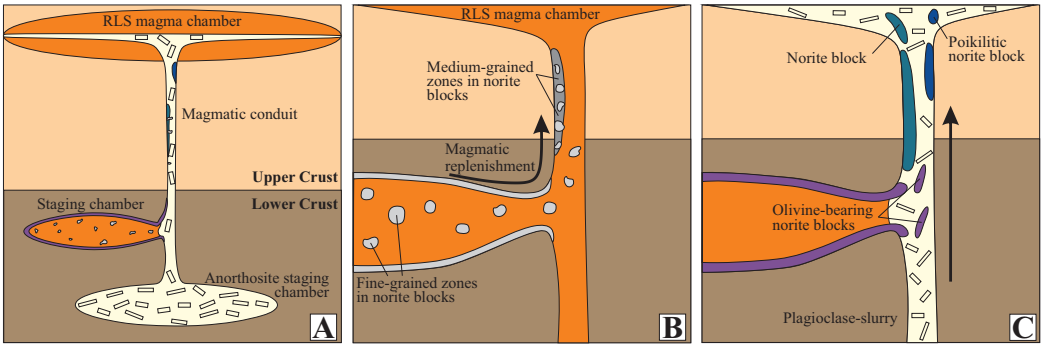

Figure 5.14 – Illustration of a proposed model of the origin and evolution of the blocks and host poikilitic anorthosite within the Bushveld magmatic plumbing system. **(A)** The Bushveld magmatic plumbing system with a few staging chambers located within the lower crust and connected to the RLS magma chamber by a conduit. Plagioclase slurries developed in a separate staging chamber below that of the blocks can explain the distinct isotopic signatures and to allow for subsequent entrainment and transport. **(B)** Origin of the norite and olivine-bearing norite blocks. Both originated in the same staging chamber with some fine-grained zones being remobilized to shallower sections of the plumbing system, where they continue to crystallize. **(C)** The olivine-bearing norite, norite and poikilitic norite blocks being entrained and transported by ascending plagioclase slurries.

chemistry, and whole-rock Sr-Nd radiogenic isotopic compositions of the blocks are examined in detail in this contribution. Whole-rock REE patterns and Sr-Nd isotopic compositions (average initial $^{87}Sr/^{86}Sr$: 0.707344 and εNd: -5.23) indicate that the cumulate blocks are cogenetic with the RLS. Both incompatible and REE patterns of the blocks are reminiscent of the B3 melt composition that is inferred to be the main feeder melt composition to the Main Zone. However, their isotopic compositions are distinct from their anorthosite (initial $^{87}Sr/^{86}Sr$: 0.707291 and εNd: -8.31) and gabbronorite (initial $^{87}Sr/^{86}Sr$: 0.707279 and εNd: -6.27) hosts. I evaluated the potential origins of these cumulate blocks such as disaggregated proto-cumulate layers, fallen roof facies rocks, and entrained sidewall cumulates, in the solidifying magma chamber. On the basis of field observations, petrography, mineral and whole-rock chemistry, isotopic compositions, density and numerical modeling constraints, I argue that the blocks represent recycled cumulate material from staging chambers and conduits in the deeper Bushveld Complex plumbing system. Numerical modeling of the terminal velocities of the blocks suggests that the absolute upper-bound hydrodynamic conditions necessary to transport the blocks (assuming spherical blocks and vertical transport) most closely resemble a plagioclase slurry (with 5 - 30 vol% crystals) that flowed at a rate of 4.38 - 0.70 cm/second. Masses of plagioclase crystals (that crystallized from a melt contaminated by the lower crust) were remobilized from deeper staging chambers and entrained the more-primitive and less-contaminated (or isotopically less radiogenic) blocks from those and/or other staging chambers through which they flowed. The blocks therefore provide important insights into the magmatic plumbing system and evolution of the Main Zone, and highlight the significance of cumulate recycling in the development of the Bushveld Complex.

6 Pyroxenite layers and blocks in the Upper Main Zone: a case of magmatic replenishment via slurries

6.1 Introduction

The vast majority of ultramafic-mafic layered intrusions are thought to have been formed through multiple pulses of replenishing magma into a differentiating magma chamber (Charlier et al., 2015 and references therein). Magmatic replenishments can be documented: 1) structurally (e.g. cross-cutting dykes and layers), 2) mineralogically (e.g. addition or loss of a crystallizing phase), 3) texturally (e.g. crystal zoning or resorption), 4) chemically, 5) isotopically, and/or 6) geochronologically. It is unknown how often magmatic replenishments take place in a magma chamber, but they are critical in the formation of long-lived intrusions and have been documented in ultramafic-mafic layered intrusions at Skaergaard (Greenland), Rum (Scotland), Stillwater (United States), Muskox (Canada), Duluth (United States) and the Bushveld (South Africa) (Cawthorn, 1996; Charlier et al., 2015).

There are mineralogical, chemical and isotopic lines of evidence that the Rustenburg Layered Suite (RLS) of the Bushveld Complex was formed through at least 4 major pulses of replenishing magma (e.g. Eales, 2002). A major pulse is thought to have been emplaced in the upper region of the Main Zone and is known as the 'Pyroxenite Marker', defined by a single or multiple (up to 4) $\leq$2 m thick orthopyroxenite layers found in the eastern, western and northern lobes of the RLS (von Gruenewaldt, 1973; Molyneux, 1974; Hayes et al., 1985; Sharpe, 1985; Kruger et al., 1987; Cawthorn et al., 1991; Maier et al., 2001; VanTongeren and Mathez, 2013; Cawthorn et al., 2016; Cawthorn, 2020). A reversal in mineral compositions (e.g. Molyneux, 1974; Hayes et al., 1985; Mitchell, 1990; VanTongeren and Mathez, 2013; Cawthorn et al., 2016) and whole-rock initial $^{87}Sr/^{86}Sr$ ratios (Sharpe, 1985; Mitchell, 1986; Kruger, 1994; Cawthorn et al., 1991) begins 200 - 400 m below the Pyroxenite Marker. Mineral compositions become more magnesian and calcic (average increase of $\sim$10 mol% in both An-content in plagioclase and Mg# in pyroxene), while initial $^{87}Sr/^{86}Sr$ ratios decreases from 0.70827 to 0.70694 (calculated at 2.056 Ga) upwards towards the Pyroxenite Marker. This major pulse is interpreted by many (e.g. Hayes et al., 1985; Cawthorn et al., 1991; VanTongeren and Mathez, 2013 and references therein) to represent the mixing of a replenishing, less differentiated magma with a resident one.

Numerous studies have explored large-scale (hectometer) aspects of the Pyroxenite Marker. However, no study has yet documented the small-scale (decimeter) aspects of individual pyroxenite layers. This study describes a series of 'pyroxenite' (*sensu lato*) layer outcrops found in an incised valley in the Mooimeisjesfontein area, $\sim$36.5 km SW of Burgersfort, in the eastern lobe of the Bushveld Complex. Pyroxenite layers are bounded by anorthosite at their base and capped by gabbronorite. Numerous transported cumulate blocks hosted in the pyroxenite layers and gabbronorite are also described in detail. This study provides detailed and diverse field, petrographical, chemical (mineral and whole-rock) and density data. Based on these data, I examine the feasibility of the Pyroxenite Marker as a result of a magmatic replenishment event, where the replenishing magma mixed with a resident one (e.g. Molyneux, 1974; Cawthorn et al., 1991; Maier et al., 2001; VanTongeren and Mathez, 2013; Cawthorn et al., 2016; Cawthorn, 2020), and the nature of the replenishing magma. Furthermore, I propose that the replenishing magma was likely crystal-bearing.

6.2 Field descriptions

The study area is dominated by unlayered gabbronorite with minor layers of anorthosite, pyroxenite (*sensu lato*) and modally-graded gabbronorite. A total of 4 outcrops exposing pyroxenite layers are located in a N-S trending incised valley, cutting into the Upper Main Zone stratigraphy (Figs. 2.5, 6.1). Lithologically-distinct blocks of transported cumulate material are found in pyroxenite layers and modally-graded gabbronorite horizons. Molyneux (1970, 1974) identified two distinct pyroxenite layers in the area separated by 60 meters of gabbronorite (Fig. 6.1). The stratigraphically-lower layer is described as a ∼2 m thick orthopyroxenite layer underlain by pure anorthosite. The second layer is described as a ∼1 m thick pyroxenite layer underlain by poikilitic anorthosite. Based on these descriptions, the pyroxenite outcrops are divided into two sequences (Fig. 6.1) which are described in detail below.

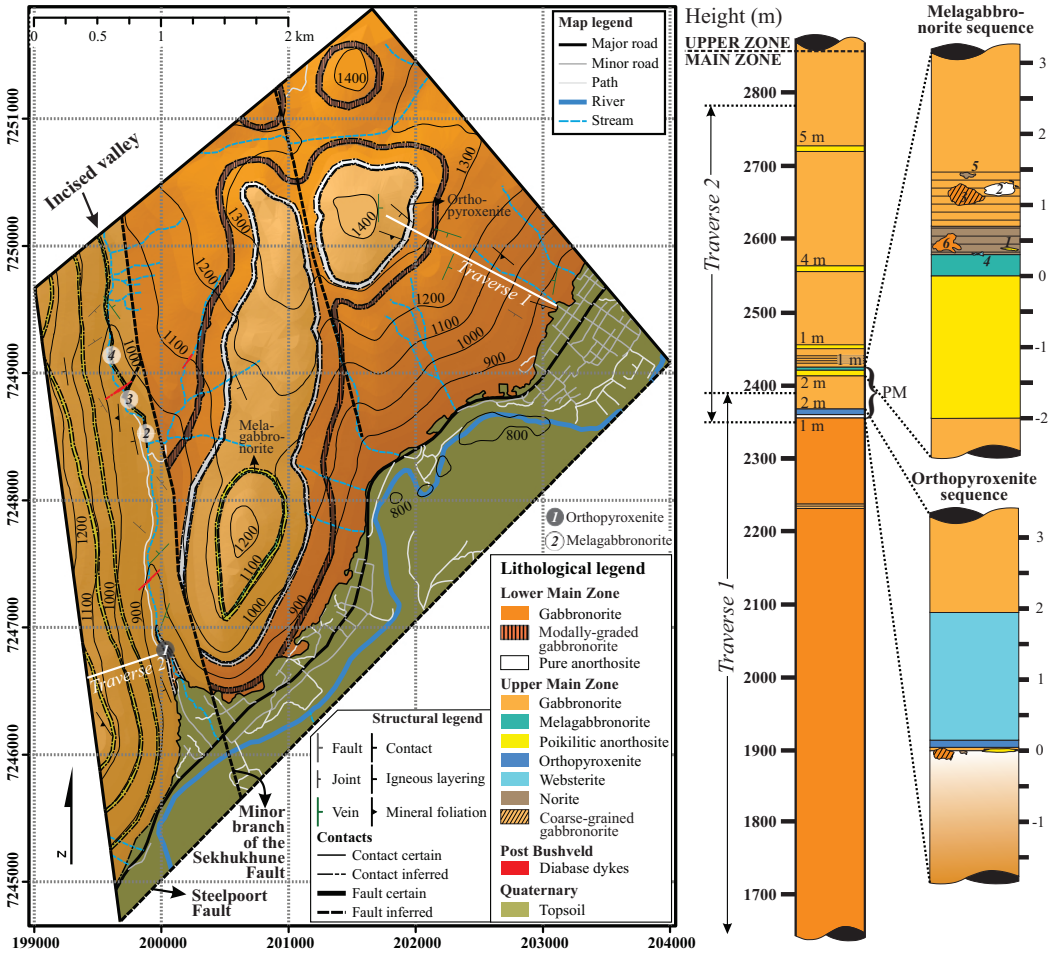

Figure 6.1 – Geology and stratigraphic succession of the Mooimeisjesfontein area. The geological map of the area (left) was updated by the author from the original base map (2430 Pilgrim's Rest geological map, 1: 250 000 Series) and from Molyneux (1974). The location of the studied pyroxenite outcrops are highlighted by shaded circles. Included are the detailed stratigraphic successions of the entire Mooimeisjesfontein area (right) and of each pyroxenite sequence (rightmost). PM, Pyroxenite Marker. Also shown in the detailed pyroxenite successions are the location and composition of cumulate blocks.

6.2.1 The orthopyroxenite sequence

This sequence is well exposed at the southern margin of the incised valley (location 1 in Fig. 2.5). The orthopyroxenite sequence begins with medium-grained unlayered gabbronorite which grades ($\sim$1 m) to pure anorthosite (Fig. 6.1). The transition is marked by modally-graded bands that can be traced for several meters along strike. Several, cm-sized, irregularly-shaped pits ($\sim$1 cm deep) in the pure anorthosite have been filled by the overlying orthopyroxenite.

The pyroxenite layer begins with strongly foliated medium-grained gabbronorite ($\sim$5 cm thick) which grades to medium-grained melanocratic orthopyroxenite - websterite (hereon called orthopyroxenite; Fig. 6.2A). The orthopyroxenite layer is $\leq$2 m in thickness and gradually thins out to $\sim$1 m along the entirety of the outcrop ($\sim$180 m). The orthopyroxenite layer transitions to unlayered gabbronorite up sequence.

6.2.2 The melagabbronorite sequence

The sequence is exposed further north in the incised valley (locations 2-4 in Fig. 2.5). The base of the sequence is marked by medium-grained unlayered gabbronorite. Overlying the basal gabbronorite is a 1 - 5 m thick layer of poikilitic anorthosite (Fig. 6.2B). The contact between the gabbronorite and anorthosite is sharp but the contact and lithologies immediate to the contact are commonly obscured by late-stage evolved pegmatoidal dykes (Hayes et al., 2018). The anorthosite is characterized by evenly distributed, pyroxene oikocrysts (4 - 10 cm; $\sim$20 vol.%) composed of both orthopyroxene and clinopyroxene, in a matrix of plagioclase laths (1 - 5 mm). Oikocrysts are spherical to irregularly-shaped and contain abundant (40%) small (1 - 2 mm) plagioclase chadacrysts.

The contact between the polikilitc anorthosite and melanocratic gabbronorite layer with up to 70% pyroxenes (hereon called melagabbronorite) is sharp and undulates slightly (average amplitude of $\sim$10 cm) along strike. The thickness of the melagabbronorite layer varies along strike, from 23 - 60 cm. Several, $\leq$70 cm high and $\leq$36 cm wide, flames of anorthosite transgress into the melagabbronorite layer (Maier et al., 2001). The melagabbronorite transitions to modally-graded gabbronorite ($\sim$1 m thick), followed by unlayered gabbronorite. Individual modally-graded bands are 1 - 10 cm thick, can be traced for several meters along strike and are the result of varying modal proportions of pyroxenes and plagioclase.

6.2.3 Blocks

Hundreds of leucocratic to melanocratic cumulate blocks are hosted at the base of the orthopyroxenite layer (Fig. 6.3A, B), in the modally-graded gabbronorite at the melagabbronorite sequence as well as in another horizon of modally-graded gabbronorite, 10 to 30 meters above the melagabbronorite sequence (Figs. 6.3C, D and 6.1). Blocks vary from centimeter to m-sized (0.05 - 20 m) and consist of anorthosite, gabbronorite, norite and websterite which are either texturally or lithologically contrasting to their host rock (Fig. 6.3). In 3 dimensions, most blocks are oblate-shaped with their two longest axes aligned parallel to layering (Appendix B). In cross-section, blocks appear oval to irregularly-shaped and some blocks appear to have deformed underlying sequences or modally-graded bands (Fig. 6.3B, D). Blocks may have rounded or very irregular margins in three dimension. Rarely some of the blocks may be fragmented or encased in a thin band of pure anorthosite (1 - 5 cm thick; Fig. 6.3C, D).

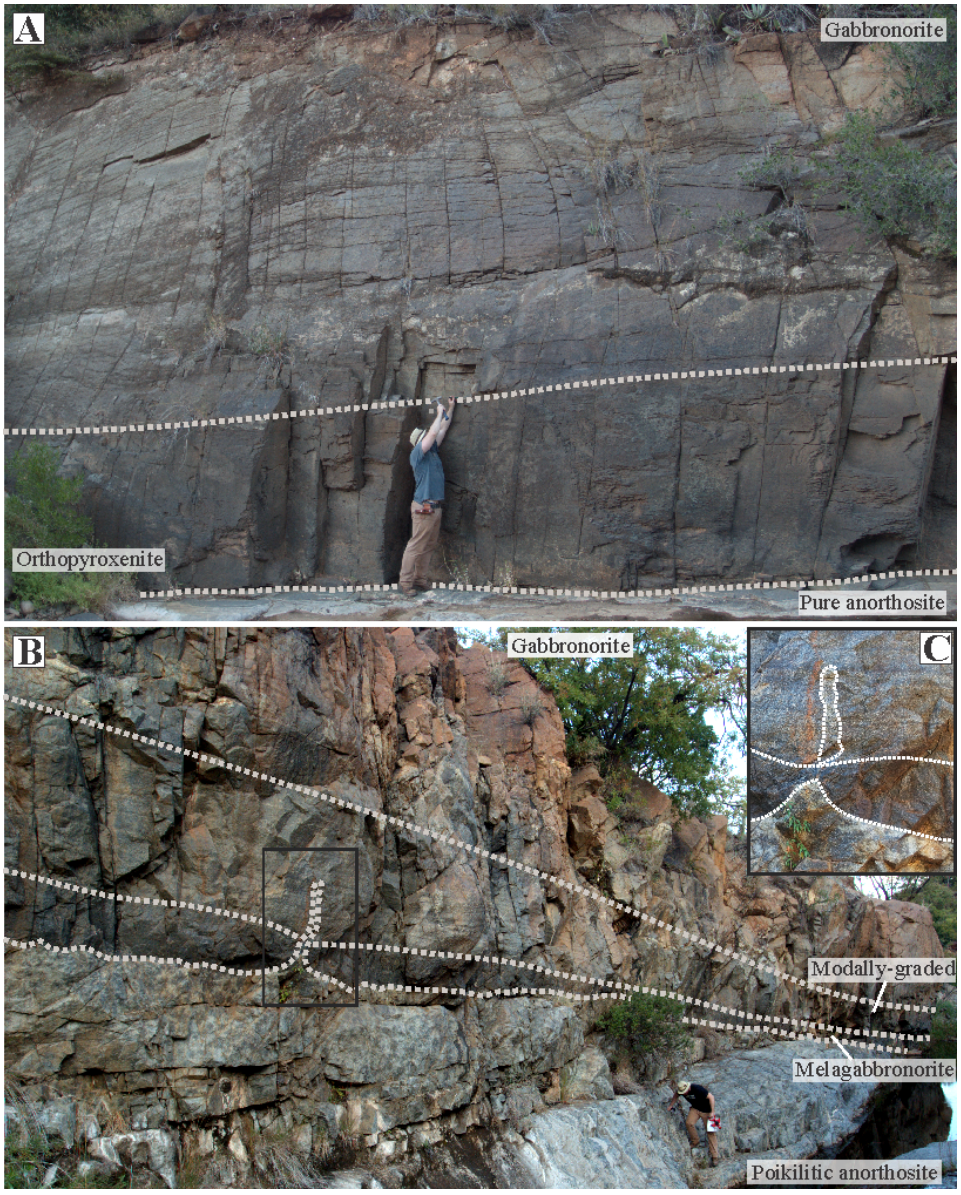

Figure 6.2 – Overview of the pyroxenite sequences. Contacts are accentuated by a dashed gray line. **(A)** The orthopyroxenite sequence (UTM: 199979 E, 7246936 N). At the base is pure anorthosite which is overlain by orthopyroxenite. The orthopyroxenite gradually transitions to unlayered gabbronorite at the top of the exposure. **(B)** The melagabbronorite sequence (UTM: 199728 E, 7248800 N). Poikilitic-textured anorthosite is overlain by melagabbronorite, followed by modally-graded gabbronorite and unlayered gabbronorite at the top. **(C)** Enlarged portion of **B** showing a 70 cm high flame (measured from the inferred undisturbed base of the melagabbronorite layer) of anorthosite which transects the melagabbronorite and some of the modally-graded gabbronorite.

6.2.4 Deformation and hydrothermal alteration

The outcrops are essentially undeformed by the Steelpoort Fault and the minor branch of the Sekhukhune Fault. However, a few small-scale faults and joints as well as en-echelon structures, aligned perpendicular to the plane of layering, striking N-S and dipping between 80 - 90° transect all layered lithologies. Hydrothermal alteration in the area is limited to in-filling of deformation structures by alteration minerals (chlorite, sericite, clinozoisite and minor quartz) or pathway exploitation by late-

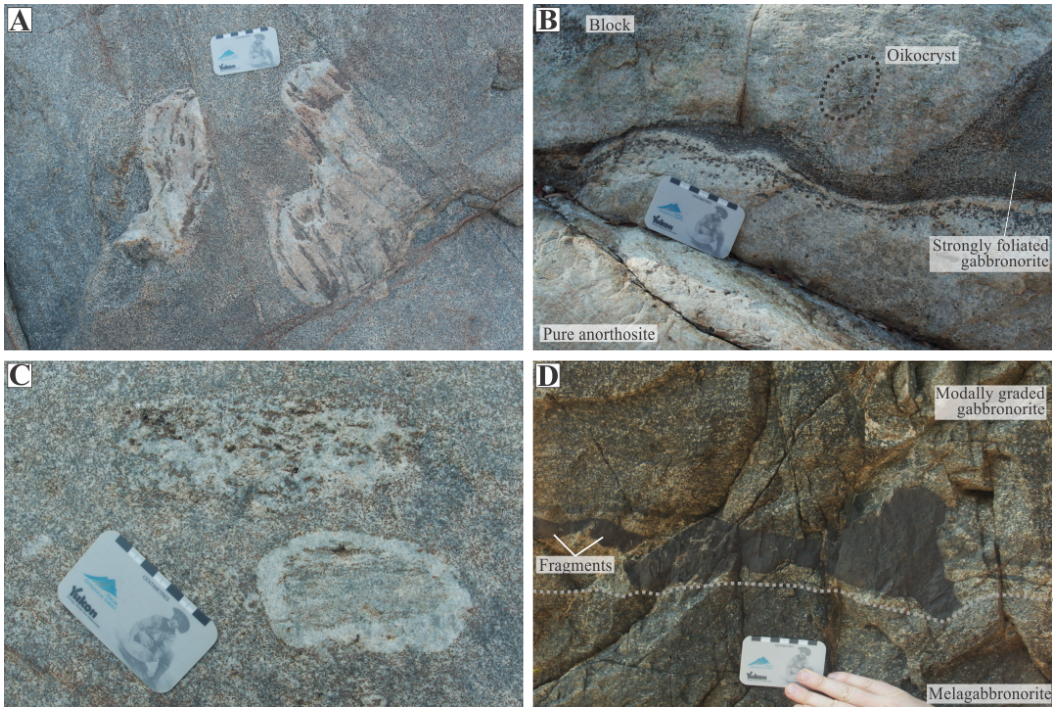

Figure 6.3 – Representative photographs of blocks found in the incised valley. **(A)** Within-plane (or parallel to the layering plane) view of banded leucocratic norite blocks at the base of the orthopyroxenite layer (UTM: 199979 E, 7246936 N). **(B)** Cross-section, close-up view of a contact between an altered poikilitic anorthosite block resting at the base of the orthopyroxenite layer (UTM: 199979 E, 7246936 N). The block slightly deforms the underlying strongly foliated gabbronorite and pure anorthosite. **(C)** Within-plane view of a gabbronorite (top) and a banded norite block (bottom) with a pure anorthosite band rimming the banded norite block. Outcrop is stratigraphically located ∼15 meters above the melagabbronorite sequence (UTM: 199688 E; 7248883 N). **(D)** A fragmented (left) websterite block in the modally-graded gabbronorite of the melagabbronorite sequence (UTM: 199728 E, 7248800 N).

stage evolved pegmatoidal dykes (Hayes et al., 2018).

6.3 Petrography and mineral chemistry

6.3.1 The orthopyroxenite sequence

Plagioclase In the basal gabbronorite to the base of the orthopyroxenite layer and including the capping gabbronorite, euhedral-subhedral plagioclase laths (0.2 - 5 mm) define a moderate to strong foliation, generally aligned parallel to the layering (Figs. 6.4A, B and 6.5A). Rarely, myrmekite textures appear at the outer edges of the laths. Rarely, laths are bent, to an angle $\leq 8°$ resulting in a slight undulose extinction. Plagioclase in the orthopyroxenite layer is interstitial, forming 0.1 - 7 mm oikocrysts with orthopyroxene chadacrysts (Fig. 6.4C). Crystals gradually become laths again at a height of ∼1.85 m above the base of the orthopyroxenite layer.

Plagioclase has an average composition of $An_{68.23}$ (anorthite; atomic 100×Ca/(Ca+Na+K)) with a 1σ of 5.54 mol% (Fig. 6.5A). Laths are compositionally zoned with a distinguishable core, mantle and rim except in the basal gabbronorite to pure anorthosite, where crystals lack a mantle. From core to mantle, laths are normally zoned, with an average decrease of 2.86 mol%. Rims are very thin (10 - 40 μm) and are reversely zoned, with an average increase of 6.77 mol% An. Albite (10 - 100 μm;

$Ab_{96.46\pm0.65}$) is found at the edges of plagioclase oikocrysts.

From the basal gabbronorite to the pure anorthosite, the An-content of plagioclase laths drops slightly from an average of 70.96 to 70.65 mol% An (core and mantle, Fig. 6.5A). The An-content drops abruptly at the base of the orthopyroxenite layer (by 2.19 mol% over 10 cm) and reaches its minimum of 58.32 mol% An at a height of 60 cm within the layer. The An-content then gradually increases and plateaus at an average of 67.70 mol% An (capping gabbronorite). The entire analyzed sequence records a decrease of 3.94 mol% An.

Orthopyroxene All orthopyroxene occurs as euhedral primocrysts (0.4 - 5 mm; Fig. 6.4A-C). Crystals commonly contain inclusions of clinopyroxene (0.06 - 0.34 mm) and more rarely plagioclase (0.1 - 0.7 mm). In the basal gabbronorite to pure anorthosite, the crystals are equant to slightly elongated. Orthopyroxene crystals at the base of the orthopyroxenite layer up to a height of 2.25 meters above the contact are lath-shaped. Generally, the elongated and lath-shaped crystals define a poor to strong foliation roughly aligned parallel to the layering. A few crystals are bent to an angle of $\leq 5^\circ$ resulting in a slight undulose extinction.

Orthopyroxene primocrysts have an average Mg# of 70.05 mol% with a 1σ of 2.37 mol% (Fig. 6.5A). Individual crystals are chemically homogeneous. From the basal gabbronorite to the pure anorthosite the Mg# decreases slightly from an average of 71.54 to 70.48 mol%. The Mg# increases to a maximum of 71.48 mol% at a height of 10 cm within the orthopyroxenite layer. The Mg# gradually decreases up-section and plateaus at an average of 68.58 mol% (capping gabbronorite). The entire analyzed sequence records a Mg# decrease of 3.39 mol%.

Clinopyroxene Clinopyroxene crystals (0.1 - 3.6 mm) appear as a mixture of sub- to anhedral primocrysts and interstitial crystals (Fig. 6.4A-C). Primocrysts tend to be elongated and aligned with the foliation defined by plagioclase and orthopyroxene. Inclusions of plagioclase (0.1 - 0.25 mm) or globular to lamellar (0.01 - 0.1 mm) exsolutions of orthopyroxene are rarely found in primocrysts. Interstitial crystals partly mantle orthopyroxene primocrysts, lack inclusions and exsolutions.

Clinopyroxene crystals average 77.65 mol% Mg# with a 1σ of 1.40 mol% (Fig. 6.5A). Individual crystals are chemically homogeneous. From the basal gabbronorite to the pure anorthosite, the Mg# decreases slightly from an average of 78.15 to 78.06 mol%. The Mg# then increases to a maximum of 79.09 mol% at a height of 10 cm within the orthopyroxenite layer. The Mg# gradually decreases up-section and plateaus at an average of 76.97 mol% (capping gabbronorite). The entire analyzed sequence records a Mg# decrease of 1.17 mol%.

Accessory minerals Accessory minerals include: phlogopite, magnesiohornblende, magnetite, ilmenite, quartz, clinochlore and clinozoisite; all in trace amounts. Phlogopite (40 - 800 μm) and magnesiohornblende (10 - 65 μm) are found throughout the sequence, partially mantling pyroxenes. Magnetite is found throughout the sequence as small (10 - 600 μm), randomly distributed anhedral crystals with oxy-exsolution lamellae (10 - 100 μm) of ilmenite. Interstitial quartz (20 - 600 μm) is found in myrmekite textures and occurs throughout the sequence with the exception of the orthopyroxenite layer. Both clinochlore (20 - 80 μm) and clinozoisite (2 - 20 μm) are only found in the capping gabbronorite as alteration minerals.

6.3.2 The melagabbronorite sequence

Plagioclase Euhedral-subhedral (0.1 - 5 mm) laths of plagioclase remain similar throughout the entire sequence (Fig. 6.4D-F). Laths in the melanogabbronorite layer show further interstitial growth

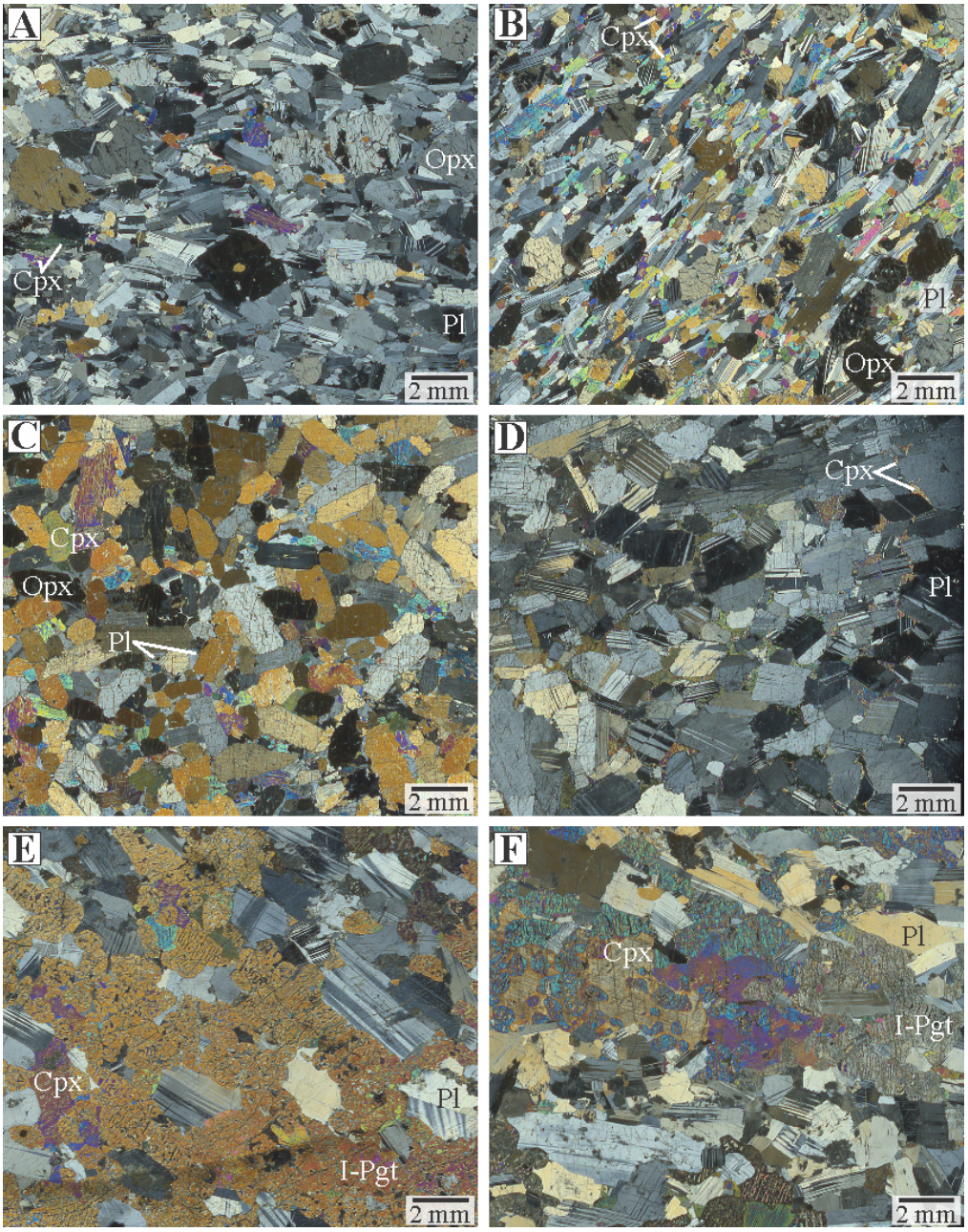

Figure 6.4 – Cross-polarized photomicrographs from the orthopyroxenite (**A-C**) and melagabbronorite (**D-F**) sequences. All photomicrographs are arranged with the stratigraphic top direction pointing towards the top of the page. **(A)** The basal gabbronorite to pure anorthosite is defined by euhedral, cumulus plagioclase (Pl) laths, crystals of orthopyroxene (Opx) and minor clinopyroxene (Cpx). Specimen is located 10 cm below orthopyroxenite layer contact. **(B)** The base of the orthopyroxenite layer is marked by a strong foliation defined by elongated crystals of plagioclase, orthopyroxene and clinopyroxene. Specimen at the contact. **(C)** The orthopyroxenite layer, composed of euhedral crystals of orthopyroxene and subhedral clinopyroxene with interstitial plagioclase. Specimen is located 1 m above the contact. **(D)** The poikilitic anorthosite, composed of plagioclase laths that define a moderate foliation, accompanied by oikocrystic clinopyroxene. Specimen is from 65 cm below the contact. **(E)** The melagabbronorite layer, composed of crystallographically-oriented inverted pigeonite primocrysts and plagioclase laths with interstitial clinopyroxene. Specimen is located 10 cm above the contact. **(F)** A melanocratic band in the modally-graded gabbronorite is caused by a modal increase of pyroxenes as opposed to plagioclase. Specimen is located 41 cm above the contact.

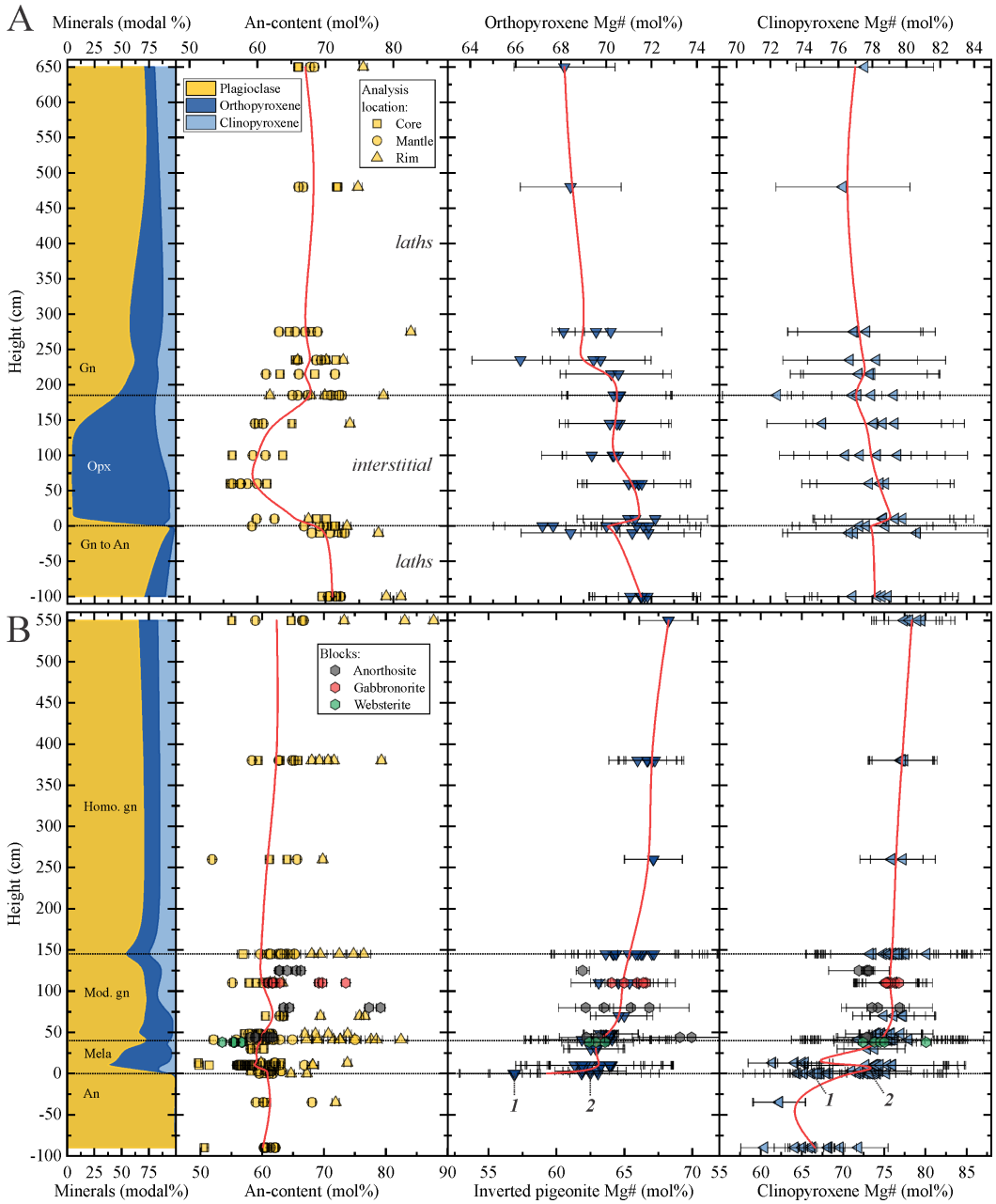

Figure 6.5 – Stratigraphic modal mineralogy and compositional variations of plagioclase, orthopyroxene (inverted pigeonite) and clinopyroxene for the **(A)** orthopyroxenite and **(B)** melagabbronorite sequences. Included in the plagioclase compositional variations in the orthopyroxenite sequence is the crystal habit of plagioclase. Included in melagabbronorite sequence are the compositional variation of blocks. Abbreviations: anorthosite (An), gabbronorite (Gn), orthopyroxenite (Opx), melagabbronorite (Mela), modally-graded (Mod.) and homogeneous (Homo.). Average compositions are given by a red line. For plagioclase, the averages includes only core and mantle analyses since rims can be associated with the myrmekite texture. The bi-modal pyroxene compositions in the melagabbronorite sequence are highlighted by number.

at their edges (Fig. 6.4E). Laths gradually decrease in size up-section, from ∼0.1 - 5 mm at the base to ∼0.1 - 3 mm at the top of the 6.5 m sequence. Altogether, the laths define a poor to strong foliation that is generally parallel to the layering. A few crystals are bent, to an angle ≤8°, resulting in a slight undulose extinction. Occasionally, the myrmekite texture appears at the crystal edges. A few, smaller (0.01 - 0.38 mm) and rounded plagioclase laths are found as inclusions in inverted pigeonite. Rarely, laths will also host a few (≤3) round inclusions of clinopyroxene (0.08 - 0.32 mm).

The average composition of plagioclase is $An_{62.96}$, with a 1σ of 8.76 mol% (Fig. 6.5B). Crystals are all reversely zoned. From core to rim, crystals steadily increase in An-content, by an average of 10.98 mol% with the increases becoming more pronounced towards the rim (6 - 30 μm thick). Plagioclase inclusions in inverted pigeonite lack rims and therefore only record a slight increase in An-content (average of 1.50 mol%). Myrmekite, found at the crystal boundaries records the highest An-content with an average of $An_{73.77}$ (1σ of 12.85 mol%).

In the poikilitic anorthosite, up to 3 cm above the melagabbronorite layer contact, the An-content of plagioclase laths remains relatively constant, averaging 60.56 mol% An (core and mantle; Fig. 6.5B). At 10 cm above the contact, the An-content reaches its minimum of 57.95 mol% An. The An-content then gradually increases and plateaus up-section at an average value of 61.28 mol% An (unlayered gabbronorite). The entire sequence records a slight increase of 3.61 mol% An. No significant lateral change (m-scale) in composition was found.

Inverted pigeonite Euhedral-subhedral inverted pigeonite primocrysts (0.1 - 4 mm) dominate the sequence, except in the poikilitic anorthosite, where crystals are oikocrysts (0.2 - 10 mm; Fig. 6.4D-F). Primocrysts tend to be slightly elongated with their long axis aligned parallel to the layering. Primocrysts form crystallographically-oriented networks (≥4 cm) or 'optical units' (von Gruenewaldt, 1970; von Gruenewaldt and Weber-Diefenbach, 1977; Fig. 6.4E, F). Primocrysts in contact with each other appear slightly fused together. Both primocrysts and oikocrysts have regularly-spaced exsolution lamellae of clinopyroxene (0.01 - 0.1 mm thick), typical of inverted pigeonite.

Orthopyroxene crystals have an average Mg# of 64.31 mol%, with a 1σ of 2.96 mol% (Fig. 6.5B). Individual crystals are chemically homogeneous. Crystals at the melagabbronorite layer contact are bimodal in Mg#s with crystals averaging 56.91 mol% (1σ: 0.06 mol%) or 62.47 mol% (1σ: 0.60 mol%). Crystals reach a maximum Mg# of 63.15 mol% at a height of 10 cm above the melagabbronorite layer contact. The Mg# gradually increases and plateaus up-section at an average of 66.88 mol% (unlayered gabbronorite). The analyzed sequence records an increase of 8.95 mol% Mg#. No significant lateral change (m-scale) in composition was noted.

Clinopyroxene Subhedral-anhedral clinopyroxene (0.1 - 8 mm) occurs either as primocrysts or interstitial crystals and as lamellar exsolutions in inverted pigeonite (Fig. 6.4D-F). Primocrysts are found in the basal and capping gabbronorite. Crystals there are slightly elongated and are aligned with the foliation defined by orthopyroxene and plagioclase. Interstitial crystals are found in the poikilitic anorthosite (as oikocrysts), the melagabbronorite layer and the modally-graded gabbronorite. These crystals partly mantle inverted pigeonite.

Clinopyroxene crystals have an average Mg# of 72.87 mol%, with a 1σ of 5.39 mol% (Fig. 6.5B). Crystals are chemically homogeneous. The Mg# of crystals in the poikilitic anorthosite decreases up-section from an average of 66.60 mol% to 62.25 mol%. At the melagabbronorite layer contact, crystals are bi-modal in Mg#s with samples centered around averages of 66.66 mol% (1σ: 1.27 mol%) and 73.22 mol% (1σ: 1.03 mol%). Crystals reach a maximum Mg# of 74.42 mol% at a height of 10 cm above the melagabbronorite layer contact. The Mg# decreases drastically at a height

of 13 cm to an average of 64.00 mol%, a value comparable to that in the poikilitic anorthosite. Subsequently, the Mg# gradually increases to a higher Mg# and plateaus up-section at an average of 76.99 mol% (unlayered gabbronorite). The entire analyzed sequence records an increase of 11.75 mol% Mg#. No significant lateral change (m-scale) in composition was noted.

Accessory minerals Accessory minerals include, in trace amounts: magnesiohornblende, magnetite, pyrite, ilmenite, quartz, clinozoisite and clinochlore. These minerals are similar to those in the Pyroxenite Marker sequence, except for the absence of phlogopite and the presence of subhedral 0.001 - 0.2 mm crystals of pyrite associated with alteration minerals found throughout the sequence (i.e. clinozoisite and clinochlore).

Table 6.1 – Representative mineral analyses from the pyroxenite layers. Single point analyses were chosen being closest to the average. The complete set of data and their respective analytical uncertainties are presented in Appendix D.

	Orthopyroxenite				**Melagabbronorite**						
Mineral	Plagioclase		Opx	Cpx	Plagioclase			Opx	Cpx	Hbl	Phl
Name	Core	Rim			Core	Mantle	Rim				
ID#	1570	1571	1576	1579	268	274	277	256	213	1751	1753
SiO_2	52.11	52.99	53.26	52.60	52.54	52.21	50.68	52.96	52.20	50.50	35.67
TiO_2	0.01	0.01	0.19	0.40	0.03	0.04	0.02	0.19	0.39	0.63	2.60
Al_2O_3	29.70	29.08	0.94	1.63	29.15	29.12	30.43	0.62	1.40	4.82	14.43
V_2O_3			0.02	0.07						0.04	0.10
Cr_2O_3			0.10	0.23	0.02	0.00	–	0.01	0.06	0.14	0.16
FeO	0.25	0.32	17.77	7.62	0.35	0.27	0.40	22.67	9.08	9.04	13.47
NiO			0.06	0.06						0.12	0.19
ZnO			–	0.00				0.07	0.04	–	–
MnO	0.00	0.01	0.38	0.20				0.52	0.25	0.11	0.11
MgO	0.00	0.01	24.92	15.00				21.91	14.28	17.94	17.77
CaO	12.53	11.96	1.62	21.75	12.50	12.45	13.86	0.90	21.82	11.97	0.12
SrO	0.02	0.07			0.01	–	0.05	–	–	0.03	0.00
BaO	0.01	0.00			–	0.05	–	0.02	0.01	0.00	0.20
Na_2O	4.20	4.76	0.01	0.36	4.04	4.08	3.44	0.02	0.27	0.65	0.05
K_2O	0.25	0.18			0.32	0.33	0.20	–	0.01	0.50	6.96
Cl										0.15	0.40
F										0.27	0.00
H_2O										1.91	0.10
OH=Cl										0.03	0.00
OH=F										0.11	0.09
Total	99.07	99.40	99.27	99.92	98.96	98.54	99.08	99.90	99.81	96.77	92.16
End-members (mol%)											
An	61.37	57.50			61.88	61.57	68.22				
Ab	37.19	41.45			36.21	36.48	30.61				
Or	1.44	1.05			1.92	1.95	1.17				
En			69.11	42.97				62.11	40.74		
Fs			27.66	12.25				36.05	14.53		
Wo			3.23	44.78				1.84	44.73		
Mg#			71.42	77.82				63.27	73.71		
Ann											29.83
Phl											70.17

All mineral and mineral group abbreviations follow Whitney and Evans (2010).
–: oxide analyzed but not detected.

6.3.3 Blocks

Blocks encountered in the incised river valley can be classified as: 1) anorthosites, 2) gabbronorites, 3) norites, and 4) websterite. The stratigraphic locations of most blocks investigated for mineral chemistry are presented in Figure 6.1). The contact between the block and host is sharp with plagioclase and/or orthopyroxene/inverted pigeonite laths in the hosts aligned parallel to the margins of

the blocks.

Anorthosite

Altered poikilitic anorthosite These blocks are composed of subhedral (0.2 - 5 mm) plagioclase crystals (average of 67 modal%) with interstitial inverted pigeonite (0.2 - 5 mm; 1%) and clinopyroxene (0.1 - 1 mm; 1%; Fig. 6.6A). Accessory minerals (0.1 - 1.4 mm) include quartz (0.5%), magnetite (0.5%) and phlogopite (0.5%). Most blocks have been significantly altered with sericite (28%) altering plagioclase, and chlorite (3%), hornblende (0.5%) and calcite (1%) altering pyroxenes. Interstitial clinopyroxene from the host has infiltrated the block up to 4.2 mm inwards from the contact.

Blocks 1 and LX-1 which is stratigraphically located in modally-graded gabbronorite $\sim$28 m above the melagabbronorite sequence (Fig. 6.1) were investigated for mineral chemistry. Plagioclase crystals have an average An-content of 60.0 mol% and 64.3 mol% for blocks 1 and LX-1, respectively (Fig. 6.5). Crystals in block 1 are normally zoned from core ($An_{60.9}$) to mantle ($An_{59.8}$; rims were too altered), whereas crystals in block LX-1 are reversely zoned with a core of $An_{61.9}$ and a rim of $An_{72.5}$. Pyroxene crystals are chemically homogeneous. Inverted pigeonite crystals have an average Mg# of 62.6 mol% and 59.7 mol% in blocks 1 and LX-1, respectively. Clinopyroxene has an average Mg# of 69.5 mol% and 69.6 mol% in blocks 1 and LX-1, respectively. Infiltrating clinopyroxene (Mg# block 1: 72.9 mol% and LX-1: 76.0 mol%) is chemically similar to the host (Mg#: 73.8 mol% and 75.7 mol%, respectively). A 2 cm band of pure anorthosite mantling block LX-1 was also chemically investigated. Plagioclase core and mantle An-contents (n = 32) in the pure anorthosite band (average An of 69.7 mol%) are indistinguishable from that of the host (gabbronorite; average An of 69.2 mol%).

Olivine alteromorph anorthosite Olivine alteromorph anorthosite blocks are less altered, coarser grained and bear olivine alteromorphs compared to the altered poikilitic anorthosite blocks. These blocks are composed of euhedral-subhedral (0.2 - 10 mm) laths of plagioclase (average of 82%), interstitial inverted pigeonite (0.1 - 6 mm; 9%), clinopyroxene (0.02 - 1 mm; 2%) and quartz (0.1 - 3 mm; 1%). Alteration minerals consisting of sericite (2%), chlorite (2%), hornblende (0.5%) and calcite (0.5%) are found in these blocks. Interstitial olivine crystals (originally 0.4 - 1.6 mm; 0.5%) were initially rimmed by symplectite magnetite (0.01 - 0.8 mm) and orthopyroxene (0.2 - 0.4 mm), and subsequently completely altered to saponite (Fig. 6.6B). Additionally, small (0.04 - 0.2 mm) round inclusions of pyroxenes are commonly found in plagioclase laths.

Blocks 2 and X2 (80 cm above the melagabbonorite contact at location 2 in Fig. 2.5) were investigated for mineral chemistry. Plagioclase crystals have average An-content of 65.1 mol% An and 69.8 mol% An in blocks 2 and X2, respectively (Fig. 6.5). Crystals in block 2 are reversely zoned, with $An_{63.2}$ at the core and $An_{69.2}$ at the rim. Crystals in block X2 are normally zoned from core ($An_{78.2}$) to mantle ($An_{63.9}$) and reversely zoned at the rim ($An_{67.2}$). Pyroxenes are chemically homogeneous. Inverted pigeonite has an average Mg# of 61.9 mol% and 63.7 mol% in blocks 2 and X2, respectively. Clinopyroxene has an average Mg# of 72.7 mol% and 72.9 mol% in blocks 2 and X2, respectively.

Gabbronorite

Altered gabbronorite Altered gabbronorite blocks are composed of plagioclase laths (0.2 - 2 mm; average of 55%) and inverted pigeonite (0.8 - 3.5 mm; 8%) accompanied by minor amounts of interstitial clinopyroxene (0.1 - 1.3 mm; 4%) and quartz (0.1 - 0.7 mm; 1%). Most altered gabbronorite

blocks have been significantly altered with sericite (22%) altering plagioclase laths, chlorite (9%) and hornblende (0.5%) altering pyroxenes. These blocks are too altered for mineral chemistry analyses.

Coarse-grained gabbronorite Coarse-grained gabbronorite blocks are comparatively coarser-grained and less altered compared to the altered gabbronorite blocks. Blocks are composed of plagioclase laths (0.2 - 5.5 mm; average of 57%) and inverted pigeonite (0.2 - 5.6 mm; 28%), accompanied by interstitial clinopyroxene (0.1 - 3.7 mm; 9%) and hornblende that partially mantle pyroxenes (0.01 - 0.04 mm; 0.5%; Fig. 6.6C). Plagioclase laths commonly host numerous (up to 20) round inclusions (0.04 - 0.2 mm) of pyroxenes. Lesser amounts of alteration minerals, consisting of sericite (5%) and chlorite (0.5%) are found in these blocks.

Block 3 was investigated for mineral chemistry. Laths of plagioclase average a composition of $An_{69.8}$ (Fig. 6.5). Laths are slightly compositionally zoned with a core, mantle and rim. From core to mantle, crystals are normally zoned (average reduction of 4.6 mol% An). The rim is reversely zoned with an average increase of 10.9 mol% An. Pyroxene crystals are chemically homogeneous. Inverted pigeonite and clinopyroxene crystals have an average Mg# of 65.4 mol% and 75.9 mol%, respectively.

Norite

All norite blocks have been significantly altered. Blocks are defined by subhedral plagioclase (0.1 - 4 mm; average of 59%), inverted pigeonite and rarely orthopyroxene (0.2 - 2 mm; 11%) with interstitial clinopyroxene (0.1 - 1 mm; 1%) and quartz (0.1 - 0.2 mm; 0.5%). Alteration minerals, consisting of chlorite (15%), sericite (11%), hornblende (0.5%) and epidote (0.5%) overprint the igneous mineralogy. Some norite blocks are banded, caused by a modal increase in pyroxenes (20 - 30% abundance). Norite blocks were too altered for mineral chemistry analyses.

Websterite

Blocks are composed almost entirely of inverted pigeonite primocrysts (0.3 - 1 mm; average of 85 modal%) with interstitial clinopyroxene (0.1 - 6 mm; 12%) and plagioclase (0.1 - 1.8 mm; 3%; Fig. 6.6D). Rarely, websterite blocks are compositionally bi-modal, divided into a websterite portion in sharp contact with anorthosite. The anorthosite is composed of moderately foliated plagioclase laths (0.2 - 3.4 mm; 77%) and are accompanied by interstitial clinopyroxene (0.1 - 0.8 mm; 2%) and inverted pigeonite (0.1 - 0.5 mm; 1%). The anorthosite is typically more altered with patches of sericite and kaolinite (20%) overprinting plagioclase.

Block 4 was investigated for mineral chemistry. Interstitial crystals of plagioclase have an average An-content of 55.1 mol% (Fig. 6.5). Plagioclase crystals are normally zoned from core to rim with an average reduction of 3.8 mol% An. Pyroxenes are chemically homogeneous. Inverted pigeonite and clinopyroxene have an average Mg# of 67.3 mol% and 74.0 mol%, respectively.

6.4 Abundance of Al_2O_3 in orthopyroxene

The average amount of Al_2O_3 in orthopyroxene crystals differs between the orthopyroxenite and melagabbronorite sequences (Fig. 6.7). Specifically, the orthopyroxenite and melagabbronorite sequences contain an average of 0.85 (1σ: 0.12 wt%; n = 34) and 0.60 wt% (1σ: 0.09 wt%; n = 63) Al_2O_3, respectively. Within individual sequences, individual rock types all contain a similar amount

Table 6.2 – Representative mineral analyses from select blocks. Single point analyses were chosen being closest to the average. The complete set of data and their respective analytical uncertainties are presented in Appendix D.

Block	1: Anorthosite			3: Gabbronorite			4: Websterite		
Mineral	Pl	Opx	Cpx	Pl	Opx	Cpx	Pl	Opx	Cpx
ID#	2337	2329	2331	2417	2403	2405	2429	2439	2438
SiO_2	52.30	52.24	51.97	50.18	52.51	52.68	53.47	52.94	52.75
TiO_2	0.00	0.16	0.41	–	0.13	0.26	0.01	0.15	0.21
Al_2O_3	30.06	0.66	1.19	31.37	0.87	0.97	29.44	0.52	1.04
V_2O_3		0.02	0.09		0.04	0.05		0.03	0.09
Cr_2O_3	–	0.02	0.00	–	0.06	0.06	–	0.03	0.05
FeO	0.37	23.13	10.38	0.31	21.98	8.38	0.23	22.41	10.18
NiO		0.03	0.03		0.02	0.02		0.03	–
MnO	–	0.56	0.27	0.01	0.48	0.23	0.01	0.53	0.32
MgO	0.03	21.37	13.02	0.02	21.98	14.30	0.02	21.96	14.99
CaO	12.73	0.66	21.80	14.48	0.58	22.32	12.16	1.03	19.87
SrO	0.07	0.01	0.01	0.12	0.02	0.00	0.08	–	0.03
BaO	0.01	–	0.01	0.02	0.00	–	0.02	0.01	–
Na_2O	4.36	–	0.23	3.47	–	0.20	4.87	–	0.22
K_2O	0.28	–	0.00	0.15	0.01	–	0.35	–	0.00
Total	100.20	98.85	99.42	100.12	98.70	99.49	100.66	99.63	99.76
End-member (%)									
An	60.77			69.18			56.83		
Ab	37.64			29.98			41.20		
Or	1.59			0.83			1.97		
En		61.37	37.72		63.28	40.81		62.25	42.86
Fs		37.27	16.87		35.51	13.41		35.64	16.33
Wo		1.36	45.41		1.21	45.77		2.10	40.81
Mg#		62.22	69.09		64.06	75.27		63.59	72.41

All mineral and mineral group abbreviations follow Whitney and Evans (2010).
–: oxide analyzed but not detected.

of Al_2O_3. Specifically, the anorthosite, orthopyroxenite and capping gabbronorite of the orthopyroxenite sequence contain an average of 0.86 wt% (1σ: 0.15 wt%; n = 7), 0.81 wt% (1σ: 0.11 wt%; n = 18) and 0.92 wt% (1σ: 0.10 wt%; n = 9) Al_2O_3, respectively. The melagabbronorite and capping gabbronorite of the melagabbronorite sequence contain an average of 0.62 (1σ: 0.08 wt%; n = 22) and 0.60 wt% (1σ: 0.10 wt%; n = 41) Al_2O_3, respectively.

Orthopyroxene crystals in the anorthosite, gabbronorite and norite blocks, hosted in the melagabbronorite sequence, contain an average of 0.63 wt% (1σ: 0.05 wt%; n = 7), 0.65 wt% (1σ: 0.18 wt%; n = 5) and 0.53 wt% (1σ: 0.01 wt%; n = 3) Al_2O_3, respectively (Fig. 5.8B).

6.5 Rock density

Average whole-rock densities of pyroxenite sequences and blocks are presented in Table 6.3. The measurements are in agreement with Main Zone densities of 2.7 g/cm^3 for anorthosite, 3.3 g/cm^3 for pyroxenite and 3.0 g/cm^3 for gabbronorite (Ashwal et al., 2005; Cawthorn and Ashwal, 2009). On average, the orthopyroxenite sequence is denser by 1.90 g/cm^3, compared to the melagabbronorite sequence (Fig. 6.8). For both sequences, densities increase drastically at the pyroxenite layer contact, reaching maximum values at a height of 60 cm and 21 cm for the orthopyroxenite and melagabbronorite sequences, respectively (Fig. 6.8). Densities progressively decrease and plateau up-section. No significant lateral change (m-scale) in density was observed within the melagabbronorite sequence.

Whole-rock densities show variations that correlate with the modal mineralogy of the blocks. No correlation between the blocks' density and its stratigraphic positions was observed.

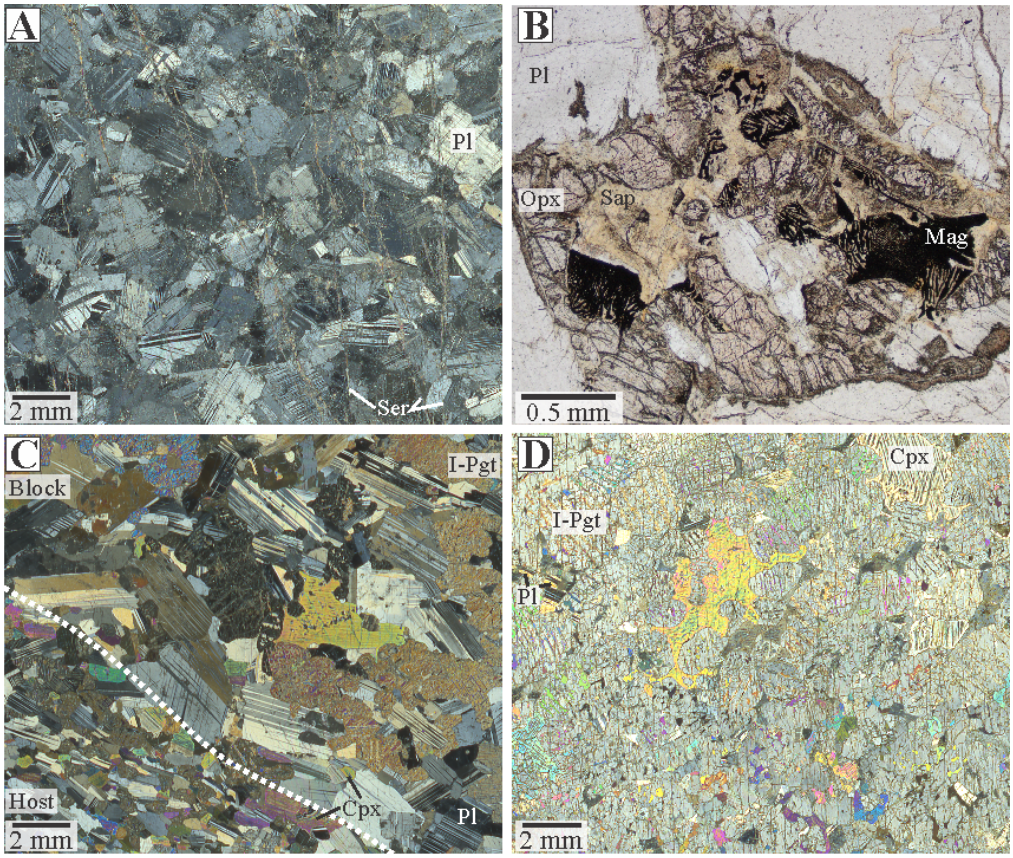

Figure 6.6 – Representative cross-polarized light photomicrographs of the blocks. All photomicrographs, except **B** are arranged with the stratigraphic top direction pointing to the top of the page. **(A)** Altered poikilitic anorthosite, composed of subhedral plagioclase (Pl) crystals. The rock is transected by veins of sericite (Ser). Specimen is from block 2. **(B)** Olivine alteromorph in an anorthosite block. Olivine crystals have been replaced by symplectite-textured magnetite (Mag) and saponite (Sap). Orthopyroxene (Opx) rims the olivine alteromorphs. Specimen is from block X2. **(C)** Coarse-grained gabbronorite, composed of euhedral-subhedral plagioclase laths, inverted pigeonite (I-Pgt) and interstitial clinopyroxene (Cpx). The contact with the gabbronorite host is highlighted by a white dashed line. Specimen is from block 3. **(D)** Websterite block. The block is dominated by crystallographically aligned inverted pigeonite with interstitial plagioclase and clinopyroxene. Specimen is from block 4.

6.6 Whole-rock chemistry

6.6.1 Major elements

Whole-rock major element oxide data shows that the pyroxenite sequences are chemically similar and follow similar trends progressing up-section (Table 6.4). At the pyroxenite layer contact, both sequences show sharp increases in: 1) TiO_2, 2) Ni, 3) Cr and 4) Mg# as well as decreases in: 1) Al_2O_3 and 2) K_2O (Fig. 6.9). No significant lateral change in composition was found within the melagabbronorite sequence.

Blocks are chemically distinct from their host (Table 6.4). Whole-rock major oxides show variations that correlate with the modal mineralogy of the blocks. No correlation between the blocks' chemistry and its stratigraphic position was noted.

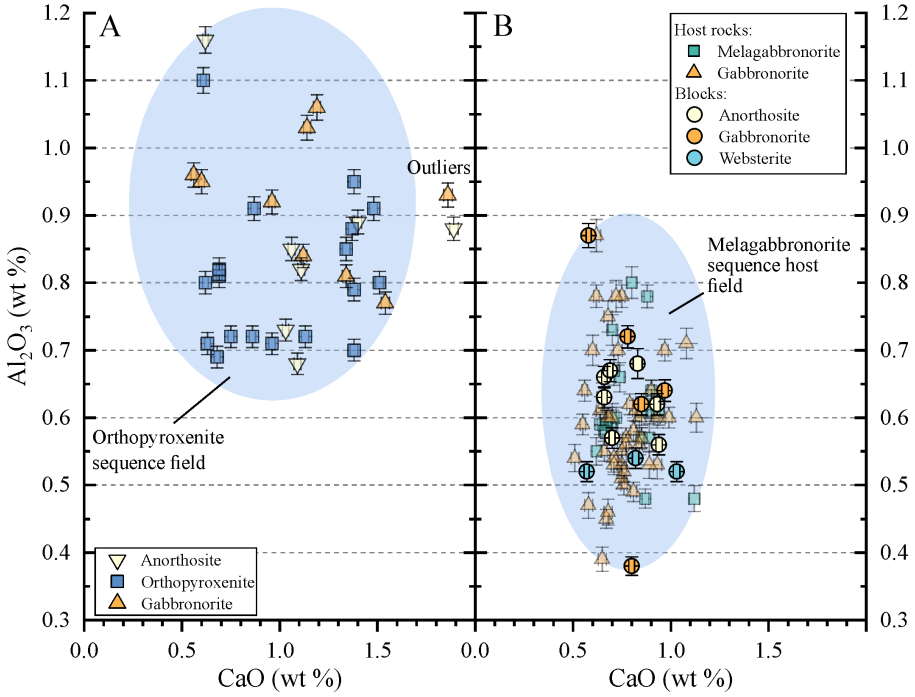

Figure 6.7 – Abundance of Al_2O_3 (wt%) versus CaO (wt%) in orthopyroxene crystals. **(A)** Comparison between anorthosite, orthopyroxenite and gabbronorite of the orthopyroxenite sequence. **(B)** Comparison between melagabbronorite and gabbronorite hosts of the melagabbronorite sequence and the anorthosite, gabbronorite and websterite blocks. Both host rocks and blocks contain similar amounts of Al_2O_3 in orthopyroxene crystals.

Table 6.3 – Average whole-rock densities of pyroxenite sequences and blocks.

	Orthopyroxenite			Melagabbronorite			Blocks			
	Average	**1σ**	**n**	**Average**	**1σ**	**n**		**Average**	**1σ**	**n**
An	2.85		1	2.72	0.03	14	**An**	2.82	0.06	11
Py	3.27	0.09	8	3.01	0.12	12	**Gn**	2.92	0.10	8
Gn	3.11	0.10	6	2.93	0.03	15	**No**	2.82	0.03	4
							Web	3.18	0.38	2

An: anorthosite, Py: pyroxenite, Gn: gabbronorite, No: norite, Web: websterite.

6.6.2 Incompatible and trace elements

The chondrite-normalized incompatible and rare earth element concentration (REE) patterns differ between comparable lithologies of the two pyroxenite sequences (Table 6.4, Fig. 6.10).

Overall, anorthosites tend to have the lowest and the pyroxenites have the highest incompatible and REE concentrations for both sequences. Chondrite-normalized REE patterns show that the orthopyroxenite layer and capping gabbronorite in the orthopyroxenite sequence have no to slightly negative Eu-anomalies whereas the remainder of the lithologies have positive Eu-anomalies. The most enriched REE patterns are found at a height of 145 cm and 10 cm in the orthopyroxenite and melagabbronorite sequences respectively.

Block trace element compositions are distinctly different to the host pyroxenite sequences (compare Figs. 6.10 to 6.11A, B). Overall blocks have a much larger range in both incompatible and REE patterns, with the anorthositic blocks being the most variable. Overall the anorthosite, gabbronorite and norite trace element patterns overlap, with similar La/Lu ratios (3.4 - 41.2) and a distinct positive Eu-anomaly (1.3 - 13.5). The websterite block (number 4) is unique with a low chondrite-normalized La/Lu ratio of 1.1 and a negative Eu-anomaly (-0.7). No correlation between

Table 6.4 – Average whole-rock geochemistry. The complete set of data and their respective errors is presented in Appendix E.

	Orthopyroxenite			Melagabbronorite			Blocks			
Rock	**An**	**Py**	**Gn**	**An**	**Py**	**Gn**	**An**	**Gn**	**No**	**Web**
n	**1**	**6**	**5**	**5**	**4**	**5**	**5**	**3**	**3**	**1**
SiO_2 (wt%)	50.53	52.16	51.74	51.81	51.77	51.74	49.36	50.04	49.72	52.01
TiO_2	0.09	0.27	0.25	0.06	0.13	0.12	0.06	0.12	0.06	0.21
Al_2O_3	24.59	5.06	11.56	27.87	16.85	16.53	27.77	19.61	25.38	3.07
$Fe_2O_{2(T)}$	4.25	14.26	10.22	1.59	9.06	8.51	1.86	6.82	3.87	19.00
MnO	0.08	0.27	0.20	0.03	0.19	0.19	0.05	0.13	0.08	0.37
MgO	5.18	19.23	13.48	0.57	8.14	8.68	1.19	7.27	3.68	18.74
CaO	12.49	7.65	10.76	12.39	10.84	11.57	13.30	11.45	12.24	6.40
Na_2O	2.33	0.53	1.23	3.97	2.30	2.17	3.20	2.00	2.52	0.34
K_2O	0.20	0.06	0.15	0.48	0.17	0.16	0.69	0.20	0.44	0.02
P_2O_5	0.01	0.02	0.03	0.01	0.01	0.01	0.01	0.02	0.01	0.02
LOI	0.24	0.20	0.35	1.03	0.58	0.33	2.00	2.26	1.80	0.16
Total	100.05	99.88	100.10	99.93	100.17	100.00	99.50	99.99	99.84	100.44
V (ppm)	34.49	151.15	128.47	21.40	141.50	172.00	26.16	93.38	52.79	283.09
Cr	137.60	643.24	502.26	6.40	76.50	120.60	16.16	137.41	72.16	212.40
Ni	88.81	312.55	221.55	9.14	103.68	145.46	19.68	117.12	68.48	260.46
Zn	22.10	86.92	59.37	14.40	47.00	51.20	16.28	49.67	33.71	125.03
Rb	1.44	2.27	2.15	6.67	1.92	1.61	11.09	2.93	5.27	0.51
Sr	108.19	49.47	109.88	471.35	324.77	277.06	262.75	194.30	169.85	36.07
Y	0.37	6.24	4.75	1.03	3.48	3.69	0.72	2.14	0.48	6.90
Zr	2.48	10.94	11.31	5.32	5.20	4.20	3.86	4.60	1.63	8.01
Nb	1.32	0.42	0.55	0.31	0.16	0.16	0.33	0.35	0.18	0.34
Ba	20.41	18.07	34.57	139.24	74.25	59.64	97.45	40.37	35.99	6.60
La	0.28	2.23	2.12	2.04	1.79	1.38	1.06	1.46	1.36	1.38
Ce	1.05	4.76	4.80	3.59	3.32	2.66	2.05	2.78	2.57	2.89
Pr	0.06	0.70	0.61	0.39	0.41	0.38	0.22	0.30	0.26	0.45
Nd	0.26	3.36	2.89	1.47	1.76	1.64	0.85	1.29	0.98	2.20
Sm	0.06	0.90	0.75	0.26	0.44	0.44	0.16	0.31	0.17	0.69
Eu	0.06	0.27	0.29	0.56	0.50	0.42	0.25	0.26	0.16	0.19
Gd	0.07	1.05	0.85	0.23	0.51	0.54	0.17	0.35	0.15	0.89
Tb	0.01	0.17	0.14	0.04	0.10	0.10	0.03	0.06	0.02	0.16
Dy	0.08	1.18	0.93	0.21	0.60	0.65	0.15	0.40	0.11	1.16
Ho	0.02	0.26	0.20	0.04	0.13	0.14	0.03	0.09	0.02	0.26
Er	0.05	0.74	0.57	0.12	0.41	0.45	0.09	0.25	0.06	0.77
Tm	0.01	0.12	0.09	0.02	0.06	0.07	0.01	0.04	0.01	0.13
Yb	0.07	0.77	0.60	0.11	0.43	0.45	0.08	0.28	0.07	0.88
Lu	0.01	0.12	0.09	0.02	0.06	0.07	0.01	0.04	0.01	0.14
Hf	0.09	0.38	0.39	0.14	0.17	0.15	0.12	0.16	0.06	0.25
Ta	0.49	0.05	0.06	0.02	0.01	0.03	0.04	0.11	0.04	0.03
Pb	0.67	1.20	1.14	2.90	2.08	1.98	2.73	5.91	3.29	1.22
Th	0.06	0.35	0.39	0.25	0.13	0.10	0.19	0.23	0.20	0.27
U	0.04	0.09	0.11	0.06	0.04	0.03	0.05	0.08	0.05	0.08
Mg#	72.85	74.83	74.23	43.20	66.61	69.38	54.54	70.03	66.78	68.46
$\sum$REE	2.07	16.67	14.92	9.10	10.50	9.39	5.17	7.91	5.93	12.12
$(La/Lu)_{cn}$	2.99	1.98	2.60	15.09	3.44	2.26	15.17	3.64	12.24	1.05
$(Eu/Eu^*)_{cn}$	3.19	-0.93	1.15	7.12	3.32	2.71	7.16	4.19	6.21	0.74

An: anorthosite, Py: pyroxenite, Gn: gabbronorite, No: norite, Web: websterite.

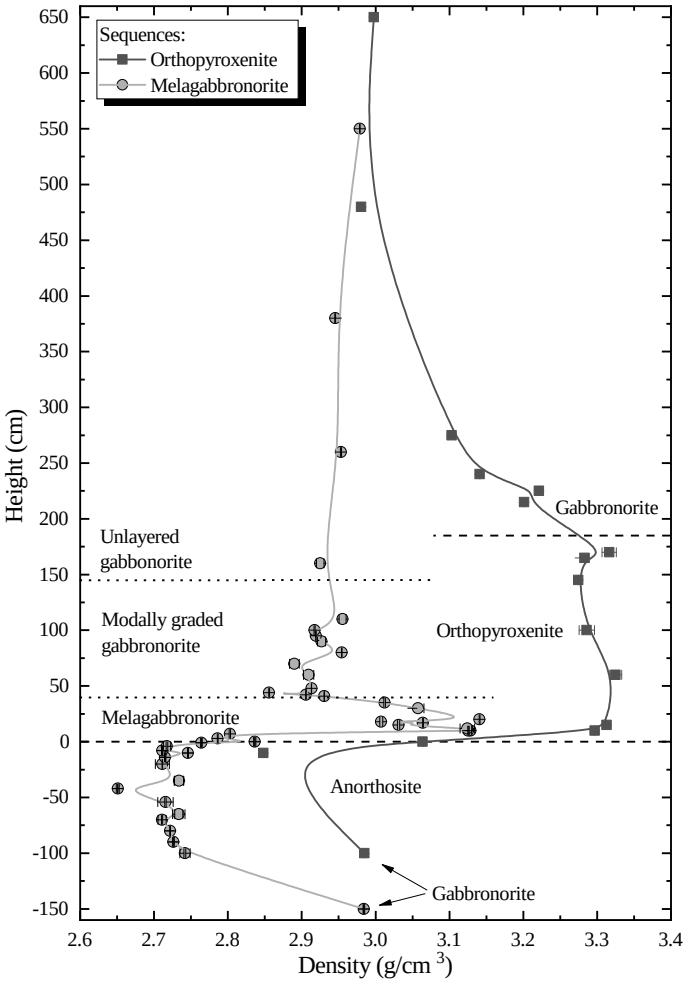

Figure 6.8 – Measured densities of the orthopyroxenite and melagabbronorite sequences. For both sequences, densities increase drastically following the pyroxenite layer contact and gradually plateau up-section in the capping gabbronorite.

the trace element pattern of the block and its stratigraphic position was found.

I compared the trace element compositions of the blocks to putative parental melts (known as B1, B2 and B3) of the RLS (Fig. 6.11C, D). The trace element patterns of the blocks best match the B3 melt composition, which is considered as the parental melt of the Main Zone (Barnes et al., 2010). However, the blocks are much more depleted in incompatible and REE compared to the B3 melt (average $\sum$REE of 6.6 ppm compared to 33.4 ppm), which is consistent with their cumulate nature.

6.7 Discussion

The Pyroxenite Marker is defined by a single or multiple (up to 4) $\leq$2 m thick orthopyroxenite, melanorite and/or melagabbronorite layers (von Gruenewaldt, 1973; Molyneux, 1974; Hayes et al., 1985; Sharpe, 1985; Kruger et al., 1987; Cawthorn et al., 1991; Maier et al., 2001; VanTongeren and Mathez, 2013; Cawthorn et al., 2016; Cawthorn, 2020). All previous studies provided a large-scale perspective (hectometer) and included only a single representative sample for each pyroxenite layer. Furthermore, types of data provided between studies vary considerably and data comparability is

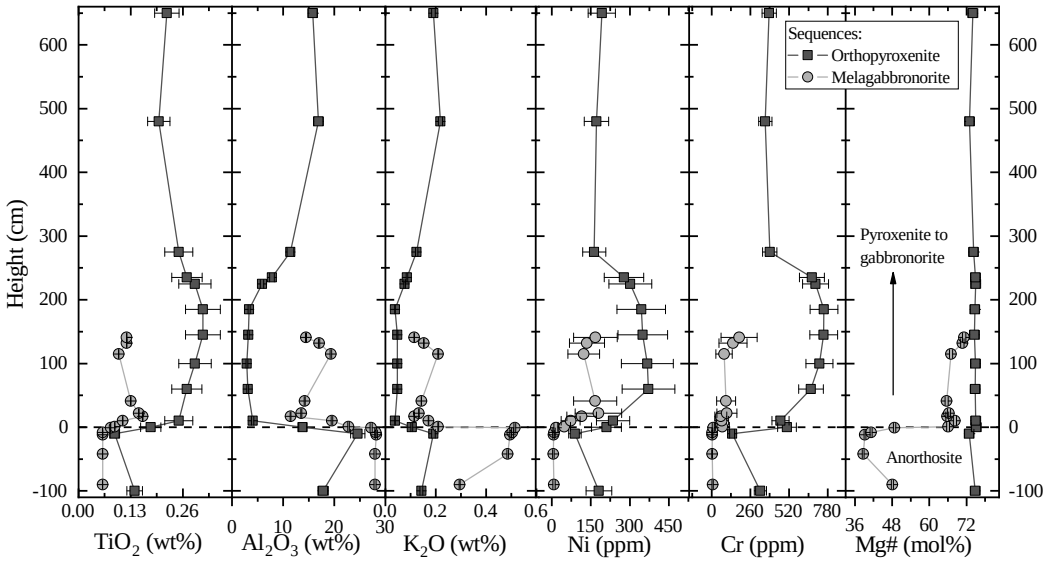

Figure 6.9 – Whole-rock major element oxide variations and molar Mg# in the pyroxenite sequences. The trend for MgO follows that of the molar Mg# presented in the figure.

problematic (i.e. modal mineralogies and/or mineral chemistries and/or whole-rock chemistry and/or initial $^{87}Sr/^{86}Sr$ ratios). Here, I presented a comprehensive and detailed series of field, textural, density and chemical observations for two pyroxenite layers and a suite of cumulate blocks on a small-scale (decimeter). In the following section, I first explore the feasibility of the magmatic replenishment with mixing model currently proposed for the origin of the Pyroxenite Marker and I explore relationships between the two pyroxenite sequences. I then discuss the relationship of the blocks to their host rocks and how they can be used to constrain the rheological conditions of the magmas, providing insights into the dynamics of magma chamber replenishment.

6.7.1 Magmatic model: Magma replenishment with mixing

The RLS was invariably formed through multiple pulses of magma, replenishing the magma chamber (e.g. Sharpe, 1985; Eales, 2002). A major pulse of less-differentiated magma, marked by a progressive (200 - 400 m thick) decrease in initial $^{87}Sr/^{86}Sr$ ratios (Sharpe, 1985; Mitchell, 1986; Kruger, 1994; Cawthorn et al., 1991) and a reversal in mineral compositions (Molyneux, 1974; Hayes et al., 1985; Mitchell, 1990; VanTongeren and Mathez, 2013; Cawthorn et al., 2016) is thought to have been emplaced at the level of the Pyroxenite Marker where it mixed with a resident magma (e.g. Molyneux, 1974; Cawthorn et al., 1991; Maier et al., 2001; VanTongeren and Mathez, 2013; Cawthorn et al., 2016; Cawthorn, 2020). Here, I test the applicability of the magmatic-replenishment-with-mixing hypothesis with insights derived from the multi-dimensional data obtained from the pyroxenite layers.

Each pyroxenite layer records a magmatic replenishment of a less-differentiated magma, as denoted by relatively abrupt changes in modal mineralogy, density, mineral and whole-rock chemistry. Relative to the underlying anorthosites at both pyroxenite layers: 1) pyroxene modal composition increases by 83 and 64%, whereas plagioclase decreases by 84 and 59% in the orthopyroxenite and melagabbronorite, respectively (Fig. 6.5), 2) plagioclase cores become more anorthitic, by an average of 12.0 mol% and 1.8 mol%, and clinopyroxene increases in Mg#, by an average of 1.0 mol% and 10.0 mol% in the orthopyroxenite and melagabbronorite, respectively, 3) whole-rock densities increase by 0.41 g/cm^3 in both layers (Fig. 6.8) and, 4) whole-rock major element oxides increase in

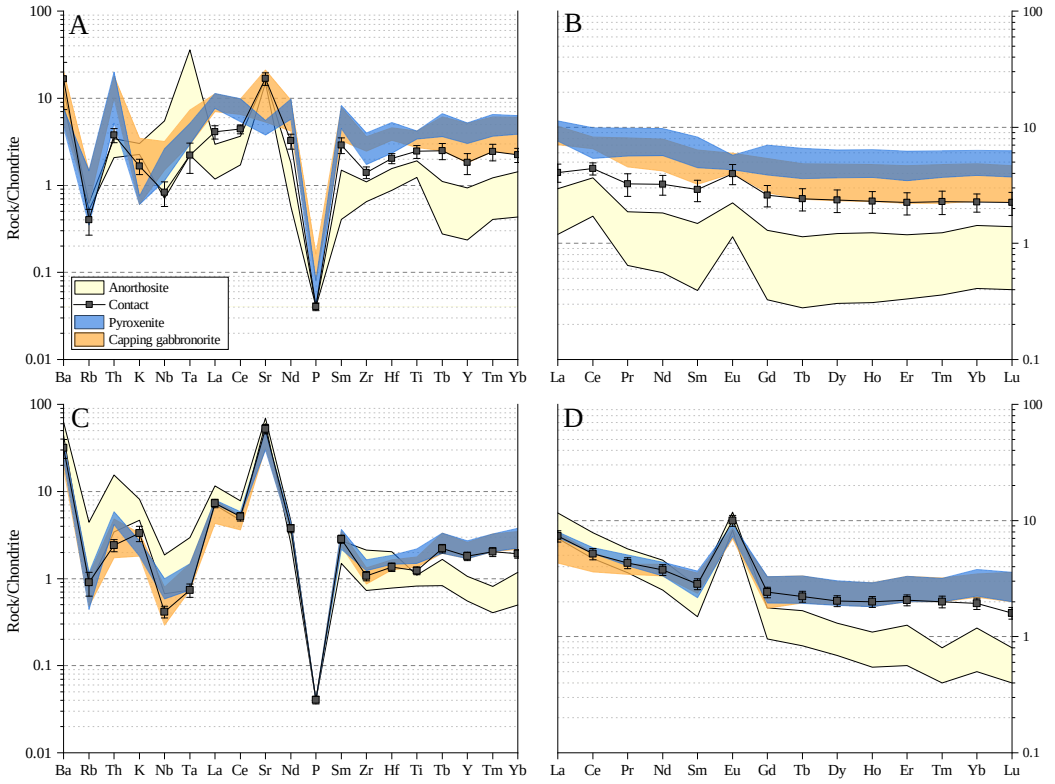

Figure 6.10 – Chondrite-normalized incompatible and rare earth element diagrams of the: **(A-B)** the orthopyroxenite sequence and **(C-D)** melagabbronorite sequences. Samples were normalized using the C1-carbonaceous chondrite values of McDonough and Sun (1995).

TiO_2, Ni, Cr and Mg#, and decrease in Al_2O_3 and K_2O in the orthopyroxenite and melagabbronorite layers, respectively (Fig. 6.9, Table 6.4).

Evidence for the presence of a resident magma suitable for mixing is found at the orthopyroxenite sequence outcrop, where small (cm-size) irregular-shaped pits filled with orthopyroxenite are observed in the pure anorthosite. At the melagabbronorite sequence outcrops (Fig. 2.5), several flames ($\leq$70 cm high) of poikilitic anorthosite transgress into the overlying melagabbronorite and modally-graded gabbronorite layers (Fig. 6.2B). These structures could have been formed from residual melt in the underlying anorthosites or from re-melting caused by the emplacement of a new, likely hotter and less-differentiated magma above the anorthosites. In either case, the presence of pit and flame structures indicate that some amount of resident magma was available for mixing.

The pyroxenite sequences demonstrate evidence consistent with magma and crystal mixing. The least-differentiated modal mineralogies, densities, mineral and whole-rock chemistries are consistently found above the lowermost pyroxenite layer contact (Figs. 6.5, 6.8, 6.9). Furthermore, the changes in modal mineralogies, densities, mineral and whole-rock chemistries all record a gradual transition to their least-differentiated or densest state, at some height within the pyroxenite layer. This is in common with the gradual reversal in mineral and whole-rock compositions that begins 200 - 400 m below the pyroxenite layers and peaks at the stratigraphic level of the Pyroxenite Marker, interpreted to represent a gradual mixing between a resident and a new, less-differentiated magma (Molyneux, 1974; Hayes et al., 1985; Mitchell, 1990; VanTongeren and Mathez, 2013; Cawthorn et al., 2016). However, the gradual change in modal mineralogies, densities, mineral and whole-rock chemistries is relatively abrupt (decimeter-scale), suggesting that a comparatively limited amount of resident magma was mixed with the new, less-differentiated and more-voluminous magma. Specific

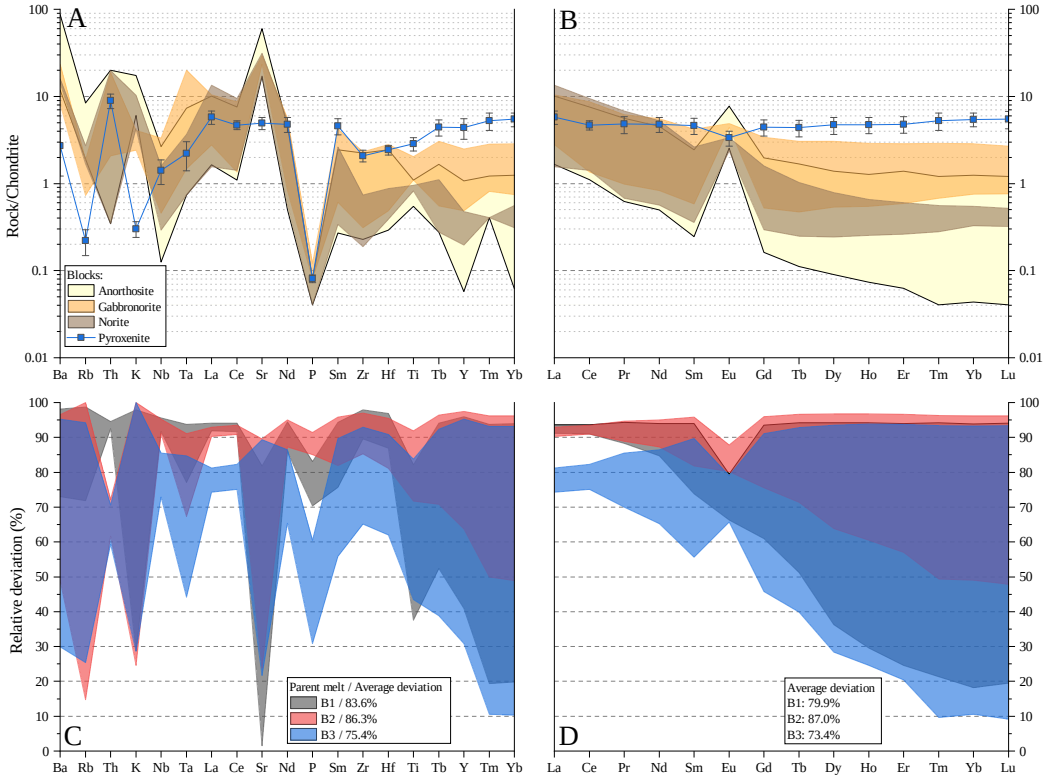

Figure 6.11 – Chondrite-normalized rare earth element diagrams of the blocks. **(A-B)** Ranges are provided for the blocks. Samples were normalized using the C1-carbonaceous chondrite values of McDonough and Sun (1995). **(C-D)** Relative deviation of incompatible elements (**C**) and REE (**D**) of all blocks with respect to the putative RLS parental melts (B1, B2, B3) proposed by Barnes et al. (2010). A lower relative deviation means a closer match.

to the melagabbornorite sequence, both orthopyroxene and clinopyroxene record bi-modal mineral chemistries immediately above the lowermost melagabbronorite layer contact (Fig. 6.5). A similar pattern could not be observed in plagioclase, as compositions (core and mantle) in the underlying anorthosite chemically overlap with that of the melagabbronorite layer. The bi-modal mineral chemistry in pyroxenes cannot be attributed to the trapped liquid shift effect (Barnes, 1986) or sub-solidus diffusion as such processes are unlikely to produce chemical bi-modal distributions. Rather, the bi-modal distribution suggests that crystals from both the resident and the new, less-differentiated magma mixed together.

6.7.2 Relationship between the pyroxenite sequences

Whole-rock normalized incompatible and REE patterns for each lithology (i.e. anorthosite, pyroxenite and gabbronorite) are very similar between the pyroxenite sequences, suggesting that the sequences crystallized from magmas with similar compositions, and in this sense are co-magmatic. However, slight differences are found in the anorthosite and pyroxenite lithologies between the sequences. Specifically, the anorthosite (upper range in Fig. 6.10B) at the orthopyroxenite sequence has a lower $(La/Lu)_{cn}$ slope (2.99) as compared to the poikilitic anorthosite at the melagabbnonorite sequence (15.09). This difference can be attributed to a larger modal abundance of pyroxenes (13%) as compared to the poikilitic anorthosite (2%). The orthopyroxenite supports a slightly negative $(Eu/Eu^*)_{cn}$ anomaly (-0.93) as compared to the melagabbonorite layer (3.32). This difference can

be attributed to a lower modal abundance of plagioclase (4%) in the orthopyroxenite layer as compared to the melagabbornorite layer (30%). As such, the matching trace element chemistries between the anorthosite, pyroxenite and gabbronorite layers suggest that all of these lithologies are from the same parental magma with each pyroxenite layer representing a separate magmatic pulse. Whole-rock normalized REE patterns of all lithologies are comparable to the Main Zone cumulate REE patterns published by Roelofse and Ashwal (2012) and Maier and Barnes (1998).

The melagabbronorite sequence was emplaced in an slightly more differentiated magma chamber as compared to the orthopyroxenite sequence. Plagioclase compositions, which are known to remain unaffected by subsequent diffusion and/or reaction processes (e.g. trapped liquid shift effect; Barnes, 1986), in the unlayered gabbronorite of the orthopyroxenite sequence, they average 67.80 mol% An (core and mantle only), whereas in the melagabbronorite sequence they average 60.73 mol%. The values are roughly in agreement with the decreasing An-content trends recorded up-section from the Pyroxenite Marker by Molyneux (1974); Lundgaard et al. (2006); VanTongeren and Mathez (2013); Cawthorn et al. (2016) in the northern half of the eastern lobe of the RLS. Unfortunately, trends in the Mooimeisjesfontein area documented by VanTongeren and Mathez (2013) were insufficiently detailed for a direct comparison, but significant variations in An-content ($\sim$15 mol%) were recorded in the vicinity of the Pyroxenite Marker. The slightly more albitic An-contents in the melagabbronorite sequence are further supported by consistently more differentiated whole-rock chemistries as compared to the orthopyroxenite sequence (Fig. 6.9).

6.7.3 Relationship of the blocks with the host rocks and putative RLS parent magmas

The blocks are lithologically and/or texturally (Fig. 6.3), petrologically (compare Figs. 6.4 to 6.6) and chemically distinct from their host rocks. Some altered poikilitic anorthosite blocks (e.g. block 1 in Fig. 6.1) resemble the poikilitic anorthosite documented at the melagabbronorite sequence. However, the blocks' mineral chemistries are more calcic ($An_{65.1}$) and magnesian (Mg#: 62.0 mol% for orthopyroxene and 71.2 mol% for clinopyroxene) compared to the anorthosite layer ($An_{59.9}$, Mg#: 60.9 mol% for orthopyroxene and Mg# 64.4 mol% for clinopyroxene). The same, slightly more calcic and magnesian mineral compositions are observed in most other blocks as compared to the nearest stratigraphically-matching lithology (i.e. melagabbronorite sequence; Fig. 6.5). These results suggest that the blocks are not related to their immediate host sequences.

Despite the differences between the blocks and their hosts, the blocks are still chemically affiliated with the RLS, and in this sense are cognate or co-magmatic. Chondrite-normalized incompatible and REE patterns best match the putative B3 melt composition, inferred as the parental melt of the Main Zone (Fig. 6.11C, D; Maier and Barnes, 1998; Barnes et al., 2010). Most blocks demonstrate a similar enrichment in LREE (average $(La/Lu)_{cn}$ = 5.07) as compared to Main Zone rocks (average $(La/Lu)_{cn}$ = 3.29 - 4.81; Maier and Barnes, 1998; Roelofse and Ashwal, 2012). Both whole-rock densities, mineral and whole-rock chemistries are also in agreement with Main Zone ranges. The presence of olivine alteromorphs in some of the anorthosite blocks are unusual for the Main Zone, which is normally devoid of olivine (Eales and Cawthorn, 1996). Nonetheless, the results suggests that the blocks may represent parts of the B3 melt system, derived from other sections, either from along strike or from deeper in the Main Zone of the RLS.

Constraints using the Al-in-orthopyroxene barometry

Here, I use the amount of Al_2O_3 in orthopyroxene to test if the blocks were derived from deeper sections of the RLS. Previous studies by Fram and Longhi (1992); Longhi et al. (1993, 1999) and Charlier et al. (2010) have demonstrated that the wt% amount of Al_2O_3 in orthopyroxene megacrysts hosted in Proterozoic massif-type anorthosite plutons can be used to estimate their depths of crystallization (in kbar).

Longhi et al. (1993) and Charlier et al. (2010) calibrated the Al-in-orthopyroxene barometer for crystals containing $\geq$3 wt% Al_2O_3. Our studied orthopyroxene crystals in the cumulate blocks contain an average of 0.61 wt% Al_2O_3 (Fig. 6.7B). However, the idea that the amount of Al_2O_3 in orthopyroxene relates to its crystallization pressure is still exploitable, as long as certain elements/oxides that could indicate other thermodynamic processes are uncorrelated with Al_2O_3 and that orthopyroxene is in equilibrium with plagioclase.

The data indicates that CaO does not co-vary with Al_2O_3, indicating that the abundance of Al_2O_3 is independent of plagioclase melt saturation (see Chapter 5 for more details). Several outliers (i.e. $>$1.5 wt% CaO) are caused by very-fine clinopyroxene exsolutions in inverted pigeonite. Therefore, high CaO-values located near visible clinopyroxene exsolution were eliminated from Fig. 6.7. Correlations between Al_2O_3 and the Mg# in orthopyroxene for RLS lithologies have been used to suggest primary thermal and/or differentiation controls of Al_2O_3 in orthopyroxene Cawthorn (2018). However, this is not the case (Fig. 6.12). Here, Al_2O_3 is essentially uncorrelated with the Mg#, indicating that Al_2O_3 in orthopyroxene is independent from magmatic processes such as temperature and melt differentiation. Similar trends were recorded in a sequence of anorthosite layers and blocks in the Upper Main Zone of the RLS (Chapter 5). Furthermore, all studied host and block samples are composed of well defined, sub- to euhedral crystals of orthopyroxene and plagioclase. Therefore, no evidence of disequilibrium is present between these mineral phases. Hence, pressure was the most likely controlling factor in the amount of Al_2O_3 in orthopyroxene.

However, without a calibrated barometer for the range of Al_2O_3, I am unable to constrain an exact depth. Cawthorn (2018) attempted to calibrate the barometer for lesser amounts of Al_2O_3 using an assortment of natural and experimental samples. However, Cawthorn (2018) used sparse data with a relatively large variance and chose linear regressions that poorly fit the data (with no R^2 given). Thus, the barometer defined by Cawthorn (2018) is deemed unreliable. The study by Charlier et al. (2010) is statistically robust and proposed a non-linear relationship between Al_2O_3 and pressure. Since Charlier et al.'s (2010) barometer is non-linear, results from its applications outside of its intended range exhibit a larger error. However, using this equation in a semi-quantitative manner yields a range of roughly 8 km for block samples. Since Charlier et al.'s (2010) barometer is non-linear with the slope of the equation being very steep in the region spanned by the data, the range result of 8 km is likely over-estimated.

The amount of Al_2O_3 in the blocks' orthopyroxene crystals is compared with that of the melagabbronorite sequence lithologies (melagabbronorite and gabbronorite), since blocks are hosted by or are stratigraphically nearest to this sequence (Fig. 6.7B). Orthopyroxene crystals in the blocks contain a similar amount of Al_2O_3 compared with the hosts. A first possibility is that orthopyroxene crystals in the blocks crystallized at the same pressures and therefore same depths as the orthopyroxene crystals in the sequence. A second possibility is that orthopyroxene crystals in the blocks crystallized at higher pressures, but re-equilibrated at lower pressures through diffusive/infiltrative mass exchange. Rarely, blocks are fragmented or have a thin band of pure anorthosite (1 - 5 cm thick) at their outer margin (Fig. 6.3C, D). However, Al_2O_3 is known for its immobility under a wide range of hydrothermal and metamorphic conditions (Rollinson, 1993). The blocks' mineral chemistries

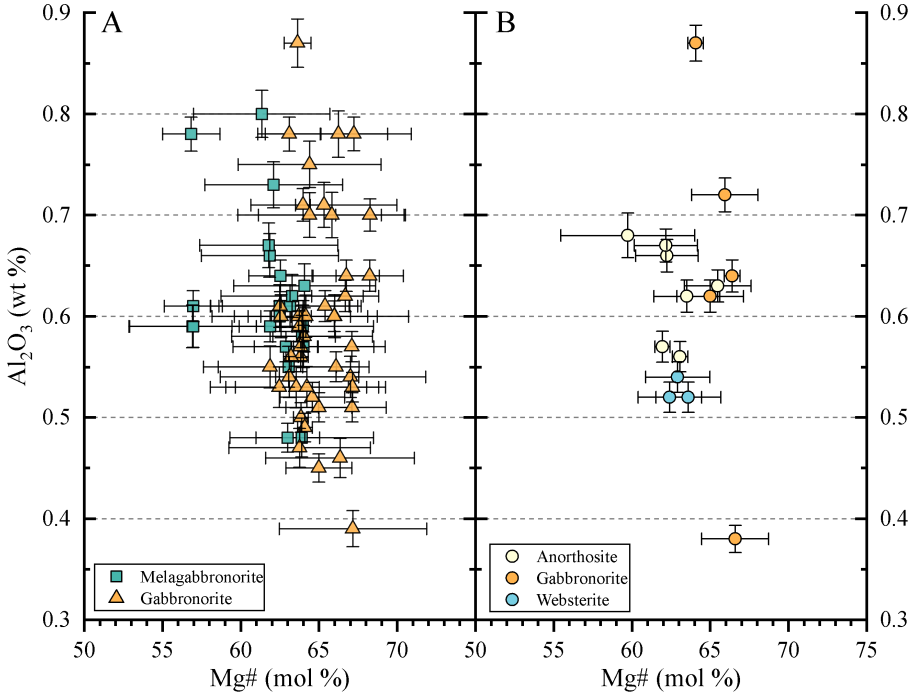

Figure 6.12 – Abundance of Al_2O_3 (wt%) versus Mg# (mol%) and in orthopyroxene crystals. **(A)** The amount of Al_2O_3 does not co-vary with the Mg# in the melagabbronorite sequence. A correlation would indicate that the Mg# and therefore temperature and/or melt differentiation is responsible for the observed change in Al_2O_3. The orthopyroxenite sequence (not shown) demonstrates the same relationship as the melagabbonorite sequence. **(B)** The amount of Al_2O_3 does not co-vary with the Mg# in the cumulate blocks hosted in the melagabbronorite sequence.

are also distinct from the thin band of pure anorthosite, suggesting limited re-equilibration. Furthermore, orthopyroxene crystals in all blocks contain similar amounts of Al_2O_3, regardless of their modal mineralogy, size and lithology. There is therefore a stronger possibility that block orthopyroxene crystals crystallized at the same pressures and therefore at similar depths as orthopyroxene crystals in the melagabbronorite sequence.

Block transport?

If the blocks were transported to their present locations from elsewhere in the Bushveld Complex magmatic system, the density of the blocks should be correlated with the density of the host. The densest block (3.34 g/cm^3) is a websterite (block 4; Figs. 6.3D, 6.6D) that is hosted in modally-graded gabbronorite (3.02 g/cm^3). To examine the hypothesis of a gabbronorite melt transporting the blocks, I employ the numerical model developed by Royse and Park (2000) and Spera (1980), which is also used in Chapter 5). With this model, it is possible to calculate a minimum transport velocity for suspending a spherical block in a column of magma (non-Newtonian) by balancing frictional forces with gravitational forces.

The density and viscosity of a gabbronorite melt may be estimated within a range by assuming that the melt was emplaced at a temperature of $\sim$1200° (Cawthorn et al., 1998). At its upper bound, if the host magma was similar to the modally-graded gabbronorite host (average of 3.02 g/cm^3), then its density is likely better approximated by the whole-rock measurements. A lower bound for host magma density can also be thermodynamically modeled using alphaMELTs (Ghiorso and Sack, 1995; Asimow and Ghiorso, 1998), which yields a gabbronorite magma host density of 2.67 g/cm^3.

Both experimental melt viscosity measurements by Getson and Whittington (2007) of chemically comparable samples and thermodynamic modeling using alphaMELTs (Ghiorso and Sack, 1995; Asimow and Ghiorso, 1998) yield a gabbronorite melt viscosity between 50 to 100 Pa·s. Assuming that this is representative of the melt, adopting the lowest viscosity value would ensure that the model produces an upper-bound estimate and also take into consideration that the melt could have originated from greater depths at higher temperatures and therefore ensures a conservative model assumption on the hydrodynamic requirements of the melt. This approach underestimates the sizes of transportable blocks and presents a favorable margin for interpretation. The numerically modeled terminal velocities of the block as a function of magma velocity at various crystal fractions for two hypothesized magma densities is presented in Figure 6.13.

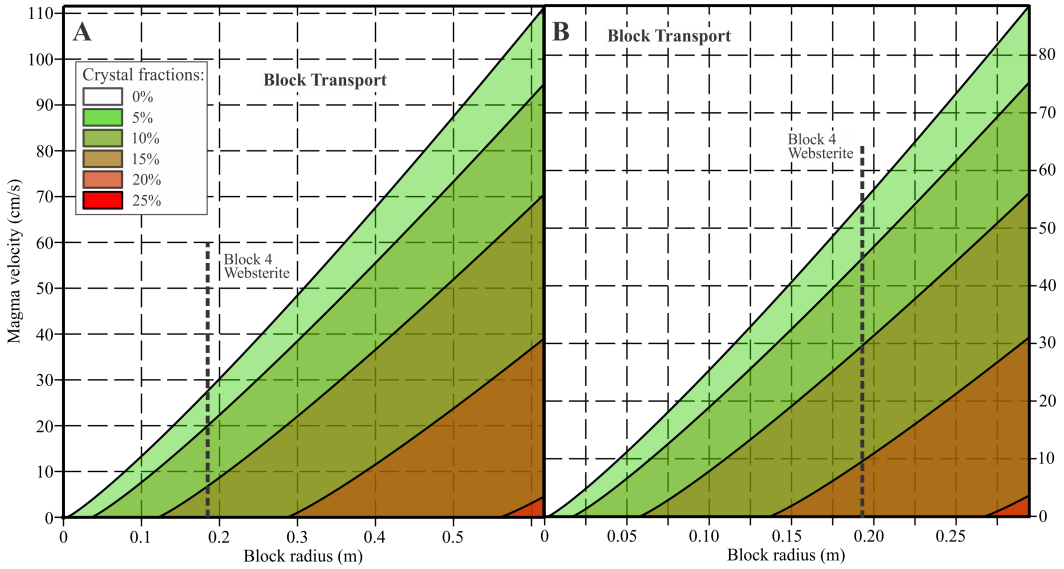

Figure 6.13 – Numerically modeled minimum magma velocity necessary to transport a range of sizes of blocks in a gabbronorite magma with crystals fractions ranging from 0 to 25 vol%. Each color corresponds to the maximum size of the block that can be transported in the slurry given a certain crystal fraction. Vertical dashed line corresponds to the radii of the densest block, the websterite block 4 (19 cm). **(A)** Lower bound of the model. Model parameters: host magma viscosity = 50 Pa·s, websterite block density = 3.34 g/gm^3, average gabbronorite density = 3.02 g/cm^3. **(B)** Upper bound of the model. Model parameters: host magma viscosity = 50 Pa·s, websterite block density = 3.34 g/gm^3, modeled gabbronorite density = 2.67 g/cm^3.

Figure 6.13 demonstrates two key observations: (1) blocks are increasingly likely to be entrained and transported in a gabbronorite magma with increasing crystal fractions and within a realistic range (e.g. 5 - 20%), mainly due to the low density contrast between the blocks and the host melt; and (2) the flow rates need to be substantially faster to transport known blocks compared to blocks being transported by a plagioclase slurry, see Chapter 5, due to the low viscosity of the hypothetical gabbronorite host magma. Since most blocks are oblate-shaped and therefore exhibit greater drag coefficients than equivalent masses of spheres, the model substantially over-estimates the magma velocities and crystallinities that are necessary to sustain vertical transport of the blocks. For physical blocks that are mostly oblate-shaped, the drag is several times that of the spherical equivalent, and therefore, the required transport velocity is a fraction of the maximum constraint via a spherical approximation. This has several geological consequences that are not mutually exclusive: (1) the required crystallinity is lower than predicted by the model; (2) the required viscosity is lower than predicted by the model; and, (3) the required flow rate is much lower than that predicted by the

model. Furthermore, orthopyroxene crystals likely crystallized at similar depths as the crystals in the host sequence (Fig. 6.7). Transport along an incline or horizon requires less hydrodynamic force than that is required vertically. However, the estimates provide a semi-quantitative and realistic constraint on magma velocity and crystal fraction. Therefore, an absolute maximum upper-bound estimate indicates a probable range of 5 to 20 vol% crystallinity and a corresponding magma ascent velocity of 54 to 9 cm/s, respectively (Fig. 6.13B). This is a highly over-estimated constraint that would allow vertical transport of the most dense block to its present location from deeper.

The most dense block would be automatically entrained at crystal fractions greater than 15 vol% at any ascent velocity or host gabbronorite magma density. The calculated velocities correspond to the minimal magma ascent rates, such that the blocks would remain neutrally buoyant in the magma. For transport to occur vertically, the magma needs to travel faster than the calculated terminal velocities and/or increase its crystal fractions and/or break up the blocks into smaller pieces. A significant portion of the blocks are however of lesser or similar densities than the host (Table 6.3). Blocks that are of lesser or similar densities as compared to their host would be automatically entrained at any velocity and crystallinity. Although if the blocks were buoyant, then an additional mechanism is necessary to retain the blocks near the bottom of respective layers.

These magma hydrodynamic conditions are reasonable compared to extensively studied volcanic systems, such as Mount St. Helens. The estimated magma ascent velocities of the May 18^{th} 1980 eruption is between 0.7 - 70 cm/s from a 8 - 11 km deep staging chamber (Scandone and Malone, 1985; Rutherford, 2008). Furthermore, recent U-Pb zircon dating reveal that the RLS was likely emplaced rapidly, in $\leq$100 ka, implying an accumulation rate of 5 - 13 km^3/year (Cawthorn et al., 1998; Zeh et al., 2015), which indirectly suggests that episodic conditions when and where ascending magma with sufficient velocity to transport blocks vertically could exist. Therefore, the numerical model of magma transport dynamics supports the hypothesis that the blocks could have been transported in a crystal-bearing gabbronorite magma.

Origin of the blocks?

The blocks are comagmatic with the RLS and can therefore be regarded as cognate xenoliths or autoliths. The blocks' trace element chemistries also best match the putative B3 parent melt composition (Fig. 6.11C, D), which suggests that the blocks were most likely derived from the same parental melt as the Main Zone. Further evidence relating the blocks to the Main Zone is the presence of variable but pervasive lithological and/or textural resemblances to their nearest-matching lithologies in the pyroxenite sequences, despite their overall more calcic and magnesian mineral chemistries (Fig. 6.5). Mineral chemistries vary laterally in the RLS, where the least-differentiated chemistries are recorded further north, near the Thabazimbi-Murchison Lineament (Lundgaard et al., 2006; Clarke et al., 2009; Cawthorn et al., 2016; Setera and VanTongeren, 2018). The range of Al_2O_3-content in orthopyroxene crystals overlaps with that of host lithologies, indicating a similar depth of crystallization (Fig. 6.7). Additionally, numerical modeling reveals that the blocks are suitably transported in a crystal-bearing gabbronorite magma. Considering all perspectives, I suggest that the blocks were likely sourced and subsequently transported from other parts of the Main Zone, either from proximal lithologies underlying the pyroxenite sequences or from elsewhere along strike, further north, as to account for their mineral chemistries.

6.7.4 Implications for the style of magmatic replenishment

The studied pyroxenite layers likely originated from separate magmatic replenishments where a less-differentiated magma mixed with a resident one. The proposed model follows the much larger-

scale and widely accepted notion of a major replenishment event in the upper portions of the Main Zone and subsequent magma mixing with a resident magma (Molyneux, 1974; Cawthorn et al., 1991; Maier et al., 2001; VanTongeren and Mathez, 2013; Cawthorn et al., 2016; Cawthorn, 2020). However, the style of magmatic replenishment remains poorly understood and is highly debated across a continuum of models. At one end of the continuum is a model that necessitates superheated aphyric melts that crystallized *in situ* after emplacement into the chamber (e.g. Campbell et al., 1978; McBirney and Noyes, 1979; Latypov et al., 2017). Another more flexible model that spans across the remainder of the continuum is the emplacement of crystal-bearing slurries (e.g. Maier and Barnes, 1998; Barnes et al., 2010; Roelofse and Ashwal, 2012; Roelofse et al., 2015; Eales and Costin, 2012; Hayes et al., 2017; Yuan et al., 2017). Here, I discuss the feasibility of each model.

Emplacement of a superheated aphyric melt that crystallized *in situ*

It is unclear what features could be solely attributable to *in situ* crystallization of a superheated aphyric magma that could not be otherwise attributed to a non-aphyric magma, since the behavior of both models greatly overlap and indeed, there is a continuum of crystallinities and thermal states available to any hypothetical magma. Upon emplacement, a superheated magma that is aphyric quickly becomes a slurry *in situ* after thermal, chemical and modal mixing with the resident magma. Additionally, the hydrodynamic conditions of the parental magma are unconstrained through any existing data and effects attributable to superheated, aphyric magmas can be present in a slurry through changes in magma composition, e.g. viscosity through addition of volatiles.

Some specific evidence that are inconsistent with *in situ* crystallization of a superheated aphyric magma include shape-preferred alignment of primocrysts in both pyroxenite sequences. von Gruenewaldt (1970) noted that pre-inversion exsolution lamellae in inverted pigeonite crystals are generally oriented perpendicular to the plane of layering, indicating that the original crystals settled with their long-axis oriented parallel to the plane of layering. Such is the case for primocrysts in both pyroxenite sequences. I consider the alignment of the primocrysts to be the result of magmatic flow as opposed to the compaction of homogeneously-nucleated and epitaxially grown crystals, since primocrysts are relatively free of deformation microstructures. Additionally, the blocks and any other solid matter in the chamber would have presented ideal heterogeneous nucleation surfaces, on which new crystals would grow during *in situ* crystallization. Thermodynamically, even if these blocks were at the same temperature as the surrounding magma, they would still lower the nucleation energy barrier by presenting crystalline surfaces. However, instead of observing well-attached crystals anchored to the blocks, the blocks are in contact with crystals that are indistinguishable to those in the bulk of the pyroxenite sequences (i.e. morphology, chemistry, zonation) and with the long axes of the host crystals resting parallel to the contact surface (Fig. 6.6C). If the blocks were transported from deeper origins, such as from a conduit or from lower stratigraphic sequences, then an aphyric magma is less suitable, unless the density contrast was reversed. However, in this case, the blocks would float to the top of the chamber, which is contrary to the observed reality, where blocks clearly settled as evidenced by the deformation of layering beneath the blocks (e.g. Fig. 6.3B, D). One known mechanism by which a denser host rock can surround blocks is via the formation of a cumulate layer, which traps and buries the blocks in dense cumulate material and thus retains the blocks at the bottom of the magma chamber. For this process to result in the observed configuration of the blocks, concomitant block transport and crystallization is necessary. For these reasons, I do not think the replenishing magmas were superheated aphyric melts that crystallized *in situ*.

Emplacement of a crystal-bearing slurry

I documented numerous blocks contained in the pyroxenite sequences as well as a modally-graded gabbronorite horizon, ∼10 to 30 m above the melagabbronorite sequence (Fig. 6.1). Field evidence supporting the notion of slurries are preserved magmatic flow textures, expressed by the alignment of primocrysts with their long axis orientated parallel to the plane of layering (Fig. 6.4) and the observation of modally-graded layers which drape and smooth across the blocks (e.g. Fig. 6.3D). The presence of modally-graded layers attest to turbulent emplacement dynamics, with magmatic currents capable of keeping crystals in suspension (e.g. Irvine et al., 1998; Quadling and Cawthorn, 1994; Maier et al., 2013). The numerical model of magma transport also supports the idea that the blocks could have been transported in a slurry. Specifically, upper bounds of the model yields realistic magma ascent velocities between 9 - 54 cm/s for crystal fractions between 20 - 5 vol%, respectively, assuming vertical transport and spherical blocks (Fig. 6.13B). Magmatic viscosity is strongly dependent on its crystal load (Marsh, 1981; Spera, 1980; Getson and Whittington, 2007). Therefore, it stands to reason that the more viscous and therefore crystalline a magma is, the better it can dislodge and entrain blocks. As blocks in the orthopyroxenite sequence are only found at the base of the orthopyroxenite layer (Fig. 6.1), the idea that the initial pulses of magma were more capable of block transport compared to subsequent pulses, by being more crystalline and/or faster flowing is probable. In addition, the thermodynamic environment experienced by subsequent blocks and proto-block material may have been disadvantageous for the preservation of blocks. In summary, it is likely that the magma replenishments that formed the pyroxenite sequences in the Mooimeisjesfontein area were slurries. Additional crystallization in the magma chamber after magma emplacement was probably rapid, due to the observation of buoyant blocks in their present locations. The rapid formation of a cumulate layer ensures that some blocks are entrapped by the settling crystals. If this idea is correct, then the density and cross-sectional horizontal surface areas of the blocks can be an effective proxy for the study of an exact rate of crystallization. However, field study of the surface areas of the blocks is outside of the scope of this chapter.

6.8 Conclusions

The Pyroxenite Marker in the Mooimeisjesfontein area is defined by two lithologically and texturally distinct pyroxenite layers that are stratigraphically separated by ∼60 m of unlayered gabbronorite. Progressing up-section, the first pyroxenite layer is a ∼2 m thick orthopyroxenite underlain by pure anorthosite, whereas the second is a ∼40 cm-thick melagabbronorite underlain by poikilitic anorthosite. Hundreds of lithologically and/or texturally distinct transported cumulate blocks are also found in the pyroxenite sequences as well as in a modally-graded gabbronorite horizon, ∼10 to 30 m above the melagabbronorite layer. The blocks' petrography, density, mineral and whole-rock compositions are also examined in detail in this contribution. Mineral and whole-rock chemistries (major and trace elements) indicate that the blocks are cogenetic with the RLS. Both incompatible and REE patterns of the blocks are closest to the putative B3 melt composition, suggesting that the blocks were derived from the same parental melt as the remainder of the Main Zone. Combined data from field, petrographic, density, mineral and whole-rock chemistry, and its associated analyses suggest that the blocks were likely sourced from other parts of the Main Zone, either from proximal lithologies underlying the pyroxenite sequences or from elsewhere along strike. Both pyroxenite layers demonstrate field, petrographic, mineral and whole-rock chemical evidence that they formed through separate magmatic replenishment events with subsequent magma mixing. On the basis of field observations, petrography, mineral and whole-rock chemistry combined with numerical model-

ing for the transport of the blocks, I suggest that the replenishing magmas were most likely emplaced as crystal-bearing slurries (5 - 20 vol% crystals) that flowed at a rate of 54 - 9 cm/s (assuming spherical blocks and vertical transport). Furthermore, the buoyancy of the blocks within the Pyroxenite Marker indicates that they could not have been in-fallen roof and/or sidewall material within the chamber, and instead, transport and trapping by concomitant crystal settling is a much more plausible mechanism within the magma chamber. This study therefore provides novel insights into the dynamics of magma chamber replenishment in the evolution of the Rustenburg Layered Suite.

7 Conclusions

Numerous aspects of the RLS have been documented or have been the subject of scientific research over the last century. In comparison to the other zones of the RLS, the Main Zone is often described as an unspectacular, 3000 m thick succession of unlayered gabbronorite. Several studies by von Gruenewaldt (1973); Molyneux (1970, 1974); Mitchell (1986, 1990) and Nex et al. (1998) have established a detailed stratigraphic succession for the Main Zone and mentioned minor successions/layers of modally-graded gabbronorite, anorthosite and pyroxenite. The Main Zone has been divided into a lower and an upper sub-zones with the Pyroxenite Marker delineating the boundary between the two (Mitchell, 1990). This study explored several unique outcrops found in the Upper Main Zone using an integrated, multidisciplinary approach.

Chapter 4 described a sequence of 8 texturally distinct poikilitic anorthosite layers and a layer of norite, all of which are bounded by unlayered gabbronorite. The sequence is stratigraphically correlated to near the top of the Upper Main Zone, ∼166 m below the base of the Upper Zone. Each layer of anorthosite represents a separate magmatic pulse, based on sharp contacts combined with abrupt mineral composition changes. Furthermore, the anorthosite layers are all related to a single parental magma that fractionated slightly prior to each emplacement as observed by the identical chondrite-normalized incompatible and REE patterns. The layers of anorthosite were likely emplaced as plagioclase slurries, as evidenced by unvarying plagioclase crystal morphologies and relatively constant mineral and whole-rock chemistries observed throughout the sequence.

Chapter 5 described a total of 16, cm- to m-sized norite cumulate blocks hosted in the layered sequence of poikilitic anorthosites. Field observations, petrography, mineral and whole-rock chemistry and whole-rock Sr-Nd radiogenic isotopic compositions revealed that the blocks are cogenetic with the RLS, specifically the B3 magma, an inferred parental melt of the Main Zone. However, the blocks' mineral chemistry and isotopic compositions are overall more primitive and less contaminated (or isotopically less-enriched) compared to both the host rocks and other values measured in the Main Zone. Therefore, the blocks likely represent transported and recycled cumulate material from staging chambers, deeper in the Bushveld Complex plumbing system. Numerical modeling of the absolute upper bound of the terminal velocities of the blocks suggests that they were likely transported in a plagioclase slurry (5 - 30 vol% crystals), which ascended at a minimal rate of 4.38 - 0.70 cm/s, respectively. Therefore, masses of plagioclase slurries ascended from deeper staging chambers and entrained the blocks from the original and/or other staging chambers, through which the recharge magma flowed.

Chapter 6 centered on the Pyroxenite Marker, located at the base of the Upper Main Zone. The Pyroxenite Marker in the Mooimeisjesfontein area is characterized by two distinct pyroxenite layers, separated by ∼60 m of unlayered gabbronorite. Progressing up-section, the first pyroxenite layer is a ∼2 m-thick orthopyroxenite underlain by pure anorthosite. The second pyroxenite layer is a ∼40 cm-thick melagabbronorite underlain by poikilitic anorthosite. Both pyroxenite layers gradually transition to gabbronorite up-section. At a minimum, hundreds of lithologically and/or texturally distinct transported cumulate blocks are present in the pyroxenite sequences as well as a modally-graded gabbronorite horizon, ∼10 to 30 m above the melagabbronorite layer. The blocks' mineral chemistry, incompatible and REE patterns are reminiscent of the inferred B3 parental magma of the Main Zone. Combined results of field observations, petrographic, density, mineral and whole-rock chemistry data together with an application of the principles of the Al-in-orthopyroxene barometer, suggests that the blocks were likely sourced from other parts of the Main Zone, either from lithologies underlying the pyroxenite sequences or from elsewhere along the strike. Each pyroxenite layer likely formed through a magmatic replenishment event, where a new and less-differentiated

magma mixed with a resident magma, based on whole-rock density, modal mineralogies, mineral and whole-rock chemistry data. Numerical modeling of the absolute upper bound of terminal velocities of the blocks suggests that the replenishing magmas were likely crystal-bearing slurries (5 - 15 vol% crystals) that flowed at a rate of 27 - 7 cm/s, respectively.

This study first examined the hypotheses that the Upper Main Zone either resulted from a single or multiple injections of magma. Chapter 4 provided field, petrographic and chemical evidence that each layer of anorthosite at the road-cut was the result of a separate injection of magma. Furthermore, chapter 6 demonstrated that each pyroxenite layer is the result of a separate magmatic replenishment, as evidenced by field, petrography, whole-rock density, mineral and whole-rock chemistries. Given this evidence, the most probable scenario is that the Upper Main Zone formed from multiple, discrete pulses of magma. This interpretation based on an integrated and multidisciplinary approach is concordant with interpretations within several studies for the Lower Main Zone and the Upper Zone (Mitchell, 1990; Ashwal et al., 2005; Hayes et al., 2017; Scoon and Mitchell, 2012; Roelofse and Ashwal, 2012; VanTongeren and Mathez, 2013; Yuan et al., 2017).

This study also contributed to the ongoing debate regarding the initial nature of the RLS magmas at the time of their emplacement - superheated aphyric melts that crystallized *in situ* versus crystal-bearing slurries. The discovery and detailed documentation of hundreds of blocks in the Upper Main Zone (Chapters 5 and 6) provided new insights into the nature of the magma injections, especially regarding crystallinity ranges of the host magmas. Numerical modeling produced the absolute maximum upper-bound constraints on the hydrodynamic conditions suitable for the transport of the blocks via entrainment, which are magma velocities between 0.7 - 4.4 cm/s for an anorthositic slurry and 7 - 27 cm/s for a gabbronorite slurry, and corresponding crystal fractions between 30 - 5 vol% for the anorthosite and 15 - 5 vol% for the gabbronorite magma, respectively. Additional field and petrographic evidence supporting slurries includes the: 1) alignment of primocrysts with their long axis oriented parallel to the plane of layering, as documented for all study areas, 2) alignment of crystals around the margins of the blocks, which are characteristic of magma flow and not epitaxial growths, as documented for all study areas, 3) morphologically consistent (e.g. size, habit, zonation) plagioclase crystals, as documented in the anorthosite layers at the road-cut, and 4) modally graded gabbronorite layers that drape and smooth over blocks, as documented in the incised valley. All lines of evidence are fully consistent with magmatic injections that were crystal-bearing for the Upper Main Zone, and inconsistent with superheated aphyric melts that crystallized *in situ*.

An unexpected surprise in this study was found with the transported cumulate blocks. To date, only a single study on the origin of blocks in large layered ultramafic-mafic intrusions has been published. Irvine et al.'s (1998) large-scale field and petrographic study of the Skaergaard intrusion (Greenland) made landmark contributions by using blocks to propose a novel magmatic crystal-liquid suspension mechanism. Regarding the blocks, Irvine et al. (1998) proposed that they represent in-fallen roof and sidewall materials, which were scattered over the intrusion's floor by magmatic crystal-liquid suspension currents. Contrary to the Skaergaard intrusion, the studied blocks in the Upper Main Zone either originated from staging chamber(s) deeper in the Bushveld magmatic plumbing system (anorthosite sequence, Chapter 5) or from relatively proximal origins (pyroxenite sequences, Chapter 6). Such differing origins between and within intrusions highlight a much more dynamic and nuanced origin, in terms of magma chamber dynamics and evolution that may be applicable to other layered ultramafic-mafic intrusions.

Of particular interest, this study used a multidisciplinary approach to gain a broad perspective on the frequency, origin and dynamics of magma emplacement. In this manner, I aimed to avoid serious common pitfalls of mono-disciplinary and specialized studies, whereby a single line of evidence, and often data outliers (e.g. isotopes, field or petrography) leads to over-interpretation, and especially

causal models without contextual or quantitative constraints. In my opinion, to further evolve geology, researchers should strive to adopt a more quantitative, integrated and multidisciplinary approach to avoid over-interpretation, which leads to poorly constrained and sometimes highly polarized, and seemingly irreconcilable ideas.

Comparatively little research is available for the Main Zone as compared to the other zones of the RLS, despite its intrigue and whimsy as demonstrated in this study. In the spirit of future research, several outstanding questions remain. How well does the replenishment mechanism as identified in this study generalize and apply to remainder of the Main Zone? Was slurry emplacement prevalent in the Main Zone and what are the hydrodynamic conditions that blocks can elucidate on a per-layer basis? At what depth are slurries generated? Are blocks in other RLS lithologies also from staging chambers, or are they from elsewhere? What are the most probable ranges of magma crystalinity in any given case, and what are the best methods to constrain this quantitatively? Did the unspectacular thick sequences of gabbronorite crystallize from a single or multiple pulses of magma? These questions highlight a few pertinent questions following this study, but also reveal how much remains to be explored and discovered, not only in the Main Zone but for the whole of the Bushveld Complex and other similar layered ultramafic-mafic intrusions in the world.

A List of samples

The tables below include all samples that were taken and submitted to various analytical methods for this thesis. All coordinates reported here follow the UTM coordinate system, specifically the World Geodetic System (WGS84) ellipsoid. The zones encompassing the Phosiri Dome area is under J35 and the Mooimeisjesfontein area is under J36. All size and height measurements are reported in centimeter. EMPA = Electron microprobe analysis; Geochem = geochemical analysis.

Table A.1 – List of samples from the anorthosite sequence.

Sample	Location	Easting	Northing	Rock	Height	Layer	EMPA	Geochem	Isotope
JB060	West	782602	7300424	Gabbronorite	5090			X	
AR-1-1	West	782666	7300503	Anorthosite	2450	8		X	
AR-3-8	West	782666	7300503	Norite	1500	8		X	
ARS-2-1	West	782660	7300468	Anorthosite	1490	7	X	X	
ARS-2-2	West	782660	7300468	Anorthosite	1440	7			
ARS-2-3	West	782660	7300468	Anorthosite	1410	7			
ARS-2-4	West	782660	7300468	Anorthosite	1370	7	X	X	X
ARS-2-5	West	782660	7300468	Anorthosite	1330	7			
ARS-2-6	West	782660	7300468	Anorthosite	1290	7	X	X	
ARS-2-7	West	782660	7300468	Anorthosite	1260	7			
ARS-2-8	West	782660	7300468	Anorthosite	1220	7			
ARS-2-9	West	782660	7300468	Anorthosite	1180	7	X	X	
ARN-3-1	East	782646	7300534	Anorthosite	1180	6	X	X	
ARN-3-2	East	782646	7300534	Anorthosite	1120	6	X		
ARN-3-3	East	782646	7300534	Anorthosite	1070	6	X	X	X
ARN-3-4	East	782646	7300534	Anorthosite	1020	6	X		
ARN-3-5	East	782646	7300534	Anorthosite	970	6			
ARN-2	East	782666	7300503	Anorthosite	950	6	XX	X	
ARN-3-6	East	782646	7300534	Anorthosite	920	6	X	X	
ARN-3-7	East	782646	7300534	Anorthosite	870	6	X		
ARN-3-8	East	782646	7300534	Anorthosite	820	6	X	X	
ARN-3-9	East	782646	7300534	Anorthosite	770	6			
ARN-1-1	East	782666	7300503	Anorthosite	740	6		X	
ARN-3-10	East	782646	7300534	Anorthosite	720	6	X	X	
ARN-4-1	East	782636	7300554	Anorthosite	720	5	X	X	
ARN-4-2	East	782636	7300554	Anorthosite	700	5			
ARN-4-3	East	782636	7300554	Anorthosite	680	5			
ARN-4-4	East	782636	7300554	Anorthosite	660	5	X	X	
ARN-4-5	East	782636	7300554	Anorthosite	640	5			
ARN-4-6	East	782636	7300554	Anorthosite	620	5			
ARN-4-7	East	782636	7300554	Anorthosite	610	5	X	X	
ARN-4-8	East	782636	7300554	Anorthosite	600	5			
ARN-4-9	East	782636	7300554	Anorthosite	580	5	X	X	
ARN-4-10	East	782636	7300554	Anorthosite	560	5			
ARN-4-11	East	782636	7300554	Anorthosite	540	5	X	X	
ARN-5-1	East	782625	7300563	Anorthosite	540	4	X	X	
ARN-5-2	East	782625	7300563	Anorthosite	520	4			
ARN-5-3	East	782625	7300563	Anorthosite	500	4			
ARN-5-4	East	782625	7300563	Anorthosite	490	4	X	X	X
ARN-3	East	782666	7300503	Anorthosite	480	4		X	
ARN-5-5	East	782625	7300563	Anorthosite	480	4			
ARN-5-6	East	782625	7300563	Anorthosite	460	4	X	X	
AR-5	East	782625	7300563	Anorthosite	445	4		X	
ARN-5-7	East	782625	7300563	Anorthosite	440	4			
ARN-5-8	East	782625	7300563	Anorthosite	420	4	X	X	
AR-7-1	West	782666	7300503	Anorthosite	230	2		X	
AR-13	West	782666	7300503	Pure anorthosite	0	1	X		
AR-9(-1)	West	782666	7300503	Gabbronorite	-470		X	XX	X

Table A.2 – List of samples from blocks in the anorthosite sequence.

Sample	Location	Easting	Northing	Rock	Layer	Layer Height	Block size Length	Block size Height
ARS-X1	West	728662	7300450	Poikilitic norite	8	350	51	18
ARS-X2	West	782629	7300509	Olivine norite	7	0	335	44
ARS-X3	West	782577	7300572	Norite	1	0	464	70
ARS-X4	West	782581	7300580	Olivine norite	Gn	-180	100	50
ARS-X5	West	782585	7300588	Olivine norite	1	5	575	60
ARS-X6	West	782581	7300588	Norite	1	10	100	17
ARN-X7	East	782578	7300603	Olivine norite	1	10	215	30
ARN-X8	East	782615	7300594	Olivine norite	7	0	430	30
ARN-X9	East	782708	7300440	Norite	8	940	266	80
							120	30
ARS-X10	West	782681	7300391	Poikilitic norite	8	735	167	40
ARN-X11	East	782646	7300534	Norite	7	15	265	150
ARN-X12	East	782646	7300534	Norite	6	410	80	50
ARN-X13	East	782659	7300502	Olivine norite	7	0	266	17
ARS-X14	West	782629	7300509	Unknown	1	300	165	15
ARS-X15	West	782666	7300503	Unknown	8	5	200	10
ARS-X16	West	728662	7300450	Norite	8	340	18	3

Sample	EMPA	Geochem	Isotope
ARS-X1	X	X	X
ARS-X2	X	X	X
ARS-X3	X	X	X
ARS-X4		X	X
ARS-X5	X	X	X
ARS-X6		X	
ARN-X7		X	
ARN-X8		X	
ARN-X9	X	X	X
ARS-X10		X	X
ARN-X11	X	X	X
ARN-X12	X	X	
ARN-X13		X	X
ARS-X14			
ARS-X15			
ARS-X16			

Table A.3 – List of samples from pyroxenite sequences.

Sample	Easting	Northing	Rock	Height	EMPA	Geochem
JB031-A1	199979	7246936	Anorthosite	-100	X	X
JB031-A2	199979	7246936	Anorthosite	-10	X	X
JB031-T	199979	7246936	Transition	0	X	X
JB031-P1	199979	7246936	Orthopyroxenite	10	X	X
JB031-P2	199979	7246936	Pyroxenite	15		
JB031-P3	199979	7246936	Pyroxenite	60	X	X
JB031-P4	199979	7246936	Websterite	100	X	X
JB031-P5	199979	7246936	Pyroxenite	145	X	X
JB031-P6	199979	7246936	Pyroxenite	165		
JB031-P7	199979	7246936	Pyroxenite	185	X	X
JB031-P8	199979	7246936	Pyroxenite	215		
JB031-P9	199979	7246936	Pyroxenite	225	X	X
JB031-G1	199979	7246936	Gabbronorite	235	X	X
JB031-G2	199979	7246936	Gabbronorite	275	X	X
JB031-G3	199979	7246936	Gabbronorite	480	X	X
JB031-G4	199979	7246936	Gabbronorite	650	X	X
PM-GN	199742	7248826	Gabbronorite	-300		
PM-100	199742	7248826	Anorthosite	-100		
PM-90	199742	7248826	Anorthosite	-90	X	X
PM-80	199742	7248826	Anorthosite	-80		
PM-70	199742	7248826	Anorthosite	-70		
PM-65	199742	7248826	Anorthosite	-65		
PM-54	199742	7248826	Anorthosite	-54		
PM-42	199742	7248826	Anorthosite	-42		X
PM-35	199742	7248826	Anorthosite	-35	X	
PM-20	199742	7248826	Anorthosite	-20		
PM-14	199742	7248826	Anorthosite	-14		
PM-12	199742	7248826	Anorthosite	-12		X
PM-10	199742	7248826	Anorthosite	-10		
PM-8	199742	7248826	Anorthosite	-8		X
PM-4	199742	7248826	Anorthosite	-4		
PM-1	199742	7248826	Anorthosite	-1	X	X
PM-0	199742	7248826	Pyroxenite	0	XX	
PM+3	199742	7248826	Pyroxenite	3		XX
PM+7	199742	7248826	Pyroxenite	7		
PM+10	199742	7248826	Pyroxenite	10	X	
PM+12	199742	7248826	Pyroxenite	12		
PM+13	199742	7248826	Pyroxenite	13	X	X
PM+15	199742	7248826	Pyroxenite	15		
PM+17	199742	7248826	Pyroxenite	17		
PM+18	199742	7248826	Pyroxenite	18		
PM+21	199742	7248826	Pyroxenite	21		X
PM+30	199742	7248826	Norite	30	X	
PM+35	199742	7248826	Gabbronorite	35		
PM+41	199742	7248826	Norite	41	X	X
PM+44	199742	7248826	Norite	44		
PM+45	199742	7248826	Norite	45		
PM+48	199742	7248826	Norite	48	X	X
PM+60	199742	7248826	Norite	60		
PM+70	199742	7248826	Norite	70	X	
PM+80	199742	7248826	Gabbronorite	80		
PM+90	199742	7248826	Gabbronorite	90		
PM+95	199742	7248826	Gabbronorite	95		
PM+100	199742	7248826	Gabbronorite	100		
PM+110	199742	7248826	Gabbronorite	110	X	
PM+133	199742	7248826	Gabbronorite	133		X
PM+145	199742	7248826	Gabbronorite	145	X	X
PM+160	199742	7248826	Gabbronorite	160		
PM+260	199742	7248826	Gabbronorite	260	X	
PM+380	199742	7248826	Gabbronorite	380	X	
PM+550	199742	7248826	Gabbronorite	550	X	
JB019-P	199894	7248548	Pyroxenite	0		
JB019-B	199894	7248548	Pyroxenite	50		
JB024-P	199610	7249328	Pyroxenite	0		

Table A.4 – List of samples from blocks in feldspathic pyroxenite sequences or in modally-graded gabbronorite. The hight is measured from the start of the melagabbronorite layer.

Sample	Easting	Northing	Rock	Height	Block size			EMPA	Geochem
					Length	Length	Height		
LX-1-1	199651	7249000	Anorthosite	2785	2164		203	X	
LX-1-2	199651	7249000	Gabbronorite	2583	124		64		X
LX-1-3-1	199651	7249000	Anorthosite	2990	880	380			
LX-1-3-2	199651	7249000	Anorthosite	3054	880	380			
LX-1-4	199651	7249000	Anorthosite	2728	2164		203		X
LX-1-5	199651	7249000	Norite	2288	110		64		X
LX-1-6	199651	7249000	Norite	2233	68		29		X
LX-1-7	199651	7249000	Norite	2327	8		5		
LX-1-8	199651	7249000	Gabbronorite	1930	32	17			
LX-2-1	199697	7248868	Anorthosite	500	680	218			X
PM-X1	199728	7248794	Anorthosite	44	56		9	X	X
PM-X2	199725	7248802	Anorthosite	125	107		40	X	X
PM-X3	199728	7248806	Gabbronorite	110	150		80	X	X
PM-X4	199728	7248808	Pyroxenite	38	37		13	X	X
PM-X5	199745	7248817	Norite	144	50		20		X
PM-X6	199736	7248827	Gabbronorite	45	90		60		X
PM-X7	199743	7248769	Gabbronorite	300	35		20		
PM-X8	199744	7248787	Pyroxenite	200	14		24		
JB017-X	199646	7248922	Gabbronorite	700	190	50			
JB019-X1	199894	7248548	Gabbronorite	60	119	24	23		
JB019-X2	199894	7248548	Anorthosite	80	34		22	X	X
JB019-X3	199894	7248548	Anorthosite	190	64	65			
JB019-X4	199894	7248548	Anorthosite	200	60	109	12		
JB023-X	199610	7249248	Norite	1500	115	115	20		
JB024-X1	199610	7249328	Gabbronorite	114	30		9		
JB024-X2	199610	7249328	Anorthosite	156	493		160		
JB024-X4	199610	7249328	Pyroxenite	150	33	10			

B Mooimeisjesfontein block outcrop maps

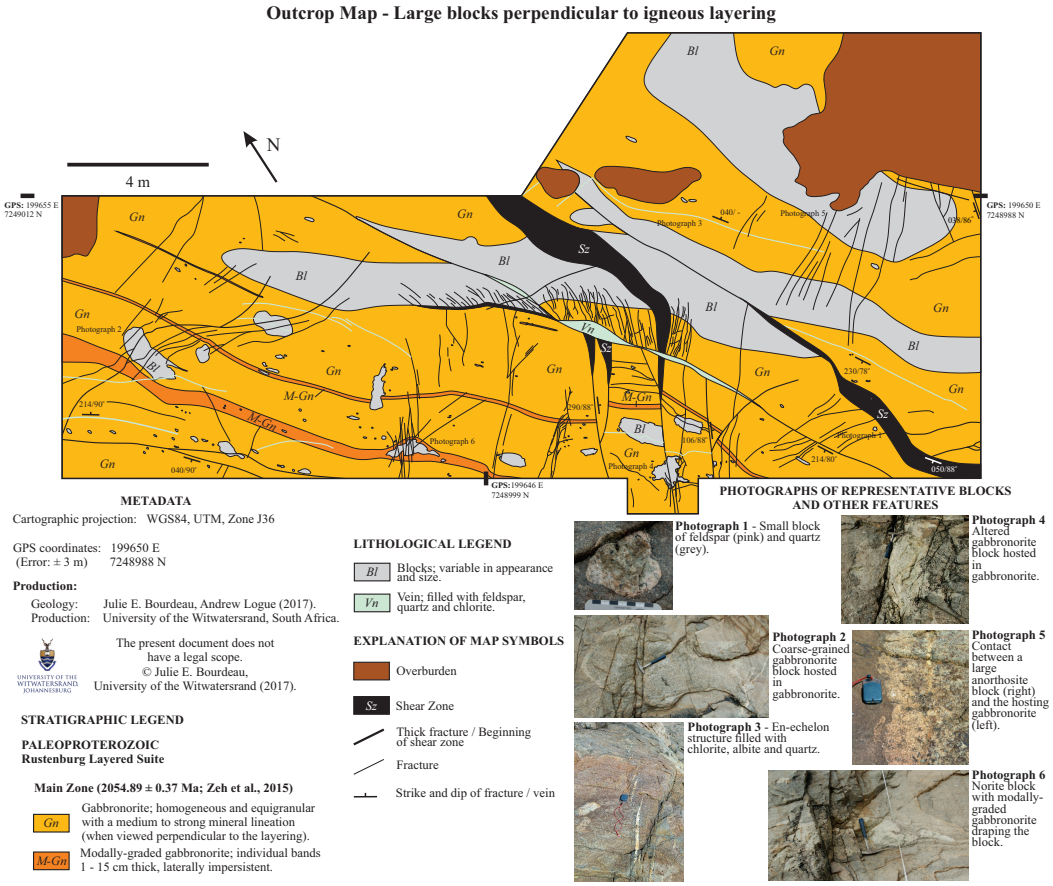

Figure B.1 – Outcrop map of large blocks in the Mooimeisjesfontein area. The surface of the outcrop is aligned perpendicular to igneous layering.

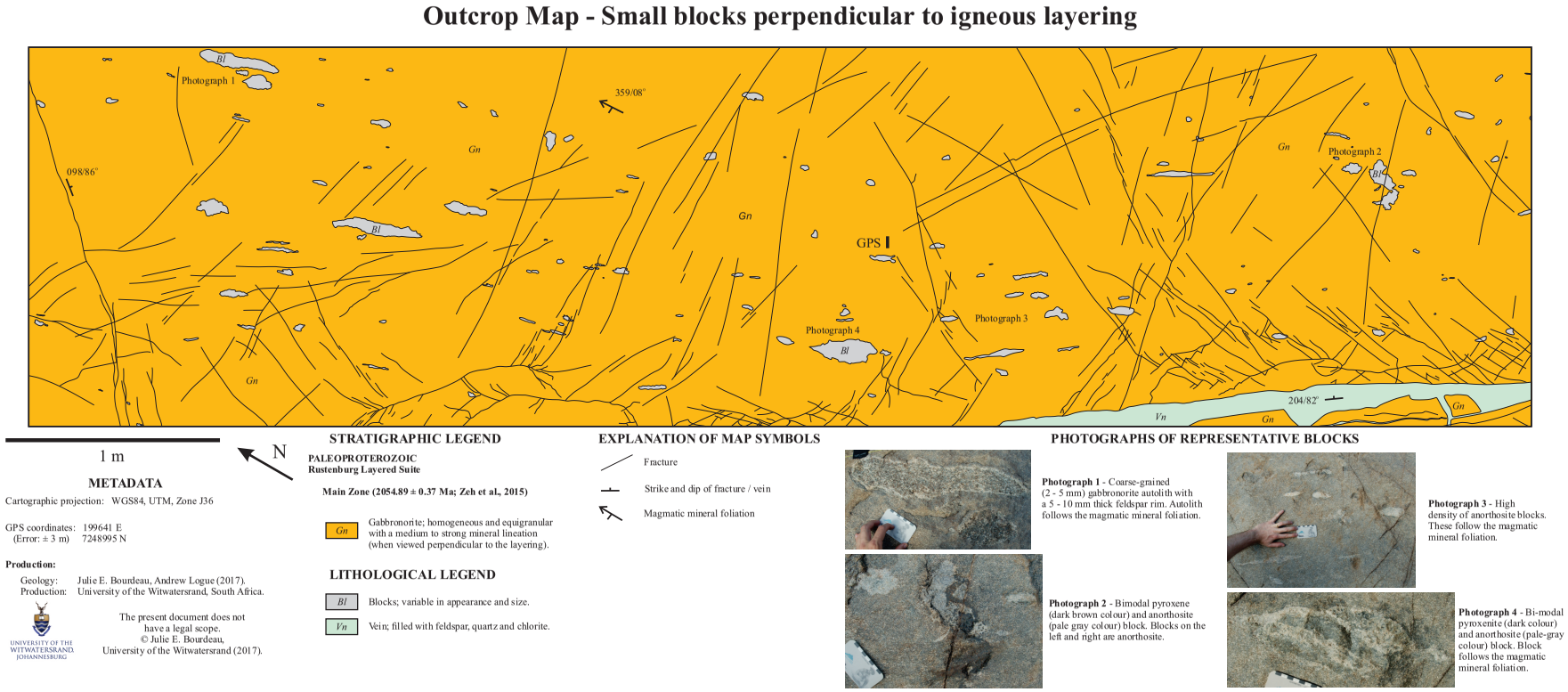

Figure B.2 – Outcrop map of small blocks in the Mooimeisjesfontein area. The surface of the outcrop is aligned perpendicular to igneous layering.

Outcrop Map - Blocks parallel to igneous layering

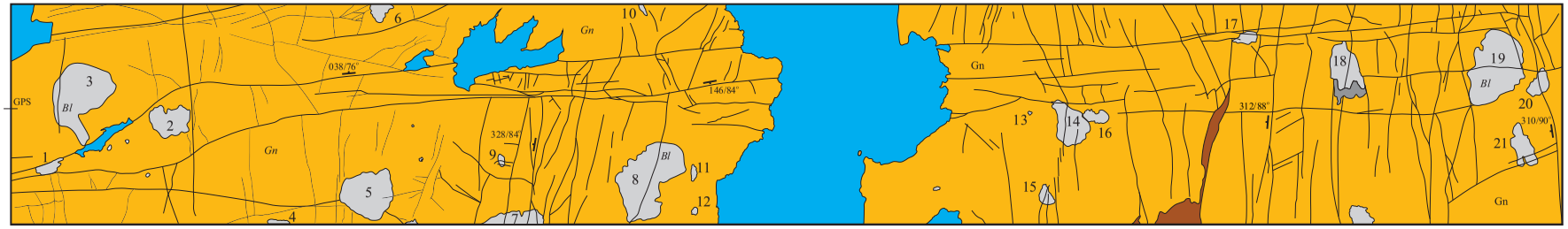

1 m

N

METADATA

Cartographic projection: WGS84, UTM, Zone J36

GPS coordinates: 199622 E
(Error: ± 3 m) 7249047 N

Production:

Geology: Julie E. Bourdeau, Andrew Logue (2017).
Production: University of the Witwatersrand, South Africa.

UNIVERSITY OF THE WITWATERSRAND, JOHANNESBURG

The present document does not have a legal scope.
© Julie E. Bourdeau, University of the Witwatersrand (2017).

STRATIGRAPHIC LEGEND

PALEOPROTEROZOIC
Rustenburg Layered Suite

Main Zone (2054.89 ± 0.37 Ma; Zeh et al., 2015)

Gn — Gabbronorite; homogeneous and equigranular with a medium to strong mineral lineation (when viewed perpendicular to the layering).

LITHOLOGICAL LEGEND

Bl — Blocks; variable in appearance and size.

EXPLANATION OF MAP SYMBOLS

Water / Overburden

Fracture

Strike and dip of fracture

Size of blocks (cm):

1: 10 × 5	8: 36 × 33	15: 6.5 × 9
2: 18 × 10	9: 5 × 3	16: 6 × 11.5
3: 37 × 27	10: 10 ×2	17: 6 × 15
4: 12 × 5	11: 8 × 3	18: 17 × 30
5: 24 × 22	12: 4 × 2	19: 32 × 36
6: 21 × 10	13: 1.5 × 1.5	20: 8 × 16
7: 29 × 9	14: 15 × 23	21: 7 × 18

PHOTOGRAPHS OF REPRESENTATIVE BLOCKS

Block 3 - Anorthosite block. Block is composed of beige, slightly tabular feldspar (1 - 4 mm) which have been slightly sericitized (pale green colour) With dark green chlorite in the matrix.

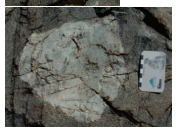

Block 5 - Anorthosite block. Block is aphanitic, feldspathic and pale green in colour (sericite).

Block 8 - Altered gabbronorite block. Block is composed of beige feldspar laths (2 - 5 mm) hosted in a chloritized matrix. Block has a poorly-developed anorthosite rim.

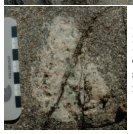

Block 15 - Anorthosite block. Block is composed of beige coloured (1 - 2 mm) feldspars with small green-coloured chlorite patches near the transecting fracture.

Figure B.3 – Outcrop map of blocks in the Mooimeisjesfontein area. The surface of the outcrop is aligned parallel to igneous layering.

C Calculation of mineral formula and error propagation

C.1 Calculation of a mineral formula

A mineral formula can be calculated using the following function:

$$\alpha(Z_i) = \frac{N(Y_j) \cdot \left(\frac{C_{wt\%}(X_i)}{M(X_i)}\right)}{\sum_{i=1}^{n}\left(\frac{q}{M(X_i)} \cdot C_{wt\%}(X_i)\right)} \tag{C.1}$$

Where Z_i is the element calculated in atoms per formula unit (*apfu*), $N(Y_j)$ is the number of anions (O, OH, F, Cl) per mineral formula, $C_{wt\%}(X_i)$ is the given raw wt% of an oxide, $M(X_i)$ is the molar weight of the oxide. For the sum function, all detected oxides are included, where q is the number of oxygens per oxide. The above formula can be applied to all non-ferromagnesian minerals.

Unfortunately, microprobe analyses cannot detect the two oxidation states of iron (Fe^{3+}/Fe^{2+}). Consequently, the equation and method presented by Droop (1987) is used, where:

$$C^{apfu}_{Fe^{3+}} = 2 \cdot N(Y_j) \cdot \left(\frac{1 - T(Y_j)}{\sum_{i=1}^{n}\alpha(Z_i)}\right) \tag{C.2}$$

Where T(Y_j) is the total number of cations per mineral formula. Note that if: $\sum_{i=1}^{n}\alpha(Z_i) < T(Y_j)$, then the calculation needs to be abandoned and all Fe needs to be set as Fe^{2+}, as otherwise negative Fe^{3+} will appear. Once the concentration of Fe^{3+} has been determined, Fe^{2+} is corrected by:

$$C^{apfu}_{Fe^{2+}} = \alpha(Fe^{2+}) - C^{apfu}_{Fe^{3+}} \tag{C.3}$$

However, note that if: $\alpha(Fe^{2+}) < C^{apfu}_{Fe^{3+}}$, then negative Fe^{2+} will appear and all iron is to be set as Fe^{3+}. Once iron concentrations have been corrected, the mineral formula needs to be re-normalized to T(Y_j) cations, where:

$$\beta(Z_i) = \alpha(Z_i) \cdot \left(\frac{T(Y_j)}{\sum_{i=1}^{n}\alpha(Z_i)}\right) \tag{C.4}$$

At this point the mineral formula may be cast into end-members (mol%). For example the end-members of pyroxene may be calculated:

$$\begin{aligned}
\text{Enstatite} : En(mol\%) &= \left(\frac{\beta(Mg)}{\beta(Mg) + \beta(Fe^{3+}) + \beta(Fe^{2+}) + \beta(Ca)}\right) \cdot 100\% \\
\text{Ferrosilite} : Fs(mol\%) &= \left(\frac{\beta(Fe^{3+}) + \beta(Fe^{2+})}{\beta(Mg) + \beta(Fe^{3+}) + \beta(Fe^{2+}) + \beta(Ca)}\right) \cdot 100\% \\
\text{Wollastonite} : Wo(mol\%) &= \left(\frac{\beta(Ca)}{\beta(Mg) + \beta(Fe^{3+}) + \beta(Fe^{2+}) + \beta(Ca)}\right) \cdot 100\%
\end{aligned} \tag{C.5}$$

C.2 Calculation of error propagation for a mineral formula

The error associated with the calculation of a mineral formula can be obtained, whereby:

$$\begin{aligned} \Delta\alpha =& \frac{N(Y_j)}{M(X_i)} \cdot \frac{C_{wt\%}(X_i)}{S_o} \cdot \sqrt{\left(\frac{\Delta C_{wt\%}(X_i)}{C_{wt\%}(X_i)}\right)^2 + \left(\frac{\Delta S_o}{S_o}\right)^2} \\ \text{Where: } S_o =& \sum_{i=1}^{n} \left(\frac{C_{wt\%}(X_i)}{M(X_i)} \cdot q\right); \qquad \Delta S_o = \sqrt{\sum_{i=1}^{n} \left(\frac{\Delta C_{wt\%}(X_i)}{M(X_i)} \cdot q\right)^2} \end{aligned} \tag{C.6}$$

The mineral formula error calculated using this equation above is sufficient for non-ferromagnesian minerals. Ferromagnesian minerals require a few extra steps to calculate the errors associated with the estimation of Fe^{3+}/Fe^{2+}. The first step involves calculating the error associated with Fe^{3+}:

$$\begin{aligned} \Delta C_{Fe^{3+}}^{apfu} =& \sqrt{\left(\frac{2 \cdot N(Y_j) \cdot T(Y_j)}{(S_{ON})^2}\right)^2 \cdot (\Delta S_{ON})^2} \\ \text{Where: } S_{ON} =& \sum_{i=1}^{n} \alpha(Z_i)^2; \qquad \Delta S_{ON} = \sqrt{\sum_{i=1}^{n} \Delta\alpha(Z_i)^2} \end{aligned} \tag{C.7}$$

Now, that the amount of Fe^{3+} has been determined we can correct the amount of Fe^{2+}:

$$\Delta C_{Fe^{2+}}^{apfu} = \sqrt{(\Delta\alpha(Fe^{2+}))^2 + \left(\Delta C_{Fe^{3+}}^{apfu}\right)^2} \tag{C.8}$$

Once the amounts of Fe^{3+}/Fe^{2+} have been determined, the last step involved the re-normalization of the formula to T(Y_j) cations (Equation C.4). The same can be done with the errors by using this formula:

$$\Delta\beta(Z_i) = \sqrt{\left(\frac{T(Y_j)}{S_{ON}}\right)^2 \cdot (\Delta\alpha(Z_i))^2 + \left(\frac{\alpha(Z_i) \cdot T(Y_j)}{(S_{ON})^2}\right)^2 \cdot (\Delta S_{ON})^2} \tag{C.9}$$

Finally, the error associated with the end-members can be calculated. The equation below apply

to the pyroxene end-members (Equation C.5):

$$
\begin{aligned}
\Delta\text{En} = &\left[\left(\frac{\Delta\beta(Mg)}{\beta(Mg)}\right)^2 + \right. \\
&\left.\left(\frac{\Delta\beta(Mg)+\Delta\beta(Fe^{3+})+\Delta\beta(Fe^{2+})+\Delta\beta(Ca))}{\beta(Mg)+\beta(Fe^{3+})+\beta(Fe^{2+})+\beta(Ca))}\right)^2\right]^{1/2} \cdot En(mol\%) \\
\Delta\text{Fs} = &\left[\left(\frac{\Delta\beta(Fe^{3+})+\Delta\beta(Fe^{2+})}{\beta(Fe^{3+})+\beta(Fe^{2+})}\right)^2 + \right. \\
&\left.\left(\frac{\Delta\beta(Mg)+\Delta\beta(Fe^{3+})+\Delta\beta(Fe^{2+})+\Delta\beta(Ca))}{\beta(Mg)+\beta(Fe^{3+})+\beta(Fe^{2+})+\beta(Ca))}\right)^2\right]^{1/2} \cdot Fs(mol\%) \\
\Delta\text{Wo} = &\left[\left(\frac{\Delta\beta(Ca)}{\beta(Ca)}\right)^2 + \right. \\
&\left.\left(\frac{\Delta\beta(Mg)+\Delta\beta(Fe^{3+})+\Delta\beta(Fe^{2+})+\Delta\beta(Ca))}{\beta(Mg)+\beta(Fe^{3+})+\beta(Fe^{2+})+\beta(Ca))}\right)^2\right]^{1/2} \cdot Wo(mol\%)
\end{aligned}
\tag{C.10}
$$

C.3 Step by step process used in this study

Table C.1 – Steps taken in the calculation of a mineral formula for this study.

Step	**Formula**	**Definitions**
Base Units	wt% = $C_{wt\%}(X_i)$	$X_i \equiv$ oxide (e.g. SiO_2, Al_2O_3, ...)
Oxygen Moles	$mol_o(X_i) = \frac{C_{wt\%}(X_i)}{M(X_i)} \cdot q$	q ≡ number of charges per oxide M≡ Molar weight
Sum	$S_o = \sum_1^n mol_o(X_i)$	
Correction factor	$\kappa(Y_j) = \frac{N(Y_j)}{S_o}$	$N(Y_j)\equiv$ number of oxygens per mineral
Normalization	$\alpha(Z_i) = \frac{\kappa(Y_j)\cdot mol_o(X_i)}{q}$	$Z_i\equiv$ element (e.g. Si^{4+}, Al^{3+}, ...)
If iron correction needed:		
Sum of elements	$S_{ON} = \sum_1^n \alpha(Z_i)$*	
Fe^{3+} correction	$C_{Fe^{3+}}^{apfu} = 2 \cdot N(Y_j) \cdot \left[\frac{1-T(Y_j)}{S_{ON}}\right]$	
Fe^{2+} correction	$C_{Fe^{2+}}^{apfu} = \alpha Fe^{2+} - C_{Fe^{3+}}^{apfu}$	
Re-normalization	$\beta(Z_i) = \alpha(Z_i) \cdot \left[\frac{T(Y_j)}{S_{ON}}\right]$	

* = Specific for amphibole (Si, Ti, Al, Cr, Fe, Mn, Mg, Ca)

Table C.2 – Steps taken in the calculation of error propagation for this study.

Step	Formula
ΔOxygen moles	$\Delta mol_o(X_i) = \frac{\Delta C_{wt\%}(X_i)}{M(X_i)} \cdot q$
ΔSum	$\Delta S_o = \sqrt{\sum_1^n \Delta mol_o(X_i)}$
ΔQuadrature	$\Delta\gamma(Z_i) = \sqrt{\left(\frac{\Delta C_{wt\%}(X_i)}{C_{wt\%}(X_i)}\right) + \left(\frac{\Delta S_o}{S_o}\right)}$
ΔError	$\Delta\alpha(Z_i) = \frac{C_{wt\%}(X_i)}{S_o} \cdot \Delta\gamma(Z_i) \cdot \frac{N(Y_j)}{M(X_i)}$
If iron correction needed:	
ΔSum of elements	$\Delta S_{ON} = \sqrt{\sum_1^n \Delta\alpha(Z_i)^2}$*
ΔFe^{3+} correction	$\Delta C_{Fe^{3+}}^{apfu} = \sqrt{\left(\frac{2 \cdot N(Y_j) \cdot T(Y_j)}{(S_{ON})^2}\right)^2 \cdot (\Delta S_{ON})^2}$
ΔFe^{2+} correction	$\Delta C_{Fe^{2+}}^{apfu} = \sqrt{(\Delta\alpha Fe^{2+})^2 + (\Delta C_{Fe^{3+}}^{apfu})^2}$
ΔRe-normalization	$\Delta\beta(Z_i) = \sqrt{\left(\frac{T(Y_j)}{S_{ON}}\right)^2 \cdot (\Delta\alpha(Z_i))^2 + \left(\frac{\alpha(Z_i) \cdot T(Y_j)}{(S_{ON})^2}\right)^2 \cdot (\Delta S_{ON})^2}$

* = Specific for amphibole (Si, Ti, Al, Cr, Fe, Mn, Mg, Ca)

D Mineral chemistry data and analytical uncertainties

The tables below include all mineral chemistry data collected and used in this thesis. The data below is unnormalized. To calculate the analytical uncertainties see appendix C. Minerals analyzed include: epidote, hornblende, micas (phlogopite and chlorite), olivine, plagioclase, pyroxenes (clinopyroxene and orthopyroxene) and spinel (ilmenite and magnetite). Data tables for the minerals are arranged alphabetically. Note for all tables: – = element not detected.

Table D.1 – Mineral chemistry for epidote. This table only includes the data (wt%). Note: NiO and ZrO were also analyzed, but were not detected. Tag list: 1 = Inclusion in plagioclase; 2 = Rimming clinopyroxene with alteration minerals.

Tag	Sample	ID	SiO2	TiO2	Al2O3	V2O3	Cr2O3	FeOT	MnO	MgO	CaO	SrO	BaO	Na2O	K2O	Cl	F	Total
Anorthosite sequence near the Phosiri Dome																		
2	ARN-4-11	1618	38.10	0.00	26.23	–	–	8.31	0.13	0.02	24.00	0.04	–	0.08	0.00	0.01	0.09	96.98
2	ARN-4-11	1619	37.44	0.00	26.53	0.04	–	2.08	0.23	2.94	23.25	0.01	–	0.02	0.01	0.00	–	92.56
2	ARN-4-11	1620	37.47	0.00	26.25	–	–	8.69	0.10	0.03	23.93	0.03	0.01	0.01	–	0.01	0.05	96.55
2	ARN-4-11	1622	37.94	–	25.99	–	0.00	8.80	0.32	0.00	23.71	0.07	–	0.02	–	0.03	–	96.88
Pyroxenite Layers in the Mooimeisjesfontein area																		
1	PM+30	1979	38.33	–	30.68	–	–	3.46	0.81	0.00	23.86	0.03	–	–	0.00	0.04	0.11	97.28

Table D.2 – Mineral chemistry for epidote. This table only includes the analytical uncertainties (%).

ID	Si	Ti	Al	V	Cr	Fe	Mn	Mg	Ca	Sr	Ba	Na	K	Cl	F
Anorthosite sequence near the Phosiri Dome															
1618	0.25	299.74	0.28	-709.08	-47.00	0.97	13.49	52.38	0.31	64.23	-49.05	17.43	154.92	65.37	99.37
1619	0.25	1698.33	0.28	57.72	-284.31	2.02	8.59	1.13	0.32	235.75	-127.95	58.97	74.77	76.49	-215.83
1620	0.25	233.90	0.28	-678.70	-95.81	0.95	16.15	33.72	0.31	101.95	111.43	105.87	-383.51	44.08	194.65
1622	0.25	-460.98	0.29	-149.11	2945.55	0.94	6.87	287.85	0.32	39.00	-101.38	65.67	-59.94	14.37	-90.72
Pyroxenite Layers in the Mooimeisjesfontein area															
1979	0.25	-96.81	0.26	-122.95	-159.33	1.53	3.77	259.40	0.32	102.00	-170.65	-313.90	10081.70	10.82	82.62

Table D.3 – Mineral chemistry for hornblende. This table only includes the data (wt%). Tag list: 1 = Rimming clinopyroxene; 2 = Rimming orthopyroxene; 3 = Rimming clinopyroxene with quartz; 4 = Rimming orthopyroxene with quartz.

Tag	Tag*	Sample	ID	SiO2	TiO2	Al2O3	V2O3	Cr2O3	FeOT	NiO	ZnO	MnO	MgO	CaO	SrO	BaO	Na2O	K2O	Cl	F	Total
Anorthosite sequence near the Phosiri Dome																					
1		AR-9	1538	49.50	0.46	5.51	0.06	0.07	10.90	0.07	–	0.13	16.22	12.18	0.01	0.01	0.55	0.55	0.18	0.18	96.46
1		AR-9	1539	49.20	0.46	5.68	0.08	0.12	11.23	0.08	–	0.12	15.92	12.00	0.00	0.01	0.65	0.51	0.21	0.04	96.24
2		ARS-2-1	1310	47.73	0.66	8.67	0.11	0.06	13.52	0.03	0.04	0.15	13.93	11.57	–	0.01	0.82	0.70	0.18	–	98.17
2		ARS-2-1	1311	50.14	0.25	6.10	0.03	0.02	12.59	0.05	–	0.19	15.25	11.39	–	–	0.54	0.43	0.08	0.14	97.22
2		ARS-2-1	1313	49.27	0.44	7.41	0.10	0.04	12.67	0.03	0.00	0.15	14.69	11.65	0.00	–	0.69	0.48	0.07	0.15	97.83
1		ARS-2-4	1450	46.85	0.70	6.90	0.07	0.01	14.13	0.03	–	0.16	13.55	12.33	0.02	0.01	0.62	0.59	0.05	0.13	96.08
1		ARS-2-4	1451	51.52	0.31	3.26	0.03	0.01	11.48	0.02	–	0.13	16.21	12.36	0.01	0.00	0.28	0.20	0.02	–	95.82
1		ARS-2-4	1452	51.15	0.31	3.51	0.05	0.03	12.17	0.04	0.02	0.14	15.88	12.12	0.02	–	0.28	0.25	0.02	–	96.00
1		ARS-2-6	1319	50.41	0.37	5.36	0.05	0.00	14.22	0.02	–	0.18	14.40	11.66	0.02	–	0.51	0.35	0.03	0.05	97.63
1		ARS-2-6	1320	54.62	0.20	2.69	0.04	–	12.40	0.02	0.02	0.23	16.32	11.54	0.02	–	0.25	0.16	0.02	0.12	98.65
1		ARS-2-6	1321	55.27	0.16	1.86	0.03	0.01	13.39	0.00	–	0.32	16.99	10.24	–	–	0.14	0.09	0.01	0.06	98.57
1		ARN-3-8	1415	50.64	0.32	4.77	0.02	–	12.38	0.02	–	0.21	15.78	11.87	–	0.01	0.36	0.38	0.10	0.14	96.92
1		ARN-3-8	1416	52.12	0.22	3.68	0.01	–	11.86	0.03	–	0.20	16.74	11.66	–	0.01	0.25	0.25	0.09	0.09	97.15
1		ARN-3-8	1418	50.18	0.34	4.79	0.09	0.01	12.59	0.03	–	0.22	15.87	11.89	0.04	–	0.39	0.38	0.11	0.09	96.95
1	3	ARN-2-2'	923	48.40	0.72	6.37	0.09	0.04	11.75		–	0.17	14.70	11.70	–	–	0.68	0.59	0.07	0.17	95.43
1	3	ARN-2-2'	924	47.14	1.05	7.18	0.06	0.02	12.99		–	0.12	13.62	11.82	0.02	0.00	0.65	0.75	0.08	0.12	95.62
1	3	ARN-2-2'	914	50.91	0.40	5.70	0.04	0.04	11.40		–	0.16	15.39	11.89	–	0.02	0.44	0.47	0.04	–	96.88
2	6	ARN-2-2'	900	49.67	0.93	6.42	0.05	0.05	10.75		0.02	0.12	15.30	11.82	–	0.03	0.60	0.59	0.04	0.19	96.59
2	6	ARN-2-2'	901	52.47	0.53	4.88	0.05	0.05	10.88		–	0.12	16.27	11.83	–	0.01	0.47	0.39	0.06	0.11	98.12

Tag	Tag*	Sample	ID	SiO2	TiO2	Al2O3	V2O3	Cr2O3	FeOT	NiO	ZnO	MnO	MgO	CaO	SrO	BaO	Na2O	K2O	Cl	F	Total
2	6	ARN-2-2'	902	52.90	0.42	4.46	0.02	0.03	10.24		–	0.11	16.71	11.87	–	0.01	0.42	0.33	0.03	0.17	97.72
1	15	ARN-2-2'	943	46.60	0.81	6.98	0.05	0.10	11.99		–	0.10	13.95	12.06	–	0.02	0.50	0.70	0.05	0.08	93.98
2	15	ARN-2-2'	944	49.91	0.33	5.02	0.05	0.05	10.24		–	0.14	16.16	11.92	–	–	0.37	0.39	0.04	0.15	94.76
1	22	ARN-2-2'	949	46.40	0.98	7.87	0.09	0.03	12.19		–	0.12	13.70	11.92	–	0.02	0.74	0.81	0.09	0.15	95.11
1	22	ARN-2-2'	950	49.54	0.72	6.02	0.06	0.07	11.04		–	0.11	15.21	12.18	–	0.01	0.43	0.51	0.05	0.23	96.18
1	22	ARN-2-2'	951	49.36	0.48	4.94	0.06	0.06	11.35		–	0.16	15.02	12.02	–	0.00	0.40	0.39	0.04	0.13	94.40
1	7	ARN-2-2	990	50.43	0.57	5.53	0.07	0.10	11.68		–	0.16	15.26	11.82	–	–	0.56	0.49	0.06	0.06	96.78
1	7	ARN-2-2	991	50.56	0.52	5.09	0.01	0.06	11.52		–	0.13	15.46	11.99	–	0.00	0.48	0.43	0.04	–	96.28
1	26	ARN-2-2	1014	51.61	0.60	4.71	0.03	0.01	11.54		–	0.13	15.53	12.24	–	0.01	0.30	0.40	0.06	0.08	97.25
1	26	ARN-2-2	1015	47.35	1.21	7.86	0.09	0.06	13.83		–	0.12	13.40	11.93	–	–	0.67	0.85	0.12	0.06	97.55
1	26	ARN-2-2	1016	46.71	1.22	8.31	0.11	0.04	14.04		–	0.13	13.07	11.90	–	–	0.74	0.93	0.15	0.03	97.38
4		ARN-4-7	1361	47.99	0.57	7.37	0.06	0.00	13.05	0.05	0.02	0.15	14.42	11.68	–	0.00	0.75	0.85	0.29	–	97.25
4		ARN-4-7	1362	55.00	0.19	2.40	–	0.01	10.11	0.03	–	0.17	18.12	11.59	0.00	–	0.19	0.16	0.07	0.03	98.06
4		ARN-4-7	1363	47.97	0.62	7.97	0.05	0.00	13.01	0.04	0.01	0.12	14.34	11.71	–	0.02	0.74	0.78	0.28	0.26	97.92
3		ARN-4-7	1364	47.31	0.67	7.82	0.06	0.03	14.06	0.05	–	0.16	13.55	11.98	0.00	–	0.68	0.86	0.29	0.17	97.69
3		ARN-4-7	1365	50.93	0.43	5.14	0.11	0.03	12.55	0.05	0.00	0.14	15.11	12.32	–	–	0.31	0.44	0.14	–	97.70
1		ARN-4-9	1342	49.09	0.70	6.57	0.10	0.02	12.98	0.05	–	0.15	14.50	11.88	0.01	0.01	0.51	0.61	0.15	–	97.33
1		ARN-4-9	1343	46.76	0.95	7.71	0.09	0.03	14.20	0.02	–	0.16	13.19	11.87	0.03	0.01	0.75	0.86	0.23	0.03	96.88
1		ARN-4-9	1344	52.09	0.39	4.37	0.03	0.04	11.69	0.03	–	0.15	16.06	12.14	–	–	0.36	0.33	0.07	0.11	97.85
1		ARN-4-11	1624	47.53	0.68	6.71	0.06	0.03	13.31	0.03	–	0.15	14.54	11.84	0.02	–	0.66	0.68	0.18	–	96.38
1		ARN-4-11	1625	52.89	0.17	1.91	0.03	0.01	10.30	0.05	–	0.17	17.62	11.86	0.00	–	0.15	0.12	0.04	0.05	95.33
2		ARN-5-1	1522	48.50	0.66	5.55	0.07	0.05	11.41	0.04	–	0.11	15.54	12.03	0.00	0.00	0.55	0.56	0.15	–	95.19
1		ARN-5-1	1523	47.18	0.83	6.72	0.08	0.04	12.29	0.07	–	0.13	14.68	12.12	0.05	0.02	0.59	0.65	0.20	0.23	95.73
1		ARN-5-1	1524	44.62	1.16	8.16	0.09	0.05	13.47	0.05	0.02	0.10	13.81	11.88	0.03	0.01	0.75	0.91	0.26	0.16	95.40
1		ARN-5-4	1478	53.51	0.27	2.40	0.04	0.05	9.44	0.04	–	0.14	17.93	12.08	0.04	–	0.18	0.17	0.05	0.17	96.42
2		ARN-5-4	1479	48.54	0.90	6.31	0.09	0.04	11.81	0.06	0.02	0.15	15.31	11.97	0.01	0.01	0.59	0.64	0.15	0.09	96.61
1		ARN-5-6	1588	48.65	0.58	6.08	–	0.00	12.76	0.05	–	0.14	14.82	12.14	0.01	0.01	0.54	0.60	0.23	0.13	96.65
1		ARN-5-6	1589	46.46	0.73	7.84	0.09	0.02	13.76	0.07	–	0.13	13.57	12.12	–	0.02	0.65	0.83	0.31	0.09	96.57
1		ARN-5-6	1590	49.86	0.49	5.18	0.05	0.00	12.06	0.07	0.00	0.13	15.68	12.21	0.01	–	0.42	0.47	0.18	0.13	96.84
2		ARN-5-8	1493	51.75	0.29	3.91	0.07	0.01	9.74	0.09	–	0.12	17.88	11.79	–	–	0.35	0.29	0.09	0.36	96.57
2		ARN-5-8	1494	49.09	0.51	6.26	0.06	0.04	11.71	0.04	–	0.13	15.35	12.19	–	0.01	0.45	0.53	0.18	0.03	96.53
1		ARN-5-8	1495	49.73	0.46	5.57	0.09	0.03	11.57	0.07	–	0.13	15.70	11.97	0.02	–	0.45	0.47	0.18	0.04	96.41

Tag*: Distance (mm) from the core of oikocryst.

Pyroxenite Layers in the Mooimeisjesfontein area																					
2		JB031-A1	1698	52.30	0.67	3.69	0.06	0.12	8.13	0.09	–	0.12	18.65	12.21	0.00	–	0.35	0.39	0.14	0.21	97.02
2		JB031-A1	1699	47.54	0.92	8.40	0.08	0.07	9.54	0.11	0.00	0.08	15.26	12.62	0.06	0.01	0.55	0.80	0.26	0.32	96.43
2		JB031-A2	1706	51.30	0.34	5.45	0.07	0.10	8.14	0.10	–	0.07	18.10	12.29	–	–	0.45	0.53	0.16	0.42	97.31
2		JB031-A2	1707	52.15	0.34	4.67	0.06	0.12	7.79	0.09	–	0.09	18.69	12.28	0.01	–	0.39	0.41	0.14	0.33	97.38
1		JB031-T	1653	51.18	0.65	4.30	0.09	0.26	9.49	0.12	–	0.09	17.48	12.26	0.00	–	0.31	0.33	0.04	0.02	96.60
1		JB031-T	1654	49.46	0.90	5.40	0.08	0.22	10.35	0.10	0.01	0.12	16.34	12.00	–	0.01	0.57	0.47	0.09	0.18	96.20
1		JB031-T	1655	52.34	0.50	3.34	0.06	0.13	8.89	0.09	–	0.13	18.18	12.19	–	–	0.30	0.23	0.04	0.21	96.53
2		JB031-T	1656	53.52	0.31	3.27	0.01	0.09	7.68	0.08	–	0.10	19.50	12.00	0.01	–	0.29	0.25	0.03	0.30	97.29
2		JB031-T	1657	53.74	0.29	2.58	0.05	0.13	7.58	0.08	–	0.11	19.35	12.19	0.02	0.01	0.25	0.19	0.04	0.07	96.63
2		JB031-T	1658	47.98	0.72	7.34	0.05	0.08	10.01	0.09	0.01	0.12	16.75	12.04	0.03	–	0.77	0.66	0.12	0.14	96.83
2		JB031-P5	1751	50.50	0.63	4.82	0.04	0.14	9.04	0.12	–	0.11	17.94	11.97	0.03	0.00	0.65	0.50	0.15	0.27	96.77
2		JB031-P5	1752	52.88	0.32	2.70	0.05	0.10	7.78	0.08	0.01	0.10	18.91	12.00	0.00	–	0.35	0.22	0.08	0.14	95.63
2		JB031-G3	1933	50.47	0.71	4.69	0.05	0.13	10.12	0.10	–	0.13	16.45	12.45	0.03	0.01	0.26	0.40	0.19	0.18	96.24
2		JB031-G3	1934	48.66	1.21	5.81	0.09	0.17	10.32	0.09	–	0.14	16.40	11.95	–	0.01	0.65	0.66	0.19	0.12	96.39
1		JB031-G3	1935	52.37	0.70	3.56	0.05	0.12	8.29	0.08	–	0.11	18.31	12.05	0.02	–	0.37	0.31	0.12	0.18	96.54
2		JB031-G4	1862	47.88	0.98	7.35	0.11	0.12	11.03	0.11	–	0.09	15.76	12.00	0.01	0.01	0.60	0.79	0.26	0.22	97.17
2		JB031-G4	1863	51.45	0.54	4.35	0.04	0.09	8.92	0.09	–	0.10	17.77	12.29	0.00	0.01	0.31	0.36	0.16	0.11	96.52
2		PM-0-2	1834	46.51	0.70	8.53	0.14	0.03	12.52	0.03	0.04	0.12	14.27	11.60	0.02	–	0.85	0.86	0.11	0.49	96.59
2		PM-0-2	1835	51.93	0.36	3.84	0.05	0.03	9.25	0.06	–	0.14	17.62	12.22	–	0.00	0.37	0.34	0.04	0.69	96.65

Tag	Tag*	Sample	ID	SiO2	TiO2	Al2O3	V2O3	Cr2O3	FeOT	NiO	ZnO	MnO	MgO	CaO	SrO	BaO	Na2O	K2O	Cl	F	Total
2		PM-0-2	1857	50.17	1.02	4.98	0.18	0.06	9.86	0.06	0.01	0.13	17.06	11.86	0.00	–	0.70	0.27	0.08	0.45	96.68
1		PM+70	2006	52.66	0.39	3.30	0.08	0.05	8.80	0.08	–	0.15	18.52	12.14	0.04	–	0.36	0.29	0.09	0.47	97.20
2		PM+70	2007	51.77	0.37	4.15	0.09	0.04	9.30	0.07	–	0.16	17.99	11.89	0.03	0.01	0.49	0.37	0.16	0.74	97.28
2		PM+110	2097	52.53	0.72	3.83	0.17	0.09	9.29	0.08	–	0.13	18.37	12.01	0.03	0.00	0.47	0.33	0.11	0.61	98.49
2		PM+110	2098	53.43	0.61	3.08	0.11	0.07	9.03	0.08	–	0.15	18.64	12.07	0.02	0.01	0.45	0.21	0.10	0.58	98.37
1		PM+260	1990	54.45	0.28	2.03	0.01	0.02	7.73	0.08	–	0.17	19.97	11.76	0.04	0.00	0.14	0.13	0.06	0.39	97.09
1		PM+260	1991	53.10	0.43	2.57	0.07	0.04	8.58	0.07	–	0.10	18.41	12.48	0.03	–	0.17	0.17	0.07	0.58	96.60
1		PM+380	2054	48.52	0.91	6.27	0.06	0.07	12.16	0.05	–	0.16	15.52	11.78	–	–	0.81	0.37	0.17	0.21	96.94
1		PM+380	2055	54.27	0.38	2.01	0.08	0.07	9.05	0.07	–	0.15	19.07	11.88	–	–	0.28	0.05	0.06	0.46	97.68
1		PM+380	2056	50.00	0.70	5.31	0.12	0.06	11.28	0.06	–	0.17	16.39	11.75	0.03	0.01	0.72	0.29	0.18	0.02	97.04
1		PM+380	2057	51.60	0.26	4.20	0.06	0.02	9.55	0.07	–	0.17	17.87	12.06	0.03	0.00	0.44	0.28	0.12	0.52	96.99

Table D.4 – Mineral chemistry for hornblende. This table only includes the analytical uncertainties (%).

ID	Si	Ti	Al	V	Cr	Fe	Ni	Zn	Mn	Mg	Ca	Sr	Ba	Na	K	Cl	F
Anorthosite sequence near the Phosiri Dome																	
1538	0.21	2.35	0.68	39.38	26.92	0.84	20.29	-51.80	12.97	0.48	0.44	248.07	131.59	4.36	2.26	3.81	48.09
1539	0.22	2.36	0.66	29.17	16.47	0.82	18.56	-188.47	14.10	0.49	0.44	1039.23	141.39	3.97	2.39	3.41	212.76
1310	0.22	1.83	0.53	22.58	30.61	0.74	44.25	89.26	11.80	0.53	0.45	-433.96	124.86	3.51	1.95	3.85	-651.03
1311	0.21	3.65	0.64	64.86	76.94	0.77	28.68	-117.85	9.78	0.50	0.45	-387.52	-755.74	4.45	2.63	6.33	64.46
1313	0.22	2.41	0.58	24.04	45.31	0.76	52.71	785.12	12.05	0.51	0.45	1205.90	-283.84	3.87	2.44	7.23	58.30
1450	0.22	1.76	0.60	33.95	184.08	0.73	51.49	-301.11	11.42	0.53	0.44	116.18	93.63	4.15	2.17	10.10	67.94
1451	0.21	3.12	0.89	75.24	168.37	0.81	75.57	-229.19	12.87	0.48	0.44	419.17	390.14	6.81	4.42	25.19	-115.60
1452	0.21	3.13	0.86	41.87	53.62	0.79	34.78	155.84	12.42	0.49	0.44	111.74	-124.86	6.84	3.73	17.88	-1845.70
1319	0.21	2.74	0.68	46.65	1369.53	0.72	80.85	-76.42	10.09	0.52	0.45	112.34	-92.69	4.69	2.97	14.80	193.29
1320	0.20	4.35	0.99	52.61	-205.91	0.77	60.86	181.14	8.50	0.48	0.45	125.83	-54.38	7.38	5.18	19.13	76.34
1321	0.20	5.44	1.22	64.17	183.66	0.74	457.43	-115.46	6.68	0.47	0.48	-83.56	-109.11	11.34	7.86	28.23	132.46
1415	0.21	3.04	0.73	104.55	-717.34	0.78	55.87	-153.53	9.18	0.49	0.45	-531.29	143.28	5.76	2.88	5.49	58.33
1416	0.21	4.07	0.84	287.08	-285.09	0.80	50.17	-50.78	9.41	0.47	0.45	-370.84	221.35	7.28	3.79	6.17	89.71
1418	0.21	2.93	0.73	25.96	249.79	0.78	39.85	-53.45	8.93	0.49	0.45	73.19	-624.08	5.48	2.88	5.34	87.17
923	0.22	1.78	0.64	26.57	52.01	0.81		-181.17	10.74	0.49	0.46	-50.14	-76.10	3.66	2.24	5.36	49.23
924	0.22	1.40	0.60	35.76	77.18	0.77		-73.14	14.20	0.51	0.46	168.65	904.66	3.88	1.93	4.94	69.42
914	0.21	2.67	0.67	44.98	44.17	0.83		-109.74	11.08	0.47	0.46	-29.56	76.93	4.85	2.55	9.49	-79.65
900	0.21	1.51	0.63	42.45	36.77	0.85		150.28	14.54	0.47	0.46	-34.05	41.96	4.02	2.21	8.06	41.38
901	0.21	2.16	0.73	42.01	38.58	0.85		-147.67	14.96	0.46	0.46	-134.11	210.08	4.62	2.88	6.15	71.10
902	0.20	2.57	0.77	113.25	58.42	0.87		-463.16	15.38	0.45	0.46	-87.02	118.06	4.86	3.16	10.91	45.92
943	0.22	1.65	0.61	41.34	18.67	0.81		-30.61	16.74	0.50	0.45	-42.61	66.92	4.52	2.00	7.07	101.99
944	0.21	3.06	0.72	40.37	36.11	0.87		-161.40	12.92	0.46	0.46	-51.01	-73.99	5.32	2.84	8.04	53.02
949	0.22	1.46	0.57	23.39	61.35	0.80		-84.26	14.52	0.50	0.46	-56.81	60.48	3.55	1.85	4.91	56.46
950	0.21	1.78	0.65	34.64	26.02	0.84		-73.48	15.94	0.47	0.45	-30.58	94.84	4.93	2.42	6.93	35.15
951	0.21	2.35	0.73	39.15	29.24	0.83		-167.40	11.21	0.48	0.45	-44.10	369.75	5.06	2.84	7.92	60.93
990	0.21	2.11	0.69	30.06	18.59	0.82		-209.50	11.66	0.48	0.46	-28.92	-94.48	4.18	2.48	6.59	121.87
991	0.21	2.20	0.72	153.32	31.69	0.82		-55.56	13.19	0.47	0.45	-33.77	376.85	4.54	2.73	7.92	-106.04
1014	0.21	2.01	0.75	66.24	185.47	0.82		-75.17	12.99	0.47	0.45	-26.50	100.54	6.24	2.80	6.50	99.53
1015	0.22	1.28	0.57	27.40	29.88	0.75		-65.61	14.32	0.51	0.45	-86.56	-659.21	3.79	1.81	3.72	124.66
1016	0.22	1.28	0.55	21.76	40.79	0.74		-40.36	13.02	0.52	0.46	-54.97	-215.50	3.60	1.70	3.31	249.32
1361	0.22	2.02	0.58	38.59	380.28	0.75	27.55	227.86	11.90	0.52	0.45	-197.35	4305.88	3.69	1.74	2.82	-614.13
1362	0.20	4.59	1.05	-604.81	227.84	0.86	45.91	-89.69	10.84	0.45	0.45	924.21	-223.77	8.92	5.09	7.38	309.01
1363	0.22	1.90	0.55	41.19	2885.79	0.75	33.93	665.98	14.21	0.52	0.45	-311.63	80.28	3.70	1.83	2.89	33.41
1364	0.22	1.81	0.56	35.07	64.16	0.72	28.69	-359.26	11.35	0.54	0.44	546.64	-208.33	3.92	1.73	2.83	48.42
1365	0.21	2.46	0.70	21.33	60.99	0.77	29.47	963.36	12.51	0.50	0.44	5000.00	-74.25	6.46	2.60	4.39	-1827.50

ID	Si	Ti	Al	V	Cr	Fe	Ni	Zn	Mn	Mg	Ca	Sr	Ba	Na	K	Cl	F
1342	0.22	1.76	0.61	23.28	79.75	0.76	31.69	-323.73	11.62	0.52	0.44	296.75	113.05	4.63	2.13	4.23	-199.73
1343	0.22	1.45	0.56	26.31	49.30	0.72	61.86	-158.73	11.33	0.55	0.44	93.65	239.91	3.72	1.74	3.28	305.38
1344	0.21	2.62	0.76	74.11	44.49	0.80	52.77	-62.02	11.69	0.49	0.44	-113.27	-367.32	5.70	3.12	7.18	80.50
1624	0.22	1.82	0.61	38.27	53.49	0.76	50.57	-176.88	11.70	0.52	0.45	118.12	-279.86	4.00	2.00	3.79	-166.48
1625	0.21	5.17	1.21	81.38	129.16	0.87	30.98	-2524.80	10.92	0.46	0.45	811.98	-1933.90	10.54	6.29	10.24	165.39
1522	0.22	1.83	0.67	30.89	33.20	0.82	32.95	-123.73	15.08	0.49	0.44	623.71	282.26	4.38	2.25	4.32	-69.66
1523	0.22	1.58	0.61	27.70	43.15	0.79	22.21	-197.24	13.23	0.51	0.44	53.10	67.89	4.24	2.05	3.54	34.91
1524	0.23	1.28	0.55	25.88	33.62	0.75	26.62	206.83	16.60	0.53	0.45	93.39	142.51	3.70	1.69	2.99	51.52
1478	0.20	3.51	1.05	58.12	33.63	0.90	36.65	-108.24	12.47	0.45	0.44	69.98	-54.27	9.12	4.82	8.84	50.46
1479	0.22	1.50	0.63	27.23	40.49	0.80	22.82	149.08	12.11	0.50	0.44	426.56	204.42	4.22	2.07	4.23	93.79
1588	0.22	2.02	0.64	-278.92	378.95	0.78	26.94	-161.37	12.63	0.51	0.44	192.89	133.53	4.50	2.15	3.25	66.76
1589	0.22	1.73	0.56	27.10	95.39	0.75	20.30	-92.97	13.10	0.54	0.44	-74.41	74.23	4.08	1.78	2.75	94.07
1590	0.21	2.28	0.70	40.83	1663.76	0.80	21.39	711.47	13.10	0.50	0.44	271.71	-91.76	5.23	2.50	3.83	68.79
1493	0.21	3.33	0.81	31.82	187.95	0.89	16.54	-143.55	14.10	0.45	0.45	-866.09	-81.65	5.79	3.39	5.86	23.91
1494	0.22	2.19	0.63	35.36	42.26	0.81	31.33	-55.90	13.25	0.49	0.44	-464.31	210.87	4.96	2.33	3.81	257.41
1495	0.21	2.35	0.67	25.96	61.64	0.81	20.14	-556.02	13.23	0.49	0.45	162.24	-583.09	4.99	2.52	3.81	239.08
Pyroxenite Layers in the Mooimeisjesfontein area																	
1698	0.21	1.84	0.84	39.23	16.49	0.98	15.67	-199.98	14.14	0.45	0.44	571.22	5000.00	5.71	2.80	4.40	43.12
1699	0.22	1.50	0.54	29.75	25.45	0.90	14.05	803.82	18.88	0.50	0.44	46.11	133.10	4.34	1.82	3.02	28.59
1706	0.21	2.93	0.68	31.76	20.24	0.98	14.93	-176.51	21.06	0.45	0.44	-388.83	-107.09	4.88	2.31	4.09	22.21
1707	0.21	2.95	0.74	35.98	16.73	1.00	15.71	-239.66	18.10	0.45	0.44	460.10	5000.00	5.31	2.72	4.52	27.15
1653	0.21	1.87	0.77	26.96	9.44	0.91	13.26	-72.58	18.08	0.46	0.44	766.95	-160.11	6.25	3.13	10.85	390.24
1654	0.22	1.51	0.69	30.45	10.50	0.87	15.18	344.58	13.78	0.48	0.45	-288.73	163.07	4.29	2.50	5.83	44.92
1655	0.21	2.22	0.89	40.09	16.30	0.94	15.85	-435.01	13.10	0.45	0.44	-3980.10	-63.43	6.31	3.95	11.44	41.53
1656	0.21	3.19	0.90	246.89	21.35	1.01	17.40	-153.04	16.09	0.43	0.45	290.88	-311.28	6.40	3.71	14.18	29.99
1657	0.21	3.29	1.02	47.95	15.65	1.02	17.89	-91.45	15.64	0.44	0.45	161.86	194.06	7.13	4.54	11.79	122.00
1658	0.22	1.75	0.58	47.50	23.99	0.88	16.29	292.34	14.13	0.48	0.45	82.99	-176.80	3.55	2.02	4.93	61.99
1751	0.21	1.92	0.73	61.19	14.88	0.93	12.63	-54.82	15.46	0.46	0.45	96.04	294.28	3.90	2.40	4.35	32.30
1752	0.21	3.09	0.99	46.60	20.45	1.00	18.34	320.60	15.90	0.44	0.45	5000.00	-130.89	5.72	4.08	6.76	63.48
1933	0.21	1.77	0.74	43.07	15.99	0.88	14.56	-253.64	13.08	0.48	0.44	91.36	145.35	7.07	2.75	3.74	49.61
1934	0.22	1.26	0.66	26.05	12.70	0.87	17.26	-62.50	12.48	0.48	0.45	-91.43	147.45	3.95	2.02	3.70	74.29
1935	0.21	1.77	0.85	43.85	16.57	0.97	17.85	-115.14	15.25	0.45	0.45	107.88	-73.29	5.50	3.24	5.07	48.95
1862	0.22	1.44	0.58	22.20	16.96	0.84	14.26	-169.86	17.43	0.50	0.45	483.43	203.15	4.17	1.83	3.06	39.25
1863	0.21	2.12	0.77	49.75	22.44	0.94	16.45	-921.48	16.07	0.46	0.44	2987.04	169.26	6.25	2.92	4.12	81.22
1834	0.22	1.78	0.54	18.69	54.46	0.79	48.08	104.03	13.78	0.53	0.46	110.80	-93.93	3.44	1.74	5.44	20.13
1835	0.21	2.82	0.82	45.21	54.30	0.92	23.92	-764.80	12.32	0.46	0.45	-261.12	297.30	5.53	3.08	11.18	14.32
1857	0.21	1.40	0.72	15.25	29.98	0.89	22.97	285.95	13.16	0.47	0.45	818.45	-188.49	3.78	3.56	6.45	21.91
2006	0.21	2.68	0.89	29.98	35.94	0.94	17.79	-574.67	11.96	0.45	0.45	69.60	-49.57	5.68	3.36	6.07	20.49
2007	0.21	2.77	0.79	27.65	47.85	0.92	20.27	-261.25	11.34	0.46	0.45	76.55	95.56	4.65	2.86	4.10	13.04
2097	0.21	1.75	0.82	15.99	20.52	0.92	17.55	-217.73	12.92	0.45	0.45	100.42	755.61	4.77	3.11	5.15	15.65
2098	0.21	1.96	0.92	22.44	26.47	0.93	17.44	-93.81	11.81	0.45	0.45	164.30	168.42	4.86	4.25	5.57	16.76
1990	0.20	3.46	1.16	203.79	86.12	1.01	18.47	-60.22	10.81	0.43	0.45	68.77	387.21	10.68	5.84	8.63	23.39
1991	0.21	2.50	1.02	32.14	47.26	0.95	20.95	-119.03	16.82	0.45	0.44	95.63	-195.70	9.42	4.98	7.01	16.00
2054	0.22	1.50	0.63	35.87	26.14	0.80	28.49	-240.83	11.38	0.50	0.45	-4159.40	-268.47	3.52	2.86	3.93	42.57
2055	0.20	2.74	1.17	28.19	25.19	0.93	19.35	-667.26	11.90	0.44	0.45	-366.09	-2211.90	6.67	13.28	7.98	20.91
2056	0.21	1.78	0.69	20.90	30.79	0.83	22.83	-366.11	10.97	0.49	0.45	79.03	224.39	3.74	3.35	3.85	392.06
2057	0.21	3.63	0.78	36.36	77.36	0.90	21.17	-1545.50	10.87	0.46	0.45	86.97	1425.00	5.00	3.48	4.90	16.59

Table D.5 – Mineral chemistry for micas, including phlogopite and chlorite. This table only includes the data (wt%). Tag list: 1 = Rimming clinopyroxene; 2 = Rimming magnetite; 3 = Pseudomorphing pyroxenes.

Tag	Tag*	Sample	ID	SiO2	TiO2	Al2O3	V2O3	Cr2O3	FeOT	NiO	ZnO	MnO	MgO	CaO	SrO	BaO	Na2O	K2O	Cl	F	Total
Anorthosite sequence near the Phosiri Dome																					
1		AR-9	1540	37.29	2.75	13.95	0.13	0.13	14.25	0.20	–	0.06	16.07	0.17	–	0.15	0.05	8.50	0.48	0.40	94.30
1		ARS-2-1	1308	31.97	1.50	16.15	0.06	0.01	17.89	0.10	–	0.15	15.75	1.80	–	–	0.03	0.25	0.06	0.05	85.78
1		ARS-2-1	1309	33.50	2.48	15.29	0.06	0.01	17.72	0.33	0.00	0.10	14.35	1.86	–	0.02	0.05	0.53	0.08	–	86.37
1		ARS-2-4	1453	28.19	1.57	15.89	0.08	–	20.91	0.07	–	0.31	15.61	1.01	–	–	0.02	0.15	0.06	–	83.84
2		ARS-2-6	1331	34.89	4.36	13.64	0.05	–	18.96	0.08	–	0.10	10.85	0.50	0.02	0.20	0.08	5.19	0.35	–	89.27
2		ARS-2-6	1332	36.88	3.27	12.71	0.03	–	19.53	0.05	–	0.10	11.70	0.44	0.01	0.26	0.07	6.02	0.39	0.29	91.76
1		ARN-3-8	1417	36.36	0.08	14.87	0.04	0.01	18.00	0.05	0.02	0.49	10.28	6.04	0.02	–	0.05	0.07	0.03	–	86.41
1		ARN-2-2'	948	31.34	4.46	14.12	0.05	0.05	16.25		–	0.10	15.28	2.23	–	0.05	0.03	1.05	0.04	0.18	85.22
1		ARN-2-2'	952	33.19	3.42	14.05	0.04	0.04	16.62		0.05	0.07	14.70	0.48	–	0.07	0.08	2.90	0.13	0.20	86.05
1		ARN-2-2'	963	34.42	3.55	13.97	0.11	0.09	15.91		0.15	0.09	14.48	0.63	–	0.08	0.06	2.81	0.13	0.20	86.67
1		ARN-2-2'	964	30.75	2.36	14.91	0.05	0.04	18.21		–	0.13	16.20	1.17	–	0.02	0.06	0.47	0.12	0.08	84.57
1	32	ARN-2-2'	972	32.66	3.66	14.00	0.10	0.04	16.89		0.10	0.08	14.81	0.45	–	0.08	0.05	2.61	0.18	0.17	85.88
1	32	ARN-2-2	1025	34.18	2.66	14.50	0.10	0.01	18.47		0.03	0.13	14.55	0.41	–	0.11	0.02	4.36	0.24	0.03	89.78
1	32	ARN-2-2	1026	34.93	2.80	14.33	0.11	0.01	18.87		–	0.08	13.53	–	–	0.15	0.04	6.49	0.33	0.02	91.68
1	37	ARN-2-2	1029	34.51	2.21	13.16	0.10	0.03	17.03		0.08	0.08	14.55	0.31	–	0.13	0.04	3.89	0.45	0.05	86.62
1	37	ARN-2-2	1030	36.54	2.23	13.40	0.05	0.01	16.83		–	0.08	13.96	–	0.02	0.21	0.07	6.30	0.49	0.23	90.43
1	37	ARN-2-2	1031	33.50	2.14	12.68	0.08	–	16.88		0.05	0.10	13.30	–	–	0.19	0.07	5.64	0.42	0.22	85.26
1	37	ARN-2-2	1032	36.44	2.17	14.15	0.06	–	17.62		–	0.09	14.08	–	–	0.18	0.05	7.75	0.56	0.32	93.45
1	37	ARN-2-2	1033	33.96	2.10	14.25	0.10	–	19.61		–	0.16	15.00	0.06	0.01	0.08	0.04	3.91	0.38	0.06	89.70
1		ARN-2-2	1034	30.64	2.51	14.59	0.09	0.02	20.09		–	0.14	15.30	1.46	0.02	0.01	0.02	0.56	0.23	–	85.69
1		ARN-4-11	1615	37.03	2.78	15.32	0.04	0.00	12.42	0.12	0.02	0.10	15.94	0.59	–	0.03	0.09	3.54	0.30	–	88.23
1		ARN-4-11	1614	29.51	0.04	18.18	0.21	0.12	17.63	0.12	–	0.23	17.44	0.62	0.02	–	0.00	0.02	–	–	84.13
1		ARN-4-11	1616	34.78	2.71	14.56	0.04	0.02	14.67	0.12	0.03	0.09	14.49	1.59	0.00	0.01	0.10	1.40	0.23	–	84.78
1		ARN-4-11	1617	37.78	1.81	17.32	0.06	0.04	14.08	0.04	–	0.12	11.62	1.76	0.01	–	0.18	0.34	0.04	–	85.20
1		ARN-5-8	1506	38.86	1.45	18.04	0.05	0.01	15.53	0.09	0.02	0.08	9.24	1.11	–	–	0.34	0.25	0.14	0.03	85.19
Tag*: Distance (mm) from the core of an oikocryst.																					
Pyroxenite Layers in the Mooimeisjesfontein area																					
1		JB031-P1	1790	35.69	2.33	13.59	0.12	0.21	13.45	0.12	–	0.11	18.84	0.24	–	0.10	0.07	6.71	0.32	0.00	91.83
1		JB031-P5	1753	35.67	2.60	14.43	0.10	0.16	13.47	0.19	–	0.11	17.77	0.12	0.00	0.20	0.05	6.96	0.40	0.00	92.16
2		JB031-P5	1754	35.12	3.54	13.27	0.07	0.18	11.93	0.24	–	0.05	17.64	0.51	–	0.08	0.07	4.50	0.36	0.21	87.60
1		JB031-G1	1669	38.16	2.62	13.75	0.12	0.06	12.44	0.18	–	0.05	17.58	0.05	–	0.25	0.01	9.24	0.53	0.45	95.20
1		JB031-G2	1916	32.91	2.61	14.71	0.15	0.36	14.21	0.20	–	0.21	18.51	1.25	–	0.04	0.01	3.14	0.39	–	88.63
1		JB031-G2	1918	32.99	1.99	13.38	0.12	0.41	16.95	0.20	–	0.11	17.77	0.17	–	0.02	0.00	2.74	0.29	0.11	87.13
1		JB031-G2	1917	31.64	2.06	15.53	0.10	0.37	13.58	0.18	–	0.42	20.03	0.90	0.01	0.03	0.04	1.45	0.40	0.21	86.78
1		JB031-G3	1937	35.69	2.42	13.93	0.09	0.27	14.85	0.18	–	0.07	17.12	0.10	0.01	0.12	0.03	7.18	0.57	0.03	92.52
1		JB031-G3	1938	36.36	2.89	13.95	0.10	0.24	14.29	0.18	–	0.07	16.27	0.16	–	0.15	0.06	8.14	0.62	0.19	93.44
1		JB031-G3	1939	36.61	2.94	13.97	0.12	0.25	14.05	0.19	0.02	0.04	15.87	0.10	–	0.16	0.06	8.84	0.64	–	93.72
1		JB031-G3	1940	35.86	2.38	13.76	0.10	0.19	14.00	0.20	–	0.07	16.97	0.20	0.01	0.11	0.04	7.01	0.49	0.27	91.44
1		JB031-G3	1941	35.79	1.84	14.15	0.08	0.07	14.19	0.18	–	0.09	17.55	0.13	–	0.08	0.05	6.80	0.52	0.00	91.40
1		JB031-G3	1936	30.36	1.52	14.81	0.08	0.07	18.07	0.17	–	0.22	19.39	0.79	–	–	0.00	0.41	0.23	0.03	86.09
1		JB031-G4	1869	35.54	3.39	14.04	0.13	0.12	15.34	0.19	–	0.08	14.82	0.20	0.02	0.16	0.04	7.86	0.70	–	92.46
1		JB031-G4	1870	34.27	3.12	14.17	0.15	0.10	17.25	0.19	–	0.13	15.51	0.37	–	0.12	0.03	6.47	0.55	0.01	92.32
1		PM-90	1084	31.55	0.01	14.76	0.01	0.02	23.71		0.03	0.34	16.42	0.39	–	0.00	0.00	0.03	0.01	–	87.29
1		PM-90	1085	30.93	–	14.95	0.04	0.02	24.03		–	0.37	15.96	0.40	0.01	–	0.03	0.04	0.01	–	86.80
1		PM-90	1068	30.04	0.00	15.82	0.02	0.00	24.01		–	0.37	15.61	0.33	0.07	–	0.01	0.01	0.01	–	86.30
1		PM-90	1069	34.31	0.03	13.15	–	0.02	22.61		–	0.30	16.70	2.56	–	0.00	0.05	0.01	0.02	–	89.77

Table D.6 – Mineral chemistry for micas, including phlogopite and chlorite. This table only includes the analytical uncertainties (%).

ID	Si	Ti	Al	V	Cr	Fe	Ni	Zn	Mn	Mg	Ca	Sr	Ba	Na	K	Cl	F
Anorthosite sequence near the Phosiri Dome																	
1540	0.25	0.77	0.42	18.57	15.57	0.73	8.48	-345.60	27.38	0.48	5.59	-281.17	9.77	28.10	0.52	2.12	22.06
1308	0.28	1.07	0.40	34.93	140.58	0.64	15.30	-1011.50	11.71	0.50	1.19	-418.02	-67.95	44.30	3.78	8.14	150.09
1309	0.28	0.80	0.41	34.11	262.73	0.64	5.85	5000.00	16.32	0.53	1.17	-147.31	70.00	30.42	2.33	6.91	-111.47
1453	0.30	1.04	0.41	28.53	-295.69	0.59	21.01	-650.89	6.87	0.51	1.66	-88.70	-125.54	77.77	5.58	8.73	-1915.70
1331	0.27	0.59	0.42	39.96	-553.80	0.62	18.42	-200.29	16.59	0.61	2.59	161.92	7.72	18.37	0.67	2.52	-81.02
1332	0.26	0.69	0.44	67.71	-120.27	0.61	30.10	-65.51	16.84	0.59	2.82	359.00	6.06	21.78	0.62	2.36	27.69
1417	0.26	9.50	0.41	46.93	164.06	0.64	29.65	228.89	5.09	0.62	0.63	157.00	-37.42	27.99	10.29	14.05	-53.04
948	0.28	0.60	0.43	47.52	36.73	0.69		-113.84	15.81	0.48	1.11	-112.42	25.35	36.92	1.60	7.79	43.74
952	0.27	0.70	0.43	50.99	40.10	0.68		73.55	20.98	0.49	3.38	-116.02	20.69	18.54	0.92	3.60	38.38
963	0.27	0.68	0.43	23.72	20.79	0.69		28.81	17.20	0.50	2.73	-685.25	17.98	23.56	0.94	3.53	39.55
964	0.29	0.85	0.42	42.21	45.51	0.65		-112.24	13.13	0.47	1.59	5000.00	57.66	21.19	2.55	3.77	94.61
972	0.27	0.67	0.43	21.56	46.87	0.67		40.29	20.41	0.49	3.49	-99.98	18.09	24.38	0.98	2.85	43.79
1025	0.27	0.80	0.43	23.97	132.31	0.64		115.86	14.17	0.50	4.12	-124.86	13.64	76.33	0.75	2.45	225.32
1026	0.26	0.78	0.43	19.84	135.08	0.64		-41.01	19.93	0.52	-6.82	-48.82	10.15	32.67	0.61	2.00	382.11
1029	0.27	0.89	0.45	22.33	47.75	0.67		49.41	19.78	0.50	5.17	-412.10	11.39	31.95	0.79	1.69	160.57
1030	0.26	0.88	0.44	39.74	142.78	0.67		-213.32	21.67	0.50	-28.35	177.82	7.61	20.20	0.62	1.61	34.36
1031	0.27	0.91	0.45	28.91	-76.73	0.67		79.63	15.92	0.52	-34.97	-58.73	8.29	19.39	0.65	1.75	33.63
1032	0.26	0.90	0.43	33.97	-116.46	0.66		-74.22	18.63	0.50	-4.08	-58.19	8.87	28.71	0.56	1.50	25.04
1033	0.27	0.91	0.43	23.20	-262.43	0.62		-40.60	10.54	0.49	23.37	299.96	18.98	35.79	0.79	1.85	111.16
1034	0.29	0.82	0.43	22.75	89.23	0.61		-131.78	12.23	0.49	1.39	141.89	128.83	79.99	2.29	2.52	-166.70
1615	0.26	0.77	0.40	58.28	328.11	0.78	13.27	178.25	16.47	0.49	2.35	-196.70	47.61	16.42	0.82	2.81	-112.96
1614	0.30	20.57	0.38	12.89	16.39	0.65	12.76	-156.09	8.59	0.48	2.26	158.88	-51.09	5000.00	36.87	-375.73	-29.16
1616	0.27	0.77	0.42	54.41	103.82	0.72	13.32	130.64	17.17	0.52	1.30	2381.07	178.76	15.04	1.34	3.29	-487.72
1617	0.26	0.97	0.37	34.08	38.04	0.74	38.78	-736.56	13.80	0.58	1.22	207.36	-451.88	9.45	3.08	11.43	-77.06
1506	0.25	1.10	0.36	42.30	203.49	0.69	16.25	218.95	18.94	0.65	1.58	-104.68	-443.09	6.04	3.87	4.57	260.57
Pyroxenite Layers in the Mooimeisjesfontein area																	
1790	0.26	0.85	0.43	21.23	10.88	0.76	12.67	-64.39	14.87	0.45	4.34	-165.06	14.78	19.88	0.59	2.69	1801.33
1753	0.26	0.80	0.42	23.63	13.13	0.75	8.75	-137.16	14.64	0.47	7.46	1036.87	7.89	26.39	0.58	2.36	1826.23
1754	0.27	0.67	0.44	33.12	11.96	0.80	7.38	-117.48	28.48	0.47	2.57	-293.20	16.79	20.87	0.72	2.52	39.97
1669	0.25	0.80	0.43	20.37	29.69	0.79	9.27	-230.83	28.27	0.46	15.26	-109.33	6.43	101.53	0.50	2.01	21.67
1916	0.28	0.79	0.42	16.71	7.30	0.73	8.45	-181.00	8.99	0.46	1.49	-209.79	31.65	118.00	0.87	2.38	-81.52
1918	0.28	0.92	0.44	20.39	6.66	0.67	8.63	-60.84	15.28	0.47	5.64	-55.27	65.68	269.50	0.93	2.85	68.78
1917	0.28	0.90	0.41	23.16	7.06	0.75	9.21	-60.82	5.58	0.44	1.80	289.19	50.57	34.36	1.31	2.35	35.44
1937	0.26	0.83	0.43	27.10	9.02	0.72	9.18	-80.83	21.47	0.48	8.81	370.18	12.14	45.70	0.57	1.93	252.62
1938	0.26	0.75	0.42	23.35	9.78	0.73	9.17	-56.77	22.98	0.49	6.09	-104.89	10.24	24.04	0.53	1.83	44.43
1939	0.26	0.75	0.42	21.15	9.40	0.74	8.91	211.32	36.75	0.50	8.79	-470.49	9.21	23.05	0.51	1.80	-369.48
1940	0.26	0.84	0.43	23.49	11.67	0.74	8.61	-314.09	22.18	0.48	5.05	224.51	13.33	36.91	0.58	2.11	30.86
1941	0.26	0.97	0.42	27.61	25.54	0.73	9.36	-109.39	17.94	0.47	6.83	-616.68	18.20	27.06	0.59	2.03	5000.00
1936	0.29	1.07	0.42	27.74	26.64	0.65	9.88	-93.01	8.81	0.45	1.94	-481.93	-115.08	273.57	2.76	3.28	217.83
1869	0.26	0.69	0.42	19.69	16.87	0.71	8.93	-263.49	21.08	0.52	5.06	149.60	9.51	33.54	0.54	1.73	-134.44
1870	0.27	0.72	0.42	17.57	18.66	0.66	8.77	-215.03	13.31	0.51	3.25	-147.60	12.22	51.62	0.60	1.98	625.20
1084	0.28	50.14	0.43	148.69	84.87	0.56		131.39	6.44	0.48	3.05	-148.91	278.47	748.24	23.30	31.22	-38.08
1085	0.29	-511.59	0.43	47.13	70.63	0.56		-736.30	6.09	0.48	3.03	205.54	-82.52	41.10	14.96	21.02	-52.24
1068	0.29	159.54	0.42	121.37	344.26	0.56		-140.57	5.92	0.49	3.36	42.56	-146.22	107.70	46.01	30.31	-56.02
1069	0.27	20.83	0.46	-332.30	65.18	0.58		-413.11	7.13	0.47	1.00	-130.19	372.55	28.32	44.68	19.32	-26.57

Table D.7 – Mineral chemistry for olivine, including analytical uncertainties. Tag list: 1 = Core; 2 = Mantle; 3 = Rim. Note: TiO_2, Al_2O_3 and Na_2O were also analyzed, but were not detected.

			Data (wt%)												Analytical uncertainty (%)										
Tag	**Sample**	**ID**	**SiO2**	**V2O3**	**Cr2O3**	**FeO**	**NiO**	**ZnO**	**MnO**	**MgO**	**CaO**	**SrO**	**BaO**	**K2O**	**Total**	**Si**	**V**	**Cr**	**Fe**	**Ni**	**Zn**	**Mn**	**Mg**	**Ca**	**Sr**	**Ba**	**K**
Blocks in the anorthosite sequence																										
1	ARS-X2	2280	37.78	–	0.00	27.05	0.25	–	0.40	34.94	0.02	0.00	–	–	100.45	0.26	-110.23	316.82	0.52	7.26	-94.88	5.65	0.34	42.76	4661.54	-91.33	-565.76
2	ARS-X2	2281	37.90	0.01	–	27.02	0.25	–	0.38	35.14	0.02	–	0.01	0.00	100.74	0.26	134.77	-2006.80	0.52	7.19	-175.74	5.85	0.34	39.86	-146.77	117.53	205.17
2	ARS-X2	2282	37.80	–	–	26.86	0.23	0.05	0.40	35.03	0.01	0.03	–	0.00	100.41	0.26	-1873.30	-66.90	0.52	7.74	90.35	5.71	0.34	76.56	80.73	-253.90	151.93
2	ARS-X2	2283	37.93	0.01	–	26.73	0.25	–	0.43	35.12	0.01	0.01	–	–	100.50	0.26	243.55	-184.01	0.52	7.25	-253.46	5.50	0.34	102.17	195.47	-111.77	-644.52
2	ARS-X2	2284	37.70	0.00	0.01	26.77	0.27	–	0.39	35.17	0.01	–	–	–	100.33	0.27	1313.07	162.68	0.53	6.85	-78.55	5.93	0.35	57.99	-755.09	-86.27	-1162.10
1	ARS-X2	2286	37.80	–	–	26.37	0.29	–	0.40	35.56	0.10	–	–	0.01	100.53	0.27	-2470.70	-323.17	0.54	6.57	-160.42	5.88	0.35	9.02	-1863.60	-80.11	92.71
2	ARS-X2	2287	37.91	0.01	–	26.43	0.26	–	0.38	35.32	0.02	0.01	–	0.00	100.34	0.27	140.84	-285.92	0.53	7.12	-102.56	5.96	0.34	43.34	524.40	-59.86	375.59
3	ARS-X2	2288	37.86	–	0.01	26.98	0.22	0.02	0.40	35.11	0.02	0.01	–	–	100.65	0.27	-126.79	120.56	0.52	8.02	242.16	5.76	0.35	31.19	204.37	-103.32	-122.77
1	ARS-X2	2289	38.10	0.01	0.01	27.08	0.24	0.04	0.38	35.22	0.03	0.04	–	–	101.15	0.26	372.70	114.32	0.52	7.55	115.85	5.94	0.34	27.32	62.90	-104.43	-253.57
3	ARS-X2	2290	37.99	0.00	–	26.37	0.22	–	0.39	35.75	0.02	–	–	–	100.74	0.26	485.86	-630.25	0.53	8.01	-102.58	5.90	0.34	30.63	-208.51	-111.03	-104.44
2	ARS-X5	2248	38.51	–	–	23.31	0.25	–	0.35	37.58	0.01	–	–	0.00	100.01	0.27	-274.89	-429.70	0.57	7.35	-64.53	6.31	0.33	65.56	5000.00	-114.39	124.81
2	ARS-X5	2249	38.10	–	0.01	23.11	0.26	–	0.39	37.43	0.02	–	0.01	0.01	99.34	0.27	-533.49	269.12	0.57	7.07	-146.28	5.86	0.33	41.26	-758.76	124.40	75.92
3	ARS-X5	2250	38.43	0.00	–	23.54	0.24	–	0.39	36.99	0.01	–	0.01	–	99.61	0.26	513.54	-89.10	0.56	7.42	-241.02	5.85	0.33	51.46	-303.43	248.31	-590.03
1	ARS-X5	2251	38.32	–	–	22.94	0.24	–	0.38	37.59	0.02	–	–	–	99.48	0.27	-341.64	-106.31	0.57	7.60	-75.75	5.97	0.33	38.57	-425.57	-196.72	-669.08
2	ARS-X5	2252	38.27	0.00	0.00	23.21	0.28	–	0.33	37.20	0.01	–	–	0.00	99.30	0.26	791.92	503.47	0.56	6.70	-67.20	6.57	0.33	68.45	-759.91	-167.59	255.54
2	ARS-X5	2253	38.58	–	–	22.79	0.28	–	0.39	37.91	0.00	0.01	0.01	–	99.96	0.26	-392.74	-147.17	0.57	6.68	-1268.60	5.84	0.33	230.40	316.68	117.76	-199.67
2	ARS-X5	2254	38.62	–	–	22.71	0.26	–	0.40	38.18	0.02	–	0.00	–	100.20	0.26	-2359.00	-150.80	0.57	7.02	-256.92	5.70	0.32	35.45	-210.36	1480.26	-292.14

Table D.8 – Mineral chemistry data for plagioclase. Tag list: 1 = Core; 2 = Mantle; 3 = Rim; 4 = Inclusion in pyroxene; 5 = Inclusion in hornblende; 6 = Albite/Orthoclase; 7 = Overgrowth; 8 = Myrmekite.

				Data (wt%)											Analytical uncertainty (%)										
Tag	**Tag***	**Sample**	**ID**	**SiO2**	**TiO2**	**Al2O3**	**FeO**	**MnO**	**MgO**	**CaO**	**SrO**	**BaO**	**Na2O**	**K2O**	**Total**	**Si**	**Ti**	**Al**	**Fe**	**Mn**	**Mg**	**Ca**	**Sr**	**Ba**	**Na**	**K**
Anorthosite sequence near the Phosiri Dome																										
1		AR-9	1541	49.61	–	31.96	0.29	0.01	0.07	14.79	0.08	–	3.13	0.19	100.12	0.22	-75.71	0.25	6.70	150.31	12.20	0.40	36.29	-700.47	1.54	4.55
1		AR-9	1542	49.27	0.01	32.44	0.35	0.00	0.02	15.12	0.05	0.02	2.75	0.19	100.23	0.22	49.11	0.25	5.83	328.99	40.19	0.40	51.36	67.67	1.65	4.47
3		AR-9	1543	49.85	0.01	31.81	0.32	0.01	0.01	14.55	0.06	0.02	3.07	0.22	99.93	0.22	136.12	0.25	6.21	136.25	49.60	0.41	48.05	68.73	1.56	3.99
2		AR-9	1544	49.28	–	31.99	0.28	0.00	0.01	14.69	0.07	–	3.10	0.19	99.61	0.22	-615.07	0.25	6.88	556.67	60.41	0.40	40.07	-1077.70	1.55	4.41
3		AR-9	1545	47.89	–	33.11	0.31	0.01	0.01	16.17	0.06	–	2.38	0.11	100.04	0.22	-139.51	0.24	6.47	239.03	74.96	0.38	49.52	-98.35	1.79	6.70
1		AR-9	1546	49.72	–	31.77	0.38	–	0.01	14.56	–	0.01	3.15	0.22	99.82	0.22	-244.37	0.25	5.54	-311.50	51.36	0.41	-606.71	94.78	1.54	4.05
4		AR-9	1547	48.98	0.01	32.10	0.36	0.00	0.01	14.97	0.05	0.01	2.94	0.20	99.62	0.22	78.56	0.25	5.76	421.04	102.12	0.40	57.53	219.71	1.60	4.35
4		AR-9	1548	49.47	–	32.05	0.41	0.01	0.01	14.77	0.01	–	3.10	0.19	100.03	0.22	-323.49	0.25	5.24	93.85	54.29	0.40	179.84	-205.20	1.55	4.54
1		AR-13	2157	48.67	–	30.66	0.38	0.01	0.01	14.38	0.07	0.02	3.57	0.57	98.34	0.23	-495.76	0.26	5.64	128.27	70.57	0.42	40.08	58.91	1.54	2.17
2		AR-13	2158	49.10	0.01	31.46	0.36	0.03	0.02	12.41	0.07	0.03	3.29	1.26	98.05	0.22	104.66	0.25	5.66	49.75	39.73	0.44	38.32	38.89	1.58	1.37
1		AR-13	2159	47.83	0.00	31.73	0.34	0.01	0.00	15.08	0.09	0.01	3.02	0.15	98.26	0.23	549.52	0.25	6.00	127.73	282.92	0.40	30.80	107.87	1.66	5.08
2		AR-13	2160	48.98	0.01	31.32	0.38	0.01	0.01	14.60	0.06	0.01	3.37	0.11	98.86	0.22	94.66	0.26	5.47	196.80	56.41	0.41	45.81	156.88	1.56	6.20
1		AR-13	2162	48.80	0.00	31.55	0.40	–	0.02	14.74	0.08	0.01	3.12	0.17	98.90	0.22	1147.54	0.25	5.30	-598.32	37.04	0.40	33.68	130.01	1.63	4.62
2		AR-13	2163	48.54	–	31.77	0.39	–	0.02	15.03	0.06	0.02	3.01	0.13	98.97	0.22	-558.94	0.25	5.38	-779.24	50.16	0.40	44.87	68.04	1.66	5.59
3		AR-13	2164	47.83	0.00	32.23	0.38	0.02	0.01	15.58	0.08	0.03	2.66	0.15	98.96	0.22	947.11	0.25	5.52	79.05	75.05	0.39	34.17	47.40	1.77	5.15
1		AR-13	2165	49.81	0.01	30.77	0.37	0.01	0.03	13.94	0.05	0.00	3.65	0.22	98.87	0.22	52.29	0.26	5.60	191.20	23.95	0.41	51.22	421.39	1.50	3.90
3		AR-13	2166	48.12	–	32.08	0.29	0.01	0.01	15.21	0.06	–	2.82	0.09	98.68	0.22	-25.54	0.25	6.70	164.18	113.35	0.40	42.18	-385.69	1.73	7.40
1		ARS-2-1	1286	49.28	0.05	30.93	0.56	0.02	0.01	14.36	0.04	0.02	2.97	0.27	98.51	0.22	13.86	0.25	4.25	59.86	75.49	0.41	62.82	69.17	1.59	3.46
1		ARS-2-1	1287	49.92	–	31.94	0.30	0.00	0.01	14.75	0.09	–	3.02	0.11	100.14	0.22	-490.18	0.25	6.44	285.15	53.16	0.40	32.78	-338.41	1.57	6.53
3		ARS-2-1	1288	49.12	–	32.56	0.31	–	0.00	15.50	0.07	0.00	2.62	0.09	100.28	0.22	-93.47	0.25	6.35	-3984.70	143.63	0.39	41.91	581.83	1.70	7.59

				Data (wt%)												Analytical uncertainty (%)										
Tag	**Tag***	**Sample**	**ID**	**SiO2**	**TiO2**	**Al2O3**	**FeO**	**MnO**	**MgO**	**CaO**	**SrO**	**BaO**	**Na2O**	**K2O**	**Total**	**Si**	**Ti**	**Al**	**Fe**	**Mn**	**Mg**	**Ca**	**Sr**	**Ba**	**Na**	**K**
3		ARS-2-1	1289	49.56	–	32.47	0.33	–	0.00	15.23	0.05	–	2.62	0.12	100.38	0.22	-79.64	0.25	6.09	-146.43	213.53	0.39	56.94	-157.14	1.70	6.31
1		ARS-2-1	1290	50.35	0.02	31.60	0.32	0.01	0.01	14.68	0.09	0.00	3.02	0.14	100.25	0.22	40.66	0.25	6.11	111.18	130.52	0.40	30.96	326.53	1.58	5.42
3		ARS-2-1	1291	49.80	–	32.01	0.30	0.00	0.01	15.05	0.07	0.02	2.79	0.13	100.17	0.22	-32.31	0.25	6.47	297.36	70.16	0.40	40.94	81.68	1.64	5.93
2		ARS-2-1	1292	51.26	0.01	31.54	0.27	0.01	0.01	14.36	0.07	0.01	3.20	0.17	100.91	0.21	97.43	0.25	6.90	156.18	96.32	0.41	42.16	102.85	1.53	4.75
4		ARS-2-1	1314	49.38	0.01	32.30	0.26	0.01	0.01	15.05	0.04	0.00	2.86	0.09	100.01	0.22	83.79	0.25	7.15	160.16	119.24	0.40	64.71	266.03	1.62	7.90
2		ARS-2-1	1315	50.17	0.02	31.99	0.28	–	0.01	14.90	0.06	0.01	2.97	0.11	100.50	0.22	45.70	0.25	6.72	5000.00	52.18	0.40	49.16	176.56	1.59	6.85
2		ARS-2-1	1316	50.66	0.00	31.54	0.25	–	0.01	14.24	0.06	0.01	3.26	0.14	100.17	0.22	422.38	0.25	7.29	-232.72	115.84	0.41	47.45	96.83	1.51	5.59
1		ARS-2-1	1317	51.39	0.00	31.16	0.24	–	0.01	13.91	0.06	–	3.43	0.15	100.36	0.21	268.97	0.25	7.47	-156.37	72.78	0.41	47.51	-184.78	1.47	5.18
3		ARS-2-1	1318	49.25	–	32.60	0.26	–	0.01	15.40	0.07	0.00	2.61	0.09	100.29	0.22	-348.18	0.25	7.07	-163.29	74.00	0.39	40.75	644.04	1.70	8.05
1		ARS-2-4	1441	48.59	0.01	31.65	0.37	–	0.02	14.71	0.06	0.01	3.13	0.12	98.68	0.22	101.36	0.25	5.62	-106.83	39.30	0.40	43.64	106.54	1.54	6.23
2		ARS-2-4	1442	48.49	0.01	31.84	0.37	0.00	0.01	15.02	0.04	–	2.94	0.13	98.85	0.22	84.26	0.25	5.68	1064.32	79.28	0.40	76.56	5000.00	1.60	5.84
3		ARS-2-4	1443	48.45	–	31.87	0.30	0.00	0.01	14.70	0.03	0.01	3.07	0.13	98.57	0.22	-116.59	0.25	6.56	313.93	109.19	0.40	97.84	215.03	1.56	5.86
5		ARS-2-4	1444	44.08	–	31.71	6.21	0.04	1.18	13.52	0.04	0.01	1.98	0.07	98.85	0.23	-68.08	0.25	1.12	34.22	1.84	0.42	66.91	245.84	2.04	9.95
1		ARS-2-4	1445	49.79	–	30.79	0.28	0.01	0.01	13.66	0.06	0.00	3.56	0.17	98.32	0.22	-282.07	0.25	6.87	144.71	60.29	0.42	46.43	713.21	1.44	4.95
2		ARS-2-4	1446	48.40	0.00	32.27	0.26	–	0.01	15.20	0.05	–	2.96	0.13	99.27	0.22	151.60	0.25	7.17	-296.87	89.60	0.40	53.02	-207.61	1.59	6.00
3		ARS-2-4	1447	48.00	–	32.48	0.31	0.01	0.01	15.25	0.05	0.00	2.80	0.10	99.01	0.22	-60.36	0.25	6.41	101.51	84.26	0.40	57.13	725.83	1.64	7.00
5		ARS-2-4	1448	46.74	–	32.84	0.62	0.00	0.01	16.05	0.04	0.00	2.18	0.05	98.55	0.22	-63.74	0.25	4.04	390.80	82.53	0.39	65.52	268.09	1.88	11.75
5		ARS-2-4	1449	46.28	–	33.58	0.56	–	0.01	16.66	0.05	–	2.23	0.06	99.43	0.23	-69.21	0.24	4.29	-397.67	74.82	0.38	57.11	-124.74	1.86	10.52
2		ARS-2-6	1333	51.91	0.02	31.04	0.33	0.01	0.01	13.85	0.07	0.01	3.49	0.18	100.94	0.21	33.37	0.25	5.96	139.16	56.08	0.41	38.90	96.11	1.46	4.54
1		ARS-2-6	1334	50.62	0.02	31.08	0.41	0.01	0.01	14.02	0.06	0.02	3.30	0.18	99.72	0.22	39.28	0.25	5.16	118.99	122.01	0.41	47.69	79.98	1.50	4.55
2		ARS-2-6	1335	51.93	0.01	30.93	0.33	–	0.01	13.86	0.04	0.02	3.45	0.20	100.78	0.21	66.81	0.25	6.04	-236.70	73.02	0.41	62.80	76.81	1.47	4.26
3		ARS-2-6	1336	49.60	–	32.39	0.32	–	0.00	15.43	0.06	–	2.69	0.12	100.62	0.22	-63.75	0.25	6.10	-3974.90	3633.08	0.39	47.58	-194.29	1.67	6.29
1		ARS-2-6	1337	50.06	0.01	31.97	0.37	0.01	–	14.97	0.06	0.01	2.84	0.13	100.42	0.22	123.42	0.25	5.56	211.07	-252.14	0.40	44.78	145.93	1.63	5.88
1		ARS-2-6	1338	50.90	0.01	31.64	0.34	0.01	–	14.35	0.05	0.01	3.23	0.13	100.68	0.22	49.62	0.25	5.95	118.81	-586.13	0.41	52.92	222.57	1.52	5.72
2		ARS-2-6	1339	51.24	0.00	31.49	0.31	0.01	0.02	14.21	0.06	0.00	3.30	0.20	100.84	0.21	302.36	0.25	6.29	197.43	47.29	0.41	49.24	582.03	1.50	4.26
1		ARS-2-6	1340	50.03	–	32.21	0.28	0.01	0.01	15.18	0.08	0.00	2.90	0.10	100.81	0.22	-64.37	0.25	6.81	91.57	79.76	0.39	34.34	693.64	1.61	7.19
2		ARS-2-6	1341	51.86	–	29.79	0.22	0.01	0.02	12.70	0.04	0.02	4.09	0.15	98.89	0.21	-42.18	0.26	8.04	243.48	41.61	0.43	65.20	65.81	1.34	5.13
1		ARS-2-9	1261	50.64	0.01	31.26	0.33	0.01	0.01	14.58	0.06	0.01	3.05	0.14	100.09	0.22	90.50	0.25	6.09	95.93	119.95	0.40	47.76	99.60	1.57	5.61
2		ARS-2-9	1262	50.31	0.01	31.36	0.32	–	0.01	14.65	0.08	–	3.04	0.16	99.93	0.22	127.32	0.25	6.10	5000.00	77.20	0.40	33.65	5000.00	1.57	5.04
2		ARS-2-9	1263	50.59	0.00	31.28	0.34	0.01	0.01	14.40	0.08	–	3.13	0.15	99.99	0.22	256.95	0.25	5.96	95.52	81.66	0.41	35.99	-92.28	1.55	5.34
7		ARS-2-9	1264	50.30	–	31.36	0.31	0.02	0.00	14.70	0.06	0.01	3.12	0.08	99.97	0.22	-57.29	0.25	6.23	80.56	197.87	0.40	49.26	118.79	1.55	8.14
2		ARS-2-9	1265	50.63	0.01	31.37	0.34	–	0.00	14.51	0.07	0.02	3.16	0.14	100.25	0.22	66.29	0.25	5.91	-691.83	152.72	0.40	40.94	82.56	1.54	5.46
1		ARS-2-9	1266	50.33	–	31.09	0.35	0.02	0.12	11.56	0.06	–	3.08	1.06	97.66	0.22	-587.19	0.25	5.81	86.21	8.06	0.45	43.91	-122.55	1.55	1.55
1		ARS-2-9	1267	49.99	0.02	31.57	0.34	–	0.01	14.79	0.08	–	2.96	0.13	99.89	0.22	36.79	0.25	5.90	-223.43	72.73	0.40	35.15	-157.44	1.59	5.90
7		ARS-2-9	1268	50.64	–	30.74	0.28	0.00	0.00	14.17	0.10	–	3.38	0.14	99.46	0.22	-78.05	0.25	6.72	272.55	167.93	0.41	28.72	-270.49	1.48	5.55
2		ARS-2-9	1269	50.21	–	31.51	0.35	0.00	0.01	14.77	0.03	0.01	2.92	0.14	99.96	0.22	-69.54	0.25	5.78	284.52	115.98	0.40	76.48	94.21	1.60	5.56
7		ARS-2-9	1270	51.14	–	30.71	0.29	–	–	14.00	0.10	–	3.52	0.09	99.83	0.22	-55.36	0.25	6.64	-238.02	-1579.70	0.41	29.78	-58.02	1.45	7.54
7		ARS-2-9	1271	52.08	–	29.54	0.33	0.02	0.01	13.23	0.06	0.01	4.06	0.13	99.46	0.21	-93.11	0.26	5.98	87.11	99.21	0.42	46.38	94.17	1.35	5.98
1		ARS-2-9	1272	49.78	0.02	31.57	0.33	0.01	0.01	14.63	0.06	0.01	3.04	0.15	99.61	0.22	33.20	0.25	6.00	236.41	61.70	0.40	44.51	196.49	1.57	5.22
1		ARS-2-9	1273	50.24	0.01	30.99	0.31	–	0.02	14.36	0.03	0.02	3.29	0.13	99.39	0.22	132.33	0.25	6.36	-353.35	34.87	0.41	98.88	62.44	1.50	5.87
2		ARS-2-9	1274	50.15	0.01	31.32	0.27	0.01	0.01	14.46	0.05	0.01	3.26	0.14	99.68	0.22	102.38	0.25	6.85	128.22	109.45	0.41	59.43	112.34	1.51	5.60
2		ARS-2-9	1275	50.36	0.00	30.98	0.35	0.01	0.01	14.02	0.05	0.01	3.42	0.17	99.37	0.22	212.43	0.25	5.81	101.05	111.28	0.41	59.42	159.59	1.48	4.70
1		ARN-3-1	1253	50.05	0.01	31.42	0.38	0.01	0.01	14.90	0.09	0.00	2.95	0.14	99.96	0.22	67.55	0.25	5.50	161.57	88.31	0.40	31.01	685.52	1.60	5.42
1		ARN-3-1	1254	49.44	0.01	31.62	0.40	–	0.01	15.15	0.04	0.01	2.85	0.14	99.68	0.22	55.41	0.25	5.30	-163.69	59.83	0.40	59.82	149.42	1.63	5.40
2		ARN-3-1	1255	50.34	0.02	31.51	0.38	0.01	0.00	14.79	0.07	0.01	3.03	0.15	100.32	0.22	33.63	0.25	5.44	90.96	1061.40	0.40	40.99	195.30	1.57	5.33
2		ARN-3-1	1256	49.95	0.03	31.36	0.37	0.01	0.00	14.65	0.02	0.00	3.00	0.15	99.54	0.22	25.29	0.25	5.60	119.29	948.79	0.40	107.10	356.59	1.58	5.20
2		ARN-3-1	1257	50.39	0.02	31.56	0.37	–	0.01	14.82	0.09	–	3.04	0.15	100.45	0.22	37.18	0.25	5.57	-266.15	50.71	0.40	30.97	-1031.60	1.57	5.27
1		ARN-3-1	1258	49.88	0.00	31.83	0.32	–	0.01	15.18	0.02	0.01	2.81	0.14	100.20	0.22	218.73	0.25	6.21	-65.08	61.40	0.40	116.91	91.66	1.64	5.64
3		ARN-3-1	1259	49.20	–	32.06	0.32	0.01	0.02	15.30	0.03	–	2.77	0.13	99.84	0.22	-113.01	0.25	6.11	112.04	49.35	0.39	91.45	-2896.80	1.65	5.78
2		ARN-3-1	1260	50.58	0.02	31.39	0.33	0.02	0.00	14.52	0.08	0.01	3.09	0.16	100.20	0.22	35.40	0.25	5.97	72.92	201.01	0.40	34.40	143.66	1.56	4.99
1		ARN-3-2	2184	49.60	0.01	31.52	0.33	0.01	0.02	14.70	0.05	0.00	3.16	0.17	99.57	0.22	84.14	0.25	6.12	158.30	38.02	0.40	56.20	678.08	1.62	4.57
2		ARN-3-2	2185	50.89	0.01	30.95	0.31	0.01	0.01	14.12	0.06	0.01	3.56	0.16	100.09	0.22	95.98	0.26	6.44	143.33	101.91	0.42	47.48	116.31	1.53	4.79
1		ARN-3-3	1424	48.37	0.00	32.41	0.33	0.00	0.01	15.49	0.03	–	2.82	0.10	99.57	0.22	151.33	0.25	6.13	5000.00	53.42	0.39	80.81	-153.85	1.63	6.94

				Data (wt%)											Analytical uncertainty (%)									
Tag	**Tag***	**Sample**	**ID**	**SiO2**	**TiO2**	**Al2O3**	**FeO**	**MnO**	**MgO**	**CaO**	**SrO**	**BaO**	**Na2O**	**K2O**	**Total**	**Si**	**Ti**	**Al**	**Fe**	**Mn**	**Mg**	**Ca**	**Sr**	**Ba**	**Na**	**K**
2		ARN-3-3	1425	47.59	0.01	31.84	0.35	0.02	0.06	15.19	0.06	–	2.61	0.14	97.88	0.22	55.28	0.25	5.89	66.75	13.85	0.40	43.70	-649.13	1.70	5.62
2		ARN-3-3	1426	48.74	0.01	31.42	0.39	0.00	0.01	14.36	0.06	0.00	3.35	0.20	98.55	0.22	48.62	0.25	5.44	932.85	52.03	0.41	49.44	554.30	1.49	4.34
2		ARN-3-3	1427	49.13	0.01	31.68	0.38	–	0.02	14.65	0.06	0.01	3.10	0.16	99.20	0.22	124.43	0.25	5.51	-245.65	39.31	0.40	45.06	160.10	1.55	5.08
6		ARN-3-3	1428	66.81	–	19.47	0.02	–	0.00	0.12	0.04	–	11.42	0.03	97.91	0.18	-55.62	0.32	76.01	-1552.60	1292.12	6.85	66.11	-310.14	0.77	17.97
6		ARN-3-3	1429	67.20	–	19.50	0.02	0.01	0.00	0.26	0.02	0.00	11.47	0.04	98.52	0.18	-59.30	0.32	76.08	124.98	181.75	3.93	144.11	264.27	0.76	15.92
6		ARN-3-3	1430	67.19	–	19.62	0.05	0.00	0.00	0.28	0.04	–	11.44	0.05	98.67	0.18	-46.59	0.32	25.74	5000.00	207.03	3.71	63.31	-100.97	0.77	13.82
1		ARN-3-3	1431	48.06	0.01	32.45	0.41	0.02	0.02	15.50	0.07	0.00	2.66	0.16	99.38	0.22	60.17	0.25	5.32	64.33	36.83	0.39	38.12	1244.55	1.69	5.02
2		ARN-3-3	1432	47.76	0.02	32.39	0.36	–	0.02	15.14	0.02	0.02	2.87	0.16	98.75	0.22	46.53	0.25	5.71	-63.63	48.52	0.40	138.20	69.37	1.62	5.15
2		ARN-3-3	1433	48.41	0.00	32.17	0.36	0.01	0.01	15.11	0.08	0.01	2.90	0.16	99.22	0.22	147.54	0.25	5.80	128.77	84.09	0.40	35.45	96.14	1.61	5.12
1		ARN-3-4	2167	48.67	–	31.98	0.36	–	0.03	14.90	0.03	0.00	2.99	0.16	99.14	0.22	-703.92	0.25	5.73	-142.29	27.05	0.40	74.32	451.55	1.68	4.84
2		ARN-3-4	2168	48.60	–	32.17	0.35	0.01	0.01	15.47	0.08	0.00	2.93	0.14	99.76	0.22	-45.46	0.25	5.85	151.70	82.33	0.40	36.07	458.80	1.70	5.42
2		ARN-3-4	2169	48.63	–	32.06	0.34	0.01	0.01	14.91	0.11	–	3.00	0.14	99.22	0.22	-241.57	0.25	5.97	160.58	57.14	0.41	26.22	-128.98	1.68	5.28
1		ARN-3-4	2170	48.84	–	31.87	0.35	–	0.00	14.88	0.07	0.01	3.07	0.16	99.24	0.22	-127.17	0.26	5.88	-675.93	948.69	0.41	40.39	198.02	1.67	4.97
2		ARN-2’	895	50.23	0.03	31.16	0.37		0.17	13.97	–	0.02	2.95	0.28	99.18	0.22	21.30	0.26	5.77		5.70	0.42	-151.87	73.98	1.46	3.54
2		ARN-2’	896	49.55	0.02	32.19	0.35		0.02	15.08	–	–	2.84	0.16	100.21	0.22	44.13	0.25	5.87		32.56	0.41	-113.61	-239.31	1.49	5.23
1		ARN-2’	910	51.27	0.03	31.79	0.27		0.01	14.48	0.02	–	3.17	0.13	101.16	0.21	25.56	0.25	7.08		99.81	0.41	139.32	-265.87	1.40	6.34
1		ARN-2’	911	50.74	0.04	31.84	0.34		0.02	14.72	0.03	–	2.98	0.18	100.91	0.21	20.00	0.25	5.91		36.31	0.41	98.83	-100.90	1.45	4.91
2		ARN-2’	909	50.52	0.01	31.74	0.28		0.02	14.74	–	0.01	3.07	0.13	100.52	0.21	55.82	0.25	7.19		48.08	0.41	-190.04	196.96	1.43	6.09
4		ARN-2’	929	48.86	0.02	32.11	0.34		0.02	15.23	–	0.01	2.83	0.14	99.54	0.22	30.06	0.25	5.97		41.64	0.40	-230.79	156.34	1.50	5.93
4		ARN-2’	930	49.17	0.01	31.92	0.33		0.01	14.73	0.00	0.01	2.99	0.16	99.32	0.22	62.36	0.25	6.24		107.37	0.41	686.31	110.01	1.46	5.19
2		ARN-2’	931	48.92	0.03	31.89	0.32		0.00	14.83	0.02	0.02	2.97	0.14	99.13	0.22	27.09	0.25	6.42		178.19	0.41	198.48	82.36	1.46	5.77
1		ARN-2’	939	48.94	0.02	32.15	0.34		0.02	15.20	0.04	–	2.70	0.14	99.54	0.22	40.40	0.25	5.91		44.84	0.40	77.36	-181.79	1.54	5.63
2		ARN-2’	940	48.84	0.02	32.05	0.36		0.02	15.10	0.04	–	2.86	0.14	99.44	0.22	44.17	0.25	5.78		37.34	0.41	70.00	-308.80	1.48	5.61
3		ARN-2’	941	47.82	0.01	32.43	0.33		0.02	15.41	0.02	–	2.63	0.14	98.81	0.22	63.67	0.25	6.27		39.61	0.40	198.45	-1056.60	1.55	5.58
1		ARN-2’	942	47.35	0.02	32.34	0.31		0.02	15.14	–	0.01	2.80	0.15	98.15	0.22	32.37	0.25	6.33		45.10	0.40	-81.70	123.80	1.51	5.41
4		ARN-2’	937	49.15	0.02	31.86	0.35		0.01	14.84	–	0.01	3.06	0.16	99.45	0.22	46.52	0.25	5.78		71.07	0.41	-148.59	248.05	1.44	5.38
2		ARN-2’	938	47.48	0.03	32.98	0.35		0.02	16.09	–	0.01	2.38	0.11	99.45	0.22	28.50	0.25	5.76		41.18	0.39	-155.07	99.34	1.64	7.02
4		ARN-2’	945	48.31	0.01	31.93	0.29		0.01	14.74	0.03	0.01	2.95	0.16	98.44	0.22	79.42	0.25	6.69		65.83	0.41	111.19	93.33	1.46	5.21
2		ARN-2’	946	49.14	0.01	31.42	0.33		0.02	14.65	0.02	0.01	3.03	0.16	98.79	0.22	72.24	0.26	6.34		35.02	0.41	200.53	172.66	1.44	5.07
2		ARN-2’	947	48.89	0.03	31.59	0.34		0.02	14.68	–	0.02	3.01	0.17	98.75	0.22	21.65	0.26	5.93		42.67	0.41	-94.95	68.28	1.45	5.01
4		ARN-2’	956	49.02	0.03	32.08	0.35		0.01	14.75	0.04	0.02	3.00	0.16	99.46	0.22	24.75	0.25	5.95		52.56	0.41	82.14	80.10	1.45	5.08
2		ARN-2’	957	48.87	0.01	31.95	0.35		0.00	14.99	0.03	–	2.83	0.15	99.18	0.22	81.34	0.25	5.79		276.10	0.41	95.45	-2160.40	1.50	5.49
1		ARN-2’	958	49.54	0.03	31.68	0.40		0.10	14.94	0.02	0.00	2.92	0.17	99.80	0.22	21.05	0.25	5.22		9.12	0.41	144.26	401.73	1.47	5.06
2		ARN-2’	959	49.69	0.01	31.81	0.32		0.01	14.73	0.05	0.01	3.00	0.16	99.79	0.22	54.18	0.25	6.41		52.16	0.41	64.41	250.28	1.44	5.09
6		ARN-2’	961	66.17	0.01	18.50	0.05		0.00	–	–	0.07	0.54	16.08	101.42	0.18	69.79	0.33	30.02		236.48	-1.74	-99.10	22.05	3.76	0.39
2		ARN-2’	962	49.03	0.03	31.75	0.32		0.02	14.92	0.02	–	2.93	0.15	99.17	0.22	24.80	0.25	6.48		33.98	0.41	137.14	-96.35	1.46	5.42
1		ARN-2’	979	48.93	0.03	32.27	0.31		0.03	14.74	0.04	0.02	2.94	0.17	99.49	0.22	25.94	0.25	6.36		29.81	0.41	72.12	59.28	1.47	4.94
2		ARN-2’	980	50.84	0.03	31.31	0.35		0.00	14.23	–	0.03	3.14	0.22	100.14	0.21	27.28	0.26	5.94		155.04	0.42	-166.68	48.02	1.41	4.14
3		ARN-2’	981	49.02	0.04	31.86	0.34		0.01	14.90	–	–	3.01	0.15	99.34	0.22	19.85	0.25	6.09		89.86	0.41	-77.76	-2158.80	1.45	5.62
1		ARN-2	998	51.24	0.02	31.81	0.32		0.02	14.91	0.01	0.00	2.91	0.16	101.41	0.21	31.88	0.25	6.30		31.69	0.41	350.32	612.26	1.47	5.23
2		ARN-2	999	50.15	0.02	31.67	0.35		0.02	14.76	0.05	0.02	3.02	0.17	100.24	0.22	41.62	0.25	5.76		40.00	0.41	58.63	75.31	1.44	4.96
1		ARN-2	1000	49.69	0.02	31.92	0.34		0.03	14.75	–	0.01	3.09	0.16	100.01	0.22	30.86	0.25	5.81		29.11	0.41	-101.49	105.24	1.43	5.00
1		ARN-2	1001	49.80	0.03	32.00	0.32		0.02	15.12	0.01	0.01	2.85	0.16	100.30	0.22	25.73	0.25	6.27		43.74	0.41	474.82	228.35	1.49	5.13
1		ARN-2	985	50.13	0.02	31.21	0.32		0.03	14.31	0.05	0.00	3.25	0.20	99.53	0.22	36.78	0.26	6.24		22.38	0.42	61.33	470.71	1.39	4.50
4		ARN-2	986	49.77	0.02	31.71	0.30		–	14.75	0.01	0.01	3.09	0.15	99.80	0.22	29.53	0.25	6.54		-793.48	0.41	475.46	123.35	1.43	5.29
1		ARN-2	996	50.32	0.03	32.02	0.35		0.03	14.91	–	–	2.95	0.16	100.79	0.22	23.55	0.25	5.80		23.06	0.41	-273.29	-252.06	1.46	5.13
2		ARN-2	997	50.80	0.02	31.83	0.33		0.01	14.73	0.02	0.04	3.00	0.20	100.99	0.21	30.01	0.25	6.22		49.57	0.41	145.59	38.41	1.45	4.42
2		ARN-2	1002	50.59	0.03	32.08	0.35		0.02	15.01	0.00	–	2.83	0.16	101.06	0.21	23.42	0.25	5.98		48.98	0.41	715.29	-128.00	1.50	5.19
2		ARN-2	1003	50.08	0.01	32.11	0.34		0.04	15.01	–	–	2.98	0.18	100.78	0.22	91.14	0.25	6.00		21.05	0.41	-51.00	-201.84	1.46	4.62
4		ARN-2	1006	50.02	0.01	32.04	0.31		0.01	15.16	0.04	–	2.88	0.15	100.63	0.22	62.29	0.25	6.36		61.15	0.40	74.25	-205.18	1.48	5.42
1		ARN-2	1007	49.63	0.03	31.97	0.37		0.02	15.15	0.01	0.02	2.86	0.15	100.21	0.22	27.13	0.25	5.68		39.50	0.41	255.43	79.18	1.49	5.32
2		ARN-2	1008	49.00	0.03	31.62	0.37		0.04	14.96	–	0.00	2.87	0.17	99.06	0.22	25.16	0.26	5.73		17.53	0.41	-627.77	839.24	1.49	4.88
3		ARN-2	1009	50.52	0.02	31.65	0.33		0.02	14.64	–	–	3.05	0.17	100.41	0.21	34.09	0.25	5.96		43.06	0.41	-195.27	-726.76	1.43	4.95

				Data (wt%)												Analytical uncertainty (%)										
Tag	Tag*	Sample	ID	SiO2	TiO2	Al2O3	FeO	MnO	MgO	CaO	SrO	BaO	Na2O	K2O	Total	Si	Ti	Al	Fe	Mn	Mg	Ca	Sr	Ba	Na	K
2		ARN-2	1010	49.60	0.03	32.09	0.32		0.02	15.02	0.00	0.01	2.92	0.16	100.20	0.22	24.38	0.25	6.35		32.32	0.41	1450.91	147.94	1.47	5.23
2		ARN-2	1027	50.04	0.02	31.70	0.33		0.01	14.40	0.02	–	3.26	0.16	99.95	0.22	40.22	0.25	6.14		53.07	0.42	139.27	-50.88	1.39	5.17
2		ARN-2	1028	50.10	0.02	31.78	0.40		0.01	14.52	–	0.02	3.10	0.19	100.15	0.22	29.77	0.25	5.24		76.45	0.41	-66.80	72.44	1.42	4.48
2		ARN-2	1039	49.54	0.02	32.01	0.37		0.01	14.84	–	0.00	3.00	0.14	99.93	0.22	34.13	0.25	5.50		65.95	0.41	-115.40	355.99	1.46	5.90
2		ARN-2	1040	49.15	0.04	31.66	0.36		0.02	14.64	0.01	0.00	3.09	0.14	99.12	0.22	17.56	0.25	5.59		37.61	0.41	290.68	693.40	1.43	5.80
1		ARN-3-6	1276	50.06	0.02	31.56	0.40	0.01	0.02	14.87	0.07	–	2.89	0.16	100.05	0.22	42.27	0.25	5.28	143.94	48.73	0.40	38.78	-2220.00	1.61	4.96
1		ARN-3-6	1277	50.78	0.01	31.06	0.40	–	0.01	14.47	0.06	0.01	3.14	0.19	100.13	0.22	105.78	0.25	5.26	-88.97	62.49	0.41	44.78	100.95	1.55	4.49
3		ARN-3-6	1278	47.70	0.00	32.96	0.37	0.01	0.01	16.54	0.05	0.01	2.13	0.10	99.89	0.22	302.64	0.24	5.54	194.85	132.60	0.38	54.69	99.61	1.90	7.12
1		ARN-3-6	1279	50.47	0.00	31.33	0.36	–	0.01	14.58	0.04	0.01	3.18	0.14	100.12	0.22	559.39	0.25	5.66	-152.21	54.42	0.40	71.99	99.33	1.53	5.45
1		ARN-3-6	1280	49.42	0.02	32.01	0.43	–	0.01	15.38	0.09	–	2.72	0.17	100.25	0.22	41.13	0.25	5.02	-68.00	60.70	0.39	30.91	-355.02	1.67	4.86
2		ARN-3-6	1281	50.74	0.01	31.21	0.38	0.00	0.01	14.35	0.08	0.02	3.23	0.20	100.23	0.22	47.41	0.25	5.50	344.44	50.74	0.41	34.35	66.87	1.52	4.30
3		ARN-3-6	1282	48.93	–	32.91	0.34	0.00	0.01	15.98	0.07	0.00	2.39	0.11	100.74	0.22	-55.76	0.24	5.97	541.33	95.93	0.38	40.70	2275.15	1.79	6.49
2		ARN-3-6	1283	49.85	0.01	31.57	0.43	0.02	0.02	14.82	0.08	0.02	2.96	0.17	99.92	0.22	128.06	0.25	5.08	64.19	37.37	0.40	36.80	81.63	1.60	4.89
1		ARN-3-7	2186	49.19	–	32.17	0.37	–	0.01	14.98	0.02	–	3.07	0.16	99.96	0.22	-1419.10	0.25	5.63	-170.58	55.20	0.40	134.24	-230.01	1.64	4.91
3		ARN-3-7	2187	48.73	–	32.61	0.32	0.02	0.01	15.15	0.03	0.01	2.94	0.14	99.95	0.22	-211.86	0.25	6.21	59.27	77.86	0.40	96.27	146.51	1.68	5.42
1		ARN-3-7	2188	49.43	–	32.07	0.27	0.00	0.00	14.82	0.09	–	3.10	0.12	99.90	0.22	-134.34	0.25	7.07	263.13	420.83	0.40	30.66	-604.17	1.63	5.83
2		ARN-3-7	2189	49.47	–	32.09	0.31	0.01	0.02	14.66	0.06	–	3.18	0.15	99.94	0.22	-148.20	0.25	6.44	202.20	44.59	0.41	47.98	-546.57	1.62	5.14
2		ARN-3-8	1407	49.26	0.00	31.78	0.38	0.01	0.00	14.65	0.02	0.01	3.23	0.18	99.51	0.22	1579.83	0.25	5.58	150.77	143.39	0.40	106.65	197.71	1.52	4.67
1		ARN-3-8	1408	49.14	0.03	31.48	0.34	0.01	0.02	14.40	0.10	0.00	3.31	0.20	99.03	0.22	23.08	0.25	5.97	137.18	47.98	0.41	30.62	464.39	1.50	4.30
2		ARN-3-8	1409	48.13	0.01	32.06	0.36	0.01	0.01	15.12	0.04	–	2.93	0.15	98.82	0.22	65.97	0.25	5.74	154.64	63.53	0.40	62.48	-134.57	1.60	5.33
3		ARN-3-8	1410	48.71	0.02	31.65	0.40	–	0.01	14.67	0.06	–	3.13	0.19	98.84	0.22	37.84	0.25	5.35	-530.30	72.35	0.40	46.39	-980.25	1.55	4.49
1		ARN-3-8	1412	47.89	0.09	32.34	0.45	0.01	0.00	15.34	0.02	0.02	2.69	0.16	99.00	0.22	9.07	0.25	4.99	235.67	246.49	0.39	115.95	65.22	1.68	5.14
3		ARN-3-8	1413	48.54	–	32.13	0.40	0.01	0.01	15.06	0.08	0.02	2.93	0.15	99.34	0.22	-89.84	0.25	5.35	141.48	52.01	0.40	36.31	64.24	1.60	5.26
2		ARN-3-8	1414	48.33	0.03	32.07	0.44	0.00	0.02	15.05	0.05	0.02	2.80	0.17	98.97	0.22	24.95	0.25	5.00	452.15	43.27	0.40	53.31	69.54	1.64	4.82
1		ARN-3-10	1245	49.75	–	31.49	0.34	–	0.01	14.78	0.06	–	2.97	0.12	99.51	0.22	-68.44	0.25	5.96	-455.26	98.72	0.40	47.47	-150.88	1.59	6.13
2		ARN-3-10	1246	50.55	0.00	31.01	0.36	–	0.01	14.38	0.04	0.00	3.28	0.16	99.79	0.22	289.43	0.25	5.68	-357.05	55.28	0.41	72.23	1631.41	1.51	4.90
2		ARN-3-10	1247	49.68	0.02	31.71	0.39	–	0.01	15.15	0.07	0.02	2.81	0.13	99.97	0.22	39.79	0.25	5.38	-145.82	103.05	0.40	39.86	78.86	1.64	5.91
3		ARN-3-10	1248	51.05	0.02	31.05	0.41	–	0.02	14.21	0.06	0.00	3.40	0.17	100.39	0.22	36.54	0.25	5.22	-282.44	40.12	0.41	44.66	259.77	1.48	4.82
1		ARN-3-10	1249	49.41	0.03	30.97	0.26	–	0.00	14.47	0.05	0.01	3.22	0.18	98.60	0.22	25.60	0.25	7.23	-89.00	303.64	0.41	50.87	143.99	1.52	4.63
2		ARN-3-10	1250	50.55	0.02	31.19	0.33	0.01	0.01	14.56	0.06	0.00	3.24	0.12	100.08	0.22	30.32	0.25	6.06	232.64	72.67	0.40	44.71	931.95	1.52	6.09
3		ARN-3-10	1251	49.97	0.01	30.71	0.36	0.02	0.02	14.22	0.05	–	3.25	0.16	98.76	0.22	51.74	0.25	5.69	80.16	35.46	0.41	52.98	-994.95	1.52	5.06
2		ARN-3-10	1252	49.78	0.01	31.54	0.31	0.01	0.01	14.78	0.04	–	2.99	0.14	99.60	0.22	126.12	0.25	6.33	177.22	69.76	0.40	65.11	-136.19	1.58	5.66
1		ARN-4-1	1626	49.25	0.01	31.36	0.37	0.01	0.02	14.58	0.04	–	3.19	0.15	98.99	0.22	74.19	0.25	5.66	121.78	38.82	0.41	60.90	-147.69	1.54	5.23
2		ARN-4-1	1627	48.73	0.01	31.52	0.43	0.01	0.02	14.86	0.08	0.01	3.03	0.17	98.89	0.22	55.17	0.25	5.17	137.20	35.29	0.40	35.57	110.02	1.59	4.75
3		ARN-4-1	1628	49.69	–	31.30	0.37	0.01	0.02	14.55	0.05	0.00	3.19	0.18	99.36	0.22	-154.07	0.25	5.66	121.52	45.01	0.41	58.51	2279.99	1.54	4.58
1		ARN-4-1	1629	48.88	0.01	32.36	0.41	0.01	0.02	15.42	0.07	0.02	2.71	0.15	100.05	0.22	118.33	0.25	5.32	194.93	35.93	0.40	42.65	83.75	1.68	5.15
2		ARN-4-1	1630	49.08	0.01	31.77	0.38	0.01	0.00	14.96	0.05	–	2.97	0.14	99.37	0.22	94.03	0.25	5.60	217.22	331.85	0.40	53.87	-127.74	1.60	5.66
2		ARN-4-1	1631	49.17	–	31.76	0.34	0.01	0.02	14.90	0.05	0.00	2.96	0.14	99.35	0.22	-155.54	0.25	6.04	134.02	44.92	0.40	55.95	1051.87	1.60	5.45
1		ARN-4-4	1400	47.59	0.01	32.30	0.41	–	0.04	14.79	0.09	0.01	2.67	0.29	98.19	0.22	106.92	0.25	5.27	-90.10	18.29	0.40	33.81	100.55	1.68	3.37
2		ARN-4-4	1401	49.44	0.00	31.16	0.36	0.00	0.01	14.20	0.03	0.00	3.34	0.21	98.76	0.22	1730.29	0.25	5.74	308.26	104.23	0.41	76.93	5000.00	1.49	4.19
3		ARN-4-4	1402	48.55	–	32.46	0.34	0.02	–	15.62	0.07	0.01	2.74	0.11	99.91	0.22	-99.40	0.25	6.04	77.03	-126.27	0.39	41.37	180.38	1.66	6.47
2		ARN-4-4	1403	48.68	0.01	32.00	0.35	–	0.01	14.98	0.03	–	2.91	0.16	99.12	0.22	47.82	0.25	5.86	-178.29	55.46	0.40	86.32	-55.66	1.61	5.13
1		ARN-4-4	1404	47.99	0.02	32.11	0.44	–	0.01	15.54	0.04	0.02	2.62	0.14	98.92	0.22	35.99	0.25	5.06	-226.61	104.65	0.39	66.15	79.20	1.70	5.62
2		ARN-4-4	1405	48.30	0.01	32.02	0.46	0.00	0.01	15.07	0.06	0.01	2.89	0.17	99.00	0.22	59.25	0.25	4.87	1287.27	64.22	0.40	48.04	237.14	1.61	4.91
3		ARN-4-4	1406	48.10	–	32.14	0.35	0.00	0.01	15.66	0.06	0.02	2.62	0.14	99.08	0.22	-55.95	0.25	5.93	285.40	49.88	0.39	49.88	81.22	1.70	5.61
2		ARN-4-7	1373	50.65	0.01	31.60	0.35	–	0.01	14.42	0.11	0.02	3.11	0.18	100.45	0.22	60.30	0.25	5.78	-147.58	77.74	0.41	25.97	83.78	1.55	4.58
2		ARN-4-7	1374	51.57	0.01	31.20	0.33	0.00	0.02	13.88	0.03	0.03	3.17	0.21	100.47	0.21	50.08	0.25	6.01	444.44	34.05	0.41	86.90	47.21	1.53	4.18
1		ARN-4-7	1375	49.77	0.02	32.25	0.39	0.03	0.01	15.04	0.02	0.02	2.76	0.15	100.46	0.22	29.99	0.25	5.36	51.91	54.53	0.40	128.28	78.35	1.65	5.14
2		ARN-4-7	1376	50.62	0.01	31.52	0.36	0.01	0.02	14.33	0.02	0.01	3.07	0.17	100.14	0.22	46.90	0.25	5.64	177.10	41.06	0.41	107.48	119.48	1.56	4.81
2		ARN-4-7	1377	50.28	0.01	31.63	0.40	0.00	0.01	14.64	0.02	0.02	3.01	0.17	100.20	0.22	49.23	0.25	5.27	367.99	80.81	0.40	162.12	60.74	1.58	4.75
2		ARN-4-7	1378	50.05	0.01	32.10	0.34	0.00	0.01	14.89	0.06	–	2.82	0.15	100.44	0.22	86.68	0.25	5.84	1804.70	54.20	0.40	44.67	-328.61	1.63	5.29
1		ARN-4-7	1379	49.50	0.01	31.96	0.33	0.00	0.01	14.82	0.07	0.01	2.81	0.16	99.68	0.22	61.48	0.25	6.04	377.24	60.31	0.40	39.79	149.76	1.64	5.00
2		ARN-4-7	1380	49.74	0.02	32.17	0.39	0.01	0.02	14.96	0.10	0.01	2.67	0.16	100.25	0.22	30.29	0.25	5.34	165.65	49.16	0.40	29.25	163.52	1.68	5.10

				Data (wt%)											Analytical uncertainty (%)									
Tag	**Tag***	**Sample**	**ID**	**SiO2**	**TiO2**	**Al2O3**	**FeO**	**MnO**	**MgO**	**CaO**	**SrO**	**BaO**	**Na2O**	**K2O**	**Total**	**Si**	**Ti**	**Al**	**Fe**	**Mn**	**Mg**	**Ca**	**Sr**	**Ba**	**Na**	**K**
1		ARN-4-9	1353	49.97	0.25	31.92	0.67	0.01	0.01	14.97	0.04	0.01	2.79	0.15	100.80	0.22	3.64	0.25	3.78	107.35	62.29	0.40	65.97	104.88	1.65	5.36
1		ARN-4-9	1354	49.92	0.02	32.38	0.42	0.00	0.01	15.21	0.07	0.00	2.71	0.14	100.88	0.22	33.43	0.25	5.14	533.88	62.73	0.39	40.93	334.61	1.67	5.52
2		ARN-4-9	1355	50.82	0.02	31.56	0.36	0.01	0.01	14.29	0.04	0.03	3.23	0.17	100.54	0.22	41.15	0.25	5.67	235.78	68.57	0.41	59.75	49.61	1.52	4.80
3		ARN-4-9	1356	49.90	0.00	32.31	0.34	0.02	0.01	15.09	0.08	0.00	2.72	0.13	100.60	0.22	582.13	0.25	5.89	70.52	105.18	0.40	36.84	559.59	1.67	5.86
1		ARN-4-9	1357	49.70	0.01	31.50	0.44	–	0.09	14.60	0.03	0.00	2.83	0.17	99.37	0.22	64.01	0.25	4.93	-120.29	10.00	0.40	86.28	344.25	1.63	4.82
2		ARN-4-9	1358	50.55	0.00	31.74	0.42	0.01	0.01	14.61	0.07	–	3.02	0.18	100.62	0.22	141.62	0.25	5.08	181.08	80.94	0.40	38.85	-194.78	1.58	4.58
2		ARN-4-9	1359	50.58	0.00	31.83	0.37	0.01	0.01	14.73	0.04	–	3.01	0.13	100.72	0.22	250.94	0.25	5.59	96.61	67.89	0.40	62.47	-79.13	1.58	5.73
2		ARN-4-9	1360	49.93	0.03	31.22	0.47	0.00	0.02	14.55	0.04	0.02	2.99	0.20	99.47	0.22	23.54	0.25	4.75	813.61	38.70	0.40	60.12	64.24	1.58	4.35
1		ARN-4-11	1600	48.98	–	31.97	0.38	0.00	0.00	15.18	0.06	0.00	2.79	0.12	99.48	0.22	-67.93	0.25	5.59	268.58	180.81	0.40	45.65	615.47	1.66	6.32
2		ARN-4-11	1601	49.81	0.03	31.18	0.38	–	0.02	14.20	0.02	0.01	3.32	0.15	99.12	0.22	25.82	0.25	5.61	-209.99	48.47	0.41	113.40	198.43	1.51	5.18
2		ARN-4-11	1602	49.56	0.02	31.50	0.38	0.01	0.02	14.68	0.07	0.00	3.22	0.13	99.60	0.22	38.89	0.25	5.55	135.73	41.99	0.41	38.46	801.55	1.53	5.79
3		ARN-4-11	1603	49.26	–	31.78	0.39	0.02	0.01	14.88	0.08	0.00	2.88	0.15	99.45	0.22	-95.66	0.25	5.53	62.53	91.46	0.40	35.74	280.82	1.63	5.26
6		ARN-4-11	1604	66.25	–	20.55	0.03	–	0.00	1.39	0.13	–	10.81	0.03	99.21	0.18	-50.12	0.32	40.19	-235.35	165.30	1.41	22.31	-632.51	0.80	17.43
1		ARN-4-11	1606	49.07	0.01	31.77	0.37	0.00	0.02	14.91	0.04	0.00	2.95	0.16	99.30	0.22	55.80	0.25	5.70	4472.09	42.61	0.40	61.41	610.29	1.61	5.11
3		ARN-4-11	1607	50.20	0.00	31.20	0.36	0.02	0.01	14.48	0.06	0.01	3.29	0.16	99.78	0.22	146.79	0.25	5.80	81.83	93.48	0.41	45.77	191.07	1.52	5.14
1		ARN-4-11	1608	49.42	0.02	31.80	0.40	0.01	0.02	14.83	0.06	–	3.05	0.16	99.77	0.22	47.06	0.25	5.44	92.99	32.27	0.40	45.56	-143.54	1.58	4.99
6		ARN-4-11	1609	66.96	–	19.99	–	–	0.00	0.78	0.10	0.02	11.18	0.04	99.07	0.18	-37.34	0.32	-304.70	-404.66	324.28	1.96	28.43	54.44	0.78	16.97
6		ARN-4-11	1610	67.60	–	19.79	0.03	0.01	0.00	0.59	0.10	0.01	11.26	0.04	99.42	0.18	-31.40	0.32	50.67	196.57	370.79	2.32	27.97	93.02	0.78	16.18
1		ARN-5-1	1507	47.79	0.02	32.07	0.39	0.01	0.01	15.48	0.02	0.01	2.56	0.17	98.52	0.22	37.86	0.25	5.46	89.88	54.10	0.39	126.89	201.50	1.72	4.85
2		ARN-5-1	1508	48.48	0.02	31.60	0.36	0.02	0.01	14.92	0.05	–	2.72	0.21	98.38	0.22	35.98	0.25	5.79	83.85	63.85	0.40	55.38	-695.38	1.67	4.18
2		ARN-5-1	1509	48.17	0.02	31.57	0.38	0.00	0.01	14.96	0.11	0.00	2.84	0.19	98.27	0.22	31.67	0.25	5.53	333.40	57.32	0.40	26.61	317.88	1.63	4.50
3		ARN-5-1	1510	48.13	0.00	31.91	0.37	0.00	–	14.69	0.04	0.03	2.90	0.18	98.25	0.22	300.75	0.25	5.68	409.49	-584.55	0.40	68.12	47.75	1.61	4.72
1		ARN-5-1	1511	48.24	0.02	31.73	0.38	0.01	0.02	15.12	0.05	–	2.78	0.17	98.52	0.22	37.08	0.25	5.56	172.32	41.44	0.40	57.61	-145.20	1.65	4.86
2		ARN-5-1	1512	49.13	0.02	30.81	0.35	–	0.02	14.09	0.08	–	3.43	0.22	98.14	0.22	37.98	0.25	5.84	-318.62	46.07	0.41	35.47	-1504.50	1.47	4.02
3		ARN-5-1	1513	48.54	0.02	31.63	0.39	0.01	0.03	15.17	0.06	–	2.74	0.16	98.76	0.22	46.50	0.25	5.44	139.97	23.75	0.40	49.81	-1260.30	1.66	4.95
1		ARN-5-4	1462	48.15	0.00	32.37	0.38	0.01	0.01	15.35	0.07	0.02	2.66	0.14	99.16	0.22	243.62	0.25	5.52	158.84	103.98	0.39	42.48	80.83	1.69	5.45
1		ARN-5-4	1463	48.68	0.01	31.98	0.39	0.01	0.02	14.82	0.03	–	2.93	0.18	99.04	0.22	58.40	0.25	5.46	171.45	42.67	0.40	86.17	-1520.90	1.60	4.65
2		ARN-5-4	1464	49.62	0.01	31.91	0.37	0.02	0.03	14.57	0.06	0.01	3.25	0.18	100.03	0.22	60.33	0.25	5.67	79.30	28.92	0.40	46.46	164.66	1.51	4.67
1		ARN-5-4	1465	49.77	0.01	31.53	0.40	–	0.02	14.60	0.05	0.01	3.12	0.21	99.72	0.22	60.88	0.25	5.38	-141.45	42.22	0.40	60.60	87.14	1.55	4.16
3		ARN-5-4	1466	48.57	–	32.52	0.33	0.01	0.01	15.41	0.04	0.01	2.63	0.15	99.67	0.22	-171.55	0.25	6.08	199.06	55.68	0.39	68.98	239.35	1.70	5.24
2		ARN-5-4	1467	49.89	0.02	31.40	0.39	0.01	0.02	14.47	0.09	0.01	3.28	0.18	99.75	0.22	44.01	0.25	5.50	126.44	44.42	0.41	30.76	132.55	1.51	4.63
4		ARN-5-4	1468	49.93	–	31.10	0.70	0.00	0.38	13.91	0.07	0.00	3.23	0.21	99.55	0.22	-303.23	0.25	3.73	264.84	3.53	0.41	40.31	361.74	1.52	4.13
4		ARN-5-4	1469	49.91	–	31.35	0.27	–	0.01	14.28	0.04	0.01	3.20	0.20	99.26	0.22	-48.41	0.25	7.13	-409.97	78.98	0.41	63.10	126.49	1.53	4.30
1		ARN-5-6	1591	49.13	0.02	31.84	0.42	0.01	0.03	14.78	0.07	0.01	2.93	0.17	99.39	0.22	37.78	0.25	5.26	222.06	25.48	0.40	42.87	138.76	1.61	4.80
2		ARN-5-6	1592	49.01	0.01	31.76	0.43	0.01	0.02	15.00	0.06	0.01	2.99	0.17	99.47	0.22	54.79	0.25	5.12	194.10	45.23	0.40	45.64	222.62	1.60	4.81
3		ARN-5-6	1593	49.39	0.01	31.80	0.42	–	0.01	14.67	0.11	–	3.09	0.18	99.68	0.22	59.85	0.25	5.25	-83.38	62.94	0.41	26.18	-133.90	1.57	4.60
3		ARN-5-6	1594	47.73	–	32.79	0.35	–	0.01	15.89	0.07	0.02	2.50	0.10	99.47	0.22	-55.30	0.25	5.92	-646.48	56.91	0.39	41.52	79.89	1.76	7.33
1		ARN-5-6	1595	48.42	0.01	32.04	0.39	0.03	0.01	15.14	0.08	–	2.86	0.16	99.16	0.22	60.69	0.25	5.47	44.88	49.84	0.40	34.81	-105.62	1.63	5.10
3		ARN-5-6	1596	49.06	–	31.51	0.39	–	0.02	14.79	0.05	0.02	3.10	0.14	99.08	0.22	-469.34	0.25	5.49	-236.48	34.05	0.40	56.49	64.24	1.57	5.43
1		ARN-5-6	1597	49.62	0.01	31.53	0.37	0.01	0.01	14.72	0.08	0.01	3.13	0.15	99.66	0.22	86.06	0.25	5.71	99.05	53.35	0.41	34.14	124.59	1.56	5.33
3		ARN-5-6	1598	49.35	–	31.74	0.43	0.01	0.01	14.91	0.05	–	2.99	0.15	99.65	0.22	-205.18	0.25	5.16	99.35	55.15	0.40	52.31	-463.13	1.60	5.19
2		ARN-5-6	1599	49.88	0.01	31.55	0.37	0.02	0.02	14.67	0.10	0.02	3.12	0.19	99.95	0.22	57.59	0.25	5.65	87.66	33.64	0.41	30.20	74.48	1.56	4.53
2		ARN-5-8C	1481	48.55	0.02	32.37	0.35	–	0.02	15.22	0.06	0.00	2.88	0.16	99.63	0.22	39.38	0.25	5.90	-200.78	36.94	0.40	49.62	5000.00	1.62	4.96
2		ARN-5-8C	1482	49.46	0.02	31.74	0.37	0.01	0.01	14.45	0.08	0.01	3.28	0.20	99.65	0.22	29.78	0.25	5.63	138.56	52.89	0.41	33.98	163.44	1.51	4.31
1		ARN-5-8C	1483	47.85	0.03	32.22	0.35	–	0.01	15.16	0.05	–	2.89	0.15	98.71	0.22	27.18	0.25	5.87	-154.13	50.96	0.40	55.20	-75.56	1.61	5.25
3		ARN-5-8C	1484	48.31	0.01	32.64	0.36	0.01	–	15.30	0.06	0.00	2.82	0.12	99.63	0.22	109.90	0.25	5.77	141.85	-1388.50	0.39	46.32	788.88	1.63	6.31
1		ARN-5-8C	1496	48.82	0.01	32.09	0.40	–	0.01	15.06	0.06	0.03	2.86	0.17	99.51	0.22	95.02	0.25	5.35	-80.27	52.86	0.40	44.87	48.73	1.62	4.91
2		ARN-5-8C	1497	48.87	0.02	31.96	0.42	0.01	0.02	14.74	0.07	0.01	3.01	0.19	99.33	0.22	36.41	0.25	5.17	115.40	47.54	0.40	41.04	218.57	1.58	4.45
3		ARN-5-8C	1498	48.68	–	32.06	0.40	0.01	0.02	14.74	0.06	0.01	3.03	0.17	99.19	0.22	-819.49	0.25	5.37	167.64	38.60	0.40	43.33	130.60	1.57	4.76
4		ARN-5-8C	1499	48.89	0.00	32.04	0.35	–	0.02	14.91	0.03	0.01	2.91	0.13	99.32	0.22	153.51	0.25	5.85	-93.05	36.87	0.40	85.22	103.66	1.61	5.76
1		ARN-5-8C	1500	48.68	0.01	32.03	0.45	–	0.02	14.94	0.06	–	2.95	0.17	99.30	0.22	88.61	0.25	4.95	-159.43	45.83	0.40	47.68	-163.38	1.60	4.80
2		ARN-5-8C	1501	49.48	0.02	31.67	0.39	–	0.01	14.65	0.03	0.03	3.06	0.22	99.56	0.22	38.51	0.25	5.50	-183.57	67.54	0.40	81.02	48.34	1.57	4.08
3		ARN-5-8C	1502	47.42	–	32.29	0.41	–	0.01	15.84	0.02	0.01	2.61	0.12	98.73	0.22	-297.11	0.25	5.28	-478.45	55.55	0.39	115.10	150.58	1.71	6.33

				Data (wt%)											Analytical uncertainty (%)										
Tag	**Tag***	**Sample**	**ID**	**SiO2**	**TiO2**	**Al2O3**	**FeO**	**MnO**	**MgO**	**CaO**	**SrO**	**BaO**	**Na2O**	**K2O**	**Total**	**Si**	**Ti**	**Al**	**Fe**	**Mn**	**Mg**	**Ca**	**Sr**	**Ba**	**Na**	**K**
1		ARN-5-8C	1503	49.97	0.02	31.12	0.41	–	0.01	14.00	0.06	0.01	3.52	0.21	99.32	0.22	31.76	0.25	5.30	-1172.40	51.91	0.41	49.46	245.34	1.45	4.21
3		ARN-5-8C	1504	48.91	–	31.82	0.40	–	0.01	14.63	0.01	0.01	3.19	0.19	99.18	0.22	-2400.30	0.25	5.36	-407.11	132.28	0.40	203.60	127.17	1.53	4.44
2		ARN-5-8C	1505	48.31	–	32.11	0.32	0.01	0.01	14.88	0.04	0.01	2.87	0.17	98.71	0.22	-78.22	0.25	6.20	150.63	81.99	0.40	68.07	134.59	1.62	4.93
Blocks in the anorthosite sequence																										
4		ARS-X1	2291	50.34	–	31.47	0.25	0.02	0.03	14.47	0.08	0.03	3.56	0.16	100.42	0.22	-52.82	0.25	7.28	70.83	29.98	0.41	35.29	41.10	1.51	4.75
2		ARS-X1	2292	50.54	–	31.13	0.18	0.01	0.04	14.18	0.06	0.01	3.53	0.19	99.87	0.22	-60.75	0.26	9.29	145.34	20.49	0.41	43.97	132.64	1.52	4.25
1		ARS-X1	2293	50.66	–	30.20	1.54	0.10	0.08	12.96	0.08	0.03	3.97	0.21	99.84	0.22	-96.87	0.26	2.33	15.40	10.81	0.43	33.29	49.12	1.43	4.01
1		ARS-X1	2294	51.75	–	30.33	0.13	0.01	0.02	13.22	0.09	0.02	4.20	0.22	99.99	0.21	-392.00	0.26	12.16	159.68	35.69	0.43	30.20	56.88	1.38	3.85
3		ARS-X1	2295	49.48	–	32.13	0.16	0.02	0.01	14.36	0.05	0.03	3.43	0.16	99.84	0.22	-31.78	0.25	10.13	67.72	60.96	0.41	48.77	45.94	1.54	4.73
3		ARS-X1	2296	48.09	–	33.35	0.17	–	0.01	15.45	0.06	–	2.85	0.13	100.11	0.22	-28.59	0.25	9.67	-374.43	109.32	0.39	45.23	-273.61	1.70	5.62
1		ARS-X1	2297	53.18	–	29.49	0.26	–	0.02	12.32	0.07	0.03	4.83	0.26	100.45	0.21	-28.52	0.26	7.12	-83.14	41.67	0.44	36.39	52.05	1.28	3.49
2		ARS-X2	2269	46.54	–	33.58	0.27	–	0.03	17.04	0.09	–	1.97	0.02	99.54	0.23	-21.03	0.24	6.96	-206.96	24.94	0.37	31.50	-441.94	2.08	25.29
2		ARS-X2	2270	46.49	–	33.37	0.26	–	0.02	16.98	0.04	0.00	1.98	0.03	99.17	0.23	-29.01	0.24	7.09	-391.74	32.92	0.37	63.54	1298.33	2.07	19.56
1		ARS-X2	2271	46.69	–	33.66	0.23	0.01	0.02	17.05	0.07	0.01	1.91	0.03	99.68	0.23	-34.86	0.24	7.81	112.31	39.67	0.37	40.65	135.90	2.10	19.14
3		ARS-X2	2272	43.83	–	35.71	0.12	0.01	0.00	19.52	0.09	0.01	0.55	0.00	99.84	0.23	-20.86	0.24	13.07	188.76	253.28	0.35	31.00	256.68	4.29	368.95
2		ARS-X2	2273	46.61	–	33.59	0.23	0.01	0.03	17.23	0.11	–	1.95	0.03	99.76	0.23	-36.75	0.24	7.92	223.86	29.36	0.37	26.74	-173.63	2.08	21.74
2		ARS-X2	2274	46.86	–	33.70	0.31	0.01	0.02	17.14	0.12	0.01	1.96	0.02	100.16	0.23	-32.26	0.24	6.31	100.53	31.04	0.37	23.59	133.37	2.07	34.33
4		ARS-X2	2275	46.43	–	33.59	0.36	0.01	0.02	17.10	0.05	0.00	2.00	0.05	99.62	0.23	-47.85	0.24	5.65	92.82	43.66	0.37	51.64	549.40	2.05	11.99
4		ARS-X2	2276	44.84	–	33.55	0.26	0.00	0.02	17.26	0.08	–	1.67	0.07	97.74	0.23	-25.74	0.24	7.21	1349.82	46.62	0.37	34.68	-97.24	2.27	8.63
2		ARS-X2	2277	46.69	–	33.45	0.21	0.03	0.02	16.84	0.07	–	2.07	0.03	99.40	0.23	-18.97	0.24	8.32	51.29	31.92	0.37	40.88	-215.64	2.01	18.60
4		ARS-X2	2278	46.82	–	33.26	0.34	0.02	0.04	16.74	0.07	0.01	2.19	0.05	99.54	0.23	-22.16	0.24	5.95	53.76	21.86	0.37	38.89	114.20	1.95	12.98
4		ARS-X2	2279	47.06	–	33.62	0.27	0.01	0.03	16.75	0.06	–	2.14	0.04	99.97	0.22	-30.64	0.24	6.85	230.61	22.69	0.37	46.78	-492.66	1.97	14.31
2	1	ARS-X3	2218	46.86	–	33.64	0.24	0.01	0.01	16.79	0.06	–	2.16	0.06	99.82	0.23	-27.46	0.25	7.77	100.13	105.12	0.38	47.84	-322.92	1.99	9.86
1	1	ARS-X3	2219	47.14	–	33.52	0.26	0.01	0.02	16.81	0.11	0.01	2.04	0.05	99.97	0.23	-28.89	0.25	7.15	115.51	39.37	0.38	26.98	187.54	2.06	11.26
4	1	ARS-X3	2220	46.58	–	31.69	1.57	0.01	0.22	15.18	0.05	–	1.84	0.17	97.33	0.23	-76.28	0.26	2.33	90.88	5.14	0.40	51.88	-348.80	2.19	4.78
1	1	ARS-X3	2221	47.03	–	33.16	0.25	0.03	0.01	16.75	0.05	0.03	2.08	0.07	99.45	0.23	-40.60	0.25	7.58	53.80	73.80	0.38	57.46	50.85	2.04	9.06
1	1	ARS-X3	2222	47.12	–	33.30	0.24	0.00	0.01	16.67	0.08	0.00	2.13	0.07	99.63	0.23	-39.97	0.25	7.61	626.18	58.70	0.38	33.66	2484.91	2.01	9.00
2	2	ARS-X3	2223	50.33	–	31.18	0.26	0.02	0.02	14.13	0.07	0.01	3.55	0.16	99.72	0.22	-64.43	0.26	7.18	84.08	48.03	0.42	40.31	138.62	1.53	4.95
1	2	ARS-X3	2224	48.87	–	32.02	0.30	0.01	0.01	15.33	0.05	0.01	2.88	0.15	99.63	0.22	-75.10	0.25	6.51	105.24	50.61	0.40	55.13	191.47	1.72	5.11
1		ARS-X5	2255	46.28	–	33.69	0.30	0.01	0.02	17.11	0.09	–	1.82	0.03	99.34	0.23	-24.91	0.24	6.54	120.61	40.04	0.37	32.32	-671.09	2.18	20.36
2		ARS-X5	2256	46.28	–	33.64	0.31	–	0.01	17.30	0.05	–	1.77	0.03	99.40	0.23	-20.19	0.25	6.32	-95.63	73.67	0.37	53.48	-454.63	2.21	19.13
1		ARS-X5	2257	46.08	–	34.15	0.33	0.01	0.03	17.33	0.06	0.01	1.68	0.03	99.73	0.23	-26.57	0.24	6.04	105.06	24.19	0.37	46.19	121.86	2.27	16.85
2		ARS-X5	2258	46.90	–	33.61	0.29	0.02	0.03	16.87	0.08	0.01	2.15	0.04	100.00	0.23	-32.41	0.25	6.59	70.37	27.29	0.38	34.17	108.55	1.98	15.27
1		ARS-X5	2259	45.99	–	34.19	0.35	–	0.03	17.39	0.08	0.01	1.70	0.03	99.76	0.23	-23.84	0.24	5.82	-2261.90	30.00	0.37	34.41	118.49	2.25	18.55
2	1	ARN-X9	2346	46.34	–	34.18	0.29	0.01	0.01	17.34	0.06	0.03	1.82	0.03	100.11	0.23	-42.49	0.24	6.60	203.56	61.80	0.37	43.31	39.42	2.15	17.56
2	1	ARN-X9	2347	46.01	–	34.19	0.30	–	0.02	17.54	0.08	0.01	1.67	0.03	99.84	0.23	-24.41	0.24	6.44	-1030.00	40.87	0.36	34.02	222.52	2.25	16.92
1	1	ARN-X9	2348	46.38	–	33.82	0.21	0.01	0.03	17.14	0.07	0.01	1.85	0.04	99.55	0.23	-33.35	0.24	8.20	199.31	28.75	0.37	37.56	133.14	2.13	15.62
1	1	ARN-X9	2349	46.13	–	33.71	0.33	0.00	0.02	17.09	0.09	0.02	1.87	0.04	99.29	0.23	-28.05	0.24	6.00	291.38	37.72	0.37	30.54	67.32	2.12	15.76
2	2	ARN-X9	2350	50.16	–	31.73	0.26	–	0.03	14.55	0.05	0.03	3.44	0.16	100.42	0.22	-42.79	0.25	7.01	-271.40	26.24	0.40	53.87	44.07	1.52	4.75
1	2	ARN-X9	2351	50.45	–	31.01	0.18	0.02	0.02	14.00	0.08	0.01	3.68	0.19	99.65	0.21	-151.50	0.25	9.40	56.71	35.92	0.41	33.34	90.17	1.47	4.28
2	1	ARN-X11	2358	46.96	–	33.73	0.20	0.01	0.01	17.10	0.07	–	2.00	0.05	100.13	0.22	-75.52	0.24	8.64	138.01	74.76	0.37	37.57	-272.13	2.04	12.27
2	1	ARN-X11	2359	46.68	–	33.91	0.21	0.01	0.02	17.18	0.12	0.00	1.84	0.05	100.02	0.22	-29.44	0.24	8.37	117.53	35.88	0.37	23.57	386.96	2.13	12.30
1	1	ARN-X11	2360	46.88	–	33.81	0.17	0.00	–	17.05	0.05	0.02	1.88	0.03	99.90	0.22	-27.71	0.24	9.68	272.09	-425.52	0.37	47.97	64.40	2.10	18.90
1	1	ARN-X11	2361	46.79	–	33.83	0.22	0.02	0.02	17.11	0.06	0.01	1.88	0.04	99.99	0.22	-35.47	0.24	7.94	62.60	43.11	0.37	42.09	161.29	2.11	13.93
2	1	ARN-X11	2362	46.62	–	34.16	0.25	0.02	0.01	17.31	0.09	0.01	1.83	0.05	100.35	0.22	-26.83	0.24	7.32	84.38	57.01	0.37	29.90	87.68	2.14	12.85
2	1	ARN-X11	2363	46.72	–	33.25	0.39	0.01	0.19	16.80	0.06	0.01	1.99	0.05	99.47	0.22	-24.83	0.24	5.39	108.28	5.67	0.37	40.88	169.77	2.04	11.10
3	1	ARN-X11	2364	44.39	–	35.65	0.17	0.00	0.00	19.04	0.06	0.01	0.75	0.01	100.08	0.23	-25.31	0.23	9.66	433.93	2111.04	0.35	44.70	217.06	3.54	97.29
2	1	ARN-X11	2365	46.81	–	33.67	0.20	–	0.01	17.09	0.05	0.01	1.90	0.04	99.77	0.22	-26.17	0.24	8.74	-190.32	73.20	0.37	56.14	139.35	2.09	14.92
2	1	ARN-X13	2310	47.34	–	33.13	0.21	0.01	0.01	16.47	0.05	0.02	2.32	0.06	99.63	0.22	-34.77	0.24	8.22	102.19	67.13	0.38	52.98	72.92	1.88	9.81
4	1	ARN-X13	2311	47.40	–	33.28	0.25	0.01	0.01	16.44	0.05	0.01	2.29	0.06	99.81	0.22	-34.75	0.24	7.30	95.46	58.17	0.38	50.88	107.12	1.90	9.57
1	1	ARN-X13	2312	47.42	–	33.14	0.17	0.00	0.02	16.45	0.04	0.02	2.29	0.05	99.61	0.22	-119.38	0.24	9.66	287.46	35.76	0.38	60.26	70.08	1.90	11.63
3	1	ARN-X13	2313	47.22	–	33.30	0.14	–	0.01	16.51	0.03	0.01	2.19	0.05	99.46	0.22	-30.51	0.24	11.31	-128.11	91.15	0.38	89.96	150.55	1.94	11.51
1	1	ARN-X13	2314	47.54	–	33.29	0.20	–	0.01	16.53	0.06	–	2.28	0.05	99.97	0.22	-26.84	0.24	8.70	-306.39	99.87	0.38	41.75	-1112.60	1.90	11.61

				Data (wt%)											Analytical uncertainty (%)									
Tag	**Tag***	**Sample**	**ID**	**SiO2**	**TiO2**	**Al2O3**	**FeO**	**MnO**	**MgO**	**CaO**	**SrO**	**BaO**	**Na2O**	**K2O**	**Total**	**Si**	**Ti**	**Al**	**Fe**	**Mn**	**Mg**	**Ca**	**Sr**	**Ba**	**Na**	**K**
2	1	ARN-X13	2315	47.56	–	33.33	0.17	0.01	0.02	16.48	0.06	0.01	2.20	0.06	99.91	0.22	-31.91	0.24	9.55	131.12	32.54	0.38	45.97	153.12	1.93	10.53
Tag*: 1 = Fine-grained, 2 = Medium-grained.																										
Pyroxenite Layers in the Mooimeisjesfontein area																										
1		JB031-A1	1675	50.40	–	31.61	0.29	0.00	0.02	14.34	0.06	–	3.35	0.20	100.29	0.22	-511.00	0.25	6.76	281.47	34.90	0.41	43.41	-149.60	1.50	4.25
1		JB031-A1	1676	49.87	–	31.44	0.36	0.01	0.01	14.43	0.06	0.02	3.17	0.22	99.60	0.22	-296.47	0.25	5.84	120.64	51.52	0.41	43.59	84.11	1.55	4.04
1		JB031-A1	1677	49.72	0.01	31.34	0.36	0.01	0.01	14.43	0.08	0.00	3.16	0.21	99.35	0.22	50.77	0.25	5.78	161.11	72.00	0.41	36.14	1454.88	1.55	4.12
3		JB031-A1	1678	48.10	–	32.98	0.30	–	0.01	16.07	0.04	0.01	2.29	0.12	99.91	0.22	-66.13	0.25	6.56	-1640.80	100.03	0.39	62.72	152.03	1.84	6.29
2		JB031-A1	1679	50.06	–	31.67	0.39	–	0.01	14.47	0.06	0.02	3.21	0.18	100.08	0.22	-2738.70	0.25	5.47	-142.86	50.22	0.41	44.85	65.28	1.54	4.68
3		JB031-A1	1680	47.37	–	33.12	0.60	0.01	0.21	16.24	0.07	0.01	2.04	0.08	99.74	0.22	-104.44	0.25	4.17	111.07	5.37	0.39	40.99	200.38	1.96	8.88
4		JB031-A1	1681	49.82	–	31.78	0.38	–	0.01	14.81	0.09	–	3.03	0.17	100.08	0.22	-183.91	0.25	5.62	-63.14	106.90	0.40	31.65	-699.41	1.58	4.83
4		JB031-A1	1682	49.76	–	31.75	0.46	–	0.01	14.65	0.11	0.01	3.10	0.18	100.04	0.22	-96.37	0.25	4.92	-298.91	75.98	0.41	26.83	133.12	1.56	4.54
2		JB031-A1	1683	49.76	–	32.06	0.39	0.00	0.01	14.88	0.07	0.00	3.05	0.19	100.41	0.22	-243.02	0.25	5.48	302.61	96.81	0.40	39.91	4157.72	1.58	4.45
1		JB031-A1	1684	49.84	0.01	31.54	0.39	0.01	0.02	14.67	0.08	0.01	3.07	0.20	99.84	0.22	56.59	0.25	5.48	184.72	43.90	0.41	36.18	93.61	1.57	4.26
4		JB031-A1	1685	49.73	0.01	31.72	0.37	0.02	0.01	14.59	0.05	–	3.10	0.20	99.80	0.22	54.86	0.25	5.66	80.76	55.59	0.41	57.52	-116.16	1.57	4.33
4		JB031-A1	1686	49.73	0.01	31.45	0.47	–	0.02	14.48	0.04	–	3.18	0.22	99.59	0.22	122.71	0.25	4.85	-211.80	39.53	0.41	65.95	-152.86	1.55	4.02
4		JB031-A1	1687	49.95	0.00	31.58	0.30	–	0.01	14.47	0.05	0.01	3.22	0.22	99.82	0.22	714.37	0.25	6.58	-99.64	61.27	0.41	51.21	129.55	1.53	4.00
1		JB031-A2	1708	50.46	0.01	31.14	0.40	0.01	0.03	14.27	0.06	0.02	3.36	0.24	100.00	0.22	59.07	0.25	5.40	111.00	29.31	0.41	47.97	61.04	1.50	3.84
2		JB031-A2	1709	50.93	0.00	31.00	0.37	0.00	0.02	13.94	0.08	–	3.47	0.23	100.05	0.22	558.32	0.25	5.69	349.86	45.02	0.42	36.99	-288.17	1.47	3.88
3		JB031-A2	1710	49.85	0.01	31.69	0.41	0.01	0.03	14.73	0.04	–	3.05	0.20	100.03	0.22	124.15	0.25	5.29	103.85	28.95	0.41	65.81	-279.18	1.58	4.25
1		JB031-A2	1711	49.58	0.01	31.61	0.47	0.00	0.03	14.96	0.07	0.00	3.01	0.20	99.95	0.22	51.75	0.25	4.88	312.96	26.26	0.40	42.34	263.94	1.59	4.25
2		JB031-A2	1712	49.54	0.02	31.10	0.48	0.00	0.02	14.46	0.03	0.02	3.17	0.22	99.06	0.22	47.44	0.25	4.79	302.85	37.09	0.41	87.65	64.03	1.55	3.97
6		JB031-A2	1713	52.60	–	29.61	0.37	0.00	0.03	12.34	0.07	0.00	4.38	0.35	99.74	0.21	-639.89	0.26	5.69	872.43	26.21	0.44	38.92	274.93	1.30	3.00
3		JB031-A2	1714	47.79	–	32.82	0.40	–	0.01	15.94	0.07	0.01	2.43	0.13	99.60	0.22	-138.82	0.25	5.42	-227.41	58.77	0.39	38.72	199.55	1.79	5.75
2		JB031-A2	1715	49.15	–	31.89	0.41	–	0.02	15.08	0.05	0.01	2.99	0.18	99.78	0.22	-161.25	0.25	5.32	-536.03	47.08	0.40	55.18	217.46	1.60	4.53
1		JB031-T	1634	49.34	0.01	31.86	0.37	0.00	0.02	14.57	0.03	0.01	3.17	0.19	99.56	0.22	91.02	0.25	5.71	534.51	46.23	0.41	87.70	99.65	1.55	4.52
2		JB031-T	1635	52.76	–	29.49	0.26	0.00	0.02	12.16	0.06	0.03	4.37	0.39	99.56	0.21	5000.00	0.26	7.24	2671.41	34.82	0.45	48.44	42.23	1.30	2.76
1		JB031-T	1636	49.22	0.01	31.27	0.37	0.00	0.03	14.35	0.08	0.00	3.25	0.19	98.78	0.22	112.22	0.25	5.66	871.12	24.37	0.41	33.80	1515.91	1.52	4.46
3		JB031-T	1637	48.84	–	31.78	0.37	–	0.01	15.00	0.09	0.02	2.94	0.15	99.20	0.22	-81.39	0.25	5.67	-363.46	84.15	0.40	33.14	85.32	1.61	5.23
2		JB031-T	1638	50.24	0.01	30.92	0.31	0.00	0.02	13.83	0.08	–	3.65	0.22	99.28	0.22	67.31	0.25	6.45	736.15	39.86	0.42	33.81	-4903.80	1.43	4.03
1		JB031-T	1639	49.79	0.00	31.59	0.33	0.01	0.01	14.45	0.09	0.02	3.06	0.19	99.55	0.22	171.54	0.25	6.22	104.75	49.89	0.41	31.77	61.33	1.58	4.51
2		JB031-T	1640	50.19	–	31.36	0.31	–	0.01	14.39	0.06	0.01	3.33	0.19	99.86	0.22	-58.09	0.25	6.40	-313.84	52.17	0.41	45.19	237.58	1.51	4.39
1		JB031-T	1641	49.94	0.02	31.67	0.37	0.01	0.02	14.65	0.06	0.00	3.12	0.19	100.05	0.22	34.79	0.25	5.67	184.88	48.47	0.41	46.66	500.13	1.56	4.46
2		JB031-T	1642	49.86	0.00	31.45	0.34	–	0.02	14.27	0.08	0.02	3.39	0.21	99.65	0.22	206.07	0.25	6.04	-3517.20	36.79	0.41	34.57	57.51	1.49	4.17
1		JB031-P1	1779	49.67	–	31.08	0.29	–	0.01	14.12	0.08	0.02	3.43	0.19	98.90	0.22	-437.99	0.25	6.73	-147.95	58.72	0.42	33.66	85.63	1.49	4.43
2		JB031-P1	1780	52.10	0.01	29.55	0.28	0.00	0.01	12.27	0.06	0.01	4.38	0.25	98.92	0.21	54.12	0.26	7.00	711.80	80.73	0.45	44.96	129.70	1.30	3.68
3		JB031-P1	1781	50.47	0.01	30.95	0.31	–	0.01	13.80	0.06	0.02	3.52	0.22	99.38	0.22	66.32	0.26	6.44	-230.00	56.36	0.42	43.64	55.83	1.47	4.01
1		JB031-P1	1782	49.49	0.03	31.54	0.50	0.01	0.01	14.45	0.07	0.01	3.27	0.20	99.59	0.22	26.30	0.25	4.66	178.07	52.63	0.41	40.01	140.30	1.53	4.34
2		JB031-P1	1783	51.92	0.01	30.11	0.30	0.01	0.01	12.96	0.03	–	4.12	0.28	99.75	0.21	111.79	0.26	6.58	179.12	52.87	0.43	78.32	-232.32	1.35	3.46
1		JB031-P3	1565	53.22	–	28.82	0.18	–	0.01	11.53	0.10	0.01	4.87	0.21	98.95	0.21	-210.40	0.26	9.52	-250.01	62.72	0.46	29.16	119.62	1.23	4.21
2		JB031-P3	1566	52.04	0.00	29.51	0.27	–	0.02	12.47	0.09	–	4.43	0.26	99.09	0.21	423.63	0.26	7.14	-170.79	44.63	0.44	32.16	-3239.80	1.29	3.63
2		JB031-P3	1567	52.27	–	27.42	2.16	–	0.11	11.30	0.02	0.01	4.27	0.24	97.79	0.21	-52.67	0.27	1.97	-649.69	8.60	0.46	155.81	163.12	1.33	3.78
4		JB031-P3	1568	52.90	–	28.92	0.27	0.01	0.01	11.83	0.06	0.00	4.64	0.28	98.91	0.21	-175.03	0.26	7.06	132.64	100.31	0.45	49.16	554.40	1.26	3.48
2		JB031-P3	1569	53.69	–	28.84	0.35	0.00	0.01	11.79	0.06	0.00	4.91	0.22	99.87	0.21	-255.35	0.26	5.93	531.36	55.94	0.45	49.25	728.01	1.22	4.00
1		JB031-P3	1570	52.11	0.01	29.70	0.25	0.00	0.00	12.53	0.02	0.01	4.20	0.25	99.07	0.21	72.85	0.26	7.58	4379.43	158.54	0.44	140.87	133.38	1.33	3.72
2		JB031-P3	1571	52.99	0.01	29.08	0.32	0.01	0.01	11.96	0.07	0.00	4.76	0.18	99.40	0.21	111.10	0.26	6.30	112.68	77.47	0.45	38.68	265.71	1.24	4.57
6		JB031-P3	1572	67.15	0.02	19.22	0.42	–	0.25	0.31	0.07	0.01	11.10	0.23	98.78	0.18	42.88	0.33	5.21	-372.55	4.70	3.56	40.88	190.00	0.79	3.92
6		JB031-P3	1573	67.94	0.01	19.50	0.19	–	0.00	0.40	0.07	0.00	11.41	0.04	99.55	0.18	82.60	0.33	9.10	5000.00	1230.40	2.97	40.75	537.20	0.77	16.44
1		JB031-P4	1759	50.19	0.02	30.27	0.24	–	–	12.93	0.11	–	3.90	0.25	97.91	0.22	45.80	0.26	7.83	-134.66	-1413.60	0.43	25.96	-177.55	1.39	3.65
2		JB031-P4	1760	51.77	–	29.78	0.44	0.02	0.03	12.56	0.05	0.00	4.24	0.25	99.14	0.21	-82.05	0.26	5.07	77.35	30.67	0.44	58.76	443.47	1.33	3.68
1		JB031-P4	1761	52.73	0.01	28.83	0.22	–	0.01	11.41	0.08	0.01	4.66	0.36	98.31	0.21	60.31	0.26	8.14	-324.38	97.73	0.46	36.37	90.49	1.26	2.94
4		JB031-P4	1762	52.33	–	29.34	0.39	0.01	0.03	12.19	0.11	0.00	4.44	0.27	99.11	0.21	-549.46	0.26	5.47	250.79	27.23	0.45	27.40	448.02	1.29	3.52
3		JB031-P5	1737	48.45	0.00	32.34	0.27	0.00	0.02	14.91	0.07	–	2.86	0.15	99.08	0.22	193.12	0.25	7.14	273.58	35.39	0.40	38.39	-1774.70	1.63	5.13

				Data (wt%)											Analytical uncertainty (%)										
Tag	**Tag***	**Sample**	**ID**	**SiO2**	**TiO2**	**Al2O3**	**FeO**	**MnO**	**MgO**	**CaO**	**SrO**	**BaO**	**Na2O**	**K2O**	**Total**	**Si**	**Ti**	**Al**	**Fe**	**Mn**	**Mg**	**Ca**	**Sr**	**Ba**	**Na**	**K**
2		JB031-P5	1738	52.23	0.00	29.45	0.38	–	0.00	12.33	0.06	0.00	4.41	0.32	99.19	0.21	366.72	0.26	5.57	-1376.20	175.31	0.44	44.71	417.66	1.30	3.16
1		JB031-P5	1739	52.26	0.01	29.70	0.27	–	0.02	12.28	0.11	–	4.33	0.25	99.23	0.21	99.73	0.26	7.10	-110.31	34.21	0.45	26.21	-220.09	1.31	3.69
2		JB031-P5	1740	51.68	0.02	29.77	0.30	–	0.02	12.49	0.04	0.02	4.28	0.25	98.86	0.21	40.97	0.26	6.62	-342.40	41.06	0.44	68.48	80.84	1.32	3.69
2		JB031-P7	1880	50.77	0.01	30.88	0.30	0.00	0.01	13.78	0.02	0.01	3.51	0.26	99.56	0.22	92.43	0.26	6.67	439.74	83.19	0.42	113.80	146.32	1.47	3.56
3		JB031-P7	1881	50.54	0.00	31.32	0.34	0.01	0.01	14.34	0.05	0.01	3.28	0.20	100.10	0.22	2199.11	0.25	6.08	118.41	65.63	0.41	56.37	107.50	1.52	4.25
1		JB031-P7	1882	49.44	0.01	31.48	0.33	–	0.01	14.52	0.09	0.01	3.06	0.18	99.13	0.22	60.07	0.25	6.17	-990.44	115.56	0.41	32.43	109.39	1.58	4.66
3		JB031-P7	1883	48.01	–	32.90	0.34	0.01	0.01	16.10	0.06	0.00	2.37	0.09	99.88	0.22	-71.85	0.25	6.08	171.43	135.75	0.39	48.34	301.86	1.81	7.52
2		JB031-P7	1884	50.18	0.02	31.43	0.31	–	0.01	14.33	0.10	0.02	3.15	0.18	99.73	0.22	47.32	0.25	6.41	-213.04	119.99	0.41	29.95	75.45	1.55	4.60
2		JB031-P7	1885	51.47	0.00	30.67	0.30	0.02	0.01	13.42	0.07	–	3.67	0.25	99.89	0.21	144.75	0.26	6.53	67.47	50.72	0.43	40.32	-404.79	1.43	3.69
2		JB031-P7	1886	51.23	0.01	30.44	0.30	–	0.01	13.25	0.08	–	3.75	0.25	99.33	0.22	67.37	0.26	6.54	-767.17	56.98	0.43	34.65	-1354.70	1.42	3.67
8		JB031-P7	1887	47.80	0.00	33.41	0.37	0.00	0.02	16.52	0.08	0.01	2.13	0.09	100.43	0.22	297.89	0.24	5.76	1505.60	37.70	0.38	34.61	191.26	1.92	7.90
8		JB031-P7	1888	47.44	–	33.45	0.35	–	0.00	16.62	0.06	0.01	2.07	0.09	100.09	0.22	-121.13	0.24	5.98	-434.75	187.49	0.38	43.86	146.20	1.95	7.97
1		JB031-P7	1889	50.16	0.01	31.32	0.30	0.01	0.02	14.26	0.04	0.02	3.20	0.22	99.55	0.22	59.02	0.25	6.62	141.52	32.90	0.41	64.14	76.66	1.54	4.04
2		JB031-P7	1890	49.48	0.01	31.95	0.37	–	0.01	14.78	0.10	0.00	2.99	0.19	99.88	0.22	78.37	0.25	5.72	-2964.00	92.14	0.41	29.90	278.85	1.60	4.51
2		JB031-P7	1891	49.79	0.01	31.74	0.36	–	0.01	14.71	0.06	0.02	3.03	0.20	99.92	0.22	63.43	0.25	5.84	-306.30	70.03	0.41	48.47	84.08	1.59	4.26
3		JB031-P7	1892	52.16	0.02	30.11	0.28	0.01	0.03	12.54	0.08	0.01	4.12	0.24	99.61	0.21	36.65	0.26	6.93	103.48	27.51	0.44	33.81	149.71	1.35	3.76
3		JB031-P7	1893	49.87	–	31.03	0.37	0.02	0.01	13.97	0.08	0.01	3.52	0.21	99.07	0.22	-192.17	0.25	5.76	71.96	106.05	0.42	35.40	239.21	1.47	4.18
1		JB031-P9	1767	49.94	0.02	30.89	0.37	0.00	0.02	14.02	0.07	–	3.43	0.22	98.98	0.22	41.61	0.26	5.72	1510.88	43.79	0.42	39.17	-94.77	1.49	3.97
2		JB031-P9	1768	50.36	0.02	30.61	0.33	–	0.02	13.60	0.07	0.01	3.72	0.21	98.96	0.22	47.44	0.26	6.19	-272.33	37.81	0.42	40.19	95.33	1.42	4.17
1		JB031-P9	1769	50.45	0.02	30.03	0.32	–	0.01	12.97	0.07	0.01	3.98	0.26	98.12	0.22	32.91	0.26	6.37	-103.22	57.09	0.43	39.04	203.65	1.37	3.61
2		JB031-P9	1770	49.01	0.01	31.36	0.34	–	0.01	14.64	0.08	0.02	3.12	0.18	98.78	0.22	70.84	0.25	6.00	-180.22	56.66	0.41	35.42	72.77	1.56	4.54
6		JB031-P9	1771	65.10	–	19.22	1.83	0.03	0.95	0.43	0.03	0.06	10.77	0.85	99.29	0.19	-35.59	0.33	2.16	47.67	2.14	2.85	75.72	22.81	0.81	1.78
6		JB031-P9	1772	67.81	0.03	19.13	0.09	–	0.02	0.42	0.05	0.01	11.32	0.05	98.93	0.18	24.38	0.33	16.83	-276.36	47.36	2.88	48.05	161.69	0.78	12.55
2		JB031-P9	1773	51.77	0.02	29.60	0.32	–	0.01	12.58	0.05	0.01	4.25	0.23	98.83	0.21	44.21	0.26	6.33	-115.39	59.71	0.44	58.35	148.84	1.33	3.97
1		JB031-G1	1660	49.81	0.01	31.04	0.40	0.01	0.02	14.30	0.05	0.02	3.25	0.22	99.12	0.22	134.76	0.25	5.42	208.11	37.42	0.41	53.56	58.04	1.53	4.07
3		JB031-G1	1661	49.43	0.00	30.67	0.32	–	0.02	14.08	0.05	0.02	3.18	0.21	97.98	0.22	3223.27	0.26	6.31	-423.81	34.04	0.42	55.64	77.33	1.54	4.13
2		JB031-G1	1662	49.77	0.01	31.14	0.39	–	0.02	13.98	0.07	0.00	3.36	0.25	99.00	0.22	64.58	0.25	5.48	-630.62	46.17	0.42	41.03	919.62	1.50	3.68
2		JB031-G1	1663	51.19	0.01	30.48	0.36	0.01	0.02	13.50	0.09	0.00	3.68	0.27	99.62	0.21	47.60	0.26	5.76	154.10	38.82	0.42	33.09	375.55	1.43	3.48
1		JB031-G1	1664	50.51	0.00	30.70	0.35	0.01	0.02	13.24	0.05	0.02	3.63	0.32	98.86	0.22	252.04	0.26	5.90	194.57	34.64	0.43	53.13	66.08	1.44	3.17
3		JB031-G1	1665	50.42	–	30.54	0.39	0.00	0.03	13.45	0.03	0.00	3.69	0.23	98.79	0.22	-141.55	0.26	5.50	435.42	25.77	0.43	87.14	591.51	1.43	3.96
3		JB031-G1	1666	49.33	–	31.44	0.28	–	0.01	14.89	0.10	0.01	2.98	0.19	99.22	0.22	-72.42	0.25	6.89	-2942.90	120.38	0.40	29.90	151.22	1.60	4.51
4		JB031-G1	1667	50.43	0.02	31.23	0.45	0.00	0.02	14.27	0.04	0.00	3.34	0.22	100.01	0.22	46.10	0.25	5.03	1689.88	35.94	0.41	69.60	811.33	1.51	4.03
1		JB031-G1	1668	50.18	0.01	31.49	0.31	–	0.03	14.62	0.06	0.02	3.08	0.19	99.99	0.22	58.78	0.25	6.39	-117.10	26.34	0.41	45.05	62.93	1.57	4.38
1		JB031-G2	1901	50.74	0.01	30.90	0.30	0.00	0.02	13.96	0.07	0.00	3.52	0.19	99.70	0.22	110.24	0.25	6.61	1080.78	39.52	0.42	41.11	4521.41	1.46	4.51
2		JB031-G2	1902	50.82	0.02	30.66	0.27	–	0.03	13.72	0.06	–	3.60	0.21	99.39	0.22	32.53	0.26	7.10	-124.57	28.22	0.42	43.55	-300.64	1.44	4.13
2		JB031-G2	1903	51.28	–	30.71	0.35	–	0.01	13.44	0.08	0.02	3.74	0.25	99.87	0.21	-230.13	0.25	5.92	-514.05	104.63	0.42	34.43	81.41	1.41	3.70
4		JB031-G2	1905	52.05	0.01	30.12	0.37	0.02	0.03	13.06	0.08	–	4.03	0.27	100.04	0.21	89.56	0.26	5.66	63.82	30.55	0.43	33.73	-2324.60	1.36	3.51
2		JB031-G2	1906	50.43	–	31.10	0.35	0.00	0.02	14.23	0.06	–	3.43	0.21	99.83	0.22	-217.35	0.25	5.87	626.91	39.06	0.41	49.57	-287.62	1.48	4.14
3		JB031-G2	1907	46.93	–	33.43	0.30	–	0.01	16.97	0.06	–	1.92	0.09	99.71	0.23	-33.43	0.24	6.65	-715.18	55.96	0.38	44.80	-99.46	2.02	8.06
1		JB031-G2	1908	51.99	0.02	30.21	0.31	0.01	0.02	13.30	0.09	–	3.83	0.28	100.06	0.21	47.00	0.26	6.48	97.15	31.67	0.43	33.04	-1085.80	1.40	3.42
2		JB031-G3	1923	51.18	0.01	30.80	0.31	–	0.02	13.65	0.08	0.01	3.57	0.28	99.91	0.21	77.92	0.25	6.43	-115.08	32.38	0.42	36.82	123.18	1.45	3.41
2		JB031-G3	1924	50.77	0.02	30.67	0.35	0.01	0.01	13.67	0.06	0.00	3.71	0.27	99.55	0.22	40.73	0.26	5.90	97.19	50.00	0.42	43.28	507.44	1.42	3.53
6		JB031-G3	1925	64.32	0.02	18.66	0.06	0.00	–	0.09	0.08	1.02	0.42	15.53	100.20	0.18	42.13	0.32	23.55	367.50	-340.40	9.61	33.37	2.18	4.86	0.39
1		JB031-G3	1930	49.38	0.01	31.60	0.34	0.02	0.01	14.61	0.07	0.00	3.06	0.21	99.31	0.22	69.96	0.25	6.07	65.04	50.47	0.41	38.60	292.35	1.58	4.21
3		JB031-G3	1931	48.63	–	32.31	0.32	0.01	0.02	15.19	0.08	0.00	2.73	0.15	99.44	0.22	-60.73	0.25	6.30	232.25	38.62	0.40	34.11	303.57	1.67	5.37
1		JB031-G3	1932	49.15	–	31.73	0.39	0.02	0.02	14.74	0.08	–	3.09	0.17	99.38	0.22	-139.89	0.25	5.54	62.58	49.38	0.41	36.65	-520.47	1.57	4.74
1		JB031-G4	1864	50.92	0.03	30.71	0.42	–	0.01	13.46	0.08	0.02	3.65	0.28	99.58	0.22	26.80	0.26	5.24	-1395.20	59.43	0.43	35.46	80.57	1.44	3.40
2		JB031-G4	1865	50.21	–	31.26	0.32	0.00	0.00	13.84	0.04	–	3.51	0.20	99.38	0.22	-169.96	0.25	6.38	335.46	234.48	0.42	63.52	-1876.10	1.47	4.37
1		JB031-G4	1866	50.67	0.01	30.87	0.39	0.01	0.01	13.52	0.07	0.01	3.67	0.25	99.50	0.22	48.03	0.26	5.50	100.00	71.00	0.42	40.17	107.96	1.43	3.67
2		JB031-G4	1867	50.58	0.02	31.19	0.37	–	0.02	14.00	0.07	–	3.44	0.21	99.90	0.22	38.74	0.25	5.71	-221.87	43.67	0.42	42.56	-588.78	1.48	4.15
3		JB031-G4	1868	48.26	–	32.50	0.39	0.01	0.01	15.47	0.08	–	2.68	0.13	99.53	0.22	-68.83	0.25	5.52	92.52	76.13	0.40	34.51	5000.00	1.70	5.77
1		PM-90	1080	53.34	0.04	29.97	0.30		0.02	12.50	0.02	–	4.32	0.29	100.80	0.21	21.07	0.26	6.62		44.15	0.45	172.34	-352.33	1.19	3.50
8		PM-90	1072	50.46	0.00	31.68	0.35		0.01	14.54	0.02	0.03	3.12	0.17	100.40	0.21	49.22	0.26	6.25		48.92	0.45	296.03	-40.04	1.21	3.57

				Data (wt%)											Analytical uncertainty (%)									
Tag	Tag*	Sample	ID	SiO2	TiO2	Al2O3	FeO	MnO	MgO	CaO	SrO	BaO	Na2O	K2O	Total	Si	Ti	Al	Fe	Mn	Mg	Ca	Sr	Ba	Na	K
2		PM-90	1073	53.80	0.05	30.04	0.30		0.01	12.46	0.03	–	4.28	0.28	101.26	0.21	50.39	0.26	7.09		93.21	0.44	-146.08	48.96	1.22	3.77
8		PM-90	1074	50.75	0.01	31.70	0.35		0.00	14.41	0.02	0.02	3.27	0.19	100.71	0.21	40.97	0.26	6.94		35.15	0.45	76.47	-2089.90	1.20	3.88
2		PM-90	1070	53.54	0.02	29.74	0.50		0.01	12.80	–	–	4.15	0.28	101.06	0.21	32.56	0.26	4.65		49.93	0.44	-174.88	-149.74	1.22	3.53
2		PM-90	1071	53.56	0.01	29.93	0.32		0.01	12.55	0.01	–	4.19	0.27	100.88	0.21	49.22	0.26	6.25		48.92	0.45	296.03	-40.04	1.21	3.57
2		PM-90	1053	53.31	0.01	30.20	0.27		0.01	12.78	–	0.03	4.14	0.26	101.03	0.21	50.39	0.26	7.09		93.21	0.44	-146.08	48.96	1.22	3.77
2		PM-90	1054	53.15	0.02	29.95	0.28		0.02	12.34	0.04	–	4.31	0.25	100.36	0.21	40.97	0.26	6.94		35.15	0.45	76.47	-2089.90	1.20	3.88
2		PM-90	1055	54.32	0.03	29.81	0.29		0.03	12.57	–	–	4.34	0.29	101.67	0.21	25.00	0.26	6.92		23.53	0.45	-348.06	-465.88	1.19	3.48
1		PM-90	1051	56.98	0.02	28.01	0.30		0.02	10.46	0.03	–	5.35	0.45	101.63	0.20	29.90	0.27	6.53		31.97	0.49	117.26	-290.28	1.06	2.66
2		PM-90	1052	53.79	0.02	29.76	0.36		0.03	12.38	–	0.01	4.29	0.29	100.96	0.21	31.80	0.26	5.77		25.53	0.45	-500.00	235.66	1.20	3.43
2		PM-90	1041	52.83	0.03	29.77	0.33		0.02	12.35	–	0.02	4.32	0.28	99.95	0.21	28.44	0.26	6.15		38.27	0.45	-474.15	84.80	1.19	3.54
2		PM-90	1042	52.71	0.02	30.25	0.29		0.02	12.81	–	0.00	4.18	0.23	100.52	0.21	34.26	0.26	6.50		41.37	0.44	-66.13	610.53	1.21	4.00
8		PM-35	1949	49.02	–	31.66	0.41	0.02	0.01	14.60	0.05	–	3.21	0.17	99.15	0.22	-101.89	0.25	5.30	57.58	84.87	0.41	52.45	-84.82	1.54	4.87
2		PM-35	1950	50.50	–	31.18	0.37	–	0.01	14.03	0.05	0.01	3.51	0.20	99.86	0.22	-92.63	0.25	5.69	-543.60	70.26	0.42	50.75	135.61	1.46	4.31
8		PM-35	1951	49.62	0.00	31.90	0.41	0.01	0.01	14.69	0.06	0.01	3.27	0.16	100.15	0.22	460.18	0.25	5.32	106.70	73.09	0.41	47.23	137.92	1.52	4.94
1		PM-35	1952	52.15	0.02	29.84	0.38	0.02	0.01	12.55	0.05	0.00	4.28	0.32	99.63	0.21	32.79	0.26	5.60	55.57	65.71	0.44	54.84	307.25	1.32	3.16
6		PM-35	1953	66.74	–	20.08	0.05	–	0.00	0.88	0.07	0.02	11.22	0.04	99.11	0.18	-77.20	0.32	29.02	-174.72	222.41	1.83	37.18	57.29	0.78	15.01
2		PM-35	1954	52.89	–	29.70	0.34	–	0.02	12.21	0.08	0.00	4.49	0.30	100.02	0.21	-196.40	0.26	6.07	-490.61	38.39	0.45	35.80	1847.93	1.28	3.25
1		PM-35	1955	52.39	–	30.02	0.38	0.01	0.01	12.60	0.06	0.00	4.34	0.30	100.11	0.21	-318.70	0.26	5.62	152.91	52.76	0.44	45.89	1477.31	1.31	3.28
3		PM-35	1956	49.28	0.00	31.83	0.39	0.00	0.02	14.77	0.02	0.01	3.07	0.19	99.59	0.22	299.20	0.25	5.55	1112.99	32.76	0.40	106.79	191.72	1.57	4.41
8		PM-35	1957	49.29	–	31.92	0.40	0.01	0.01	14.95	0.10	0.01	2.99	0.19	99.87	0.22	5000.00	0.25	5.42	89.01	61.19	0.40	30.19	204.48	1.60	4.50
8		PM-35	1958	38.37	–	26.22	8.59	0.12	0.00	23.69	0.15	–	0.03	0.01	97.18	0.25	-58.84	0.28	0.95	14.37	380.80	0.32	21.19	-326.87	45.41	59.80
8		PM-35	1959	49.17	–	31.95	0.31	–	0.02	14.75	0.09	0.02	3.06	0.17	99.54	0.22	-93.06	0.25	6.44	-730.50	44.56	0.41	33.33	54.40	1.58	4.80
2		PM-35	1960	52.43	0.01	29.71	0.31	0.00	0.02	12.41	0.06	0.00	4.32	0.33	99.61	0.21	85.02	0.26	6.38	619.57	40.11	0.44	44.49	713.75	1.31	3.10
8		PM-35	1961	49.42	–	31.60	0.34	0.01	0.01	14.53	0.10	0.03	3.19	0.20	99.42	0.22	-57.73	0.25	6.07	115.83	79.76	0.41	29.57	45.53	1.54	4.31
2		PM-0-1	1815	51.78	0.03	30.05	0.36	0.01	0.02	12.74	0.07	0.01	4.20	0.25	99.51	0.21	28.27	0.26	5.81	96.67	38.31	0.44	42.45	230.68	1.34	3.67
1		PM-0-1	1816	52.42	0.02	29.68	0.34	–	0.01	12.35	0.08	0.03	4.32	0.29	99.55	0.21	39.89	0.26	6.00	-562.65	59.80	0.45	33.84	51.24	1.31	3.36
8		PM-0-1	1818	50.18	–	31.30	0.39	–	0.01	14.21	0.07	–	3.30	0.19	99.65	0.22	-64.78	0.25	5.56	-118.77	63.06	0.41	42.52	-253.00	1.52	4.41
8		PM-0-1	1819	49.65	0.00	31.54	0.44	–	0.00	14.73	0.08	0.00	3.09	0.17	99.71	0.22	493.32	0.25	5.12	-141.23	171.01	0.41	34.64	425.34	1.57	4.84
8		PM-0-1	1820	49.89	0.00	31.64	0.43	0.01	0.01	14.50	0.03	0.03	3.10	0.18	99.84	0.22	257.43	0.25	5.13	102.70	66.66	0.41	78.96	41.84	1.57	4.67
3		PM-0-1	1822	51.37	–	30.53	0.34	–	0.01	13.26	0.05	0.00	3.84	0.25	99.65	0.21	-390.28	0.26	6.07	-827.60	68.73	0.43	49.93	823.77	1.40	3.73
2		PM-0-1	1823	52.52	0.01	29.77	0.31	0.02	0.01	12.28	0.09	0.00	4.42	0.30	99.75	0.21	48.13	0.26	6.38	63.11	52.06	0.45	31.04	636.54	1.30	3.28
2		PM-0-1	1824	52.44	0.01	29.82	0.36	0.01	0.01	12.48	0.08	–	4.19	0.30	99.70	0.21	48.45	0.26	5.78	144.57	117.89	0.44	33.85	-216.27	1.34	3.32
3		PM-0-1	1825	50.93	0.01	30.88	0.36	0.01	0.02	13.76	0.06	0.01	3.57	0.20	99.82	0.22	58.99	0.26	5.82	137.89	43.16	0.42	45.26	101.79	1.45	4.23
2		PM-0’	422	53.09	0.04	28.93	0.38			12.42	–	0.04	4.17	0.34	99.41	0.71	26.35	0.37	8.28			0.64	-54.91	44.06	1.77	4.50
3		PM-0’	424	51.88	0.03	30.55	0.38			14.12	–	0.01	3.49	0.22	100.68	0.72	31.52	0.36	8.25			0.60	-1173.30	158.43	1.94	6.23
1		PM-0’	426	53.00	0.03	29.37	0.48			12.96	0.03	0.02	3.89	0.29	100.10	0.71	28.99	0.37	6.91			0.62	169.64	100.38	1.84	5.01
3		PM-0’	427	50.53	0.03	30.49	0.43			14.06	0.08	0.00	3.43	0.20	99.28	0.73	30.18	0.36	7.73			0.60	65.24	2999.09	1.96	6.82
3		PM-0’	461	51.43	0.01	30.23	0.31			13.91	–	–	3.50	0.24	99.66	0.72	93.23	0.37	9.17			0.60	-108.59	-83.22	1.93	5.72
3		PM-0’	462	51.02	0.01	30.24	0.35			13.56	–	0.00	3.74	0.25	99.17	0.73	165.14	0.37	8.80			0.61	-76.87	737.25	1.87	5.36
2		PM-0’	463	53.73	0.04	29.16	0.32			11.88	–	0.04	4.33	0.34	99.87	0.71	25.91	0.37	9.15			0.65	-44.55	47.99	1.73	4.55
2		PM-0’	464	52.90	–	29.01	0.25			12.23	–	0.01	4.29	0.30	99.01	0.71	-87.02	0.37	10.76			0.64	-67.88	147.11	1.73	5.01
1		PM-0’	428	52.33	0.05	29.26	0.50			12.78	–	0.03	3.92	0.33	99.20	0.72	23.46	0.37	6.86			0.63	-75.49	76.88	1.82	4.67
3		PM-0’	429	50.49	0.01	30.86	0.38			14.20	–	–	3.26	0.20	99.42	0.73	86.24	0.36	7.97			0.60	-34.04	-64.21	2.01	6.31
8		PM-0’	430	49.53	0.02	31.19	0.30			14.86	0.04	–	2.97	0.17	99.09	0.74	41.20	0.36	9.58			0.58	123.24	-47.07	2.11	7.14
8		PM-0’	435	49.77	0.00	31.82	0.35			15.33	–	–	2.74	0.13	100.14	0.74	311.40	0.36	8.77			0.57	-52.69	-116.51	2.20	8.70
8		PM-0’	436	48.94	0.01	32.09	0.25			15.59	–	0.00	2.60	0.12	99.60	0.74	80.40	0.35	11.24			0.57	-233.99	2965.39	2.27	9.32
2		PM-0’	437	54.05	0.05	28.82	0.29			11.86	–	0.03	4.52	0.30	99.92	0.70	20.35	0.38	9.59			0.65	-61.40	73.58	1.68	4.97
3		PM-0’	452	49.28	0.02	31.46	0.36	0.02	0.02	14.96	–	0.01	2.77	0.16	99.04	0.74	45.79	0.36	8.55	124.97	63.86	0.58	-560.81	267.59	2.19	7.43
2		PM-0’	453	52.61	0.02	29.31	0.34	0.01	0.03	12.84	–	–	4.02	0.24	99.42	0.71	50.69	0.37	8.94	190.76	35.58	0.63	-73.32	-608.79	1.79	5.73
4		PM-0’	454	52.58	0.00	29.70	0.35	0.02	0.04	12.74	–	0.04	3.95	0.25	99.69	0.71	5000.00	0.37	8.47	87.65	28.90	0.63	-119.93	44.35	1.81	5.51
3		PM-0’	443	48.62	0.01	31.80	0.33			15.51	–	–	2.27	0.36	98.91	0.75	129.31	0.36	9.08			0.57	-101.36	-109.91	2.45	4.42
2		PM-0’	444	53.25	0.02	28.35	0.27			11.90	0.05	0.03	4.82	0.23	98.91	0.71	64.40	0.38	10.35			0.65	106.43	74.41	1.63	5.91
3		PM-0’	445	47.82	0.01	32.47	0.26			16.23	0.02	–	2.27	0.11	99.18	0.75	86.74	0.35	11.18			0.56	276.38	-75.08	2.43	10.68

				Data (wt%)												Analytical uncertainty (%)										
Tag	**Tag***	**Sample**	**ID**	**SiO2**	**TiO2**	**Al2O3**	**FeO**	**MnO**	**MgO**	**CaO**	**SrO**	**BaO**	**Na2O**	**K2O**	**Total**	**Si**	**Ti**	**Al**	**Fe**	**Mn**	**Mg**	**Ca**	**Sr**	**Ba**	**Na**	**K**
2		PM-0'	446	53.12	0.02	29.39	0.29			12.58	–	0.02	4.11	0.29	99.82	0.71	61.27	0.37	10.11			0.63	-86.65	121.37	1.78	5.07
3		PM-0'	477	49.52	0.01	33.52	0.32			15.70	0.04	0.02	2.40	0.15	101.72	0.74	82.64	0.35	9.40			0.57	122.27	122.32	2.37	7.99
3		PM-0'	478	49.65	0.01	33.52	0.35			15.50	–	0.03	2.61	0.13	101.82	0.74	88.94	0.35	8.67			0.57	-91.32	61.73	2.27	9.39
2		PM-0'	479	52.42	0.01	30.98	0.40			12.78	–	–	4.00	0.28	100.88	0.72	118.67	0.37	7.62			0.63	-106.40	-83.52	1.81	5.17
1		PM-0-2	1836	52.90	0.02	29.22	0.35	0.00	0.03	11.91	0.10	0.01	4.56	0.28	99.38	0.21	47.19	0.26	5.95	361.21	26.34	0.45	28.30	100.77	1.28	3.45
2		PM-0-2	1837	52.54	0.02	29.40	0.31	0.01	0.02	12.03	0.07	0.01	4.37	0.28	99.06	0.21	41.80	0.26	6.44	157.64	45.42	0.45	38.13	114.06	1.30	3.41
2		PM-0-2	1838	51.46	–	30.14	0.31	–	0.02	13.04	0.05	0.02	4.04	0.26	99.32	0.21	-237.18	0.26	6.44	-77.76	37.51	0.43	56.07	69.68	1.36	3.62
2		PM-0-2	1839	51.50	0.01	29.96	0.31	–	0.03	12.97	0.06	0.01	4.04	0.24	99.12	0.21	132.56	0.26	6.43	-113.58	29.30	0.43	45.25	236.02	1.36	3.84
1		PM-0-2	1840	52.58	0.01	29.72	0.31	0.00	0.03	12.60	0.05	0.01	4.16	0.27	99.75	0.21	66.06	0.26	6.45	2214.84	25.62	0.44	56.36	156.85	1.34	3.47
2		PM-0-2	1841	52.42	0.01	29.61	0.35	–	0.02	12.59	0.07	0.02	4.17	0.29	99.54	0.21	48.55	0.26	5.95	-539.51	31.09	0.44	39.32	77.48	1.34	3.36
2		PM-0-2	1842	52.03	–	29.78	0.31	0.01	0.01	12.55	0.06	0.01	4.25	0.28	99.30	0.21	-244.12	0.26	6.52	102.94	58.42	0.44	45.22	96.57	1.33	3.43
2		PM-0-2	1843	52.63	0.00	29.70	0.28	0.00	0.02	12.49	0.07	0.01	4.28	0.29	99.76	0.21	172.32	0.26	7.02	2061.90	39.46	0.44	41.46	173.56	1.32	3.33
1		PM-0-2	1844	52.40	0.00	29.90	0.33	–	0.03	12.62	0.11	0.01	4.23	0.28	99.92	0.21	241.49	0.26	6.16	-104.24	27.79	0.44	27.35	95.24	1.33	3.45
8		PM-0-2	1845	49.45	–	31.75	0.29	–	0.01	14.76	0.07	0.01	3.00	0.17	99.51	0.22	-41.37	0.25	6.79	-4966.50	69.77	0.41	41.30	184.40	1.60	4.71
8		PM-0-2	1846	50.10	–	31.40	0.30	0.01	0.01	14.42	0.09	0.01	3.23	0.18	99.76	0.22	-191.96	0.25	6.68	202.97	60.52	0.41	31.09	102.52	1.53	4.68
8		PM-0-2	1847	50.11	–	31.07	0.34	0.00	0.01	14.20	0.11	0.03	3.39	0.19	99.44	0.22	-426.70	0.25	6.11	364.28	122.06	0.41	26.46	50.16	1.50	4.46
4		PM+10	284	53.57	0.03	28.46	0.36			11.53	–	0.03	4.55	0.32	98.85	0.71	30.30	0.38	8.11			0.66	-146.74	56.43	1.69	4.73
4		PM+10	285	54.85	0.03	28.54	0.32			11.57	0.01	0.01	4.68	0.40	100.42	0.70	35.33	0.38	8.88			0.66	583.89	228.30	1.66	4.02
2		PM+10	286	51.29	0.03	27.91	1.96			11.28	–	–	4.19	0.37	97.03	0.72	34.57	0.38	3.02			0.67	-500.00	-292.88	1.77	4.34
4		PM+10	227	54.30	0.01	28.30	0.27			11.56	–	0.03	4.58	0.40	99.47	0.70	92.29	0.38	10.42			0.66	-96.45	66.98	1.68	4.04
4		PM+10	228	54.87	0.03	28.38	0.41			11.56	0.09	–	4.59	0.37	100.30	0.70	36.66	0.38	7.58			0.66	63.39	-64.34	1.68	4.30
4		PM+10	229	54.02	0.03	28.69	0.33			11.62	–	0.04	4.59	0.35	99.67	0.70	32.99	0.38	9.04			0.66	-145.76	54.82	1.68	4.46
4		PM+10	230	53.99	0.00	28.60	0.28			11.53	0.00	–	4.70	0.40	99.53	0.70	303.98	0.38	9.88			0.66	1154.87	-136.67	1.66	4.05
2		PM+10	207	53.07	0.02	28.65	0.29			11.59	–	0.01	4.66	0.36	98.67	0.71	52.71	0.38	10.34			0.66	-42.48	227.27	1.66	4.38
2		PM+10	208	53.53	0.01	28.69	0.19			11.51	–	0.02	4.71	0.40	99.06	0.71	105.71	0.38	13.61			0.66	-102.41	83.31	1.65	4.06
1		PM+10	209	51.94	0.03	29.66	0.22			12.93	–	–	4.07	0.28	99.14	0.72	36.99	0.37	11.97			0.63	-179.42	-65.65	1.79	5.16
2		PM+10	272	52.22	0.02	29.19	0.30			12.44	0.05	0.03	4.05	0.34	98.65	0.72	66.58	0.37	9.50			0.64	106.43	63.14	1.79	4.45
2		PM+10	273	51.87	0.05	29.34	0.25			12.58	0.00	0.04	3.94	0.31	98.38	0.72	21.99	0.37	11.54			0.64	1192.31	50.76	1.82	4.83
2		PM+10	274	52.21	0.04	29.12	0.27			12.45	–	0.05	4.08	0.33	98.54	0.72	27.11	0.37	10.37			0.64	-58.29	39.38	1.79	4.61
2		PM+10	275	52.59	0.04	29.13	0.34			12.39	–	–	4.14	0.33	98.97	0.71	22.78	0.37	8.65			0.64	-389.75	-105.09	1.77	4.58
3		PM+10	276	50.73	0.00	30.38	0.32			13.71	–	–	3.40	0.22	98.77	0.73	261.11	0.37	9.44			0.61	-76.92	-93.43	1.97	5.98
3		PM+10	277	50.68	0.02	30.43	0.40			13.86	0.05	–	3.44	0.20	99.08	0.73	57.36	0.36	7.72			0.60	114.89	-77.16	1.96	6.52
8		PM+10	279	61.63	0.02	23.45	1.51			11.75	–	0.03	1.65	0.07	100.13	0.65	46.39	0.41	3.51			0.66	-55.73	64.13	2.88	14.00
4		PM+10	270	53.23	0.03	28.60	0.46			11.66	–	0.00	4.50	0.27	98.78	0.71	30.62	0.38	7.20			0.66	-76.01	983.57	1.69	5.35
4		PM+10	271	53.57	0.01	28.62	0.30			11.43	–	–	4.73	0.32	98.99	0.71	85.84	0.38	9.59			0.67	-291.41	-149.29	1.65	4.84
4		PM+10	220	53.54	0.03	28.59	0.43			11.43	–	0.02	4.69	0.34	99.08	0.71	32.96	0.38	7.29			0.67	-81.40	102.71	1.66	4.56
4		PM+10	221	53.39	0.02	28.77	0.50			11.43	–	–	4.75	0.34	99.20	0.71	66.50	0.38	6.60			0.67	-59.31	-200.31	1.64	4.54
4		PM+10	222	54.11	0.03	28.26	0.23			11.30	0.02	0.03	4.54	0.35	98.87	0.70	32.28	0.38	11.74			0.67	274.21	54.95	1.69	4.50
4		PM+10	223	53.83	0.02	28.74	0.28			11.65	0.01	–	4.55	0.38	99.44	0.71	60.74	0.38	10.23			0.66	599.88	-757.26	1.69	4.26
4		PM+10	224	53.84	0.02	29.32	0.23			12.04	–	0.03	4.58	0.32	100.38	0.71	50.87	0.37	11.32			0.65	-221.66	61.15	1.68	4.82
4		PM+10	225	53.93	0.03	29.12	0.20			11.85	–	0.03	4.52	0.33	100.02	0.71	30.21	0.37	12.83			0.65	-64.17	69.57	1.69	4.75
4		PM+10	262	53.79	0.00	28.51	0.33			11.46	–	0.02	4.60	0.40	99.11	0.71	222.90	0.38	8.98			0.67	-67.31	101.75	1.68	4.12
4		PM+10	263	53.37	0.03	28.36	0.24			11.60	–	–	4.78	0.36	98.73	0.71	38.99	0.38	11.52			0.66	-162.19	-273.15	1.65	4.41
4		PM+10	264	53.11	0.03	28.43	0.36			11.70	0.00	0.01	4.59	0.39	98.63	0.71	31.33	0.38	8.24			0.66	1188.79	371.17	1.67	4.21
2		PM+10	258	52.50	0.02	29.69	0.28			12.47	0.13	–	4.15	0.31	99.54	0.72	52.04	0.37	10.18			0.64	39.71	-96.48	1.77	4.87
4		PM+10	259	53.18	0.02	28.75	0.68			11.77	–	–	4.46	0.35	99.19	0.71	61.18	0.38	5.48			0.66	-72.43	-81.48	1.71	4.40
4		PM+10	260	53.86	0.01	29.05	0.70			11.76	–	–	4.48	0.37	100.24	0.71	132.41	0.37	5.46			0.66	-143.59	-69.90	1.70	4.31
1		PM+10	261	52.33	0.02	29.21	0.37			12.55	–	0.02	4.00	0.35	98.84	0.72	67.04	0.37	8.51			0.63	-118.38	97.02	1.81	4.52
4		PM+10	265	53.31	0.05	28.77	0.28			11.61	–	0.03	4.44	0.33	98.86	0.71	18.21	0.38	10.36			0.66	-30.00	71.90	1.71	4.61
4		PM+10	266	53.74	0.05	28.50	0.26			11.62	–	0.01	4.50	0.31	99.04	0.71	22.00	0.38	10.58			0.66	-56.12	165.72	1.69	4.87
2		PM+10	267	52.57	0.02	28.89	0.24			12.02	–	0.00	4.38	0.32	98.45	0.71	41.19	0.37	11.62			0.65	-110.41	434.35	1.71	4.66
1		PM+10	268	52.54	0.03	29.15	0.35			12.50	0.01	–	4.04	0.32	98.96	0.71	29.43	0.37	8.69			0.64	393.06	-179.78	1.80	4.81
8		PM+10	236	48.84	0.00	32.55	0.27			15.95	–	0.01	2.40	0.14	100.15	0.75	277.87	0.35	10.15			0.56	-537.79	373.68	2.38	8.28

				Data (wt%)											Analytical uncertainty (%)									
Tag	Tag*	Sample	ID	SiO2	TiO2	Al2O3	FeO	MnO	MgO	CaO	SrO	BaO	Na2O	K2O	Total	Si	Ti	Al	Fe	Mn	Mg	Ca	Sr	Ba	Na	K
2		PM+10	237	52.62	0.03	28.84	0.24			11.76	–	0.03	4.44	0.30	98.27	0.71	29.31	0.38	11.80			0.66	-140.04	74.58	1.71	5.01
8		PM+10	238	48.49	0.01	32.02	0.25			15.51	–	0.02	2.66	0.11	99.09	0.75	91.15	0.36	11.21			0.57	-82.45	109.65	2.25	10.18
8		PM+10	239	49.90	0.01	31.12	0.24			14.38	–	0.02	3.13	0.23	99.04	0.74	79.21	0.36	12.40			0.59	-75.11	116.11	2.06	5.78
8		PM+10	240	49.41	0.02	31.41	0.27			14.97	0.07	–	2.84	0.18	99.17	0.74	66.77	0.36	10.39			0.58	77.46	-95.60	2.17	7.09
8		PM+10	241	49.65	0.01	31.70	0.21			14.84	–	0.01	2.78	0.15	99.37	0.74	83.99	0.36	11.93			0.58	-199.95	142.92	2.18	8.49
2		PM+10	242	50.74	0.03	30.31	0.23			13.70	–	0.00	3.59	0.24	98.86	0.73	39.06	0.37	12.20			0.61	-556.09	1012.49	1.91	5.74
2		PM+10	243	53.44	0.01	28.98	0.25			11.87	0.00	0.01	4.36	0.33	99.26	0.71	105.67	0.37	11.14			0.65	1130.48	148.63	1.72	4.69
1		PM+10	233	56.06	0.01	27.34	0.28			10.33	–	–	5.50	0.40	99.93	0.69	84.50	0.39	10.65			0.70	-54.90	-139.68	1.53	4.12
1		PM+10	234	54.93	0.03	27.60	0.26			10.60	–	–	5.26	0.42	99.12	0.70	35.70	0.38	10.23			0.69	-116.56	-157.42	1.56	3.93
2		PM+10	235	52.17	0.04	29.43	0.22			12.69	–	0.00	4.14	0.31	99.03	0.72	24.09	0.37	12.22			0.63	-95.72	426.36	1.77	4.79
1		PM+13	2008	51.57	0.02	29.66	0.38	0.00	0.04	12.91	0.05	0.01	4.00	0.28	98.93	0.21	34.71	0.26	5.58	717.89	22.13	0.43	53.03	120.11	1.37	3.38
2		PM+13	2009	51.44	0.01	29.57	0.35	–	0.03	12.63	0.06	0.01	4.11	0.28	98.48	0.21	71.16	0.26	5.95	-147.74	27.19	0.44	47.45	107.28	1.35	3.44
3		PM+13	2010	48.29	–	31.81	0.48	0.02	0.02	15.18	0.09	–	2.87	0.16	98.91	0.22	-55.85	0.25	4.81	84.49	35.90	0.40	32.69	-472.38	1.63	5.05
2		PM+13	2011	52.08	0.01	29.44	0.34	0.00	0.01	12.22	0.05	0.01	4.31	0.31	98.79	0.21	75.32	0.26	5.99	262.19	56.32	0.45	54.79	190.54	1.31	3.20
1		PM+13	2012	54.35	–	27.44	0.34	0.00	0.02	10.20	0.05	0.01	5.48	0.36	98.26	0.21	-30.57	0.27	5.97	270.01	38.01	0.49	54.96	193.88	1.15	2.92
2		PM+13	2013	51.86	0.01	29.57	0.37	0.01	0.03	12.67	0.05	0.01	4.10	0.27	98.94	0.21	62.92	0.26	5.69	172.90	29.25	0.44	55.08	198.58	1.35	3.46
3		PM+13	2014	52.53	–	29.37	0.37	0.01	0.02	12.34	0.11	0.00	4.38	0.30	99.43	0.21	-62.98	0.26	5.71	126.03	46.94	0.44	26.27	361.09	1.30	3.30
6		PM+13	2015	66.06	–	20.65	0.05	0.01	0.01	1.25	0.05	0.03	10.71	0.59	99.40	0.19	-31.96	0.32	25.56	216.04	78.69	1.49	48.64	50.37	0.80	2.20
6		PM+13	2016	65.31	–	20.10	0.13	0.04	0.04	2.16	0.10	–	10.99	0.01	98.87	0.19	-26.40	0.32	12.57	36.57	19.08	1.10	28.96	-134.52	0.79	52.27
8		PM+13	2017	50.41	–	30.87	0.37	0.00	0.03	13.98	0.06	0.01	3.48	0.21	99.41	0.22	-44.80	0.25	5.68	2737.72	28.86	0.42	45.95	175.29	1.47	4.20
8		PM+13	2018	49.92	0.00	30.78	0.34	0.02	0.02	13.93	0.09	0.01	3.71	0.20	99.02	0.22	223.10	0.26	5.98	73.50	33.65	0.42	31.35	251.51	1.42	4.23
8		PM+13	2019	49.43	–	31.34	0.36	0.01	0.01	14.89	0.09	0.01	3.06	0.15	99.34	0.22	-48.48	0.25	5.81	126.73	70.24	0.40	32.14	178.74	1.58	5.35
1		PM+30	1963	52.79	0.01	29.15	0.26	0.00	0.02	11.79	0.08	0.01	4.47	0.32	98.90	0.21	54.60	0.26	7.31	959.95	39.53	0.45	35.82	104.66	1.29	3.15
2		PM+30	1964	51.60	0.01	29.38	0.28	–	0.01	12.09	0.09	0.01	4.45	0.34	98.25	0.21	59.66	0.26	6.92	-1699.80	127.36	0.45	30.70	125.41	1.29	3.03
8		PM+30	1967	51.00	–	30.31	0.35	0.02	0.02	12.99	0.06	–	3.91	0.22	98.88	0.22	-91.21	0.26	5.91	62.67	31.92	0.43	45.66	-1052.80	1.38	4.03
1		PM+30	1968	52.74	0.02	29.58	0.36	–	0.02	12.25	0.11	0.01	4.24	0.34	99.68	0.21	38.14	0.26	5.77	-721.01	34.25	0.45	26.24	108.68	1.32	3.00
2		PM+30	1969	53.04	0.00	29.37	0.34	–	0.02	11.87	0.09	0.01	4.47	0.39	99.61	0.21	216.05	0.26	6.04	-367.72	39.61	0.45	31.38	98.71	1.29	2.77
3		PM+41	360	50.96	0.01	30.58	0.40			13.75	0.08	0.02	3.56	0.23	99.59	0.73	77.74	0.36	7.76			0.61	71.81	111.77	1.91	5.78
2		PM+41	361	52.46	0.01	29.44	0.34			12.52	–	–	4.10	0.29	99.17	0.72	82.03	0.37	8.95			0.64	-75.70	-86.03	1.78	5.06
3		PM+41	362	47.86	0.01	32.06	0.32			15.95	–	0.02	2.35	0.11	98.69	0.75	84.44	0.35	9.50			0.56	-127.12	113.29	2.41	10.49
2		PM+41	363	53.66	0.04	28.70	0.26			11.81	–	–	4.49	0.34	99.30	0.71	27.46	0.38	11.03			0.66	-180.07	-325.22	1.69	4.49
8		PM+41	336	49.20	–	31.90	0.26			15.28	–	–	2.92	0.13	99.68	0.74	-112.36	0.36	11.05			0.57	-586.22	-323.24	2.13	9.00
8		PM+41	337	51.07	0.03	30.05	0.31			13.34	–	0.01	3.82	0.25	98.89	0.73	34.64	0.37	9.16			0.62	-132.83	169.77	1.85	5.42
2		PM+41	338	52.09	0.02	29.33	0.31			12.19	–	0.01	4.29	0.30	98.55	0.72	58.64	0.37	9.09			0.64	-500.00	130.62	1.74	4.92
2		PM+41	339	52.32	0.02	29.51	0.29			12.25	0.08	0.01	4.16	0.30	98.95	0.72	45.75	0.37	9.59			0.64	73.42	196.71	1.77	4.99
8		PM+41	340	49.17	–	31.61	0.24			15.08	–	0.01	2.86	0.17	99.14	0.74	-124.45	0.36	11.78			0.58	-299.76	306.57	2.15	7.27
2		PM+41	343	52.44	0.02	29.05	0.32			12.04	–	0.01	4.39	0.30	98.58	0.72	48.90	0.37	9.55			0.65	-128.12	243.79	1.71	4.96
3		PM+41	356	48.74	0.01	31.97	0.68			15.17	–	0.01	2.71	0.11	99.44	0.75	95.60	0.36	5.67			0.57	-232.28	139.05	2.24	10.25
2		PM+41	357	51.80	0.02	28.87	0.45			11.98	–	0.01	4.21	0.26	97.63	0.72	40.73	0.38	7.24			0.65	-191.34	249.94	1.76	5.44
2		PM+41	358	52.93	0.02	29.44	0.35			12.57	–	0.04	4.08	0.30	99.74	0.71	44.44	0.37	8.48			0.64	-160.95	47.57	1.79	4.97
2		PM+41	359	52.74	0.03	29.56	0.27			12.88	–	–	4.01	0.31	99.80	0.71	29.86	0.37	9.99			0.63	-135.74	-153.32	1.80	4.94
3		PM+41	331	50.08	0.02	30.58	0.24			14.02	–	0.01	3.33	0.21	98.50	0.73	56.70	0.36	10.87			0.60	-63.06	129.46	1.99	6.31
3		PM+41	332	47.40	–	33.22	0.30			16.90	–	0.00	1.93	0.07	99.83	0.76	-516.84	0.35	9.67			0.54	-74.47	595.02	2.66	14.57
3		PM+41	333	48.17	–	32.20	0.25			15.70	–	–	2.42	0.11	98.88	0.75	-252.14	0.35	11.71			0.57	-63.80	-1539.10	2.36	10.17
2		PM+41	334	54.05	0.02	28.53	0.26			11.40	–	0.00	4.74	0.38	99.37	0.70	61.22	0.38	10.45			0.67	-205.35	3021.20	1.64	4.29
1		PM+41	335	52.13	0.04	29.24	0.29			12.39	–	0.00	4.21	0.30	98.63	0.72	28.76	0.37	9.62			0.64	-99.15	426.38	1.75	4.95
3		PM+41	310	50.10	0.01	30.91	0.32			14.66	–	0.00	3.11	0.18	99.28	0.73	138.59	0.36	8.87			0.59	-103.22	1513.47	2.06	6.81
3		PM+41	311	48.80	0.01	30.77	0.71			14.47	–	–	2.90	0.17	97.82	0.75	182.82	0.36	5.52			0.59	-62.03	-203.59	2.14	7.40
3		PM+41	312	49.55	0.01	31.45	0.26			14.82	0.00	0.02	2.98	0.17	99.28	0.74	83.34	0.36	10.71			0.58	1189.43	96.20	2.11	7.07
2		PM+41	313	51.27	0.02	29.99	0.22			13.37	–	0.03	3.84	0.23	99.00	0.73	63.14	0.37	12.52			0.62	-88.68	56.50	1.84	5.77
2		PM+41	314	51.95	0.03	29.14	0.22			12.54	0.01	–	4.25	0.30	98.48	0.72	35.51	0.37	12.40			0.64	592.26	-494.30	1.74	5.00
3		PM+41	315	49.29	0.01	30.85	0.27			14.07	0.01	0.02	3.40	0.19	98.14	0.74	72.24	0.36	10.29			0.60	363.79	98.75	1.96	6.93
3		PM+41	316	48.40	0.02	31.90	0.26			15.30	0.07	0.00	2.72	0.16	98.86	0.75	44.25	0.36	10.83			0.57	75.72	518.50	2.21	7.49

				Data (wt%)												Analytical uncertainty (%)										
Tag	**Tag***	**Sample**	**ID**	**SiO2**	**TiO2**	**Al2O3**	**FeO**	**MnO**	**MgO**	**CaO**	**SrO**	**BaO**	**Na2O**	**K2O**	**Total**	**Si**	**Ti**	**Al**	**Fe**	**Mn**	**Mg**	**Ca**	**Sr**	**Ba**	**Na**	**K**
2		PM+41	295	53.16	0.04	29.08	0.30			12.22	0.01	0.03	4.39	0.22	99.46	0.71	23.49	0.37	9.38			0.64	344.82	75.81	1.71	6.09
2		PM+41	296	53.66	0.03	26.54	1.64			10.10	0.02	–	4.95	0.27	97.22	0.71	36.18	0.39	3.36			0.71	223.69	-1519.20	1.63	5.31
8		PM+48	1132	48.74	0.02	32.66	0.33		0.01	15.46	0.01	0.00	2.60	0.14	99.98	0.22	38.18	0.25	6.16		60.12	0.40	333.68	423.52	1.57	5.90
2		PM+48	1133	53.10	0.03	30.04	0.24		0.01	12.57	0.02	0.01	4.23	0.28	100.54	0.21	22.19	0.26	7.54		120.62	0.45	137.89	110.07	1.20	3.52
3		PM+48	1134	49.48	0.01	32.49	0.29		0.02	15.17	–	0.02	2.87	0.16	100.51	0.22	48.86	0.25	6.52		40.87	0.40	-196.26	62.34	1.49	5.16
2		PM+48	1135	53.86	0.02	29.80	0.27		0.03	12.29	–	0.01	4.41	0.30	100.99	0.21	34.44	0.26	7.04		29.63	0.45	-181.02	170.56	1.18	3.32
4		PM+48	1129	52.97	0.04	30.17	0.43		0.02	12.44	–	0.02	4.15	0.28	100.54	0.21	19.62	0.26	5.12		37.46	0.45	-433.14	82.62	1.22	3.52
4		PM+48	1130	53.71	0.02	29.85	0.41		0.02	12.27	–	0.01	4.45	0.31	101.09	0.21	36.87	0.26	5.18		30.26	0.45	-141.36	142.97	1.18	3.33
2		PM+48	1131	53.48	0.02	30.03	0.24		0.00	12.32	–	0.03	4.43	0.29	100.86	0.21	35.63	0.26	7.92		339.52	0.45	-100.46	43.40	1.18	3.48
8		PM+48	1124	48.34	0.01	29.53	0.20		0.00	17.13	0.11	0.00	3.16	0.01	98.52	0.22	61.55	0.26	9.02		595.74	0.38	32.97	357.22	1.42	39.29
2		PM+48	1125	51.23	0.03	29.14	2.14		0.66	11.38	–	0.01	4.05	0.39	99.01	0.21	21.94	0.27	1.99		2.45	0.47	-74.52	225.65	1.25	2.89
8		PM+48	1127	48.23	0.00	33.64	0.26		0.01	16.49	0.02	–	2.11	0.08	100.84	0.22	239.46	0.25	7.38		91.40	0.39	179.74	-80.64	1.74	8.80
2		PM+48	1128	53.46	0.03	30.04	0.26		0.02	12.35	0.04	0.02	4.43	0.28	100.93	0.21	28.96	0.26	7.51		46.38	0.45	87.04	57.49	1.18	3.53
2		PM+48	1121	52.61	0.02	29.55	0.32		0.03	12.19	–	0.01	4.36	0.32	99.43	0.21	36.28	0.26	6.26		28.35	0.45	-69.61	124.60	1.19	3.14
3		PM+48	1122	49.73	0.01	31.93	0.27		0.01	14.44	0.00	–	3.18	0.20	99.76	0.22	122.13	0.25	7.32		86.77	0.41	711.27	-133.51	1.41	4.43
2		PM+48	1123	53.51	0.02	29.53	0.30		0.03	12.30	–	0.01	4.40	0.29	100.38	0.21	35.04	0.26	6.74		27.91	0.45	-500.00	129.64	1.18	3.49
3		PM+48	1114	51.67	0.01	31.05	0.32		0.03	13.83	–	–	3.64	0.21	100.77	0.21	79.94	0.26	6.32		25.84	0.42	-73.13	-43.79	1.31	4.29
3		PM+48	1115	51.52	0.01	31.46	0.32		0.02	14.10	0.03	–	3.42	0.21	101.11	0.21	58.65	0.26	6.24		36.24	0.42	91.01	-93.43	1.35	4.28
2		PM+48	1116	53.67	0.01	30.22	0.29		0.01	12.62	0.04	–	4.22	0.29	101.37	0.21	68.81	0.26	6.68		52.81	0.44	71.59	-4293.90	1.21	3.51
2		PM+48	1117	52.91	0.03	30.26	0.28		0.01	12.73	0.01	0.04	4.21	0.26	100.73	0.21	20.34	0.26	6.92		70.60	0.44	337.45	37.70	1.21	3.74
2		PM+48	1102	53.09	0.02	30.05	0.35		0.02	12.53	–	0.00	4.28	0.26	100.59	0.21	31.67	0.26	5.80		51.28	0.45	-110.09	1414.50	1.20	3.69
8		PM+48	1103	49.89	0.01	31.95	0.24		0.02	14.57	0.01	0.01	3.20	0.15	100.06	0.22	118.16	0.25	7.66		49.12	0.41	283.67	157.93	1.40	5.43
2		PM+48	1104	54.27	0.03	29.72	0.29		0.03	11.88	–	–	4.58	0.32	101.12	0.21	25.83	0.26	6.72		29.01	0.46	-46.18	-239.03	1.16	3.27
8		PM+48	1097	49.83	0.01	32.46	0.28		0.02	15.16	–	0.01	2.89	0.16	100.82	0.22	49.61	0.25	6.86		43.58	0.40	-94.00	192.38	1.48	5.05
2		PM+48	1098	54.05	0.04	29.63	0.35		0.01	12.20	0.02	0.01	4.48	0.31	101.13	0.21	17.00	0.26	5.98		50.30	0.45	128.28	132.33	1.17	3.26
8		PM+48	1100	48.69	–	33.32	0.27		0.01	16.13	0.00	0.01	2.29	0.11	100.84	0.22	-345.21	0.25	7.02		48.12	0.39	711.17	129.23	1.67	7.12
2		PM+48	1101	53.83	0.04	29.44	0.32		0.00	12.07	0.05	0.00	4.59	0.31	100.67	0.21	20.49	0.26	6.18		248.16	0.46	63.31	4257.05	1.15	3.30
2		PM+48	1093	54.00	0.02	30.25	0.24		0.02	12.60	–	–	4.22	0.27	101.62	0.21	33.45	0.26	7.93		35.47	0.45	-157.48	-522.62	1.21	3.55
1		PM+48	1087	55.07	0.04	29.49	0.23		0.01	11.88	0.03	–	4.70	0.33	101.80	0.20	20.58	0.26	8.29		92.29	0.46	89.70	-614.74	1.14	3.15
2		PM+70	1992	50.89	0.00	30.34	0.25	–	0.01	12.98	0.06	–	3.99	0.22	98.73	0.22	5000.00	0.26	7.58	-87.17	77.17	0.43	48.63	-328.68	1.37	4.05
3		PM+70	1993	49.69	–	31.26	0.33	0.02	0.02	14.32	0.06	0.01	3.38	0.16	99.24	0.22	-214.19	0.25	6.13	81.67	31.34	0.41	48.87	112.89	1.50	5.01
3		PM+70	1994	48.33	–	32.56	0.32	0.01	0.01	15.58	0.08	0.00	2.67	0.12	99.67	0.22	-197.94	0.25	6.35	156.47	92.73	0.39	37.45	2323.25	1.70	6.06
2		PM+70	1995	51.70	0.00	30.23	0.30	0.01	0.02	12.93	0.10	0.01	3.98	0.24	99.51	0.21	289.94	0.26	6.54	231.20	48.35	0.43	29.57	109.20	1.37	3.74
1		PM+70	1996	52.21	0.00	29.90	0.26	0.01	0.02	12.35	0.06	0.01	4.29	0.25	99.36	0.21	299.75	0.26	7.21	218.12	32.56	0.44	42.92	128.82	1.31	3.74
1		PM+70	1997	51.25	–	30.23	0.30	–	0.01	12.97	0.05	0.01	3.97	0.24	99.02	0.21	-818.33	0.26	6.55	-451.03	80.52	0.43	56.79	104.96	1.37	3.80
3		PM+70	1998	47.70	–	32.88	0.41	0.02	0.01	15.81	0.06	0.01	2.59	0.11	99.60	0.22	-58.13	0.25	5.33	72.72	72.13	0.39	47.05	108.95	1.73	6.41
2		PM+70	1999	50.51	–	29.13	1.52	0.04	1.10	12.23	0.08	0.02	3.85	0.23	98.70	0.22	-94.27	0.26	2.39	35.18	1.93	0.45	35.05	85.42	1.40	3.86
8		PM+110	2075	49.70	–	32.13	0.22	–	0.01	15.16	0.04	–	2.86	0.12	100.25	0.22	-362.83	0.25	8.21	-1688.30	69.04	0.40	68.63	-4409.80	1.63	6.09
2		PM+110	2078	52.81	0.01	29.92	0.28	0.01	0.01	12.67	0.05	0.01	4.09	0.27	100.14	0.21	91.15	0.26	6.89	100.13	129.27	0.44	51.20	110.23	1.35	3.47
2		PM+110	2079	53.00	0.02	29.74	0.29	–	0.02	12.49	0.03	0.01	4.29	0.28	100.18	0.21	44.48	0.26	6.68	-228.38	38.86	0.44	77.03	102.55	1.31	3.43
2		PM+110	2080	53.28	0.02	29.28	0.27	–	0.03	12.26	0.05	0.02	4.34	0.25	99.82	0.21	31.51	0.26	7.05	-111.13	27.59	0.45	49.54	69.23	1.31	3.64
1		PM+110	2081	53.03	0.01	29.42	0.34	–	0.02	12.27	0.08	0.03	4.53	0.28	100.02	0.21	63.73	0.26	6.02	-341.45	30.79	0.45	34.36	48.72	1.28	3.44
3		PM+110	2082	52.82	0.01	29.69	0.23	0.00	0.02	12.72	0.06	0.00	4.29	0.23	100.06	0.21	124.83	0.26	7.99	1191.32	41.86	0.44	46.17	1711.63	1.31	3.93
2		PM+110	2083	54.35	–	28.42	0.34	0.01	0.01	11.32	0.06	0.02	4.86	0.33	99.72	0.21	-208.79	0.27	6.02	211.98	65.31	0.46	42.32	66.85	1.23	3.09
2		PM+110	2084	52.92	0.02	29.71	0.31	0.01	0.01	12.67	0.08	0.01	4.25	0.27	100.25	0.21	42.98	0.26	6.44	173.26	97.24	0.44	36.93	117.94	1.32	3.51
1		PM+110	2085	53.42	0.04	29.25	0.23	0.02	0.02	11.98	0.08	–	4.63	0.29	99.95	0.21	20.70	0.26	8.06	70.08	43.23	0.45	35.10	-323.70	1.26	3.32
3		PM+110	2086	52.37	0.01	30.23	0.32	0.00	0.02	12.90	0.04	0.02	4.21	0.25	100.38	0.21	62.38	0.26	6.28	278.26	43.99	0.43	59.76	63.43	1.33	3.72
3		PM+110	2087	52.14	–	30.07	0.32	0.01	0.01	13.03	0.07	0.01	4.02	0.24	99.92	0.21	-193.42	0.26	6.31	95.10	57.42	0.43	42.14	95.18	1.36	3.76
2		PM+145	367	52.74	0.01	29.31	0.23			12.52	–	–	4.24	0.27	99.33	0.71	70.47	0.37	11.82			0.64	-54.91	-225.89	1.75	5.39
3		PM+145	368	49.15	0.03	31.59	0.32			15.37	–	0.03	2.77	0.14	99.39	0.74	34.15	0.36	8.97			0.57	-64.16	66.61	2.20	9.03
2		PM+145	369	52.92	0.02	29.25	0.31			12.58	–	–	4.28	0.23	99.59	0.71	53.38	0.37	9.83			0.63	-43.85	-228.81	1.74	6.05
2		PM+145	391	52.82	0.02	29.50	0.24			12.85	0.02	0.04	4.09	0.23	99.82	0.71	56.16	0.37	11.91			0.63	237.58	53.06	1.79	5.99
3		PM+145	392	51.02	0.00	30.71	0.28			14.13	–	0.01	3.33	0.16	99.64	0.73	799.78	0.36	10.38			0.60	-63.81	212.86	1.98	7.82

				Data (wt%)											Analytical uncertainty (%)									
Tag	**Tag***	**Sample**	**ID**	**SiO2**	**TiO2**	**Al2O3**	**FeO**	**MnO**	**MgO**	**CaO**	**SrO**	**BaO**	**Na2O**	**K2O**	**Total**	**Si**	**Ti**	**Al**	**Fe**	**Mn**	**Mg**	**Ca**	**Sr**	**Ba**	**Na**	**K**
2		PM+145	393	52.77	0.01	29.31	0.18			12.49	–	–	4.19	0.23	99.21	0.71	73.57	0.37	14.08			0.64	-500.00	-597.56	1.76	5.88
2		PM+145	394	52.51	0.03	29.83	0.34			13.19	0.07	0.03	3.77	0.19	99.95	0.72	40.38	0.37	8.80			0.62	78.25	70.69	1.88	6.74
3		PM+145	395	48.80	0.01	32.28	0.36			15.74	–	0.05	2.61	0.11	99.98	0.75	82.64	0.35	8.13			0.56	-172.00	36.84	2.26	10.81
4		PM+145	396	51.50	0.03	29.92	0.39			12.98	–	0.02	3.91	0.23	99.00	0.72	32.70	0.37	7.93			0.62	-564.32	120.02	1.83	6.07
2		PM+145	397	51.78	0.01	29.90	0.26			13.04	–	0.01	3.86	0.25	99.11	0.72	69.61	0.37	10.97			0.62	-286.97	204.27	1.84	5.57
3		PM+145	398	48.96	0.00	30.64	0.37			14.64	0.04	–	2.95	0.18	97.78	0.74	261.91	0.36	8.56			0.59	120.19	-68.79	2.13	7.11
8		PM+145	407	51.59	0.01	30.21	0.18			14.60	–	0.01	2.18	0.09	98.89	0.72	114.75	0.36	14.54			0.59	-51.02	307.55	2.47	11.84
2		PM+145	408	52.88	0.01	29.08	0.36			12.17	0.08	–	4.37	0.26	99.20	0.71	111.03	0.37	8.91			0.65	72.35	-75.07	1.72	5.63
8		PM+145	409	49.55	–	31.91	0.12			15.58	–	0.02	2.09	0.09	99.38	0.74	5000.00	0.35	19.78			0.57	-177.92	85.96	2.55	12.51
2		PM+145	410	52.26	0.03	29.44	0.23			12.77	–	–	4.00	0.24	98.98	0.72	29.32	0.37	11.78			0.63	-218.04	-595.58	1.81	5.66
2		PM+145	414	50.87	0.02	28.77	0.24			13.21	–	0.01	3.74	0.23	97.09	0.73	53.36	0.38	11.52			0.62	-135.62	216.87	1.88	6.05
3		PM+145	418	51.73	0.03	30.31	0.29			13.72	–	0.01	3.43	0.21	99.74	0.72	37.88	0.37	9.52			0.61	-53.25	185.41	1.96	6.13
2		PM+145	419	52.56	0.03	29.59	0.23			12.84	–	0.01	4.00	0.24	99.50	0.71	31.03	0.37	11.95			0.63	-36.05	140.49	1.81	5.83
1		PM+145	420	54.38	0.03	28.46	0.22			11.67	–	0.00	4.70	0.29	99.75	0.70	32.94	0.38	12.83			0.66	-85.09	990.36	1.65	5.01
1		PM+260	1980	51.79	0.00	29.80	0.26	0.00	0.02	12.49	0.08	0.01	4.25	0.21	98.91	0.21	803.31	0.26	7.40	263.02	48.07	0.44	35.68	117.38	1.32	4.18
2		PM+260	1981	53.00	0.12	28.07	1.92	0.03	0.20	10.34	0.06	0.02	5.14	0.25	99.15	0.21	6.87	0.27	2.10	53.04	5.53	0.49	47.82	60.55	1.21	3.75
4		PM+260	1982	50.60	–	30.69	0.32	0.00	0.01	13.48	0.09	0.00	3.76	0.21	99.17	0.22	-570.61	0.26	6.28	289.17	52.91	0.42	33.32	449.82	1.41	4.14
1		PM+260	1983	49.57	0.00	30.01	0.24	0.01	0.02	13.21	0.06	0.01	3.97	0.21	97.31	0.22	998.63	0.26	7.68	235.18	47.35	0.43	45.57	123.65	1.37	4.15
3		PM+260	1984	49.25	–	31.56	0.31	0.01	0.01	14.34	0.06	0.00	3.32	0.17	99.02	0.22	-201.26	0.25	6.39	186.20	98.37	0.41	42.80	5000.00	1.51	4.87
1		PM+380	2028	52.56	0.02	29.19	0.31	–	0.02	12.25	0.04	–	4.48	0.25	99.11	0.21	37.56	0.26	6.36	-286.11	45.16	0.45	72.47	-278.47	1.29	3.67
2		PM+380	2029	52.12	0.01	29.70	0.30	–	0.02	12.95	0.06	0.02	4.11	0.24	99.53	0.21	52.96	0.26	6.59	-331.56	33.12	0.43	43.39	66.07	1.35	3.84
2		PM+380	2030	52.97	0.02	29.05	0.27	0.01	0.03	12.02	0.05	0.00	4.56	0.29	99.26	0.21	41.26	0.26	7.16	122.19	27.23	0.45	55.03	307.76	1.27	3.34
2		PM+380	2031	51.78	0.02	30.00	0.29	0.00	0.02	12.97	0.11	0.01	4.10	0.25	99.54	0.21	37.62	0.26	6.75	470.30	39.60	0.43	26.66	229.24	1.35	3.72
3		PM+380	2032	49.37	–	31.54	0.33	–	0.02	14.65	0.05	–	3.13	0.11	99.20	0.22	-84.57	0.25	6.16	-2026.40	40.72	0.41	59.31	-850.69	1.56	6.50
3		PM+380	2033	49.48	–	31.38	0.32	0.00	0.01	14.48	0.08	0.00	3.23	0.14	99.13	0.22	-302.92	0.25	6.29	415.91	124.99	0.41	34.14	269.75	1.53	5.46
2		PM+380	2034	51.42	0.00	30.22	0.32	0.01	0.02	13.31	0.05	–	3.85	0.20	99.42	0.21	187.25	0.26	6.27	128.55	30.83	0.43	52.85	-329.65	1.39	4.26
1		PM+380	2035	52.23	0.01	29.79	0.26	0.01	0.02	12.83	0.07	0.01	4.05	0.22	99.51	0.21	88.52	0.26	7.22	107.53	38.10	0.44	38.72	129.75	1.36	3.99
3		PM+380	2036	50.87	–	30.68	0.31	0.01	0.01	13.93	0.05	0.01	3.51	0.17	99.56	0.22	-57.91	0.26	6.42	103.87	61.96	0.42	55.12	97.47	1.47	4.78
3		PM+380	2037	50.40	–	31.12	0.32	0.01	0.01	14.26	0.10	0.02	3.39	0.17	99.81	0.22	-85.81	0.25	6.29	124.10	50.44	0.41	28.09	83.14	1.49	4.78
8		PM+380	2039	47.52	–	32.58	0.24	0.01	0.02	16.49	0.10	–	2.32	0.08	99.36	0.22	-47.34	0.25	7.75	147.87	42.35	0.38	28.10	-1130.50	1.83	8.31
3		PM+380	2042	47.41	–	33.00	0.38	–	0.01	16.28	0.03	–	2.31	0.06	99.47	0.22	-66.28	0.25	5.65	-3476.60	74.58	0.39	85.81	-169.71	1.83	11.30
2		PM+380	2043	50.77	0.00	30.40	0.35	–	0.01	13.47	0.07	–	3.84	0.18	99.09	0.22	303.54	0.26	5.89	-406.82	65.51	0.42	38.61	-242.41	1.40	4.65
1		PM+380	2044	51.26	0.00	30.45	0.29	0.02	0.02	13.68	0.07	0.02	3.81	0.18	99.80	0.21	146.81	0.26	6.78	76.46	41.22	0.42	39.77	73.29	1.40	4.56
1		PM+550	2058	54.36	0.00	28.54	0.26	0.01	0.02	11.40	0.08	0.01	4.92	0.34	99.95	0.21	211.92	0.27	7.27	131.11	34.40	0.46	36.02	168.52	1.22	3.05
2		PM+550	2059	51.42	–	30.82	0.34	0.01	0.03	13.73	0.07	0.00	3.69	0.21	100.32	0.21	-110.03	0.25	5.99	181.77	27.60	0.42	39.72	319.65	1.43	4.18
3		PM+550	2060	47.29	–	33.41	0.36	–	0.01	17.04	0.03	0.01	1.88	0.06	100.08	0.22	-79.46	0.24	5.86	-137.76	52.56	0.38	100.10	236.28	2.05	10.30
2		PM+550	2061	51.28	0.01	30.49	0.35	0.01	0.03	13.80	0.08	0.01	3.66	0.21	99.92	0.21	76.84	0.26	5.88	212.22	29.04	0.42	36.02	108.58	1.43	4.16
2		PM+550	2062	53.37	0.03	29.22	0.29	–	0.01	12.30	0.10	0.00	4.61	0.20	100.14	0.21	21.20	0.26	6.70	-1786.90	61.98	0.44	29.17	5000.00	1.27	4.26
1		PM+550	2063	51.90	0.01	30.13	0.35	–	0.03	13.35	0.07	0.01	3.90	0.20	99.95	0.21	101.49	0.26	5.90	-253.37	28.67	0.43	39.90	101.99	1.38	4.23
3		PM+550	2064	46.08	–	34.47	0.24	0.00	0.00	17.91	0.05	0.00	1.35	0.04	100.14	0.23	-59.15	0.24	7.66	1311.44	602.65	0.37	59.43	705.91	2.45	15.17
Blocks in the Mooimeisjesfontein area																										
2	-3	PM-X1	2333	52.30	0.00	30.04	0.31	0.02	0.03	12.82	0.09	0.01	4.34	0.24	100.21	0.21	266.82	0.26	6.26	68.23	27.46	0.43	29.44	100.37	1.34	3.59
2	-3	PM-X1	2334	52.86	0.01	29.74	0.27	0.01	0.01	12.30	0.03	0.02	4.67	0.27	100.19	0.21	76.60	0.26	6.82	105.09	96.21	0.44	75.79	59.69	1.29	3.37
1	0	PM-X1	2335	52.13	–	30.28	0.28	0.01	0.01	12.82	0.09	0.01	4.36	0.26	100.26	0.21	-407.85	0.26	6.63	126.74	50.83	0.43	30.53	119.57	1.34	3.43
2	0	PM-X1	2336	52.68	0.01	29.71	0.33	0.02	0.03	12.36	0.08	0.01	4.54	0.30	100.07	0.21	89.35	0.26	5.98	70.64	26.50	0.44	31.92	108.45	1.31	3.17
1	0	PM-X1	2337	52.30	0.00	30.06	0.37	–	0.03	12.73	0.07	0.01	4.36	0.28	100.20	0.21	857.73	0.26	5.51	-161.26	29.80	0.43	39.84	162.67	1.34	3.28
2	5	PM-X1	2338	52.97	0.00	29.63	0.30	0.02	0.03	12.18	0.08	0.02	4.65	0.31	100.19	0.21	282.27	0.26	6.45	81.87	24.45	0.44	33.34	55.67	1.29	3.05
2	5	PM-X1	2339	52.74	–	29.51	0.36	0.01	0.03	12.28	0.07	0.02	4.54	0.31	99.86	0.21	-193.74	0.26	5.68	137.46	27.08	0.44	37.78	67.69	1.31	3.10
2	15	PM-X1	2340	52.09	–	29.85	0.36	0.00	0.04	12.73	0.04	0.01	4.29	0.25	99.66	0.21	-163.50	0.26	5.65	714.08	21.88	0.43	61.63	100.64	1.35	3.56
2	17	PM-X1	2341	52.08	–	29.95	0.37	0.00	0.03	13.07	0.07	0.01	4.32	0.24	100.14	0.21	-214.88	0.26	5.49	289.71	29.97	0.42	39.98	213.86	1.35	3.58
1	-14	PM-X1	2342	52.58	0.00	30.04	0.28	–	0.04	12.47	0.04	0.02	4.58	0.23	100.27	0.21	-500.00	0.26	6.70	-191.56	20.75	0.43	61.19	70.97	1.30	3.75
2	-14	PM-X1	2343	52.57	0.01	29.64	0.31	0.01	0.03	12.36	0.12	0.02	4.68	0.30	100.06	0.21	60.16	0.26	6.20	100.30	28.43	0.44	23.31	59.63	1.29	3.12
2	-8	PM-X1	2344	52.53	0.01	29.58	0.32	0.02	0.02	12.31	0.09	0.02	4.57	0.28	99.75	0.21	61.85	0.26	6.04	64.66	31.10	0.44	30.02	82.30	1.31	3.29

				Data (wt%)												Analytical uncertainty (%)										
Tag	**Tag***	**Sample**	**ID**	**SiO2**	**TiO2**	**Al2O3**	**FeO**	**MnO**	**MgO**	**CaO**	**SrO**	**BaO**	**Na2O**	**K2O**	**Total**	**Si**	**Ti**	**Al**	**Fe**	**Mn**	**Mg**	**Ca**	**Sr**	**Ba**	**Na**	**K**
1	-8	PM-X1	2345	52.84	0.01	29.55	0.32	0.00	0.03	12.16	0.05	0.02	4.60	0.31	99.88	0.21	135.69	0.26	6.14	1188.25	26.97	0.44	51.95	71.19	1.30	3.06
1		PM-X2	2389	52.27	–	30.10	0.26	0.01	0.02	13.17	0.06	–	4.18	0.22	100.30	0.21	-163.87	0.26	7.21	160.59	31.52	0.43	42.07	5000.00	1.39	3.88
1		PM-X2	2390	52.03	–	30.31	0.31	0.01	0.02	13.25	0.06	0.00	4.21	0.19	100.40	0.21	-212.99	0.26	6.31	103.92	34.59	0.43	43.45	545.66	1.38	4.37
2		PM-X2	2391	51.53	–	30.64	0.36	–	0.02	13.68	0.05	0.01	3.86	0.18	100.34	0.21	-129.07	0.26	5.67	-215.68	31.40	0.42	48.18	111.94	1.45	4.53
2		PM-X2	2392	51.42	–	30.79	0.38	–	0.03	13.86	0.07	0.00	3.79	0.17	100.52	0.22	-58.49	0.26	5.53	-141.77	30.30	0.42	37.61	260.28	1.46	4.73
1		PM-X2	2393	51.52	–	30.65	0.30	–	0.02	13.60	0.06	0.01	4.11	0.17	100.44	0.22	-39.33	0.26	6.45	-454.10	39.20	0.42	43.35	113.94	1.40	4.58
3		PM-X2	2394	50.51	–	31.20	0.40	0.01	0.02	14.44	0.09	0.02	3.47	0.13	100.31	0.22	-38.44	0.26	5.32	144.68	33.80	0.41	29.92	65.82	1.54	5.49
2	20	PM-X3	2414	52.22	–	29.98	0.27	–	0.03	12.91	0.06	0.01	4.41	0.25	100.15	0.21	-120.73	0.26	7.04	-454.20	22.79	0.43	45.40	99.17	1.36	3.62
2	20	PM-X3	2415	51.99	0.02	30.18	0.25	0.01	0.04	13.11	0.08	0.00	4.36	0.24	100.28	0.21	40.30	0.26	7.47	188.78	21.79	0.43	32.61	364.04	1.36	3.69
2	7	PM-X3	2416	49.46	–	32.02	0.32	0.02	0.03	15.23	0.04	0.01	2.94	0.13	100.20	0.22	-165.69	0.25	6.27	55.98	28.06	0.40	68.86	124.45	1.69	5.53
1	7	PM-X3	2417	50.18	–	31.37	0.31	0.01	0.02	14.48	0.12	0.02	3.47	0.15	100.12	0.22	-53.40	0.26	6.38	204.39	47.00	0.41	24.56	72.82	1.55	5.20
2	7	PM-X3	2418	49.20	–	30.65	0.32	–	0.07	14.60	0.08	0.00	3.30	0.31	98.52	0.22	-559.81	0.26	6.26	-135.26	13.15	0.41	35.85	1241.90	1.59	3.14
2	7	PM-X3	2419	51.69	–	30.26	0.21	–	0.03	13.28	0.06	0.01	4.18	0.24	99.96	0.22	-123.82	0.26	8.44	-232.14	26.01	0.43	43.41	127.97	1.40	3.74
2	3	PM-X3	2420	52.28	–	30.11	0.26	0.01	0.02	12.99	0.04	0.02	4.31	0.22	100.26	0.21	-273.45	0.26	7.18	158.83	31.11	0.43	68.48	72.65	1.38	3.93
3	3	PM-X3	2421	48.39	–	32.60	0.32	–	0.03	15.80	0.04	0.00	2.77	0.10	100.05	0.22	-41.30	0.25	6.29	-780.80	26.58	0.39	64.31	311.25	1.74	7.09
2	0	PM-X3	2422	52.09	–	30.18	0.33	0.01	0.03	12.94	0.08	0.03	4.28	0.23	100.20	0.22	-78.80	0.26	6.16	208.70	23.12	0.43	34.74	47.42	1.38	3.79
1	-2	PM-X3	2423	52.93	0.01	29.04	0.27	0.01	0.04	12.21	0.08	0.02	4.67	0.28	99.54	0.21	132.21	0.27	7.00	107.19	22.12	0.45	34.09	63.39	1.32	3.38
1	-3	PM-X3	2424	53.08	0.00	29.44	0.26	0.00	0.03	12.41	0.04	–	4.47	0.27	100.01	0.21	386.55	0.26	7.17	749.59	25.83	0.44	62.09	-1940.20	1.35	3.41
1	-5	PM-X3	2425	52.51	–	29.87	0.28	0.01	0.02	12.85	0.09	0.01	4.29	0.23	100.16	0.21	-45.80	0.26	6.87	109.50	39.49	0.44	29.87	101.06	1.38	3.86
2		PM-X4	2428	54.08	–	29.05	0.38	0.02	0.02	11.66	0.09	0.02	4.89	0.39	100.60	0.21	-67.50	0.27	5.53	77.94	35.06	0.46	31.93	59.48	1.29	2.72
1		PM-X4	2429	53.47	0.01	29.44	0.23	0.01	0.02	12.16	0.08	0.02	4.87	0.35	100.66	0.21	115.66	0.26	7.99	107.20	41.16	0.45	33.29	69.81	1.29	2.89
2		PM-X4	2431	53.68	–	29.25	0.29	0.02	0.02	11.93	0.07	0.04	5.01	0.41	100.73	0.21	-188.83	0.27	6.59	61.96	37.54	0.45	38.91	36.57	1.27	2.65
2		PM-X4	2432	53.50	–	29.38	0.31	0.00	0.01	11.98	0.09	–	4.79	0.41	100.49	0.21	-51.59	0.27	6.30	369.42	55.44	0.45	29.96	-4089.40	1.30	2.64
4		PM-X4	2433	53.91	–	29.23	0.34	0.01	0.02	11.90	0.03	0.02	5.07	0.38	100.90	0.21	-56.92	0.27	5.99	93.15	43.14	0.45	96.13	72.68	1.26	2.76
2		PM-X4	2434	54.42	0.01	28.74	0.25	–	0.01	11.48	0.06	0.06	5.28	0.35	100.67	0.21	70.10	0.27	7.47	-156.20	52.03	0.46	42.54	23.53	1.23	2.89
3		PM-X4	2435	54.28	–	28.91	0.29	0.01	0.02	11.52	0.08	0.04	5.42	0.32	100.89	0.21	-168.34	0.27	6.66	196.66	42.35	0.46	34.15	35.42	1.22	3.05
6		PM-X4	2436	66.79	–	20.11	0.10	0.01	–	0.98	0.06	0.00	12.19	0.04	100.29	0.19	-21.53	0.33	14.89	92.73	-223.80	1.71	46.01	366.98	0.78	13.61
3		JB019-X2	2446	50.59	–	30.93	0.30	0.02	0.01	13.95	0.05	0.00	3.81	0.22	99.88	0.22	-70.59	0.26	6.54	74.31	55.46	0.42	52.31	567.21	1.47	3.91
1		JB019-X2	2447	47.41	–	33.05	0.40	0.00	0.03	16.40	0.05	0.01	2.32	0.10	99.77	0.23	-106.30	0.25	5.34	293.57	28.46	0.38	50.15	166.72	1.92	6.85
2		JB019-X2	2448	51.44	–	30.46	0.27	–	0.02	13.34	0.10	0.02	4.12	0.19	99.95	0.22	-85.93	0.26	6.98	-325.22	37.77	0.43	29.32	65.36	1.41	4.30
3		JB019-X2	2449	50.46	–	31.23	0.34	0.01	0.03	14.49	0.06	0.02	3.58	0.20	100.41	0.22	-83.53	0.26	5.95	206.44	29.10	0.41	43.77	71.28	1.52	4.16
1		JB019-X2	2450	48.02	–	32.85	0.38	0.01	0.02	16.18	0.09	0.02	2.54	0.13	100.24	0.23	-56.56	0.25	5.54	128.76	35.20	0.39	31.87	79.18	1.83	5.77
2		JB019-X2	2451	51.09	0.02	30.48	0.34	0.02	0.02	13.55	0.03	0.01	3.98	0.25	99.79	0.22	39.16	0.26	5.92	77.31	30.67	0.42	77.62	197.76	1.44	3.60
2	20	LX-1-1	533	51.03	0.01	29.74	0.33			13.70	0.06	0.05	3.39	0.26	98.57	0.72	70.15	0.37	9.17			0.61	93.54	40.93	1.97	5.48
6	20	LX-1-1	534	66.85	–	19.66	0.23			1.10	–	0.02	10.79	0.03	98.69	0.62	-139.27	0.46	11.25			2.36	-88.01	95.20	1.05	35.23
2	20	LX-1-1	536	51.85	0.05	29.80	0.37			13.08	0.03	0.02	3.93	0.21	99.35	0.72	20.65	0.37	8.46			0.62	200.04	90.32	1.82	6.35
1	19	LX-1-1	527	52.88	0.04	28.80	0.32			12.25	0.08	0.01	4.31	0.21	98.89	0.71	22.89	0.37	9.31			0.64	76.55	188.71	1.73	6.40
3	19	LX-1-1	528	49.94	0.02	30.55	0.43			14.24	0.06	–	3.15	0.22	98.60	0.73	54.99	0.36	7.48			0.59	99.31	-153.42	2.04	6.19
2	19	LX-1-1	529	50.93	0.05	30.08	0.47			13.75	–	0.01	3.45	0.22	98.98	0.73	21.70	0.37	7.02			0.60	-42.09	189.14	1.94	5.98
3	17	LX-1-1	537	49.20	0.02	31.84	0.38			14.76	0.04	–	2.94	0.12	99.30	0.74	45.09	0.36	8.14			0.58	132.89	-115.88	2.14	10.16
3	17	LX-1-1	538	49.00	0.01	31.11	0.39			15.18	–	0.03	2.82	0.10	98.65	0.74	70.67	0.36	8.09			0.57	-62.37	69.82	2.17	11.28
3	17	LX-1-1	539	49.32	0.01	31.59	0.34			15.02	–	0.02	2.96	0.12	99.40	0.74	83.11	0.36	8.58			0.58	-52.60	86.40	2.11	9.96
2	15	LX-1-1	550	51.15	0.03	30.00	0.30			13.34	–	0.00	3.55	0.19	98.58	0.73	36.07	0.37	9.35			0.62	-1000.00	3004.38	1.92	6.80
1	15	LX-1-1	551	53.65	0.02	28.56	0.29			11.92	–	0.03	4.56	0.19	99.23	0.71	45.31	0.38	9.38			0.65	-48.60	65.85	1.68	6.64
1	15	LX-1-1	552	52.21	0.03	27.88	0.29			12.16	0.00	–	5.01	0.08	97.67	0.72	31.37	0.38	9.62			0.64	1199.25	-299.26	1.60	13.48
2	14	LX-1-1	542	51.99	0.02	29.82	0.41			13.36	–	–	3.57	0.24	99.42	0.72	51.96	0.37	7.41			0.61	-65.75	-428.29	1.92	5.82
1	14	LX-1-1	543	50.15	0.02	30.36	0.46			13.96	–	0.04	3.36	0.20	98.55	0.73	60.57	0.36	6.96			0.60	-1088.80	50.35	1.97	6.46
2	14	LX-1-1	544	50.95	0.02	30.63	0.36			13.92	–	–	3.33	0.23	99.43	0.73	52.59	0.36	8.36			0.60	-61.59	-108.78	1.98	5.93
2	11	LX-1-1	559	50.90	0.02	30.74	0.26			14.21	0.01	0.01	3.40	0.10	99.68	0.73	58.21	0.36	10.30			0.59	375.74	152.63	1.96	11.29
2	7	LX-1-1	561	51.73	0.04	29.40	0.37			12.71	–	0.01	4.03	0.28	98.59	0.72	24.64	0.37	8.36			0.63	-500.00	366.97	1.79	5.17
3	7	LX-1-1	562	50.02	0.04	30.10	0.53			14.05	–	–	3.41	0.17	98.32	0.73	25.29	0.37	6.65			0.60	-55.93	-333.06	1.96	7.42
1	3	LX-1-1	563	51.23	0.03	30.03	0.44			13.62	–	–	3.67	0.20	99.20	0.72	39.47	0.37	7.27			0.61	-101.34	-142.25	1.90	6.65
1	3	LX-1-1	564	54.83	0.01	28.06	0.37			11.41	–	0.03	4.76	0.32	99.81	0.70	123.83	0.38	8.18			0.67	-162.22	58.01	1.65	4.84

				Data (wt%)											Analytical uncertainty (%)									
Tag	Tag*	Sample	ID	SiO2	TiO2	Al2O3	FeO	MnO	MgO	CaO	SrO	BaO	Na2O	K2O	Total	Si	Ti	Al	Fe	Mn	Mg	Ca	Sr	Ba	Na	K
2	3	LX-1-1	565	51.71	0.02	29.87	0.45			13.62	–	0.01	3.52	0.25	99.48	0.72	40.34	0.37	7.22			0.61	-384.08	177.53	1.93	5.49
1	3	LX-1-1	566	52.90	0.01	28.95	0.41			12.46	0.00	0.02	4.19	0.25	99.20	0.71	101.24	0.37	7.53			0.64	1198.61	115.10	1.76	5.60
1	2	LX-1-1	568	50.31	0.01	29.91	0.46			13.72	–	–	3.57	0.24	98.24	0.73	144.12	0.37	7.31			0.61	-93.50	-112.36	1.92	5.77
2	2	LX-1-1	569	50.41	0.01	30.54	0.46			13.94	–	–	3.41	0.21	99.01	0.73	67.41	0.36	7.26			0.60	-81.98	-141.61	1.96	6.08
3	2	LX-1-1	571	49.04	0.02	31.29	0.42			15.08	0.02	–	2.72	0.12	98.76	0.74	55.31	0.36	7.62			0.58	295.86	-42.40	2.23	9.02
1	0	LX-1-1	592	52.71	0.01	28.18	0.38			11.88	0.06	0.03	4.28	0.28	97.84	0.71	88.22	0.38	8.45			0.65	85.34	63.81	1.74	5.13
1	0	LX-1-1	593	48.20	0.02	31.77	0.44			15.22	–	0.01	2.66	0.14	98.48	0.75	44.15	0.36	7.42			0.57	-171.95	140.68	2.24	8.37
1	0	LX-1-1	594	49.77	0.05	30.64	0.38			14.41	–	0.02	2.89	0.16	98.32	0.74	19.86	0.36	7.98			0.59	-150.95	91.29	2.16	7.66
1	0	LX-1-1	595	48.58	0.01	32.81	0.40			15.54	–	0.02	2.55	0.14	100.10	0.75	75.06	0.35	7.99			0.57	-235.62	112.15	2.29	8.71
2	0	LX-1-1	596	49.80	0.02	30.54	0.42			13.92	0.09	0.02	3.29	0.22	98.33	0.74	45.16	0.36	7.30			0.60	60.23	128.67	2.00	6.12
1	0	LX-1-1	597	48.24	0.04	29.27	1.11			14.83	–	0.03	3.16	0.53	97.22	0.75	24.38	0.37	4.19			0.58	-43.69	66.28	2.07	3.39
1	0	LX-1-1	582	52.07	0.03	28.82	0.37			12.34	–	–	4.08	0.26	97.96	0.72	39.02	0.38	8.26			0.64	-43.70	-1458.90	1.79	5.45
2	0	LX-1-1	583	49.86	0.03	30.88	0.41			14.34	–	–	3.11	0.19	98.82	0.74	30.74	0.36	7.90			0.59	-500.00	-341.44	2.06	6.87
2	0	LX-1-1	584	50.12	0.02	30.69	0.38			14.15	0.05	–	3.22	0.19	98.82	0.73	49.70	0.36	8.11			0.60	116.62	-250.49	2.02	6.70
2	-2	LX-1-1	572	49.92	0.03	30.52	0.29			14.12	0.03	0.02	3.40	0.23	98.57	0.74	34.73	0.36	10.12			0.60	155.86	121.23	1.96	6.00
2	-2	LX-1-1	573	50.94	0.02	30.62	0.27			14.14	–	0.00	3.39	0.19	99.58	0.73	55.32	0.36	10.33			0.60	-140.29	735.74	1.97	6.40
1	-7	LX-1-1	576	50.84	0.03	30.52	0.25			13.95	–	–	3.23	0.20	99.01	0.73	35.58	0.36	10.93			0.60	-201.24	-62.95	2.02	6.78
2	-7	LX-1-1	577	50.63	0.01	31.01	0.24			14.31	0.06	0.01	3.31	0.14	99.72	0.73	184.49	0.36	11.06			0.59	86.60	226.72	1.99	8.77
3	-7	LX-1-1	578	49.36	–	31.66	0.28			14.98	–	0.01	2.76	0.15	99.22	0.74	-89.69	0.36	9.85			0.58	-125.15	157.05	2.20	8.04
1	-10	LX-1-1	588	50.21	0.03	30.08	0.21			13.82	0.03	–	3.31	0.23	97.92	0.73	36.50	0.37	12.39			0.60	169.60	-166.05	2.00	5.79
3	-10	LX-1-1	590	48.78	0.01	31.75	0.29			15.12	0.04	–	2.70	0.15	98.86	0.75	158.49	0.36	9.72			0.58	131.98	-93.84	2.23	7.88
3	-10	LX-1-1	591	49.60	0.02	31.15	0.26			14.65	–	0.01	2.94	0.14	98.77	0.74	49.21	0.36	10.45			0.59	-500.00	164.02	2.13	8.63

Tag*: Distance (mm) from contact. Positive values are in the autolith.

Table D.9 – Mineral chemistry for pyroxenes. This table only includes data (wt%). Tag list: 1 = Clinopyroxene; 2 = Clinopyroxene exsolution in orthopyroxene; 3 = Clinopyroxene in plagioclase; 4 = Disequilibrium clinopyroxene; 5 = Orthopyroxene; 6 = Orthopyroxene exsolution in clinopyroxene; 7 = Orthopyroxene in plagioclase; 8 = Orthopyroxene in hornblende. Al-in-Opx list: X = Uncontaminated (good); C = Contaminated (excluded); O = Oikicryst; S = Subophitic crystal.

Tag	Tag*	Al-in-Opx	Sample	ID	SiO2	TiO2	Al2O3	V2O3	Cr2O3	FeO	NiO	ZnO	MnO	MgO	CaO	SrO	BaO	Na2O	K2O	Total
Anorthosite sequence near the Phosiri Dome																				
5		X	AR-9	1527	52.22	0.17	0.81	0.00	0.05	19.74	0.05	–	0.44	24.51	0.48			–		98.48
1			AR-9	1528	52.08	0.36	1.63	0.04	0.10	8.08	0.02	–	0.22	14.83	22.13			0.30		99.78
1			AR-9	1529	51.26	0.35	1.73	0.09	0.12	7.66	0.01	–	0.22	14.72	21.74			0.30		98.20
1			AR-9	1530	51.56	0.42	1.48	0.07	0.09	7.70	0.02	–	0.20	14.51	22.43			0.29		98.77
6		X	AR-9	1531	52.45	0.17	1.09	0.03	0.08	19.04	0.05	–	0.42	23.31	2.14			0.02		98.79
6		X	AR-9	1532	52.66	0.15	0.84	0.00	0.03	20.44	0.06	–	0.43	24.06	0.55			0.00		99.23
5		X	AR-9	1533	52.76	0.17	0.85	0.03	0.04	18.54	0.03	0.00	0.39	24.81	1.06			0.00		98.70
5		X	AR-9	1534	53.02	0.17	0.70	0.01	0.07	19.25	0.04	–	0.38	24.77	0.72			–		99.13
5		X	AR-9	1535	53.19	0.21	0.74	0.00	0.06	19.35	0.05	0.02	0.41	24.78	0.97			0.01		99.80
5		X	AR-9	1536	52.85	0.20	0.70	0.02	0.03	19.44	0.02	0.00	0.39	24.59	0.80			–		99.03
5		X	AR-9	1537	53.46	0.21	0.79	0.02	0.07	18.79	0.05	0.06	0.36	24.84	0.95			0.01		99.61
1			ARS-2-1	1299	52.36	0.22	1.28	0.07	–	11.72	0.01	–	0.32	12.30	21.65			0.23		100.16
5		X/S	ARS-2-1	1300	50.71	0.13	1.09	0.03	0.01	28.71	0.03	–	0.71	16.36	1.01			0.01		98.80
5		X/S	ARS-2-1	1301	51.63	0.10	0.76	0.00	0.00	29.21	0.01	–	0.67	16.69	0.78			–		99.86
1			ARS-2-1	1303	51.91	0.31	1.67	0.07	–	12.22	0.04	–	0.28	12.13	21.29			0.23		100.15
1			ARS-2-1	1304	53.32	0.17	1.14	0.03	–	11.68	0.02	–	0.31	12.38	21.69			0.20		100.93
5		X/O	ARS-2-1	1306	52.76	0.22	0.66	0.03	0.03	24.53	0.03	–	0.46	20.18	1.17			–		100.06
5		C/O	ARS-2-1	1307	51.67	0.69	0.61	0.03	–	24.49	0.03	–	0.52	19.79	1.45			0.02		99.30
8		X/O	ARS-2-1	1312	55.30	0.04	0.35	–	0.01	20.52	0.00	–	0.46	19.76	0.74	–	–	0.01	–	97.21

Tag	Tag*	A1-in-Opx	Sample	ID	SiO2	TiO2	Al2O3	V2O3	Cr2O3	FeO	NiO	ZnO	MnO	MgO	CaO	SrO	BaO	Na2O	K2O	Total
1			ARS-2-4	1454	51.69	0.38	1.54	0.04	0.05	7.83	0.02	–	0.19	14.11	22.94			0.20		98.98
5		X/O	ARS-2-4	1455	51.79	0.20	0.85	0.02	0.03	23.30	0.02	–	0.45	21.92	0.69			–		99.28
1			ARS-2-4	1456	51.99	0.39	1.65	0.03	0.05	8.59	0.01	–	0.23	14.00	22.32			0.25		99.51
1			ARS-2-4	1459	51.56	0.27	1.34	0.06	0.04	10.09	0.00	–	0.29	13.19	22.44			0.21		99.50
6		X/O	ARS-2-4	1460	50.28	0.10	0.80	0.04	0.00	27.79	0.02	0.01	0.72	18.00	0.66			–		98.43
5		X/O	ARS-2-6	1324	52.29	0.14	0.50	0.02	0.02	27.96	–	0.04	0.83	17.88	0.63			0.00		100.32
5		X/O	ARS-2-6	1325	52.59	0.05	0.51	0.03	0.00	26.95	0.01	–	0.76	18.75	0.43			0.01		100.10
6		C/O	ARS-2-6	1326	52.30	0.17	0.89	0.02	0.04	26.11	0.02	–	0.61	18.89	1.37			–		100.41
6		X/O	ARS-2-6	1327	52.49	0.16	0.89	0.04	0.01	26.43	0.01	0.01	0.63	19.03	0.66			–		100.35
5		X/O	ARN-3-2	2152	50.82	0.20	0.69	0.01	0.03	22.86	0.01	–	0.49	22.29	0.92	0.01	0.01	–	0.01	98.35
5		C/O	ARN-3-2	2153	51.24	0.18	0.94	0.03	0.02	21.82	0.03	0.01	0.45	22.69	1.69	0.03	–	–	0.00	99.14
1			ARN-3-2	2154	51.14	0.43	1.62	0.06	0.04	8.79	0.01	–	0.20	14.68	22.30	–	0.01	0.26	0.00	99.53
2			ARN-3-2	2155	51.19	0.11	0.63	0.01	0.01	22.81	0.02	–	0.44	22.54	0.75	–	–	–	–	98.52
1			ARN-3-2	2156	50.57	0.44	1.64	0.06	0.06	9.16	–	–	0.22	14.48	21.91	0.03	–	0.27	0.00	98.82
1			ARN-3-2	2180	51.85	0.45	1.75	0.05	0.04	10.42	0.02	–	0.28	13.60	21.59	0.04	–	0.28	0.01	100.38
5		C/O	ARN-3-2	2181	51.83	0.13	0.93	0.01	0.02	23.41	0.04	–	0.54	19.97	2.86	0.03	–	0.02	–	99.80
5		X/O	ARN-3-2	2182	51.16	0.13	0.78	0.00	0.00	25.19	0.02	0.03	0.64	20.23	0.73	0.05	–	–	0.01	98.98
1			ARN-3-2	2183	51.96	0.19	1.15	0.06	0.04	9.49	0.01	–	0.26	13.72	22.63	0.03	0.01	0.23	0.01	99.77
1			ARN-3-3	1434	51.25	0.22	1.32	0.05	0.01	11.16	0.04	–	0.27	12.98	21.60			0.25		99.14
3			ARN-3-3	1435	50.77	0.26	1.24	0.04	–	10.80	0.01	–	0.27	12.78	22.20			0.26		98.62
1			ARN-3-3	1436	51.10	0.20	1.24	0.03	–	10.65	0.03	–	0.30	12.99	22.27			0.22		99.05
5		C/O	ARN-3-4	2171	52.51	0.14	0.68	0.02	0.03	21.00	0.03	–	0.43	23.06	1.42	–	–	0.01	–	99.33
5		C/O	ARN-3-4	2172	52.09	0.17	0.86	0.03	0.01	20.27	0.04	–	0.43	22.47	2.99	0.05	0.01	0.01	0.01	99.44
1			ARN-3-4	2173	51.52	0.21	1.35	0.01	0.01	9.68	0.04	–	0.30	13.69	22.29	–	0.02	0.23	–	99.36
1			ARN-3-4	2174	51.51	0.24	1.48	0.05	0.01	9.98	0.01	–	0.31	13.57	21.95	0.02	0.00	0.25	0.01	99.38
1			ARN-3-4	2175	51.76	0.36	1.54	0.06	0.01	7.87	0.03	–	0.20	14.64	22.02	0.01	0.00	0.24	0.01	98.75
5		X/O	ARN-3-7	2176	52.04	0.29	0.69	0.00	0.00	19.38	0.02	–	0.42	24.02	1.16	0.00	–	0.00	–	98.03
5		X/O	ARN-3-7	2177	52.46	0.24	0.74	0.02	0.02	19.84	0.04	–	0.45	24.08	1.29	–	0.00	0.01	0.01	99.18
1			ARN-3-7	2178	51.62	0.45	1.59	0.05	0.06	9.11	0.03	–	0.24	14.22	22.02	0.02	0.00	0.26	0.00	99.67
1			ARN-3-7	2179	51.81	0.23	1.32	0.01	0.04	8.52	0.03	–	0.24	14.18	22.61	–	–	0.26	0.00	99.23
1			ARN-3-8	1419	50.54	0.31	1.55	0.07	0.04	9.53	0.03	0.00	0.26	13.36	22.56			0.26		98.51
1			ARN-3-8	1420	51.54	0.36	1.71	0.04	0.04	10.03	0.02	–	0.28	13.34	21.76			0.26		99.38
1	3		ARN-2-2'	916	52.65	0.40	1.63		0.09	8.24		0.03	0.22	13.57	22.34	–	0.00	0.26	0.00	99.42
5	3	X/O	ARN-2-2'	917	53.04	0.14	0.75		0.01	23.32		0.04	0.51	21.05	0.66	0.02	–	0.02	–	99.55
1	3		ARN-2-2'	912	52.79	0.31	1.39		0.08	8.78		0.00	0.23	13.68	22.32	–	0.02	0.22	0.01	99.84
5	3	X/O	ARN-2-2'	913	53.81	0.09	0.63		0.02	23.94		–	0.63	20.89	0.60	–	–	–	–	100.62
1	3		ARN-2-2'	903	53.37	0.40	1.57		0.06	8.30		–	0.19	13.88	22.08	–	0.01	0.24	–	100.11
5	3	X/O	ARN-2-2'	904	53.49	0.22	0.85		0.03	21.75		–	0.49	22.28	0.68	–	0.02	–	–	99.81
2	3		ARN-2-2'	905	53.70	0.38	1.60		0.08	8.94		–	0.23	14.74	19.65	–	0.02	0.24	–	99.59
2	3		ARN-2-2'	906	54.44	0.34	1.55		0.06	9.64		–	0.27	15.10	18.99	–	–	0.25	–	100.64
1	6		ARN-2-2'	897	52.90	0.36	1.44		0.08	8.26		0.01	0.24	13.94	22.15	–	0.01	0.25	0.01	99.64
5	6	X/O	ARN-2-2'	898	53.00	0.08	0.77		0.02	23.06		–	0.54	21.42	0.54	–	–	–	–	99.43
1	7		ARN-2-2'	925	51.42	0.40	1.49		0.09	8.88		0.01	0.21	13.72	21.78	–	0.01	0.27	–	98.28
1	7		ARN-2-2'	926	51.67	0.41	1.67		0.10	9.08		–	0.24	13.79	21.25	–	0.01	0.23	0.00	98.44
6	7	X/O	ARN-2-2'	927	52.14	0.18	0.80		0.03	22.75		–	0.48	21.26	0.69	–	–	0.01	0.01	98.35
1	7		ARN-2-2'	928	52.20	0.37	1.42		0.03	8.65		–	0.24	13.71	21.94	–	–	0.26	0.00	98.82
1	13		ARN-2-2'	932	52.06	0.41	1.45		0.06	8.65		–	0.24	13.63	22.29	–	0.01	0.24	–	99.03
1	13		ARN-2-2'	933	51.85	0.43	1.60		0.07	9.13		0.00	0.24	13.69	21.45	–	0.01	0.28	–	98.75
5	13	X/O	ARN-2-2'	934	51.71	0.08	0.51		0.04	22.75		–	0.56	20.53	1.28	–	–	0.00	–	97.47
1	16		ARN-2-2'	935	51.61	0.35	1.51		0.06	7.94		0.00	0.21	13.73	22.36	–	0.00	0.25	–	98.02
5	16	X/O	ARN-2-2'	936	52.13	0.17	0.60		0.02	22.04		–	0.51	21.92	0.66	–	0.01	0.00	–	98.05
1	26		ARN-2-2'	953	51.00	0.42	1.59		0.07	9.20		–	0.28	13.47	22.05	–	0.02	0.31	0.01	98.39
5	26	X/O	ARN-2-2'	954	50.97	0.20	0.76		0.03	24.74		–	0.57	19.40	0.69	–	0.01	–	–	97.36
3	26		ARN-2-2'	955	51.72	0.28	1.26		0.05	8.88		–	0.25	13.55	21.88	–	–	0.26	0.01	98.14

Tag	Tag*	A1-in-Opx	Sample	ID	SiO2	TiO2	Al2O3	V2O3	Cr2O3	FeO	NiO	ZnO	MnO	MgO	CaO	SrO	BaO	Na2O	K2O	Total
1	27		ARN-2-2'	966	51.84	0.33	1.53		0.05	8.83		–	0.27	13.35	22.29	–	–	0.23	0.01	98.73
5	27	X/O	ARN-2-2'	967	51.83	0.11	0.70		0.01	23.99		–	0.55	20.34	0.72	–	–	–	0.01	98.26
6	32	C/O	ARN-2-2'	974	51.14	0.21	0.94		0.04	24.09		0.02	0.56	18.91	1.83	–	–	–	0.00	97.73
1	32		ARN-2-2'	975	52.39	0.49	1.74		0.06	9.57		–	0.29	13.09	22.05	–	0.01	0.31	–	100.00
1	7		ARN-2-2	987	51.72	0.29	1.40		0.08	8.77		–	0.24	13.75	22.34	–	0.01	0.21	–	98.81
5	7	X/O	ARN-2-2	988	51.06	0.24	0.77		0.04	23.63		0.00	0.59	20.11	0.91	–	–	0.02	–	97.39
1	7		ARN-2-2	989	52.38	0.34	1.51		0.06	10.04		–	0.25	14.01	20.70	–	–	0.24	–	99.54
1	8		ARN-2-2	982	52.70	0.35	1.47		0.07	8.61		–	0.20	14.23	21.82	–	–	0.22	0.00	99.69
5	8	C/O	ARN-2-2	983	53.27	0.16	0.71		0.03	18.42		–	0.42	21.37	6.34	–	0.01	0.01	0.01	100.75
1	8		ARN-2-2	984	51.99	0.36	1.51		0.10	8.48		–	0.23	13.99	21.99	–	0.02	0.27	0.00	98.94
2	10		ARN-2-2	992	52.50	0.39	1.47		0.07	8.34		–	0.24	14.30	22.11	–	0.03	0.24	–	99.68
5	10	X/O	ARN-2-2	993	52.39	0.25	0.81		0.04	21.26		–	0.49	22.10	0.81	–	–	0.01	0.00	98.17
1	10		ARN-2-2	994	52.69	0.40	1.47		0.07	8.03		–	0.22	13.88	22.53	–	–	0.28	0.01	99.58
3	10		ARN-2-2	995	52.47	0.39	1.54		0.07	8.74		–	0.25	13.98	22.19	–	0.02	0.29	0.00	99.95
1	22		ARN-2-2	1004	53.34	0.35	1.41		0.07	8.70		–	0.23	13.96	22.40	–	–	0.29	0.00	100.75
1	26		ARN-2-2	1011	52.58	0.41	1.53		0.04	9.16		–	0.23	13.72	22.17	–	0.01	0.25	–	100.11
1	26		ARN-2-2	1012	52.45	0.36	1.65		0.05	9.16		0.00	0.27	13.63	22.12	–	0.00	0.25	0.00	99.95
5	26	X/O	ARN-2-2	1013	51.48	0.14	0.70		0.03	23.85		–	0.57	20.42	0.71	–	–	–	–	97.91
1	32		ARN-2-2	1023	52.29	0.27	1.36		0.03	9.23		–	0.29	13.26	22.49	–	0.01	0.26	–	99.51
1	32		ARN-2-2	1024	51.92	0.46	1.73		0.05	10.09		–	0.25	13.31	21.48	–	–	0.26	–	99.55
1	37		ARN-2-2	1037	52.27	0.17	1.11		–	9.45		–	0.30	13.18	22.38	–	–	0.25	0.01	99.12
1	37		ARN-2-2	1038	52.24	0.22	1.29		0.05	9.39		0.05	0.26	13.12	22.65	–	–	0.26	0.00	99.54
5		C/O	ARN-4-7	1366	52.64	0.70	0.69	0.04	0.01	22.85	0.03	0.00	0.56	21.30	1.43			0.00		100.26
5		X/O	ARN-4-7	1367	53.35	0.10	0.68	0.01	0.02	22.73	0.01	0.01	0.49	21.77	0.97			0.00		100.15
2			ARN-4-7	1368	53.53	0.32	1.71	0.06	0.08	8.07	0.02	–	0.21	14.39	21.97			0.36		100.72
5		X/S	ARN-4-7	1369	53.78	0.17	0.95	0.01	0.04	21.02	0.02	–	0.43	22.80	1.19			0.02		100.43
5		C/S	ARN-4-7	1370	53.52	0.13	1.10	0.03	0.05	20.46	0.03	0.01	0.47	22.36	1.98			0.03		100.17
1			ARN-4-7	1371	52.96	0.29	1.70	0.06	0.02	8.98	0.00	–	0.25	13.46	22.46			0.26		100.46
1			ARN-4-7	1372	52.73	0.53	1.65	0.11	0.03	9.53	0.05	–	0.25	13.70	21.55			0.30		100.42
1			ARN-4-9	1345	53.06	0.17	1.26	0.04	0.03	8.57	0.02	–	0.27	13.64	22.85			0.23		100.16
1			ARN-4-9	1346	53.54	0.12	1.14	0.01	0.05	8.66	0.02	–	0.25	13.90	22.49			0.22		100.40
5		C/O	ARN-4-9	1348	52.82	0.99	0.69	0.02	0.03	21.57	0.01	0.04	0.41	22.41	1.34			0.01		100.35
1			ARN-4-9	1349	53.29	0.40	1.77	0.07	0.07	8.21	0.03	–	0.22	13.97	22.13			0.25		100.41
1			ARN-4-11	1611	51.88	0.27	1.59	0.03	0.04	9.20	0.01	–	0.30	13.48	22.39			0.30		99.48
1			ARN-4-11	1612	51.97	0.19	1.43	0.05	0.03	9.08	0.04	0.02	0.33	13.52	22.65			0.30		99.61
5		X/S	ARN-5-1	1514	52.13	0.17	0.89			20.13			0.42	22.86	1.79	0.00	–	0.03	–	98.42
5		X/S	ARN-5-1	1515	52.34	0.22	0.72			20.37			0.44	22.96	1.63	0.02	–	0.01	0.01	98.72
1			ARN-5-1	1516	51.42	0.36	1.58			8.02			0.23	13.94	22.58	–	0.00	0.26	0.01	98.39
3			ARN-5-1	1517	51.44	0.54	1.64			8.42			0.21	14.03	21.96	0.01	0.02	0.29	0.01	98.58
1			ARN-5-1	1518	51.78	0.32	1.57	0.10	0.04	8.30	0.01	–	0.21	14.09	22.57			0.25		99.23
1			ARN-5-1	1519	52.10	0.14	1.13	0.06	0.03	8.12	0.03	–	0.24	14.13	22.85			0.28		99.10
5		X/O	ARN-5-1	1520	52.31	0.17	0.71	0.02	0.01	22.61	0.04	0.05	0.49	22.02	0.97			–		99.40
5		C/O	ARN-5-1	1521	51.74	0.20	0.66	0.04	0.02	21.05	0.04	0.00	0.44	22.37	1.27			0.02		97.85
1			ARN-5-4	1470	52.00	0.36	1.70	0.03	0.11	8.57	0.02	–	0.24	13.86	22.47			0.31		99.68
5		X/S	ARN-5-4	1471	52.63	0.21	0.86	–	0.02	22.03	0.02	–	0.51	22.47	0.87			0.00		99.64
1			ARN-5-4	1472	51.51	0.35	1.74	0.04	0.05	8.80	0.04	–	0.22	14.03	21.95			0.29		99.02
5		X/S	ARN-5-4	1473	52.00	0.18	1.00	0.02	0.04	22.83	0.03	–	0.50	22.07	0.69			–		99.36
1			ARN-5-4	1474	52.54	0.12	1.22	0.06	0.05	8.48	0.02	–	0.24	13.88	22.79			0.27		99.68
1			ARN-5-4	1475	52.21	0.37	1.67	0.07	0.07	8.54	0.01	–	0.23	13.97	22.53			0.31		99.98
5		X/S	ARN-5-4	1476	52.99	0.14	0.85	0.04	0.03	21.02	0.02	–	0.44	23.14	0.74			–		99.42
5		C/S	ARN-5-4	1477	53.39	0.24	0.76	0.04	0.02	20.93	0.04	–	0.47	22.46	1.89			0.01		100.24
1			ARN-5-6	1583	52.90	0.26	1.38	0.03	–	8.36	0.01	–	0.24	13.87	22.63			0.32		99.99
1			ARN-5-6	1584	52.23	0.26	1.46	0.05	–	9.07	0.02	–	0.20	13.96	22.05			0.28		99.59
5		C/S	ARN-5-6	1585	52.54	0.17	0.91	0.02	–	20.50	0.05	–	0.41	22.82	1.77			0.02		99.21

Tag	Tag*	Al-in-Opx	Sample	ID	SiO2	TiO2	Al2O3	V2O3	Cr2O3	FeO	NiO	ZnO	MnO	MgO	CaO	SrO	BaO	Na2O	K2O	Total
5		X/S	ARN-5-6	1586	52.70	0.14	0.89	0.03	0.02	20.72	0.03	0.02	0.44	22.87	1.45			–		99.32
2			ARN-5-6	1587	52.18	0.34	1.57	0.10	0.09	8.25	0.03	–	0.19	14.45	22.34			0.28		99.82
5		C/S	ARN-5-8C	1485	52.22	0.15	0.78	0.02	0.03	20.91	0.03	–	0.40	22.43	1.53			0.00		98.51
1			ARN-5-8C	1486	52.34	0.29	1.46	0.13	0.06	8.26	0.03	–	0.20	14.04	22.74			0.25		99.81
5		X/O	ARN-5-8C	1487	51.77	0.17	0.76	0.01	–	21.90	0.03	–	0.48	22.52	0.91			–		98.54
1			ARN-5-8C	1488	52.37	0.27	1.41	0.05	0.03	8.45	0.02	–	0.22	13.90	22.82			0.27		99.81
1			ARN-5-8C	1489	51.71	0.49	1.78	0.09	0.07	8.74	0.04	–	0.20	13.95	22.17			0.29		99.53
5		X/S	ARN-5-8C	1490	51.79	0.27	0.81	0.02	–	22.04	0.04	0.02	0.48	22.32	0.91			0.01		98.70
1			ARN-5-8C	1491	51.11	0.57	1.74	0.07	0.03	8.94	0.03	0.02	0.21	13.59	22.45			0.33		99.08
1			ARN-5-8C	1492	51.40	0.29	1.49	0.05	0.03	8.90	0.02	–	0.19	13.89	21.99			0.29		98.53

Tag*: Distance (mm) from core of oikocryst.

Blocks in the anorthosite sequence																				
5		C	ARS-X1	2298	53.01	0.21	0.91	0.06	0.18	18.94	0.07	–	0.42	23.76	1.39	0.05	–	0.01	0.00	99.00
5		X	ARS-X1	2299	52.98	0.19	0.96	–	0.18	20.08	0.04	–	0.47	23.50	0.76	0.02	–	–	–	99.18
1			ARS-X1	2300	52.45	0.41	1.74	0.07	0.37	7.44	0.05	–	0.22	14.52	22.13	0.05	–	0.24	0.00	99.67
1			ARS-X1	2301	52.74	0.45	1.81	0.05	0.34	6.94	0.04	0.02	0.19	14.79	22.62	0.05	0.01	0.27	0.00	100.33
1			ARS-X1	2302	52.52	0.29	2.23	0.04	0.40	7.17	0.03	–	0.23	14.71	22.26	0.05	0.01	0.30	0.00	100.25
6		C	ARS-X1	2303	52.47	0.09	1.56	0.01	0.30	19.28	0.04	–	0.42	22.42	2.39	0.03	–	0.03	–	99.04
5		X	ARS-X1	2304	53.15	0.15	1.53	0.00	0.20	19.27	0.08	–	0.43	23.82	0.95	0.02	–	0.02	–	99.61
5		X	ARS-X1	2305	53.28	0.13	1.19	0.00	0.23	19.91	0.04	0.01	0.44	23.54	0.86	0.02	–	0.01	–	99.65
5		X	ARS-X1	2306	53.62	0.16	0.99	0.02	0.20	18.36	0.05	–	0.39	24.57	1.00	–	–	–	0.00	99.37
1			ARS-X1	2307	52.99	0.34	1.57	0.06	0.43	6.83	0.03	–	0.19	15.03	22.60	0.01	–	0.26	0.00	100.36
5		X	ARS-X1	2308	53.93	0.21	0.68	0.02	0.15	19.03	0.06	–	0.43	24.55	0.80	0.01	0.03	0.02	–	99.93
5		X	ARS-X1	2309	53.88	0.23	0.81	0.01	0.18	19.03	0.06	–	0.38	24.38	1.12	0.01	–	0.00	–	100.09
1			ARS-X2	2260	51.85	0.33	2.25	0.03	0.49	7.35	0.02	–	0.26	15.56	20.92	0.02	–	0.23	–	99.31
5		X	ARS-X2	2261	53.75	0.12	1.34	–	0.20	15.96	0.04	0.03	0.35	26.04	0.79	–	0.00	–	0.00	98.62
5		X	ARS-X2	2262	53.55	0.13	1.31	0.01	0.19	16.11	0.05	–	0.36	26.04	0.92	0.02	–	–	–	98.70
5		X	ARS-X2	2264	53.43	0.12	1.40	0.02	0.16	15.90	0.04	0.03	0.39	26.11	0.94	0.01	0.00	–	–	98.56
1			ARS-X2	2265	52.04	0.28	2.23	0.05	0.42	7.16	0.04	0.08	0.23	16.08	20.46	0.01	0.01	0.19	0.00	99.28
5		X	ARS-X2	2267	53.31	0.10	1.38	–	0.08	16.20	0.05	0.02	0.38	26.30	0.84	0.01	0.01	–	0.00	98.68
5		X	ARS-X2	2268	53.38	0.15	1.36	0.02	0.20	15.86	0.05	0.04	0.38	26.48	0.89	0.01	0.00	–	–	98.81
5	1	X	ARS-X3	2225	53.71	0.19	1.07	0.04	0.28	15.41	0.06	0.01	0.35	26.62	0.81	0.05	0.02	0.01	0.00	98.61
5	1	X	ARS-X3	2226	54.18	0.19	0.94	0.04	0.29	15.21	0.05	–	0.33	26.75	0.71	0.03	0.00	–	–	98.72
1	1		ARS-X3	2227	52.45	0.43	2.21	0.07	0.49	5.98	0.03	–	0.17	14.99	22.87	0.01	0.01	0.31	0.00	100.03
5	1	X	ARS-X3	2228	53.38	0.19	1.12	0.01	0.23	15.47	0.04	–	0.33	26.37	0.55	0.01	0.01	–	–	97.70
5	1	X	ARS-X3	2229	53.70	0.15	0.85	0.01	0.23	15.32	0.05	0.01	0.36	26.76	0.51	0.04	0.01	0.00	–	97.98
1	1		ARS-X3	2230	52.83	0.35	1.61	0.07	0.49	5.39	0.04	–	0.18	15.28	23.15	–	0.01	0.27	0.00	99.68
5	1	X	ARS-X3	2231	53.50	0.21	1.16	0.03	0.24	15.63	0.05	–	0.34	26.26	0.82	0.02	0.01	–	–	98.27
5	2	X	ARS-X3	2232	54.10	0.13	0.62	–	0.04	18.15	0.03	–	0.40	25.16	0.74	0.06	–	0.01	–	99.44
5	2	X	ARS-X3	2233	53.76	0.26	0.76	0.02	0.06	18.11	0.06	–	0.39	25.00	0.79	0.00	0.01	–	–	99.22
5	2	X	ARS-X3	2234	54.35	0.26	0.80	0.02	0.05	18.50	0.04	0.02	0.39	25.06	0.85	0.01	0.01	0.00	–	100.36
5	2	X	ARS-X3	2235	53.71	0.26	0.81	0.02	0.04	18.06	0.03	–	0.42	25.25	0.93	0.03	–	0.01	–	99.56
5	2	X	ARS-X3	2236	53.74	0.33	0.86	0.04	0.06	18.60	0.06	–	0.39	24.97	0.97	0.03	0.01	0.01	–	100.08
5		X	ARS-X5	2237	53.10	0.09	1.51	0.02	0.19	14.32	0.04	–	0.39	27.34	0.81	0.04	–	–	0.00	97.85
5		X	ARS-X5	2238	54.76	0.13	1.44	0.02	0.18	14.39	0.04	–	0.39	27.50	1.09	0.04	0.00	–	–	100.00
1			ARS-X5	2239	51.54	0.31	2.41	0.01	0.47	6.31	0.03	–	0.23	14.98	22.47	0.02	0.00	0.34	–	99.11
5		X	ARS-X5	2240	53.86	0.11	1.45	0.01	0.31	14.82	0.05	–	0.35	27.12	0.90	0.06	–	–	–	99.03
5		X	ARS-X5	2241	53.81	0.11	1.46	0.00	0.23	14.66	0.04	–	0.40	27.15	0.95	0.01	–	–	0.00	98.83
5			ARS-X5	2242	53.86	0.08	1.39	–	0.17	14.92	0.06	0.01	0.40	27.07	0.69	0.04	0.01	–	–	98.70
1			ARS-X5	2243	51.99	0.28	2.42	0.03	0.43	6.30	0.03	–	0.24	15.98	21.11	0.03	0.00	0.25	0.01	99.09
5		X	ARS-X5	2244	53.92	0.08	1.46	0.02	0.13	14.22	0.06	–	0.37	27.62	0.79	0.05	0.00	–	–	98.74
1			ARS-X5	2245	51.72	0.29	2.42	0.04	0.47	6.44	0.02	–	0.22	15.34	22.32	0.02	0.00	0.31	0.00	99.61
1			ARS-X5	2246	51.44	0.30	2.44	0.03	0.52	6.05	0.00	–	0.21	15.03	22.45	0.02	–	0.26	0.00	98.77

Tag	Tag*	A1-in-Opx	Sample	ID	SiO2	TiO2	Al2O3	V2O3	Cr2O3	FeO	NiO	ZnO	MnO	MgO	CaO	SrO	BaO	Na2O	K2O	Total
5		X	ARS-X5	2247	53.77	0.12	1.45	–	0.15	14.26	0.05	0.02	0.41	27.28	1.07	0.02	–	–	–	98.59
5	1	X	ARN-X9	2352	53.24	0.14	1.49	0.02	0.17	16.08	0.08	–	0.42	25.77	0.80	0.03	0.00	0.01	–	98.26
5	1	X	ARN-X9	2353	53.55	0.12	1.43	0.02	0.24	15.86	0.05	–	0.36	26.15	1.10	0.03	–	–	–	98.90
5	1	X	ARN-X9	2354	53.54	0.13	1.36	0.02	0.26	16.06	0.06	0.00	0.38	25.80	1.09	0.03	–	–	–	98.74
5	2	X	ARN-X9	2355	53.47	0.15	0.95	0.03	0.07	17.82	0.06	–	0.42	25.11	0.82	–	0.02	0.01	–	98.91
5	2	X	ARN-X9	2356	53.82	0.13	0.85	0.01	0.10	17.78	0.05	–	0.41	25.10	0.86	0.03	0.00	0.01	0.00	99.15
5	2	X	ARN-X9	2357	53.76	0.14	0.98	0.02	0.09	17.65	0.05	0.01	0.38	25.25	0.73	0.02	–	–	–	99.09
1	1		ARN-X11	2366	52.72	0.22	1.80	0.03	0.20	6.92	0.02	–	0.22	14.83	22.55	0.03	0.02	0.24	–	99.80
1	1		ARN-X11	2367	53.16	0.20	1.86	0.04	0.23	7.05	0.04	–	0.26	14.90	22.60	0.03	0.00	0.23	–	100.60
5	1	X	ARN-X11	2368	53.23	0.08	1.15	0.03	0.09	17.50	0.06	–	0.44	24.52	1.30	0.03	0.01	0.00	–	98.44
4	1		ARN-X11	2369	52.82	0.15	1.35	–	0.17	6.66	0.02	–	0.26	15.16	22.76	0.03	–	0.21	–	99.60
5	1	X	ARN-X11	2370	53.78	0.08	0.87	0.00	0.09	18.16	0.04	–	0.46	25.10	0.67	0.01	–	–	0.00	99.28
4	1		ARN-X11	2371	53.67	0.10	0.89	0.04	0.14	6.07	0.03	–	0.24	15.74	23.12	0.03	0.00	0.21	0.00	100.27
5	1	X	ARN-X11	2372	53.54	0.11	1.08	0.02	0.11	18.24	0.05	–	0.43	24.78	1.11	0.01	–	–	–	99.48
5	1	X	ARN-X11	2373	53.92	0.07	0.85	0.01	0.09	17.81	0.06	–	0.40	25.49	0.62	0.00	0.01	–	0.00	99.35
1	1		ARN-X11	2374	52.79	0.20	1.93	0.01	0.26	6.97	0.03	–	0.21	15.31	21.53	0.03	0.02	0.22	0.00	99.52
5	1	X	ARN-X11	2375	53.39	0.07	1.12	0.03	0.12	17.93	0.04	–	0.46	25.12	0.81	0.01	–	–	0.00	99.10
4	1		ARN-X11	2376	53.41	0.08	1.32	0.00	0.22	6.00	0.03	0.01	0.18	15.29	23.10	0.01	0.01	0.17	0.01	99.82
4	1		ARN-X11	2377	53.35	0.15	1.23	0.03	0.16	6.11	0.02	–	0.23	14.92	23.71	0.03	–	0.12	–	100.06
5	1	X	ARN-X11	2378	53.38	0.06	1.07	0.01	0.09	18.29	0.05	–	0.42	24.72	0.77	0.03	–	0.01	–	98.87
5	1	X	ARN-X13	2316	53.90	0.16	1.05	0.03	0.31	15.35	0.06	–	0.34	26.64	1.29	–	0.01	0.00	–	99.15
5	1	X	ARN-X13	2317	54.04	0.19	1.06	0.03	0.26	15.58	0.07	–	0.35	26.99	0.68	–	–	–	0.00	99.26
1	1		ARN-X13	2318	51.96	0.33	1.76	0.05	0.50	9.00	0.03	–	0.20	15.32	21.18	0.03	–	0.28	0.00	100.64
5	1	X	ARN-X13	2319	54.20	0.19	1.07	0.03	0.28	16.38	0.05	–	0.34	26.29	0.74	0.03	0.01	0.00	0.00	99.60
1	1		ARN-X13	2320	52.79	0.38	2.01	0.09	0.52	5.62	0.03	–	0.17	15.34	22.58	0.08	0.01	0.27	0.00	99.89
5	1	X	ARN-X13	2321	53.81	0.20	1.05	–	0.24	16.83	0.03	0.00	0.36	25.93	0.73	0.06	0.01	–	–	99.24
1	1		ARN-X13	2322	52.97	0.40	2.02	0.05	0.57	5.57	0.04	–	0.17	15.39	22.37	0.01	0.01	0.25	0.02	99.83
1	1		ARN-X13	2323	53.04	0.29	1.42	0.07	0.46	5.52	0.04	–	0.19	15.39	23.06	0.03	0.02	0.27	–	99.78

Tag*: 1 = Fine-grained; 2 = Medium-grained.

Pyroxenite Layers in the Mooimeisjesfontein area																				
1			JB031-A1	1688	52.26	0.38	1.84	0.05	0.29	7.42	0.04	0.01	0.19	15.00	22.31			0.32		100.11
5		X	JB031-A1	1689	53.44	0.19	0.88	–	0.11	17.59	0.06	–	0.40	24.82	1.89			0.01		99.39
5		X	JB031-A1	1690	53.68	0.16	0.73	–	0.09	18.04	0.04	–	0.39	24.86	1.03			0.02		99.04
5		C	JB031-A1	1691	53.68	0.15	0.94	0.03	0.08	17.31	0.05	–	0.36	24.76	1.97			0.03		99.37
1			JB031-A1	1692	52.62	0.38	1.55	0.11	0.24	7.01	0.04	0.03	0.23	14.72	22.81			0.31		100.04
1			JB031-A1	1693	52.62	0.32	1.83	0.07	0.29	7.05	0.04	–	0.21	14.49	22.86			0.35		100.13
5		X	JB031-A1	1694	53.60	0.16	0.85	0.02	0.12	17.72	0.08	–	0.37	25.17	1.06			–		99.15
5		C	JB031-A1	1695	53.34	0.18	0.78	0.01	0.10	17.76	0.06	–	0.38	25.08	1.76			0.02		99.47
5		X	JB031-A1	1696	53.71	0.20	0.68	0.02	0.08	18.01	0.04	0.03	0.39	25.36	1.09			–		99.61
1			JB031-A1	1697	52.24	0.39	1.69	0.04	0.24	7.91	0.05	0.00	0.21	14.72	22.34			0.29		100.12
5		X	JB031-A2	1700	53.34	0.17	0.89	0.02	0.11	17.72	0.05	–	0.36	25.39	1.40			0.01		99.45
5		X	JB031-A2	1701	53.23	0.20	0.82	0.01	0.08	18.11	0.08	0.06	0.37	25.07	1.11			–		99.15
1			JB031-A2	1702	52.88	0.19	1.20	0.07	0.09	6.46	0.04	–	0.14	15.07	23.39			0.24		99.76
1			JB031-A2	1703	52.58	0.30	1.53	0.07	0.20	7.90	0.05	–	0.21	14.78	21.92			0.33		99.87
1			JB031-A2	1704	52.27	0.41	1.92	0.05	0.23	7.92	0.05	–	0.20	14.57	22.25			0.32		100.18
6		X	JB031-A2	1705	52.84	0.18	1.16	0.00	0.09	19.91	0.06	–	0.45	24.21	0.62			0.00		99.52
1			JB031-T	1643	52.83	0.33	1.63	0.03	0.21	7.73	0.04	–	0.24	14.72	22.14			0.34		100.25
5		X	JB031-T	1644	52.72	0.15	1.10	0.00	0.10	18.50	0.07	–	0.39	24.23	0.61			0.04		97.92
5		X	JB031-T	1645	53.82	0.16	0.71	0.02	0.10	17.89	0.07	0.03	0.39	25.65	0.63			–		99.47
5		C	JB031-T	1646	53.38	0.20	0.94	0.06	0.13	17.66	0.07	0.04	0.36	25.02	1.84			0.02		99.72
5		C	JB031-T	1647	53.73	0.19	0.86	0.02	0.12	17.81	0.07	0.00	0.36	24.88	1.69			0.02		99.76
5		X	JB031-T	1648	53.52	0.18	0.91	0.01	0.11	18.50	0.08	–	0.40	24.76	1.48			0.01		99.97
1			JB031-T	1649	52.26	0.36	1.62	0.07	0.22	7.66	0.04	–	0.21	14.92	21.74			0.31		99.41

Tag	Tag*	Al-in-Opx	Sample	ID	SiO2	TiO2	Al2O3	V2O3	Cr2O3	FeO	NiO	ZnO	MnO	MgO	CaO	SrO	BaO	Na2O	K2O	Total
6		X	JB031-T	1650	52.60	0.12	0.80	0.01	0.13	20.39	0.05	–	0.45	23.42	0.62			0.01		98.61
1			JB031-T	1651	52.40	0.26	1.41	0.07	0.24	7.01	0.05	–	0.20	14.60	22.93			0.30		99.46
6		X	JB031-T	1652	52.57	0.12	0.81	–	0.14	20.37	0.04	–	0.46	23.90	0.69			–		99.12
1			JB031-P1	1784	52.25	0.36	1.60	0.09	0.23	7.37	0.05	–	0.19	15.17	21.95			0.32		99.58
5		X	JB031-P1	1785	53.04	0.17	0.91	0.02	0.08	17.66	0.06	0.05	0.39	25.69	0.87			0.01		98.96
5		X	JB031-P1	1786	52.89	0.18	0.69	0.03	0.10	18.44	0.07	0.02	0.39	25.30	0.68			0.01		98.78
1			JB031-P1	1787	52.16	0.38	1.57	0.10	0.24	6.88	0.05	0.01	0.20	14.84	22.88			0.31		99.61
5		X	JB031-P1	1788	53.24	0.17	0.80	0.04	0.14	18.03	0.06	0.00	0.38	25.11	1.51			0.01		99.48
1			JB031-P1	1789	51.88	0.41	1.69	0.08	0.27	6.64	0.05	–	0.18	14.69	22.98			0.35		99.22
1			JB031-P1	1801	51.92	0.20	1.24	0.07	0.19	7.02	0.03	0.01	0.18	14.51	23.01			0.26		98.63
5		X	JB031-P3	1574	53.84	0.20	0.71	0.02	0.05	18.27	0.04	–	0.39	25.42	0.96			0.01		99.91
5		X	JB031-P3	1575	53.79	0.19	0.79	0.01	0.11	18.25	0.06	–	0.38	25.06	1.38			0.01		100.05
5		C	JB031-P3	1576	53.26	0.19	0.94	0.02	0.10	17.77	0.06	–	0.38	24.92	1.62			0.01		99.27
5		X	JB031-P3	1577	53.47	0.22	0.85	0.04	0.12	17.90	0.07	–	0.37	24.87	1.34			0.01		99.25
1			JB031-P3	1578	52.75	0.45	1.59	0.06	0.18	7.20	0.03	–	0.20	14.98	22.32			0.34		100.10
1			JB031-P3	1579	52.60	0.40	1.63	0.07	0.23	7.62	0.06	0.00	0.20	15.00	21.75			0.36		99.92
5		X	JB031-P3	1580	53.88	0.23	0.72	0.01	0.10	17.97	0.04	–	0.41	25.37	0.75			–		99.47
5		X	JB031-P3	1581	53.52	0.23	0.72	0.03	0.11	18.13	0.06	0.01	0.40	25.45	1.13			0.00		99.79
1			JB031-P3	1582	52.29	0.41	1.75	0.06	0.23	7.06	0.03	–	0.18	14.42	22.86			0.32		99.62
5		X	JB031-P4	1755	51.97	0.22	0.88	0.01	0.10	18.34	0.07	0.02	0.40	24.40	1.37			0.01		97.79
1			JB031-P4	1756	51.21	0.49	1.64	0.03	0.20	8.06	0.06	0.01	0.20	14.63	21.91			0.31		98.73
5		X	JB031-P4	1757	52.10	0.20	0.72	0.03	0.06	19.38	0.07	0.03	0.39	24.61	0.86			0.00		98.44
1			JB031-P4	1758	51.38	0.36	1.46	0.06	0.21	7.31	0.04	–	0.21	14.78	22.45			0.31		98.58
1			JB031-P4	1763	51.98	0.43	1.65	0.07	0.23	7.78	0.05	–	0.19	14.84	22.20			0.35		99.76
5		C	JB031-P4	1764	52.71	0.18	0.88	0.02	0.13	18.31	0.08	0.02	0.37	24.58	1.87			0.01		99.15
5		X	JB031-P4	1765	53.60	0.18	0.82	0.03	0.09	19.05	0.08	0.02	0.41	25.27	0.69			–		100.23
1			JB031-P4	1766	51.85	0.18	1.31	0.04	0.23	6.80	0.03	–	0.16	14.76	23.14			0.33		98.84
1			JB031-P5	1741	52.66	0.20	1.19	0.10	0.17	10.28	0.03	–	0.26	17.36	17.50			0.24		99.99
5		X	JB031-P5	1742	52.84	0.18	0.95	0.02	0.10	18.32	0.06	0.04	0.42	24.67	1.38			–		98.98
5		X	JB031-P5	1743	52.65	0.20	0.70	0.01	0.11	18.69	0.06	–	0.43	24.66	1.38			0.02		98.93
3			JB031-P5	1744	51.79	0.46	1.54	0.07	0.23	7.41	0.05	–	0.19	14.81	22.39			0.30		99.25
5		C	JB031-P5	1745	52.73	0.17	0.88	0.03	0.10	18.31	0.05	0.04	0.38	24.52	1.81			0.01		99.04
1			JB031-P5	1746	52.71	0.22	1.35	0.10	0.24	6.97	0.03	–	0.18	15.01	22.74			0.29		99.83
1			JB031-P5	1747	52.04	0.24	1.58	0.05	0.22	7.07	0.03	0.01	0.17	14.59	22.16			0.31		98.48
1			JB031-P7	1871	51.21	0.26	2.24	0.04	0.23	11.16	0.03	0.00	0.26	16.42	16.69			0.22		98.76
1			JB031-P7	1872	52.00	0.35	1.48	0.05	0.24	7.39	0.03	–	0.23	14.64	22.73			0.33		99.48
1			JB031-P7	1873	52.73	0.35	1.53	0.08	0.18	7.92	0.05	–	0.22	14.99	21.54			0.25		99.84
5		X	JB031-P7	1874	53.64	0.18	0.81	0.03	0.10	18.44	0.05	0.00	0.37	24.83	1.34			0.02		99.81
5		C	JB031-P7	1875	53.19	0.17	0.90	0.04	0.06	18.24	0.06	0.00	0.39	24.26	2.14			0.03		99.48
5		C	JB031-P7	1876	53.20	0.18	0.93	0.03	0.11	18.20	0.05	–	0.39	24.45	1.79			0.01		99.34
5		C	JB031-P7	1877	52.93	0.17	0.87	0.03	0.11	18.14	0.06	0.01	0.39	24.45	1.71			0.00		98.86
1			JB031-P7	1878	52.33	0.30	1.54	0.06	0.21	8.11	0.04	–	0.18	15.09	21.09			0.27		99.22
1			JB031-P7	1879	52.89	0.32	1.34	0.05	0.23	6.85	0.04	–	0.18	14.69	22.71			0.25		99.56
3			JB031-P9	1774	51.73	0.44	1.63	0.05	0.25	7.32	0.05	–	0.18	14.42	22.73			0.32		99.13
5		C	JB031-P9	1775	53.07	0.20	1.02	0.03	0.10	18.02	0.08	0.02	0.42	24.21	2.24			0.04		99.45
1			JB031-P9	1776	52.07	0.43	1.70	0.08	0.23	7.59	0.03	–	0.18	14.42	22.57			0.34		99.65
1			JB031-P9	1777	51.96	0.36	1.48	0.05	0.21	7.39	0.05	–	0.18	14.66	22.48			0.34		99.15
5		X	JB031-P9	1778	53.03	0.16	0.84	0.00	0.10	18.66	0.08	0.02	0.39	24.69	1.12			0.01		99.10
5		X	JB031-G1	1670	52.61	0.18	0.92	0.02	0.10	18.91	0.07	–	0.38	24.47	0.96			–		98.64
5		X	JB031-G1	1671	52.93	0.26	1.06	0.01	0.09	18.96	0.05	0.02	0.40	24.17	1.19			0.01		99.15
1			JB031-G1	1672	52.56	0.21	1.24	0.07	0.18	7.24	0.04	–	0.21	14.60	22.88			0.27		99.49
1			JB031-G1	1673	52.41	0.40	1.69	0.06	0.21	7.82	0.04	–	0.20	14.44	22.22			0.35		99.83
6		X	JB031-G1	1674	52.68	0.11	0.96	0.04	0.11	20.93	0.06	–	0.47	23.00	0.56			–		98.92
1			JB031-G2	1909	53.13	0.34	1.45	0.06	0.20	7.76	0.05	–	0.20	14.57	22.38			0.28		100.43

Tag	Tag*	A1-in-Opx	Sample	ID	SiO2	TiO2	Al2O3	V2O3	Cr2O3	FeO	NiO	ZnO	MnO	MgO	CaO	SrO	BaO	Na2O	K2O	Total
5		X	JB031-G2	1910	53.84	0.19	1.03	0.01	0.11	18.72	0.07	–	0.39	24.74	1.14			0.01		100.25
1			JB031-G2	1911	53.09	0.35	1.61	0.04	0.25	7.46	0.04	–	0.30	14.52	22.72			0.30		100.68
6		X	JB031-G2	1912	53.87	0.14	0.95	0.02	0.08	20.00	0.08	–	0.42	23.96	0.60			0.00		100.15
1			JB031-G2	1913	52.84	0.40	1.64	0.07	0.23	7.89	0.05	–	0.19	14.75	21.81			0.31		100.17
5		X	JB031-G2	1914	53.86	0.17	0.77	0.03	0.11	18.88	0.06	0.02	0.38	24.20	1.54			0.01		100.02
5		X	JB031-G3	1942	52.34	0.19	0.93	–	0.11	19.19	0.06	–	0.39	23.33	1.86			0.02		98.42
1			JB031-G3	1943	52.16	0.42	1.68	0.11	0.23	7.96	0.02	–	0.21	14.35	22.46			0.32		99.94
5		C	JB031-G4	1858	52.63	0.36	0.85	0.03	0.13	19.56	0.04	0.02	0.42	23.48	2.00			0.02		99.54
1			JB031-G4	1859	52.19	0.27	1.51	0.07	0.21	7.52	0.04	0.02	0.18	14.57	22.64			0.27		99.48
1			JB031-G4	1860	53.03	0.40	1.53	0.05	0.24	7.90	0.04	–	0.21	14.66	22.32			0.32		100.69
1			JB031-G4	1861	52.08	0.42	1.89	0.05	0.27	7.75	0.03	0.00	0.24	14.26	22.34			0.31		99.64
1			PM-90	1082	51.81	0.22	1.19		0.03	14.08		–	0.35	12.07	20.97	–	0.01	0.23	–	100.96
1			PM-90	1076	53.14	0.25	1.33		0.01	12.15		–	0.30	12.19	21.35	–	0.02	0.26	–	100.99
1			PM-90	1065	52.39	0.26	1.29		0.01	11.28		–	0.32	12.44	22.01	–	0.01	0.24	0.01	100.25
3			PM-90	1066	53.15	0.37	1.26		0.02	11.14		–	0.30	12.27	22.10	–	–	0.26	0.01	100.87
2			PM-90	1058	52.17	0.16	0.96		–	10.44		–	0.28	12.53	22.30	–	–	0.23	0.00	99.09
2			PM-90	1063	53.16	0.24	1.26		0.01	10.28		0.02	0.23	13.22	21.91	–	–	0.23	0.00	100.57
2			PM-90	1064	52.52	0.33	1.19		0.05	10.60		–	0.26	12.81	21.93	–	–	**0.22**	0.01	99.91
1			PM-90	1046	52.11	0.17	1.08		0.02	11.24		–	0.33	12.17	21.84	–	–	0.22	–	99.17
1			PM-90	1047	51.11	0.39	2.25		–	11.09		–	0.31	11.59	22.08	–	0.01	0.29	0.00	99.11
2			PM-90	1044	52.30	0.24	1.11		0.10	9.43		–	0.24	13.50	22.26	–	–	0.20	–	99.39
1			PM-35	1945	50.83	0.31	1.50	0.07	0.01	12.48	0.02	–	0.31	11.54	21.88			0.30		99.24
1			PM-35	1946	51.36	0.32	1.48	0.13	0.01	12.81	0.01	–	0.33	11.86	21.22			0.25		99.77
2			PM-0-1	1807	52.06	0.36	1.22	0.13	0.04	11.93	0.02	–	0.35	13.33	20.88			0.23		100.55
5		X	PM-0-1	1808	51.40	0.15	0.61	0.02	0.02	26.17	0.02	–	0.57	19.43	0.90			–		99.29
2			PM-0-1	1809	51.46	0.32	1.27	0.07	0.02	10.85	0.02	–	0.24	12.95	21.83			0.22		99.25
5		X	PM-0-1	1810	51.64	0.19	0.78	0.06	0.02	26.57	0.03	–	0.58	19.63	0.88			–		100.36
1			PM-0-1	1811	51.73	0.17	1.14	0.05	0.01	11.06	0.02	–	0.32	12.61	22.11			0.23		99.46
3			PM-0-1	1813	51.26	0.34	1.34	0.08	0.01	12.18	0.06	–	0.34	12.36	21.18			0.25		99.39
1			PM-0-1	1814	51.95	0.23	1.28	0.12	–	11.27	0.04	0.01	0.34	12.35	22.12			0.24		99.94
1			PM-0'	465	52.21	0.42	1.30		–	12.16		0.03	0.37	12.79	21.27	–	0.04	0.21	0.00	100.80
1			PM-0'	455	53.05	0.28	1.23		0.05	9.18		–	0.23	13.85	22.49	–	0.00	0.28	0.01	100.66
2			PM-0'	456	52.17	0.28	1.15		0.06	9.73		–	0.21	14.08	21.88	–	–	0.20	–	99.77
2			PM-0'	457	53.13	0.23	1.12		0.07	9.39		–	0.18	13.96	22.24	–	0.01	0.23	0.00	100.58
2			PM-0'	470	53.38	0.21	0.86		0.06	8.50		0.04	0.24	14.49	22.57	–	0.01	0.19	0.00	100.54
5		X	PM-0'	471	53.03	0.13	0.55		–	22.96		0.04	0.55	21.99	0.62	–	0.02	0.00	–	99.89
1			PM-0'	432	51.41	0.33	1.87		0.05	11.49		–	0.27	13.00	21.61	–	–	0.25	–	100.28
1			PM-0'	448	52.52	0.26	1.39		0.02	10.66		–	0.28	12.94	22.02	–	–	0.29	0.01	100.38
2			PM-0'	449	53.63	0.26	1.12		0.07	9.20		0.02	0.24	14.09	21.95	–	0.02	0.22	–	100.81
5		X	PM-0'	450	52.58	0.17	0.66		–	23.73		–	0.51	21.59	0.74	–	–	0.01	–	99.99
1			PM-0'	451	52.62	0.43	1.35		0.06	9.91		0.00	0.26	14.08	21.21	–	–	0.22	0.00	100.14
5		X	PM-0'	440	51.76	0.11	0.59		0.02	26.26		0.01	0.62	19.46	0.70	–	0.00	0.01	–	99.54
6		X	PM-0'	441	51.81	0.10	0.59		0.05	26.38		0.00	0.62	19.57	0.67	–	0.02	–	–	99.81
3			PM-0'	472	52.61	0.31	1.16		0.06	8.96		–	0.32	13.77	22.07	–	–	0.24	–	99.50
1			PM-0'	473	52.42	0.29	1.10		0.09	9.26		0.01	0.24	14.30	21.35	–	0.02	0.23	0.01	99.32
3			PM-0'	474	52.49	0.30	1.08		0.04	9.00		–	0.25	14.46	22.06	–	–	0.22	–	99.90
2			PM-0'	475	52.50	0.30	1.12		0.02	9.13		0.02	0.26	14.39	21.91	–	–	0.27	0.00	99.91
5		X	PM-0'	476	52.30	0.18	0.61		0.05	23.21		–	0.48	21.69	0.85	–	0.03	–	0.00	99.39
1			PM-0-2	1831	52.69	0.26	1.08	0.09	0.04	9.94	0.03	–	0.26	13.68	22.08			0.21		100.37
5		C	PM-0-2	1832	52.69	0.14	0.74	0.07	0.03	21.71	0.04	0.02	0.47	20.73	3.33			0.02		99.97
1			PM-0-2	1833	52.56	0.24	1.10	0.10	0.01	8.85	0.04	–	0.27	14.12	22.37			0.21		99.86
2			PM-0-2	1853	52.59	0.28	1.09	0.10	0.03	9.80	0.03	–	0.31	14.08	21.60			0.18		100.09
5		X	PM-0-2	1854	52.84	0.17	0.59	0.02	0.02	23.76	0.04	–	0.52	21.64	0.64			–		100.24
2			PM-0-2	1855	52.73	0.26	1.00	0.08	0.05	8.62	0.04	–	0.24	14.07	22.57			0.23		99.90

Tag	Tag*	Al-in-Opx	Sample	ID	SiO2	TiO2	Al2O3	V2O3	Cr2O3	FeO	NiO	ZnO	MnO	MgO	CaO	SrO	BaO	Na2O	K2O	Total
5		X	PM-0-2	1856	52.42	0.15	0.60	0.04	0.02	23.32	0.05	0.01	0.55	21.80	0.72			–		99.67
5		C	PM+10	203	52.64	0.18	0.63		0.05	22.27		0.02	0.46	22.25	1.34	–	0.01	–	–	99.85
5		X	PM+10	204	52.99	0.17	0.57		0.01	22.71		0.07	0.58	22.65	0.89	0.04	0.04	–	–	100.72
5		C	PM+10	205	52.00	0.17	0.58		0.04	22.12		0.01	0.50	22.12	1.97	–	–	–	–	99.51
2			PM+10	206	52.30	0.30	1.06		0.03	9.03		–	0.25	14.78	21.52	–	0.02	0.25	0.00	99.53
3			PM+10	281	52.67	0.26	0.86		–	9.50		–	0.26	14.21	22.24	–	–	0.22	0.02	100.25
5		C	PM+10	282	52.44	0.20	0.63		0.04	22.40		0.02	0.56	21.67	1.77	–	0.00	0.04	0.01	99.79
2			PM+10	283	52.81	0.30	0.98		0.04	8.99		–	0.26	14.30	22.00	–	0.00	0.24	–	99.93
6		C	PM+10	212	52.03	0.15	0.93		0.01	21.96		0.01	0.50	20.47	3.38	–	–	0.04	0.00	99.48
1			PM+10	213	52.20	0.39	1.40		0.06	9.08		0.04	0.25	14.28	21.82	–	0.01	0.27	0.01	99.81
6		C	PM+10	214	52.45	0.15	0.88		0.02	22.85		–	0.50	20.82	2.25	–	–	0.03	–	99.97
5		X	PM+10	216	52.48	0.13	0.67		0.02	23.58		0.02	0.58	21.38	0.71	–	–	–	–	99.57
2			PM+10	219	52.80	0.28	0.95		0.05	8.65		0.02	0.26	14.85	22.30	–	0.00	0.22	0.02	100.39
1			PM+10	249	52.82	0.27	1.11		0.06	8.26		0.00	0.23	14.60	21.89	–	0.01	0.23	–	99.49
1			PM+10	250	52.53	0.25	1.16		0.04	9.09		0.03	0.26	14.37	21.72	–	–	0.22	0.01	99.68
2			PM+10	251	51.99	0.24	1.05		0.05	8.09		0.03	0.23	14.38	22.37	–	0.01	0.28	–	98.72
2			PM+10	252	52.62	0.30	1.08		0.07	8.97		0.01	0.27	14.44	22.06	–	0.03	0.24	0.00	100.11
5		X	PM+10	253	52.00	0.20	0.61		0.05	22.52		0.01	0.55	21.65	0.94	0.01	–	0.01	–	98.54
6		X	PM+10	254	51.29	0.17	0.73		–	23.29		0.06	0.57	21.41	0.70	–	–	0.00	–	98.23
6		X	PM+10	255	51.60	0.10	0.80		0.03	23.74		–	0.53	21.14	0.80	–	–	–	–	98.74
5		X	PM+10	256	52.96	0.19	0.62		0.01	22.67		0.07	0.52	21.91	0.90	–	0.02	0.02	–	99.90
5		X	PM+10	257	52.85	0.14	0.48		0.02	22.22		–	0.49	22.06	1.12	–	–	0.00	–	99.39
7		X	PM+10	245	53.21	0.15	0.59		0.01	22.66		0.06	0.52	22.56	0.67	–	–	–	–	100.43
7		X	PM+10	246	52.26	0.13	0.58		–	22.51		–	0.52	22.38	0.66	–	0.04	–	0.00	99.08
5		X	PM+10	247	52.19	0.16	0.63		0.04	22.34		0.00	0.50	22.35	0.65	–	0.01	0.03	–	98.90
2			PM+10	248	52.52	0.29	1.23		0.05	9.02		0.02	0.25	14.51	21.77	–	0.02	0.21	–	99.88
1			PM+13	2021	51.81	0.23	1.28	0.04	0.01	12.37	0.01	–	0.36	12.41	21.52			0.29		100.32
1			PM+13	2022	52.08	0.16	1.15	0.05	0.02	11.92	0.02	–	0.35	12.44	21.81			0.24		100.25
3			PM+13	2023	49.97	0.19	2.52	0.03	0.01	13.77	0.00	–	0.38	12.31	19.67			0.22		99.09
1			PM+13	2024	51.53	0.24	1.43	0.11	0.05	11.82	0.03	0.03	0.34	12.54	21.33			0.29		99.73
5		X	PM+30	1970	52.61	0.15	0.48	0.04	0.00	22.90	0.02	–	0.49	21.87	0.87			–		99.44
2			PM+30	1971	52.24	0.32	1.15	0.09	0.06	9.01	0.05	–	0.23	14.24	22.29			0.23		99.91
5		X	PM+30	1972	51.98	0.20	0.64	0.05	0.02	23.15	0.04	–	0.53	21.67	0.90			0.01		99.21
5		X	PM+30	1977	52.37	0.18	0.57	0.04	0.03	23.26	0.03	–	0.52	22.11	0.85			0.00		99.96
2			PM+30	1978	51.99	0.34	1.17	0.09	0.03	9.32	0.04	–	0.29	14.09	21.90			0.21		99.47
3			PM+41	364	52.27	0.29	1.11		0.03	9.86		0.04	0.31	14.10	21.87	–	0.03	0.21	–	100.13
1			PM+41	365	51.50	0.28	1.11		0.07	9.62		–	0.26	14.62	21.27	–	0.01	0.18	0.02	98.97
5		C	PM+41	366	51.16	0.18	1.28		0.02	22.35		–	0.43	21.97	0.80	–	0.03	0.02	0.02	98.25
1			PM+41	352	52.62	0.31	1.10		0.06	8.35		–	0.22	14.35	22.14	–	–	0.23	0.00	99.38
1			PM+41	353	52.01	0.32	1.18		0.07	8.41		0.02	0.26	14.39	22.21	–	–	0.25	0.00	99.13
1			PM+41	354	51.39	0.37	1.38		0.07	8.81		0.08	0.24	14.21	22.03	–	0.00	0.27	0.01	98.86
5		X	PM+41	355	52.42	0.12	0.54		0.00	23.20		0.00	0.46	22.27	0.51	–	0.00	–	–	99.53
7		X	PM+41	344	52.17	0.17	0.55		0.03	24.30		0.02	0.48	22.12	0.75	–	0.01	–	–	100.59
3			PM+41	345	52.56	0.19	0.90		0.04	7.46		–	0.19	14.82	22.78	–	0.03	0.16	0.01	99.14
1			PM+41	346	52.29	0.21	0.95		0.03	8.24		–	0.23	14.36	22.58	–	–	0.18	–	99.09
2			PM+41	347	52.50	0.33	1.15		0.04	9.22		–	0.27	14.54	22.15	–	0.00	0.25	–	100.44
5		C	PM+41	348	51.21	0.11	1.32		0.09	21.20		–	0.46	21.23	1.47	–	0.01	0.01	0.02	97.14
5		C	PM+41	324	52.12	0.16	0.53		0.04	22.61		0.02	0.52	22.10	0.93	–	–	0.01	0.01	99.06
2			PM+41	325	52.57	0.29	0.94		0.06	8.27		–	0.23	14.54	22.44	–	–	0.23	–	99.59
5		X	PM+41	326	51.87	0.15	0.53		0.04	23.27		0.02	0.51	21.73	0.75	–	–	0.02	0.00	98.88
5		C	PM+41	327	52.19	0.16	0.58		0.03	21.78		0.00	0.54	21.56	2.25	–	–	0.00	0.00	99.10
2			PM+41	328	52.78	0.21	0.97		0.06	8.40		–	0.25	14.41	22.29	–	0.00	0.20	0.00	99.58
3			PM+41	329	51.56	0.30	1.00		0.03	9.12		–	0.24	14.24	21.62	–	–	0.20	0.00	98.30
5		X	PM+41	330	51.79	0.16	0.60		–	23.17		0.02	0.54	21.74	0.70	–	0.00	0.02	0.00	98.74

Tag	Tag*	A1-in-Opx	Sample	ID	SiO2	TiO2	Al2O3	V2O3	Cr2O3	FeO	NiO	ZnO	MnO	MgO	CaO	SrO	BaO	Na2O	K2O	Total
1			PM+41	318	51.98	0.31	1.19		0.05	9.55		0.01	0.28	14.69	21.34	–	–	0.18	–	99.59
1			PM+41	319	51.92	0.30	0.99		0.02	8.68		0.03	0.26	14.49	21.89	–	0.04	0.21	–	98.82
1			PM+41	320	52.49	0.29	1.01		0.07	8.87		–	0.30	14.59	21.40	–	–	0.22	0.00	99.26
3			PM+41	321	52.76	0.24	0.93		0.05	8.15		–	0.18	14.40	22.45	–	–	0.21	–	99.37
6		C	PM+41	323	51.58	0.20	0.74		0.05	22.08		0.09	0.53	20.47	3.20	–	0.00	0.02	0.00	98.97
1		X	PM+41	300	52.22	0.37	1.26		0.01	8.90		0.01	0.26	14.15	21.94	–	0.02	0.26	–	99.42
5		X	PM+41	301	51.21	0.16	0.61		0.02	22.94		–	0.51	21.47	0.64	–	0.02	–	–	97.58
3			PM+41	302	52.43	0.22	1.08		0.05	8.99		0.02	0.21	14.29	21.70	–	0.01	0.17	0.01	99.18
5		X	PM+41	303	52.05	0.13	0.47		0.02	22.46		0.02	0.50	22.17	0.58	–	–	0.01	–	98.43
2			PM+41	304	52.14	0.29	1.06		0.04	8.72		–	0.23	14.44	21.97	–	0.04	0.21	–	99.14
2			PM+41	305	52.30	0.28	1.02		0.06	8.04		0.03	0.21	14.45	22.73	–	0.02	0.18	0.01	99.33
1			PM+41	297	52.28	0.23	1.11		0.04	9.30		0.01	0.26	14.20	22.32	–	0.01	0.20	–	99.96
5		C	PM+41	298	52.94	0.16	0.77		0.03	21.95		0.01	0.50	20.91	2.31	–	–	0.07	0.00	99.66
2			PM+41	299	52.81	0.40	1.14		0.06	8.62		0.06	0.26	14.58	22.24	–	–	0.25	–	100.43
2			PM+48	1137	52.96	0.31	1.09		0.10	8.83		0.05	0.27	14.10	22.17	–	–	0.23	0.01	100.13
1			PM+48	1138	52.46	0.32	1.25		0.02	8.18		0.04	0.25	14.33	22.59	–	–	0.27	–	99.71
5		X	PM+48	1139	52.13	0.19	0.60		0.03	22.17		0.01	0.52	22.10	0.93	–	–	0.01	–	98.69
2			PM+48	1140	53.27	0.31	1.05		0.06	8.17		–	0.23	14.40	22.62	–	–	0.24	–	100.34
3			PM+48	1118	53.92	0.31	1.19		0.07	8.98		–	0.24	14.26	21.75	–	–	0.25	–	100.97
2			PM+48	1119	52.78	0.33	1.24		0.09	7.56		–	0.19	14.20	23.18	–	0.00	0.21	0.00	99.77
5		X	PM+48	1120	53.73	0.20	0.50		0.04	22.43		–	0.53	22.21	0.76	–	–	0.01	–	100.40
3			PM+48	1110	53.30	0.31	1.01		0.02	8.21		0.02	0.23	14.46	22.61	–	0.03	0.25	0.00	100.44
7		X	PM+48	1111	53.26	0.18	0.59		0.00	22.50		–	0.51	22.19	0.55	–	0.02	–	0.00	99.81
1			PM+48	1112	53.08	0.32	1.06		0.04	8.64		–	0.24	14.21	22.21	–	–	0.22	–	100.03
5		C	PM+48	1113	53.30	0.20	0.71		0.07	21.84		–	0.48	21.76	1.73	–	–	–	0.01	100.10
2			PM+48	1105	53.18	0.33	1.06		0.07	8.64		–	0.24	14.22	21.81	–	–	0.25	0.01	99.82
5		X	PM+48	1106	53.78	0.18	0.49		0.06	22.23		–	0.52	22.27	0.81	–	–	–	0.00	100.34
5		X	PM+48	1107	53.33	0.19	0.56		0.06	22.34		–	0.53	22.12	0.77	–	–	–	–	99.90
5		X	PM+48	1108	53.36	0.19	0.60		0.04	22.42		–	0.55	22.08	0.68	0.03	–	–	0.01	99.95
2			PM+48	1109	52.08	0.21	1.40		0.04	8.08		–	0.21	14.14	22.07	–	–	0.21	0.05	98.48
1			PM+48	1094	53.21	0.32	1.11		0.07	8.59		–	0.26	14.19	21.87	–	0.00	0.23	–	99.85
5		X	PM+48	1095	53.16	0.21	0.58		–	22.37		–	0.53	22.35	0.81	–	–	–	0.00	100.01
2			PM+48	1096	53.44	0.28	1.02		0.09	8.59		–	0.20	14.60	21.17	–	–	0.22	–	99.61
3			PM+48	1088	53.31	0.49	1.33		0.04	8.69		–	0.19	13.99	22.37	–	0.02	0.26	–	100.68
7		X	PM+48	1089	53.28	0.20	0.56		0.01	22.72		–	0.56	21.89	0.84	–	0.02	0.01	0.01	100.09
5			PM+48	1092	53.66	0.19	0.57		0.04	22.30		–	0.52	22.08	0.85	–	0.02	0.01	–	100.24
1			PM+70	2000	52.01	0.21	1.06	0.08	0.07	8.69	0.01	–	0.28	14.56	22.15			0.23		99.37
5		X	PM+70	2001	52.69	0.12	0.51	0.07	0.02	21.90	0.06	0.02	0.48	22.81	0.75			0.01		99.43
1			PM+70	2002	52.87	0.20	0.97	0.09	0.07	7.78	0.02	–	0.25	14.76	22.68			0.23		99.92
2			PM+70	2003	53.00	0.20	0.87	0.04	0.06	7.71	0.04	–	0.22	14.73	22.84			0.22		99.94
7		X	PM+70	2004	52.33	0.11	0.45	0.02	0.02	22.32	0.04	0.01	0.51	22.82	0.67			0.00		99.33
3			PM+70	2005	52.51	0.18	0.86	0.13	0.04	8.15	0.04	–	0.25	14.59	22.39			0.23		99.37
5		X	PM+110	2088	53.10	0.16	0.52	0.05	0.04	22.38	0.05	–	0.54	22.88	0.76			0.01		100.49
1			PM+110	2089	52.60	0.28	1.03	0.11	0.10	8.57	0.03	–	0.27	14.72	22.42			0.23		100.36
1			PM+110	2090	52.76	0.30	1.39	0.11	0.06	8.60	0.03	–	0.21	14.53	22.08			0.22		100.30
5		X	PM+110	2091	52.97	0.14	0.78	0.03	0.04	23.15	0.05	–	0.52	22.21	0.75			0.01		100.65
1			PM+110	2092	52.92	0.28	1.18	0.07	0.08	8.51	0.04	–	0.26	14.64	22.58			0.21		100.76
5		X	PM+110	2093	53.19	0.15	0.61	0.04	0.03	21.81	0.05	–	0.53	23.11	0.82			0.00		100.35
2			PM+110	2094	53.29	0.26	1.13	0.11	0.05	8.24	0.05	–	0.23	14.75	22.39			0.23		100.73
2			PM+110	2095	53.13	0.26	1.09	0.13	0.06	8.59	0.02	–	0.27	14.66	22.22			0.20		100.61
5		X	PM+110	2096	53.38	0.15	0.55	0.03	0.02	21.42	0.05	–	0.46	23.41	0.66			0.00		100.13
1			PM-145	370	53.15	0.22	1.01		0.02	8.61		0.02	0.25	14.67	21.93	–	–	0.21	–	100.09
1			PM-145	371	52.48	0.25	1.07		0.08	10.06		–	0.26	15.45	19.73	–	–	0.18	0.01	99.56
5		X	PM-145	372	52.70	0.18	0.75		0.06	22.21		–	0.54	22.55	0.68	–	–	–	0.01	99.67

Tag	Tag*	Al-in-Opx	Sample	ID	SiO2	TiO2	Al2O3	V2O3	Cr2O3	FeO	NiO	ZnO	MnO	MgO	CaO	SrO	BaO	Na2O	K2O	Total
1			PM-145	373	52.20	0.27	1.16		0.12	8.15		0.00	0.22	14.73	22.09	–	–	0.19	0.02	99.14
1			PM-145	374	52.32	0.25	0.96		0.06	9.13		0.01	0.25	15.26	20.95	–	0.01	0.19	–	99.41
3			PM-145	376	53.03	0.49	1.04		0.00	8.31		–	0.25	14.77	21.77	–	–	0.21	–	99.87
3			PM-145	377	52.55	0.47	1.10		0.04	8.39		0.03	0.28	14.63	22.07	–	–	0.16	–	99.72
1			PM-145	378	52.57	0.21	1.17		0.08	7.87		0.01	0.21	14.54	22.29	–	0.01	0.22	–	99.19
5		X	PM-145	379	53.25	0.19	0.60		0.02	21.15		0.05	0.47	23.04	1.13	–	0.00	0.00	–	99.91
5		X	PM-145	380	53.14	0.17	0.71		0.02	21.55		–	0.47	22.77	1.08	–	0.02	0.01	0.01	99.95
1			PM-145	381	52.76	0.28	1.22		0.03	8.74		0.00	0.30	14.96	21.50	–	–	0.18	0.00	99.98
5		X	PM-145	382	52.42	0.18	0.78		0.01	21.17		0.02	0.47	23.30	0.72	–	0.00	0.02	0.01	99.10
1			PM-145	383	52.72	0.25	1.42		0.06	9.74		0.02	0.27	15.21	19.95	–	–	0.22	0.01	99.86
6		X	PM-145	384	53.11	0.13	0.87		0.02	22.61		–	0.52	22.19	0.62	–	–	–	–	100.08
1			PM-145	385	52.97	0.25	1.06		0.04	7.76		–	0.17	14.49	22.20	–	0.01	0.16	0.00	99.11
1			PM-145	386	53.12	0.27	1.07		0.04	7.62		0.02	0.19	14.81	22.58	–	–	0.18	–	99.88
1			PM-145	387	53.30	0.29	1.04		0.10	8.33		–	0.25	14.82	22.15	–	–	0.17	–	100.44
5		X	PM-145	388	53.37	0.17	0.53		0.05	22.30		–	0.50	22.47	0.89	–	0.02	0.00	–	100.31
5		X	PM-145	389	53.06	0.18	0.60		0.03	22.34		0.01	0.53	22.44	0.84	–	0.04	–	–	100.06
6		X	PM-145	390	53.18	0.20	0.70		0.06	22.19		–	0.61	22.53	0.73	–	–	–	0.01	100.22
1			PM-145	399	52.46	0.25	1.24		0.09	8.36		0.02	0.29	14.61	22.31	–	–	0.23	0.02	99.87
2			PM-145	400	53.15	0.23	1.06		0.08	8.07		–	0.21	14.88	22.58	–	–	0.20	–	100.46
5		X	PM-145	401	53.50	0.19	0.70		0.00	21.39		0.01	0.54	23.12	0.60	–	–	0.04	–	100.09
5		X	PM-145	402	53.10	0.13	0.39		0.03	20.84		–	0.39	23.92	0.65	–	–	–	–	99.46
5		X	PM-145	403	53.87	0.13	0.54		0.06	20.68		0.05	0.50	23.58	0.71	–	0.03	0.00	–	100.15
5		X	PM-145	404	52.89	0.13	0.46		0.08	20.88		0.01	0.52	23.09	0.68	–	–	0.01	0.02	98.79
1			PM-145	405	53.43	0.24	1.01		0.07	7.88		0.03	0.23	14.99	21.78	–	–	0.19	–	99.84
2			PM-145	406	54.50	0.18	0.79		0.04	6.81		0.02	0.13	15.41	22.88	–	–	0.20	0.01	100.96
1			PM-145	411	52.89	0.23	0.99		0.03	8.34		0.01	0.27	14.80	21.89	–	0.00	0.19	–	99.63
3			PM-145	416	52.98	0.21	0.93		0.05	8.50		–	0.22	15.05	22.12	–	–	0.19	0.01	100.27
3			PM-145	417	52.94	0.22	1.04		0.05	8.40		0.00	0.29	15.28	21.62	–	0.04	0.19	–	100.07
5		X	PM+260	1985	52.43	0.13	0.53	0.05	0.02	20.81	0.05	–	0.50	23.85	0.71			–		99.09
1			PM+260	1986	52.10	0.24	1.17	0.08	0.05	8.27	0.05	–	0.26	14.60	22.06			0.25		99.12
1			PM+260	1987	51.80	0.24	1.01	0.06	0.02	7.66	0.01	–	0.20	14.61	22.68			0.24		98.55
1			PM+260	1988	51.96	0.30	1.45	0.11	0.04	8.25	0.04	–	0.24	14.56	22.06			0.28		99.29
5		C	PM+260	1989	52.75	0.14	0.51	0.01	0.01	20.55	0.05	0.02	0.47	23.54	1.34			–		99.39
5		X	PM+380	2045	53.50	0.17	0.78	0.05	0.02	20.70	0.04	–	0.48	23.83	0.62			–		100.19
1			PM+380	2046	53.09	0.27	1.26	0.06	0.05	7.69	0.04	–	0.23	14.83	22.72			0.23		100.46
5		X	PM+380	2047	53.72	0.13	0.57	0.05	0.01	20.93	0.05	–	0.50	23.94	0.77			0.01		100.67
1			PM+380	2048	53.02	0.25	1.04	0.07	0.04	7.91	0.05	–	0.21	14.81	22.35			0.24		99.99
5		X	PM+380	2049	53.29	0.15	0.62	0.02	0.01	21.07	0.05	0.03	0.48	23.64	0.79			0.01		100.16
1			PM+380	2050	52.73	0.25	0.99	0.09	0.02	7.85	0.03	–	0.20	14.80	22.49			0.25		99.71
5		X	PM+380	2051	53.63	0.15	0.64	0.01	0.01	21.12	0.05	–	0.53	23.77	0.90			0.00		100.81
1			PM+380	2052	53.29	0.23	0.91	0.09	0.04	7.80	0.04	–	0.23	14.79	22.71			0.24		100.38
5		X	PM+380	2053	52.77	0.15	0.60	0.02	0.04	21.38	0.07	0.02	0.53	23.26	0.99			0.00		99.83
1			PM+550	2066	53.40	0.24	0.97	0.08	0.06	7.03	0.04	–	0.21	15.33	23.05			0.22		100.62
2			PM+550	2069	53.64	0.28	0.94	0.08	0.05	7.17	0.04	–	0.22	15.18	23.06			0.19		100.84
2			PM+550	2070	53.13	0.24	1.12	0.08	0.05	7.44	0.04	–	0.27	14.83	22.74			0.19		100.12
1			PM+550	2071	53.07	0.27	1.11	0.07	0.08	7.56	0.01	–	0.23	14.80	22.75			0.22		100.16
5		X	PM+550	2072	53.84	0.14	0.70	0.01	0.02	20.16	0.06	0.01	0.45	24.32	0.97			0.01		100.71
2			PM+550	2073	53.18	0.22	1.11	0.07	0.05	7.79	0.05	–	0.23	14.95	22.43			0.20		100.30
5		X	PM+550	2074	53.90	0.13	0.64	0.02	0.02	20.47	0.05	–	0.44	24.68	0.56			–		100.92
Blocks in the Mooimeisjesfontein area																				
5	-3		PM-X1	2324	52.61	0.13	0.64	0.05	0.03	22.71	0.03	–	0.53	21.86	0.62	0.02	0.01	–	–	99.25
2	-3		PM-X1	2325	52.27	0.22	1.14	0.09	0.06	8.60	0.05	–	0.28	13.74	22.63	–	–	0.20	0.00	99.28
1	-3		PM-X1	2326	52.32	0.31	1.41	0.14	0.05	8.82	0.01	–	0.24	13.74	22.42	0.01	–	0.25	0.00	99.73
1	0		PM-X1	2327	52.59	0.28	1.16	0.09	0.03	9.23	0.02	–	0.26	14.03	21.77	0.02	0.01	0.25	–	99.73

Tag	Tag*	A1-in-Opx	Sample	ID	SiO2	TiO2	Al2O3	V2O3	Cr2O3	FeO	NiO	ZnO	MnO	MgO	CaO	SrO	BaO	Na2O	K2O	Total
2	0		PM-X1	2328	52.54	0.27	1.13	0.08	0.03	9.26	0.02	–	0.29	13.94	21.88	0.01	–	0.23	–	99.67
5	0	X	PM-X1	2329	52.24	0.16	0.66	0.02	0.02	23.13	0.03	–	0.56	21.37	0.66	0.01	–	–	–	98.85
5	0	X	PM-X1	2330	52.37	0.16	0.56	0.02	0.02	22.40	0.04	–	0.50	21.46	0.94	0.01	–	0.01	–	98.47
1	4		PM-X1	2331	51.97	0.41	1.19	0.09	0.00	10.38	0.03	–	0.27	13.02	21.80	0.01	0.01	0.23	0.00	99.42
1	4		PM-X1	2332	51.89	0.40	1.21	0.06	0.02	9.97	0.04	–	0.26	13.02	22.11	0.02	0.01	0.30	0.01	99.31
3			PM-X2	2395	52.89	0.27	1.13	0.08	0.02	9.14	0.04	–	0.24	13.87	21.81	0.01	0.00	0.18	–	99.67
7		X	PM-X2	2396	52.79	0.15	0.57	0.04	–	23.23	0.03	–	0.54	21.19	0.70	0.01	–	0.01	–	99.26
3			PM-X2	2397	52.96	0.24	1.15	0.11	0.05	9.20	0.02	–	0.25	13.86	21.97	–	0.00	0.22	0.00	100.02
3			PM-X2	2398	53.01	0.24	0.96	0.07	0.04	9.05	0.01	–	0.25	13.85	22.24	0.02	–	0.21	–	99.96
3			PM-X2	2399	53.05	0.24	1.04	0.11	0.02	9.63	0.04	–	0.24	13.84	22.02	0.02	–	0.24	–	100.49
5	20	X	PM-X3	2400	54.01	0.14	0.38	0.01	0.05	21.15	0.06	–	0.48	23.65	0.80	0.04	0.00	0.01	0.00	100.79
2	20		PM-X3	2401	53.24	0.25	1.02	0.08	0.08	8.17	0.02	–	0.24	14.74	22.40	0.03	0.00	0.20	0.00	100.48
1	20		PM-X3	2402	52.88	0.26	1.17	0.11	0.07	8.50	0.05	–	0.28	14.56	21.92	0.01	0.00	0.21	0.01	100.02
6	20	X	PM-X3	2403	52.51	0.13	0.87	0.04	0.06	21.98	0.02	–	0.48	21.98	0.58	0.02	0.00	–	0.01	98.70
7	7	X	PM-X3	2404	52.63	0.18	0.62	0.06	0.03	21.58	0.04	–	0.56	22.48	0.85	0.03	–	0.02	–	99.08
3	7		PM-X3	2405	52.68	0.26	0.97	0.05	0.06	8.38	0.02	–	0.23	14.30	22.32	0.00	–	0.20	–	99.49
1	7		PM-X3	2406	52.67	0.32	1.32	0.10	0.10	7.70	0.03	–	0.23	14.29	22.90	0.05	0.01	0.20	–	99.92
5	3	X	PM-X3	2407	52.84	0.17	0.72	0.06	0.03	21.30	0.05	–	0.48	23.12	0.78	0.05	0.01	–	–	99.60
2	3		PM-X3	2408	52.57	0.25	1.12	0.11	0.06	8.27	0.04	–	0.27	14.53	22.28	0.04	–	0.20	0.00	99.74
2	1		PM-X3	2409	52.82	0.26	1.21	0.08	0.06	8.73	0.03	–	0.25	15.08	21.16	0.01	0.00	0.19	–	99.90
5	1	X	PM-X3	2410	53.60	0.14	0.64	0.03	0.04	20.88	0.06	–	0.52	23.15	0.97	0.01	–	0.00	0.00	100.03
1	-2		PM-X3	2411	52.95	0.26	1.19	0.07	0.09	8.54	0.02	–	0.26	14.53	22.24	0.03	–	0.21	0.01	100.39
1	-3		PM-X3	2412	53.06	0.25	1.06	0.10	0.09	8.06	0.02	–	0.25	14.86	22.11	0.03	–	0.20	–	100.08
5	-3		PM-X3	2413	53.15	0.15	0.58	0.01	0.04	21.03	0.05	–	0.50	23.30	0.88	0.01	–	–	–	99.71
1			PM-X4	2438	52.75	0.21	1.04	0.09	0.05	10.18	–	–	0.32	14.99	19.87	0.03	–	0.22	0.00	99.76
5		X	PM-X4	2439	52.94	0.15	0.52	0.03	0.03	22.41	0.03	–	0.53	21.96	1.03	–	0.01	–	–	99.63
2			PM-X4	2440	52.94	0.27	1.08	0.08	0.08	9.02	0.02	–	0.26	14.28	21.89	–	–	0.25	0.00	100.18
6		C	PM-X4	2441	54.89	0.32	2.07	0.11	0.02	8.45	0.07	–	0.14	19.07	12.09	0.00	0.01	0.32	0.16	97.72
2			PM-X4	2442	52.78	0.28	1.12	0.10	0.05	8.59	0.02	–	0.26	14.10	22.52	0.02	0.02	0.26	–	100.11
1			PM-X4	2443	52.63	0.27	0.97	0.08	0.07	8.43	0.04	–	0.23	14.21	22.44	0.03	0.01	0.27	0.00	99.69
5		X	PM-X4	2444	52.41	0.18	0.54	0.02	0.03	22.86	0.05	–	0.52	21.76	0.82	0.01	0.01	–	–	99.20
6		X	PM-X4	2445	52.47	0.11	0.52	0.03	0.04	23.22	0.05	–	0.55	21.63	0.57	–	–	0.00	–	99.19
5		X	JB019-X2	2452	52.09	0.19	0.62	0.02	0.02	22.37	0.04	0.01	0.51	21.84	0.93	0.02	–	0.00	0.00	98.66
1			JB019-X2	2453	51.94	0.27	1.18	0.09	0.04	8.71	0.04	–	0.23	14.06	22.43	–	0.00	0.26	0.00	99.25
5		X	JB019-X2	2454	52.93	0.13	0.63	0.02	0.00	21.41	0.05	–	0.46	22.79	0.66	0.03	0.01	–	0.00	99.14
2			JB019-X2	2455	52.79	0.23	1.03	0.06	0.05	7.84	0.03	–	0.19	14.63	22.83	0.04	–	0.22	0.00	99.94
3			JB019-X2	2456	52.25	0.24	1.25	0.09	0.05	9.23	0.01	–	0.27	14.38	21.78	0.02	0.02	0.19	0.01	99.77
7		X	JB019-X2	2457	52.04	0.12	0.67	0.05	0.01	23.24	0.05	–	0.54	21.42	0.69	–	0.00	–	–	98.86
3			JB019-X2	2458	51.83	0.32	1.51	0.08	0.02	13.93	0.03	0.01	0.30	15.74	16.02	0.00	–	0.17	–	99.97
1	20		LX-1-1	532	51.23	0.44	1.28		0.03	10.59		–	0.23	12.92	21.75		0.02	0.20	0.01	98.69
1	15		LX-1-1	554	50.51	0.44	2.04		0.07	11.17		–	0.30	12.78	21.34		–	0.22	–	98.87
2	15		LX-1-1	555	51.80	0.48	1.37		0.03	9.73		–	0.33	13.28	21.71		–	0.28	–	99.01
1	14		LX-1-1	540	51.96	0.44	1.52		0.04	10.46		–	0.22	13.11	22.11		–	0.28	0.01	100.18
1	14		LX-1-1	541	51.63	0.37	1.35		0.05	10.08		–	0.28	13.29	22.01		0.02	0.23	–	99.29
2	14		LX-1-1	546	51.88	0.51	1.40		0.01	10.69		0.02	0.27	13.09	21.05		–	0.26	0.01	99.19
2	14		LX-1-1	547	53.34	0.23	1.01		0.05	9.16		–	0.17	13.85	22.27		–	0.19	0.01	100.29
6	14	X	LX-1-1	548	51.90	0.25	0.68		0.02	24.48		0.04	0.56	20.37	0.83		0.00	–	–	99.13
1	14		LX-1-1	549	52.21	0.46	1.38		0.05	10.42		–	0.25	13.49	21.24		0.04	0.23	–	99.77
1	0		LX-1-1	585	52.68	0.30	1.19		0.02	8.61		–	0.19	14.00	22.49		–	0.26	0.01	99.76
1	0		LX-1-1	586	52.29	0.34	1.19		0.05	7.94		0.00	0.19	14.37	22.20		–	0.25	0.00	98.81
2	0		LX-1-1	587	52.23	0.34	1.09		–	7.47		–	0.18	14.34	22.73		0.02	0.21	–	98.60
1	2		LX-1-1	574	52.91	0.34	1.13		0.05	8.65		0.01	0.21	14.14	22.50		0.01	0.20	0.01	100.18
1	-7		LX-1-1	579	52.95	0.22	1.51		0.04	8.54		–	0.18	14.78	20.83		0.02	0.20	0.02	99.30
6	-7		LX-1-1	580	53.24	0.14	0.53		0.08	20.22		–	0.54	23.34	0.72		0.00	–	0.02	98.84

Tag	Tag*	Al-in-Opx	Sample	ID	SiO2	TiO2	Al2O3	V2O3	Cr2O3	FeO	NiO	ZnO	MnO	MgO	CaO	SrO	BaO	Na2O	K2O	Total
1	-7		LX-1-1	581	52.94	0.23	1.08		0.08	7.72		0.02	0.22	14.69	22.05		0.02	0.22	–	99.27

Tag*: Distance (mm) from the contact. Positive values are in the autolith.

Table D.10 – Mineral chemistry for pyroxenes. This table only includes the analytical uncertainties (%).

ID	Si	Ti	Al	V	Cr	Fe	Ni	Zn	Mn	Mg	Ca	Sr	Ba	Na	K
Anorthosite sequence near the Phosiri Dome															
1527	0.21	5.05	2.08	404.87	31.95	0.61	28.84	-177.80	5.44	0.40	2.64			-147.52	
1528	0.20	2.83	1.30	55.86	19.85	0.98	59.55	-82.26	8.95	0.50	0.33			6.51	
1529	0.21	2.88	1.25	26.96	17.41	1.01	91.36	-99.80	8.88	0.50	0.33			6.50	
1530	0.21	2.56	1.37	32.06	22.59	1.00	65.92	-98.43	9.42	0.51	0.32			6.60	
1531	0.21	4.89	1.73	69.99	23.12	0.63	29.29	-315.18	5.64	0.41	1.09			71.82	
1532	0.21	5.58	2.04	2150.08	57.74	0.60	25.22	-78.53	5.49	0.40	2.41			252.87	
1533	0.21	5.03	2.01	61.94	39.46	0.64	44.36	1986.93	5.85	0.39	1.62			355.85	
1534	0.21	4.94	2.28	137.98	25.79	0.62	39.00	-160.24	5.96	0.39	2.05			5000.00	
1535	0.21	4.20	2.20	409.80	30.59	0.62	26.37	147.50	5.65	0.39	1.71			146.43	
1536	0.21	4.39	2.27	124.31	54.44	0.62	81.51	948.62	5.88	0.39	1.92			-626.84	
1537	0.21	4.15	2.10	85.42	24.94	0.63	28.52	62.37	6.23	0.39	1.74			159.32	
1299	0.21	4.13	1.49	32.03	-2421.20	0.80	139.11	-93.80	6.86	0.56	0.33			7.99	
1300	0.22	6.18	1.73	67.09	151.22	0.50	51.21	-262.92	4.02	0.51	1.66			122.56	
1301	0.21	7.69	2.16	657.10	349.30	0.50	215.59	-225.58	4.16	0.51	1.94			-97.81	
1303	0.21	3.18	1.28	32.34	-111.89	0.78	39.43	-136.79	7.54	0.57	0.33			8.01	
1304	0.20	5.20	1.60	73.08	-361.16	0.80	81.70	-219.57	6.99	0.56	0.33			9.01	
1306	0.21	4.07	2.36	75.07	62.76	0.54	54.95	5000.00	5.24	0.45	1.53			5000.00	
1307	0.21	1.74	2.48	58.54	-1675.10	0.54	49.07	-146.49	4.86	0.46	1.35			84.04	
1312	0.21	19.29	3.59	5000.00	148.72	0.60	471.79	-331.87	5.24	0.45	2.00	-809.59	-87.51	101.80	-326.47
1454	0.21	2.76	1.34	51.36	39.80	0.99	74.03	-2693.80	10.02	0.51	0.32			8.63	
1455	0.21	4.43	2.02	80.21	53.28	0.56	64.84	-67.54	5.31	0.43	2.10			-413.47	
1456	0.20	2.69	1.28	66.17	34.69	0.95	223.78	-62.78	8.64	0.52	0.32			7.35	
1459	0.21	3.52	1.45	35.77	40.06	0.87	293.77	-126.71	7.25	0.54	0.32			8.52	
1460	0.22	7.59	2.11	46.69	313.18	0.51	71.11	283.22	3.96	0.48	2.17			-110.18	
1324	0.21	5.69	2.84	79.38	87.03	0.51	-107.13	92.51	3.65	0.49	2.21			657.60	
1325	0.21	15.56	2.83	60.47	411.80	0.52	104.68	-1169.10	3.84	0.47	2.83			117.01	
1326	0.21	5.04	1.95	88.54	41.80	0.53	92.66	-160.20	4.42	0.47	1.39			-884.48	
1327	0.21	5.11	1.96	48.80	200.82	0.52	209.55	572.37	4.32	0.47	2.16			-3164.30	
2152	0.22	4.55	2.39	149.63	61.77	0.57	97.66	-94.29	5.06	0.45	1.77	182.96	213.43	-248.89	95.52
2153	0.22	4.86	1.96	66.06	71.16	0.58	52.24	274.80	5.36	0.44	1.25	101.12	-195.84	-110.56	167.44
2154	0.21	2.58	1.35	40.83	43.17	0.94	114.08	-73.44	9.68	0.54	0.33	-948.36	270.33	7.84	121.65
2155	0.22	7.57	2.57	189.68	137.39	0.57	58.31	-130.59	5.49	0.45	2.02	-91.26	-304.78	-205.83	-307.17
2156	0.21	2.54	1.35	41.15	32.74	0.92	-1877.30	-96.14	9.03	0.55	0.33	89.88	-282.73	7.71	394.65
2180	0.21	2.46	1.28	43.75	46.99	0.85	59.82	-253.03	7.44	0.55	0.33	59.48	-444.33	7.39	98.16
2181	0.21	6.28	1.96	143.64	74.31	0.56	35.33	-157.09	4.75	0.47	0.94	77.06	-254.25	77.20	-2478.00
2182	0.22	6.71	2.23	522.22	487.64	0.55	58.40	144.94	4.31	0.47	2.06	55.70	-59.84	-230.02	82.00
2183	0.21	5.05	1.67	39.58	50.76	0.91	253.48	-86.75	7.98	0.56	0.33	102.83	217.38	8.57	85.06
1434	0.21	4.25	1.47	46.16	240.50	0.83	38.85	-83.63	7.68	0.54	0.33			7.53	
1435	0.21	3.66	1.52	60.02	-268.86	0.84	93.70	-1401.90	7.79	0.55	0.32			7.35	
1436	0.21	4.50	1.53	62.53	-163.26	0.85	41.12	-82.95	7.08	0.54	0.32			8.22	
2171	0.22	5.96	2.43	101.74	48.16	0.60	49.49	-112.69	5.60	0.44	1.40	-151.79	-69.54	198.09	-77.49
2172	0.22	5.10	2.09	70.01	305.61	0.61	33.20	-3589.00	5.57	0.44	0.93	60.39	111.27	143.18	110.43
2173	0.21	4.51	1.52	149.28	240.66	0.90	40.10	-83.60	7.26	0.56	0.33	-335.43	75.53	8.54	-102.08
2174	0.21	4.07	1.46	44.64	165.25	0.90	151.61	-673.06	7.18	0.57	0.34	134.60	1174.38	8.36	62.79

ID	Si	Ti	Al	V	Cr	Fe	Ni	Zn	Mn	Mg	Ca	Sr	Ba	Na	K
2175	0.21	2.94	1.37	36.60	167.46	0.98	49.28	-153.02	9.41	0.53	0.33	209.12	5000.00	8.16	90.37
2176	0.21	3.32	2.34	607.70	507.36	0.61	56.32	-78.96	5.53	0.41	1.52	2048.87	-297.85	1495.98	-147.80
2177	0.21	3.82	2.26	90.93	78.95	0.60	39.17	-66.09	5.29	0.41	1.44	-160.43	474.73	223.05	70.22
2178	0.21	2.44	1.34	47.47	31.73	0.90	48.51	-99.80	8.30	0.53	0.32	112.62	5000.00	7.68	195.57
2179	0.21	4.14	1.50	170.80	47.73	0.94	51.72	-344.14	8.23	0.53	0.32	-827.47	-131.32	7.74	231.07
1419	0.21	3.21	1.34	31.51	44.43	0.90	52.99	762.31	7.81	0.53	0.32			7.25	
1420	0.21	2.86	1.26	52.22	41.99	0.88	77.14	-429.81	7.59	0.53	0.33			7.21	
916	0.20	2.70	1.32		19.88	0.98		136.92	9.09	0.50	0.33	-26.81	403.32	6.55	142.92
917	0.21	6.21	2.21		118.14	0.57		109.70	4.94	0.42	2.18	169.64	-66.53	73.28	-119.60
912	0.20	3.21	1.44		24.22	0.95		780.11	8.63	0.50	0.33	-45.95	84.34	7.56	53.02
913	0.21	8.59	2.51		76.92	0.56		-60.80	4.29	0.42	2.33	-56.51	-466.20	-390.51	-54.87
903	0.20	2.74	1.34		29.39	0.97		-83.05	10.18	0.50	0.33	-39.48	98.88	6.83	-2554.50
904	0.21	4.17	2.05		49.25	0.59		-123.60	5.15	0.40	2.16	-73.26	75.38	-137.42	-636.30
905	0.20	2.77	1.33		22.16	0.94		-1502.80	8.62	0.48	0.35	-36.83	76.43	6.81	0.00
906	0.20	3.05	1.35		30.93	0.90		-243.88	7.33	0.48	0.36	-39.08	-41.98	6.63	-158.09
897	0.20	2.94	1.42		22.12	0.98		479.42	8.36	0.50	0.33	-117.24	250.32	6.73	58.25
898	0.21	10.11	2.18		72.11	0.57		-65.80	4.73	0.41	2.47	-288.97	-105.37	-78.10	-210.48
925	0.20	2.70	1.38		20.73	0.94		256.96	9.36	0.50	0.33	-66.13	225.23	6.59	-2547.00
926	0.20	2.64	1.31		17.85	0.93		-313.14	8.44	0.50	0.34	-74.97	205.15	7.40	323.99
927	0.21	4.79	2.12		60.07	0.58		-75.83	5.18	0.41	2.11	-121.59	-58.56	191.19	43.77
928	0.20	2.87	1.43		51.88	0.96		-152.36	8.52	0.50	0.33	-82.96	-319.07	6.76	279.98
932	0.20	2.66	1.40		27.15	0.95		-60.33	8.54	0.50	0.33	-85.68	279.92	7.03	-864.69
933	0.20	2.53	1.33		27.90	0.93		754.10	8.70	0.50	0.34	-44.57	136.67	6.20	-631.35
934	0.21	10.07	2.85		35.80	0.58		-180.93	4.67	0.42	1.48	-85.84	-1547.70	523.87	-321.12
935	0.20	3.00	1.37		29.90	1.00		1477.58	9.66	0.50	0.33	-60.65	365.51	6.75	-214.08
936	0.21	5.09	2.60		96.88	0.59		-98.03	4.96	0.41	2.21	-42.31	184.43	1565.13	-65.71
953	0.21	2.64	1.33		27.20	0.93		-238.10	7.25	0.51	0.33	-36.09	76.41	5.59	92.99
954	0.21	4.46	2.20		49.46	0.55		-65.79	4.71	0.44	2.14	-116.75	167.32	-83.37	-111.76
955	0.20	3.55	1.53		37.67	0.94		-61.05	8.31	0.50	0.33	-42.38	-736.50	6.50	71.87
966	0.20	3.13	1.36		40.10	0.94		-316.94	7.45	0.51	0.33	-36.69	-315.30	7.52	70.61
967	0.21	7.60	2.32		163.90	0.56		-77.46	4.75	0.43	2.07	-26.95	-52.44	-81.36	62.51
974	0.21	4.30	1.93		38.44	0.56		260.21	4.65	0.44	1.20	-71.96	-100.63	-100.67	199.52
975	0.20	2.33	1.27		31.94	0.91		-59.19	7.24	0.52	0.33	-38.17	138.93	5.91	-365.55
987	0.20	3.41	1.45		24.08	0.95		-239.26	8.42	0.50	0.33	-44.78	137.05	7.86	-120.90
988	0.21	3.78	2.20		38.32	0.57		1574.60	4.51	0.43	1.81	-233.25	-49.09	55.38	-144.23
989	0.20	3.02	1.39		32.99	0.88		-32.27	8.23	0.50	0.34	-37.57	-499.36	7.07	-103.29
982	0.20	2.97	1.40		29.80	0.96		-53.08	9.77	0.49	0.33	-53.00	-226.22	7.67	133.44
983	0.21	5.46	2.27		50.37	0.65		-53.54	5.68	0.41	0.63	-42.84	225.23	100.38	92.73
984	0.20	2.89	1.37		20.08	0.97		-45.93	8.95	0.50	0.33	-31.19	61.29	6.53	159.07
992	0.20	2.75	1.40		28.56	0.97		-62.08	8.35	0.49	0.33	-60.51	55.93	6.95	-428.10
993	0.21	3.72	2.13		46.64	0.60		-60.01	5.12	0.40	1.92	-69.21	-97.33	90.56	310.24
994	0.20	2.68	1.40		26.23	1.00		-135.15	9.05	0.50	0.33	-64.26	-84.13	6.28	49.10
995	0.20	2.81	1.37		24.98	0.95		-403.43	8.22	0.50	0.33	-23.68	63.90	5.97	178.11
1004	0.20	2.95	1.44		23.79	0.95		-364.20	8.82	0.50	0.33	-32.61	-145.84	6.06	317.66
1011	0.20	2.63	1.37		47.10	0.93		-103.99	8.54	0.50	0.33	-132.00	134.16	6.68	-360.50
1012	0.20	2.93	1.31		37.27	0.93		1515.41	7.66	0.50	0.33	-33.62	558.45	6.83	130.73
1013	0.21	6.03	2.32		44.91	0.56		-36.41	4.63	0.42	2.11	-230.91	-257.47	-228.15	-427.56
1023	0.20	3.57	1.45		65.08	0.93		-132.65	7.54	0.51	0.33	-28.32	112.88	6.67	-157.33
1024	0.20	2.43	1.28		35.50	0.88		-100.90	8.47	0.51	0.34	-39.38	-412.26	6.86	-137.95
1037	0.20	5.12	1.64		-616.23	0.91		-57.05	7.05	0.51	0.33	-52.50	-1135.10	6.55	69.94
1038	0.20	4.25	1.50		34.51	0.91		67.41	7.53	0.51	0.33	-40.50	-185.66	6.78	313.24
1366	0.21	1.72	2.28	48.10	126.05	0.56	49.73	5000.00	4.66	0.44	1.36			466.47	
1367	0.21	8.17	2.32	143.38	71.42	0.56	113.31	351.91	5.03	0.43	1.70			326.72	
1368	0.20	3.07	1.25	37.78	24.74	0.97	83.09	-244.89	9.26	0.51	0.33			5.73	

ID	Si	Ti	Al	V	Cr	Fe	Ni	Zn	Mn	Mg	Ca	Sr	Ba	Na	K
1369	0.21	4.85	1.87	139.65	46.07	0.59	59.73	-122.95	5.50	0.42	1.51			68.06	
1370	0.21	6.19	1.71	65.26	36.10	0.60	42.75	587.94	5.18	0.42	1.13			38.93	
1371	0.20	3.32	1.26	34.94	77.11	0.92	448.75	-409.59	8.19	0.53	0.32			7.23	
1372	0.20	2.15	1.28	22.89	50.24	0.89	28.86	-90.60	8.18	0.53	0.33			6.52	
1345	0.20	5.05	1.49	56.41	49.53	0.94	86.85	-75.79	7.66	0.53	0.32			7.89	
1346	0.20	6.99	1.59	188.38	37.06	0.93	60.52	-96.94	8.07	0.52	0.32			8.11	
1348	0.21	1.38	2.30	83.58	60.65	0.58	116.69	87.13	5.66	0.42	1.41			139.30	
1349	0.20	2.62	1.23	31.65	26.38	0.96	46.08	-208.77	8.92	0.52	0.32			7.48	
1611	0.21	3.61	1.32	68.55	47.24	0.92	100.41	-80.77	7.19	0.54	0.33			6.65	
1612	0.21	4.66	1.41	48.47	58.78	0.93	33.45	240.61	6.65	0.54	0.32			6.54	
1514	0.21	4.99	1.96			0.61			5.59	0.41	1.21	3645.35	-228.52	51.19	-194.58
1515	0.21	4.07	2.24			0.61			5.40	0.41	1.27	128.66	-150.80	118.23	90.55
1516	0.21	2.86	1.32			0.98			8.67	0.52	0.32	-1593.50	979.32	7.17	65.05
1517	0.21	2.12	1.29			0.96			9.14	0.52	0.33	406.10	75.06	6.61	43.02
1518	0.21	3.08	1.33	23.90	49.00	0.97	102.38	-91.46	9.35	0.52	0.32			7.29	
1519	0.20	6.01	1.60	39.02	54.38	0.98	45.60	-57.76	8.45	0.51	0.32			6.90	
1520	0.21	4.96	2.26	108.37	128.21	0.57	37.66	80.93	5.08	0.42	1.71			-334.82	
1521	0.21	4.32	2.36	58.28	79.17	0.59	34.79	1635.84	5.46	0.42	1.46			73.06	
1470	0.20	2.82	1.26	74.46	18.76	0.95	76.29	-178.40	8.33	0.52	0.32			6.37	
1471	0.21	4.20	2.01	-889.61	86.09	0.58	60.55	-286.90	4.91	0.42	1.82			360.09	
1472	0.21	2.92	1.25	59.37	33.33	0.94	33.03	-338.19	8.96	0.52	0.33			6.64	
1473	0.21	4.82	1.82	85.30	39.20	0.57	49.71	-436.63	4.99	0.42	2.10			-261.59	
1474	0.20	7.00	1.53	39.15	34.70	0.95	58.26	-84.97	8.39	0.52	0.32			7.02	
1475	0.20	2.82	1.28	33.81	27.12	0.95	97.21	-604.77	8.71	0.52	0.32			6.34	
1476	0.21	5.90	2.01	48.56	58.97	0.59	81.35	-188.73	5.43	0.41	2.01			-1872.90	
1477	0.21	3.74	2.15	51.21	78.96	0.60	38.31	-96.43	5.22	0.42	1.17			205.46	
1583	0.20	3.74	1.43	67.48	-121.12	0.97	127.56	-497.69	8.37	0.53	0.32			6.33	
1584	0.21	3.66	1.39	45.11	-1045.70	0.93	65.48	-73.36	9.46	0.53	0.33			6.93	
1585	0.21	5.12	1.94	101.90	-286.79	0.61	30.61	-309.51	5.75	0.42	1.22			67.28	
1586	0.21	5.95	1.96	66.34	79.69	0.60	45.90	188.04	5.44	0.42	1.36			-130.51	
1587	0.21	3.00	1.33	24.22	21.84	0.98	51.14	-167.75	9.97	0.51	0.33			6.84	
1485	0.21	5.65	2.13	82.16	51.16	0.60	51.43	-286.58	5.78	0.42	1.31			357.62	
1486	0.20	3.35	1.38	19.66	33.18	0.97	42.36	-430.06	9.45	0.52	0.32			7.40	
1487	0.21	5.03	2.16	264.52	-191.27	0.58	44.81	-1118.70	5.16	0.42	1.77			5000.00	
1488	0.20	3.53	1.41	42.33	57.18	0.96	62.73	-65.32	8.98	0.52	0.32			6.96	
1489	0.21	2.28	1.23	26.86	26.75	0.94	39.00	-334.94	9.50	0.52	0.32			6.60	
1490	0.21	3.37	2.08	80.24	-271.54	0.58	38.48	235.91	5.11	0.42	1.78			146.81	
1491	0.21	2.04	1.25	33.60	55.77	0.93	42.29	221.82	9.10	0.53	0.32			6.18	
1492	0.21	3.38	1.37	45.57	55.27	0.93	63.30	-103.61	10.06	0.52	0.33			6.66	
Blocks in the anorthosite sequence															
2298	0.21	4.40	1.98	36.65	11.87	0.62	20.81	-172.20	5.53	0.41	1.39	58.31	-88.44	142.69	5000.00
2299	0.21	4.60	1.92	-2264.60	11.75	0.60	33.54	-331.42	5.18	0.41	1.98	126.42	-211.48	-139.20	-142.54
2300	0.21	2.66	1.28	34.77	7.49	1.01	28.07	-400.50	8.88	0.52	0.33	47.47	-171.00	7.95	303.12
2301	0.21	2.50	1.25	42.09	7.92	1.05	34.66	198.08	9.79	0.51	0.32	47.85	247.62	7.31	135.20
2302	0.21	3.45	1.12	60.63	7.08	1.04	42.75	-105.69	8.52	0.52	0.33	52.63	240.71	6.88	678.45
2303	0.22	9.02	1.45	152.38	8.28	0.63	39.50	-113.64	5.67	0.43	1.04	82.30	-114.34	51.77	-214.00
2304	0.22	5.90	1.48	1564.82	11.31	0.63	19.03	-332.39	5.63	0.42	1.77	126.51	-100.37	82.21	-268.37
2305	0.21	6.44	1.67	570.64	9.87	0.61	38.32	667.65	5.37	0.41	1.84	126.18	-64.94	173.47	-313.48
2306	0.21	5.38	1.87	113.84	10.89	0.63	26.45	-105.59	5.78	0.40	1.69	5000.00	-349.08	-246.38	153.72
2307	0.20	3.05	1.34	35.49	6.68	1.05	43.83	-764.40	9.74	0.50	0.32	171.26	-332.60	7.41	196.17
2308	0.21	4.29	2.35	84.53	13.33	0.61	22.48	-193.96	5.41	0.40	1.90	274.30	48.95	69.46	-98.82
2309	0.21	4.01	2.10	267.66	11.54	0.61	24.31	-589.51	5.89	0.40	1.56	219.64	-749.35	946.09	-68.48
2260	0.21	3.10	1.10	63.38	6.18	1.02	58.68	-82.20	7.77	0.50	0.33	128.05	-528.18	8.08	-238.68
2261	0.21	6.86	1.55	-140.22	11.06	0.68	34.39	131.11	6.23	0.38	1.92	-148.77	460.75	-115.18	223.08

ID	Si	Ti	Al	V	Cr	Fe	Ni	Zn	Mn	Mg	Ca	Sr	Ba	Na	K
2262	0.21	6.54	1.57	150.21	11.17	0.67	28.36	-475.24	6.15	0.38	1.76	115.86	-200.28	-96.45	-126.76
2264	0.21	6.72	1.52	80.39	12.73	0.68	36.70	117.52	5.84	0.38	1.74	417.75	285.91	-406.47	-58.55
2265	0.21	3.53	1.11	40.71	6.83	1.03	39.08	47.28	8.54	0.49	0.34	278.90	252.87	9.35	210.44
2267	0.21	7.84	1.54	-1377.50	22.55	0.67	27.02	151.39	5.94	0.38	1.87	242.49	134.90	-99.89	156.34
2268	0.21	5.72	1.55	103.53	10.97	0.68	29.66	87.13	5.90	0.38	1.80	172.85	361.81	-99.37	-482.75
2225	0.21	4.67	1.81	54.85	8.70	0.70	25.38	383.25	6.36	0.38	1.93	56.10	77.45	98.03	162.51
2226	0.21	4.79	1.96	57.65	8.52	0.71	29.08	-346.94	6.57	0.38	2.09	75.84	1376.03	-1169.70	-118.19
2227	0.21	2.64	1.14	34.71	6.32	1.16	54.54	-4255.00	10.74	0.52	0.33	180.49	108.01	6.76	145.87
2228	0.21	4.75	1.74	224.78	9.91	0.69	39.06	-601.50	6.49	0.38	2.44	185.96	167.49	-126.66	-419.69
2229	0.21	5.73	2.07	358.04	9.96	0.70	28.08	569.71	6.09	0.38	2.56	69.79	185.85	545.63	-99.42
2230	0.21	3.02	1.34	31.16	6.19	1.20	38.20	-409.11	10.03	0.50	0.32	-668.71	95.91	7.25	138.17
2231	0.21	4.36	1.71	71.97	9.62	0.69	26.14	-218.79	6.36	0.38	1.89	121.65	123.21	-681.04	-145.13
2232	0.21	6.31	2.55	-416.42	40.63	0.64	46.43	-957.56	5.78	0.40	2.03	49.06	-108.74	186.98	5000.00
2233	0.21	3.64	2.25	123.39	28.47	0.65	26.25	-120.57	5.91	0.40	1.96	1292.53	132.19	-205.83	-79.17
2234	0.21	3.69	2.20	123.71	35.14	0.65	35.10	213.00	5.97	0.41	1.89	224.46	119.77	312.87	-78.87
2235	0.21	3.68	2.13	89.38	38.24	0.64	46.74	-39.31	5.58	0.39	1.75	99.85	-284.17	183.35	-615.02
2236	0.21	3.08	2.09	48.83	28.97	0.64	23.28	-101.71	5.91	0.40	1.75	77.48	135.06	146.45	-242.66
2237	0.22	8.96	1.52	116.68	12.04	0.75	33.12	-175.21	6.09	0.39	2.00	68.62	-147.92	-219.95	3113.85
2238	0.21	6.59	1.53	84.34	12.26	0.74	34.09	-200.57	5.92	0.38	1.64	65.33	5000.00	-96.60	-72.16
2239	0.21	3.35	1.08	214.11	6.43	1.12	52.30	-162.57	8.65	0.51	0.33	164.41	320.59	6.35	-92.82
2240	0.21	7.60	1.50	217.43	8.10	0.71	29.29	-146.63	6.29	0.38	1.80	42.82	-2438.60	-385.47	-415.26
2241	0.21	7.26	1.50	1330.90	9.98	0.72	36.11	-395.27	5.76	0.38	1.75	212.34	-239.43	-1035.30	344.54
2242	0.21	9.87	1.54	-223.30	12.22	0.71	24.05	529.84	5.70	0.38	2.10	73.86	219.56	-205.97	-298.10
2243	0.21	3.59	1.07	68.10	6.83	1.11	44.42	-129.44	8.30	0.49	0.34	76.42	406.55	7.70	55.86
2244	0.21	9.84	1.49	87.95	15.43	0.73	23.82	-1567.40	6.00	0.37	1.95	57.06	341.02	-74.77	-253.37
2245	0.21	3.53	1.07	57.28	6.38	1.10	66.41	-55.28	8.82	0.50	0.33	162.70	406.63	6.78	241.66
2246	0.21	3.44	1.07	81.70	6.01	1.14	785.70	-66.28	9.07	0.51	0.33	163.50	-155.26	7.57	139.41
2247	0.21	7.26	1.51	-168.25	13.90	0.73	29.60	184.16	5.70	0.38	1.63	161.84	-101.40	-3334.60	-119.26
2352	0.21	5.92	1.45	88.97	12.16	0.67	18.54	-251.25	5.51	0.38	1.89	80.01	288.78	188.71	-80.47
2353	0.21	6.96	1.48	87.49	9.60	0.67	29.69	-137.22	6.02	0.38	1.57	98.05	-95.30	-255.30	-185.77
2354	0.21	6.20	1.53	116.64	8.96	0.67	22.71	840.28	5.87	0.38	1.58	92.24	-97.74	-100.57	-631.08
2355	0.21	5.51	1.90	71.31	25.72	0.64	25.62	-141.41	5.51	0.39	1.87	-135.65	75.04	140.80	-2075.30
2356	0.21	6.31	2.04	163.20	19.27	0.64	26.32	-102.22	5.56	0.39	1.82	90.29	384.62	174.03	147.17
2357	0.21	5.93	1.86	86.22	19.85	0.64	29.91	243.90	5.81	0.39	2.01	123.89	-172.94	-128.59	-471.66
2366	0.20	4.30	1.24	69.86	11.55	1.04	59.91	-371.81	8.62	0.50	0.32	76.82	77.03	7.86	-426.85
2367	0.20	4.52	1.21	59.22	10.36	1.03	34.80	-255.96	7.80	0.50	0.32	76.77	1451.98	8.13	-514.05
2368	0.21	9.35	1.68	59.65	19.69	0.64	22.71	-817.83	5.33	0.39	1.43	84.79	246.47	344.44	-234.80
2369	0.20	6.03	1.46	-104.24	12.63	1.06	73.56	-57.32	7.64	0.50	0.32	87.38	-235.29	8.67	-717.47
2370	0.21	10.28	2.00	687.09	19.74	0.63	32.58	-877.05	5.13	0.39	2.11	334.26	-247.52	-115.88	188.00
2371	0.20	8.55	1.87	57.15	14.67	1.11	51.75	-109.92	8.25	0.49	0.31	87.10	1063.15	8.72	780.74
2372	0.21	7.45	1.76	115.16	16.66	0.63	27.53	-748.00	5.36	0.39	1.56	221.29	-933.19	-469.61	-191.11
2373	0.21	10.45	2.04	158.20	19.67	0.63	22.25	-200.07	5.61	0.39	2.21	694.24	171.57	-157.70	389.24
2374	0.20	4.52	1.19	136.83	9.49	1.03	44.27	-60.69	8.81	0.49	0.33	75.10	86.84	8.36	1557.38
2375	0.21	10.65	1.72	74.84	16.20	0.63	33.27	-2044.00	5.17	0.39	1.88	322.10	-216.90	-98.44	289.30
2376	0.20	10.71	1.48	789.61	10.78	1.12	51.60	316.70	10.07	0.49	0.32	462.87	248.70	10.08	89.79
2377	0.20	6.02	1.53	67.98	13.47	1.11	60.30	-100.77	8.40	0.50	0.31	83.20	-127.06	13.09	5000.00
2378	0.21	12.77	1.77	299.77	21.15	0.63	26.63	-153.79	5.48	0.39	1.95	97.79	-154.13	157.03	-159.49
2316	0.21	5.22	1.78	66.52	7.97	0.69	22.11	-89.55	6.28	0.38	1.43	-331.98	151.98	772.33	-73.14
2317	0.21	4.71	1.77	75.54	9.00	0.68	20.47	-235.69	6.17	0.37	2.09	-265.00	-173.38	-103.76	496.20
2318	0.21	3.07	1.26	47.81	6.04	0.91	46.46	-188.92	9.25	0.50	0.33	98.48	-1402.90	7.09	197.61
2319	0.21	4.59	1.77	68.66	8.55	0.66	27.18	-303.53	6.34	0.38	1.99	85.95	232.66	542.63	201.65
2320	0.20	2.78	1.16	26.18	5.85	1.16	49.30	-80.24	10.54	0.49	0.32	33.37	147.87	7.17	431.96
2321	0.21	4.52	1.79	-226.86	9.53	0.65	46.84	1010.66	6.03	0.38	2.01	47.26	184.53	-244.86	-234.81
2322	0.20	2.67	1.15	42.70	5.58	1.16	36.29	-113.31	10.52	0.49	0.32	173.73	122.32	7.65	31.66

ID	Si	Ti	Al	V	Cr	Fe	Ni	Zn	Mn	Mg	Ca	Sr	Ba	Na	K
2323	0.20	3.42	1.41	34.45	6.40	1.17	36.67	-172.76	9.66	0.49	0.32	86.05	87.99	7.20	-388.05
Pyroxenite Layers in the Mooimeisjesfontein area															
1688	0.21	2.77	1.21	45.24	8.75	1.03	39.46	260.87	9.99	0.50	0.33			6.26	
1689	0.21	4.51	1.97	-483.49	18.00	0.66	22.98	-181.50	5.79	0.40	1.18			141.99	
1690	0.21	5.20	2.23	-196.06	21.13	0.65	35.66	-62.39	5.92	0.40	1.66			65.56	
1691	0.21	5.46	1.89	64.08	22.97	0.66	29.64	-75.80	6.17	0.40	1.15			38.60	
1692	0.20	2.79	1.34	23.08	10.22	1.06	37.08	133.15	8.58	0.51	0.32			6.31	
1693	0.20	3.15	1.22	33.29	8.89	1.06	31.61	-503.07	9.18	0.51	0.32			5.90	
1694	0.21	5.16	2.01	117.70	16.45	0.66	18.58	-796.91	6.14	0.39	1.64			-197.54	
1695	0.21	4.70	2.13	352.12	18.92	0.65	23.59	-96.07	6.00	0.39	1.23			56.48	
1696	0.21	4.42	2.33	108.01	22.46	0.65	32.08	111.88	5.85	0.39	1.61			-459.55	
1697	0.21	2.72	1.28	58.68	9.96	1.00	29.61	1775.59	9.34	0.51	0.33			6.59	
1700	0.21	5.12	1.96	132.25	16.88	0.66	29.42	-1361.10	6.26	0.39	1.39			108.82	
1701	0.21	4.37	2.06	155.04	23.43	0.65	18.76	59.81	6.12	0.39	1.59			-109.81	
1702	0.20	4.76	1.55	32.08	22.62	1.11	36.36	-1443.00	12.90	0.50	0.32			7.49	
1703	0.20	3.30	1.35	32.58	11.34	1.00	30.10	-306.51	9.11	0.51	0.33			6.10	
1704	0.21	2.63	1.19	43.96	10.33	1.00	29.56	-135.95	9.62	0.51	0.33			6.26	
1705	0.21	4.87	1.68	407.96	20.23	0.62	24.06	-128.88	5.39	0.40	2.27			390.27	
1643	0.20	3.05	1.30	64.39	10.93	1.01	33.64	-524.27	8.45	0.51	0.33			6.00	
1644	0.21	5.45	1.72	1199.67	18.29	0.64	21.67	-297.99	5.86	0.40	2.29			35.48	
1645	0.21	5.35	2.26	82.82	18.92	0.65	21.61	127.32	5.86	0.39	2.24			-122.36	
1646	0.21	4.34	1.90	37.48	15.35	0.66	20.67	99.53	6.27	0.39	1.20			54.90	
1647	0.21	4.55	2.00	118.77	16.49	0.65	20.36	1761.35	6.17	0.39	1.25			52.87	
1648	0.21	4.69	1.93	154.26	16.99	0.64	19.45	-457.38	5.77	0.40	1.35			112.30	
1649	0.21	2.89	1.30	31.88	10.59	1.01	35.35	-126.56	9.29	0.51	0.33			6.39	
1650	0.21	6.75	2.10	227.55	15.57	0.61	28.70	-227.28	5.34	0.41	2.26			152.89	
1651	0.20	3.67	1.41	34.89	10.02	1.06	26.67	-722.22	9.67	0.51	0.32			6.50	
1652	0.21	6.71	2.08	-418.10	14.08	0.61	31.74	-116.47	5.26	0.41	2.11			-78.14	
1784	0.21	2.90	1.32	27.29	10.45	1.04	26.78	-1142.80	9.98	0.50	0.33			6.18	
1785	0.21	5.09	1.95	88.08	22.61	0.66	23.00	67.37	5.87	0.39	1.85			104.71	
1786	0.21	4.87	2.33	72.43	18.54	0.64	21.70	206.68	5.91	0.39	2.14			221.75	
1787	0.21	2.80	1.33	25.35	10.03	1.08	26.55	353.50	9.76	0.51	0.32			6.31	
1788	0.21	5.06	2.11	55.19	14.54	0.65	23.12	5000.00	6.06	0.40	1.34			152.86	
1789	0.21	2.62	1.28	29.62	9.20	1.10	29.42	-109.93	10.24	0.51	0.32			5.90	
1801	0.21	4.66	1.53	35.49	11.94	1.06	41.96	483.77	10.38	0.52	0.32			7.26	
1574	0.21	4.39	2.27	118.90	31.51	0.64	33.39	-105.29	5.86	0.39	1.74			209.04	
1575	0.21	4.50	2.11	151.67	17.77	0.65	22.54	-112.66	6.04	0.39	1.41			81.80	
1576	0.21	4.57	1.89	82.85	19.18	0.65	23.79	-133.96	5.99	0.39	1.28			133.15	
1577	0.21	4.07	2.01	58.50	16.39	0.65	21.08	-509.39	6.14	0.39	1.43			146.03	
1578	0.20	2.44	1.32	39.58	12.31	1.05	43.71	-173.31	9.60	0.50	0.33			5.99	
1579	0.21	2.64	1.30	32.65	10.46	1.02	22.94	1159.32	9.69	0.50	0.33			5.80	
1580	0.21	3.98	2.24	213.21	19.36	0.65	31.46	-260.97	5.71	0.39	2.01			-119.67	
1581	0.21	3.96	2.24	78.19	17.59	0.65	25.15	378.80	5.79	0.39	1.58			299.89	
1582	0.21	2.61	1.25	38.30	10.45	1.06	45.00	-217.85	10.39	0.51	0.32			6.18	
1755	0.21	4.09	1.98	186.57	18.32	0.64	20.84	179.63	5.85	0.40	1.41			81.70	
1756	0.21	2.30	1.30	80.50	11.41	0.99	25.61	541.94	9.63	0.51	0.33			6.45	
1757	0.21	4.43	2.26	66.38	30.20	0.63	21.91	107.42	5.86	0.40	1.86			406.75	
1758	0.21	2.87	1.39	37.24	11.17	1.04	38.81	-106.12	9.09	0.51	0.33			6.34	
1763	0.21	2.52	1.30	34.52	10.36	1.01	28.28	-525.79	9.85	0.51	0.33			5.90	
1764	0.21	4.74	1.99	98.44	15.38	0.65	18.19	227.86	6.15	0.40	1.19			161.95	
1765	0.21	4.75	2.08	73.52	20.29	0.63	18.88	217.57	5.76	0.40	2.12			-436.02	
1766	0.21	5.05	1.48	51.41	10.37	1.08	40.51	-107.24	11.40	0.51	0.32			6.14	
1741	0.21	4.45	1.58	24.79	13.05	0.87	44.36	-57.31	7.98	0.47	0.37			7.61	
1742	0.21	4.77	1.88	111.25	18.18	0.64	24.45	96.53	5.61	0.40	1.41			-499.42	

ID	Si	Ti	Al	V	Cr	Fe	Ni	Zn	Mn	Mg	Ca	Sr	Ba	Na	K
1743	0.21	4.32	2.28	141.96	16.93	0.64	22.43	-1854.00	5.57	0.40	1.40			58.04	
1744	0.21	2.39	1.34	32.31	10.25	1.03	27.73	-233.28	9.90	0.51	0.33			6.54	
1745	0.21	4.93	1.97	66.07	18.18	0.64	29.06	97.34	5.96	0.40	1.21			83.45	
1746	0.20	4.24	1.45	24.53	9.98	1.06	47.52	-240.25	10.41	0.50	0.32			6.59	
1747	0.21	3.96	1.32	43.29	10.63	1.06	47.47	270.68	10.76	0.51	0.33			6.38	
1871	0.21	3.65	1.11	56.26	10.32	0.84	46.22	5000.00	7.93	0.49	0.38			8.04	
1872	0.21	2.99	1.38	43.41	10.05	1.04	40.53	-78.12	8.63	0.51	0.32			6.11	
1873	0.21	2.94	1.35	31.11	12.23	1.00	29.29	-110.44	8.86	0.51	0.33			7.29	
1874	0.21	4.74	2.09	61.54	18.97	0.64	28.32	747.47	6.12	0.40	1.43			75.77	
1875	0.21	4.94	1.95	51.05	27.75	0.65	25.54	867.07	5.95	0.40	1.10			37.11	
1876	0.21	4.72	1.91	61.51	17.72	0.65	30.39	-482.75	5.89	0.40	1.22			85.01	
1877	0.21	5.15	1.99	64.72	17.89	0.65	24.06	526.46	5.87	0.40	1.25			495.88	
1878	0.21	3.28	1.35	38.19	11.22	0.99	35.75	-618.33	10.37	0.51	0.34			7.03	
1879	0.20	3.14	1.46	43.14	10.33	1.08	39.61	-140.94	10.25	0.51	0.32			7.27	
1774	0.21	2.48	1.30	42.25	9.89	1.04	29.34	-94.08	10.32	0.52	0.32			6.27	
1775	0.21	4.49	1.81	64.59	18.20	0.65	18.32	194.39	5.66	0.40	1.08			34.65	
1776	0.21	2.56	1.27	31.12	10.30	1.02	40.97	-67.80	10.24	0.52	0.33			6.02	
1777	0.21	2.91	1.38	43.24	10.99	1.04	31.18	-89.59	10.51	0.51	0.33			5.95	
1778	0.21	5.45	2.04	999.35	18.40	0.64	17.96	211.66	5.91	0.40	1.59			139.26	
1670	0.21	4.75	1.92	84.67	18.68	0.63	20.08	-120.39	5.95	0.40	1.74			-4951.10	
1671	0.21	3.56	1.77	230.85	19.68	0.63	28.52	177.40	5.83	0.40	1.53			145.89	
1672	0.20	4.40	1.53	32.23	12.51	1.04	37.28	-251.82	9.22	0.51	0.32			7.04	
1673	0.21	2.67	1.28	36.34	11.08	1.00	34.14	-168.83	9.49	0.52	0.33			5.92	
1674	0.21	7.48	1.88	56.91	17.08	0.60	22.48	-420.70	5.23	0.42	2.41			-124.30	
1909	0.20	3.01	1.39	36.59	11.43	1.01	26.78	-595.44	9.50	0.51	0.33			6.75	
1910	0.21	4.62	1.79	162.61	17.87	0.64	21.13	-73.41	5.90	0.40	1.56			192.22	
1911	0.20	2.94	1.31	51.46	9.70	1.03	37.95	-79.86	7.22	0.51	0.32			6.42	
1912	0.21	5.76	1.88	103.40	21.87	0.62	17.57	-63.03	5.58	0.41	2.31			454.32	
1913	0.20	2.67	1.30	33.06	10.39	1.00	27.78	-1123.00	9.87	0.51	0.33			6.40	
1914	0.21	5.15	2.15	80.29	17.73	0.63	23.07	216.74	5.99	0.40	1.32			88.79	
1942	0.21	4.66	1.91	-393.62	17.30	0.63	24.37	-62.77	5.85	0.41	1.19			54.43	
1943	0.21	2.57	1.28	22.93	10.39	0.99	54.92	-53.01	9.25	0.52	0.33			6.19	
1858	0.21	2.78	2.02	76.94	15.37	0.62	33.90	207.85	5.62	0.41	1.14			62.64	
1859	0.21	3.60	1.36	32.37	11.06	1.03	35.93	219.84	10.41	0.51	0.32			7.07	
1860	0.20	2.68	1.35	48.90	10.02	1.00	37.03	-101.55	9.28	0.51	0.33			6.21	
1861	0.21	2.57	1.20	49.05	9.23	1.01	50.73	710.89	8.37	0.52	0.33			6.36	
1082	0.20	4.19	1.60		56.21	0.74		-68.34	6.65	0.55	0.34	-35.26	140.99	7.68	-52.15
1076	0.20	3.80	1.48		167.15	0.80		-500.07	7.31	0.54	0.34	-77.76	78.61	6.99	-120.58
1065	0.20	3.77	1.52		112.44	0.83		-127.49	6.78	0.53	0.33	-26.78	105.41	7.21	103.46
1066	0.20	2.87	1.54		72.75	0.84		-99.56	7.22	0.54	0.33	-39.08	-102.42	6.38	110.54
1058	0.20	5.50	1.82		-59.68	0.87		-134.61	7.47	0.53	0.33	-39.90	-124.24	7.17	184.10
1063	0.20	3.98	1.53		143.54	0.88		161.36	8.98	0.51	0.33	-28.90	-73.24	7.51	636.30
1064	0.20	3.17	1.59		34.91	0.86		-80.63	7.84	0.52	0.33	-55.99	-275.67	7.47	109.92
1046	0.20	5.44	1.67		82.44	0.83		-181.56	6.85	0.54	0.33	-75.73	-52.27	7.80	-263.74
1047	0.21	2.74	1.10		-122.32	0.84		-93.58	6.94	0.55	0.33	-53.29	195.34	6.21	196.56
1044	0.20	3.97	1.63		19.46	0.91		-42.14	8.52	0.51	0.33	-25.80	-257.02	7.97	-198.98
1945	0.21	3.27	1.37	33.71	274.24	0.79	80.32	-164.30	7.07	0.59	0.33			6.71	
1946	0.21	3.16	1.38	19.29	134.42	0.78	265.70	-61.08	6.77	0.58	0.33			7.61	
1807	0.21	2.87	1.56	19.37	43.17	0.81	59.63	-136.41	6.43	0.55	0.34			8.01	
1808	0.22	5.62	2.52	114.23	75.13	0.54	56.82	-1088.80	4.66	0.47	1.81			-218.21	
1809	0.21	3.15	1.51	33.06	81.73	0.85	69.70	-134.42	8.31	0.55	0.33			8.41	
1810	0.21	4.71	2.16	34.60	90.05	0.53	51.43	-129.53	4.60	0.47	1.83			-108.80	
1811	0.21	5.23	1.61	48.99	130.59	0.84	60.59	5000.00	6.85	0.56	0.33			8.08	
1813	0.21	3.04	1.47	29.76	114.26	0.80	26.24	-112.59	6.63	0.57	0.33			7.73	

ID	Si	Ti	Al	V	Cr	Fe	Ni	Zn	Mn	Mg	Ca	Sr	Ba	Na	K
1814	0.21	4.11	1.51	21.62	-192.57	0.83	35.55	588.14	6.65	0.57	0.33			7.93	
465	0.70	3.67	2.08		-331.71	1.17		74.95	8.74	0.75	0.48	-36.34	48.66	11.75	1941.31
455	0.69	4.86	2.15		50.30	1.35		-667.45	13.38	0.71	0.47	-121.61	467.48	8.99	99.75
456	0.70	4.95	2.23		41.65	1.31		-390.31	13.57	0.70	0.47	-38.02	5000.00	11.75	-325.69
457	0.69	5.88	2.26		38.31	1.34		-55.31	14.62	0.71	0.47	-26.31	193.00	10.00	187.38
470	0.69	6.20	2.64		42.32	1.41		65.15	12.27	0.69	0.47	-43.44	348.33	11.80	257.99
471	0.71	8.70	3.67		-303.76	0.84		64.26	6.90	0.58	3.31	-46.28	124.24	360.51	-47.94
432	0.70	4.39	1.69		51.52	1.20		-184.29	12.21	0.74	0.48	-40.00	-801.42	10.05	-2007.40
448	0.69	5.30	2.00		143.35	1.25		-2041.30	10.97	0.74	0.47	-36.98	-136.70	9.21	142.83
449	0.68	5.25	2.26		36.00	1.35		154.03	13.08	0.70	0.47	5000.00	127.55	10.62	-156.32
450	0.72	6.80	3.26		-374.42	0.83		-344.23	7.15	0.58	3.03	-37.74	-56.31	168.45	-42.01
451	0.69	3.66	2.05		37.51	1.30		970.36	12.04	0.70	0.48	-221.96	-52.40	10.81	307.65
440	0.72	10.18	3.62		118.57	0.78		256.16	6.45	0.62	3.10	-52.80	3254.53	179.50	-158.20
441	0.72	11.38	3.54		47.43	0.78		696.80	6.32	0.62	3.18	-369.09	101.35	-123.23	-56.50
472	0.69	4.54	2.22		42.86	1.37		-110.55	9.52	0.71	0.47	-46.47	-61.65	10.34	-115.46
473	0.69	4.73	2.30		27.27	1.35		339.07	11.57	0.69	0.48	-158.36	81.94	9.99	169.53
474	0.69	4.72	2.31		66.23	1.36		-1016.90	11.87	0.69	0.47	-78.00	-1563.30	10.42	-126.53
475	0.69	4.78	2.25		131.72	1.35		157.06	11.78	0.69	0.47	-48.49	-81.19	9.18	2099.69
476	0.72	6.86	3.47		45.27	0.83		-187.81	7.45	0.58	2.72	-70.69	56.59	-227.12	1977.04
1831	0.21	3.72	1.66	26.02	45.93	0.89	47.80	-216.48	7.95	0.54	0.33			8.47	
1832	0.21	6.10	2.21	33.47	61.54	0.59	33.71	202.28	5.26	0.44	0.87			79.14	
1833	0.21	3.99	1.65	24.98	183.41	0.94	34.69	-87.80	7.70	0.53	0.33			8.54	
1853	0.21	3.51	1.65	25.14	52.41	0.90	44.76	-126.04	6.96	0.53	0.33			9.49	
1854	0.21	5.17	2.56	108.18	69.43	0.56	36.78	-59.99	4.90	0.44	2.23			-157.81	
1855	0.20	3.76	1.73	28.48	39.17	0.96	34.16	-87.50	8.47	0.53	0.32			7.85	
1856	0.21	5.56	2.55	49.20	98.27	0.57	30.56	303.79	4.76	0.43	2.07			-141.04	
203	0.72	6.77	3.39		43.01	0.85		145.33	7.67	0.58	2.09	-57.44	266.90	-519.61	-531.47
204	0.72	7.10	3.65		318.07	0.84		40.23	6.62	0.57	2.66	131.03	53.57	-145.77	-405.44
205	0.72	7.25	3.65		62.18	0.86		286.74	7.32	0.58	1.68	-36.25	-408.01	-387.23	-124.34
206	0.70	4.70	2.36		70.91	1.36		-278.10	11.92	0.69	0.48	-59.28	129.22	9.91	977.21
281	0.69	5.43	2.70		-168.51	1.33		-333.26	11.48	0.70	0.47	-66.65	-92.14	10.42	46.01
282	0.72	6.37	3.39		55.90	0.85		107.21	6.69	0.58	1.77	-78.01	536.92	44.72	87.93
283	0.69	4.70	2.48		63.08	1.37		-2022.20	11.23	0.70	0.47	-32.70	508.22	9.60	-156.69
212	0.72	8.17	2.64		303.50	0.86		340.70	7.35	0.60	1.25	-56.76	-404.53	50.11	1069.89
213	0.70	3.92	1.99		46.40	1.36		55.80	12.09	0.70	0.47	-111.65	145.71	9.22	119.81
214	0.72	7.80	2.77		103.62	0.84		-110.81	7.46	0.60	1.55	-116.57	-95.01	68.84	-54.43
216	0.72	9.04	3.28		134.75	0.83		128.67	6.43	0.59	3.07	-60.40	-544.02	-49.71	-41.45
219	0.69	5.00	2.49		54.86	1.40		148.96	11.06	0.69	0.47	-153.06	1056.78	10.68	59.41
249	0.69	5.27	2.31		39.13	1.43		1967.40	12.31	0.69	0.47	-43.51	172.47	10.51	-2017.30
250	0.69	5.58	2.22		64.67	1.36		74.89	11.86	0.70	0.48	-39.37	-75.27	10.88	162.85
251	0.70	5.69	2.37		49.49	1.45		70.94	12.43	0.70	0.47	-284.70	313.93	8.84	-186.94
252	0.69	4.71	2.33		33.74	1.37		267.60	10.89	0.70	0.47	-43.47	66.90	9.67	224.12
253	0.72	6.27	3.44		42.63	0.85		297.18	6.86	0.58	2.56	557.10	-236.60	254.88	-119.51
254	0.73	7.24	3.12		-67.55	0.83		40.79	6.78	0.59	3.08	-35.24	-3337.60	1091.86	-84.03
255	0.73	11.62	2.91		66.99	0.82		-357.39	6.91	0.59	2.88	-126.17	-1063.80	-125.20	-184.27
256	0.71	6.60	3.46		234.50	0.85		37.63	7.15	0.58	2.63	-46.70	75.84	63.74	-170.77
257	0.71	8.50	4.02		104.56	0.85		-2108.50	7.16	0.58	2.31	-68.83	-85.01	360.51	-76.34
245	0.71	7.77	3.54		188.62	0.84		43.44	7.04	0.57	3.19	-67.87	-113.92	-171.57	-158.93
246	0.72	9.26	3.55		-854.17	0.85		-380.96	7.19	0.57	3.21	-33.87	52.37	5000.00	2075.67
247	0.72	7.82	3.46		59.25	0.85		670.82	7.23	0.57	3.24	-114.85	353.63	51.52	-989.90
248	0.69	4.86	2.16		53.28	1.37		166.66	11.69	0.69	0.48	-22.22	126.64	11.01	-229.59
2021	0.21	4.09	1.51	55.19	162.94	0.79	157.44	-70.36	6.38	0.57	0.33			6.88	
2022	0.21	5.43	1.60	41.68	92.94	0.81	75.42	-151.43	6.39	0.57	0.33			7.89	
2023	0.21	4.67	1.03	72.89	153.98	0.75	317.82	-101.02	6.10	0.57	0.35			8.37	

ID	Si	Ti	Al	V	Cr	Fe	Ni	Zn	Mn	Mg	Ca	Sr	Ba	Na	K
2024	0.21	4.00	1.41	23.48	38.43	0.81	47.62	113.98	6.59	0.56	0.33			6.88	
1970	0.21	5.45	2.93	53.80	4608.48	0.57	58.63	-95.81	5.09	0.43	1.84			-362.04	
1971	0.21	3.15	1.60	27.14	30.99	0.93	30.15	-143.71	8.78	0.52	0.33			7.84	
1972	0.21	4.48	2.42	39.19	66.89	0.57	36.65	-3324.10	4.81	0.44	1.80			94.99	
1977	0.21	4.84	2.64	47.89	47.22	0.57	52.20	-231.95	4.87	0.43	1.87			274.55	
1978	0.21	3.04	1.58	26.21	54.85	0.92	39.08	-201.94	7.29	0.53	0.33			8.32	
364	0.70	4.95	2.30		94.86	1.30		65.66	9.68	0.71	0.47	-40.00	67.84	11.43	-58.37
365	0.70	5.01	2.27		35.71	1.31		-65.08	11.58	0.69	0.48	-49.15	156.99	12.82	52.73
366	0.73	6.78	2.21		136.25	0.85		-88.78	8.39	0.58	2.83	-41.07	70.50	111.35	43.55
352	0.69	4.52	2.28		43.12	1.42		-119.89	13.54	0.70	0.47	-62.49	-180.62	10.28	290.31
353	0.70	4.35	2.20		35.09	1.41		135.79	11.48	0.69	0.47	-63.80	-38.50	9.62	251.20
354	0.70	4.05	2.02		36.07	1.38		32.49	11.89	0.70	0.47	-30.05	530.69	9.35	168.30
355	0.72	10.00	3.75		5000.00	0.83		966.96	7.84	0.57	3.87	-240.77	457.78	-75.13	-501.23
344	0.72	7.11	3.73		77.66	0.81		118.36	7.24	0.58	2.94	-56.92	362.87	-214.45	-187.82
345	0.69	6.82	2.60		68.35	1.51		-99.47	14.08	0.68	0.47	-56.99	62.14	13.10	126.21
346	0.69	6.39	2.48		74.53	1.43		-119.88	12.47	0.69	0.47	-55.66	-73.12	12.85	-109.41
347	0.69	4.38	2.24		63.07	1.35		-109.13	10.70	0.69	0.47	-124.05	3083.67	9.27	-85.98
348	0.73	9.99	2.17		26.03	0.87		-48.09	7.75	0.59	1.97	-392.52	218.94	127.46	43.04
324	0.72	7.54	3.86		51.51	0.85		150.48	7.02	0.58	2.61	-39.46	-799.74	144.68	68.63
325	0.69	4.89	2.49		38.19	1.42		-108.58	12.47	0.69	0.47	-22.07	-3225.00	10.10	-53.71
326	0.72	8.26	3.80		52.28	0.83		116.01	7.27	0.58	2.90	-37.48	-71.17	98.99	229.05
327	0.72	7.57	3.53		72.84	0.86		964.33	6.82	0.58	1.55	-52.37	-318.08	314.46	410.35
328	0.69	6.27	2.45		38.57	1.42		-974.47	11.61	0.69	0.47	-30.91	534.28	10.64	999.85
329	0.70	4.71	2.45		88.58	1.35		-81.57	11.82	0.70	0.48	-134.68	-70.55	11.44	182.02
330	0.72	7.66	3.51		5000.00	0.83		158.18	6.94	0.58	3.08	-177.88	1590.40	63.11	406.38
318	0.70	4.62	2.22		52.10	1.32		186.94	10.79	0.69	0.48	-58.50	-440.90	12.54	-99.53
319	0.70	4.78	2.48		163.24	1.39		102.45	11.21	0.69	0.47	-51.36	52.64	11.07	-507.36
320	0.69	4.78	2.39		36.07	1.38		-98.98	10.72	0.69	0.48	-38.30	-186.25	10.58	285.31
321	0.69	5.56	2.53		54.44	1.44		5000.00	15.09	0.69	0.47	-44.19	-401.49	11.05	-109.51
323	0.72	6.52	3.06		50.99	0.86		29.95	6.96	0.60	1.28	-122.21	548.19	73.33	532.66
300	0.69	4.03	2.13		229.16	1.37		180.67	11.25	0.70	0.47	-65.45	119.16	9.45	-202.97
301	0.73	7.58	3.44		120.36	0.84		-201.95	7.42	0.59	3.26	-235.67	109.62	-140.68	5000.00
302	0.69	5.93	2.34		46.18	1.37		106.44	13.86	0.70	0.48	-127.24	193.63	12.93	71.02
303	0.72	8.64	4.06		80.00	0.85		132.16	7.21	0.57	3.53	-113.10	-140.13	122.22	-2022.10
304	0.70	4.94	2.35		64.27	1.39		-53.66	12.76	0.70	0.47	-38.30	51.70	11.42	-189.14
305	0.69	5.05	2.40		41.93	1.45		100.99	13.39	0.69	0.46	-375.27	123.54	12.67	89.76
297	0.69	5.73	2.27		62.89	1.34		514.70	11.31	0.70	0.47	-37.19	225.83	11.43	-139.94
298	0.71	7.51	3.03		78.71	0.86		177.89	7.07	0.59	1.52	-43.02	-1051.20	23.57	301.30
299	0.69	3.83	2.22		40.39	1.40		43.23	10.96	0.69	0.47	-45.82	-143.85	9.62	-95.10
1137	0.20	3.23	1.67		18.73	0.94		65.50	7.66	0.49	0.33	-26.32	-67.99	6.97	84.85
1138	0.20	3.22	1.53		92.12	0.98		81.01	8.04	0.49	0.33	-62.85	-264.27	6.37	-2539.50
1139	0.21	4.51	2.58		49.82	0.59		315.38	4.83	0.40	1.78	-673.24	-282.50	236.87	-128.36
1140	0.20	3.27	1.71		30.61	0.98		-121.93	8.92	0.49	0.33	-34.57	-412.05	6.96	-425.55
1118	0.20	3.26	1.57		28.29	0.94		-50.34	8.43	0.49	0.33	-35.60	-405.62	6.83	-92.30
1119	0.20	3.07	1.54		21.05	1.02		-364.06	10.38	0.49	0.32	-40.24	445.80	7.83	1262.78
1120	0.21	4.53	2.91		42.69	0.58		-112.96	4.78	0.40	2.00	-137.79	-380.74	134.89	-198.66
1110	0.20	3.25	1.75		74.63	0.98		206.46	8.85	0.49	0.33	-28.17	54.37	6.92	184.33
1111	0.21	4.96	2.59		5000.00	0.58		-385.97	5.08	0.40	2.43	-32.93	59.04	-1652.00	372.75
1112	0.20	3.18	1.69		40.08	0.96		-374.38	8.53	0.49	0.33	-51.94	-179.69	7.12	-116.76
1113	0.21	4.44	2.28		25.74	0.59		-244.93	5.11	0.41	1.24	-29.49	-377.67	-333.93	79.51
1105	0.20	3.07	1.68		25.65	0.95		-49.44	8.41	0.49	0.33	-61.93	-88.82	6.85	105.89
1106	0.21	4.74	2.90		27.67	0.58		-47.82	4.93	0.40	1.95	-34.49	-52.03	-94.29	354.79
1107	0.21	4.74	2.69		26.19	0.58		-44.41	4.86	0.40	2.00	-97.92	-219.59	-117.80	-67.19
1108	0.21	4.50	2.58		43.40	0.58		-74.24	4.66	0.40	2.14	100.60	0.00	-538.50	72.11

ID	Si	Ti	Al	V	Cr	Fe	Ni	Zn	Mn	Mg	Ca	Sr	Ba	Na	K
1109	0.20	4.45	1.44		43.75	0.99		-96.38	9.70	0.49	0.33	-71.04	-109.73	7.75	12.91
1094	0.20	3.26	1.65		27.65	0.96		-247.28	7.94	0.49	0.33	-44.63	1117.01	7.25	-231.55
1095	0.21	4.29	2.63		-617.38	0.58		-117.46	4.76	0.40	1.92	-53.57	-112.92	-110.16	226.57
1096	0.20	3.54	1.75		22.45	0.96		-83.53	9.45	0.48	0.34	-26.65	-75.23	7.41	-47.50
1088	0.20	2.32	1.48		41.51	0.95		-178.52	10.24	0.50	0.33	-30.46	85.82	6.51	-138.29
1089	0.21	4.51	2.68		137.38	0.58		-124.19	4.70	0.41	1.89	-41.30	88.58	135.40	43.14
1092	0.21	4.61	2.66		36.85	0.58		-46.90	4.90	0.40	1.86	-77.36	79.93	124.73	-135.50
2000	0.21	4.36	1.68	28.59	28.70	0.95	101.18	-159.12	7.55	0.52	0.33			7.76	
2001	0.21	6.88	2.84	32.85	74.81	0.59	23.37	226.15	5.14	0.42	2.01			92.36	
2002	0.20	4.53	1.77	25.86	26.58	1.01	69.60	-68.99	8.16	0.51	0.32			7.94	
2003	0.20	4.55	1.89	50.29	29.45	1.01	34.71	-65.73	8.86	0.51	0.32			7.96	
2004	0.21	7.18	3.06	83.03	65.19	0.58	32.74	559.09	4.94	0.42	2.15			318.95	
2005	0.20	4.90	1.91	20.07	40.37	0.98	33.34	-72.35	8.06	0.51	0.33			7.94	
2088	0.21	5.25	2.79	42.74	37.40	0.58	28.59	-58.87	4.80	0.42	1.99			115.93	
2089	0.20	3.51	1.71	22.87	20.70	0.96	43.72	-79.53	7.73	0.51	0.33			7.79	
2090	0.20	3.28	1.43	21.90	29.20	0.95	44.13	-278.02	9.09	0.52	0.33			8.22	
2091	0.21	6.05	2.13	79.03	44.39	0.57	27.63	-229.56	4.88	0.43	2.00			128.09	
2092	0.20	3.46	1.57	34.56	23.45	0.96	34.21	-75.47	7.97	0.51	0.32			8.46	
2093	0.21	5.74	2.51	51.11	59.13	0.59	26.25	-459.29	4.84	0.42	1.90			314.93	
2094	0.20	3.70	1.62	22.48	38.37	0.98	29.24	-32.17	8.57	0.51	0.33			7.82	
2095	0.20	3.72	1.65	20.17	32.15	0.96	85.76	-62.43	7.77	0.51	0.33			8.66	
2096	0.21	5.53	2.68	61.17	73.62	0.59	29.33	-104.22	5.29	0.41	2.18			848.41	
370	0.69	6.02	2.42		132.29	1.40		111.11	12.03	0.69	0.47	-80.80	-113.96	10.81	-288.19
371	0.70	5.53	2.35		31.11	1.29		-71.25	11.39	0.67	0.50	-30.91	-799.89	12.16	82.07
372	0.72	6.82	3.06		36.64	0.85		-52.34	6.83	0.57	3.09	-35.35	-70.65	-184.09	94.40
373	0.69	5.17	2.23		21.69	1.44		1931.64	12.77	0.68	0.47	-83.28	-80.79	11.24	38.17
374	0.70	5.43	2.47		51.06	1.35		247.45	11.09	0.67	0.48	-42.47	135.17	11.41	-89.75
376	0.69	3.34	2.34		841.35	1.43		-76.34	11.83	0.68	0.48	-58.50	-286.72	10.81	0.00
377	0.69	3.41	2.28		61.87	1.41		95.10	11.25	0.69	0.47	-228.69	-1038.40	14.82	-326.54
378	0.69	6.26	2.20		30.43	1.46		250.62	14.14	0.69	0.47	-590.96	313.66	11.01	-81.22
379	0.71	6.55	3.54		94.91	0.88		49.11	7.69	0.56	2.30	-47.66	792.76	565.62	-100.73
380	0.71	7.21	3.13		134.76	0.87		-506.19	7.61	0.56	2.34	-78.02	84.45	199.00	131.82
381	0.69	4.95	2.17		93.14	1.39		633.32	10.19	0.68	0.48	-235.70	-212.37	12.47	410.36
382	0.72	7.11	2.94		220.76	0.87		109.25	7.58	0.56	3.01	-56.03	3179.47	95.77	111.65
383	0.69	5.53	2.00		43.12	1.31		125.00	11.34	0.68	0.50	-26.76	-117.05	10.96	97.98
384	0.71	9.08	2.77		112.74	0.85		-127.15	7.08	0.57	3.34	-29.30	-177.73	-61.41	-122.95
385	0.69	5.43	2.37		61.86	1.47		-90.71	16.85	0.69	0.47	-293.39	181.74	14.26	397.43
386	0.69	5.09	2.33		72.13	1.49		132.14	15.00	0.68	0.47	-80.80	-124.23	12.02	-35.04
387	0.69	4.89	2.36		28.47	1.42		-318.84	11.80	0.68	0.47	-42.18	-633.94	13.69	-58.23
388	0.71	7.18	3.83		44.06	0.85		-501.08	7.52	0.57	2.65	-48.93	88.94	321.37	-254.87
389	0.71	6.94	3.51		65.60	0.85		282.44	7.09	0.57	2.76	-47.72	50.10	-115.99	-39.19
390	0.71	6.15	3.15		44.55	0.85		-126.23	6.33	0.57	3.02	-67.12	-121.00	-85.80	67.43
399	0.69	5.39	2.14		31.87	1.42		150.52	10.15	0.69	0.47	-65.50	-175.64	10.74	54.73
400	0.69	5.72	2.36		33.99	1.45		-89.45	13.05	0.68	0.47	-87.45	-1561.70	11.14	5000.00
401	0.71	6.48	3.19		805.13	0.87		279.57	6.83	0.56	3.37	-57.33	-194.80	41.38	-102.71
402	0.71	8.85	4.57		68.51	0.88		5000.00	8.71	0.55	3.28	-70.23	-1078.40	-1024.70	-513.54
403	0.71	9.10	3.80		37.31	0.89		52.70	7.23	0.55	3.06	-68.03	56.86	1126.92	-124.37
404	0.72	9.08	4.19		25.39	0.88		186.94	6.95	0.56	3.13	-142.48	-95.37	151.84	43.72
405	0.69	5.86	2.43		34.54	1.46		88.61	12.51	0.68	0.48	-34.41	-103.05	11.92	0.00
406	0.68	7.22	2.78		62.18	1.58		141.42	20.92	0.66	0.46	-46.12	-137.27	10.80	82.26
411	0.69	6.00	2.44		89.44	1.42		267.63	11.20	0.68	0.47	-47.14	1584.14	11.10	-2007.10
416	0.69	6.35	2.53		57.93	1.41		-124.05	13.30	0.68	0.47	-99.29	-264.54	11.90	107.99
417	0.69	6.05	2.38		55.49	1.41		948.53	10.55	0.67	0.48	-160.92	54.62	11.66	-202.45
1985	0.21	6.52	2.76	39.43	72.42	0.60	26.10	-98.08	5.01	0.41	2.08			-186.92	

ID	Si	Ti	Al	V	Cr	Fe	Ni	Zn	Mn	Mg	Ca	Sr	Ba	Na	K
1986	0.21	3.92	1.58	30.47	38.34	0.97	31.33	-97.17	8.00	0.51	0.33			7.33	
1987	0.21	3.89	1.72	37.13	86.19	1.01	118.31	-202.83	9.46	0.51	0.32			7.55	
1988	0.21	3.35	1.39	23.54	42.67	0.98	31.68	-112.23	8.40	0.51	0.33			6.87	
1989	0.21	6.03	2.80	195.09	124.75	0.61	29.88	222.58	5.23	0.41	1.43			-4797.40	
2045	0.21	4.99	2.13	45.13	71.89	0.60	34.33	-526.21	5.16	0.41	2.25			-55.66	
2046	0.20	3.63	1.51	37.23	33.88	1.01	36.64	-161.00	8.62	0.51	0.32			7.80	
2047	0.21	6.24	2.62	40.70	114.53	0.60	31.24	-165.91	5.04	0.41	1.98			119.77	
2048	0.20	3.82	1.69	34.32	43.74	1.00	27.48	-97.30	9.09	0.51	0.33			7.66	
2049	0.21	5.59	2.48	104.87	116.01	0.60	29.73	130.72	5.13	0.41	1.95			103.81	
2050	0.20	3.77	1.75	25.96	69.11	1.00	52.11	-627.19	9.43	0.51	0.32			7.46	
2051	0.21	5.71	2.43	199.84	115.75	0.60	29.70	-133.89	4.81	0.41	1.81			809.04	
2052	0.20	4.02	1.83	27.42	45.05	1.00	33.45	-121.05	8.71	0.51	0.32			7.52	
2053	0.21	5.67	2.52	82.74	44.47	0.59	22.27	177.61	4.85	0.42	1.70			311.63	
2066	0.20	3.89	1.77	30.99	30.97	1.06	33.63	-57.56	9.30	0.50	0.32			7.91	
2069	0.20	3.48	1.80	28.52	37.83	1.05	38.91	-239.17	9.07	0.50	0.32			8.83	
2070	0.20	3.92	1.62	29.09	40.00	1.03	36.46	-97.20	7.76	0.51	0.32			8.89	
2071	0.20	3.61	1.63	32.64	24.61	1.02	101.35	-1067.30	8.65	0.51	0.32			8.00	
2072	0.21	5.86	2.28	193.15	64.40	0.61	24.70	300.61	5.36	0.40	1.72			141.19	
2073	0.20	4.21	1.63	31.81	35.48	1.00	29.91	-53.09	8.60	0.51	0.33			8.50	
2074	0.21	6.28	2.43	102.65	74.78	0.61	26.12	-258.89	5.42	0.40	2.41			-273.29	
Blocks in the Mooimeisjesfontein area															
2324	0.21	6.33	2.45	42.62	47.51	0.56	50.77	-134.08	4.71	0.43	2.23	155.02	140.25	-108.76	-369.21
2325	0.20	4.25	1.61	26.15	32.44	0.93	29.42	-589.62	7.28	0.53	0.32	-81.68	-162.92	9.15	350.06
2326	0.20	3.23	1.42	18.70	34.62	0.92	97.10	-276.38	8.22	0.53	0.32	251.69	-151.54	7.79	250.50
2327	0.20	3.52	1.60	27.32	59.62	0.89	84.52	-236.62	7.79	0.52	0.32	126.53	138.20	7.80	-634.47
2328	0.20	3.61	1.63	29.00	65.19	0.89	84.94	-61.40	7.07	0.52	0.32	253.64	-77.76	8.36	-222.89
2329	0.21	5.47	2.40	108.35	84.07	0.55	51.84	-181.70	4.55	0.43	2.14	257.03	-215.19	-87.05	-112.22
2330	0.21	5.27	2.68	82.84	77.60	0.56	38.01	-244.65	4.89	0.43	1.72	432.59	-237.71	259.71	-100.49
2331	0.20	2.65	1.57	25.02	336.71	0.84	44.35	-110.50	7.48	0.55	0.32	227.72	134.56	8.48	157.09
2332	0.20	2.66	1.56	35.74	100.92	0.86	38.71	-173.05	7.77	0.54	0.32	132.44	126.92	7.00	72.27
2395	0.20	3.67	1.65	28.42	82.83	0.91	39.34	-94.42	8.27	0.53	0.33	208.43	341.91	9.98	-350.01
2396	0.21	5.85	2.67	54.63	-691.34	0.56	41.55	-114.43	4.74	0.44	2.09	478.26	-1040.20	117.98	-1667.30
2397	0.20	4.05	1.63	22.62	38.42	0.91	89.93	-47.33	8.06	0.53	0.33	-291.26	286.02	8.70	139.53
2398	0.20	4.04	1.82	33.13	42.78	0.92	93.42	-169.75	7.96	0.53	0.33	140.13	-219.80	9.06	-1241.10
2399	0.20	4.02	1.73	22.67	70.52	0.89	35.30	-170.40	8.34	0.53	0.33	139.23	-228.59	8.21	-209.76
2400	0.21	6.27	3.53	155.78	33.75	0.59	26.53	-76.56	5.11	0.41	1.92	63.70	772.27	147.71	195.71
2401	0.20	3.89	1.75	29.14	23.41	0.97	87.94	-121.66	8.22	0.51	0.32	86.95	378.35	9.38	108.32
2402	0.21	3.76	1.62	23.13	26.41	0.95	27.85	-1112.40	7.40	0.52	0.33	221.18	328.30	9.04	90.76
2403	0.21	6.62	2.04	48.48	27.34	0.58	60.68	-238.53	5.10	0.43	2.35	107.55	532.76	-315.72	72.97
2404	0.21	5.00	2.54	37.21	57.73	0.58	37.77	-111.11	4.63	0.43	1.85	75.54	-767.03	62.43	-112.83
2405	0.21	3.80	1.81	43.75	30.29	0.96	56.09	-183.70	8.58	0.52	0.33	856.65	-331.84	9.33	-268.77
2406	0.21	3.25	1.50	23.83	20.36	1.00	50.87	-44.80	8.47	0.52	0.32	50.94	271.46	9.08	-554.62
2407	0.21	5.17	2.31	35.82	64.37	0.59	28.24	-716.73	5.14	0.42	1.95	57.64	149.72	-426.02	-670.45
2408	0.21	3.97	1.66	23.06	32.09	0.96	35.05	-113.69	7.59	0.52	0.33	68.41	-697.43	9.21	188.56
2409	0.21	3.77	1.59	28.52	30.21	0.94	46.77	-84.00	8.08	0.51	0.33	306.56	473.48	9.51	-78.14
2410	0.21	6.15	2.50	68.66	46.97	0.59	26.29	-51.81	4.85	0.42	1.72	318.83	-132.55	471.35	127.55
2411	0.21	3.81	1.61	32.71	21.41	0.95	60.22	-208.75	7.80	0.52	0.33	86.31	-104.03	9.07	97.30
2412	0.21	3.91	1.72	25.36	21.30	0.98	84.69	-216.28	8.07	0.51	0.33	75.45	-98.89	9.21	-445.51
2413	0.21	5.75	2.67	151.49	44.01	0.59	31.02	-64.45	4.96	0.42	1.82	404.93	-166.72	-355.82	-96.23
2438	0.21	4.44	1.75	25.97	35.14	0.87	-2538.60	-38.32	6.84	0.51	0.35	88.17	-98.38	8.75	326.69
2439	0.21	5.83	2.86	75.22	59.62	0.57	48.82	-117.08	4.84	0.43	1.66	-105.86	236.08	-1722.30	-1085.90
2440	0.21	3.65	1.71	29.77	25.47	0.92	56.44	-55.10	7.84	0.53	0.33	-224.60	-76.85	7.92	534.26
2441	0.20	3.22	1.18	22.40	76.97	0.95	20.28	-162.13	12.44	0.45	0.45	513.01	220.21	6.47	5.05
2442	0.21	3.56	1.66	23.79	35.64	0.95	83.27	-219.50	7.87	0.53	0.32	127.62	82.68	7.79	-131.27

ID	Si	Ti	Al	V	Cr	Fe	Ni	Zn	Mn	Mg	Ca	Sr	Ba	Na	K
2443	0.21	3.64	1.82	29.07	26.64	0.95	33.40	-54.60	8.69	0.53	0.33	98.29	247.12	7.45	318.48
2444	0.21	4.99	2.79	105.55	60.52	0.57	31.31	-82.39	4.88	0.44	1.90	493.66	117.45	-123.47	-107.55
2445	0.21	7.84	2.86	71.74	45.69	0.56	29.09	-392.18	4.71	0.44	2.39	-115.83	-176.70	646.28	-220.30
2452	0.22	4.71	2.56	81.39	68.32	0.58	33.64	474.21	4.96	0.44	1.77	125.47	-2916.90	5000.00	290.74
2453	0.21	3.66	1.61	25.87	46.73	0.94	35.72	-101.97	8.70	0.53	0.33	-547.02	312.07	7.82	199.34
2454	0.21	6.31	2.53	82.94	1112.48	0.59	29.56	-121.18	5.24	0.43	2.19	76.50	142.04	-79.85	790.28
2455	0.21	4.24	1.75	35.59	39.81	0.99	49.96	-889.83	10.01	0.52	0.32	66.99	-66.56	8.68	170.41
2456	0.21	4.05	1.57	26.40	34.96	0.91	122.50	-264.82	7.69	0.53	0.33	154.55	74.08	9.89	96.24
2457	0.22	7.01	2.42	42.19	129.27	0.56	31.11	-70.31	4.74	0.44	2.11	-317.59	279.31	-113.65	-466.17
2458	0.21	3.18	1.42	27.75	105.69	0.74	43.41	306.29	7.08	0.51	0.39	1488.95	-147.47	10.75	-146.03
532	0.70	3.54	2.11		91.62	1.26		-139.96	13.27	0.73	0.47		130.00	11.66	85.16
554	0.71	3.62	1.63		34.94	1.22		-329.07	10.41	0.74	0.48		-126.65	11.02	-56.78
555	0.70	3.35	2.04		74.53	1.31		-108.01	10.11	0.72	0.48		-451.88	9.15	-515.97
540	0.70	3.58	1.91		63.59	1.26		-224.70	14.02	0.72	0.47		-145.75	8.65	118.89
541	0.70	3.97	2.03		49.98	1.29		-147.04	11.19	0.72	0.47		129.01	10.59	-134.78
546	0.70	3.21	1.99		166.12	1.25		169.12	11.81	0.72	0.48		-184.76	9.51	103.91
547	0.69	5.71	2.40		47.94	1.35		-119.24	17.17	0.70	0.47		-83.43	12.74	171.99
548	0.72	5.34	3.25		88.31	0.81		61.13	6.87	0.60	2.74		3298.41	-1118.00	-101.48
549	0.70	3.43	2.01		46.89	1.27		-144.59	11.96	0.71	0.48		51.89	10.44	-225.19
585	0.69	4.76	2.19		105.99	1.40		-69.98	15.29	0.70	0.47		-71.86	9.33	132.16
586	0.69	4.27	2.19		54.43	1.46		1987.45	14.05	0.68	0.47		-62.00	9.57	331.65
587	0.69	4.29	2.32		-192.80	1.50		0.00	15.11	0.68	0.47		119.36	11.10	-76.51
574	0.69	4.29	2.25		43.00	1.39		269.12	14.18	0.69	0.47		260.56	11.09	105.90
579	0.69	5.93	1.91		62.17	1.40		-49.62	14.94	0.67	0.49		86.88	11.32	60.53
580	0.71	8.48	3.78		28.81	0.90		-203.92	6.82	0.55	3.00		1598.36	-93.53	55.32
581	0.69	5.89	2.35		30.08	1.48		135.11	13.57	0.67	0.47		126.26	10.89	-197.42

Table D.11 – Mineral chemistry for spinels, including analytical uncertainties. Note: NaO was also analyzed, but was not detected. Tag list: 1 = Inclusion in clinopyroxene exsolution; 2 = Inclusion in plagioclase; 3 = Inclusion in quartz; 4 = Inclusion in alteration minerals.

				Data (wt%)											Analytical uncertainty (%)										
Tag	Tag*	Sample	ID	SiO2	TiO2	Al2O3	V2O3	Cr2O3	FeOT	NiO	ZnO	MnO	MgO	CaO	Total	Si	Ti	Al	V	Cr	Fe	Ni	Zn	Mn	Mg	Ca
Anorthosite sequence near the Phosiri Dome																										
3		AR-9	1549	0.06	42.74	0.02	0.44	0.29	50.13	0.03	0.03	5.15	0.11	0.07	99.07	21.39	0.17	47.87	7.47	8.37	0.38	57.89	233.39	1.32	13.04	11.17
3		AR-9	1550	3.11	44.47	0.29	0.47	0.27	41.88	0.03	–	6.38	0.30	2.51	99.71	0.95	0.17	4.74	7.18	9.08	0.41	50.25	-119.86	1.19	5.73	0.93
3		AR-9	1551	0.31	42.96	0.09	0.45	0.23	49.57	0.01	0.01	5.22	0.19	0.14	99.19	4.63	0.17	12.22	7.36	9.88	0.38	182.61	593.56	1.31	8.36	6.41
2		ARS-2-1	1293	–	0.31	0.39	0.18	–	93.71	0.04	0.13	0.03	0.02	–	94.81	-150.42	2.95	4.17	13.37	-146.39	0.26	39.03	56.38	61.92	57.81	-222.27
1		ARS-2-1	1295	1.49	0.50	1.80	0.33	0.01	87.89	0.04	0.05	0.07	0.68	0.08	92.94	1.61	2.09	1.49	8.60	144.10	0.27	39.76	142.12	23.50	3.69	10.77
1		ARS-2-1	1296	0.68	0.07	0.62	0.37	0.00	90.30	0.02	0.04	0.02	0.39	0.15	92.69	2.77	11.00	2.97	7.92	488.59	0.27	77.14	183.39	77.30	5.35	6.30
1		ARS-2-1	1297	1.24	1.53	0.62	0.68	0.10	86.64	0.05	0.20	0.09	0.29	0.11	91.57	1.81	0.98	2.95	5.31	16.08	0.28	33.27	37.88	19.65	6.71	8.50
1		ARS-2-1	1298	0.88	0.21	0.62	0.67	0.07	89.62	0.07	0.16	0.03	0.29	0.26	92.88	2.30	4.17	2.96	5.34	22.80	0.27	23.82	46.47	49.01	6.66	4.11
2		ARN-2-1	1294	–	50.01	–	–	–	46.82	0.01	–	2.50	–	0.00	99.34	-28.00	0.16	5000.00	-22.87	-610.94	0.39	184.99	-388.71	1.95	-324.73	216.43
2		ARS-2-6	1328	–	0.06	0.27	0.57	0.02	93.06	0.05	0.05	0.00	0.01	0.00	94.09	-68.97	13.20	5.55	5.94	83.27	0.27	32.72	132.72	5000.00	101.83	2010.69
2		ARS-2-6	1329	–	0.08	0.30	0.68	0.02	92.96	0.02	0.03	0.01	0.03	–	94.12	-428.97	9.99	5.05	5.29	58.25	0.27	82.50	266.98	190.33	53.70	-158.22
2		ARS-2-6	1330	–	49.54	0.03	0.09	0.01	46.92	0.00	0.02	2.54	–	0.03	99.19	-59.17	0.16	38.37	25.81	327.85	0.38	405.08	261.88	1.93	-124.19	22.92
1		ARN-3-3	1439	0.00	0.14	0.39	0.33	0.02	95.85	0.07	0.05	0.04	–	0.05	96.95	785.05	5.60	4.13	8.48	84.04	0.26	25.22	129.37	40.38	-123.24	17.43
2		ARN-3-3	1440	1.59	0.41	0.98	0.21	–	92.53	0.04	0.07	0.05	0.65	0.08	96.61	1.53	2.42	2.17	12.01	-769.12	0.27	38.07	101.38	32.56	3.79	10.90
1		ARN-3-8	1421	0.12	0.11	0.25	0.85	0.16	93.40	0.06	0.02	0.04	0.05	0.15	95.23	11.72	7.45	5.87	4.61	10.72	0.27	27.35	307.17	41.51	30.65	6.35
1		ARN-3-8	1422	–	0.08	0.43	0.54	0.04	94.81	0.08	0.10	0.03	0.01	0.01	96.15	-48.36	9.51	3.87	6.17	32.14	0.27	20.92	75.28	54.67	92.85	91.37
1		ARN-3-8	1423	7.06	60.92	0.13	0.11	–	15.04	0.00	–	2.75	–	9.94	95.94	0.58	0.15	8.43	22.50	-546.61	0.70	1251.80	-502.21	1.89	-65.10	0.45

				Data (wt%)												Analytical uncertainty (%)										
Tag	**Tag***	**Sample**	**ID**	**SiO2**	**TiO2**	**Al2O3**	**V2O3**	**Cr2O3**	**FeOT**	**NiO**	**ZnO**	**MnO**	**MgO**	**CaO**	**Total**	**Si**	**Ti**	**Al**	**V**	**Cr**	**Fe**	**Ni**	**Zn**	**Mn**	**Mg**	**Ca**
1	3	ARN-2-2'	918	0.02	0.40	0.95	1.03	1.41	87.98	0.04	–	0.06	0.03	0.24	92.17	58.89	5.92	2.35	2.40	1.72	0.28	41.53	-18.61	29.16	58.95	4.41
1	3	ARN-2-2'	915	–	45.42	–	0.06	0.14	48.73	–	–	3.24	0.01	0.15	97.75	-47.72	0.44	-18.85	22.30	9.80	0.39	-111.16	-53.33	1.72	94.45	5.90
1	6	ARN-2-2'	899	–	47.14	–	0.06	0.08	48.06	–	–	2.84	0.01	0.11	98.32	-71.47	0.44	-13.28	21.55	15.46	0.39	-79.89	-129.87	1.86	99.04	7.67
1	27	ARN-2-2'	965	–	0.07	0.25	0.70	0.25	89.74	0.02	–	0.04	–	0.10	91.17	-91.35	23.80	6.46	3.05	5.11	0.28	99.85	-20.68	44.27	-122.16	9.00
2	32	ARN-2-2'	968	0.05	0.07	0.26	0.56	0.09	90.53	0.05	–	0.01	0.02	0.12	91.75	30.99	22.66	6.26	3.46	11.05	0.28	37.23	-24.30	275.16	69.56	7.78
2	34	ARN-2-2'	976	0.03	0.03	0.27	0.24	0.01	90.37	0.05	–	–	0.01	0.11	91.11	49.06	50.34	5.92	6.27	127.40	0.28	34.29	-35.29	-187.05	146.50	8.74
1	26	ARN-2-2	1018	–	0.30	0.44	1.19	1.03	87.20	0.03	–	0.04	0.04	0.19	90.46	-191.12	7.27	4.12	2.19	2.05	0.28	60.88	-31.14	37.21	40.48	5.33
1	32	ARN-2-2	1019	3.25	0.15	1.43	0.63	0.08	83.18	0.05	–	0.03	0.28	1.23	90.29	0.99	12.00	1.75	3.29	13.53	0.29	38.72	-28.02	57.73	6.97	1.46
1	32	ARN-2-2	1021	–	0.19	0.35	0.67	0.10	89.91	0.03	–	0.02	–	0.09	91.34	-33.48	10.11	4.86	3.10	10.58	0.28	69.53	-32.44	81.44	-156.14	10.49
1	32	ARN-2-2	1020	–	50.30	–	0.11	0.02	41.43	0.01	0.11	5.52	0.01	0.13	97.64	-95.16	0.42	-24.96	12.72	70.26	0.42	122.47	66.76	1.30	115.97	6.73
1	37	ARN-2-2	1035	1.49	0.07	0.41	0.61	0.12	87.59	0.05	–	0.01	0.07	0.16	90.57	1.63	23.85	4.19	3.26	8.95	0.28	38.61	-27.78	127.73	23.55	6.02
1	37	ARN-2-2	1036	–	0.13	0.44	0.40	0.04	90.49	0.05	–	–	–	0.07	91.61	-70.82	13.82	3.95	4.33	22.47	0.28	38.77	-28.77	-64.99	-70.36	12.43
1		ARN-4-9	1352	0.56	8.12	0.41	0.66	0.33	80.54	0.01	0.26	0.79	0.04	0.08	91.80	3.16	0.39	3.91	5.49	6.79	0.29	149.01	28.47	3.72	33.85	10.84
1		ARN-4-9	1351	1.49	40.27	0.36	0.31	0.11	48.99	0.02	0.05	2.21	0.63	0.31	94.73	1.51	0.18	4.01	9.56	18.70	0.38	103.08	131.10	2.08	3.54	3.41
1		ARN-5-1	1525	4.03	43.10	1.36	0.37	0.24	38.60	–	–	6.30	1.13	1.14	96.25	0.82	0.17	1.62	8.45	9.83	0.43	-251.83	-598.86	1.20	2.42	1.45
1		ARN-5-1	1526	8.23	46.28	1.06	0.40	0.22	30.93	0.03	–	4.70	0.71	5.43	97.97	0.55	0.17	1.85	8.20	10.82	0.48	59.16	-64.22	1.41	3.11	0.62
1		ARN-5-4	1480	4.65	46.40	0.63	0.25	0.08	37.76	0.01	–	5.90	0.68	2.93	99.29	0.75	0.17	2.63	11.37	23.85	0.44	296.02	-1265.00	1.24	3.27	0.85

Tag*: Distance (mm) from core of oikocryst.

Pyroxenite Layers in the Mooimeisjesfontein area																										
1		JB031-A2	1716	0.00	0.13	0.22	0.28	0.15	94.55	0.29	0.00	0.02	0.00	0.23	95.87	954.88	6.33	6.49	9.79	11.17	0.27	7.13	1770.46	79.23	1678.94	4.61
1		JB031-A2	1717	0.02	18.70	0.15	0.41	0.07	73.27	–	0.07	0.15	0.02	0.34	93.22	80.07	0.26	8.53	7.68	24.54	0.31	-64.34	93.35	12.63	55.16	3.31
1		JB031-A2	1718	0.56	16.31	0.24	0.51	0.06	74.31	0.01	–	0.18	0.02	0.92	93.14	3.06	0.28	5.83	6.70	29.15	0.31	234.91	-181.68	11.03	58.08	1.71
1		JB031-T	1659	0.22	2.00	0.90	1.08	1.84	88.52	0.20	0.07	0.09	0.05	0.25	95.25	6.65	0.85	2.31	4.10	2.30	0.28	9.61	101.44	19.11	27.22	4.26
1		JB031-P5	1750	–	0.35	0.66	1.19	6.83	84.43	0.30	0.32	0.51	0.03	0.05	94.67	-727.72	2.72	2.84	3.89	1.16	0.29	6.88	24.25	5.01	54.35	16.59
1		JB031-P5	1748	2.92	43.63	0.14	0.41	0.84	44.42	0.00	0.09	5.12	0.12	2.30	100.00	0.99	0.17	8.83	7.93	4.24	0.40	455.97	68.56	1.34	11.87	0.98
1		JB031-P5	1749	–	43.93	–	0.41	0.58	48.89	0.01	–	5.07	0.04	0.07	99.03	-29.11	0.17	-99.07	7.87	5.27	0.38	106.46	-177.97	1.34	31.38	12.01
1		JB031-G1	1720	0.24	17.56	0.27	0.90	1.08	73.86	0.04	0.06	0.68	0.19	0.03	94.90	6.07	0.27	5.34	4.66	3.34	0.31	42.80	121.36	4.16	8.94	26.22
1		JB031-G1	1719	–	43.00	0.07	0.30	0.34	53.33	0.03	–	2.89	0.02	0.04	100.03	-49.49	0.17	15.76	9.97	7.50	0.37	53.14	-1160.50	1.81	52.89	19.15
1		JB031-G2	1919	4.42	46.49	0.06	0.36	0.52	39.82	0.01	0.04	4.11	0.02	3.96	99.83	0.78	0.17	18.33	8.75	5.82	0.43	138.75	164.75	1.51	63.91	0.73
1		JB031-G2	1920	4.49	46.39	0.05	0.38	0.49	39.74	0.02	–	4.18	0.04	4.11	99.90	0.77	0.17	20.48	8.55	6.02	0.43	89.01	-278.62	1.50	30.36	0.71
1		JB031-G2	1921	0.64	48.12	–	0.33	0.43	44.31	0.01	–	4.90	0.04	1.00	99.78	2.63	0.16	-480.51	9.30	6.52	0.40	140.62	-238.85	1.37	30.22	1.57
1		JB031-G2	1922	11.32	43.85	0.06	0.61	0.92	29.20	0.01	–	3.04	0.02	10.64	99.68	0.46	0.18	17.74	6.31	4.13	0.50	149.19	-200.86	1.79	68.71	0.44
1		JB031-G3	1944	0.41	46.01	0.02	0.30	0.43	46.20	0.03	0.09	5.00	0.02	0.86	99.35	3.71	0.17	59.51	9.97	6.54	0.40	58.79	66.97	1.36	74.66	1.72
1		PM-90	1086	–	0.40	1.11	0.76	0.05	92.15	0.04	–	0.02	–	0.10	94.62	-35.03	5.79	2.08	2.87	20.70	0.27	46.45	-18.74	85.01	-110.11	8.62
1		PM-90	1078	0.13	0.10	0.57	0.86	0.03	91.92	0.06	–	0.03	0.01	0.11	93.82	11.26	16.57	3.45	2.65	27.08	0.27	28.07	-54.63	62.29	224.47	8.52
1		PM-90	1079	–	0.13	0.84	0.91	0.02	89.43	–	–	0.01	0.01	0.14	91.49	-82.50	14.44	2.55	2.56	44.67	0.28	-172.17	-25.33	231.81	167.63	6.54
1		PM-90	1067	–	0.20	0.49	0.72	0.06	92.21	–	–	0.02	0.00	0.11	93.82	-69.84	9.61	3.70	2.99	16.41	0.27	-2930.00	-28.40	63.24	704.74	8.17
1		PM-90	1057	–	0.18	0.49	0.78	0.02	89.78	–	–	0.03	–	0.13	91.40	-56.32	9.92	3.77	2.84	45.72	0.28	-568.83	-21.79	62.80	-62.40	7.06
1		PM-90	1056	0.00	0.17	–	0.81	0.03	93.26	0.05	–	0.02	–	0.12	94.47	588.47	10.94	-197.59	2.75	25.87	0.27	33.24	-63.29	108.23	-94.56	7.36
1		PM-90	1048	–	0.18	0.39	0.88	0.04	92.40	0.04	–	0.03	–	0.05	94.01	-24.95	10.28	4.44	2.67	21.15	0.27	50.26	-43.29	53.41	0.00	17.36
1		PM-90	1049	0.24	0.21	0.54	0.89	0.07	88.96	0.03	–	0.03	0.16	0.13	91.25	6.78	8.99	3.40	2.61	14.23	0.28	69.58	-23.24	58.38	11.05	7.51
1		PM-90	1050	–	0.10	0.29	0.50	0.02	89.84	0.01	–	0.01	–	0.14	90.92	-47.97	17.25	5.53	3.75	44.52	0.28	128.37	-19.38	158.54	-107.53	6.98
1		PM-35	1947	0.10	0.54	0.47	1.09	0.08	93.79	0.04	0.02	0.03	0.10	0.23	96.51	13.48	1.98	3.63	4.03	20.38	0.27	38.25	321.79	63.27	15.32	4.57
1		PM-35	1948	–	0.30	0.26	1.14	0.05	94.88	0.04	0.16	0.01	–	0.09	96.93	-301.56	3.08	5.71	3.92	29.37	0.27	44.43	45.21	125.34	-182.65	10.27
1		PM-0-1	1826	–	0.10	0.33	0.65	0.10	95.80	0.11	0.17	0.04	0.00	0.05	97.36	-95.53	8.12	4.71	5.51	16.43	0.27	16.81	43.21	42.59	363.18	17.33
1		PM-0-1	1828	–	0.13	0.42	0.76	0.07	93.91	0.08	0.10	0.05	0.00	0.14	95.66	-162.13	6.12	3.99	5.01	20.94	0.27	22.36	70.03	34.29	373.24	6.88
1		PM-0-1	1829	0.00	0.14	0.51	0.95	0.08	94.92	0.10	0.04	0.03	0.01	0.17	96.99	343.55	5.76	3.41	4.36	20.11	0.27	17.93	181.09	62.26	132.41	5.74
1		PM-0-1	1830	0.52	0.28	0.47	0.54	0.03	93.93	0.08	0.18	0.07	0.31	0.16	96.57	3.37	3.31	3.66	6.25	54.88	0.27	21.13	41.44	23.13	6.44	6.17
1		PM-0-1	1827	0.00	49.92	0.02	0.04	0.01	36.32	0.01	–	13.88	0.01	0.11	100.32	303.64	0.16	50.44	59.77	245.54	0.45	142.93	-256.31	0.80	116.28	7.61
3		PM-0'	425	–	0.43	0.14	0.53	0.02	95.19	0.02	0.00	0.02	0.03	0.22	96.61	0.00	7.99	13.24	5.18	51.98	0.39	127.22	2511.67	138.54	63.87	7.10
3		PM-0'	460	–	0.22	0.19	0.80	0.13	90.87	0.05	–	0.04	0.06	0.14	92.49	0.00	12.62	10.43	3.98	11.57	0.40	51.21	-187.60	62.97	37.49	10.57
3		PM-0'	466	1.52	0.49	0.43	1.13	0.18	89.15	0.09	0.05	0.06	0.41	0.50	94.02	4.76	7.22	5.34	3.25	9.24	0.41	28.01	64.56	38.29	7.06	3.84

				Data (wt%)												Analytical uncertainty (%)										
Tag	**Tag***	**Sample**	**ID**	**SiO2**	**TiO2**	**Al2O3**	**V2O3**	**Cr2O3**	**FeOT**	**NiO**	**ZnO**	**MnO**	**MgO**	**CaO**	**Total**	**Si**	**Ti**	**Al**	**V**	**Cr**	**Fe**	**Ni**	**Zn**	**Mn**	**Mg**	**Ca**
3		PM-0'	467	0.12	0.23	0.37	0.91	0.07	91.01	0.09	0.05	0.03	0.05	0.16	93.10	34.33	12.50	6.22	3.75	20.80	0.40	28.33	59.15	70.35	41.81	9.07
3		PM-0'	480	–	0.31	0.37	0.82	0.07	94.44	0.12	–	0.09	–	0.12	96.34	0.00	10.11	6.04	3.87	22.43	0.39	20.97	-62.02	31.01	-135.11	11.71
3		PM-0'	482	–	0.32	0.15	1.22	0.31	90.38	0.09	–	0.02	0.01	0.24	92.73	0.00	9.60	12.63	3.10	6.34	0.40	29.47	-859.37	163.65	138.92	6.70
3		PM-0'	433	–	0.09	0.33	0.79	0.03	91.77	0.12	0.00	0.01	–	0.04	93.18	0.00	30.16	6.67	3.95	39.26	0.40	19.83	877.48	453.38	-63.62	33.42
3		PM-0'	434	–	0.13	0.38	0.37	0.02	91.37	0.08	–	0.04	0.00	0.12	92.52	0.00	18.71	6.00	6.54	78.79	0.40	29.88	-357.11	62.98	774.59	12.13
3		PM-0'	447	–	0.15	0.46	0.70	0.07	95.59	0.15	–	0.11	–	0.07	97.31	0.00	17.18	4.99	4.24	20.13	0.39	17.28	-155.34	22.58	-799.79	18.47
3		PM-0'	438	–	0.59	0.22	1.03	0.19	94.76	0.08	0.07	0.13	–	0.12	97.19	0.00	6.31	9.46	3.39	8.79	0.39	30.78	42.85	21.36	-542.46	11.90
1		PM+10	287	–	45.12	0.17	0.65	0.18	37.61	0.01	–	9.12	0.64	2.34	95.83	0.00	0.64	9.51	4.97	11.75	0.64	421.47	-197.51	1.46	4.67	1.40
1		PM+10	210	–	47.99	0.01	0.58	0.17	36.93	0.01	0.01	12.67	0.03	0.06	98.46	0.00	0.62	246.10	5.34	12.34	0.65	145.38	402.67	1.23	63.41	20.43
1		PM+10	226	–	45.62	0.04	0.64	0.16	40.31	–	–	11.00	–	0.26	98.02	0.00	0.63	32.71	4.99	13.51	0.62	-848.73	-75.30	1.32	-228.11	6.00
2		PM+10	231	–	44.42	0.01	0.97	0.01	42.64	–	–	9.59	0.02	0.36	98.03	0.00	0.64	96.58	3.87	137.35	0.60	-48.48	-101.20	1.42	76.33	4.59
2		PM+10	232	–	37.66	0.23	1.22	0.07	47.08	0.02	–	8.82	0.19	0.14	95.45	0.00	0.69	7.69	3.31	24.14	0.57	98.11	-178.53	1.47	11.02	9.97
1		PM+13	2025	–	0.22	0.59	0.42	0.02	94.21	0.04	0.08	0.03	–	0.02	95.67	-102.59	3.93	3.09	7.31	71.48	0.27	38.79	87.37	51.85	-745.34	35.55
1		PM+13	2026	1.86	0.06	1.22	0.46	0.06	90.30	0.06	0.04	0.05	0.88	0.47	95.53	1.39	12.39	1.91	6.89	23.95	0.28	28.35	188.52	32.40	3.14	2.69
1		PM+13	2027	0.10	0.47	0.74	0.57	0.07	93.07	0.06	0.06	0.04	0.01	0.19	95.42	13.23	2.19	2.64	5.96	20.99	0.27	26.55	112.67	41.91	112.65	5.26
1		PM+41	349	–	45.06	0.01	0.80	0.25	41.10	0.01	0.01	9.87	0.02	0.27	97.39	0.00	0.64	244.50	4.30	9.23	0.61	207.54	235.76	1.40	68.96	5.76
1		PM+41	350	–	43.23	0.03	0.65	0.29	40.55	0.02	–	10.82	0.05	0.17	95.81	0.00	0.65	44.97	4.92	8.12	0.62	92.20	-71.76	1.33	38.42	8.29
1		PM+41	309	–	45.38	0.00	0.54	0.12	40.47	0.05	0.00	9.74	0.00	0.10	96.41	0.00	0.64	475.39	5.44	15.92	0.62	40.35	1176.82	1.41	1705.74	13.45
1		PM+41	307	–	42.53	0.11	0.36	0.15	41.74	–	–	10.86	0.04	0.51	96.31	0.00	0.66	14.20	7.29	13.32	0.61	-156.87	-161.78	1.33	38.98	3.66
1		PM+41	308	–	43.30	0.04	0.37	0.15	41.76	0.00	0.02	10.70	0.01	0.49	96.84	0.00	0.65	33.24	7.00	13.45	0.61	1444.14	175.83	1.34	156.20	3.69
1		PM+41	294	–	45.37	0.05	0.51	0.16	43.57	–	0.02	4.89	0.20	0.25	95.02	0.00	0.64	30.26	5.64	12.36	0.60	-173.65	117.88	2.02	10.86	6.18
2		PM+145'	375	–	47.47	0.01	0.31	0.08	40.51	0.03	0.02	8.89	0.01	0.33	97.66	0.00	0.62	95.90	8.17	24.77	0.62	78.06	130.08	1.48	140.91	4.95
Blocks in the Mooimeisjesfontein area																										
2		LX-1-1	526	–	46.59	0.03	0.26	–	48.84	–	0.01	1.20	–	0.13	97.05	5000.00	0.63	45.55	9.02	-427.51	0.56	-415.81	391.51	4.49	-348.07	10.01
1		LX-1-1	556	0.66	0.00	0.27	0.99	0.53	88.88	0.12	–	0.05	0.50	0.07	92.07	8.22	1252.68	7.72	3.50	4.40	0.41	20.49	-149.57	44.96	6.18	21.03
1		LX-1-1	557	2.51	0.06	0.73	0.93	0.47	86.06	0.15	–	0.01	2.06	0.16	93.13	3.63	35.57	3.65	3.71	4.75	0.41	17.13	-418.23	455.77	2.52	9.57
1		LX-1-1	545	0.08	0.24	0.38	0.79	0.23	93.69	0.11	–	0.02	–	0.19	95.73	37.12	11.21	5.90	4.01	8.10	0.40	25.38	-2515.50	123.65	-325.57	8.15

E Whole-rock chemical data and analytical uncertainties

The table below includes all whole-rock geochemistry data collected and used in this thesis. The data below is unnormalized. To calculate the analytical uncertainties (1σ), the relative errors from Earth Lab and the coefficients for expanded uncertainties from Intertek are presented at the end. Abbreviations EL = Earth Lab and I = Intertek.

Table E.1 – Whole-rock chemical data.

	Anorthosite sequence near the Phosiri Dome									
Samples	JB060	AR-1-1	AR-3-8	ARS-2-1	ARS-2-4	ARS-2-6	ARS-2-9	ARN-3-1	ARN-3-3	ARN-3-5
Lab	EL	I	I	EL	EL	EL	EL	EL	EL	EL
SiO_2 (wt%)	51.63	50.76	50.39	49.35	50.47	46.95	50.55	49.82	50.04	49.78
TiO_2	0.21	0.09	0.12	0.10	0.12	0.12	0.12	0.07	0.12	0.12
Al_2O_3	17.40	28.07	19.99	26.74	25.46	24.67	25.53	30.36	28.13	27.18
$Fe_2O_{3\,T}$	7.38	2.52	8.76	2.62	3.73	2.67	3.84	1.01	2.19	2.30
MnO	0.15	0.04	0.15	0.04	0.06	0.04	0.06	0.02	0.05	0.04
MgO	7.87	1.67	7.79	1.75	2.72	1.88	2.60	0.33	1.51	1.66
CaO	12.94	14.03	10.58	13.56	13.49	13.00	13.09	13.97	13.67	12.93
Na_2O	2.04	2.77	1.85	2.60	2.49	2.59	2.47	2.92	2.63	2.54
K_2O	0.20	0.20	0.10	0.23	0.25	0.31	0.20	0.29	0.21	0.21
P_2O_5	0.04	0.01	0.01	0.02	0.02	0.03	0.02	0.02	0.03	0.02
LOI	0.21	0.12	0.21	2.14	0.79	0.66	1.07	1.01	1.16	2.92
Total	100.10	100.39	100.09	99.16	99.63	92.94	99.58	99.84	99.75	99.72
Ba (ppm)		79.80	53.00							
Be		0.28	0.20							
Cd		0.03	0.07							
Ce		4.29	3.53							
Co		11.30	51.10							
Cr		20.00	51.00							
Cs		0.08	–							
Cu		28.10	149.20							
Dy		0.33	0.46							
Er		0.26	0.38							
Eu		0.43	0.33							
Ga		21.89	15.32							
Gd		0.35	0.41							
Ge		0.75	0.90							
Hf		0.21	0.17							
Ho		0.08	0.11							
La		2.47	1.95							
Li		5.00	3.00							
Lu		0.03	0.06							
Mo		0.10	0.10							
Nb		0.37	0.28							
Nd		2.02	1.69							
Ni		29.90	150.30							
Pb		1.60	1.90							
Pr		0.50	0.41							
Rb		2.44	0.60							
Sc		6.00	16.40							
Sm		0.35	0.35							
Sn		0.10	0.10							
Sr		404.18	267.39							
Ta		0.03	0.03							
Tb		0.06	0.08							
Th		0.29	0.15							
Tm		0.03	0.06							
U		0.06	0.03							
V		28.00	70.00							
W		–	–							
Y		1.97	2.93							
Yb		0.20	0.41							
Zn		19.00	58.00							
Zr		7.40	4.80							

	Anorthosite sequence									
Samples	ARN-2	ARN-3-8	ARN-1-1	ARN-3-10	ARN-4-1	ARN-4-4	ARN-4-7	ARN-4-9	ARN-4-11	ARN-5-1
Lab	I	EL	I	EL	EL	EL	EL	EL	EL	EL
SiO_2 (wt%)	50.26	50.13	50.35	49.43	50.00	50.24	50.18	50.58	49.94	50.58
TiO_2	0.09	0.10	0.13	0.14	0.14	0.15	0.16	0.15	0.10	0.13
Al_2O_3	29.22	27.35	28.27	26.92	27.80	26.97	24.10	27.21	28.72	25.85
Fe_2O_{3T}	1.95	2.52	2.01	2.35	1.96	2.47	5.08	2.79	1.62	3.83
MnO	0.03	0.04	0.04	0.04	0.04	0.04	0.09	0.05	0.03	0.07
MgO	1.16	1.86	1.20	1.55	1.32	1.78	4.31	2.12	1.04	3.46
CaO	13.86	13.38	14.15	13.14	13.89	13.48	11.89	13.48	13.69	12.85
Na_2O	2.75	2.55	2.61	2.43	2.58	2.61	2.18	2.45	2.62	2.42
K_2O	0.24	0.21	0.32	0.19	0.29	0.28	0.17	0.24	0.30	0.16
P_2O_5	0.03	0.02	0.02	0.03	0.03	0.02	0.03	0.03	0.02	0.03
LOI	0.42	1.65	0.73	1.85	1.14	1.82	1.69	1.32	1.61	0.82
Total	100.11	99.83	99.94	98.10	99.21	99.89	99.90	100.45	99.70	100.22
Ba (ppm)	89.30		100.70							
Be	0.29		0.30							
Cd	0.02		0.03							
Ce	6.87		8.33							
Co	8.20		8.30							
Cr	8.00		17.00							
Cs	0.17		0.25							
Cu	23.50		22.00							
Dy	0.35		0.59							
Er	0.21		0.37							
Eu	0.43		0.47							
Ga	22.57		21.56							
Gd	0.40		0.61							
Ge	0.71		0.75							
Hf	0.26		0.37							
Ho	0.07		0.12							
La	3.79		4.50							
Li	3.80		4.80							
Lu	0.03		0.04							
Mo	0.10		0.10							
Nb	0.44		0.93							
Nd	2.78		3.57							
Ni	21.30		24.50							
Pb	2.90		2.20							
Pr	0.73		0.96							
Rb	3.39		6.39							
Sc	3.10		6.90							
Sm	0.44		0.69							
Sn	0.20		0.20							
Sr	399.10		381.29							
Ta	0.04		0.06							
Tb	0.06		0.10							
Th	0.53		0.75							
Tm	0.03		0.04							
U	0.05		0.09							
V	21.00		35.00							
W	–		–							
Y	1.90		3.13							
Yb	0.17		0.28							
Zn	19.00		15.00							
Zr	8.90		14.40							

	Anorthosite sequence								Blocks	
Samples	ARN-5-4	ARN-3	ARN-5-6	AR-5-1	ARN-5-8	AR-7-1	AR-9-1	AR-9	ARS-X1	ARS-X2
Lab	EL	I	EL	I	EL	I	I	EL	EL	EL
SiO_2 (wt%)	49.96	50.49	50.07	50.03	50.23	49.84	50.87	50.95	51.75	48.95
TiO_2	0.10	0.12	0.12	0.14	0.12	0.12	0.18	0.18	0.23	0.13
Al_2O_3	26.51	26.45	26.37	25.83	24.04	26.18	18.00	18.40	6.01	12.08
$Fe_2O_{3\,T}$	3.06	3.43	3.02	3.95	5.13	3.28	6.52	6.16	15.93	12.83
MnO	0.05	0.06	0.06	0.07	0.09	0.06	0.14	0.13	0.26	0.24
MgO	2.77	2.98	2.73	3.19	5.02	2.65	8.46	8.31	18.46	17.28
CaO	13.43	13.66	13.61	13.08	11.53	13.93	13.44	13.60	5.30	7.09
Na_2O	2.48	2.47	2.48	2.43	2.20	2.49	1.69	1.72	0.54	0.57
K_2O	0.17	0.20	0.18	0.20	0.16	0.15	0.19	0.20	0.04	0.04
P_2O_5	0.02	0.01	0.03	0.02	0.02	0.01	0.01	0.02	0.01	0.02
LOI	0.75	0.27	0.93	0.53	1.12	1.23	0.35	0.48	1.16	0.86
Total	99.31	100.26	99.61	99.58	99.70	100.05	100.00	100.21	100.08	100.39
Ba (ppm)		80.00		79.40		70.20	68.60	45.10	22.49	35.07
Be		0.30		0.27		0.30	0.27			
Cd		0.02		0.05		0.03	0.06			
Ce		5.63		7.07		5.97	8.19	5.26	1.78	1.98
Co		18.30		20.20		17.90	41.40	38.61	51.24	71.63
Cr		41.00		26.00		27.00	176.00	201.35	1119.39	1330.07
Cs		0.13		0.22		0.18	0.23	0.19	0.13	0.17
Cu		23.70		24.50		27.70	24.30	28.42	578.73	9.61
Dy		0.48		0.56		0.49	1.02	0.57	0.64	0.24
Er		0.33		0.37		0.30	0.68	0.33	0.48	0.19
Eu		0.46		0.46		0.45	0.38	0.18	0.16	0.13
Ga		20.86		20.24		20.59	14.88	10.74	4.36	8.79
Gd		0.47		0.56		0.48	0.93	0.54	0.48	0.22
Ge		0.80		0.79		0.76	1.05			
Hf		0.31		0.43		0.28	0.36	0.33	0.18	0.13
Ho		0.10		0.11		0.10	0.22	0.12	0.15	0.05
La		3.05		3.79		3.30	4.19	1.67	1.09	1.09
Li		4.30		2.80		3.00	4.00	2.01		
Lu		0.05		0.06		0.04	0.10	0.05	0.09	0.04
Mo		0.10		0.10		–	0.10			
Nb		0.50		0.79		0.43	0.40	0.40	0.28	0.13
Nd		2.59		3.01		2.71	3.70	1.90	1.37	0.84
Ni		50.00		51.30		49.40	152.70	139.38	354.69	349.83
Pb		4.30		2.40		2.90	1.80	1.70	15.45	3.45
Pr		0.64		0.79		0.69	0.86	0.42	0.30	0.22
Rb		3.18		3.74		1.65	3.45	3.00	0.59	0.80
Sc		10.20		9.20		9.40	31.30	14.93	32.98	20.59
Sm		0.50		0.60		0.52	0.88	0.48	0.40	0.19
Sn		0.40		0.20		0.20	0.30	0.29		
Sr		358.06		353.05		350.68	236.73	138.68	57.09	149.40
Ta		0.04		0.06		0.04	0.04	0.06	0.02	0.01
Tb		0.09		0.10		0.08	0.17	0.09	0.09	0.04
Th		0.47		0.81		0.48	0.38	0.25	0.12	0.09
Tm		0.04		0.06		0.04	0.09	0.05	0.08	0.03
U		0.08		0.13		0.07	0.10	0.10	0.04	0.03
V		43.00		46.00		42.00	115.00	112.86	166.55	75.32
W		–		–		–	–	0.09	0.04	0.04
Y		2.73		3.09		2.65	5.72	2.95	3.80	1.41
Yb		0.28		0.35		0.30	0.62	0.34	0.54	0.24
Zn		24.00		36.00		23.00	42.00	40.47	56.32	142.88
Zr		12.10		15.30		10.10	12.40	10.60	4.98	4.59

	Blocks in the anorthosite sequence near the Phosiri Dome									
Samples	ARS-X3	ARS-X4	ARS-X5	ARS-X6	ARN-X7	ARN-X8	ARN-X9	ARS-X10	ARN-X11	ARN-X12
Lab	EL	EL	EL	EL	EL	EL	EL	EL	EL	EL
SiO_2 (wt%)	50.78	49.35	48.58	50.66	52.03	48.90	49.40	48.31	49.55	51.27
TiO_2	0.16	0.15	0.15	0.12	0.20	0.13	0.12	0.14	0.08	0.17
Al_2O_3	12.24	10.93	10.97	18.06	7.17	12.21	12.44	11.51	17.67	12.49
Fe_2O_{3T}	11.30	13.22	13.12	8.21	15.80	13.33	12.50	13.94	9.18	11.76
MnO	0.21	0.24	0.25	0.13	0.29	0.23	0.23	0.28	0.18	0.20
MgO	16.36	17.21	18.36	10.34	18.94	16.68	16.74	18.12	11.65	15.93
CaO	7.13	6.28	7.47	9.31	5.15	6.91	5.91	6.59	9.69	7.15
Na_2O	0.72	0.51	0.43	1.43	0.56	0.56	0.45	0.51	0.90	0.78
K_2O	0.05	0.06	0.07	0.09	0.05	0.06	0.02	0.05	0.02	0.04
P_2O_5	0.02	0.01	0.02	0.01	0.01	0.01	0.02	0.02	0.01	0.02
LOI	1.02	2.20	1.17	1.98	0.33	1.28	1.89	0.44	0.76	0.61
Total	100.24	100.51	100.91	100.38	100.70	100.63	100.00	100.23	99.78	100.65
Ba (ppm)	19.36	34.60	28.81	48.98	29.13	31.00	43.27	34.39	23.14	20.98
Be										
Cd										
Ce	1.49	2.84	2.16	2.05	1.98	1.75	2.88	2.62	1.20	2.31
Co	44.88	84.50	89.77	50.22	86.43	86.33	75.03	98.92	65.28	75.89
Cr	846.58	1624.13	1422.15	139.76	1535.27	1378.63	1296.71	635.48	442.95	952.50
Cs	0.19	0.48	0.22	0.22	0.26	0.09	0.04	0.25	0.05	0.07
Cu	6.38	4.13	7.65	18.54	3.01	3.11	33.83	69.32	14.91	32.48
Dy	0.33	0.42	0.37	0.24	0.36	0.24	0.34	0.60	0.15	0.39
Er	0.24	0.30	0.24	0.18	0.25	0.19	0.28	0.43	0.12	0.27
Eu	0.15	0.19	0.16	0.21	0.19	0.15	0.21	0.20	0.12	0.18
Ga	6.26	8.57	8.78	12.16	9.32	9.34	9.37	6.64	15.83	9.12
Gd	0.25	0.37	0.31	0.21	0.31	0.18	0.30	0.43	0.13	0.30
Ge										
Hf	0.13	0.14	0.14	0.09	0.11	0.13	0.24	0.20	0.07	0.20
Ho	0.07	0.09	0.08	0.05	0.08	0.05	0.08	0.14	0.03	0.09
La	1.19	1.94	1.25	1.25	1.74	1.23	1.72	1.50	0.67	1.53
Li	0.88	1.32	0.46		1.09	0.36		0.37		1.36
Lu	0.05	0.06	0.04	0.03	0.04	0.04	0.06	0.09	0.02	0.05
Mo										
Nb	0.49	0.12	0.09	0.27	0.11	0.07	0.06	0.08	0.20	0.56
Nd	0.92	1.40	1.12	0.83	1.31	0.72	1.18	1.37	0.51	1.06
Ni	180.67	354.41	386.67	155.60	377.15	376.96	363.53	299.35	262.15	286.36
Pb	0.73	1.77	1.20	2.47	0.51	1.45	3.18	5.36	1.01	0.60
Pr	0.22	0.33	0.27	0.22	0.31	0.18	0.31	0.31	0.13	0.26
Rb	0.63	1.47	1.08	1.15	0.89	0.40	0.21	0.51	0.33	0.42
Sc	15.79	17.54	19.33	16.58	19.58	21.66	22.09	22.45	24.60	17.52
Sm	0.21	0.33	0.29	0.19	0.28	0.16	0.25	0.37	0.13	0.24
Sn	0.13	0.10	0.13		0.58	0.22		0.18		0.12
Sr	98.18	114.46	117.15	195.80	130.49	125.30	179.79	82.95	288.98	113.21
Ta	0.20	0.01	0.01	0.05	0.01	0.00	0.01	0.00	0.07	0.12
Tb	0.04	0.06	0.05	0.04	0.05	0.03	0.05	0.08	0.02	0.05
Th	0.07	0.09	0.05	0.02	0.06	0.04	0.03	0.07	0.08	0.07
Tm	0.04	0.05	0.04	0.03	0.04	0.03	0.05	0.08	0.02	0.05
U	0.01	0.02	0.02	0.01	0.02	0.02	0.01	0.03	0.02	0.02
V	87.69	82.14	74.14	70.21	94.59	80.83	85.37	129.36	46.75	91.26
W	0.02	0.08	0.07	0.05	0.00	0.00	0.04	0.03	0.06	0.38
Y	1.97	2.59	2.19	1.40	2.31	1.52	2.14	3.80	0.87	2.37
Yb	0.30	0.34	0.28	0.22	0.29	0.24	0.37	0.56	0.14	0.32
Zn	48.18	112.68	96.89	49.79	88.27	115.52	126.65	108.98	70.83	67.22
Zr	3.82	4.88	4.89	2.62	4.10	4.27	8.75	5.98	2.46	6.44

	Blocks	Pyroxenite sequences in the Mooimeisjesfontein area								
Samples	ARN-X13	JB031-A1	JB031-A2	JB031-T	JB031-P1	JB031-P3	JB031-P4	JB031-P5	JB031-P7	JB031-P9
Lab	EL	EL	EL	EL	EL	EL	EL	EL	EL	EL
SiO_2 (wt%)	49.86	51.19	50.53	51.10	52.53	52.72	52.52	52.17	51.93	52.50
TiO_2	0.16	0.14	0.09	0.18	0.25	0.27	0.29	0.31	0.31	0.29
Al_2O_3	11.12	17.85	24.59	13.77	4.04	3.08	2.91	3.19	3.35	5.92
Fe_2O_{3T}	13.75	7.54	4.25	8.70	15.40	15.92	15.45	15.07	14.99	13.31
MnO	0.25	0.15	0.08	0.18	0.29	0.30	0.29	0.29	0.29	0.25
MgO	17.75	10.16	5.18	11.94	20.94	21.47	20.90	20.06	20.09	18.08
CaO	6.01	11.03	12.49	11.90	5.89	5.65	6.77	7.71	7.96	9.23
Na_2O	0.45	1.67	2.33	1.37	0.43	0.34	0.31	0.35	0.36	0.64
K_2O	0.04	0.15	0.20	0.11	0.04	0.05	0.05	0.05	0.04	0.08
P_2O_5	0.02	0.01	0.01	0.01	0.02	0.01	0.02	0.02	0.04	0.03
LOI	0.56	0.24	0.24	0.17	0.01	0.01	0.35	0.48	0.16	0.25
Total	100.31	100.23	100.05	99.56	100.03	100.02	100.07	99.89	99.71	100.76
Ba (ppm)	47.06	29.86	20.41	39.87	14.50	18.15	11.24	12.57	12.07	15.79
Be										
Cd										
Ce	4.89	2.25	1.05	2.70	3.30	4.96	5.62	6.04	5.95	5.49
Co	81.46	44.87	22.60	54.24	55.47	104.06	99.24	94.69	92.54	81.35
Cr	1606.20	328.09	137.60	503.17	462.24	666.84	723.88	751.22	752.08	702.86
Cs	0.09	0.07	0.10	0.08	0.09	0.74	1.03	0.90	0.88	0.27
Cu	6.61	6.73	5.56	7.87	5.23	9.82	14.41	15.64	13.97	14.27
Dy	0.43	0.30	0.08	0.58	0.90	1.18	1.38	1.57	1.49	1.31
Er	0.30	0.19	0.05	0.36	0.56	0.74	0.86	0.99	0.92	0.81
Eu	0.24	0.13	0.06	0.22	0.24	0.27	0.28	0.31	0.32	0.32
Ga	8.88	9.72	13.01	7.77	3.17	4.05	3.91	4.23	4.31	5.44
Gd	0.44	0.26	0.07	0.52	0.77	1.01	1.22	1.40	1.37	1.18
Ge										
Hf	0.23	0.16	0.09	0.21	0.24	0.38	0.46	0.54	0.47	0.46
Ho	0.10	0.07	0.02	0.13	0.20	0.26	0.31	0.35	0.33	0.29
La	2.89	0.70	0.28	0.96	1.81	2.60	2.70	2.67	2.65	2.49
Li	1.36	0.98	0.65	0.95	0.18	0.33	0.71	0.75	0.41	0.38
Lu	0.06	0.04	0.01	0.06	0.09	0.12	0.14	0.16	0.14	0.13
Mo										
Nb	0.16	0.17	1.32	0.20	0.27	0.37	0.54	0.63	0.49	0.77
Nd	2.12	0.83	0.26	1.47	2.61	3.34	4.02	4.46	4.29	3.81
Ni	380.56	181.38	88.81	209.30	235.00	371.51	367.25	349.32	342.90	303.92
Pb	2.87	0.73	0.67	0.97	0.68	2.10	1.21	1.08	1.13	0.89
Pr	0.57	0.17	0.06	0.30	0.53	0.72	0.85	0.91	0.87	0.79
Rb	0.69	1.21	1.44	0.92	0.80	2.95	3.32	3.38	2.23	1.84
Sc	14.40	10.21	3.29	15.99	37.78	45.26	52.38	56.43	57.86	41.69
Sm	0.44	0.22	0.06	0.43	0.66	0.88	1.06	1.22	1.16	1.01
Sn	0.19	0.23	0.23	0.14	0.86	0.46	0.21	0.23	0.27	0.19
Sr	153.98	120.08	108.19	120.91	40.31	38.19	27.30	31.89	38.21	66.49
Ta	0.05	0.04	0.49	0.03	0.07	0.04	0.05	0.06	0.06	0.10
Tb	0.06	0.04	0.01	0.09	0.13	0.17	0.20	0.24	0.22	0.20
Th	0.07	0.10	0.06	0.11	0.15	0.34	0.51	0.58	0.40	0.52
Tm	0.05	0.03	0.01	0.06	0.09	0.12	0.13	0.16	0.15	0.13
U	0.02	0.04	0.04	0.05	0.04	0.10	0.13	0.14	0.10	0.13
V	83.78	78.32	34.49	118.45	142.72	141.76	157.24	175.77	170.95	156.67
W	0.00	0.10	0.81	0.08	0.07	0.05	0.12	0.10	0.13	0.15
Y	2.67	1.48	0.37	2.85	4.73	6.27	7.38	8.13	8.09	6.72
Yb	0.37	0.23	0.07	0.36	0.62	0.78	0.89	1.02	0.97	0.85
Zn	163.60	44.77	22.10	52.02	59.52	105.33	104.36	103.70	96.60	85.61
Zr	10.91	4.19	2.48	5.34	6.59	11.16	13.51	15.27	13.75	13.33

	Pyroxenite sequences									
Samples	JB031-G1	JB031-G2	JB031-G3	JB031-G4	PM-90	PM-42	PM-12	PM-8	PM-1	PM+3-1
Lab	EL	EL	EL	EL	I	I	I	I	I	I
SiO_2 (wt%)	51.72	51.70	51.17	51.59	52.07	51.79	51.77	51.64	51.78	51.50
TiO_2	0.27	0.25	0.20	0.22	0.06	0.06	0.06	0.06	0.08	0.09
Al_2O_3	7.80	11.46	16.81	15.82	27.99	27.95	28.16	28.12	27.15	22.80
Fe_2O_{3T}	12.06	10.23	7.64	7.88	1.76	1.43	1.33	1.35	2.07	4.31
MnO	0.23	0.21	0.14	0.16	0.03	0.03	0.03	0.03	0.04	0.08
MgO	16.31	13.41	9.38	10.22	0.74	0.41	0.39	0.43	0.90	3.81
CaO	9.94	11.02	11.52	12.07	12.41	12.48	12.26	12.52	12.28	13.10
Na_2O	0.82	1.21	1.81	1.68	3.98	3.97	4.07	3.99	3.86	3.15
K_2O	0.09	0.13	0.23	0.20	0.31	0.51	0.52	0.53	0.54	0.22
P_2O_5	0.02	0.02	0.03	0.03	0.01	0.01	0.01	0.01	0.01	0.01
LOI	0.42	0.43	0.49	0.17	0.61	1.26	1.13	1.21	0.92	0.83
Total	99.86	100.20	99.52	100.14	100.06	100.00	99.84	99.99	99.76	100.03
Ba (ppm)	29.76	32.11	48.13	47.08	105.90	147.00	149.20	149.90	144.20	76.30
Be					0.30	0.35	0.35	0.41	0.37	0.24
Cd					–	–	–	–	0.05	0.04
Ce	5.02	3.99	4.83	4.66	2.88	3.13	3.58	3.56	4.79	3.16
Co	74.33	34.77	45.29	50.07	7.60	4.60	4.30	4.70	9.00	28.20
Cr	671.67	390.92	358.70	387.16	7.00	4.00	5.00	5.00	11.00	72.00
Cs	0.19	0.15	0.18	0.11	0.23	0.71	0.83	0.70	0.50	0.13
Cu	14.76	12.38	15.67	23.15	13.90	11.00	14.80	13.90	17.80	9.50
Dy	1.18	0.97	0.57	0.63	0.17	0.17	0.18	0.19	0.32	0.50
Er	0.74	0.57	0.35	0.39	0.09	0.11	0.10	0.09	0.20	0.33
Eu	0.33	0.34	0.22	0.23	0.51	0.46	0.58	0.59	0.66	0.56
Ga	6.43	5.54	9.66	9.17	24.00	23.41	24.66	25.50	24.45	20.47
Gd	1.07	0.88	0.54	0.60	0.19	0.21	0.21	0.21	0.35	0.48
Ge					0.77	0.74	0.78	0.81	0.84	0.98
Hf	0.42	0.34	0.38	0.36	0.08	0.17	0.13	0.10	0.21	0.14
Ho	0.26	0.21	0.13	0.14	0.04	0.03	0.03	0.03	0.06	0.11
La	2.43	2.35	1.67	1.67	1.66	1.71	2.06	2.04	2.74	1.74
Li	1.18	0.95	1.39	1.32	4.00	3.80	4.00	4.10	5.90	5.20
Lu	0.12	0.09	0.06	0.06	0.02	0.02	0.01	0.01	0.02	0.04
Mo					0.20	0.20	0.20	0.20	0.20	0.20
Nb	0.44	0.36	0.59	0.58	0.16	0.41	0.31	0.23	0.45	0.10
Nd	3.61	3.08	1.91	2.03	1.15	1.27	1.48	1.37	2.08	1.72
Ni	277.04	163.26	171.14	192.40	8.40	5.90	7.20	8.50	15.70	47.70
Pb	1.05	1.04	1.47	1.26	2.80	2.80	2.60	2.50	3.80	1.70
Pr	0.75	0.65	0.42	0.43	0.33	0.33	0.39	0.39	0.53	0.40
Rb	1.55	1.42	3.33	2.60	1.87	6.77	7.91	6.69	10.12	2.07
Sc	28.59	22.09	13.71	15.07	3.10	1.50	1.60	2.00	4.90	24.20
Sm	0.94	0.77	0.48	0.52	0.22	0.22	0.23	0.25	0.40	0.42
Sn	0.21	0.17	0.16	0.20	0.20	0.20	0.20	0.20	0.20	0.10
Sr	85.94	103.84	151.32	141.83	448.96	434.60	475.15	497.60	500.45	378.92
Ta	0.04	0.06	0.04	0.06	0.01	0.03	0.02	0.02	0.04	0.01
Tb	0.18	0.14	0.09	0.10	0.04	0.03	0.03	0.03	0.06	0.08
Th	0.37	0.29	0.45	0.34	0.10	0.33	0.20	0.18	0.45	0.07
Tm	0.12	0.09	0.06	0.06	0.02	0.01	0.02	0.01	0.02	0.05
U	0.10	0.06	0.14	0.13	0.03	0.09	0.05	0.04	0.11	0.02
V	152.16	124.72	94.51	114.31	26.00	17.00	16.00	16.00	32.00	121.00
W	0.07	0.07	0.18	0.09	0.10	–	–	–	–	–
Y	6.13	4.83	2.82	3.26	0.88	0.88	0.87	0.87	1.67	2.84
Yb	0.78	0.60	0.37	0.41	0.09	0.10	0.08	0.09	0.19	0.31
Zn	77.53	37.58	47.48	48.66	14.00	12.00	12.00	12.00	22.00	26.00
Zr	11.69	9.46	11.22	10.84	2.80	6.60	4.80	4.30	8.10	4.10

	Pyroxenite sequences								Blocks	
Samples	PM+3-2	PM+13	PM+21	PM+41	PM+48	PM+133	PM+145	PM-GN	LX-1-2	LX-1-4
Lab	I	I	I	I	I	I	I	I	EL	EL
SiO_2 (wt%)	51.22	52.04	52.33	51.95	51.78	51.67	51.97	51.33	50.09	48.98
TiO_2	0.11	0.16	0.15	0.13	0.10	0.12	0.12	0.12	0.15	0.07
Al_2O_3	19.49	11.48	13.63	14.26	19.35	17.05	14.48	17.49	18.64	28.03
$Fe_2O_{3\,T}$	5.71	14.07	12.15	11.96	7.84	7.15	8.62	6.96	6.71	1.94
MnO	0.12	0.29	0.25	0.25	0.17	0.16	0.20	0.15	0.15	0.05
MgO	5.59	12.29	10.87	10.36	7.24	7.82	9.69	8.30	7.28	0.81
CaO	13.43	8.08	8.73	9.01	10.14	12.97	12.49	13.22	12.70	13.15
Na_2O	2.68	1.53	1.83	1.95	2.63	2.33	1.90	2.06	2.02	3.13
K_2O	0.18	0.12	0.14	0.15	0.22	0.16	0.12	0.13	0.27	1.15
P_2O_5	0.01	0.01	0.01	0.01	0.01	0.01	0.01	0.01	0.02	0.02
LOI	1.10	0.13	0.25	0.11	0.44	0.47	0.33	0.32	1.53	2.18
Total	99.80	100.36	100.50	100.30	100.05	100.07	100.09	99.49	99.62	99.36
Ba (ppm)	75.30	89.90	55.50	63.80	89.40	60.60	44.40	40.00	56.08	209.60
Be	0.25	0.21	0.19	0.19	0.23	0.20	0.16	0.16		0.28
Cd	0.06	0.06	0.05	0.06	0.05	0.07	0.06	0.04		–
Ce	3.58	3.34	3.21	2.85	3.26	2.82	2.21	2.18	5.29	4.61
Co	39.10	54.60	81.30	78.90	54.10	51.10	61.50	49.60	43.05	7.10
Cr	69.00	62.00	103.00	97.00	84.00	143.00	185.00	94.00	95.15	27.00
Cs	0.14	0.16	0.06	0.08	0.16	0.12	0.06	–	0.22	1.47
Cu	10.70	15.50	23.70	17.00	15.40	10.30	9.10	7.10	19.32	13.80
Dy	0.74	0.46	0.71	0.66	0.46	0.71	0.73	0.71	0.75	0.34
Er	0.46	0.32	0.53	0.51	0.32	0.49	0.53	0.42	0.45	0.22
Eu	0.52	0.49	0.41	0.39	0.48	0.46	0.41	0.34	0.27	0.43
Ga	18.61	18.21	12.92	13.31	17.39	15.80	13.35	14.81	11.62	21.68
Gd	0.65	0.39	0.51	0.53	0.35	0.65	0.64	0.55	0.67	0.39
Ge	1.02	0.94	1.13	1.22	1.08	1.25	1.33	1.25		0.74
Hf	0.18	0.15	0.19	0.17	0.15	0.17	0.13	0.13	0.29	0.25
Ho	0.15	0.10	0.16	0.15	0.10	0.16	0.15	0.15	0.16	0.07
La	1.81	1.90	1.70	1.54	1.86	1.38	1.02	1.10	2.46	2.37
Li	5.00	4.30	3.50	3.40	4.20	5.00	5.30	4.50	3.74	6.80
Lu	0.06	0.05	0.09	0.09	0.05	0.07	0.07	0.06	0.07	0.03
Mo	0.10	–	0.10	0.10	0.10	–	0.10	1.00		2.40
Nb	0.14	0.15	0.24	0.19	0.17	0.11	0.07	0.24	0.80	0.64
Nd	2.00	1.53	1.78	1.53	1.57	1.92	1.61	1.56	2.54	2.06
Ni	72.10	114.90	180.00	166.90	122.80	134.90	167.80	134.90	131.24	16.20
Pb	1.90	3.10	1.60	1.60	3.40	2.90	1.30	0.70	12.53	3.10
Pr	0.47	0.38	0.40	0.35	0.37	0.39	0.32	0.46	0.57	0.52
Rb	1.87	2.70	1.02	1.19	2.53	1.82	1.11	1.40	4.30	19.30
Sc	35.50	22.10	33.30	33.20	22.10	41.10	46.00	33.10	16.92	3.00
Sm	0.54	0.32	0.49	0.39	0.35	0.52	0.50	0.46	0.62	0.36
Sn	0.10	0.20	0.30	0.10	0.20	0.10	–	0.10	0.36	0.10
Sr	345.00	357.43	217.71	253.77	346.70	290.42	228.33	266.09	199.87	433.85
Ta	0.01	0.01	0.02	0.02	0.02	0.01	–	0.06	0.27	0.04
Tb	0.12	0.07	0.11	0.10	0.07	0.12	0.12	0.09	0.11	0.06
Th	0.12	0.14	0.17	0.14	0.13	0.09	0.05	0.08	0.54	0.58
Tm	0.06	0.05	0.08	0.08	0.05	0.07	0.08	0.06	0.07	0.03
U	0.03	0.04	0.05	0.04	0.04	0.02	0.02	0.02	0.17	0.15
V	171.00	102.00	172.00	174.00	110.00	200.00	231.00	145.00	103.13	26.00
W	–	–	–	–	–	–	–	–	0.11	0.50
Y	4.12	2.66	4.28	4.07	2.66	4.08	4.10	3.54	3.89	1.67
Yb	0.42	0.36	0.61	0.56	0.35	0.46	0.50	0.38	0.46	0.20
Zn	35.00	51.00	76.00	78.00	54.00	42.00	46.00	36.00	65.92	13.00
Zr	5.70	4.70	6.30	5.10	4.70	4.10	3.30	3.80	8.79	8.50

	Blocks in the pyroxenite sequences or modally graded gabbronorite in the Mooimeisjesfontein area									
Samples	LX-1-5	LX-1-6	LX-2-1	PM-X1	PM-X2	PM-X3	PM-X4	PM-X5	PM-X6	JB019-X2
Lab	EL	EL	EL	EL	EL	EL	EL	EL	EL	EL
SiO_2 (wt%)	50.47	50.50	48.38	51.15	48.97	50.47	52.01	48.20	49.57	49.32
TiO_2	0.06	0.06	0.07	0.04	0.04	0.12	0.21	0.07	0.08	0.08
Al_2O_3	24.62	27.76	27.10	28.92	27.59	18.58	3.07	23.77	21.62	27.21
Fe_2O_{3T}	4.11	2.20	2.14	0.81	1.58	8.11	19.00	5.30	5.64	2.85
MnO	0.09	0.04	0.07	0.02	0.05	0.15	0.37	0.10	0.10	0.05
MgO	4.30	1.69	1.22	0.26	1.25	8.80	18.74	5.06	5.73	2.39
CaO	12.03	12.69	14.02	12.72	13.28	10.22	6.40	12.00	11.43	13.34
Na_2O	2.54	3.07	3.33	3.82	3.11	2.01	0.34	1.95	1.97	2.60
K_2O	0.36	0.68	0.75	0.46	0.71	0.16	0.02	0.28	0.16	0.40
P_2O_5	0.01	0.01	0.01	0.01	0.01	0.03	0.02	0.02	0.02	0.02
LOI	1.51	1.17	2.53	1.05	2.44	1.51	0.16	2.71	3.75	1.82
Total	100.13	99.89	99.74	99.27	99.06	100.23	100.44	99.51	100.11	100.09
Ba (ppm)	35.15	38.39	176.20	37.61	35.39	45.19	6.60	34.42	19.83	28.44
Be			0.28							
Cd			0.04							
Ce	0.87	5.78	3.07	0.67	0.71	2.23	2.89	1.05	0.83	1.17
Co	23.08	9.68	8.80	2.13	6.72	53.24	131.79	38.07	25.96	15.10
Cr	48.22	13.98	18.00	1.77	14.60	243.46	212.40	154.27	73.63	19.42
Cs	0.29	0.39	1.30	0.44	0.65	0.20	0.05	0.35	0.24	0.33
Cu	2.32	18.99	9.10	14.19	0.56	27.38	31.32	11.90	1.03	15.77
Dy	0.06	0.19	0.24	0.02	0.05	0.31	1.16	0.06	0.13	0.09
Er	0.04	0.10	0.14	0.01	0.03	0.22	0.77	0.04	0.09	0.06
Eu	0.13	0.15	0.37	0.15	0.16	0.26	0.19	0.19	0.25	0.14
Ga	14.19	16.75	20.72	19.12	13.87	10.94	3.99	18.61	10.07	12.23
Gd	0.06	0.32	0.28	0.03	0.05	0.26	0.89	0.06	0.10	0.09
Ge			0.86							
Hf	0.05	0.09	0.17	0.03	0.03	0.15	0.25	0.04	0.05	0.12
Ho	0.01	0.04	0.05	0.00	0.01	0.07	0.26	0.01	0.03	0.02
La	0.37	3.19	1.65	0.39	0.45	1.25	1.38	0.51	0.66	0.44
Li	2.77	2.50	9.80	2.49	7.42	5.77	0.69	15.09	22.26	6.61
Lu	0.01	0.01	0.02	0.00	0.00	0.04	0.14	0.01	0.02	0.01
Mo			0.20							
Nb	0.10	0.38	0.38	0.03	0.03	0.11	0.34	0.07	0.12	0.55
Nd	0.26	2.40	1.37	0.23	0.23	0.96	2.20	0.30	0.38	0.38
Ni	67.88	25.15	22.10	5.13	16.04	155.69	260.46	112.41	64.45	38.93
Pb	2.54	3.93	7.10	1.37	1.43	4.71	1.22	3.40	0.49	0.66
Pr	0.06	0.63	0.35	0.06	0.06	0.22	0.45	0.08	0.09	0.09
Rb	3.86	5.78	18.85	6.60	6.30	1.67	0.51	6.19	2.82	4.41
Sc	3.71	1.21	4.70	0.24	1.68	13.80	67.25	5.10	9.08	2.59
Sm	0.05	0.39	0.26	0.04	0.05	0.22	0.69	0.05	0.09	0.08
Sn	0.05	0.47	0.20	0.03	0.04	0.06	0.13	1.17	0.09	0.18
Sr	161.07	123.96	424.15	172.40	121.60	170.23	36.07	224.53	212.81	161.76
Ta	0.01	0.05	0.03	0.02	0.01	0.02	0.03	0.05	0.04	0.10
Tb	0.01	0.04	0.05	0.00	0.01	0.04	0.16	0.01	0.02	0.01
Th	0.03	0.57	0.29	0.01	0.01	0.09	0.27	0.01	0.06	0.05
Tm	0.01	0.01	0.02	0.00	0.00	0.04	0.13	0.01	0.02	0.01
U	0.03	0.11	0.08	0.01	0.01	0.03	0.08	0.01	0.03	0.03
V	31.07	16.78	31.00	7.73	25.99	111.56	283.09	110.54	65.46	40.06
W	0.03	0.09	0.10	0.03	0.02	0.11	0.04	0.05	0.07	0.19
Y	0.31	0.75	1.24	0.09	0.20	1.77	6.90	0.37	0.76	0.42
Yb	0.05	0.09	0.13	0.01	0.03	0.26	0.88	0.06	0.12	0.06
Zn	29.67	21.16	36.00	5.34	11.29	62.13	125.03	50.29	20.97	15.79
Zr	1.36	2.81	5.90	0.97	0.86	3.81	8.01	0.72	1.19	3.07

Table E.2 – Relative errors form Earth Lab and coefficients for expanded uncertainties from Intertek.

Lab	Earth Lab	Intertek	Intertek
Coefficient		S02	S12
SiO_2 (wt%)	9.39E-03	2.07E-04	9.25E-06
TiO_2	6.98E-02	7.70E-06	4.45E-06
Al_2O_3	2.86E-02	4.11E-05	1.22E-05
$Fe_2O_{3\,T}$	1.45E-02	3.18E-05	1.16E-05
MnO	6.20E-02	1.13E-06	8.03E-05
MgO	7.97E-03	2.00E-05	1.42E-05
CaO	3.86E-02	2.39E-06	9.14E-06
Na_2O	3.20E-02	3.62E-05	8.78E-05
K_2O	1.89E-02	9.66E-07	4.89E-05
P_2O_5	5.19E-02	1.90E-06	7.18E-06
LOI	4.79E-01	1.17E-06	1.23E-05
Total			
Ba (ppm)	2.72E-01	4.74E-02	1.24E-03
Be		4.38E-05	2.03E-03
Cd		2.63E-05	8.52E-04
Ce	3.29E-02	2.76E-04	2.14E-03
Co	2.97E-02	2.97E-03	8.29E-04
Cr	6.22E-02	4.24E-01	7.17E-03
Cs	7.86E-02	6.02E-06	6.74E-04
Cu	1.23E-01	4.08E-01	7.56E-04
Dy	9.93E-02	6.66E-07	1.43E-03
Er	9.50E-02	1.22E-06	1.67E-03
Eu	8.39E-02	2.19E-06	1.43E-03
Ga	4.20E-02	2.86E-04	1.53E-03
Gd	9.09E-02	2.91E-06	1.41E-03
Ge		6.77E-04	1.29E-02
Hf	4.06E-02	1.55E-05	2.83E-03
Ho	9.18E-02	6.03E-07	1.74E-03
La	7.17E-02	4.25E-05	2.24E-03
Li	5.28E-02	1.21E-03	1.06E-03
Lu	1.01E-01	1.82E-06	2.86E-03
Mo		1.60E-03	1.22E-03
Nb	1.39E-01	7.10E-05	3.65E-04
Nd	8.31E-02	1.26E-05	9.17E-04
Ni	1.36E-01	2.48E-01	8.94E-04
Pb	2.26E-01	3.07E-02	6.22E-04
Pr	9.82E-02	1.45E-06	1.27E-03
Rb	7.04E-02	1.17E-03	1.36E-03
Sc	8.80E-02	3.21E-04	1.81E-03
Sm	9.15E-02	1.84E-06	1.33E-03
Sn	2.86E-01	7.26E-04	4.17E-03
Sr	6.39E-02	3.86E-03	1.03E-03
Ta	1.75E-01	4.74E-06	7.54E-03
Tb	9.55E-02	5.78E-07	1.37E-03
Th	5.70E-02	2.77E-05	1.75E-03
Tm	1.01E-01	9.37E-07	3.25E-03
U	5.31E-02	7.49E-06	5.71E-04
V	1.78E-02	1.54E-01	1.40E-03
W	8.85E-02	2.65E-04	9.21E-04
Y	1.25E-01	2.00E-05	3.25E-03
Yb	7.49E-02	3.33E-06	2.01E-03
Zn	7.99E-02	5.14E-01	1.51E-03
Zr	5.59E-02	1.34E-03	3.08E-03

F Whole-rock density data and analytical uncertainties

The table below includes all whole-rock density data collected and used in this thesis. The analytical uncertainty (1σ) is found to the right of the calculated density.

Sample	Weight g (dry)	Weight g (wet)	Density g/cm^3	Error g/cm^3	Sample	Weight g (dry)	Weight g (wet)	Density g/cm^3	Error g/cm^3
Anorthosite sequence near Phosiri Dome									
JB060	115.96	39.28	2.95	0.00	ARN-3-10	6.7	2.45	2.73	0.01
AR-1-1	346.90	124.44	2.79	0.00		5.63	2.1	2.68	0.01
AR-3-8	70.25	24.38	2.88	0.00	ARN-4-1	9.66	3.58	2.70	0.01
	161.54	52.84	3.06	0.00		8.48	3.07	2.76	0.01
ARS-2-1	15.23	5.72	2.66	0.00		8.74	3.15	2.77	0.01
	9.69	3.56	2.72	0.01		8.87	3.21	2.76	0.01
	5.12	1.90	2.69	0.02		4.87	1.78	2.74	0.02
	6.70	2.45	2.73	0.01		6.26	2.30	2.72	0.01
	5.63	2.10	2.68	0.01	ARN-4-2	11.17	4.11	2.72	0.01
	50.45	18.36	2.75	0.00		9.61	3.56	2.70	0.01
ARS-2-2	513.91	183.24	2.80	0.00		7.47	2.78	2.69	0.01
	119.31	43.88	2.72	0.00		6.56	2.44	2.69	0.01
ARS-2-3	228.89	83.10	2.75	0.00		7.88	2.91	2.71	0.01
ARS-2-4	77.87	28.31	2.75	0.00		9.12	3.39	2.69	0.01
ARS-2-5	48.53	17.80	2.73	0.00	ARN-4-3	84.54	31.05	2.72	0.00
ARS-2-6	50.12	18.18	2.76	0.00	ARN-4-4	22.96	8.56	2.68	0.00
ARS-2-7	66.88	24.68	2.71	0.00		12.12	4.56	2.66	0.01
ARS-2-8	11.47	4.07	2.82	0.01		5.50	2.01	2.74	0.01
ARS-2-9	8.45	3.09	2.73	0.01		2.90	1.08	2.69	0.03
	7.51	2.72	2.76	0.01		5.70	2.15	2.65	0.01
	10.98	4.06	2.70	0.01	ARN-4-5	8.58	3.19	2.69	0.01
	10.49	3.79	2.77	0.01		7.04	2.60	2.71	0.01
	35.48	12.69	2.80	0.00		7.72	2.91	2.65	0.01
	38.34	14.04	2.73	0.00		9.00	3.35	2.69	0.01
ARN-3-1	49.49	18.14	2.73	0.00		5.90	2.20	2.68	0.01
	49.44	18.19	2.72	0.00		7.50	2.84	2.64	0.01
ARN-3-2	7.47	2.67	2.80	0.01	ARN-4-6	113.14	42.39	2.67	0.00
	11.52	4.15	2.78	0.01		113.05	42.72	2.65	0.00
	7.27	2.65	2.74	0.01	ARN-4-7	107.59	38.85	2.77	0.00
	7.88	2.83	2.78	0.01	ARN-4-8	81.64	29.54	2.76	0.00
	7.26	2.64	2.75	0.01		81.64	29.60	2.76	0.00
	7.75	2.78	2.79	0.01	ARN-4-9	289.71	107.32	2.70	0.00
ARN-3-3	29.48	10.85	2.72	0.00	ARN-4-10	283.55	103.82	2.73	0.00
ARN-3-4	91.59	34.60	2.65	0.00	ARN-4-11	128.81	47.93	2.69	0.00
ARN-3-5	7.98	2.97	2.69	0.01		91.97	34.11	2.70	0.00
	13.65	5.07	2.69	0.01	ARN-5-1	33.00	11.94	2.76	0.00
	10.79	4.06	2.66	0.01	ARN-5-2	108.24	39.03	2.77	0.00
	9.39	3.51	2.68	0.01	ARN-5-3	134.90	49.96	2.70	0.00
	8.74	3.27	2.67	0.01		134.90	49.96	2.70	0.00
	6.13	2.31	2.65	0.01	ARN-5-4	77.95	28.39	2.75	0.00
ARN-2	276.22	101.56	2.72	0.00	ARN-5-5	122.63	44.80	2.74	0.00
ARN-3-6	43.93	16.16	2.72	0.00	ARN-3	73.56	26.66	2.76	0.00
ARN-3-7	88.54	32.25	2.75	0.00	ARN-5-6	49.42	18.00	2.75	0.00
ARN-3-8	53.30	19.80	2.69	0.00	ARN-5-7	106.61	38.84	2.74	0.00
ARN-3-9	95.89	35.54	2.70	0.00	ARN-5-8	176.54	64.96	2.72	0.00
ARN-3-10	9.88	3.63	2.72	0.01	AR-7-1	469.69	174.01	2.70	0.00
	15.23	5.72	2.66	0.00	AR-13	174.34	63.92	2.73	0.00
	9.69	3.56	2.72	0.01	AR-9	136.39	46.17	2.95	0.00
	5.12	1.9	2.69	0.02					
Blocks in the anorthosite sequence near Phosiri Dome									
ARS-X1	10.64	3.35	3.18	0.01	ARS-X4	9.09	3.06	2.97	0.01
	9.90	2.90	3.41	0.01		14.07	4.65	3.03	0.01
	3.65	1.15	3.17	0.03		7.67	2.55	3.01	0.01
	5.08	1.59	3.19	0.02	ARS-X5	187.26	59.17	3.16	0.00
	3.26	1.05	3.10	0.03	ARS-X6	303.07	106.03	2.86	0.00
	6.74	2.17	3.11	0.02	ARN-X7	108.87	35.61	3.06	0.00
	7.10	2.22	3.20	0.02	ARN-X8	264.76	83.70	3.16	0.00

Sample	Weight g (dry)	Weight g (wet)	Density g/cm^3	Error g/cm^3	Sample	Weight g (dry)	Weight g (wet)	Density g/cm^3	Error g/cm^3
ARS-X2	7.64	2.51	3.04	0.01	ARN-X9	168.54	55.08	3.06	0.00
	7.87	2.51	3.14	0.01	ARS-X10	147.21	44.84	3.28	0.00
	7.60	2.47	3.08	0.01	ARN-X11	114.92	38.58	2.98	0.00
	5.61	1.83	3.07	0.02	ARN-X12	13.06	4.23	3.09	0.01
	8.66	2.77	3.13	0.01		9.15	3.02	3.03	0.01
	5.07	1.63	3.11	0.02		9.21	3.07	3.00	0.01
	9.16	2.99	3.06	0.01		9.81	3.21	3.06	0.01
ARS-X3	16.58	5.40	3.07	0.01		8.27	2.69	3.07	0.01
	13.95	4.54	3.07	0.01		10.06	3.26	3.09	0.01
	6.56	2.14	3.07	0.02	ARN-X13	14.21	4.52	3.14	0.01
	9.44	3.07	3.07	0.01		10.88	3.44	3.16	0.01
	10.72	3.49	3.07	0.01		11.43	3.60	3.18	0.01
	10.67	3.51	3.04	0.01		11.48	3.66	3.14	0.01
ARS-X4	9.51	3.08	3.09	0.01		8.19	2.59	3.16	0.01
	9.06	2.95	3.07	0.01		9.72	3.09	3.15	0.01
	9.23	3.15	2.93	0.01					
Pyroxenite sequences in the Mooimeisjesfontein area									
JB031-A1	97.13	32.54	2.98	0.00	PM-4	73.48	27.04	2.72	0.00
JB031-A2	73.99	25.98	2.85	0.00	PM-1	68.66	24.84	2.76	0.00
JB031-T	89.06	29.07	3.06	0.00	PM-0	58.03	20.46	2.84	0.00
JB031-P1	219.49	66.58	3.30	0.00		216.65	72.77	2.98	0.00
JB031-P2	10.18	3.05	3.34	0.01	PM+3	115.71	41.53	2.79	0.00
	18.97	5.73	3.31	0.01	PM+7	90.84	32.41	2.80	0.00
	8.03	2.43	3.30	0.01	PM+10	63.79	20.39	3.13	0.00
	11.15	3.38	3.30	0.01	PM+10	413.03	132.16	3.13	0.00
JB031-P3	10.86	3.26	3.33	0.01	PM+12	5.89	1.95	3.02	0.02
	7.86	2.37	3.32	0.01		7.89	2.42	3.26	0.01
	6.72	2.02	3.33	0.02		5.04	1.63	3.09	0.02
JB031-P4	4.63	1.42	3.26	0.02	PM+15	68.87	22.72	3.03	0.00
	10.15	3.08	3.30	0.01	PM+17	162.43	53.01	3.06	0.00
	6.99	2.12	3.30	0.02	PM+18	47.49	15.79	3.01	0.00
	4.08	1.24	3.29	0.03	PM+21	175.50	55.88	3.14	0.00
JB031-P5	381.28	116.44	3.27	0.00	PM+30	7.15	2.35	3.04	0.01
JB031-P6	17.53	5.34	3.28	0.01		13.80	4.51	3.06	0.01
JB031-P7	7.93	2.39	3.32	0.01		5.68	1.85	3.07	0.02
	9.62	2.91	3.31	0.01	PM+35	88.38	29.34	3.01	0.00
	5.32	1.6	3.33	0.02	PM+41	335.44	114.46	2.93	0.00
JB031-P8	117.74	36.78	3.20	0.00	PM+44	149.25	52.26	2.86	0.00
JB031-P9	249.59	77.48	3.22	0.00	PM+45	277.95	95.66	2.91	0.00
JB031-G1	413.07	131.51	3.14	0.00	PM+48	592.93	203.53	2.91	0.00
JB031-G2	20.18	6.52	3.10	0.00	PM+60	8.01	2.77	2.89	0.01
	14.13	4.57	3.09	0.01		10.11	3.47	2.91	0.01
	8.68	2.78	3.12	0.01		6.02	2.06	2.92	0.01
JB031-G3	242.73	81.44	2.98	0.00	PM+70	8.39	2.90	2.89	0.01
JB031-G4	195.89	65.35	3.00	0.00		11.42	3.96	2.88	0.01
PM-GN	185.22	62.07	2.98	0.00		5.93	2.05	2.89	0.01
PM-100	5.86	2.13	2.75	0.01	PM+80	195.27	66.10	2.95	0.00
	6.63	2.42	2.74	0.01	PM+90	13.50	4.67	2.89	0.01
	6.45	2.35	2.74	0.01		7.48	2.58	2.90	0.01
	5.59	2.05	2.73	0.01		7.62	2.59	2.94	0.01
	8.35	3.04	2.75	0.01		7.32	2.46	2.98	0.01
PM-90	163.85	60.10	2.73	0.00	PM+95	223.14	76.44	2.92	0.00
PM-80	158.41	58.20	2.72	0.00	PM+100	153.60	52.65	2.92	0.00
PM-70	105.37	38.87	2.71	0.00	PM+110	10.48	3.57	2.94	0.01
PM-65	5.67	2.08	2.73	0.01		13.31	4.50	2.96	0.01
	5.96	2.17	2.75	0.01		14.24	4.82	2.95	0.01
	18.51	6.80	2.72	0.00		6.60	2.22	2.97	0.01
	7.67	2.80	2.74	0.01	PM+133	55.69	18.99	2.93	0.00
PM-54	80.46	29.63	2.72	0.00	PM+145	626.43	209.56	2.99	0.00
PM-42	36.37	13.72	2.65	0.00	PM+160	18.23	6.26	2.91	0.00
PM-35	8.33	3.05	2.73	0.01		10.87	3.72	2.92	0.01
	9.18	3.37	2.72	0.01		7.94	2.70	2.94	0.01
	5.52	2.01	2.75	0.01	PM+260	128.96	43.67	2.95	0.00
	5.44	1.99	2.73	0.01	PM+380	225.46	76.55	2.95	0.00
PM-20	188.89	69.67	2.71	0.00	PM+550	242.49	81.41	2.98	0.00
PM-14	171.64	63.22	2.71	0.00	JB019-P	204.07	64.95	3.14	0.00
PM-10	147.21	53.61	2.75	0.00	JB019-B	94.69	32.52	2.91	0.00
PM-8	85.59	31.57	2.71	0.00	JB024-P	650.78	209.30	3.11	0.00

Sample	Weight g (dry)	Weight g (wet)	Density g/cm^3	Error g/cm^3	Sample	Weight g (dry)	Weight g (wet)	Density g/cm^3	Error g/cm^3
Blocks in the pyroxenite sequences or modally graded gabbronorite in the Mooimeisjesfontein area									
LX-1-1	153.08	54.49	2.81	0.00	PM-X4	8.21	2.45	3.35	0.01
LX-1-2	103.27	35.36	2.92	0.00		5.51	1.66	3.32	0.02
LX-1-3-1	166.98	59.37	2.81	0.00	PM-X5	242.93	85.45	2.84	0.00
LX-1-3-2	96.89	32.52	2.98	0.00	PM-X6	225.08	78.78	2.86	0.00
LX-1-4	226.51	79.00	2.87	0.00	PM-X7	165.71	57.56	2.88	0.00
LX-1-5	186.14	65.90	2.82	0.00	JB017-X	339.00	113.56	2.99	0.00
LX-1-6	59.67	21.50	2.78	0.00	JB019-X1	92.39	30.98	2.98	0.00
LX-1-8	35.51	11.53	3.08	0.00	JB019-X2	9.22	3.28	2.81	0.01
LX-2-1	41.90	14.91	2.81	0.00		13.94	5.00	2.79	0.01
PM-X1	9.07	3.31	2.74	0.01		12.07	4.32	2.79	0.01
	6.47	2.37	2.73	0.01	JB019-X3	323.51	117.22	2.76	0.00
	5.87	2.13	2.76	0.01	JB019-X4	183.85	65.36	2.81	0.00
	6.57	2.39	2.75	0.01	JB023-X	125.65	44.19	2.84	0.00
PM-X2	115.30	41.85	2.76	0.00	JB024-X1	121.45	44.13	2.75	0.00
PM-X3	134.39	46.53	2.89	0.00	JB024-X2	184.40	64.83	2.84	0.00
PM-X4	11.18	3.40	3.29	0.01	JB024-X4	66.87	22.09	3.03	0.00
	12.36	3.76	3.29	0.01					

References

Armstrong, J.T., 1988. Quantitative analysis of silicate and oxide minerals: comparison of Monte Carlo, ZAF and phi-rho-z procedures. Microbeam Analysis 23, 239–246.

Ashwal, L.D., 1993. Anorthosites. Springer-Verlag.

Ashwal, L.D., Bybee, G.M., 2017. Crustal evolution and the temporality of anorthosites. Earth-Science Reviews 173, 307–330. doi:10.1016/j.earscirev.2017.09.002.

Ashwal, L.D., Webb, S.J., Knoper, M.W., 2005. Magmatic stratigraphy in the Bushveld Northern Lobe: continuous geophysical and mineralogical data from the 2950 m Bellvue drillcore. South African Journal of Geology 108, 199–232. doi:10.2113/108.2.199.

Asimow, P.D., Ghiorso, M.S., 1998. Algorithmic modifications extending MELTS to calculate subsolidus phase relations. American Mineralogist 83, 1127–1132. doi:10.2138/am-1998-9-1022.

Barnes, S.J., 1986. The effect of trapped liquid crystallization on cumulus mineral compositions in layered intrusions. Contributions to Mineralogy and Petrology 93, 524–531. doi:10.1007/BF00371722.

Barnes, S.J., Wolfgang, M.D., Curl, E.A., 2010. Composition of the marginal rocks and sills of the Rustenberg Layered Suite, Bushveld Complex, South Africa: Implications for the formation of the Platinum-Group Element deposits. Economic Geology 105, 1491–1511. doi:10.2113/econgeo.105.8.1491.

Bergantz, G.W., Schleicher, J.M., Burgisser, A., 2015. Open-system dynamics and mixing in magma mushes. Nature Geoscience 8, 793–796. doi:10.1038/ngeo2534.

Boudreau, A.E., 2016. The Stillwater Complex, Montana - Overview and the significance of volatiles. Mineralogical Magazine 80, 585–637. doi:10.1180/minmag.2016.080.063.

Buchanan, P.C., 2006. Chapter 12: The Rooiberg Group, in: Johnson, M.R., Anhaeusser, C.R., Thomas, R.J. (Eds.), The Geology of South Africa. South African Council for Geosciences and the Geological Society of South Africa, pp. 283–289.

Buchanan, P.C., Reimold, W.U., Koeberl, C., Kruger, F.J., 2004. Rb-Sr and Sm-Nd isotopic compositions of the Rooiberg Group, South Africa: early Bushveld-related volcanism. Lithos 75, 373–388. doi:10.1016/j.lithos.2004.03.007.

Burger, A.J., Coertze, F.J., 1975. Age determinations - April 1972 to March 1974. Technical Report. Annals of the Geological Survey of South Africa.

Button, A., 1973. A regional study of the stratigraphy and development of the Transvaal Basin in the eastern and northeastern Transvaal. Ph.D. thesis. University of the Witwatersrand.

Cameron, E.N., 1978. The Lower Zone of the Eastern Bushveld Complex in the Olifants River trough. Journal of Petrology 19, 437–462. doi:10.1093/petrology/19.3.437.

Campbell, I.H., 1977. Some problems with the cumulus theory. Lithos 11, 311–323. doi:10.1016/0024-4937(78)90038-5.

Campbell, I.H., Roeder, P.L., Dixon, J.M., 1978. Plagioclase buoyancy in basaltic liquids as determined with a centrifuge furnace. Contributions to Mineralogy and Petrology 67, 369–377. doi:10.1007/BF00383297.

Cashman, K.V., Sparks, S.J., Blundy, J.D., 2017. Vertically extensive and unstable magmatic systems: a unified view of igneous processes. Science 355, 1–9. doi:10.1126/science.aag3055.

Cawthorn, R. G. Lundgaard, K.L., Tegner, C., Wilson, J.R., 2016. Lateral variations in plagioclase compositions, Main Zone, Bushveld Complex, South Africa: Evidence for slow mixing of magmas in basinal structures. Mineralogical Magazine 80, 213–225. doi:10.1180/minmag.2015.079.7.12.

Cawthorn, R.G. (Ed.), 1996. Layered Intrusions. Elsevier.

Cawthorn, R.G., 2015. Chapter 6: The Bushveld Complex, South Africa, in: Charlier, B., Namur, O., Latypov, R., Tegner, C. (Eds.), Layered Intrusions. Springer, pp. 517–587.

Cawthorn, R.G., 2018. A non-horizontal floor during accumulation of the Bushveld Complex - evidence and implications. Lithos 316-317, 323–329. doi:10.1016/j.lithos.2018.07.030.

Cawthorn, R.G., 2020. Massive pyroxenite compositional oscillations on a meter scale in the Pyroxenite Marker, northern limb, Bushveld Complex, South Africa. Lithos 356-357, 1–8. doi:10.1016/j.lithos.2020.105392.

Cawthorn, R.G., Ashwal, L.D., 2009. Origin of anorthosite and magnetitite layers in the Bushveld Complex, constrained by major element compositions of plagioclase. Journal of Petrology 50, 1607–1637. doi:10.1093/petrology/egp042.

Cawthorn, R.G., Cooper, G.R.J., Webb, S.J., 1998. Connectivity between the western and eastern limbs of the Bushveld Complex. South African Journal of Geology 101, 291–298. doi:10.1016/S0040-1951(00)00227-4.

Cawthorn, R.G., Eales, H.V., Uken, R., Watkeys, M.K., 2006. Chapter 11: The Bushveld Complex, in: Johnson, M.R., Anhaeusser, C.R., Thomas, R.J. (Eds.), The Geology of South Africa. South African Council for Geosciences and the Geological Society of South Africa, pp. 261–281.

Cawthorn, R.G., Lee, C.A., Schouwstra, R.P., Mellowship, P., 2002. Relationship between PGE and PGM in the Bushveld Complex. The Canadian Mineralogist 40, 311–328. doi:10.2113/gscanmin.40.2.311.

Cawthorn, R.G., Meyer, P.S., Kruger, F.J., 1991. Major addition of magma at the Pyroxenite Marker in the Western Bushveld Complex, South Africa. Journal of Petrology 32, 739–763. doi:10.1093/petrology/32.4.739.

Cawthorn, R.G., Spies, L., 2003. Plagioclase content of cyclic units in the Bushveld Complex, South Africa. Contributions to Mineralogy and Petrology 145, 47–60. doi:10.1007/s00410-002-0431-0.

Charlier, B., Duchesne, J.C., Vander Auwera, J., Strome, J.Y., Maquil, R., Longhi, J., 2010. Polybaric fractional crystallization of high-alumina basalt parental magmas in the Egersund-Ogna massif-type anorthosite (Rogaland, SW Norway) constrained by plagioclase and high-alumina

orthopyroxene megacrysts. Journal of Petrology 51, 2515–2546. doi:10.1093/petrology/egq066.

Charlier, B., Namur, O., Latypov, R., Tegner, C. (Eds.), 2015. Layered Intrusions. Springer Geology.

Cheadle, M.J., Elliott, M.T., McKenzie, D., 2004. Percolation threshold and permeability of crystallizing igneous rocks: the importance of textural equilibration. Geology 32, 757–760. doi:10.1130/G20495.1.

Clague, D.A., 1987. Hawaiian xenolith populations, magma supply rates, and development of magma chambers. Volcanology 49, 577–587. doi:10.1007/BF01079963.

Clarke, B., Uken, R., Reinhardt, J., 2009. Structural and compositional constraints on the emplacement of the Bushveld Complex, South Africa. Lithos 111, 21–36. doi:10.1016/j.lithos.2008.11.006.

Coertze, F.J., Walraven, F., Marlow, A.G., MacCaskie, D.R., Burger, A.J., 1978. Field relations and age determinations in the Bushveld Complex. Transactions of the Geological Society of South Africa 81, 1–11.

Czamanske, G.D., Bohlen, S.R., 1990. The Stillwater Complex and its anorthosites: An accident of magmatic underplating? American Mineralogist 75, 37–45.

Donovan, J.J., Snyder, D.A., Rivers, M.L., 1993. An improved interference correction for trace element analysis. Microbeam Analysis 2, 23–28.

Droop, G.T.R., 1987. A general equation for estimating fe^3 concentrations in ferromagnesian silicates and oxides from microprobe analyses, using stoichiometric criteria. Mineralogical Magazine 51, 431–435. doi:10.1180/minmag.1987.051.361.10.

Eales, H.V., 2002. Caveats in defining the magmas parental to the mafic rocks of the Bushveld Complex, and the manner of their emplacement: review and commentary. Mineralogical Magazine 66, 815–832. doi:10.1180/0026461026660062.

Eales, H.V., Cawthorn, R.G., 1996. Chapter 12: The Bushveld Complex, in: Cawthorn, R.G. (Ed.), Layered Intrusions. Elsevier. Developments in Petrology 15, pp. 181–229.

Eales, H.V., Costin, G., 2012. Crustally contaminated komatiite: primary source of the chormitites and Marginal, Lower, and Critical Zone magmas in a staging chamber beneath the Bushveld Complex. Economic Geology 107, 645–665. doi:10.2113/econgeo.107.4.645.

Engelbrecht, J.P., 1985. The chromites of the Bushveld Complex in the Nietverdiend area. Economic Geology 80, 896–910. doi:10.2113/gsecongeo.80.4.896.

Eriksson, P.G., Altermann, W., Hartzer, F.J., 2006. Chapter 10: The Transvaal Supergroup and its precursors, in: Johnson, M.R., Anhaeusser, C.R., Thomas, R.J. (Eds.), The geology of South Africa. South African Council for Geosciences and the Geological Society of South Africa, pp. 237–260.

Eriksson, P.G., Reczko, B.F.F., 1995. The sedimentary and tectonic setting of the Transvaal Supergroup floor rocks to the Bushveld Complex. Journal of African Earth Sciences 21, 487–504. doi:10.1016/0899-5362(95)00111-5.

Eriksson, P.G., Schreiber, U.M., Reczko, B.F.F., Snyman, C.P., 1994. Petrography and geochemistry of sandstones interbedded with the Rooiberg Felsite Group (Transvaal Sequence, South Africa): implications for provenance and tectonic setting. Journal of Sedimentary Research A64, 836–846. doi:10.1306/D4267EDD-2B26-11D7-8648000102C1865D.

Fram, M.S., Longhi, J., 1992. Phase equilibria of dikes associated with proterozoic anorthosite complexes. American Mineralogist 77, 605–616.

Gerya, T.V., Uken, R., Reinhardt, J., Watkeys, M.K., Maresch, W.V., Clarke, B.M., 2003. Cold fingers in hot magma: Numerical modeling of country-rock diapirs in the Bushveld Complex, South Africa. Geology 31, 753–756. doi:10.1130/G19566.1.

Getson, J.M., Whittington, A.G., 2007. Liquid and magma viscosity in the anorthite-forsterite-diopside-quartz system and implications for the viscosity-temperature paths of cooling magmas. Journal of Geophysical Research 112, 1–19. doi:10.1029/2006JB004812.

Ghiorso, M.S., Sack, R.O., 1995. Chemical mass-transfer in magmatic processes IV. A revised and internally consistent thermodynamic model for the interpolation and extrapolation of liquid-solid equilibria in magmatic systems at elevated temperatures and pressures. Contributions to Mineralogy and Petrology 119, 197–210. doi:10.1007/BF00307281.

von Gruenewaldt, G., 1970. On the phase-change orthopyroxene-pigeonite and the resulting textures in the Main and Uuuper Zones of the Bushveld Complex un the eastern Transvaal, in: The Geological Society of South Africa, Special Publication 1. Symposium on the Bushveld Igneous Complex and other layered intrusions, pp. 67–73.

von Gruenewaldt, G., 1973. The Main and Upper Zones of the Bushveld Complex in the Roossenekal area, Eastern Transvaal. Transactions of the Geological Society of South Africa 76, 207–227.

von Gruenewaldt, G., Weber-Diefenbach, K., 1977. Coexsisting Ca-poor pyroxenes in the Main Zone of the Bushveld Complex. Contributions to Mineralogy and Petrology 65, 11–18. doi:10.1007/BF00373565.

Hall, A.L., 1932. The Bushveld Igneous Complex of the Central Transvaal. volume 28. South Africa Geological Survey Memoir.

Harmer, R.E., von Gruenewaldt, G., 1991. A review of magmatism associated with the Transvaal Basin - implications for its tectonic setting. South African Journal of Geology 94, 104–122.

Harmer, R.E., Sharpe, M.R., 1985. Field relations and strontium isotope systematics of the marginal rocks of the Eastern Bushveld Complex. Economic Geology 80, 813–837. doi:10.2113/gsecongeo.80.4.813.

Hart, R.J., Andreoli, M.A.G., Tredoux, M., DeWitt, M.J., 1990. Geochemistry across an exposed section of the Archean crust at the Vredefort, South Africa: with implications for mid-crustal discontinuities. Chemical Geology 82, 21–50. doi:10.1016/0009-2541(90)90072-F.

Hart, R.J., Welke, H.J., Nicolaysen, L.O., 1981. Geochronology of the deep profile through Achean basement at Vredefort, with implications for early crustal evolution. Journal of Geophysical Research 81, 10663–10680. doi:10.1029/JB086iB11p10663.

Hatton, C.J., Schweitzer, J.K., 1995. Evidence for synchronous extrusive and intrusive Bushveld magmatism. Journal of African Earth Sciences 21, 579–594. doi:10.1016/0899-5362(95)00103-4.

Hayes, B., Ashwal, L.D., Webb, S.J., Bybee, G.M., 2017. Large-scale magmatic layering in the Main Zone of the Bushveld Complex and episodic downward magma infiltration. Contributions to Mineralogy and Petrology 172, 1–16. doi:10.1007/s00410-017-1334-4.

Hayes, B., Bybee, G.M., Mawela, M., Nex, P.A.M., van Niekerk, D., 1985. Implication of vertical and lateral compositional variations across the Pyroxenite Marker and its associated rocks in the upper part of the Main Zone in the Eastern Bushveld Complex. Economic Geology 80, 1007–1015. doi:10.2113/gsecongeo.80.4.1007.

Hayes, B., Bybee, G.M., Mawela, M., Nex, P.A.M., van Niekerk, D., 2018. Residual melt extraction and out-of-sequence differentiation in the Bushveld Complex, South Africa. Journal of Petrology 59, 2413–2434. doi:10.1093/petrology/egy101.

Henderson, P., 1984. General geochemical properties and abundances of the Rare Earth Elements, in: Henderson, P. (Ed.), Rare earth element geochemistry. Elsevier, pp. 1–32.

Hess, H.H., 1960. Stillwater Igneous Complex, Montana. 80, The Geological Society of America.

Humphreys, M.C.S., 2009. Chemical evolution of intercumulus liquid, as recorded in plagioclase overgrowth rims from the Skaergaard Intrusion. Journal of Petrology 50, 127–145. doi:10.1093/petrology/egn076.

Irvine, T.N., 1974. Petrology of the Duke Island Ultramafic Complex Southeastern Alaska. The Geological Society of America, volume 138.

Irvine, T.N., Andersen, J.C.O., Brooks, C.K., 1998. Included blocks (and blocks within blocks) in the Skaergaard intrusion: Geologic relations and the origins of rhythmic modally graded layers. Geological Society of America Bulletin 110, 1398–1447. doi:10.1130/0016-7606(1998)110<1398:IBABWB>2.3.CO;2.

Jackson, E.D., 1961. Primary textures and mineral associations in the Ultramafic Zone of the Stillwater Complex, Montana. Technical Report 358. Geological Survey Professional Paper.

Jaupart, C., Mareschal, J.C., 2011. Heat generation and transport in the Earth. Cambridge University Press.

de Klerk, W.J., 1995. Textures exhibited by feldspars in the Giant Mottled Anorthosite (GMA) of the bastard unit in the Upper Critical Zone, Western Bushveld Complex. Mineralogy and Petrology 54, 25–34. doi:10.1007/BF01162755.

Kruger, F.J., 1990. The stratigraphy of the Bushveld Complex: a reapprisal and relocation of the Main Zone boundaries. South African Journal of Geology 93, 376–381.

Kruger, F.J., 1994. The Sr-isotopic stratigraphy of the western Bushveld Complex. South African Journal of Geology 97, 393–398.

Kruger, F.J., Cawthorn, R.G., Walsh, K.L., 1987. Strontium isotopic evidence against magma addition in the Upper Zone of the Bushveld Complex. Earth and Planetary Science Letters 84, 51–58. doi:10.1016/0012-821X(87)90175-0.

Latypov, R., Chistyakova, S., Barnes, S.J., Hunt, E.J., 2017. Origin of platinum deposits in layered intrusions by *in situ* crystallization: evidence from undercutting Merensky Reef of the Bushveld Complex. Journal of Petrology 58, 715–761.

Latypov, R., O'Driscoll, B., Lavrenchuk, A., 2013. Towards a model for the in situ origin of PGE reefs in layered intrusions: insights from chromitite seams of the Rum Eastern Layered Intrusion, Scotland. Contributions to Mineralogy and Petrology 166, 309–327.

Lesego Platinum Mining Ltd., MSA, 2011. Geological map of the Phosiri Dome and surrounding area. Unpublished geological map and data.

Lightfoot, P.C., Keays, R.R., Morrison, G.D., Bite, A., Farrell, K.P., 1997. Geologic and geochemical relationships between the Contact Sublayer Iclusions, and the main mass of the Sudbury Igneous Complex: a case study of the Whistle Mine Embayment. Economic Geology 92, 647–673. doi:10.2113/gsecongeo.92.6.647.

Longhi, J., Fram, M.S., Vander Auwera, J., Montieth, J.N., 1993. Pressure effects, kinetics, and rheology of anorthositic and related magmas. American Mineralogist 78, 1016–1030.

Longhi, J., Vander Auwera, J., Fram, M.S., Duchesne, J.C., 1999. Some phase equilibrium constraints on the origin of Proterozoic (massif) anorthosites and related rocks. Journal of Petrology 40, 339–362. doi:10.1093/petroj/40.2.339.

Lundgaard, K.L., Tegner, C., Cawthorn, R.G., Kruger, F.J., Wilson, J.R., 2006. Trapped intercumulus liquid in the Main Zone of the eastern Bushveld Complex, South Africa. Contributions to Mineralogy and Petrology 151, 352–369. doi:10.1007/s00410-006-0063-x.

Maaloe, S., 1978. The origin of rhythmic layering. Mineralogical Magazine 42, 337–345. doi:10.1180/minmag.1978.042.323.03.

Maier, W.D., Arndt, N.T., Curl, E.A., 2000. Progressive crustal contamination of the Bushveld Complex: evidence from Nd isotopic analyses of the cumulate rocks. Contributions to Mineralogy and Petrology 140, 316–327. doi:10.1007/s004100000186.

Maier, W.D., Barnes, S.J., 1998. Concentrations of rare earth elements in silicate rocks of the Lower, Critical and Main Zones of the Bushveld Complex. Chemical Geology 150, 85–103. doi:10.1016/S0009-2541(98)00054-0.

Maier, W.D., Barnes, S.J., Groves, D.I., 2013. The Bushveld Complex, South Africa: formation of platinum, palladium, chrome- and vanadium-rich layers via hydrodynamic sorting of a mobilized cumulate slurry in a large, relatively slow cooling, subsiding magma chamber. Mineralium Deposita 48, 1–56. doi:10.1007/s00126-012-0436-1.

Maier, W.D., Barnes, S.J., van der Merwe, M.J., 2001. Platinum-group elements in the Pyroxenite Marker, Bushveld Complex: implications for the formation of the Main Zone. South African Journal of Geology 104, 301–308. doi:10.2113/gssajg.104.4.301.

Maier, W.D., Karykowski, B.T., Yang, S.H., 2016. Formation of transgressive anorthosite seams in the Bushveld Complex via tectonically induced mobilisation of plagioclase-rich crystal mushes. Geoscience Frontiers 7, 875–889. doi:10.1016/j.gsf.2016.06.005.

Marsh, B.D., 1981. On the crystallinity, probability of occurence and rheology of lava and magma. Contributions to Mineralogy and Petrology 78, 85–98. doi:10.2113/gselements.2.5.287.

Marsh, B.D., 2006. Dynamics of magmatic systems. Elements 2, 287–292. doi:10.2113/gselements.2.5.287.

Martin, L.E., 1999. The attenuation of the Main Zone at the Phosiri Dome, Bushveld Complex. Master's thesis. University of the Witwatersrand.

McBirney, A.R., Noyes, R.M., 1979. Crystallization and layering of the Skaergaard Intrusion. Journal of Petrology 20, 487–554. doi:10.1093/petrology/20.3.487.

McCallum, I.S., 1996. The Bushveld Complex, in: Cawthorn, R.G. (Ed.), Layered Intrusions. Elsevier, pp. 441–483.

McCallum, I.S., Raedeke, L.D., Mathez, E.A., 1980. Investigations of the Stillwater Complex: Part I. Stratigraphy and structure of the Banded Zone. American Journal of Science 280-A, 59–87.

McDonald, I., Holwell, D.A., 2007. Did lower zone magma conduits store PGE-rich sulphides that were later supplied to the Platreef. South African Journal of Geology 110, 611–616. doi:10.2113/gssajg.110.4.611.

McDonough, W.F., Sun, S.S., 1995. The composition of the Earth. Chemical Geology 120, 223–253. doi:10.1016/0009-2541(94)00140-4.

Miller, J.D.J., Weiblen, P.W., 1990. Anorthositic rocks of the Duluth Complex: Examples of rocks formed from plagioclase crystal mush. Journal of Petrology 31, 295–339. doi:10.1093/petrology/31.2.295.

Mitchell, A.A., 1986. The petrology, mineralogy and geochemistry of the Main Zone of the Bushveld Complex at Rustenburg Platinum Mines, Union Section. Ph.D. thesis. Rhodes University.

Mitchell, A.A., 1990. The stratigraphy, petrology and mineralogy of the Main Zone of the north-western Bushveld Complex. South African Journal of Geology 93, 818–831.

Mitchell, A.A., 1996. Compositional cyclicity in a pyroxenitic layer from the Main Zone of the Western Bushveld Complex: evidence for repeated magma influx. Mineralogical Magazine 60, 149–161. doi:10.1180/minmag.1996.060.398.10.

Mitchell, A.A., Henckel, J., Mason-Apps, A., 2019. The Upper Critical Zone of the Rustenburg Layered Suite in the Swartklip sector, north-western Bushveld Complex, on the farm Wilgerspruit 2JQ: I stratigraphy and PGE mineralization patterns. South African Journal of Geology 122, 117–142. doi:10.25131/sajg.122.0010.

Mitchell, A.A., Manthree, R., 2002. The Giant Mottled Anorthosite: a transitional sequence at the top of the Upper Critical Zone of the Bushveld Complex. South African Journal of Geology 105, 15–24. doi:10.2113/1050015.

Molyneux, T.G., 1964. The geology and the structure of the area in the vicinity of Magnet Heights, Eastern Transvaal, with special reference to the magnetic iron ore. Master's thesis. University of Pretoria.

Molyneux, T.G., 1970. A geological investigation of the Bushveld Complex in Sekhukhueland and part of the Steelpoort Valley, Eastern Transvaal with particular reference to the oxide minerals. Ph.D. thesis. University of Pretoria.

Molyneux, T.G., 1974. A geological investigation of the Bushveld Complex in Sekhukhueland and part of the Steelpoort Valley. Transactions of the Geological Society of South Africa 77, 329–338.

Molyneux, T.G., 2008. Geology of the Eastern compartment of the Bushveld Complex. One hundred years of geology at the University of Pretoria (1908-2008). Special publication of the Johannes Willemse Bushveld Intelligence Centre, University of Pretoria.

Morse, S.A., 1973. The Nain anorthosite project, Labrador: field report 1972. Technical Report 11. University of Massachusetts.

Morse, S.A., 1979a. Kigmapait geochemistry I: Systematics, sampling and density. Journal of Petrology 20, 555–590. doi:10.1093/petrology/20.3.555.

Morse, S.A., 1979b. Kigmapait geochemistry II: Petrography. Journal of Petrology 20, 591–624. doi:10.1093/petrology/20.3.591.

Morse, S.A., Nolan, K.M., 1984. Origin of strongly reversed rims on plagioclase in cumulates. Earth and Planetary Science Letters 68, 485–498. doi:10.1016/0012-821X(84)90132-8.

Mungall, J.E., Kamo, S.L., McQuade, S., 2016. U-Pb-geochronology documents out-of-sequence emplacement of ultramafic layers in the Bushveld Igneous Complex of South Africa. Nature Communications 7, 1–13. doi:10.1038/ncomms13385.

Nex, P.A., Kinnaird, J.A., Ingle, L.J., van der Vyver, B.A., Cawthorn, R.G., 1998. A new stratigraphy of the Main Zone for the Bushveld Complex, in the Rustenburg area. South African Journal of Geology 101, 215–223.

Nguuri, T.K., Gore, J., James, D.E., Webb, S. J. Wright, C., Zengeni, T.G., Gwavava, O., Snoke, J.A., 2001. Crustal structure beneath southern Africa and its implications for the formation and evolution of the Kaapvaal and Zimbabwe cratons. Geophysical Research Letters 28, 2501–2504. doi:10.1029/2000GL012587.

Petford, N., Mirhadizadeh, S., 2017. Image-based modelling of lateral magma flow: the Basement Sill, Antarctica. Royal Society Open Science 4, 1–18. doi:10.1098/rsos.161083.

Prevec, S.A., Ashwal, L.D., Mkaza, M.S., 2005. Mineral disequilibrium in the Merensky Reef, western Bushveld Complex, South Africa; new Sm-Nd isotopic evidence. Contributions to Mineralogy and Petrology 149, 306–315. doi:10.1007/s00410-005-0650-2.

Price, J., 2016. PGM distribution and reef characterization of the Merensky Reef and the Phosiri Dome, Bushvled Complex, South Africa. Master's thesis. Cardiff University.

Quadling, K., Cawthorn, R.G., 1994. The layered gabbronorite sequence, Main Zone, eastern Bushveld Complex. South African Journal of Geology 97, 442–454.

Richardson, S.H., Gurney, J.J., Erlank, A.J., Harris, J.W., 1984. Origin of diamonds in old enriched mantle. Nature 310, 198–202.

Richardson, S.H., Harris, J.W., Gurney, J.J., 1993. Three generations of diamonds from old continental crust. Nature 366, 256–258.

Richardson, S.H., Shirey, S.B., 2008. Continental mantle signature of Bushveld magmas and coveal diamonds. Nature 453, 910–913. doi:10.1038/nature07073.

Roelofse, F., Ashwal, L.D., 2012. The Lower Main Zone in the Northern Limb of the Bushveld Complex - a >1.3 thick sequence of intruded and variably contaminated crystal mushes. Journal of Petrology 53, 1449–1476. doi:10.1093/petrology/egs022.

Roelofse, F., Ashwal, L.D., Romer, R.L., 2015. Multiple, isotopically heterogeneous plagioclase populations in the Bushveld Complex suggest mush intrusion. Chemie der Erde 75, 357–364. doi:10.1016/j.chemer.2015.07.001.

Rollinson, H., 1993. Using geochemical data: evaluation, presentation, interpretation. Pearson, Prentice Hall.

Royse, K.R., Park, R.G., 2000. Emplacement of the Nain anorthosite: diapiric versus conduit ascent. Canadian Journal of Earth Sciences 37, 1195–1207. doi:10.1139/e00-025.

Rutherford, M.J., 2008. Magma ascent rates. Reviews in Mineralogy and Geochemistry 69, 241–271. doi:10.2138/rmg.2008.69.7.

SACS, 1980. Lithostratigraphy of the Republic of South Africa, South West Africa/Namibia and the Republics of Bophuthatswana, Transkei and Venda. Geological Survey of South Africa, Handbook 8, Part 1.

Scandone, R., Malone, S.D., 1985. Magama supply, magma discharge and readjustment of the feeding system of Mount St. Helens during 1980. Journal of Volcanology and Geothermal Research 23, 239–262. doi:10.1016/0377-0273(85)90036-8.

Schoenberg, R., Kruger, F.J., Nägler, T.F., Miesel, T., Kramers, J.D., 1999. PGE enrichment in chromitite layers and the Merensky Reef of the western Bushveld Complex; a Re-Os and Rb-Sr isotope study. Earth Planetary Science Letters 172, 49–64. doi:10.1016/S0012-821X(99)00198-3.

Schweitzer, J.K., Hatton, C.J., 2005. Chemical alteration within the volcanic roof rocks of the Bushveld Complex. Economic Geology 90, 2218–2231. doi:10.2113/gsecongeo.90.8.2218.

Scoates, J.A., Wall, C.J., 2015. Chapter 1: Geochronology of layered intrusions, in: Charlier, B., Namur, O., Latypov, R., Tegner, C. (Eds.), Layered Intrusions. Springer, pp. 3–74.

Scoates, J.S., 2000. The plagioclase-magma density paradox re-examined and the crystallization of Proterozoic anorthosites. Journal of Petrology 41, 627–649. doi:10.1093/petrology/41.5.627.

Scoon, R.J., 2002. A new occurrence of Merensky Reef on the flanks of the Zaaikloof Dome, Northeastern Bushveld Complex: Relationship between diapirism and magma replenishment. Economic Geology 97, 1037–1049. doi:10.2113/gsecongeo.97.5.1037.

Scoon, R.J., Costin, G., 2018. Chemistry, morphology and origin of the magmatic-rection chromite strigners associated with anorthosite in the Upper Critical Zone at Winnaarshoek, Eastern Limb of the Bushveld Complex. Journal of Petrology 59, 1551–1578. doi:10.1093/petrology/egy071.

Scoon, R.J., Mitchell, A.A., 2012. The Upper Zone of the Bushveld Complex at Roossenekal, South Africa: geochemical stratigraphy and evidence of multiple episodes of magma replenishment. South African Journal of Geology 155, 515–534. doi:10.2113/gssajg.115.4.515.

Setera, J.B., VanTongeren, J.A., 2018. Lateral variability on the Upper Main Zone, Bushveld Complex, owing to directional magma recharge and emplacement from North to South. Journal of Petrology 59, 1763–1786. doi:10.1093/petrology/egy081.

Sharpe, M.R., 1985. Strontium isotope evidence for preserved density stratification in the Main Zone of the Bushveld Complex, South Africa. Nature 316, 119–126. doi:10.1038/316119a0.

Sharpe, M.R., Chadwick, B., 1982. Structures in Transvaal sequence rocks within and adjacent to the Eastern Bushveld Complex. Transactions of the Geological Society of South Africa 85, 29–41.

Sparks, R.S.J., Pinkerton, H., Macdonald, R., 1977. The transport of xenoliths in magmas. Earth and Planetary Science Letters 35, 234–238. doi:10.1016/0012-821X(77)90126-1.

Spera, F.J., 1980. Chapter 7: Aspects of magma transport, in: Hargraves, R.B. (Ed.), Physics of magmatic processes. Princeton University Press, pp. 265–314.

Spera, F.J., 2000. Physical properties of magma, in: Sigurdsson, H. (Ed.), Encyclopedia of Volcanoes. Academic Press, pp. 171–190.

Stickel, J.J., Powell, R.L., 2005. Fluid mechanics and rheology of dense suspensions. Annual Reviews of Fluid Mechanics 37, 129–149. doi:10.1146/annurev.fluid.36.050802.122132.

Streckeisen, A., 1976. To each plutonic rock its proper name. Earth-Science Reviews 12, 1–33. doi:10.1016/0012-8252(76)90052-0.

Sunagawa, I., 2005. Crystals: growth, morphology and perfection. Cambridge University Press.

Takeuchi, S., 2011. Preeruptive magma viscosity: an important measure of magma eruptibility. Journal of Geophysical Research 11, 1–19. doi:10.1029/2011JB008243.

Tanaka, T., Togashi, S., Kamioka, H., Amakawa, H., Kagami, H., Hamamoto, T., Yuhara, M., Orihashi, Y., Yoneda, S., Shimizu, H., et al., 2000. JNdi-1: a neodymium isotopic reference in consistency with LaJolla neodymium. Chemical Geology 168, 279–281. doi:10.1016/S0009-2541(00)00198-4.

Uken, R., Watkeys, M.K., 1997. Diapirism initiated by the Bushveld Complex, South Africa. Geology 25, 723–726. doi:10.1130/0091-7613(1997)025<0723:DIBTBC>2.3.CO;2.

VanTongeren, J.A., Mathez, E.A., 2013. Incoming magma composition and style of recharge below the Pyroxenite Marker, Eastern Bushveld Complex, South Africa. Journal of Petrology 54, 1585–1605. doi:10.1093/petrology/egt024.

Vermaak, C.F., 1976. The Merensky Reef - thoughts in its environment and genesis. Economic Geology 71, 1270–1298. doi:10.2113/gsecongeo.71.7.1270.

Vukmanovic, Z., Holness, M.B., Monks, K., Andersen, J.C.O., 2018. The Skaergaard through layering: sedimentation in a convecting magma chamber. Contributions to Mineralogy and Petrology 173, 1–18. doi:10.1007/s00410-018-1466-1.

Wager, L.R., Brown, G.M., 1968. Chapter 14: The Bushveld Intrusion, South Africa, in: Layered igneous rocks. W. H. Freeman and Company, San Francisco, pp. 343–407.

Wall, C.J., Scoates, J.S., Weis, D., Freidman, R.M., M., A., Meurer, W.P., 2018. The Stillwater Complex: integrating zircon geochronological and geochemical constraints on the age, emplacement history and crystallization of a large, open-system layered intrusion. Journal of Petrology 59, 153–190. doi:10.1093/petrology/egy024.

Walraven, F., 1985. Genetic aspects of the granophyric rocks of the Bushveld Complex. Economic Geology 80, 1166–1180. doi:10.2113/gsecongeo.80.4.1166.

Walraven, F., 1997. Geochronology of the Rooiberg Group, Transvaal Supergroup, South Africa. Technical Report. University of the Witwatersrand, Informal circular on economic geology resources.

Walraven, F., Armstrong, R.A., Kruger, F.J., 1990. A chronostratigraphic framework of the north-central Kaapvaal Craton, the Bushveld Complex and the Vredefort structure. Tectonophysics 171, 23–48. doi:10.1016/0040-1951(90)90088-P.

Walraven, F., Hattingh, E., 1993. Geochronology of the Nebo Granite, Bushveld Complex. South African Journal of Geosciences 96, 31–41.

Walraven, F., Retief, E.A., Burger, A.J., Swanepoel, D.J.d.V., 1987. Implications of new U-Pb zircon age dating on the Nebo Granite of the Bushveld Complex. Transactions of the Geological Society of South Africa 90, 344–351.

Webb, S.J., Ashwal, L.D., Cawthorn, R.G., 2011. Continuity between eastern and western Bushveld Complex, confirmed by xenoliths from kimberlite. Contributions to Mineralogy and Petrology 162, 101–107. doi:10.1007/s00410-010-0586-z.

Whitney, D.L., Evans, B.W., 2010. Abbreviations for names of rock-forming minerals. American Mineralogist 95, 185–187. doi:10.2138/am.2010.3371.

Wilson, A.H., 2012. A chill sequence to the Bushveld Complex: insight into the first stage of emplacement and implications for the parental magmas. Journal of Petrology 53, 1123–1168. doi:10.1093/petrology/egs011.

Wright, T.L., Okamura, R.T., 1977. Cooling and crystallization of tholeiitic basalt, 1965 Makaopuhi lava lake, Hawaii. Technical Report 1004. Geological Survey Professional Paper.

Yang, S.H., Maier, W.D., Lahaye, Y., O'Brien, H., 2013. Strontium isotope disequilibrium of plagioclase in the Upper Critical Zone of the Bushveld Complex: evidence for mixing of crystal slurries. Contributions to Mineralogy and Petrology 166, 959–974. doi:10.1007/s00410-013-0903-4.

Yoshinobu, A.S., Wolak, J.M., Paterson, S.R., Pignotta, G.S., Anderson, H.S., 2009. Determining relative magma and host rock xenolith rheology during magmatic fabric formation in plutons: Examples from the middle and upper crust. Geosphere 5, 270–285. doi:10.1130/GES00191.1.

Yuan, Q., Namur, O., Fischer, L.A., Roberts, R.J., Lü, X., Charlier, B., 2017. Pulses of plagioclase-laden magmas and the stratigraphic evolution in the Upper Zone of the Bushveld Complex, South Africa. Journal of Petrology 58, 1619–1644. doi:10.1093/petrology/egx067.

Zeh, A., Ovtcharova, M., Wilson, A.H., Schaltegger, U., 2015. The Bushveld Complex was emplaced and cooled in less than one million years - results of zirconology, and geotectonic implications. Earth and Planetary Science Letters 418, 103–114. doi:10.1016/j.epsl.2015.02.035.

Zeh, A., Wilson, A.H., Gudelius, D., Gerdes, A., 2020. Hafnium isotopic composition of the Bushveld Complex requires mantle melt - upper crust mixing: new evidence from zirconology of mafic, felsic and metasedimentary rocks. Journal of Petrology Accepted manuscript, 1–76. doi:10.1093/petrology/egaa004.

Zindler, A., Hart, S., 1986. Chemical geodynamics. Annual Review of Earth and Planetary Sciences 14, 493–571. doi:10.1146/annurev.ea.14.050186.002425.